Radar Design Principles

Signal Processing and the Environment

Fred E. Nathanson
Georgia Tech Research Institute
Rockville, Maryland

with

J. Patrick Reilly
The Johns Hopkins University
Applied Physics Laboratory
Laurel, Maryland

Marvin N. Cohen
Georgia Tech Research Institute
Georgia Institute of Technology
Atlanta, Georgia

Second Edition

SciTECH
PUBLISHING, INC.
MENDHAM, NEW JERSEY

This is a reprinting of the 1991 edition
originally published by McGraw-Hill, Inc.

Printed in the United States of America

10 9 8 7 6 5 4 3 2 1

ISBN 1-891121-09-X

SciTech books may be purchased at quantity discounts for educational, business, or sales promotional use. For information, contact the publisher:

SciTech Publishing, Inc.
89 Dean Road
Mendham, NJ 07945
e-mail: scitech@worldnet.att.net
www.scitechpub.com

IEEE members may order directly from the association.

The Institute of Electrical and Electronics Engineers, Inc.
PO Box 1331, 445 Hoes Lane
Piscataway, NJ 08855-1331 USA
e-mail: customer.service@ieee.org
www.ieee.org
IEEE Order No.: PC5822

Acknowledgments

The dramatic advances in radar systems and especially in radar signal processing are the result of the efforts of many individuals in many fields. To help me assimilate this information, I enlisted the aid of a number of knowledgeable coworkers in the radar field.

The primary credit goes to J. Patrick Reilly of the Johns Hopkins University, Applied Physics Laboratory, for both the original book and this edition. He authored Chap. 9 and significant portions of Chap. 1, 2, 3, 5, 6, and 7. Dr. Marvin Cohen of Georgia Tech Research Institute (GTRI) contributed a new version of Chap. 12 and contributed to the rewrite of Chap. 13.

I thank Dr. Mark Richards (GTRI) who contributed the new section on pulse Doppler signal processor architecture; Mel Belcher (GTRI) for the CFAR section in Chap. 4; A. Corbeil, J. DiDomizio, and R. DiDomizio of Technology Service Corporation, Trumbull, Connecticut for the new material on track before detect in Chap. 4; and Allen Sinsky of Allied-Signal for updating the ambiguity function material in Chap. 8.

I remain indebted to those at the Applied Physics Laboratory who assisted with the first edition, and to my colleagues during 18 years at Technology Service Corporation where much of the new material evolved from various programs and short courses.

I wish to thank Drs. E. K. Reedy, J. L. Eaves, and Jim Wiltse of Georgia Tech Research Institute for their encouragement and support in preparing this edition.

I greatly appreciate the assistance of Janice Letow for typing, assembling, and keeping the manuscript on track.

My final thanks to the patience and understanding of my wife, Lila, who supported me while I underestimated the effort of a new edition. Finally, thanks to my daughter and son-in-law, and to my son who expected me to build him a radar 20 years ago. I still do not know if I will ever get to build him one.

McGraw-Hill Reference Books of Interest

Handbooks

AVALONE AND BAUMEISTER • *Standard Handbook for Mechanical Engineers*
COOMBS • *Basic Electronic Instrument Handbook*
COOMBS • *Printed Circuits Handbook*
CROFT AND SUMMERS • *American Electricians' Handbook*
DI GIACOMO • *Digital Bus Handbook*
DI GIACOMO • *VLSI Handbook*
FINK AND BEATY • *Standard Handbook for Electrical Engineers*
FINK AND CHRISTIANSEN • *Electronics Engineers' Handbook*
HICKS • *Standard Handbook of Engineering Calculations*
INGLIS • *Electronic Communications Handbook*
JOHNSON AND JASIK • *Antenna Engineering Handbook*
JURAN • *Quality Control Handbook*
KAUFMAN AND SEIDMAN • *Handbook for Electronics Engineering Technicians*
KAUFMAN AND SEIDMAN • *Handbook of Electronics Calculations*
KURTZ • *Handbook of Engineering Economics*
SKOLNIK • *Radar Handbook*
STOUT AND KAUFMAN • *Handbook of Microcircuit Design and Application*
STOUT AND KAUFMAN • *Handbook of Operational Amplifier Design*
TUMA • *Engineering Mathematics Handbook*
WILLIAMS • *Designer's Handbook of Integrated Circuits*
WILLIAMS AND TAYLOR • *Electronic Filter Design Handbook*

Dictionaries

Dictionary of Computers
Dictionary of Electrical and Electronic Engineering
Dictionary of Engineering
Dictionary of Scientific and Technical Terms
MARKUS • *Electronics Dictionary*

Other Books

BOITHIAS • *Radiowave Propagation*
GENTILE • *Microwave Amplifiers and Oscillators*
JOHNSON AND JASIK • *Antenna Applications Reference Guide*
MILLIGAN • *Modern Antenna Design*
SKOLNIK • *Introduction to Radar Systems*

ABOUT THE AUTHOR

A specialist in radar search techniques, radar systems, radar signal processing, and electro-optical devices, Fred E. Nathanson has supervised laboratory and prototype search and radar development and served with numerous evaluation and advisory groups. He is currently Principal Research Engineer with Georgia Tech Research Institute in Rockville, Maryland. Mr. Nathanson holds a B.E. in Electrical Engineering from John Hopkins University, and an M.S. from Columbia. A Fellow of the IEEE "for contributions to radar systems" and a member of the Radar Systems Panel, he has published many technical articles and taught intensive short courses worldwide.

Preface

The first version of this book was written in the late 1960s. At that time the relationships between the radar waveform, the carrier frequency, the signal processing, and the environment were understood well enough to project some highly capable systems. The digital age was just beginning, but implementation was still cumbersome and expensive. During the late 1970s and early 1980s a number of sophisticated but highly successful radars were developed using the knowledge of the environment to select the waveforms and taking advantage of the rapid progress in digital technology.

As the 1980s evolved, radar was beginning to be called a mature technology until the Exocet missile, "stealth" targets, sophisticated electronic countersurveillance measures (ECM), drug interdiction requirements, etc., demanded a new look at radar design and technology. This in turn requires further knowledge of the details of target reflectivity, natural clutter and clutter artifacts, and a radar's susceptibility to electronic interference. The potential of remote sensing and space-based radars also requires a better understanding of the environment and signal processing.

Thus the emphasis of this book is on radar design to cope with the "total environment" rather than any single performance goal. The *total environment,* as defined here, includes the unwanted reflections from the sea, land areas, precipitation, and chaff, as well as thermal noise and jamming. It also recognizes that mapping, weather sensing, terrain avoidance, altimetry, etc., may be designed for a single-function radar or as modes of a multifunction radar.

As in the first edition, the book is divided into three parts. The first four chapters contain an introduction to radar; expanded material on the fundamentals of antennas, transmitters, multipath and ducting problems; and a review of the radar equations for the detection of targets in the presence of noise and natural and man-made interference. This is followed by descriptions of the statistics of target detection and the techniques for obtaining automatic detection with considerable new material on advanced constant false alarm techniques and track-before-detect.

Chapter 5 contains a mostly new and thorough survey and analysis of the available material on the reflectivity of both natural and man-made targets. It includes the spectral, polarization, and wavelength properties since they all have been shown to have a substantial effect on the choice of processing technique. Chapter 6 contains greatly expanded material on propagation and the reflectivity from precipitation and chaff. This includes statistics on their occurrence, carrier-frequency selection, and frequency-agility effects, wind shear phenomena, the bright band, anomalous echoes, etc. with statistical descriptors to evaluate signal-processing techniques. Chapter 7 follows in the same format to describe sea and land clutter with new models, and statistical descriptions that must be included when analyzing high-resolution radar detection of low-flying targets. Reflectivity is related to carrier frequency, polarization, and ducting effects. Bistatic data are included.

Chapters 8 through 13 contain descriptions of the various signal-processing techniques that are widely used or proposed for future radar systems. After a general discussion of processing concepts, specific techniques are discussed for the detection of moving targets by use of the Doppler effect (CW, MTI, pulse Doppler), FFTs, and fast convolvers and the pulse compression techniques (phase-coding, frequency-coding, and linear FM). In most of these signal-processing chapters there is a discussion of the theory of operation, and diagrams of typical processors with emphasis on the new digital implementations and the limitations and losses. The equations for performance evaluation, along with advantages and disadvantages of each technique, are generally included.

Chapter 14 describes some newer or more specialized techniques such as the moving target detector (MTD) and clutter maps; ground, airborne, and space-based meteorological radars often using pulse-pair processors; and surveillance radars on aerostats. The final section contains a description on how to analyze or simulate coherent radars including the limitations and related loss terms.

It is not suggested that there is an optimum radar or even a generally optimum waveform, but that in the impending era of adaptive radar, the radar will sense the environment and adapt to this information.

While not specifically written as a textbook, the earlier edition was used for a number of graduate courses on radar and in many intensive short courses. An attempt has been made to better organize the material, while retaining the chapter structure for those familiar with the first edition. Supplementary material and further derivations are available in the 800 references.

Fred E. Nathanson

Contents

Chapter

2

Review of Radar Range Performance Computations

F. E. Nathanson

J. P. Reilly

This chapter reviews the basic forms of the radar equation and the variations needed to calculate the performance of a radar that is attempting to detect targets masked by the basic thermal noise of the radar receiver. Subsequently this development is extended to cover a general environment, which includes the multitude of superfluous returns that often exceed the basic receiver noise. These returns include electronic countermeasures, friendly interference, sky noise, and the backscatter from atmospheric effects, land, seas, and chaff.

2.1 General Radar Range Equation

The following general radar equation for pulse radars shown includes a larger number of parameters than is commonly used in current radar texts by Barton [39], Blake [75], and Skolnik [671]. The separation of certain loss terms from the basic parameters facilitates rewriting the equations for the various external environments. The loss terms in this book are less than unity or are subtracted from the numerator when

the equation is expressed in decibel form. The backscattered power received from a target of radar cross section σ_t at the first mixer or preamplifier can be written

$$\hat{P}_r = \frac{\hat{P}_T G_T L_T G_R L_R \lambda^2 L_P L_S L_L L_a \sigma_t}{(4\pi)^3 R^4} \tag{2.1}$$

where $\hat{P}_r$ is peak received power.

Before elaborating on the terms of this equation, it is useful to convert the received power $\hat{P}_r$ to the minimum detectable received power $S_{\min}$ and to rewrite the equation in terms of the detection range R for a pulse radar. Then

$$R^4 = \frac{\hat{P}_T G_T L_T G_R L_R \lambda^2 L_P L_S L_L L_a \sigma_t}{(4\pi)^3 S_{\min}} \tag{2.2}$$

where R = the detection range of the desired target with the statistics of detection to be defined later.

$\hat{P}_T$ = the peak transmit power (the average power during the pulse) at what is arbitrarily defined as the output of the transmitter unit.

G_T = the transmit power gain of the antenna with respect to an omnidirectional radiator. This is a dimensionless quantity equal to $4\pi A_e/\lambda^2$. This term generally refers to the centerline of the antenna beam. The pattern factor F_1^2 is included in L_p in this book.

A_e = the effective aperture of the antenna, which is equal to the projected area in the direction of the target times the efficiency. This includes the fractional losses due to spill over and tapering of the aperture to reduce the sidelobes. Then considering the losses, $A_e = \epsilon A$ where A is the physical projection of the antenna area and $\epsilon \approx 0.4$ to 0.8. A_e can also be defined as the area that, when multiplied by the power density at the receive aperture, equals the received power.

λ = the wavelength of the radiation.

L_T = the losses between the transmitter output and free space including transmit/receive duplexers, power dividers, waveguide or coax, radomes, and any other losses not included in A_e. It is preferred to include in this term any losses that do not affect the beamwidth of the radar. L_T is less than unity, or negative in decibel terms.

G_R = the receive power gain of the radar defined in a manner similar to the transmit gain.

L_R = the receive antenna losses defined in a manner similar to the transmit losses. However, in the case of sensitive receivers, the losses must be included in the effective system noise temperature T_s. These are defined in conjunction with the minimum detectable signal.

L_P = the beam shape and scanning and pattern factor losses,* which include several factors to compensate for the antenna-gain terms being calculated on the centerline or *nose* of the beam. A typical target for a search radar tends to have an arbitrary position with respect to this line, and the ground and sea reflections create a lobing pattern resulting from the relative phase of the free space and reflected signals. An analogous loss occurs in conical scan tracking radars where the beam is *nutated,* or scanned such that the full gain of the antenna is not continuously pointed at the target. A typical value for search radars is 1.6 dB for each dimension of scan and for 50-percent detection probability. Similar losses caused by finite range gates and Doppler filters are covered in the chapters on processing techniques.

The pattern factors caused by forward scatter are quite complex, as described in Sec. 1.12. They are dependent on the grazing angle with respect to the land or sea and the height of terrain objects (trees, hills, buildings) or ocean waves at the point of reflection. Chapter 7 on sea clutter effects gives additional experimental data for rough sea conditions and some of the basic properties of the reflected signal. There is further discussion of lobing effects as they affect detection of targets near the horizon in Secs. 1.7, 5.6, and 7.8.

The description of beam shape losses is slightly expanded in the section on detection statistics. A more thorough treatment is found in Barton [39] and Blake [74].

L_a = the two-way pattern absorption or propagation losses of the medium. These are calculated separately since they are usually a function of the target range, the elevation of the target, and the type of interference. It is a common practice to compute the free-space range and then adjust for these losses, as in Fig. 2.1, rather than complicate the radar equation. L_a is often expressed as $\exp(-2\alpha R)$, where α is the attenuation constant of the medium and the factor 2 is for a two-way path.

* Including F of Blake's notation. See Barton [39], Blake [74], and Skolnik [673].

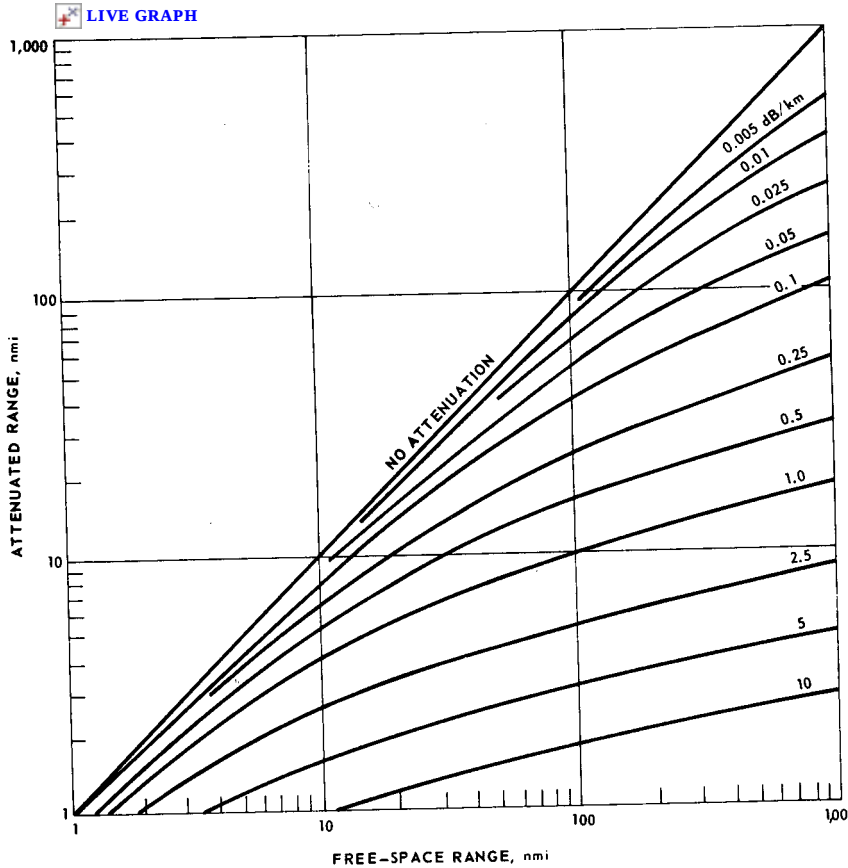

Figure 2.1 Free-space radar range versus attenuated radar range for one-way attenuation rates of α dB/km. (*From Skolnik* [*671*])

L_S = signal-processing losses that occur for virtually every waveform and implementation. The typical values are discussed with the processors in Chaps. 9 through 14.

L_L = lens-effect loss for radars located near the earth's surface. The atmosphere acts as a lens, and the beam divergence in the vertical plane reduces the power density on a target near the horizon. Schrader and Weil [760] show loss curves for surface radars amounting to 0.9 dB at 200 nmi for a 0° elevation beam and about 0.5 dB for a 1.5° elevation. At 400 nmi these are almost doubled. The losses are halved for distributed atmospheric target (rain and chaff). This loss may be pessimistic for pencil-beam phased arrays or radars with "stacked" beams in elevation as it slightly reduces the pattern loss (L_P in elevation). This loss is dropped from later versions of the radar equation and

should probably be folded into L_P or the pattern factors F_1 F_2 used in other texts.

σ_t = the radar cross-sectional area of the object that is being detected and is equal to

$$\sigma_t = \frac{\left(\begin{array}{c}\text{power reflected toward the receiving} \\ \text{aperture/unit solid angle}\end{array}\right)}{(\text{incident power density}/4\pi)}$$

The definition has a simple physical significance only for the case of a large metallic sphere, in which the physical cross section is equal to the radar cross section (when the diameter is large with respect to the radar wavelength). (See Chap. 5.) The use of the term *cross section* is expanded to include the amplitude and spectral distributions of the reflectivity in the chapter on targets. The radar return from land or cultural features appears as the target for an airborne mapping radar but often forms the *noise* level for an Airborne Early-Warning System (AEW) or surface-surveillance radar.

$S_{\min}$ = the minimum detectable target-signal power that, with a given probability of success, the radar can be said to *detect, acquire,* or *track* in the presence of its own thermal noise or some external interference. Since all these factors (including the target return itself) are generally noiselike, the criterion for a detection can be described only by some form of probability distribution with an associated probability of detection P_D and a probability that, in the absence of a target signal, one or more noise or interference samples will be mistaken for the target of interest. This latter probability is often called the false alarm probability P_F or P_N. The related term of false alarm time T_F or n' is elaborated on in the next chapter. The use of this terminology implies a threshold detector, which is established with respect to the noise level.

The most definitive treatments of the statistical problem of target detection by a pulse radar are the works of Marcum and Swerling presented from 1947 through 1954 and republished by the IRE [461]. Numerous graphs have been presented in the technical journals with slight variations; the most appropriate ones are presented in Chap. 3. Figure 2.2 gives the signal-to-noise ratio to achieve a given probability of detection of a target signal in a single look. The false alarm number n' is the parameter. The solid lines apply when the target echo is a

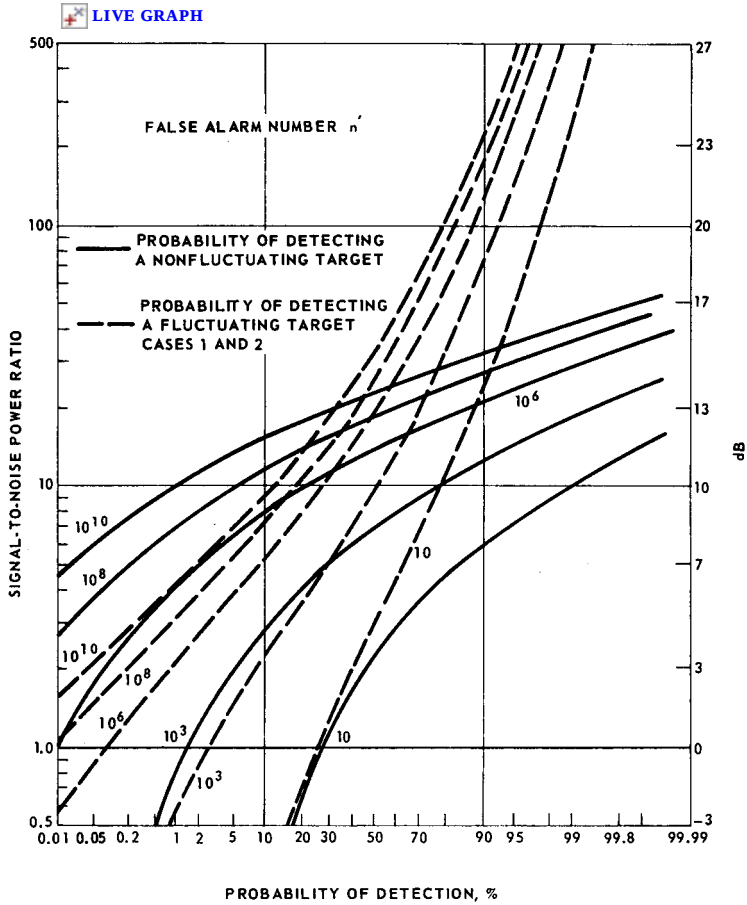

Figure 2.2 Signal-to-noise ratio versus probability of detection in a single look. (*After Fehlner [225] and Marcum and Swerling [461]*)

constant sinusoid and the noise is gaussian; the dashed lines apply when the target echo is fluctuating. These curves are for single-pulse detection. Multipulse detection curves with a more detailed explanation are given in Chap. 3.

The classic radar equation is based on the assumption that the thermal noise of the receiver is the fundamental limitation on minimum detectable target signal. As more sensitive receivers have been developed, the effects of antenna noise and sky noise and the effects of the sun, galaxies, and the earth must be included, Blake [74]. Since this text emphasizes signal processing, it suffices to define the thermal noise power of the receiver as

$$N = KT_sB_N \tag{2.3}$$

where K = Boltzmann's constant [equal to 1.38×10^{-23} W/(Hz)(°K)].

T_s = system noise temperature, including the antenna temperature, environmental effects, and the noise of the receiver itself. It should be remembered that the effective temperature T_e of the receiver noise itself is not simply equated to the noise factor (or noise figure) $\bar{F}$ by $T_0\bar{F}$. T_e can usually be replaced by $T_0(\bar{F} - 1)$, where T_0 is the reference temperature of the system and is assumed to be 290°K. It is also assumed that the receiver *does not* respond to the noise at the image frequency of a heterodyne receiver.* Then

$$T_e = (\bar{F} - 1)290°\text{K} \quad \text{or} \quad T_s \doteq T_e + T_A$$

where T_A is the antenna noise temperature with appropriate consideration for losses between the antenna and receiver.† (See [63, 45, 75].) If T_A is small compared to T_e, the term T_0 is sometimes combined with K and then expressed in decibels.

$$KT_0 = -204 \text{ dBW/Hz}$$
$$KT_s = -204 \text{ dBW/Hz} + 10 \log(\bar{F} - 1)$$

The noise figure of typical solid-state microwave receivers is shown in Fig. 2.3. Various GaAs FET and *high electron mobility transistors* (HEMT) are represented.

B_N = noise bandwidth of the receiver in hertz after amplification but before envelope detection. The actual noise bandwidth varies with the transfer function of the filter or set of filters prior to detection and with the type of waveform. For a simple radar transmitting a rectangular pulse, the *optimum* B_N is the bandwidth of the matched filter that is described in Sec. 8.1. In practice the matched filter is not frequently implemented since the filter skirts (or sidelobes) do not fall off rapidly and the receiver becomes more susceptible to jamming or interference. In the same vein, transmit pulses are trapezoidal rather than rectangular to minimize the spectral interference to other receivers. In the United States there are requirements on the maximum transmitted signals allowed at frequencies away from the carrier.

---

* See "Description of Noise Performance of Amplifiers and Receiving Systems," *Proc. IEEE*, vol. 51, no. 3, pp. 436–442, 1963.

† In this equation T_A is often written as T_A/L_R.

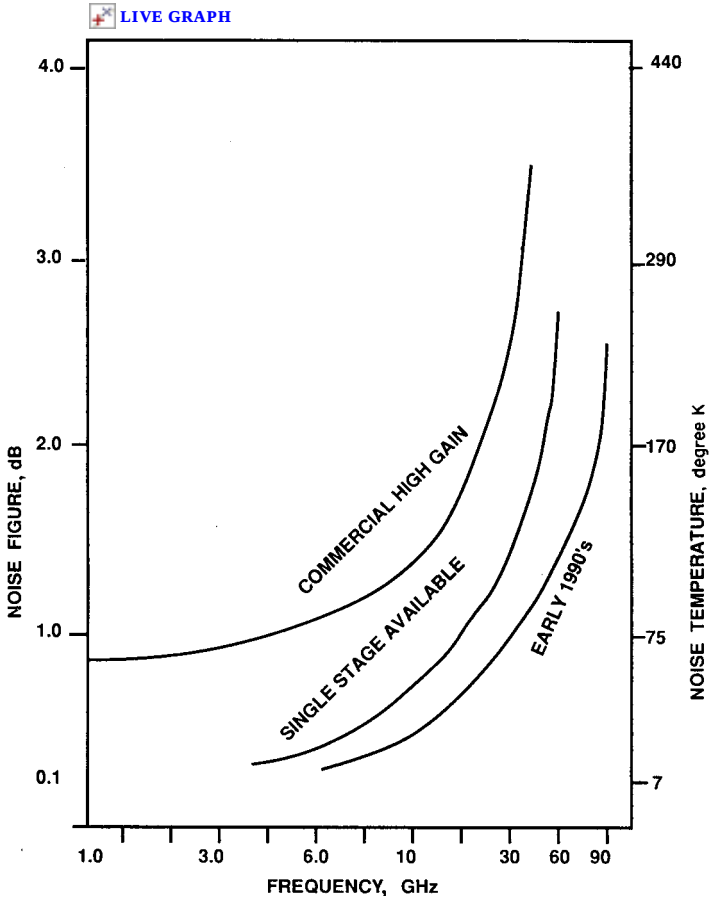

Figure 2.3 Solid-state uncooled low-noise receivers from various manufactures. Various G_aA_s FET and HEMT (high electron mobility transistors) technologies are represented.

Many filter responses are utilized for nearly rectangular pulses. There is optimization to minimize loss in detectability in noise and also the minimization of clutter responses. While performance in clutter is discussed later in the chapter, Fig. 2.4 illustrates the double tradeoff. The ordinate is the normalized clutter output of the receiver or the effective pulse duration τ' in a distributed-clutter environment. This is a quantity that should be minimized. The abscissa is the 3-dB bandwidth times the duration of the rectangular pulse, which is denoted by τ throughout this book. The curve labeled sin x/x is the matched filter where the effective pulse duration is 0.667τ. Note that the only other comparable filter in clutter is the rectangular bandpass. The optimum bandwidth for minimum loss in noise (~0.6 dB) is for the double tuned filter if the $B\tau = 0.6$, but the clutter response is quite poor for this

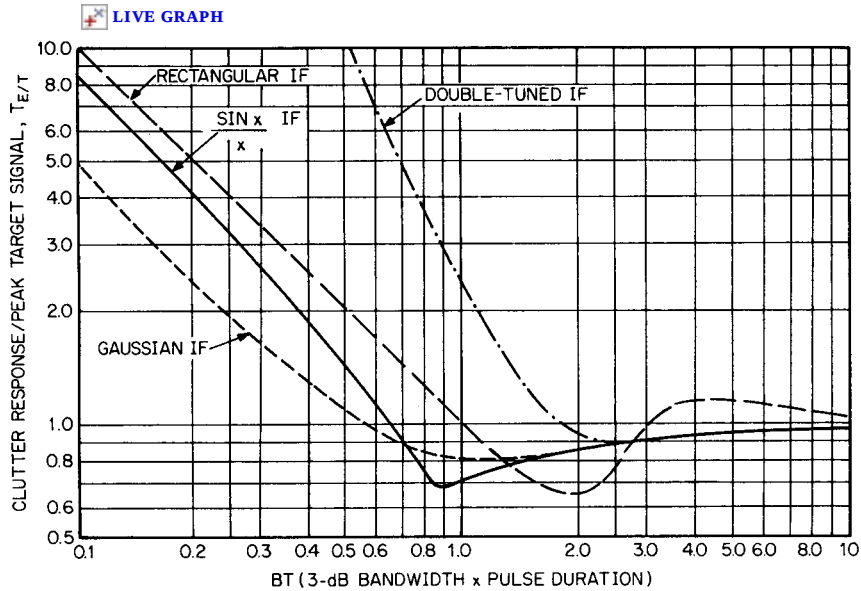

Figure 2.4 Equivalent pulse length for rectangular pulse and various if bandwidth filters. (*Courtesy L. W. Brooks*)

bandwidth. For the rectangular band-pass filter, the optimum $B\tau \approx 1.3$ for noise and the loss is 0.8 to 0.9 dB. This is also near optimum for clutter. The use of trapezoidal pulses alters these values slightly. Also, the noise bandwidth B_N is somewhat greater than the 3-dB bandwidth B. In most computations B_N is assumed to be $1/\tau$ unless more exact calculations are necessary. In clutter calculations, τ' should be used for more accuracy. A physical way of observing Fig. 2.4 is that a narrow filter smears the clutter in range while an overly wide filter has little effect.

In practice, receiver filters are generally slightly wider than optimum to allow for target Doppler and slight mistuning of the transmitter or local oscillator. The matched-filter loss can be entered into the radar equation in L_S or by increasing B_N.

With the preceding assumptions, the minimum detectable signal can be written

$$S_{\min} = KT_s B_N (S/N) \left(\frac{1}{L_c}\right) \tag{2.4}$$

where (S/N) = a dimensionless parameter that is the acceptable value by which the desired signal exceeds the rms noise level with respect to the function of the overall radar system.*

* In detection equations (S/N) is usually the required signal-to-noise ratio or visibility factor, and in this text S/N represents the actual power ratio for the stated conditions.

L_c = collapsing loss, which results when two or more samples of unwanted noise, interference, or clutter are added to the desired signal. Several examples occur when the bandwidth of the receiver is excessive compared to the *matched-filter bandwidth,* when numerous elevation beams are "collapsed" onto a conventional *plan position indicator* (PPI) display, or when numerous azimuth positions are "collapsed" onto a *range height indicator* (RHI).

This term is expanded to include the undesired backscatter from clouds, rain, or electronic counter-measures, which occur in several radar beams. A special, but not uncommon, case is when there is no interference in the beam in which the target is located, but interference may be present only in the *collapsed* beam positions.

The radar return from a low flying aircraft may be obscured on a PPI by rain clouds at 10,000-ft altitude, even though there is no rain at the target location.

The collapsing ratio ρ, another common term, is defined as

$$\rho = \frac{m + n}{n}$$

where m is the number of samples containing noise alone and n is the number of samples containing signal plus noise. The collapsing loss (in dB) can then be found from the curves on integration loss for n samples integrated incoherently (Chap. 3). The loss L_c is determined for $n + m$ samples (in dB) and then subtracted from the loss (in dB) for n samples.

Similar collapsing losses for PPI displays, as taken from Barton [45], are based on

$$\rho = \frac{1/\tau + 2B_v}{2B_v}$$

for insufficient video bandwidth where B_v is the video bandwidth (Hz). In the foregoing cases the increase in the total number of noise samples presented to the detector or operator must be taken into account when evaluating the statistics of the detection process. This type of calculation is expanded on in Chap. 3. The collapsing loss L_c is expressed here as a fraction less

than unity or in decibel form where this loss should be subtracted from the numerator of the radar equations.

Before discussing what constitutes an acceptable value of (S/N) it is useful to write the full radar equation and some of its variations. The *pulse radar equation* is

$$R^4 = \frac{\hat{P}_T G_T L_T G_R L_R \lambda^2 L_P L_a L_c L_s \sigma_t}{(4\pi)^3 K T_s B_N (S/N)} \tag{2.5}$$

for the receiver (and antenna) noise limited case, and where L_s is the signal processing loss, which will be loosely defined as the deviation from a linear receiver with a perfectly matched filter. The numerical value to be used is expanded on in Chap. 4 on automatic and adaptive detection and in the various signal processing chapters. This loss varies in the presence of clutter and jamming because of the change in the power spectrum and amplitude distribution of the interference.

Since the noise bandwidth B_N is approximately equal to $1/\tau$ for a system approximating a matched filter, a more descriptive presentation of the detection properties of a radar system is to replace

$$\frac{\hat{P}_T}{B_N} \quad \text{with} \quad \hat{P}_T \tau = E$$

where E is the transmitted energy per pulse in joules. This substitution illustrates that the detection properties of a particular radar (for target obscured by receiver noise) are dependent only on the transmitted energy and the noise per Hz (KT_s). It can be shown that the relationship is essentially independent of the pulse length or transmitted waveform. This substitution also allows simpler extension to the CW (continuous wave), FM, and pulse Doppler radars, where it can be shown that the average power determines the detection performance if the receiver can be made to approach the *matched* filter.

The radar equation expressed in the foregoing form is somewhat misleading in that it implies a λ^2 dependence on detection range by using the gain of the antenna as a parameter. In a search radar, higher gain with the resulting narrower beamwidth means that less time or energy or fewer pulses can be radiated in any one direction if it is necessary to search a volume that is large compared to the cross-sectional area of any one beam. Another common form of the radar equation substitutes $4\pi A_e/\lambda^2$ for G_R and results in the *preferred search radar equation*

$$R^4 = \frac{\hat{P}_T G_T L_T A_e L_R L_P L_a L_c L_s \sigma_t}{(4\pi)^2 K T_s B_N (S/N)} \tag{2.6}$$

which has no wavelength dependence.

Hall [302] has shown (with different notation) that to search a solid angle Ψ with a given observation time for a single beam T, the minimum total search time (T_{sc}) is

$$T_{sc} = T\frac{\Psi}{\Omega}$$

where Ω = the solid angle of the radar beam
Ψ = the total solid angle to be searched
T_{sc} = time allowed in seconds to search a total solid angle Ψ

The solid angle of the radar beam, however, can be expressed as $\Omega = 4\pi/G_T$. The average power $\overline{P}_T$ is equal to $\hat{P}_T\tau/T$ for a pulse radar, and $B_N\tau \approx 1$ from Eq. (2.4). Then substituting for B_N in Eq. (2.6) gives the *volume search-radar equation*

$$R^4 = \frac{\overline{P}_T L_T A_e L_R L_P L_a L_c L_s \sigma_t T_{sc}}{4\pi K T_s (S/N)\Psi} \tag{2.7}$$

In a similar manner the transmit gain G_T can be converted to aperture area. This form also has misleading effects in countermeasures and in clutter-limited situations but applies where there is a firm constraint on antenna size. For a common transmit-and-receive antenna, Eq. (2.6) becomes the *antenna size limited equation*

$$R^4 = \frac{\hat{P}_T L_T A_e^2 L_R L_P L_a L_c L_s \sigma_t}{4\pi\lambda^2 K T_s B_N (S/N)} \tag{2.8}$$

This form with the inverse λ^2 dependence is useful for aircraft, satellite, and missile radar computations where transmit frequencies of over 10,000 MHz are common. The greater detection range implied for higher-frequency radars is often negated by increased atmospheric and weather attenuation and a tendency of receiver noise temperatures to increase with frequency. In addition, the number of beam positions to search a given volume increases, and time may become a major constraint.

2.2 Radar Detection with Noise Jamming or Interference

It is convenient at this point to introduce the detection equations for noise jamming or interference as they follow the basic radar equation in form and do not require the introduction of statistical distributions other than wideband gaussian noise. The simplest geometry to consider

is where the target is carrying a relatively high-power noise source to attempt to deny knowledge of the target's location to a search radar or to prevent a tracking radar from *acquiring* the target.*

The noise power radiated from a broadband jammer (barrage jammer) has a power density at the search radar of

$$\text{Power density at radar} = \frac{\bar{P}_J G_J}{4\pi R_J^2} \text{ W/unit area} \tag{2.9}$$

where $\bar{P}_J$ = the average power of jammer at its antenna input
G_J = gain of jammer antenna, including losses
R_J = range from jammer to radar

$\bar{P}_J G_J$ is commonly called effective radiated power (ERP). The power entering the radar and added to the receiver noise is dependent on the aperture area of the radar and the relative bandwidth of the jammer B_J and the radar receiver B_N. It is convenient to assume that $B_J \geq B_N$ (otherwise the jammer would be a *spot jammer* and the radar system response would become intimately involved with the type of signal processing). At the receiver input the total noise power is

$$N = KT_s B_N + \frac{\bar{P}_J G_J B_N A_e L_R L_a'}{4\pi R_J^2 B_J} \tag{2.10}$$

where L_a' is the one-way propagation loss. This term can replace $KT_s B_N$ in the previous radar equations, but it is more common to replace $\bar{P}_J/B_J$ by the jammer power per unit bandwidth.†

If the barrage jammer is to have any effect on the radar it must be large enough to make

$$\frac{\bar{P}_J G_J A_e L_R L_a'}{4\pi R_J^2 B_J} > KT_s$$

that is, the jamming noise density must be greater than the system noise density. With this simplification the radar equation can be written for the jammer at the target range and angle as the *self-screening range equation*

$$R_{SS}^2 = \frac{\hat{P}_T G_T L_T L_P' L_a' L_c' L_s'}{4\pi B_N (S/J)} \left(\frac{\sigma_t}{P_J G_J} \right) \tag{2.11}$$

* For general references see Waddell [738], Schlesinger [637].

† Despite the confusion of units, $\bar{P}_J/B_J$ is often called P_J and is usually expressed in W/MHz if B_N and B_J are in MHz. It is also assumed in all discussions that the total jamming noise does not saturate the receiver.

where R_{SS} = *self-screening* range of the radar, or the range at which a target of cross section σ_t can be detected in jamming noise
L'_P = one-way scanning and pattern losses of the radar since the jamming signal also has similar losses
L'_a = one-way atmospheric or weather losses from radar to target
(S/J) = signal-to-jam ratio, which is defined in a manner analogous to (S/N)
L'_c = collapsing losses only in the receiver itself since the jammer is assumed to occupy only one beam
L'_s = signal-processing losses applicable to jamming (includes image losses, etc.)
P_J = jammer power density (W/MHz if B_N in MHz)

In operational analysis it has been found convenient to express the self-screening equation as

$$R_{SS} = \alpha \left(\frac{\sigma_t}{P_J G_J}\right)^{1/2} (L'_a)^{1/2}$$

where $(P_J G_J/\sigma_t)$ is expressed in W/(MHz)(m^2) and the remaining terms form α if B_N is expressed in MHz. The term α is then the range on a 1-m^2 target radiating 1 W/MHz.

$$\alpha = \left(\frac{\hat{P}_T G_T L_T L'_P L'_c L'_s}{4\pi B_N (S/J)}\right)^{1/2} \tag{2.11a}$$

If the jammer is attempting to screen another target (stand-off jammer) at another range the equation is rewritten and sometimes called the "burn-through" range equation. Neglecting atmospheric losses, the *stand-off jammer equation* is

$$R_{BT} = (\alpha R_J)^{1/2} \left(\frac{\sigma_t}{P_J G_J}\right)^{1/4} \tag{2.12}$$

where R_{BT} is the detection range of the target that is not carrying the jammer. If the jammer is in the radar antenna receive sidelobes, as is the common case for a stand-off jammer, the range equation is written

$$R_{BT} = (\alpha R_J)^{1/2} \left(\frac{\sigma_t}{P_J G_J}\right)^{1/4} \left(\frac{G_R}{G'}\right)^{1/4} \tag{2.13}$$

where (G_R/G') is the ratio of the antenna gain in the direction of the target to the antenna gain in the direction of the jammer.

It can also be shown that the fractional range with barrage jamming is

$$\left(\frac{R_{BT}}{R}\right)^4 = \frac{4\pi K T_s R_J^2}{P_J G_J A_e L_R L_a' + 4\pi K T_s R_J^2} \tag{2.14}$$

or

$$\left(\frac{R_{BT}}{R}\right)^4 = \frac{(4\pi)^2 K T_s R_J^2}{\lambda^2 P_J G_J G_R L_R + (4\pi)^2 K T_s R_J^2} \tag{2.15}$$

If the jammer is in the radar sidelobes, $P_J G_J$ is reduced by the appropriate sidelobe ratio.

It is also useful to derive the volume search radar equation for the self-screening jammer environment in the same manner as Eq. (2.8). If a solid angle Ψ is believed to contain a jamming target and the search time is defined as T_{sc}, it is convenient to assume that

$$T_{sc} = \frac{\hat{P}\tau\Psi}{\bar{P}\Omega} \qquad \Omega = \frac{4\pi}{G_T} \qquad \tau \approx \frac{1}{B_N}$$

Substituting for G_T in Eq. (2.11), the equation for the detection range of a jamming target located within a solid angle Ψ becomes the *volume search equation in jamming*

$$R_{SS}^2 = \frac{\bar{P}_T L_T L_P' L_a' L_c' L_s' T_{sc}}{\Psi(S/J)} \left(\frac{\sigma_t}{\bar{P}_J G_J}\right)$$

where $\bar{P}_J$ is the jammer power density in W/Hz.

It should be noted that this equation is *independent of both transmit frequency and antenna size* with the assumption that the jammer has a constant power density.

A sample calculation for a typical S-band surveillance radar against a moderately powerful jammer is

$$R_{SS}^2 = \frac{\hat{P}_T G_T B_j \sigma_t}{4\pi P_j G_j B_N (S/J)_{\text{req}}}$$

where $\hat{P}_T = 10^6$ W
$\lambda = 0.1$ m
$P_j = 10^3$ W
$B_j = 500$ MHz
$G_T = 1.78 \times 10^4$
$\sigma_t = 1$ m^2
$B_N = 10^6$ Hz

$$G_j = 10$$
$$(S/J)_{\text{req}} = 10$$

The self-screening range R_{SS} is 2.68 km.

2.3 Beacon and Repeater Equations

The radar echoes from targets are often augmented as for tracking satellites, for air traffic control, and for identification purposes. These augmentors may be passive reflectors, beacon transponders, or repeaters.

The common passive reflectors include Luneburg lenses with partial metallic coatings, corner reflectors, and sometimes directive antennas with appropriate termination. The beacon transponder generates a return signal on the appropriate frequency when it receives an adequate illumination signal from the radar. Since only one-way transmission losses need be considered if the beacon power is high enough to be detected by the radar, the simple *radar beacon illumination* equation is

$$R_B^2 = \frac{\hat{P}_T G_T L_T A_B L_a' L_P'}{4\pi S_B} \tag{2.16}$$

where R_B = radar-to-beacon detection range
A_B = receive aperture area of the beacon antenna including losses
L_a' = one-way atmospheric loss
L_P' = antenna pattern losses one way
S_B = minimum detectable signal to beacon

The return signal from the beacon can be calculated by inserting the appropriate parameters in the same equation.

A more complicated equation is needed for the case of the repeater, which amplifies the radar signals and retransmits them to the radar. These repeaters may be used for enhancing the signal at the radar or may be used by an enemy as a jamming technique. Two calculations must be made to cover the two cases when

1. The maximum power output of the repeater is insufficient to be detected by the radar.
2. The noise level of the repeater itself is sufficiently high compared to the signal it receives from the radar [Eq. (2.16)] that the noise output of the repeater is essentially jamming the radar.

If neither of these limitations is reached, the search-radar equation [Eq. (2.6)] can be written

$$R^4 = \frac{\hat{P}_T G_T L_T A_e L_R L_P L_a L_c L_s A_B G_B G_E}{(4\pi)^2 K T_s B_N (S/N)} \tag{2.17}$$

if $P_{RB}G_E \leq \hat{P}_{\max}$ of the repeater and $P_{RB}/S_B >> S/N$ in the appropriate bandwidth, which depends on the type of processing and

where G_B = retransmit gain including losses of the beacon or repeater antenna *
G_E = electronic gain of the repeater including losses
P_{RB} = receive power at the beacon calculated by solving Eq. (2.16) with P_{RB} substituted for S_B
$\hat{P}_{\max}$ = maximum peak power output of the repeater transmitter

The detection range for the power-output-limited case of the repeater can be obtained by using the one-way equation [Eq. (2.16)] and by substituting $\hat{P}_{\max}$ for $\hat{P}_T$, G_B for $G_T L_T$, and $S_{\min}$ (for the radar) for S_B.

The equations for the repeater-noise-limited case can be solved from the appropriate jamming equations by replacing $KT_sG_EG_B$ with P_JG_J with selection of the proper receiver bandwidth and by replacing σ_t in the same manner as was used in obtaining Eq. (2.17).

2.4 Bistatic Radar

While the majority of this text relates mainly to monostatic radars (common location of transmit and receive antennas), it has become increasingly important to study the performance of bistatic radars where there is considerable separation of transmit and receive antennas. The advent of the *antiradiation missile* (ARM) is making it desirable to separate the transmitter from the remainder of the system by placing it on an aircraft or satellite. The other, and most common, application of this technique is the semiactive *homing* missile system in which the transmitter and its antenna are located on the ground or in an airplane and the receiver or *seeker* is located in a missile. This generally allows a larger transmitter and transmit antenna to be used while keeping the size and weight of the receiver system to a minimum. The basic radar detection range for this case is obtained from Eq. (2.5) of Sec. 2.1 and is the *bistatic range equation*

$$(R_T R_R)^2 = \frac{\hat{P}_T G_T L_T G_R L_R \lambda^2 L_P L_{aT} L_{aR} L_c \sigma_{tb}}{(4\pi)^3 K T_s B_N S/N} \tag{2.18}$$

* The total gain for small signals is G_BG_E.

where $(R_T R_R)$ = *range product* of the system
R_T = range from the transmitter to the target
R_R = range from the target to the receiver
L_{aT} = propagation loss from the transmitter to the target
L_{aR} = propagation loss from the target to the receiver
σ_{tb} = the bistatic radar cross section of the target

The range computation is quite similar to that for the monostatic radar with the exception of the propagation loss terms and the target cross-section definition. Since in general the propagation paths are not the same and since the receiver may be at high altitude, both the atmospheric and the propagation losses are considerably reduced. The bistatic cross section is defined in a similar manner to the monostatic cross section. They usually have a comparable *average* value with respect to all aspect angles of the target if the bistatic angle* is small with respect to 180° and the wavelength is small compared with the dimensions of the target. For a discussion of bistatic cross sections of targets and the unique case of forward scatter (where the bistatic angle $\approx$ 180°) see Willis [778] and Chaps. 1 and 5.

When a self-screening jammer is used, the self-screening range is independent of R_R if proper adjustment is made for the gain of the jammer in the direction of the receiver. Then from Eq. (2.11)† the *bistatic self-screening range* is

$$R_{SS}^2 = R_T^2 = \frac{\hat{P}_T G_T L_T L'_P L'_c L_{aT}}{4\pi B_N (S/J)} \left(\frac{\sigma_{tb}}{P_J G'_J}\right) \tag{2.19}$$

where G'_J is the jammer gain in the direction of the receiver. If the jammer is at a different location than the target, the burn-through range can be written as the *bistatic burn-through range*

$$R_{BT}^2 = \left(\frac{\hat{P}_T G_T L_T L'_P L'_c}{4\pi B_N (S/J)}\right) \left(\frac{\sigma_{tb}}{P_J G_J}\right) \left(\frac{L_{aT}}{L_{JR}}\right) \left(\frac{R_{JR}}{R_{TR}}\right)^2 \tag{2.20}$$

where R_{BT} = radar transmitter to target range at which the target will be detected with the probabilities associated with (S/J) neglecting receiver noise
L_{JR} = fractional propagation loss between the jammer and the receiver
R_{JR} = range between the jammer and the receiver
R_{TR} = range between the target and the receiver

* The angle between the transmitter and receiver as seen from the target.

† Jamming-noise power density is assumed to be $\gg KT_s$.

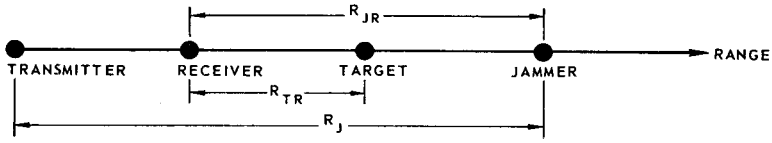

Figure 2.5 Stand-off jammer diagram.

Substituting α^2 for the first bracket per Eq. (2.11a)

$$R_{BT} = \alpha\left(\frac{\sigma_{tb}}{P_J G_J}\right)^{1/2}\left(\frac{L_{aT}}{L_{JR}}\right)^{1/2}\left(\frac{R_{JR}}{R_{TR}}\right) \tag{2.21}$$

In many cases the ratio R_{JR}/R_{TR} is not known, but it can often be assumed that the four locations are in a straight line as shown in Fig. 2.5.

In this case

$$R_{BT} = \frac{\alpha(R_{TR} + R_J)(L_{aT}/L_{JR})^{1/2}}{\alpha(L_{aT}/L_{JR})^{1/2} + R_{TR}(P_J G_J/\sigma_{tb})^{1/2}} \tag{2.22}$$

where R_J is the range from transmitter to jammer.

In many cases the factor L_{aT}/L_{JR} can be assumed to be unity because of the short ranges involved and their tendency to cancel each other for typical geometries.

Again it must be emphasized that if $P_J G_J/\sigma_{tb}$ is expressed in the conventional W/(MHz)(m^2) the term α should be calculated with B_N in MHz.

2.5 Radar Detection Equations in Distributed Clutter (Volume Reflectors) for Pulse Radars

If a radar target is situated in a region of space that contains a large number of undesired radar scatterers, such as raindrops, snowflakes, or chaff dipoles, the summation of the reflected radar signals from these objects may well determine the minimum detectable target signal of the radar. Signals reflected from these scatterers form part of the *environmental noise* and are commonly called radar *clutter*. These objects, however, may be the targets of interest, as, for example, in a weather radar. This section defines the equations that can be used to determine the received power from clutter and the range at which a target will be detected in the presence of clutter signals. Chapter 6 contains the scattering coefficients and other statistics that are required to solve the radar detection equations and describe the spectra of the clutter.

The power density that is incident on a volume of scatterers at a range R (see Fig. 1.2) is

$$P_\alpha = \frac{\hat{P}_T G_T |f(\theta, \phi)|^2 L_T L_a'}{4\pi R^2} \tag{2.23}$$

where P_α = power density at the clutter cell

$G_T|f(\theta, \phi)|^2$ = transmit gain of the antenna with respect to an omnidirectional radiator including the effects of the decreases* in gain at angles θ and ϕ from the beam centerline, where

$$G_T = 4\pi \frac{A_e}{\lambda^2}$$

L_a' = the one-way attenuation loss in the transmission medium

Then, the reflected power from an elemental volume of scatterers in the far zone of the radar aperture is

$$\frac{\hat{P}_T G_T |f(\theta, \phi)|^2 L_T L_a' \Sigma\sigma dV}{4\pi R^2}$$

where $\Sigma\sigma$ is the backscattering cross-section coefficient per unit volume (preferably in m^2/m^3) assuming that the scatterers fill the volume dV. The symbol η is often used interchangeably with $\Sigma\sigma$, but often with different units.

Similarly, the echo received by the receive antenna of effective aperture $A_e|f(\theta, \phi)|^2$ can be expressed as

$$dP_C = \frac{\hat{P}_T G_T |f(\theta, \phi)|^4 L_T L_a A_e L_R \Sigma\sigma dV}{(4\pi)^2 R^4} \tag{2.24}$$

This equation includes the assumptions that there are no *ambiguous* or *second-time-around* clutter signals and that the transmitter and receiver are at the same location. For Eq. (2.24)

P_C = returned power from the clutter.

$A_e|f(\theta, \phi)|^2$ = effective aperture as a function of angle from the clutter cell to the radar beam centerline.

dV = volume element of the clutter cell.

* This factor constitutes part of the pattern loss for targets L_P described earlier.

Note that for pulse lengths short with respect to R, $dV = R^2(c\tau/2)d\Omega$, $c\tau/2$ is the pulse length or cell length in distance units, and $d\Omega$ is the elemental solid angle of the beam.

To obtain the total clutter power for long pulse or continuous wave systems, an integration of Eq. (2.24) should be performed over range. In the chapter on CW radars this is carried out, but for the present it is assumed that $c\tau/2 \ll R$.

To eliminate the antenna pattern shape $|f(\theta, \phi)|^4$ term and integrate over the solid angle Ω, Probert-Jones [563] has shown that for a gaussian beam pattern and a circular antenna

$$\int_\Omega |f(\theta, \phi)|^4 d\Omega = \frac{\pi\theta_1 \phi_1}{8 \ln 2} \tag{2.25}$$

where θ_1 and ϕ_1 are the one-way, 3-dB beamwidths of the beam pattern. Almost identical results are obtained for a uniformly illuminated circular aperture including the clutter power from the first few sidelobes. The factor for rectangular apertures should be somewhat smaller than this value when using the usual definitions for beamwidth. Substituting in Eq. (2.24) yields the *clutter return power for single-aperture radar**

$$P_C = \left[\frac{\hat{P}_T G_T L_T A_e L_R L_a}{(4\pi)^2 R^2}\right]\left[\frac{\Sigma\sigma(c\tau/2)'\pi\theta_1 \phi_1}{8 \ln 2}\right] \tag{2.26}$$

or by substituting for A_e

$$P_C = \left[\frac{\hat{P}_T G_T L_T G_R L_R \lambda^2 L_a}{(4\pi)^3 R^2}\right]\left[\frac{\Sigma\sigma(c\tau/2)'\pi\theta_1 \phi_1}{8 \ln 2}\right] \tag{2.27}$$

A note of caution: The foregoing equations are valid only for equal transmit and receive beamwidths and antennas with a high ratio of main beam to sidelobe gain. If the antenna beamwidth or the gains of the antennas are not known, a good approximation can be obtained by substituting

$$G = \frac{\pi^2}{\theta_1 \phi_1}$$

The foregoing equations are adequate for measuring the rain, snow, or chaff backscattered power using the values of $\Sigma\sigma$ from Chap. 6. In most cases these reflectors are *clutter* and act as noise with a similar amplitude distribution to receive noise. If the backscatter noise P_C is small compared to the system noise $KT_S B_N$, the effect on detection range is negligible. In the usual case of interest $P_C >> KT_S B_N$. Then

* The τ' is used when accuracy is required. See Fig. 2.4.

the received power from the target can be expressed from Eq. (2.1) of Sec. 2.1 as

$$P_R = \frac{\hat{P}_T G_T L_T G_R L_R \lambda^2 L_a}{(4\pi)^3 R^2} \left(\frac{\sigma_t L_P L_c}{R^2} \right) \tag{2.28}$$

where L_c is the collapsing loss introduced since distributed clutter is often folded onto a two-dimensional display from radar beams other than the one of interest.

To detect a target in a volume of uniformly distributed clutter, the ratio of the target power P_R to that of the clutter return P_C must exceed a value (S/C) in a similar manner to the requirements on signal-to-noise ratio (S/N) or the signal-to-jam ratio (S/J). Then from Eqs. (2.27) and (2.28)

$$(S/C) = \frac{P_R L_s'}{P_C} = \frac{L_P L_c L_s' \sigma_t (8 \ln 2)}{\pi R^2 \Sigma\sigma (c\tau/2)' \theta_1 \phi_1} \tag{2.28a}$$

where L_s' is the signal processing loss for clutter greater than receiver noise. Solving for range gives the *detection range in clutter noise for pulse radars*

$$R^2 = \frac{L_P L_c L_s' \sigma_t \, 2 \ln 2}{(\pi/4)\theta_1 \, \phi_1 \, (c\tau/2)' (S/C) \, \Sigma\sigma} \quad \text{if } P_C >> KT_s B_N \tag{2.29}$$

The term $(\pi/4)\theta_1 \, \phi_1$ is the usual 3-dB beamwidth definition of the cross section of a circular radar beam and $(c\tau/2)'$ is the effective pulse length. The remaining undefined term (2 ln 2)* is effectively the inverse of the beam pattern loss for the clutter. The fractional pattern loss for the target was defined as L_P, but its numerical value is a complex function of the beam shape, scanning pattern, and the number of pulses in a search or acquisition radar. While the pattern losses L_P for the target often exceed the factor of (2 ln 2) for rain in a pencil-beam search radar, a useful approximation for a pulse radar is the *detection range in rain, snow, or chaff*

$$R^2 \approx \frac{\sigma_t L_c L_s'}{(\pi/4)\theta_1 \, \phi_1 \, (c\tau/2)' (S/C) \, \Sigma\sigma} \tag{2.30}$$

where σ_t = the radar cross section, m^2
$c\tau/2$ = the pulse length, m
$\Sigma\sigma$ = backscatter coefficient of the scatterers, m^2/m^3

* Numerically equal to 1.39 or 1.4 dB.

$\theta_1\ \phi_1$ = the 3-dB beamwidths in radians for a circular aperture *
R = the detection range of the target located in a volume filled with clutter, m
(S/C) = the ratio of the required target echo power to the power received from the clutter cell for detection
L_s' = the signal-processing loss based on the spectrum and distribution function of the clutter returns

By substituting $G/(\pi^2)$ for $1/(\theta_1\ \phi_1)$

$$R^2 = \frac{4G\sigma_t L_c L_s'}{\pi^3 (c\tau/2)'(S/C)\ \Sigma\sigma} \tag{2.31}$$

The detection range in the case in which the clutter return does not substantially exceed the noise can be found by adding P_C to KT_sB_N; substituting this sum in Eq. (2.5), Sec. 2.1; and solving for R.

The single pulse (S/C) required for detection in Rayleigh distributed clutter for matched-filter receivers† is usually assumed to be equal to the single pulse (S/N) with respect to detection in noise. This is not generally the case with integration of multiple pulses since the clutter returns are partially correlated from pulse to pulse.

Another problem in defining (S/C), which is expanded on in Chap. 4 on automatic detection, is caused by the effective clutter bandwidth not always being equal to the noise bandwidth of the receiver. The determination of the target detection statistics from the signal-to-clutter ratio (S/C) and the processing loss L_s' varies with the transmitted waveform and the implementation of the receiver.

2.6 Pulse-Radar Detection Equations for Area Clutter

The development of the range equation for targets in area clutter is similar to that for volume clutter; however, in this case the integral involving the beam pattern shape is usually programmed on a computer. Therefore, the approach used in this section is somewhat simplified. This development also neglects effects of sidelobe clutter and is valid only in the far-field region. Furthermore, because of the simplifications used, the results must be restricted to a pulse radar system.

The power density at a clutter element is given by Eq. (2.32). (Since

* A similar approximation for the case in which the transmit and receive beamwidths are different is to use the smaller set of the beamwidths assuming that the target is in the smaller beam.

† This is the most common distribution for rain, chaff, or snow.

the pattern shape factor is not used in this development, a closer approximation is the use of the two-way, rather than the one-way, beamwidth.)

$$P_d = \frac{\hat{P}_T G_T L_T L_a'}{4\pi R^2} \tag{2.32}$$

The reflected clutter power is*

$$P_{\text{refl}} = \frac{\hat{P}_T G_T L_T L_a' [\sigma_0 A_c]}{4\pi R^2} \tag{2.33}$$

where σ_0 = the backscatter cross section per unit area (m^2/m^2) of a reflecting surface; the mean value unless stated otherwise.
A_c = area of the cluttered cell.

The clutter power at the receiver preamplifier is

$$P_c = \frac{\hat{P}_T G_T L_T L_a L_R A_e}{(4\pi)^2 R^4} (\sigma_0 A_c) \tag{2.34}$$

In considering the clutter area A_c, two cases are of interest depending on whether the pulse length is large or small compared with the projected length in the radial direction of the beam. These two cases lead to different results. In either case the formulation is based on a flat earth approximation, in which case grazing and depression angles are identical. For greater accuracy, the $\frac{4}{3}$ earth approximation may be used (Chap. 1).

As suggested by Fig. 2.6, the intercepted clutter area may be approximated by the *clutter cell limited by beamwidths*

$$A_c \cong \pi R^2 \tan\frac{\theta_2}{2} \tan\frac{\phi_2}{2} \csc\Psi \quad \text{for} \quad \tan\Psi > \frac{\tan\phi_2 R}{c\tau'/2} \tag{2.35}$$

or by the *clutter cell limited by pulse length*

$$A_c \cong 2R\frac{c\tau'}{2} \tan\frac{\theta_2}{2} \sec\Psi \quad \text{for} \quad \tan\Psi < \frac{\tan\phi_2 R}{c\tau'/2} \tag{2.36}$$

The choice of either Eq. (2.35) or (2.36) depends on the grazing angle Ψ. For small, two-way beamwidths θ_2 ϕ_2 (less than $\approx 10°$) A_c is defined by

* The complete equation, including the beam-shape factor and antenna sidelobes, is derived in the chapter on CW systems and in [325].

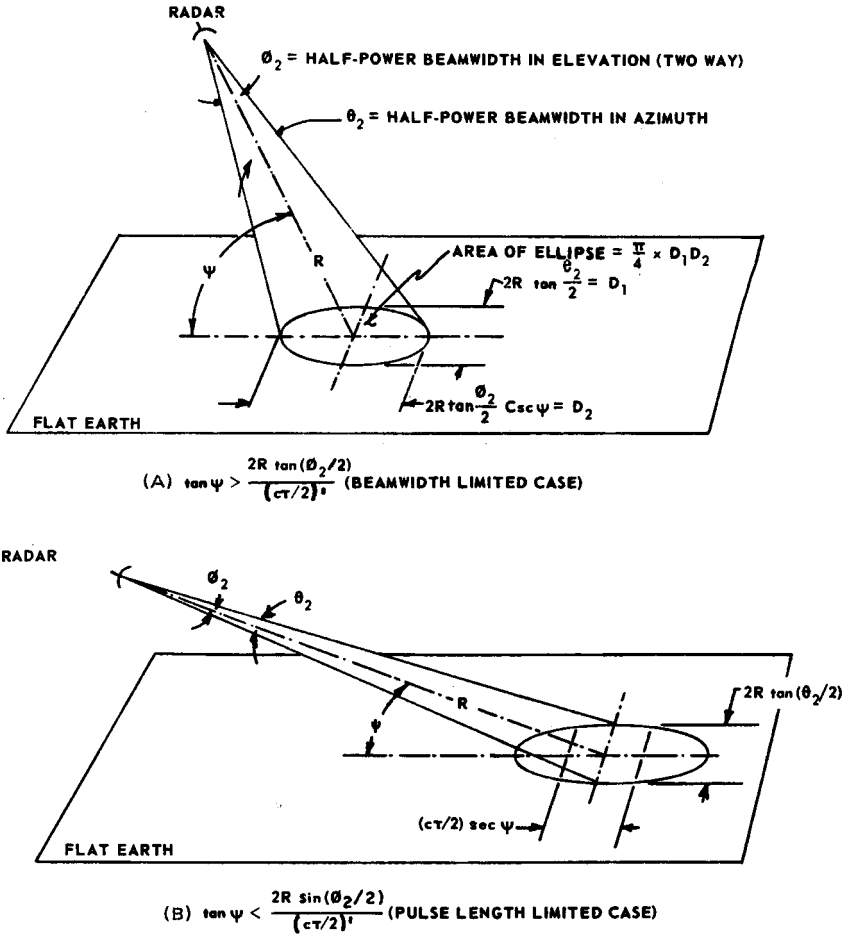

Figure 2.6 Area illustration for pulse radar. (A) Beamwidth limited case; (B) pulse length limited case.

$$A_c \cong \frac{\pi R^2}{4} \theta_2 \phi_2 \csc \Psi \quad \text{for} \quad \tan \Psi > \frac{\phi_2 R}{c\tau'/2} \tag{2.37}$$

$$A_c \cong R \theta_2 \frac{c\tau'}{2} \sec \Psi \quad \text{for} \quad \tan \Psi < \frac{\phi_2 R}{c\tau'/2} \tag{2.38}$$

Combining Eqs. (2.37) and (2.38) with (2.34), the expression for receiver clutter power in a pulsed radar is

$$P_c = \frac{\hat{P}_T G_T L_T L_a L_R A_e (\pi/4) \theta_2 \phi_2 \sigma_0}{(4\pi)^2 R^2 \sin \Psi} \quad \text{for} \quad \tan \Psi > \frac{\phi_2 R}{c\tau'/2} \tag{2.39}$$

$$P_c = \frac{\hat{P}_T G_T L_T L_a L_R A_e (c\tau/2)' \theta_2 \sigma_0}{(4\pi)^2 R^3 \cos \Psi} \quad \text{for} \quad \tan \Psi < \frac{\phi_2 R}{c\tau/2} \tag{2.40}$$

Using a procedure similar to that used in the previous section, the ratio of the equations for P_R and P_c [Eq. (2.39)] results in the following range equation for area clutter-limited cases. This equation applies only when $P_c >> KT_sB_N$, and the target is in the clutter. The *pulse radar range equation for area clutter* is

$$R^2 = \frac{L_s' L_P L_c (\sin \Psi)\sigma_t}{(\pi/4)\theta_2 \phi_2 (S/C)\sigma_0} \quad \text{for} \quad \tan \Psi > \frac{\phi_2 R}{c\tau/2} \tag{2.41}$$

where L_P = beam pattern losses for the target echo.
L_s' = signal-processing loss in a clutter limited environment.

For a circular aperture* $G \cong \pi^2/\theta_2 \phi_2$ 2 ln 2 and using the approximation† as explained in the previous section, we have

$$R^2 \cong \frac{4GL_s' L_c (\sin \Psi)\sigma_t}{\pi^3 (S/C)\sigma_0} \tag{2.42}$$

Another form may be obtained by substituting $\sin \Psi = h/R$, where h is the antenna height, and assuming a flat earth

$$R^3 = \frac{4GL_s' L_c h\sigma_t}{\pi^3 (S/C)\sigma_0} \tag{2.43}$$

The equation for the case in which ($\tan \Psi < \theta_2 R/c\tau/2$) is obtained by taking the ratio of P_R to P_c [Eq. (2.40)] and solving for R. The *pulse-radar range equation for area clutter* is

$$R = \frac{L_s' L_P L_c \cos \Psi \sigma_t}{(S/C)(c\tau/2)\theta_2 \sigma_0} \quad \text{for} \quad \tan \Psi < \frac{\phi_2 R}{c\tau'/2} \tag{2.44}$$

As stated previously, the symbols are defined as

G_T = transmit gain of antenna
L_s' = signal-processing loss in the clutter-limited case
L_P = beam shape and pattern losses for the target echo
L_c = collapsing loss of processor or display
Ψ = grazing angle of radiation on clutter cell

* For different transmit and receive antennas the gain corresponding to the smaller beamwidth should be used.

† $L_P \approx \frac{1}{2}$ ln 2.

(S/C) = signal-to-clutter power ratio required for detection.
σ_0 = reflectivity per unit cross section of clutter (dimensionless).
θ_2, ϕ_2 = 3-dB beamwidth in azimuth and elevation, respectively (two-way path). In general, $\theta_2 \approx 0.71\theta_1$, $\phi_2 \approx 0.71\phi_1$.

In later sections the prime in $c\tau'/2$ is dropped, but it is assumed that a calculation will be made where accuracy is deemed important.

Chapter

3

Statistical Relationships for Various Detection Processes

F. E. Nathanson

J. P. Reilly

3.1 Introduction and Definitions*

As alluded to in the previous chapter, the detection of signals in noise or interference is best described in statistical terms although the use of gaussian wideband noise is not always sufficient to describe performance in a given environment. The first part of this chapter describes the statistics for detection of steady targets in white gaussian† noise. The discussion is then extended to target signals that have a fluctuating amplitude with various correlation times. This case is essential to prediction of the performance where the target's returns are immersed in clutter signals. This is followed by a brief summary of radar displays and human operator performance. The techniques of

* For general references see Marcum and Swerling [461], Siebert [654], Fehlner [225], Wainstein and Zubakov [740], Barton [45], Nolan et al. [513], DiFranco and Rubin [179].

† See Berkowitz [63, Chaps. 2, 3, and 4 by W. R. Bennett].

detection by sequential, adaptive, or automatic means are covered in Chap. 4.

There is a multitude of excellent texts and papers on the statistics of radar detection [514, 461, 75, 179]. The purpose of this chapter is to summarize the useful relationships on this topic in engineering terms rather than to delve into the theory. Before proceeding, it is essential to define the terminology to be used here. When in parentheses, (S/N) refers to the required signal-to-noise ratio to achieve certain detection statistics.

1. *Signal-to-noise ratio S/N:* The ratio of the signal power (when the signal is present) to the average noise power after the matched filter but before detection or postdetection integration.

2. *Radar cell:* A term used to describe a *volume* from which return signals are received. The most common usage is for a pulse radar where the *cell volume* is defined by the pulse length and the half-power beamwidth of the antennas. A *clutter cell* is a volume of this size containing undesired scatterers. The *target cell* is the same volume containing a target even though it may occupy only a portion of the cell. The number of cells of a simple pulse radar in a given time such as the scan time of the radar, neglecting Doppler cells, can be written

$$\text{Number of cells in one scan} = \frac{(\text{PRF})(\text{scan time})(\text{display time/sweep})}{\text{pulse duration}}$$

The PRF is the *pulse repetition frequency*. It is assumed that the display time per beam is less than the interpulse period.

3. *Pulse integration:* The summation of target return signals (from the same location) and noise from two or more successive transmit pulses. The purpose is usually to improve the probability of detection or to permit more accurate parameter estimation.

4. *Coherent:* (a) Two or more radar signals are said to be *coherent* when the amplitudes and relative phases of the signals have a known relationship* even though they may be considerably separated in time. (b) This term is applied to an oscillator that is sufficiently stable to predict the phase at a given time later than the start of the transmission. (c) Signals on two or more frequencies may be called *coherent* if they were derived, by frequency multiplication or mixing, from the same basic frequency which is stable as specified in (b).

5. *Coherent integration* (*predetection integration*): The addition of coherent radar signals prior to envelope detection where the signals are summed vectorially (voltagewise). For perfect integration of con-

* Phase shifts due to unknown target velocity do not alter this definition.

stant-amplitude coherent signals the S/N increases linearly as the number of these signals, assuming that the noise is uncorrelated. A predetection matched filter can be considered as a coherent integrator for complex signals. For example, a narrow-band IF filter is a coherent integrator for a single-frequency signal. Coherent signals on different frequencies can be added coherently with certain restrictions on the times that this can occur (see Chap. 13) with respect to the relative phases.

6. *Correlated:* While coherency implies a complete predictability of relative phase (and sometimes amplitude) between a set of radar signals, the term *correlated* is used in a number of cases where the second, third, fourth, etc., signal of a set is in some way related in phase, amplitude, or power to the first of the set or to each other. The terminology derives from the autocorrelation and cross-correlation functions of signals.

7. *Correlation functions and related distributions:* (a) *Temporal*—describes to what degree the value of a time function $f(t)$ at one time is correlated with another value τ time units later. Usually, unless otherwise specified, the term *autocorrelation function* refers to the temporal function. For a random function $f(t)$

$$R(\tau) = \lim_{T\to\infty} \frac{1}{2T} \int_{-T}^{T} f(t)\, f(t + \tau)\, dt$$

In practice the finite limits are taken long enough so that a sufficient degree of accuracy is obtained. As stated by the Wiener-Kintchine theorem, the autocorrelation function is simply the Fourier transform of the power spectral density function. Other properties are

$$\rho(\tau) = \frac{R(\tau)}{R(0)}, \qquad \text{the normalized autocorrelation function}$$

$$R(\tau) \leq R(0)$$

$$R(\tau) = R(-\tau)$$

(b) *Frequency*—describes how well a signal corresponding to a certain transmitted frequency f_0 is correlated* with another signal whose transmitted frequency is different by Δf units. (The two signals are assumed to occur close enough together in time and space so that they are not decorrelated because of the time interval or spatial separation.) The mathematical form is identical to that for the temporal function except that the temporal variable t is replaced by a frequency variable f and

* Since the correlation in phase of these signals is dependent on the coherency and time delays involved, *correlated* radar returns generally refer to the power of the returns.

the frequency separation Δf replaces τ. (c) *Spatial*—describes how well the signal reflected from one cell is correlated with another signal reflected from a distant cell. (The two signals are assumed to occur close enough together in time and transmit frequency so that they are not decorrelated because of the time interval or frequency spacing.) The mathematical form is identical with that for the temporal function, except that the temporal variables t and τ are replaced by spatial variables.

8. *Probability density function* $p(x)$—defines the probability of a random variable taking on a value within a small interval. The expression $p(x)\,dx$ gives the probability that a random variable X will lie in the interval $x \leq X \leq x + dx$. The gaussian distribution, often called the *normal distribution,* has the density function

$$p(x) = \frac{1}{\sqrt{2\pi\,\sigma^2}} \exp\left[-\frac{(x - \bar{x})^2}{2\sigma^2}\right]$$

where $\bar{x}$ is the mean value. The variance (second central moment) is

$$\sigma^2 = \overline{(x - \bar{x})^2}$$

3.2 Target Detection by a Pulsed Radar

J. I. Marcum and P. Swerling [461] treated the statistical problem of target detection by a pulse radar. Their papers have withstood the test of time. Similar studies were made by Rice [592, 593], Blake [75], Kaplan [384], Hall [302], North [514], and others and with proper interpretation are in close agreement.

Swerling [689] extended Marcum's results to the case of a radar target with an echo of fluctuating strength. Swerling's analytic results are used in this section to extend the numerical data beyond that given in [461].

The text and graphs of these papers, however, are presented in terms so highly mathematical that the results may not appear as useful as they really are. The majority of this section is paraphrased from Fehlner's report [225], which clarified the earlier papers.

Marcum's contribution is the definition of the relationship between a threshold value of radar return signal-to-noise power S/N and of the probability that values in excess of the threshold will exist in the presence of both noise and echoes. These threshold crossings will be reported as target detections and will include both false and real reports of targets.

The problem starts with noise. Suppose that the voltage caused by

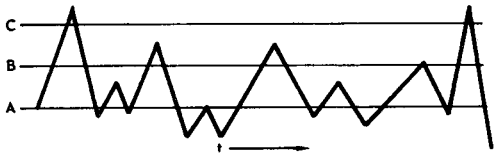

Figure 3.1 Threshold detection of noise.

noise alone varies with time as shown in Figure 3.1. During the period shown, the noise exceeded threshold voltage level A seven times; level B, five times; and level C, only twice. Obviously, the higher the threshold, the longer will be the average time between occasions when noise alone exceeds the threshold. This time is of considerable concern because if it is too short the system will be too frequently faced with false alarms and, if too long, excessive radiated energy will be required to achieve reasonable probabilities of target detection. Marcum defined it as the time during which the probability is P_0 that there will not be a false alarm. For purposes of standardization, P_0 is taken to be 0.5. (Not all authors use this definition.)

P_N is the probability that a false alarm is obtained each time there is an opportunity. The false-alarm number n' is the number of independent opportunities for a false alarm in the false-alarm time. Then

$$P_0 = (1 - P_N)^{n'} = 0.5 \qquad \text{(Marcum, Eq. 10)*} \tag{3.1}$$

where P_0 = the probability of no false alarm during the false-alarm time.
P_N = the probability of a false alarm on each opportunity.
n' = the false-alarm number, the number of independent opportunities for detection.

For a pulse radar (one Doppler channel)

$$n' = \frac{n}{mN} \approx \frac{T_{FA}}{\tau mN} \tag{3.2}$$

where n = the number of pulse lengths τ in the false-alarm time T_{FA}.
m = the number of pulses integrated coherently (≥ 1).
N = the number of pulses integrated incoherently (≥ 1).

The probability of a false alarm in the absence of echoes is given by Eq. (3.1). For $n' \gg 1$, a very close approximation is

* These references are to equations in *Rand Res. Memo* RM 753 from [461], but they are not necessarily quoted verbatim. For example, Marcum used n for false-alarm number instead of n'.

$$P_N \approx \frac{1}{n'} \ln_e \frac{1}{P_0} \qquad \text{(Marcum, Eq. 21)} \tag{3.3}$$

The value of false-alarm probability when $P_0 = 0.5$ is

$$P_N \approx \frac{0.69}{n'}$$

The probability P_N that noise alone will exceed a given bias level of voltage is a function of the bias level, the combined law of the detector and integrator, and the characteristics of the noise. The detector referred to here is the envelope detector, the output of which is a given function of the envelope of the carrier wave. The integrator characteristic also affects the statistical problem. The function of the signal voltage that is integrated is called the law of the integrator, e.g., the square of the pulse voltage might be integrated. So long as the same weight is applied to each of the N pulses the integrator is called linear.

A functional block diagram of a pulse radar with automatic detection is shown in Fig. 3.2. The output of the matched filter is fed to the detector and also to a device that measures rms noise,* the value of which must not be unduly influenced by echoes. This value is multiplied by a factor Y_b to obtain the bias level. The integrated output of the detector is compared to the bias level in the threshold device. If the output is larger, an alarm is sounded indicating the probable presence of a target. Marcum's analysis applies to only that part of the functional block diagram downstream of the matched filter. If m pulses are integrated coherently, Marcum's data apply to $1/m$ of the pulses, each of which has m times the energy of a single pulse. This analysis applies to integrators that are dumped after the integration period.

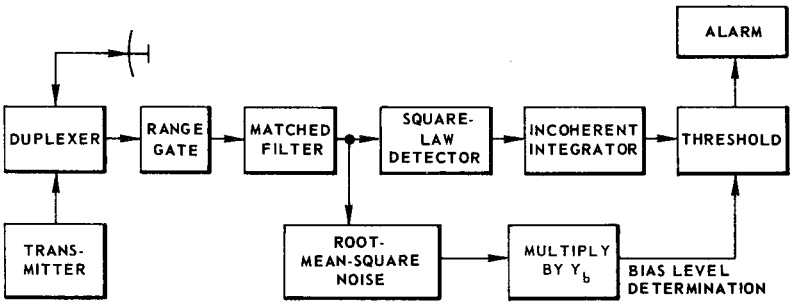

Figure 3.2 Pulse integrator block diagram.

* If the root-mean-square noise level is changing as a function of time (because of jamming, etc.), a sufficient number of samples must be averaged before the bias level is determined. This is covered in Chap. 4 on automatic detection. The range gate is not necessary for simple-pulse radars.

Since the relationships have been established among the bias level, the false alarm number n', and the number of pulses integrated N; the probability of detection can now be related to n' and N. These relationships are shown in Figs. 3.3 through 3.6, which also show fluctuating target-detection curves. The single-pulse case was shown as Fig. 2.2. Simple expressions for determining thresholds are given in [306].

Hansen [306] derived a simple method for calculating the bias level for either a square law or linear detector for virtually all values of P_N and N. With gaussian noise he reports the accuracy to be better than 0.1 dB.

3.3 Additional Results of the Marcum and Swerling Analysis

Marcum made a limited number of calculations for a linear detector and integrator. A comparison with the square-law results shows very small differences. For example, at a detection probability of 0.5, the

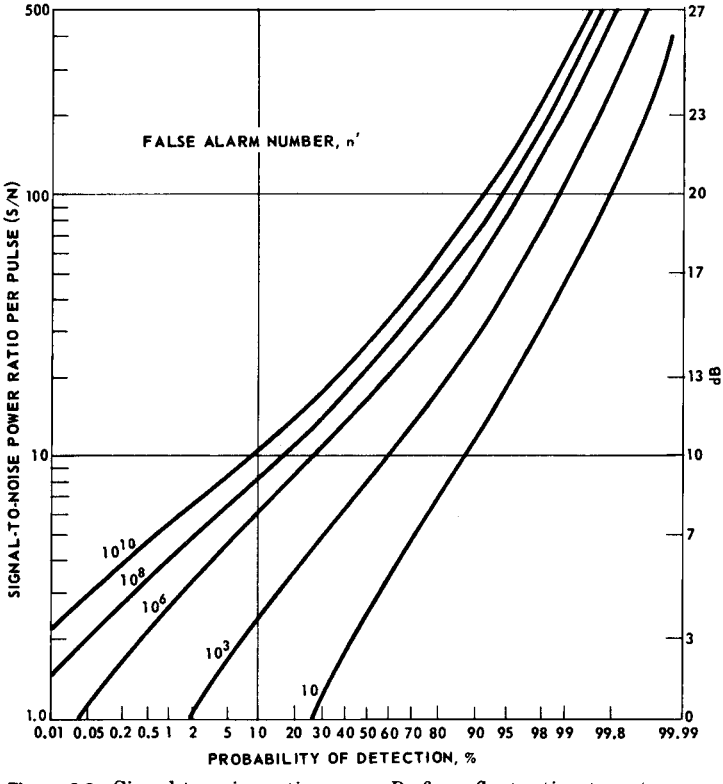

Figure 3.3 Signal-to-noise ratio versus P_D for a fluctuating target—cases 3 and 4 ($N = 1$). (*After Fehlner* [225])

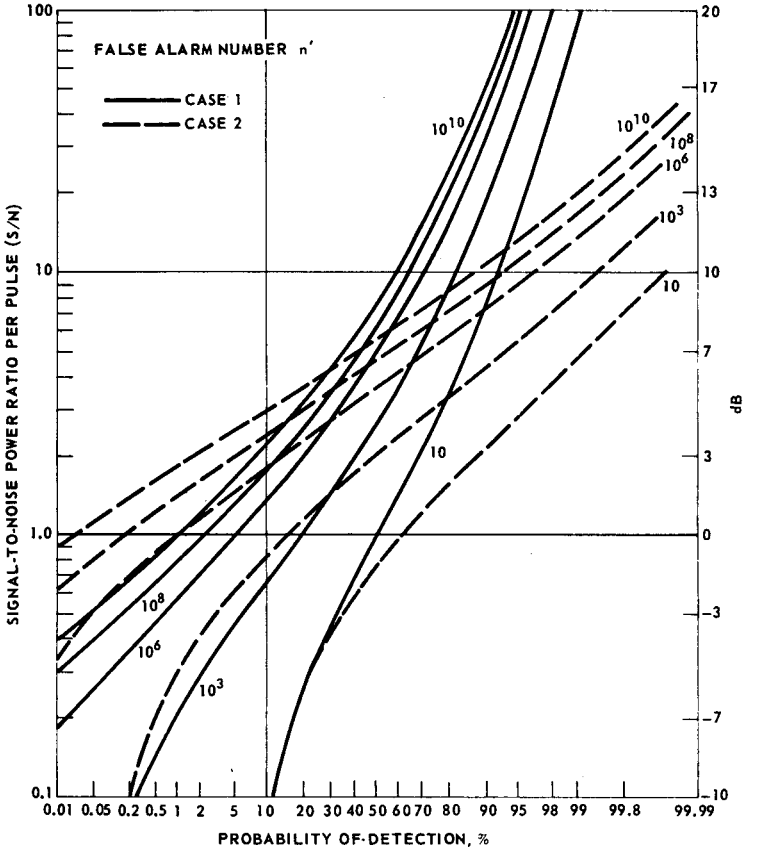

Figure 3.4 Signal-to-noise ratio versus P_D for a fluctuating target ($N = 6$). (*After Fehlner* [225])

required signal-to-noise ratio is the same for both laws for $N = 1$ and $N = 70$, where N is the number of pulses integrated. For $N = 10$, the square law requires about 2.5 percent more power ratio than the linear law. For very large N the linear law approaches a requirement of about 4.5 percent more signal-to-noise ratio than the square law. These results are ample justification for preferring the more easily obtained square-law data. Graphs of the linear-rectifier detector *detectability factor* with an explanation of the relationships to (S/N) are given in Blake [75, 74].

Marcum proves rigorously that there is a best possible detector law for each signal strength (Marcum, Eq. 217). For small signals the best possible law closely approximates the square law. For large signals, it is the linear law. The numerical results for these extreme cases, however, are not very different, so that if faced with a choice, there is not

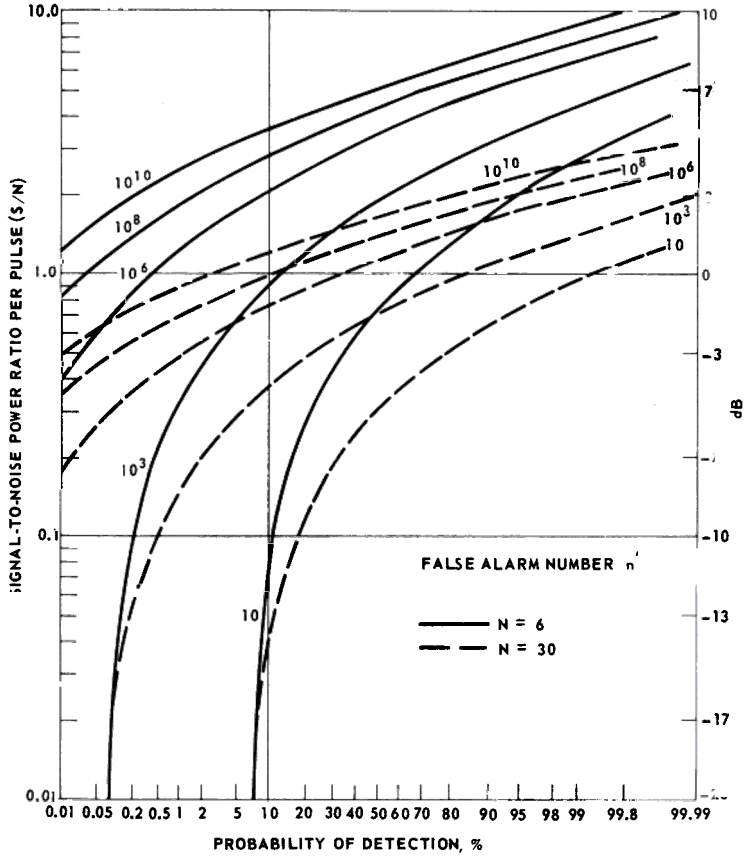

Figure 3.5 Signal-to-noise ratio versus P_D for a steady target. (*After Fehlner* [225])

much reason to prefer one to the other on the basis of detection probability. (See DiFranco and Rubin [179, p. 370].) The linear law, however, has one practical advantage in that a linear detector requires less dynamic range.

Swerling extended Marcum's square-law results to four different cases in which targets return echoes of fluctuating strength.* Cases 1 and 2 apply to targets that can be represented as a number of independently fluctuating reflectors of about equal echoing area. The density function is the *chi-square* distribution with two degrees of freedom.

$$w(x, \bar{x}) = \frac{1}{\bar{x}} \exp\left(-\frac{x}{\bar{x}}\right) \qquad x \geq 0 \tag{3.4}$$

* A detailed discussion of these cases is given in Chap. 5 on targets.

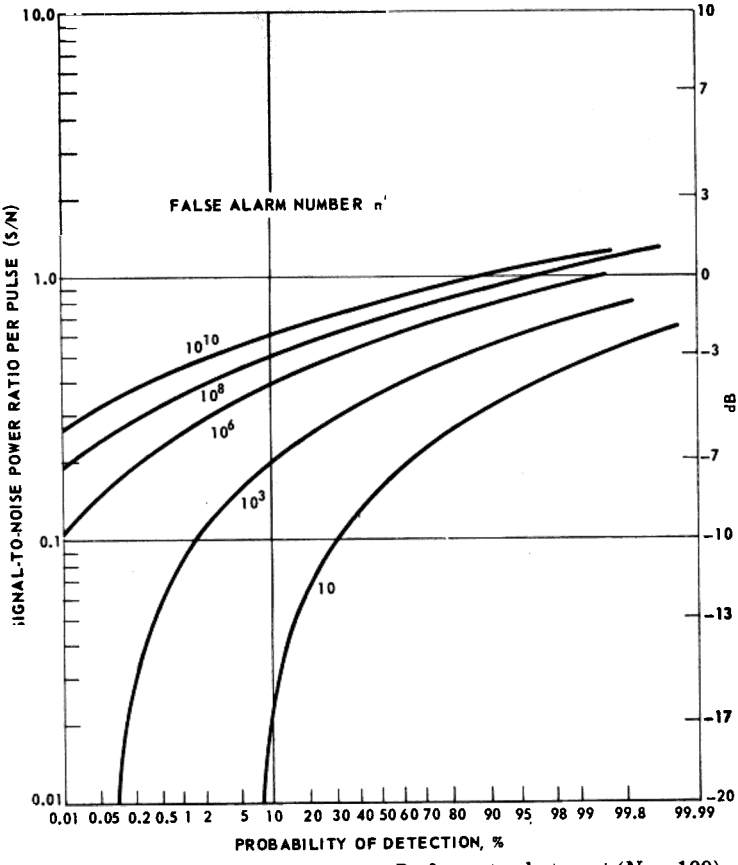

Figure 3.6 Signal-to-noise ratio versus P_D for a steady target ($N = 100$).

where $\bar{x}$ is the average signal-to-noise ratio over all target fluctuations. (See Chap. 5.)

Cases 3 and 4 were derived from the density function of Eq. (3.5). It was said to apply to targets that can be represented as one large reflector together with a number of small reflectors or as one large reflector subject to small changes in orientation.

$$w(x, \bar{x}) = \frac{4x}{\bar{x}^2} \exp\left(-\frac{2x}{\bar{x}}\right) \qquad x \geq 0 \tag{3.5}$$

Cases 1 and 3 apply when echo fluctuations are statistically independent from scan to scan, but perfectly correlated pulse to pulse. *Cases 2 and 4 apply when fluctuations occur from pulse to pulse.*

Swerling did not give the exact expression for P_N for case 4. The

equations were derived by Roll [225] from the characteristic function for case 4 given in [461].

The relationships among P_D, $\bar{x}$, N, and n' are shown in Figs. 3.3 through 3.6. A far more extensive set is available in Fehlner [225].

In practice, the false-alarm rate is established, in the absence of a target, by a counter at the output of the threshold circuit of Fig. 3.2.

The preceding discussion has assumed that the integrator was linear. Other integrator types are:

1. A recursive delay line integrator with a feedback gain of less than unity, which permits the older information to decay as new information is added. This is common with mechanically scanning radars.
2. A digital integrator in which the input amplitude is quantized into several levels with the integration performed in a digital memory.

It can be shown that the additional loss introduced by these techniques is small while a considerable saving in hardware is obtained.

3.4 Noncoherent Integration Losses

The graphs shown in Figs. 3.3 to 3.6 can be used to obtain the required signal-to-noise ratios per pulse for a given detection criterion. It is often more interesting to know the integration loss or the difference between perfect coherent integration and incoherent techniques. Before this loss can be determined, it is necessary to define the false alarm statistics in more consistent terms in order to resolve differences in the reported curves of integration loss. The primary reason for the discrepancy is that after integration of many noise samples, the number of opportunities for a false alarm is reduced by the number of integrations. If it is desired to keep the time between false alarms T_{fa} constant, the threshold or bias level can be lowered, and a higher probability of a single sample of noise exceeding this threshold P_N can be accepted. Barton [44] has shown that this accounts for most of the differences between earlier publications. The graphs published in this section are for a constant false alarm probability P_N and for the false alarm time increasing with the number of integrations. This allows the estimation of the number of false alarms per beam position to be computed from a knowledge of the number of noise samples in the instrumented range.

It has also been shown [44] that the fluctuation losses* of the various Swerling cases are essentially independent of the loss from incoherent

* The increase in target echo to achieve the same detection statistics as a steady target of the same radar cross section.

integration of many pulses. Since these losses are dependent on the various detection and false alarm criteria, the required (S/N) per pulse as a function of the number of pulses can be drawn only for special cases. Figures 3.7 and 3.8 are from Barton [44] (see also [39]), who used Fehlner's computations of the Marcum and Swerling equations.

Figure 3.7 shows the required (S/N) per pulse for N pulses for a detection probability P_D of 50 percent and a false alarm probability P_N of 10^{-6}. This is a common case for a low-resolution search radar. Both coherent and incoherent integration are included. The integration loss is the difference in the ordinate between the two cases for a given number of pulses integrated. Figure 3.8 is for a $P_D = 80$ percent and $P_N = 10^{-6}$. This is a common value for acquisition by a tracking radar.

Another comparison is the required signal-to-noise ratio (Fig. 3.9) for the single-pulse case for the various fluctuation models. At desired single-scan detection probabilities P_D between 0.2 and 0.4 it makes little difference which target fluctuation model is assumed; however, at a $P_D = 0.9$ an average of 8 dB more S/N is required to detect a slowly fluctuating target for the illustrated case of 10^6 false alarm number.

The choice of a particular false alarm number n' has not been emphasized as it is generally less important than the fluctuation model of the target when using search radars and when the number of integrations is small.

The required signal-to-noise ratio versus the false alarm number for P_D equal to 0.5 is shown in Fig. 3.10 [782] in which the number of pulses integrated N is the parameter. The target model is the Swerling case 1.

It can be seen that even for the case of 0.5 detection probability and a fluctuating target, only a 2-dB increase in S/N is required to increase the false alarm number from 10^5 to 10^9 for 10 pulses integrated. At the 10^5 false alarm number, a 7-dB smaller signal-to-noise ratio would be required to detect a constant echo.

Since these curves were also drawn from Fehlner's [225] computations, they can be used to interpolate the previous figures in this chapter.

3.5 Postdetection Integration with Partially Correlated Noise

Marcum and Swerling [461] showed that for postdetection integration the required signal-to-noise ratio per pulse may be reduced by a factor somewhat between $\sqrt{N}$ and N (the number of pulses integrated). These results were obtained for white, gaussian noise; and it was assumed that every pulse processed contained a statistically independent sample

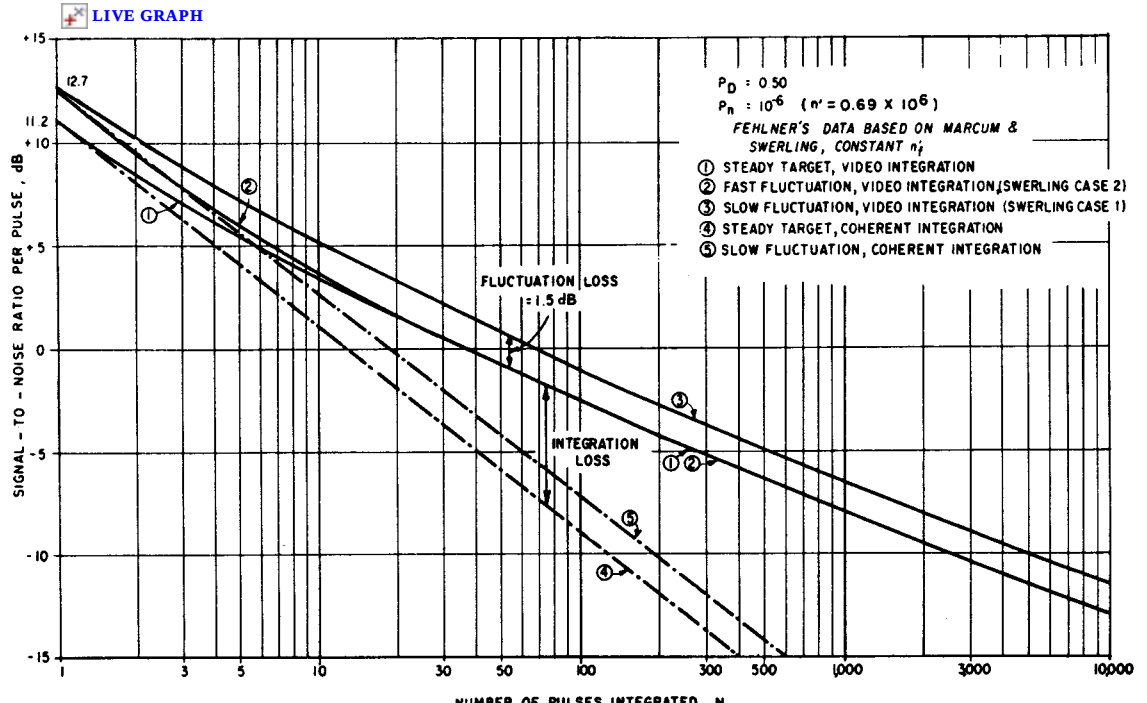

Figure 3.7 Detectability factor (S/N) versus number of pulses ($P_D = 0.5$).

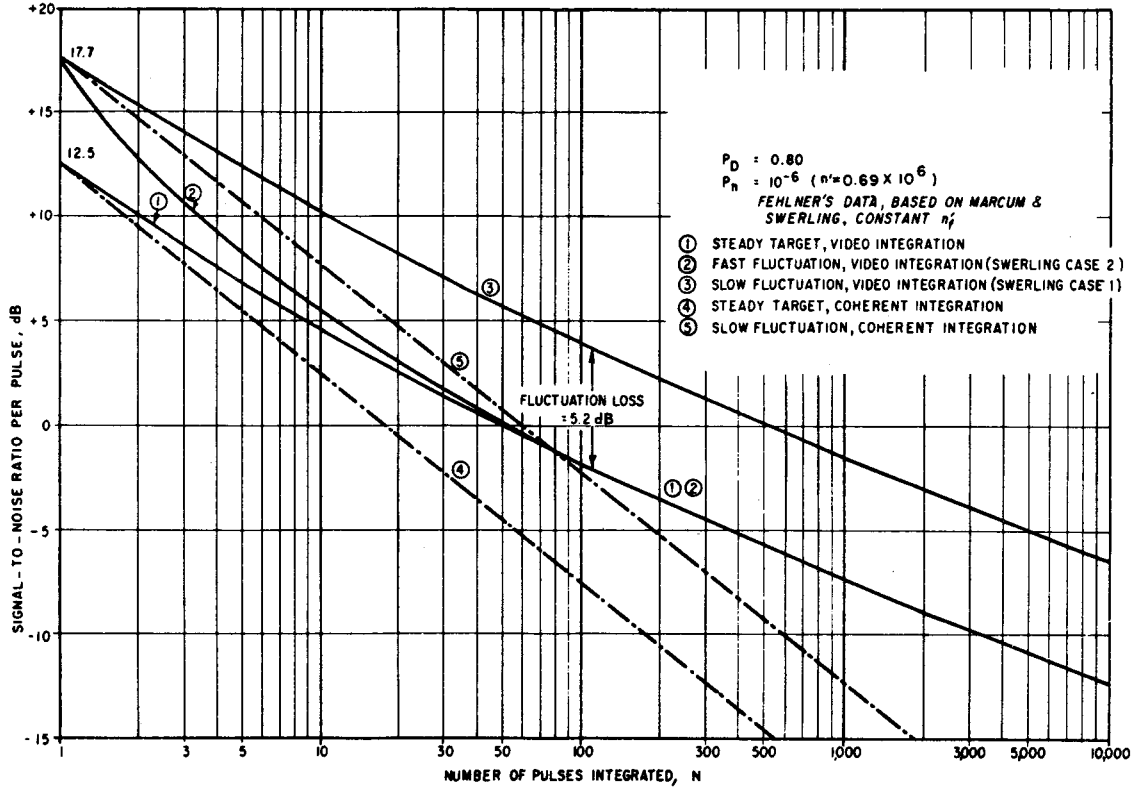

Figure 3.8 Detectability factor (S/N) versus number of pulses ($P_D = 0.8$).

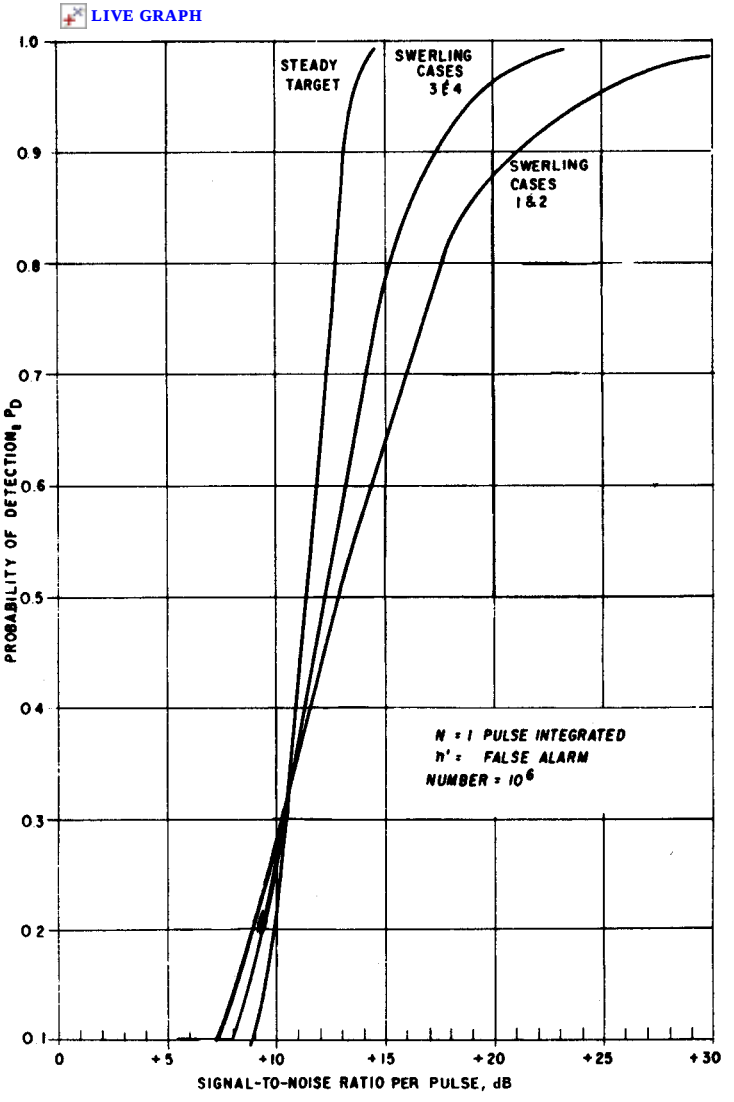

Figure 3.9 Detection probabilities for various target fluctuation models.

of the noise. The theory may be extended to include interference that is time correlated, such as clutter echoes, by accounting for the fact that the number of independent samples of the interference may be much smaller than the actual number of pulses processed.

The basic incoherent processor that was illustrated in Fig. 3.2 consists of a square-law detector followed by a linear integrator that forms the sample average of N samples in each resolution cell. Figure 3.11 illustrates the signal that might be observed on an A scope. To simplify

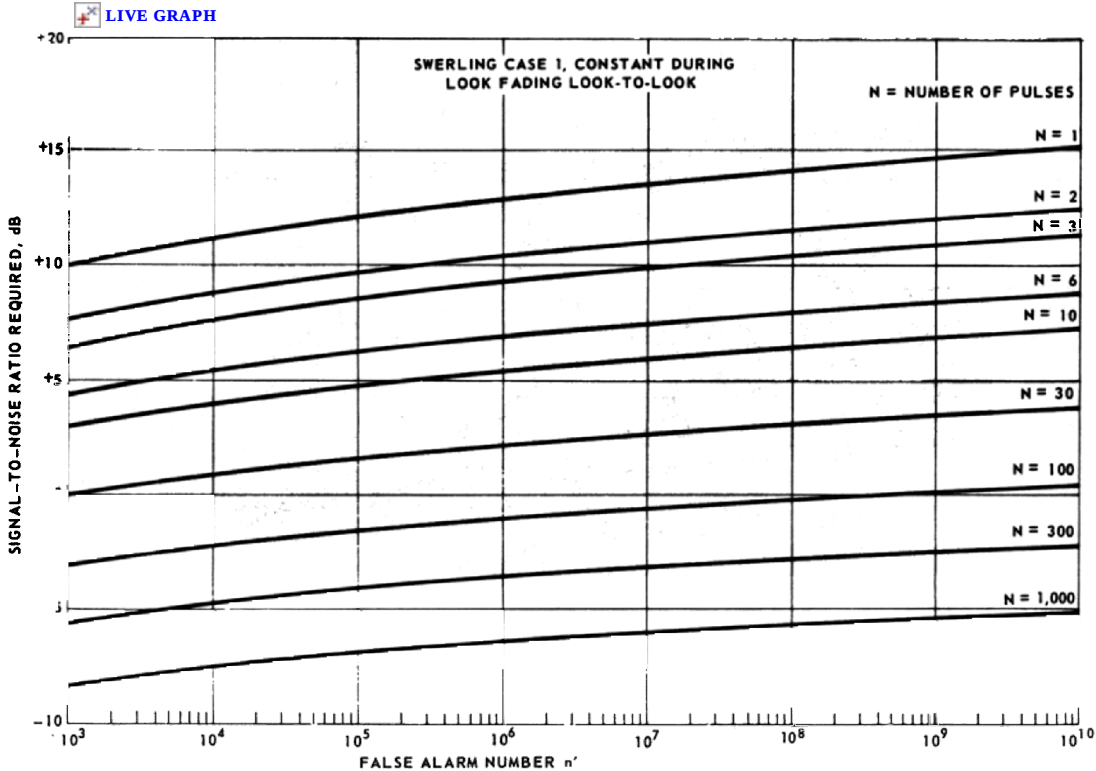

Figure 3.10 Signal-to-noise ratio versus n' for $P_D = 0.5$ (*After Young* [782])

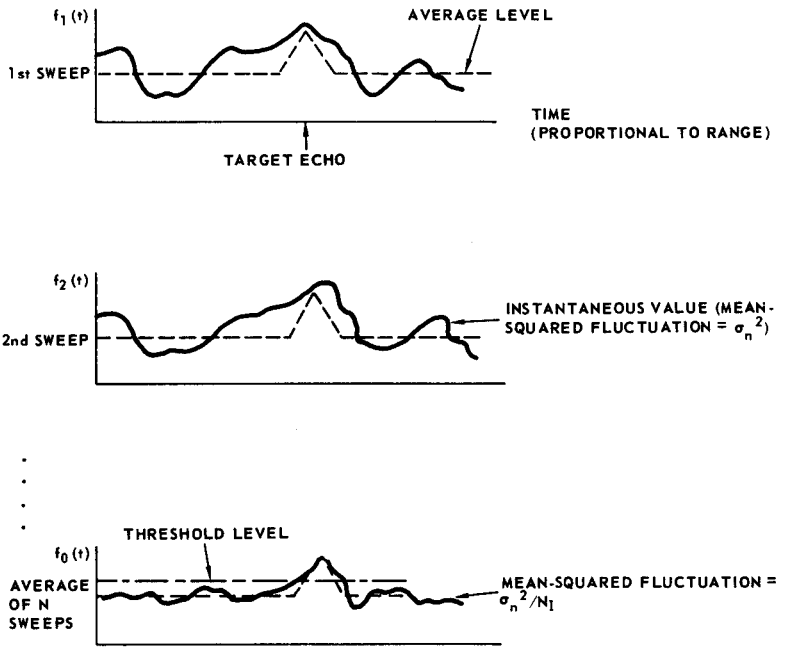

Figure 3.11 Voltage waveforms of an automatic detection process with correlated noise.

matters, the average value of the signal is shown as a constant except at a range cell in which a target is assumed to exist. The temporal variance of noise about its mean value is designated σ_n^2. The variance of the ensemble average is σ_n^2/N_I, where N_I is the number of independent samples obtained at any one range interval. To obtain the significance of this relationship consider a random process consisting of noise samples $x_1, x_2, x_3, \ldots, x_N$ with variance σ_x^2. The sample mean is defined by

$$\bar{x} = \frac{1}{N}\sum_{i=1}^{N} x_i \tag{3.6}$$

For statistically independent x_i the variance of the sample mean, designated $\sigma_{\bar{x}}^2$, depends on N, the number of samples averaged

$$\sigma_{\bar{x}}^2 = \frac{\sigma_x^2}{N} \qquad \text{(independent samples)} \tag{3.7}$$

When x_i and x_j are correlated,* however, the variance of the sample mean also depends on their correlation [426, Chap. 11]. Assuming a stationary process,

* Correlated samples obey the property $(x_i - \bar{x})(x_j - \bar{x}) \neq 0$.

$$\sigma_{\bar{x}}^2 = \sigma_x^2 \sum_{k=-(N-1)}^{N-1} \frac{N - |k|}{N^2} \rho(kT) \qquad \text{(dependent samples)} \tag{3.8}$$

where

$$\rho(kT) = \frac{\overline{[x_i - \bar{x}][x_{i+k} - \bar{x}]}}{\sigma_x^2}$$
$$T = \text{sampling interval} \tag{3.9}$$

The quantity $\rho(kT)$ is the normalized autocorrelation coefficient. It follows that an equivalent number of independent samples N_I may be expressed as

$$N_I = \frac{1}{N^2} \sum_{k=-(N-1)}^{N-1} [N - |k|]\rho(kT) \tag{3.10}$$

As the actual number of samples averaged in a given integration time T_s becomes very large, the sample variance becomes that for continuous sampling (continuous integration)

$$\sigma_{\bar{x}}^2 = \sigma_x^2 \int_{-T_s}^{T_s} \frac{T_s - |\tau|}{T_s^2} \rho(\tau)\, d\tau \tag{3.11}$$

where

$$\rho(\tau) = \frac{1}{2T} \int_{-T_s}^{T_s} \frac{[x(t) - \bar{x}][x(t+\tau) - \bar{x}]\, dt}{\sigma_x^2}$$
$$T_s = \text{total integration time.}$$

The quantity T_s is also referred to as the observation time. By analogy with Eq. (3.7) the definition for the equivalent number of independent samples is

$$\frac{1}{N_I} = \frac{\sigma_{\bar{x}}^2}{\sigma_x^2} = \int_{-T_s}^{T_s} \frac{T_s - |\tau|}{T_s^2} \rho(\tau)\, d\tau \tag{3.12}$$

Thus, Eq. (3.12) demonstrates that the number of statistically independent samples obtainable in the interval T_s is dependent on the normalized autocorrelation function $\rho(\tau)$; this in turn depends on the power spectral density function of the clutter.

3.6 Independent Sampling of Clutter Echoes

The gaussian power spectral density* function has been shown to provide a reasonable description of clutter spectra, namely,

$$S(f) = S_0 e^{-f^2/2\sigma_f{}^2} \tag{3.13}$$

where σ_f^2 is the second moment of the spectrum. By taking the Fourier transform of Eq. (3.13), the normalized autocorrelation function, which is also a gaussian function, is obtained

$$\rho(\tau) = e^{-\tau^2/2\sigma_\tau{}^2} \tag{3.14}$$

where σ_τ^2 is the second moment of the correlation function. Equations (3.13) and (3.14) are related by

$$\sigma_\tau = \frac{1}{2\pi\sigma_f} \tag{3.15}$$

By substituting the correlation function into Eq. (3.12), one obtains

$$\frac{1}{N_I} = \frac{1}{\sqrt{2\pi}\,\sigma_f T_s} \operatorname{erf}(\sqrt{2}\pi\sigma_f T_s) - \frac{1}{2\pi^2\sigma_f^2 T_s^2}\left[\exp(-2\pi^2\sigma_f^2 T_s^2) - 1\right] \tag{3.16}$$

where erf is the error function.

Lhermitte [435] has shown that for correlated samples, the difference between continuous integration [Eq. (3.16)] and the sum of N_I discrete samples equally spaced in time T_s [Eq. (3.8)] is small. Thus, in Eq. (3.16) we make the substitutions

$$T_s = \frac{N}{f_r} \qquad \text{(for dependent sampling)}$$

and

$$\sigma_f = \frac{2\sigma_v}{\lambda} \qquad \text{(the Doppler equation)}$$

---

* Although this section analyzes independent sampling for clutter having gaussian spectra, the results are not very sensitive to the precise spectrum shape. Lhermitte [435], for example, shows that nearly identical results are obtained for triangular or rectangular spectra.

where N = the actual number of samples.
f_r = the sampling frequency.
σ_v = the standard deviation of the velocity distribution of the clutter scatterers.
λ = the radar wavelength.

As the total observation time is increased, the second term of Eq. (3.16) becomes insignificant compared with the first. At the same time $\text{erf}(\sqrt{2\pi}\,\sigma_f T_s) \cong 1$. Thus,

$$N_I \cong \sqrt{2\pi}\,\sigma_f T_s = 2\sqrt{2\pi}\,\frac{\sigma_v T_s}{\lambda} \qquad \text{(for } T_s \text{ large)} \tag{3.17}$$

This result leads to the definition of the equivalent time for independence

$$T_I = \frac{T_s}{N_I} = \frac{1}{\sqrt{2\pi}\,\sigma_f} = \frac{\lambda}{2\sqrt{2\pi}\,\sigma_v} \tag{3.18}$$

Equation (3.18) is illustrated in Fig. 3.12. We may interpret T_I as the time required between samples for independence; sampling at a more rapid rate gives practically no new information.

Assume that a given sampling frequency gives independent samples. As that frequency is increased, a point is reached at which the samples become dependent. The transition between independent and dependent sampling is quite abrupt, as shown in Fig. 3.13, occurring approxi-

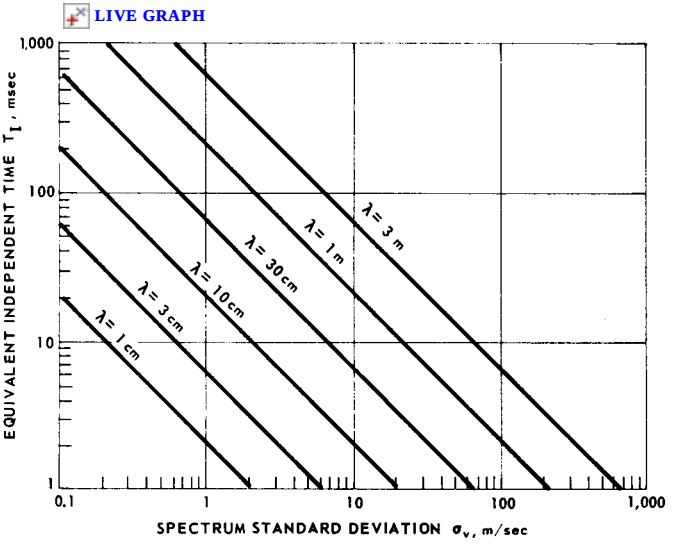

Figure 3.12 Equivalent independent sampling time for radar clutter.

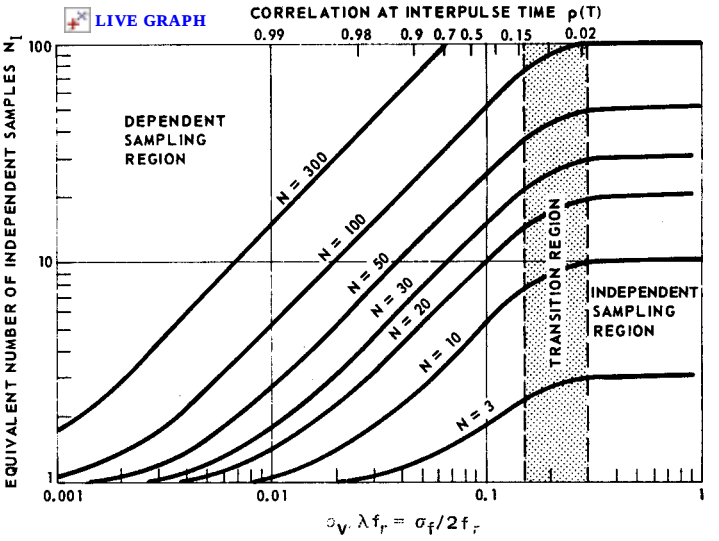

Figure 3.13 Independent samples for partially correlated waveforms (gaussian correlation function assumed).

mately at $\sigma_v/\lambda f_r = 0.2$. This figure has been derived from Eq. (3.8).* Thus, we may state, with only a small error, for

$$\frac{\sigma_f}{f_r} < 0.4 \qquad \text{or} \qquad \frac{\sigma_v}{\lambda f_r} < 0.2$$

N_I may be determined by using Eq. (3.16) or Fig. 3.13. For

$$\frac{\sigma_f}{f_r} > 0.4 \qquad \text{or} \qquad \frac{\sigma_v}{\lambda f_r} > 0.2$$

N_I may be determined by $N_I = N$. Alternately N_I may be exactly determined from Eq. (3.10).

The concept of independent sampling may be applied to detection calculations in clutter where, for target models with scan-to-scan independence, the number of pulses integrated is understood to equal N_I. Marcum and Swerling's results were obtained for noise with a chi-squared distribution of degree $2N$, which is the distribution one obtains (after low-pass filtering) when adding N independent squared gaussian variates. To be completely rigorous, one must also show that the mean

* Adapted from Lhermitte [435]. The spectrum width parameter σ_v used in this section refers to the width after envelope detection. If the predetection spectral width is available it should be multiplied by $\sqrt{2}$.

value over the period T of a correlated variable follows the chi-squared distribution of degree $2N_I$. This seems to be a reasonable assumption, since N_I was defined in such a way that the second moment of the distribution of the mean correlated variates corresponds to that of the $2N_I$-degree chi-squared distribution, but equality of higher-order moments is not necessarily assured. Residues of moving target indicator (MTI) processors are partly correlated and discussed in Chap. 14.

3.7 Digital Integrators and Limits on Independent Sampling

Virtually all postdetection integration is currently performed digitally. The actual implementation depends on the speed, and the architecture at the radar processor. The memory of the detected signals at all range gates is stored for one or more interpulse periods. This can be accomplished in a shift register configuration or in a random-access memory. With a phased array, it is often convenient to add the linear (or square-law detected) signals for the duration of the transmissions in a given duration and test the sums against a threshold. These integrated values are then "dumped" before the beam is pointed in the next direction. This is sometimes called *integrate and dump.*

With a rotating antenna, the values at each range gate are added, but $1/K$ times the sum at each range is subtracted after each transmission. This is a recursive or *leaky* integrator. K is a value that is smaller than or equal to the number of pulses transmitted per beamwidth. The value of K is usually a binary value for simplicity of implementation. The summation is tested against a threshold after every transmission. There is a small loss in this latter technique, but the ideal is difficult to achieve since the power at a given range is not constant from pulse to pulse due to the shape of the beam pattern (two-way).

The previous sections show that there are several benefits to postdetection of independent samples. In observing the target models, it was shown that detection is easier if the target fluctuates from pulse to pulse rather than fluctuates slowly if a high detection probability is desired. With a slow fluctuation, there is a significant probability that the target will be at an aspect angle that yields low reflections, and that its aspect may not change sufficiently in the integration time. If the target echo is decorrelated, the high echoes will average with the low ones. With clutter, the echo at any given time may be at a peak, and if there is little decorrelation, it may stay there for the integration time. Thus, if postdetection integration is to yield its full benefit, both target and clutter echoes should be uncorrelated. In the foregoing discussion we are referring to the temporal correlation.

Two important phenomena limit signal-to-clutter improvements by pulse integration. One is the nonstationary and nonergodic nature of the clutter statistics. The mean radar cross section of land and weather is nonuniform in space. Therefore, although pulse integration can reduce the time fluctuation of the clutter signals, this technique has no effect on spatial nonuniformities. Thus, one must set the threshold according to the statistics of the spatial fluctuation as well as those of the temporal fluctuation.

The second limitation is due to long-term correlations of some types of clutter. Sea clutter has some residual spatial and temporal correlation even after several seconds. (Ocean waves are physical structures that persist for many seconds.) Thus, the correlation functions have "tails" for several seconds and numerous range gates.

In a clutter-free environment, the threshold can be set based on the noise level and number of pulses. This is much more complicated in a clutter-plus-noise environment. One must have a measure of the number of independent samples of clutter plus noise. The best way to obtain this is to measure after the integration by determining at least the mean and variance of the output and assuming that this output belonged to some distribution family. An alternate procedure is to assume some minimum spectral width that results in a minimum number of independent samples and accept the small loss. Other procedures are given in Chap. 4.

3.8 Cumulative Detection of a Radar Target

In the previous chapter the radar equations were written to determine the range at which a target can be detected with a certain probability P_D on a single scan. In many radar situations the primary purpose is to detect approaching targets *before* they reach a given range. In general, the typical surveillance radar has been searching for targets for a considerable period of time before the S/N ratio has increased to a level that yields the desired detection probability. The probability that the target has been detected on at least one of j scans (or *dwells*)* can be written

$$P_c = 1 - (1 - P_D)^j \tag{3.19}$$

where P_c is the cumulative probability of at least one detection in j scans and P_D is the single-scan (or dwell) detection probability.

* The term *dwell* is introduced here since a surveillance radar often transmits several pulses in a single direction during one scan. Thus, the time between dwells is generally a few milliseconds, while the time between scans is a few seconds.

The first question to be addressed in this section is whether to build a linear integrator or simply to wait for a detection to occur in one of j scans. The false alarm number n' for the entire process is 10^6 in the examples.

The efficiency of looking more often and setting a higher threshold per dwell versus using a linear integrator is a function of the fluctuation characteristics of the targets and the desired certainty of detecting the target.

The required value of (S/N) per dwell has been calculated using Fehlner's [225] curves for a fluctuating target. The overall detection probability P_D is 0.9. Table 3.1 shows the (S/N) per dwell required for 1 through 1000 dwells. In one case, the threshold is slightly raised, and 90 percent of the time the target signal plus noise (at the target location) will add and exceed the threshold on one or more of the dwells. The required S/N per dwell is shown in the fourth column. The second case assumes the use of a linear integrator as discussed in Sec. 3.2. The last column in the table shows the relative improvement obtained by the use of the linear integrator.

The steady or nonfluctuating target is not very common in radar. Table 3.2 shows the relative performance of waiting for a detection versus linear integration for the Swerling case 2 fluctuating target (independent fluctuation from pulse to pulse). The last column shows that there is relatively less improvement for linear integrators with fluctuating targets. If the fluctuation is slow compared to the interpulse period, the computation becomes more difficult; but Johnson [375] has shown that cumulative detection allows only a 2-dB reduction in the required signal-to-noise ratio for $j = 4$, $P_D = 0.9$, $P_N = 10^{-6}$ and a Swerling case 3 target. If the target had the same amplitude distribution but fluctuated rapidly (case 4), the required signal-to-noise ratio

TABLE 3.1 Cumulative Detection and Incoherent Integration for Steady Targets*

Number of dwells, j	Cumulative detection statistics			Incoherent integration (S/N) per dwell, dB	Integration improvement factor, dB
	P_{Di}	n'	(S/N) per dwell, dB		
1	0.90	10^6	13.1	13.1	
2	0.684	2×10^6	12.2	10.8	1.4
3	0.535	3×10^6	11.8	9.4	2.4
4	0.44	4×10^6	11.4	8.5	2.9
6	0.32	6×10^6	11.1	7.0	4.1
10	0.206	10^7	10.6	5.5	5.1
30	0.074	3×10^7	9.7	2.0	7.7
100	0.023	10^8	9.2	−1.2	10.4
1000	0.002	10^9	8.0	−6.8	14.8

* Steady-target detection probability = 0.9, and overall false alarm number $n' = 10^6$.

TABLE 3.2 Cumulative Detection and Incoherent Integration for Fluctuating Targets*

Number of dwells, j	Cumulative detection statistics			Incoherent integration (S/N) per dwell, dB	Integration improvement factor, dB
	P_{Di}	n'	(S/N) per dwell, dB		
1	0.90	10^6	21.1	21.1	
2	0.684	2×10^6	15.6	15.0	0.6
3	0.535	3×10^6	13.5	12.4	1.1
6	0.32	6×10^6	11.1	8.9	2.1
10	0.206	10^7	9.7	6.8	2.9
30	0.074	3×10^7	7.5	2.8	4.7
100	0.023	10^8	6.0	−0.5	6.5
1000	0.002	10^9	3.9	−6.0	9.9

* Fluctuating-target detection probability = 0.9, and Swerling case 2; overall $n' = 10^6$.

is reduced by about 5.8 dB. This emphasizes the need for obtaining several *independent* looks on targets that fluctuate slowly if high detection probabilities are desired. This can be accomplished by mechanically (or electronically) scanning the antenna more rapidly so that there are several scans (and probably independent observations of the target) in the desired detection time. Alternate techniques are pulse-to-pulse frequency or polarization shifting.

Barton [45] discusses the apportionment of the number of pulses per beamwidth per scan for a given total number of pulses, and he concludes that about four scans should be used for $P_D = 0.9$, $P_N = 10^{-8}$. This is based on the rapidly fluctuating target and also considers beam shape losses. It would seem that $j = 4$ to 6 is also a good value for the slowly fluctuating target since the fluctuation loss vanishes* at $P_D \approx 0.33$. This assumes that the target return is uncorrelated from scan to scan. If there is clutter or interference, the fluctuation rate of the clutter would also have to be accounted for in the optimization of the number of scans. The linear integrator has the additional advantage of reducing the *relative* fluctuations of the clutter (discussed in Sec. 3.5).

3.9 Detection Range for an Approaching Target

Another implication of the use of cumulative detection is that the basic volume search radar equation must be modified for the case of an approaching target with uniform radial velocity. The volume search radar equation from Chap. 2 was written as

* For values of P_D of less than 0.33 at $P_N = 10^{-6}$, less (S/N) is needed for fluctuating than for steady targets.

$$R^4 = \frac{\overline{P}_T L_T A_e L_R L_P L_a L_c \sigma_t T_{SC}}{4\pi K T_s \psi (S/N)} \tag{3.20}$$

where T_{SC} is the scan time of the surveillance radar and ψ is the total solid angle to be searched.

In the approaching target case, the time that the target is within the instrumented maximum range may well be many times T_{SC}. Mallett and Brennan [459] showed that there is an optimum choice of T_{SC} (the frame time in their paper) for a constant velocity target and with the other radar parameters fixed. They make the substitution

$$\frac{\Delta}{V_c} = T_{SC}$$

where Δ = the radial distance traversed by the target in the scan time T_{SC}.
V_c = the radial closing velocity of the target.

They then define (in the notation of the previous sections)

$$R_0^4 = \Delta R_1^3 \tag{3.21}$$

$$R_1^3 = \frac{\overline{P}_T L_T A_e L_R L_P L_a L_c \sigma_t}{4\pi K T_s \psi V_c} Q_i^3 \tag{3.22}$$

where R_0 = the detection range for $(S/N) = 1$.
R_1 = an artificial range used in their optimization of Δ including the parameters of the radar.
Q_i^3 = a correction factor less than unity relating to the amount of incoherent integration performed during one scan and for false alarm numbers other than 10^6.

The interesting feature derived from this equation is that for coherent integration on each beam position, the detection range varies as the cube root of the power-aperture product for the optimum scan time.

The optimization parameter δ is then defined

$$\delta = \frac{\Delta}{R_1} \tag{3.23}$$

and varies with the desired P_c and the fluctuation model but is independent of the beamwidth, transmit frequency, waveform, and receiver bandwidth. The value of Δ for optimum performance is thus proportional to R_1, and longer-range radars should have longer frame times for a given target velocity. The frame time expression is

$$T_{SC} = \frac{\delta R_1}{V_c} \tag{3.24}$$

Coherent integration is assumed during each dwell ($Q_i = 1$). The optimum values of δ are not critical for P_c less than or equal to 90 percent, and the detection range will decrease by less than 7 percent for a range of 0.5δ to 2δ for this cumulative probability.

The resulting detection ranges with respect to R_1 for the optimum values of δ are shown in Fig. 3.14 for values of P_c from 0.5 to almost unity. The detection range varies from 0.155 to 0.196 for $P_c = 90$ percent for the three cases.

The detection range for unity (S/N) and coherent integration during each frame is expressed by

$$R_0^4 = \Delta R_1^3 = \delta R_1^4 \tag{3.25}$$

and the detection range is then

$$\begin{aligned} R^4 &= \frac{\delta R_1^4}{(S/N)} \\ \left(\frac{S}{N}\right) &= \frac{\delta}{(R/R_1)^4} \end{aligned} \tag{3.26}$$

where (S/N) is the required signal-to-noise ratio per scan.

For $P_c = 0.9$, $n' = 10^6$, and Swerling case 1, the optimum value of $\delta \approx 0.042$, and $R/R_1 \approx 0.155$. Then from Eq. (3.24)

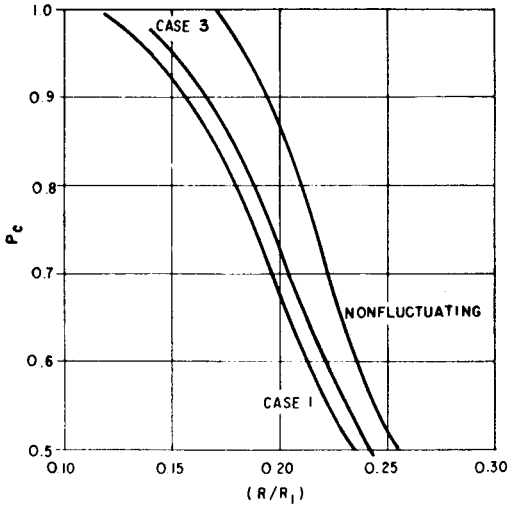

Figure 3.14 Normalized range (R/R_1) at optimum δ versus cumulative probability of detection (*After Mallett and Brennan* [*459*])

$$T_{SC} = \frac{(0.042)R}{V_c(0.155)} \approx \frac{0.27R}{V_c}$$

For a 200,000-ft detection range (≈33 nmi) and V_c = 2000 ft/s, T_{SC} = 27 s. For very high-velocity targets, such as ballistic missiles with V_c = 20,000 ft/s, the optimum scan time for 2 × 10^6 ft detection (330 nmi) is also about 27 s, showing that coherent integration should be carried out as long as possible even for the fluctuating target with P_c = 0.9 and n' = 10^8. The signal-to-noise ratio required is about 18.7 dB as compared to 21.1 dB for the single look.* For the same criteria and a steady target, the optimum scan time would be about 41 s. The use of the term *optimum* is not intended to imply an optimum detection process since it will be shown in Sec. 4.7 that track-before-detect or *sequential detection* can further increase the detection range. The detrimental case of a slowly fluctuating target can also be avoided for many targets by changing the transmit frequency from pulse to pulse. This has the effect of changing a Swerling case 1 or 3 target to a rapidly fluctuating target. This effect is expanded on in Chap. 5 on radar targets.

The discussion in Chap. 2 dealt with the basic range equation and the losses involved in detecting targets. The *S/N* ratio graphs (Figs. 2.2 and 3.3) considered the *single*-target pulse detection cases. In most radar displays the multiplicity of return pulses per beam position reduces the required (*S/N*) considerably for given detection criteria. The operator or the *cathode-ray tube* (CRT) display also acts as an integrator in a manner similar to integration in the mathematical sense as described by Marcum [461].

Detectability on displays is degraded by correlated clutter in a similar fashion to threshold devices, but the statistics are not known. In practice an operator usually can obtain the results attributed to cumulative detection probabilities. By focusing attention on a *peak* of a scintillating target, the operator can usually track the target through the nulls since the observations are localized on the display.

3.10 Summary

The basic statistics of the detection problem have been summarized without regard to the type or complexity of the receiver, the processing technique, or the transmitted waveform. It has also been shown that the amplitude distribution and fluctuating characteristics of the target have a strong effect on the required (*S/N*) and thus the detection range.

* The assumption in this case is that the target is uncorrelated after time T_{SC}.

These characteristics are discussed in Chap. 5 on the available experimental measurements and some of the theories.

The statistics of environmental noise with a significant correlation time have been covered; specific values are given in the individual chapters on clutter. The chapters on sea and land clutter also indicate where the amplitude and spatial distributions deviate from the Rayleigh law.

Various losses from coherent processing have been shown for incoherent linear integration and for displays, but it must be emphasized that detection was the criterion. In the cases where parameter estimation is the goal, the input S/N is usually high with respect to unity, and the detector losses may become trivial.

The basic shortcoming of all the information in this chapter is the assumption that there is a prior knowledge of the rms value of the noise. With clutter or jamming and in some cases when looking near the sun, galaxies, or even the surface of the earth, this information is not available; and a measurement of the total noise in any portion of space is required when setting a threshold for detection. This uncertainty also occurs with radar displays that generally have 12- to 15-dB dynamic range above receiver noise. Several of the techniques for automatically or adaptively setting a threshold are discussed in the next chapter.

Chapter

4

Automatic Detection by Nonlinear, Sequential, and Adaptive Processes

4.1 Introduction

The radar equations and the statistics of detection described in the previous chapters were based on the return signal from a target exceeding a fixed threshold. It was assumed that this threshold was established with respect to either the rms value of the system noise or the environmental noise prior to searching for the target.* In the typical surface-radar situation, environmental effects or electronic countermeasures make that assumption of limited value. Figure 4.1 shows, in an overly simplified way, the effects of the range dependence of the mean radar backscatter from various types of clutter at a transmit frequency of 3000 MHz (S-band). In this figure backscatter is normalized to the radar cross section of a target at a given range (left-hand ordinate); the right-hand ordinate is an estimate of the radar cross section of a target that can be detected in the presence of the clutter at the corresponding range. The required target signal-to-clutter ratio

* The block diagram used with the Marcum and Swerling analysis (Chap. 3) shows that the mean-square noise is measured at the time of arrival of the target echo.

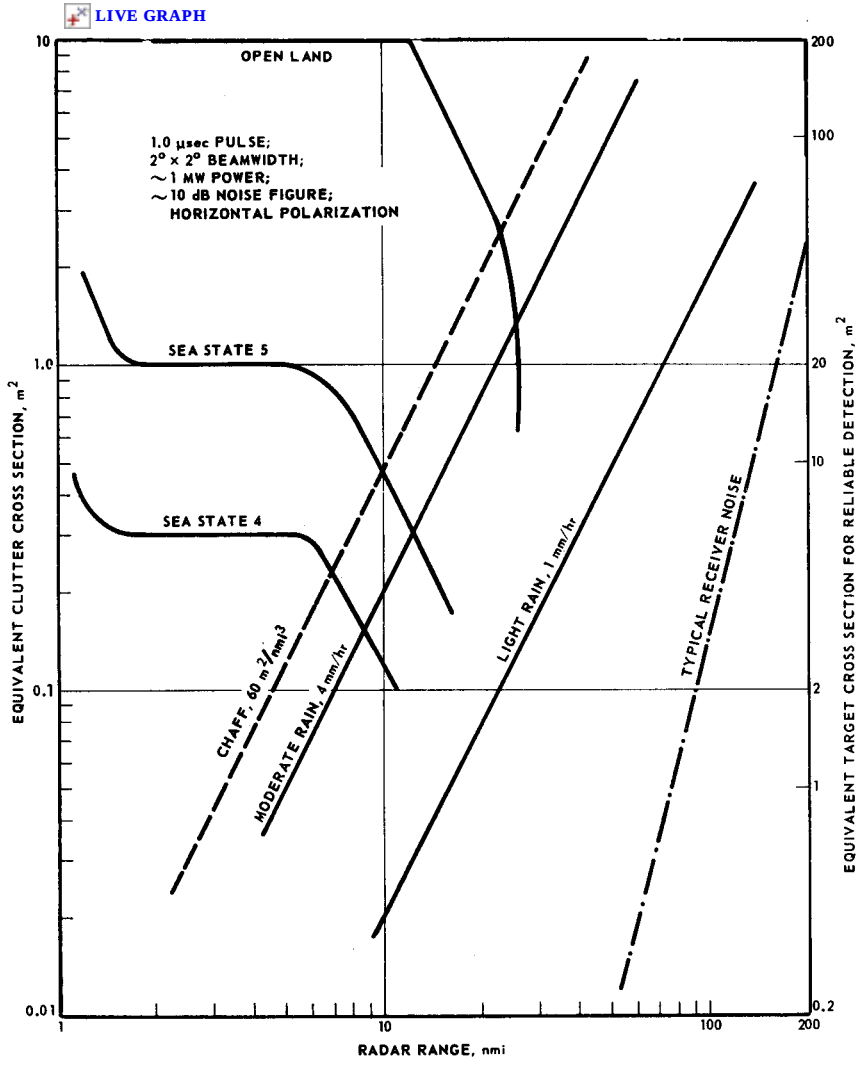

Figure 4.1 Environment for typical S-band surveillance radar (3000 MHz).

is assumed to be 20 to 1 (13 dB). This is a typical value for a narrow-beam surveillance radar. The purpose of this plot is to illustrate that:

1. The various types of radar clutter have different range dependencies and considerable time variations of intensity (rainfall rate, chaff density, sea state).
2. For the chosen parameters of the radar, the clutter effects exceed the receiver noise by several orders of magnitude.

3. The radar cross section of rural clutter is comparable to that of small aircraft (1 to 10 m^2) and far exceeds the cross sections attributed to small missiles or reentry bodies. Cultural features can be two to three orders of magnitude higher.

A graph of this nature (see also Fig. 1.2) can be prepared from the clutter equations of Chap. 2 and the clutter cross sections of Chaps. 6 and 7. It illustrates the dynamic range requirements of the receiver and the amount of clutter rejection that should be obtained with signal processing. This graph was drawn for a surface radar that is scanning the horizon* from an elevation of about 150 ft, but a similar situation exists in airborne radars. While radars for detection or tracking of satellites or planets receive less clutter backscatter, they are usually one to two orders of magnitude more sensitive and are subject to variable solar and galactic noises, atmospheric anomalies, and varying antenna system temperatures, especially at low elevation angles.

The electronic jamming problem can easily be illustrated by assuming a noise jammer with 1-W/MHz power density (P_J) and a 10-dB antenna gain (G_J). If the jammer is located at a range of 50 nmi from the radar and the radar receiver bandwidth is 1.0 MHz, the jamming noise power will exceed the receiver noise by about 50 dB.

It is obvious then that *in addition* to being designed for clutter rejection, the radar must ultimately include a threshold detector that adapts in some way to the interference at the time when (or location where) the statistical test for detection is to be carried out.

The following sections summarize some methods for accomplishing this, including the use of various nonlinear amplifiers and truly "adaptive" techniques.

4.2 Dynamic Range Problems—STC and IAGC

The dynamic range limitation of radar receivers was one of the first problems encountered in radar design. The dynamic range of a system is defined here as the larger of two ratios: the ratio of the return signal power that will saturate the receiver to the minimum detectable signal; or the ratio of the saturation signal power to the mean-square noise level.

The best operator performance is obtained with the receiver noise

* The rapidly sloping plot of sea and land clutter backscatter beyond the horizon is arbitrary. The land horizon from a ship effectively occurs at greater range than the sea clutter horizon because of hills, etc., which extend above the geometric horizon. Quantitative values of reflectivity are given in Sec. 5 on ship targets and in Chaps. 6 and 7.

visible on a PPI display. The dynamic range under these conditions is only 15 to 20 dB for the PPI and perhaps 20 to 30 dB for the A scope. Since the hypothetical radar environment shown in Fig. 4.1 has a ratio of signals in excess of 10^7 (70 dB) at a range of 5 nmi, some form of compression of the amplitude of the signals must precede the display.

One of the earliest and most widespread techniques used to cope with this problem is the *sensitivity time control* (STC) circuit. This circuit simply reduces the gain of the amplifiers at close range where maximum sensitivity is not generally required. The gain may be varied as R^n, where n may be chosen between a value of 2 for weather effects and as much as 4 for land and sea clutter. The maximum gain is reached at the range where the clutter barely exceeds the noise. Modern radars have the value of n selected by an operator. Some manufacturers have the STC before the low-noise preamplifier, while others have it following. The choice is partially dependent on the dynamic range of the receiver system.

A second technique for eliminating saturation is the *instantaneous automatic gain control* (IAGC). IAGC acts in a similar manner to the automatic volume control on a radio or TV receiver. The rectified output of the detector is integrated for several pulse widths in a low-pass filter, and this output is used as negative feedback to vary the gain of the amplifier that precedes the detector. This reduces the overall gain for extensive clutter with a slight loss in the detectability of the target signal. An alternate version of this technique can be used to counteract rapid variations in the noise level due to broadband electronic jamming. If the bandwidth of the system, including the IF amplifiers, is wider than that of the matched filter, the noise level can be sampled prior to the matched filter. If the total input noise is sufficiently broadband, the number of independent samples of the noise can be increased by the ratio of the IF to matched-filter bandwidths. This allows a better estimate of the mean-square noise. A study of such a system with a bandwidth ratio of 5 was reported by Manske [472]. With Monte Carlo methods, he showed that the degradation in the required signal-to-noise ratio was less than 1 dB compared with having a complete knowledge of the mean noise power for signal-to-noise ratios of less than 10 dB.

A third technique is based on the knowledge that the target return signal for a pulse radar has approximately the same width as the transmit pulse. By contrast, clutter returns or interference may be many pulse widths in duration. The optimization of the receiver for a given pulse width may take the form of a high-pass filter [fast-time-constant (FTC) circuit] or a pulse-width discriminator. The pulse-width discriminator inhibits return signals that are either shorter or longer than the expected target return signal. Since the spatial distribution

of most clutter returns includes many signals with an extent comparable to the pulse width, clutter rejection by these techniques alone is quite limited.

The fourth of the basic techniques is the use of a logarithmic amplifier to reduce the dynamic range of the input signals. The logarithmic receiver, when used by itself (prior to the detector), has little effect on detection* or on performance in clutter. The log-FTC circuit is discussed in [498].

4.3 Effects of Limiters on Target Detection

The use of a bandpass limiter† in the IF amplifiers of a receiver in order to compress the dynamic range of radar target signals, noise, and clutter appears to be one of the simplest means available to achieve automatic or adaptive detection of targets. On the other hand, the choice of waveform and receiver parameters (bandwidths, location, and characteristics of the matched filters, limiting level, etc.) and the calculation of the losses incurred in detection are quite complex. This section describes some of the general properties of limiters and the classes of radar waveforms that are amenable to various forms of limiting. In the absence of a detailed nonlinear analysis or simulation, it is possible only to place upper and lower bounds on some of the effects. The emphasis is on the target detection properties as a function of the various parameters, rather than on the maintenance of the fidelity of the input signal. The ability to maintain a constant false alarm rate (CFAR) for a wide dynamic range of input signals is also emphasized, along with some of the design compromises that are necessary.

The basic block diagram of a bandpass limited receiver is shown in Fig. 4.2.

Not all the blocks are necessary for all waveforms, and in some cases the functions are combined:

$S_1(t)$ = target signal of interest at a carrier frequency f_1.
$S_2(t)$ = interfering signal, such as clutter, jamming, or interference from other radars.
$N_1(t)$ = system noise (gaussian) with a bandwidth $\gg S_1(t)$ prior to filter B_1.

---

* When the outputs of a logarithmic amplifier are added incoherently, it has been shown [294] that there is 0.5-dB loss in detectability for 10-pulse integration and a 1.0-dB loss for 100-pulse integration.

† The terminology is standard but awkward. The amplitude of the waveform is *limited* by a symmetrical clipper, and, simultaneously, the bandpass of the waveform is *limited* in the frequency domain by a linear filter.

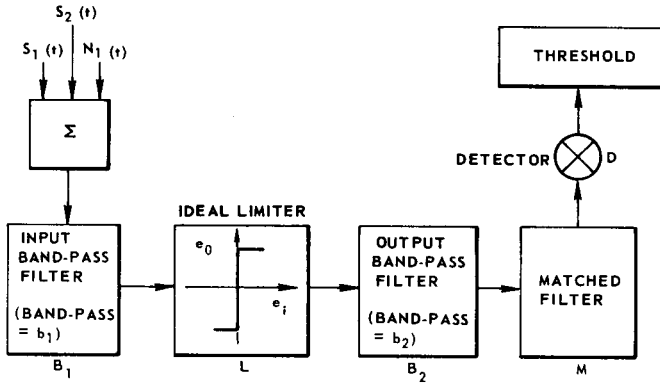

Figure 4.2 Block diagram of bandpass limited receiver.

B_1 = linear symmetrical bandpass filter with bandwidth b_1 and center frequency f_1. This may be the bandpass characteristic of the limiter itself.

L = limiter, which generally will be a "hard" limiter, by definition having the property that the output signal $e_0 = +1$ if $e_i > 0$, $= 0$ if $e_i = 0$, and $= -1$ if $e_i < 0$, where e_i = the total input signal. (The limiter bandwidth is assumed to be greater than b_1.)

B_2 = linear symmetrical bandpass filter with bandwidth b_2 (less than b_1). The bandpass filter may be the matched filter.

M = filter that is matched to the transmit waveform.

D = linear envelope or square-law detector.

T = threshold device.

Davenport [162]* analyzed the effects of hard limiting on sinusoidal signals and gaussian noise. The spectrum of the noise is assumed to be narrow and to be centered on the carrier frequency f_1 of the CW signal. The bandpass filter B_2 has an ideal rectangular passband and is also centered on f_1. The ratio of the output signal-to-noise power ratio $(S/N)_0$, prior to the detector, to the input signal-to-noise $(S/N)_i$ was shown to asymptotically approach the following values:

$$\begin{aligned} \left(\frac{S}{N}\right)_0 &\approx \left(\frac{\pi}{4}\right)\left(\frac{S}{N}\right)_i \quad \text{for} \quad \left(\frac{S}{N}\right)_i \to 0 \\ \left(\frac{S}{N}\right)_0 &\approx 2\left(\frac{S}{N}\right)_i \quad \text{for} \quad \left(\frac{S}{N}\right)_i \to \infty \end{aligned} \tag{4.1}$$

* Based on analysis techniques of Rice [593] and Middleton (see [729]). See also Sevy [647] for a discussion of modulated signals.

The output $(S/N)_0$ is almost a linear function of the input $(S/N)_i$, and the maximum loss compared with a linear receiver is $\pi/4$ or 1.0 dB.* Davenport also showed that if the hard limiter were replaced by a "softer" square-root circuit, the maximum loss would be considerably smaller than 1.0 dB.

The analyses of Davenport were extended by Manasse, Price, and Lerner [428], who showed that the 1-dB loss occurred only if the noise out of B_1 was narrow-band. They showed that, if the input signal-to-noise ratio was small and the bandwidth of the noise (at the output of B_1) approached infinity, the loss in S/N approaches 0. When the signal and noise bandwidths are about equal, the maximum loss is only 0.6 dB.† They also indicated that the limiter degradation could be reduced by proper choice of the spectrum of the noise or even by adding noise whose spectrum fell outside of the filter B_2.

4.4 Effects of Interfering Signals in Systems with Limiters

Cahn [101] showed that there is an additional degradation in the signal-to-noise ratio if there is an interfering signal $S_2(t)$ in addition to the desired signal $S_1(t)$ and receiver noise. His analysis applies when the desired signal $S_1(t)$ is much smaller than $S_2(t)$ at the limiter output. When $S_2(t)$ is also small compared to the noise, the loss approaches the 1.0-dB value reported by Davenport. On the other hand, when $S_2(t)$ is much larger than the noise [and also the desired signal $S_1(t)$] the loss in the ratio of S_1/S_2 approaches 6 dB. This is the *small-signal suppression* effect that is common in FM radio systems. In radar problems, $S_2(t)$ may represent clutter returns, the echoes from an undesired target, or interference from other radars.

Jones [377] also examined the case of two signals $S_1(t)$ and $S_2(t)$ and noise in a hard-limited receiver; two of his graphs are reproduced as Figs. 4.3 and 4.4. Figure 4.3 shows the ratio of the output signal-to-noise $(S/N)_0$ to the input signal-to-noise $(S/N)_i$ as a function of $(S/N)_i$ with the ratio of the interference S_2/S_1 as a parameter.‡

The uppermost curve $S_2/S_1 = 10^{-3}$ is the same as that derived by Davenport and shows a 1-dB maximum loss. When the interference ratio reaches 0.2 and both signals are above the noise, $S_2(t)$ affects the signal-to-noise ratio of the desired signal. When $S_2/S_1 \geq 10$ and both

* The curve illustrating this effect can be seen as the uppermost one in Fig. 4.3.

† If the interference had a distribution function other than gaussian, the maximum loss remains quite small.

‡ Rubin and Kamen [623] have analyzed the case where $S_1(t)$ and $S_2(t)$ are separately filtered after limiting.

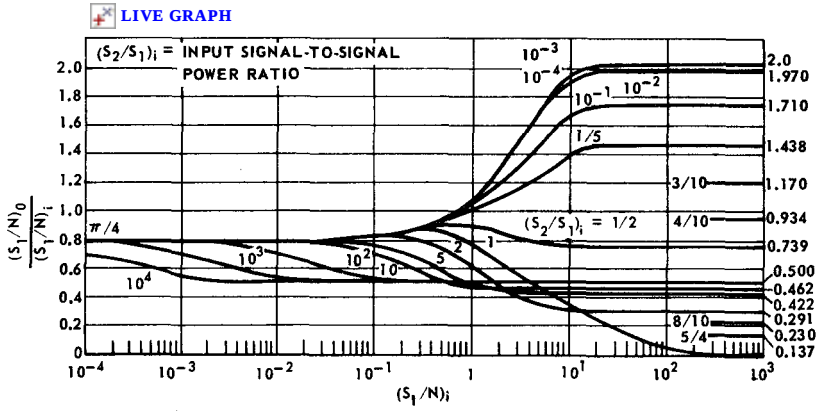

Figure 4.3 Ratio of the output SNR to the input SNR as a function of the latter for the ideal bandpass limiter. (*From Jones* [*377*])

are much greater than the noise, the signal-to-noise ratio of the desired signal is reduced by 3 dB. The intermediate cases are best described by the graph itself.

In Fig. 4.4 the ratios of the output signals are shown versus the signal-to-noise ratio of the larger signal. If both signals are less than the noise, the limiter is essentially a linear device. For two large signals, the smaller signal is suppressed by 6 dB. Some tentative conclusions would include:

1. If $(S/N)_i$ is very small, the limiting loss approaches $\pi/4$ until $S_2(t)$ dominates the limiter.

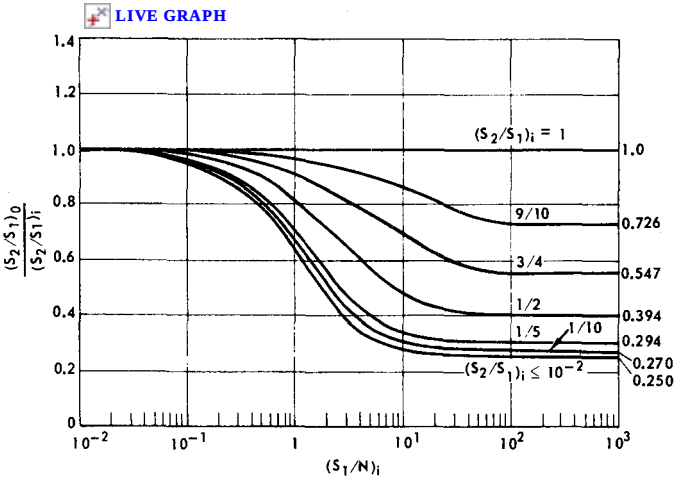

Figure 4.4 Ratio of output signal-to-signal power ratio to the input signal-to-signal ratio as a function of the larger input SNR. (*From Jones, IRE* [*377*])

2. If the interference ratio S_2/S_1 is large and $(S/N)_i$ is also large, the loss in the $(S/N)_0$ of the desired signal is 3 dB.
3. If the interference ratio is much less than unity, the loss of the desired signal in all cases is small; there is actually an improvement in $(S/N)_0$ for $(S/N)_i$ greater than unity. The increase in the $(S/N)_0$ for large $(S/N)_i$ does not improve detectability and may be applicable only to problems involving parameter estimation. An analogy can be drawn with the square-law envelope detector, which increases the output signal-to-noise ratio for large input signal-to-noise ratios but does not improve detectability, which is determined by the amplitude distribution of signal plus noise.
4. If $S_1(t)$ is within about 20 percent of $S_2(t)$ and they are both *large* with respect to the rms noise, the loss in signal strength of *either* the signal or the interference may exceed 6 dB with respect to the noise.* The loss in S/N never exceeds 6 dB for the desired signal $S_1(t)$, assuming that $S_2(t)$ is the *noise* of the system.
5. The effects of the limiter are determined by the signals and noise levels at the limiter input. The *limiter loss* (i.e., loss in signal-to-noise ratio) and the suppression of the desired signal can be reduced by increasing the prelimiter bandwidth to a point where it is much greater than b_2.

The previous discussion was based on CW systems, and the results are not easily related to the general pulse-radar detection problem. It is difficult to interpret the output of a *threshold detector* following a limiter and bandpass filter B_2 where the input is continuous, and its bandwidth and the noise bandwidth are identical. If the signal and noise spectra were identical and at the same carrier frequency, the amplitude of the limiter output would be almost constant with or without the signal being present. The implementation of a threshold type of detection system can be more easily visualized if the input noise bandwidth is much larger than the spectrum of the input signal, and the output passband b_2 is very small compared to b_1 (B_1 will be assumed to limit the noise bandwidth). In this case, the output of B_2 will be small† compared with the *maximum possible* output of the limiter.‡ It is then easy to picture a threshold device that is set well above the

* Both $(S/N)_1$ and $(S/N)_2$ at the output will remain greater than unity.

† The output noise power of the filter B_2 will be approximately b_2/b_1 times the maximum power output of the limiter for hard limiting in the absence of signal.

‡ By definition, the power output of a hard limiter has a constant value for any nonzero level of input signal, noise, or combination thereof. Alternatively, since noise, at least, is always present, a hard limiter is always saturated.

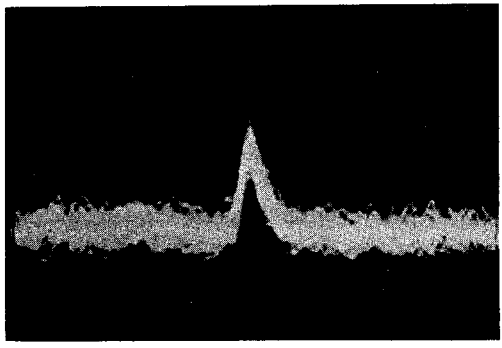

Figure 4.5 Postdetection integration of 32 hard-limited pulses. 10 dB limiting, 10-μs trace; $b_1/b_2 = 4$; $(S/N)_i = -3$ dB in b_1.

detected output of B_2 for noise alone, but below the maximum output for limiter-filter combination for $S_1(t)$ alone. As the input signal $S_1(t)$ is increased, the output of B_2 will increase almost linearly until the input signal is about equal to the total noise power into the limiter. The linear behavior of the output as $S_1(t)$ is increased is caused by the "softening" of the limiter by the wideband noise that is passed by B_1. On the other hand, the output at the detector will not be increased by an increase in noise alone if the noise spectrum is flat over the entire passband of B_1 since the added noise is mostly outside of B_2. An example of this effect is illustrated in Fig. 4.5 where b_1/b_2 is a factor of 4 and there is postdetection integration of 32 pulses. Even though the mean-square value of the input noise was 10 times that needed to limit, the output from each pulse was only about one-fourth the maximum signal output. The noise level on the display remained constant, and a signal equal to the noise could easily be seen. This represents one case of a constant false-alarm rate (CFAR) system in which the number of threshold crossings due to noise (or jammming) is independent of the total power of the input noise as long as the noise spectrum is flat.

4.5 Limiting in Pulse Compression and Pulse Doppler Systems

Experimental results were reported by Bogotch and Cook [80] who used a linear FM pulse compression signal (chirp) having a time-bandwidth product (compression ratio) of 35 to 1. In their limiter tests, $b_1 = b_2$ = the frequency deviation of the FM pulse. With a dispersed signal, the *instantaneous* signal input to the limiter is smaller than the equivalent simple pulse by the compression ratio (for the same pulse energy). Their detection tests were concerned with the case of input signal-to-noise ratios less than unity, which is common in pulse compression (PC) systems. They showed that to achieve a given probability of detection, an increase in signal-to-noise ratio of 1.0 to 2.0 dB above a

linear system was required for various values of limiting level above the rms noise.* In other tests, they report that the (S/N) for detection, with the PC system, was 1.0 dB poorer than a linear pulsed CW mode followed by a $1.2/\tau$ bandpass filter. It appears from their experiments that for a typical pulse compression system the sum of the filter mismatch and limiting losses can be held below 1.5 dB if the compression ratio is large enough and if there is no interference other than broadband noise.

In multiple-pulse coherent radar systems, such as pulse Doppler systems, the limiting loss can be minimized by a small *increase* in predetection bandwidth above a matched filter. It has been reported by Silber [661] that for a 30-pulse system with single pulse $(S/N)_i = 0.5$ and $b_1/b_2 = 2$, the detection probability dropped from 0.9 (linear system) to 0.7 (limiting). The noise was limited at its rms value, and the false-alarm probability was 10^{-9}. For higher numbers of pulses the loss in detectability drops rapidly even with small bandwidth ratios.

When the number of pulses integrated in a hard-limited coherent pulse radar system is small, the prelimiter bandwidth must be widened to permit a threshold to satisfy two conditions:

1. The threshold level must be well above the sum of the detected rms noise samples out of the filter B_2 to achieve the desired false-alarm probability.
2. The threshold level must be set below the maximum possible output of the combination of the limiter, postlimiter filter B_2, and the detector.

If there were only 10 pulses to be integrated, and $b_2/b_1 = 1$, the average sum of the noise samples would be only about 10 dB below the sum of the 10 coherently integrated signal pulses if there were no noise. The two conditions stated above could not be met for low false-alarm probabilities. The same difficulty exists for pulse compression systems with low compression ratios.

The effect of increasing the prelimiter bandwidth can be seen in Table 4.1, derived from Silber's analysis. The false-alarm probability is 10^{-9}, the limiting is *hard,* and the desired detection probability is 0.5 for 20 pulses coherently integrated.

The limiting loss in this case is the deviation of the required input signal-to-noise from the computations for a linear system. The results are pessimistic because of the low false-alarm probability $(P_N = 10^{-9})$

* The 1.0-dB value was for limiting at the rms noise level, and the 2.0-dB loss was for about 40 dB of limiting. (The rms noise was 40 dB greater than a signal that would barely limit.) The false-alarm probability was 2×10^{-4}.

TABLE 4.1 Limiting Loss for Multiple-Pulse Coherent Radar

b_1/b_2	Nb_1/b_2	$(S/N)_1$	Limiting loss, dB
1	20	$\gg 10$	$\rightarrow \infty$
2	40	1.1	≈ 3.2
3	60	0.57	2.1
4	80	0.38	1.6
5	100	0.29	1.4
∞	∞	0	1.0

NOTES: $N = 20$ pulses
rms noise = 20 times the limit level
$P_D = 0.5, P_N = 10^{-9}$
$(S/N)_1$ = ratio of the signal power to total noise power in filter B_1 (per pulse)

and the assumption that the rms noise is at least 13 dB above the limit level (very hard limiting). It can be seen that as the prelimiter bandwidth is increased and the input signal-to-noise ratio approaches zero, the 1-dB loss figure reported by Davenport is reached.

A more general curve from Silber [661] (Fig. 4.6) shows the limiting loss as a function of the ratio of rms noise-to-limit level for several values of input signal-to-noise ratio. As the input noise-to-limit level ratio is decreased, the limiting loss is decreased; however, at the same time the CFAR action of the limiter is degraded, and an increase in the input noise level due to narrow-band jamming or clutter increases the false-alarm rate P_N by several orders of magnitude. The 1.0-dB increase in the limiting loss in going from 0 to 40 dB limiting, reported by Bogotch and Cook [80], is in agreement with Fig. 4.6. Their input signal-to-noise ratio varied from -15 dB to unity.

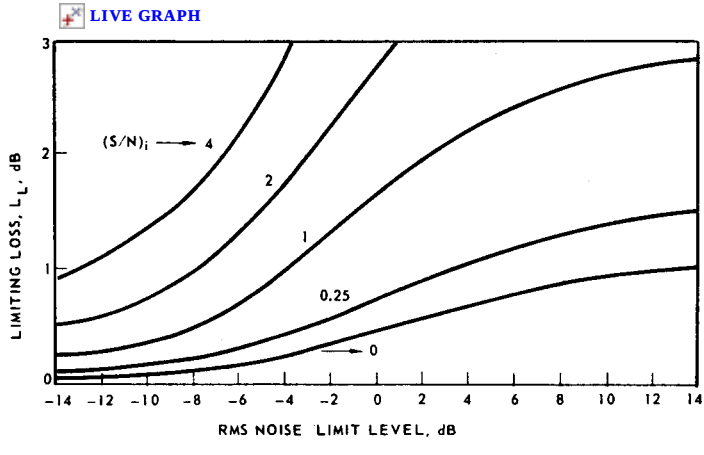

Figure 4.6 Signal loss due to limiting as a function of hardness of limiting with input signal to noise as a parameter. (*From Silber, IEEE [661]*)

4.6 Summary of Limiter Effects

The broadening of the spectrum of the *noise* input to the limiter has been shown to be effective in minimizing the limiter loss while maintaining a constant false alarm probability P_N. The retention of a low value of P_N in the presence of clutter $S_2(t)$ is a much more difficult problem. The spectrum of the clutter echoes has approximately the same width as the transmit signal $S_1(t)$ in pulse radar systems, and a widening of the input filter will only have a second-order effect unless both $S_1(t)$ and $S_2(t)$ are small. Since the clutter looks like a signal, the output of the postlimiter filter B_2 can also approach the maximum signal output for simple pulse radar systems with only clutter signals.

In multipulse or pulse compression systems, radar clutter often appears noiselike at the limiter. If the clutter is similar to noise and the number of pulses *or* the compression ratio is very large, the loss would seem to revert to the 1.0-dB maximum of Davenport's continuous signal analysis with *narrow-band noise*. The results of an experimental work on the influence of strong interference is the previously cited paper by Bogotch and Cook [80]. They added a second chirp signal $S_2(t)$ to their limiter, displaced in time from the desired chirp signal $S_1(t)$, and measured the detection probabilities of $S_1(t)$ as a function of the overlap of the signals and the ratio $S_2(t)/S_1(t)$. The probability of detection of the desired signal dropped rapidly as $S_2(t)/S_1(t)$ exceeded unity for the case of 75-percent overlap. The limiting loss in these cases was quite high when the input signal-to-noise ratio $(S/N)_i = +0.8$ dB, and was substantial even when $(S/N)_i$ was -5.2 dB. These severe losses can be attributed to two design requirements that are of great importance in the use of limiters for pulse radars as contrasted with communication systems:

1. The compression ratio or time-bandwidth product in the Bogotch and Cook experiment [80] was only 35 to 1 and leaves little margin between the threshold and the maximum signal output. This can be seen from Table 4.1 (from Silber's analysis) by noting the loss for values of Nb_1/b_2 between 20 and 40. High pulse compression ratios are needed for CFAR action in the presence of clutter echoes. The required ratio depends on P_N.
2. In a pulse radar detection system, the important criterion is the false-alarm rate in the absence of a target signal. The suppression of the noise by interference allows a reduced threshold *only* if the interference exists continuously. The cited studies of continuous interference can only lead to quantitative clutter calculations if the results can be modified for intermittent interference. If the system designer is to take advantage of the noise reduction by intermittent

interference, the threshold level must be adaptive. This is discussed in Sec. 4.10.

Some special cases of limiting and digital quantization are expanded in connection with phase coding and digital processors, described in Chaps. 12 and 14 and in Ref. [695].

4.7 Sequential Detection and Track-Before-Detect Processing

In the previous discussions of detection by means of setting a threshold after the detector, no justification was given as to what constitutes an optimal decision procedure. A technique, which has enjoyed wide acceptance in hypothesis testing, is known as the method of *maximum likelihood* or *probability ratio test* [161]. The likelihood function is the ratio of the probability density of signal-plus-noise to noise alone. From this function a statistical test for radar detection can be established that minimizes two errors:

1. Declaring that a target is present when in fact there is only noise (or clutter, jamming, etc.). The probability of this occurrence is the false alarm probability P_N.
2. Declaring that a target is not present when in fact there is a target signal. The probability of this "false dismissal" is simply 1 minus the probability of detection P_D.

From the likelihood function (or its logarithm) it is possible to compute the signal-to-noise ratio out of a matched filter that is required for a given P_D and P_N. This procedure will yield graphs similar to Figs. 3.3 through 3.6. If the returns from N incoherent pulses are collected and the signal-to-noise ratio on each pulse is small, a square-law detector followed by a linear integrator is a good approximation to a maximum-likelihood detection criterion [328].

Sequential detection

In the analysis of Chap. 3 it was assumed that N was fixed for a given beam position. In sequential testing the same procedures may be followed except that the sample size N is not fixed and two thresholds are used [742, 561]. One pulse is transmitted, and the echo is observed for a given range cell. A decision as to whether a target is or is not present can often be made on this information, and there is no need for further transmissions in that beam position. If, on the other hand, the signal has an intermediate value and a decision cannot be made,

a second pulse is transmitted in the same direction as the first, and its echo is added to the first. This is illustrated by Fig. 4.7 [561]. The upper and lower thresholds are represented by the dashed lines, and the ordinate is the integrated video voltage. A "decision" is made whenever the integrated video either exceeds the upper threshold (a detection) or falls below the lower threshold, indicating that a target echo of a given strength is not likely (a dismissal). Pulses are transmitted in the same direction until one or the other decision is made in the range cell of interest. It was shown that on the average fewer are required (less transmission time) in a given beam position than with a fixed sample size [328]. For a single range bin Preston [551] has shown that for $P_D = 0.9$ and $P_N = 10^{-8}$, less than one-tenth the time of that of a classical detector is needed to determine the absence of a threshold signal. In the presence of a threshold signal about one-half the time is required. Alternately, the time saving can be traded for increased sensitivity.

In a search radar, numerous range cells must be observed in a given beam position, and the absence of a signal crossing the lower threshold in any one of these bins becomes less likely. For a $P_D = 0.86$ and $P_N = 3 \times 10^{-11}$ with 30-, 100-, and 300-range cells per sweep, the probability ratio sequential detector yielded 4.4-dB, 3.6-dB, and 3.2-dB improved sensitivity. These values were for binary quantized video and would be somewhat higher for linear integration. Similar improvements are reported by Helstrom [328].

With a rotating radar the practical improvement is less dramatic since the time saved cannot be used to transmit pulses in another beam position. Alternately, if both thresholds are lowered to increase the sensitivity, the number of samples may increase to where the test has

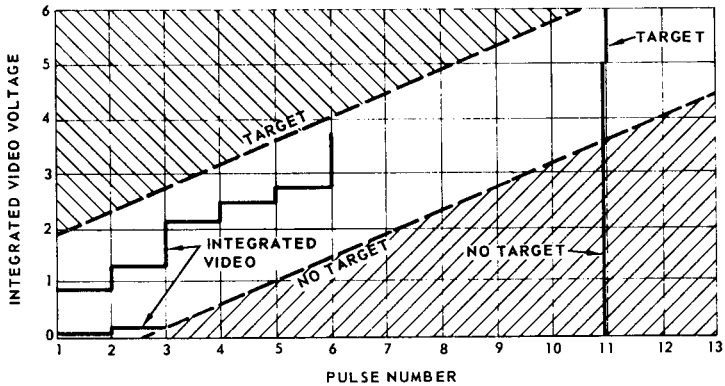

Figure 4.7 Pulse sequence illustrating probability ratio sequential detector for single range bin. (*After Preston, IRE [561]*)

not been completed before the antenna has moved to a new beam position because of near-threshold signals or clutter. For these reasons the primary interest in sequential detection is in array radars or in cases where average transmitter power needs to be reduced part of the time.

The problems of the time-varying threshold of the radar "hanging up" in a given beam direction have precluded the recommendation of "basic" sequential detection even for array radars. Several simpler procedures have been proposed to limit the number of decisions and the maximum time per beam position. Helstrom [327] proposed a two-step procedure in which the integrated sum of n pulses is compared with a threshold. If the threshold is not crossed in any of the range cells, the antenna beam is moved to the next sector. If the threshold is crossed in one of the cells, m additional pulses are transmitted and added to the previous n. The sum is then compared to a second threshold, and a firm decision is made as to whether there is a target. Essentially "most signal detection takes place in the first stage, with the second stage serving to keep down the rate of false alarms" [327]. The improvement over a single-threshold system varies with the input signal-to-noise ratio and the choice of n and m, but 2- to 3-dB improvement is reasonable.

A somewhat similar procedure has been described by Finn, which he calls *energy variant sequential detection* [228, 231]. A single pulse (or pulse train if more energy is required) is transmitted, and the return compared with a threshold. If the threshold is crossed, a second, higher-energy pulse is transmitted and the signals compared with a second threshold. If both thresholds are crossed in the same range bin, a detection is declared. For 100- or 300-range bins per sweep 3- to 4-dB power savings are obtained. An additional 0.5 dB is gained by adding a third step to the process. Brennan and Hill [89] studied the cumulative detection probability using this technique for the four Swerling target models. Similar improvements are obtained, and they show that for the slowly fluctuating targets (cases 1 and 3), it is desirable to transmit the second pulse immediately after the first, since first-pulse detection implies a favorable target cross section σ_t at that time. Unfortunately, if a clutter echo has crossed the first threshold, it will probably cross the second one as a result of the relatively long correlation times of clutter echoes. Finn and Johnson [231] studied the situation in which strong clutter signals are present, but these clutter signals are uncorrelated from pulse to pulse. Significant improvement is still obtained over the simple threshold if the clutter can be decorrelated by leaving sufficient time between transmissions or by frequency agility; however, both types of detections till suffer from the existence of the strong clutter signals.

A final limitation on the use of sequential detection is the current tendency toward high-resolution radar. For most of the sequential techniques, the improvement drops to about 2.5 dB for 1000 range or Doppler cells per sweep and even less for 10,000 cells (with energy variant sequential detection). With 100 or more cells per sweep the second transmission should have considerably more energy than the first. When high resolution (many cells) is a requirement for target sorting, it is desirable to use a lower-resolution waveform for the first pulse followed by a second or third waveform of higher resolution.

Track-before-detect processing*

Track-before-detect (TBD) processing accomplishes many of the goals of noncoherent integration. As with other forms of integration, the primary objective of TBD is to enhance target detectability, either by increasing the detection range for a given *radar cross section* (RCS) or by maintaining the detection range of the system as the RCS is reduced. Unlike other forms of integration. TBD is applied over multiple observation intervals, or dwells, of the radar rather than over the multiple-pulse repetition intervals of the radar waveform that constitute an individual dwell. Consequently, the time between updates of the TBD process is typically on the order of seconds, not milliseconds. Significant target motion can occur between updates. Thus, it is necessary to associate over several updates the resolution cells that correspond to possible target motions. The name *track-before-detect* is derived from the fact that a sequence of associated resolution cells, comprising a time history of target position or track, exists in the memory of the radar signal processor before a detection is declared.

To minimize the processing load that is imposed by TBD, integration of the signal from dwell to dwell is performed by means of coincidence, or M-out-of-N, methods rather than by direct summation of the amplitudes of the received signals. For each value of N there is an optimum value of M, which has been shown to yield an integration gain of, nominally, N to 1.

Assuming a scanning coherent radar with the ability to measure the range (R), range rate (v), and azimuth angle (Θ) of the target, the TBD algorithm consists of the following set of procedures:

1. Coherently integrate the received radar signals over the dwell time of the scanning radar beam.

---

* Contributed by A. Corbeil, J. DiDomizio, and R. DiDomizio; Technology Service Corporation, Trumbull, Connecticut.

2. Compare the integrated signals in each resolution cell on each scan to an amplitude threshold, which is set lower than normal.
3. Over a number of scans N, form sets of associated cells, called *templates,* which correspond to possible target motions.
4. In each template, count the number of scans for which the amplitude threshold is exceeded, calling this number m.
5. Declare a target detection if in a template $m \geq M$, where M is a selected integer less than N.
6. Continue to form new templates and extend those that have yielded detections by repeated application of the rules of association.

The pulse-to-pulse integration in the first step is typically performed in each range-azimuth resolution cell by means of a pulse Doppler processor often using the complex FFT algorithm. In each range-azimuth-Doppler cell that results, a magnitude is computed from the in-phase and quadrature outputs of the FFT and compared to the amplitude threshold. The amplitude threshold is typically set 0.5 to 1.0 dB lower than normal to increase the detectability of the target. The increased number of potential false alarms that are generated is eliminated by the formation of the templates in steps 3, 4, and 5.

Template formation involves predicting the future position of a target from measured data and postulated maneuvers. The predicted positions are accompanied by multidimensional windows to allow for the uncertainties in target motion. Any given threshold crossing is associated with a previous threshold crossing if it falls within the association window. Range-Doppler and range-azimuth windows are shown in Figs. 4.8 and 4.9. The windows are projected ahead from the range, velocity, and azimuth values (R_i, v_i, and Θ_i) for each threshold crossing on scan i. The size of the windows is a function of the radar measurement errors (δ_R, δ_V, and $\delta_S = R\delta_\theta$), the elapsed time between threshold crossings (Δt), and the maximum velocity and acceleration ($v_{\max}$ and a) that are assumed for the target. If it is assumed that the range change between successive threshold crossings is related to the velocities measured on the two scans, then the rectangular range-Doppler association window in Fig. 4.8 is reduced to the narrow diagonal strip, or correlation window, as shown.

The simulated range-azimuth and range-Doppler displays of Figs. 4.10 to 4.13 illustrate the advantages of the correlation form of TBD processing. Each range-azimuth display extends from 10 km to 70 km, and covers a sector of 120°. Each range-Doppler map covers the same 60-km range swath, and extends from -160 m/s to $+160$ m/s. The radar is assumed to have a scan period of 5 s and resolutions of

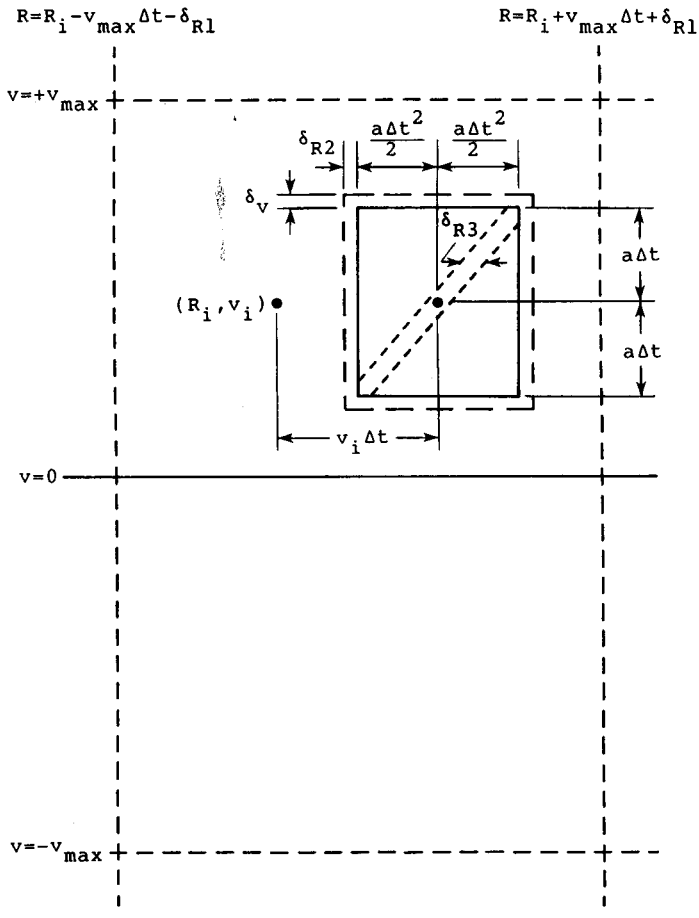

Figure 4.8 Definition of range-Doppler windows.

$$\Delta R = 150.0 \text{ m}$$
$$\Delta v = 5.0 \text{ m/s}$$
$$\Delta \Theta = 2.5°$$

in range, range-rate, and azimuth, for a total of 1.2×10^6 resolution cells. The target enters the surveillance coverage on the first scan, at a range of 70 km and a signal-to-noise ratio (SNR) of 3 dB. Flying a diagonal trajectory, at a constant velocity of 140 m/s, the target exits the surveillance coverage after 100 scans at a range of 36.6 km and a SNR of 14.3 dB.

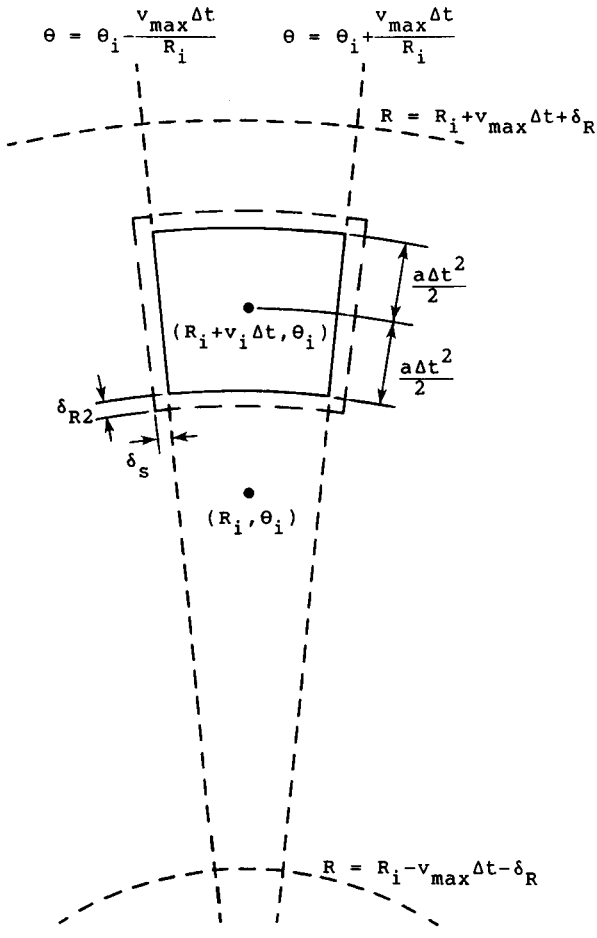

Figure 4.9 Definition of range-azimuth windows.

Figures 4.10 and 4.11 show the threshold crossings on all 100 scans for the normal setting, which yields an input probability of false alarm in each resolution cell (P_{fa}) of 10^{-7}, and the TBD correlation setting, for which $p_{fa} = 1.9 \times 10^{-6}$. The association windows, which are generated for each threshold crossing, are shown in Fig. 4.12, assuming a maximum target velocity of 160 m/s and a maximum target acceleration of 10 m/s^2. The TBD outputs are shown in Fig. 4.13, for a 2-of-10 coincidence logic, which is optimum for a 10-scan process. The number of false alarms in Fig. 4.13 is, on the average, equal to the number of false alarms in Fig. 4.10.

A quantitative assessment of TBD processing is provided in Table 4.2, assuming an output probability of detection (P_D) of 0.8 and an

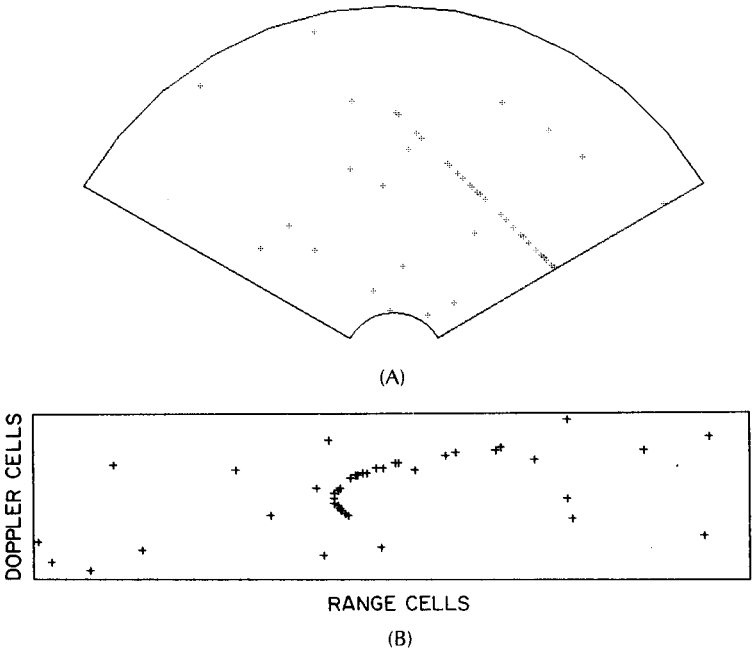

Figure 4.10 Single-scan threshold crossings. (A) Range-azimuth coordinates; (B) range-Doppler coordinates.

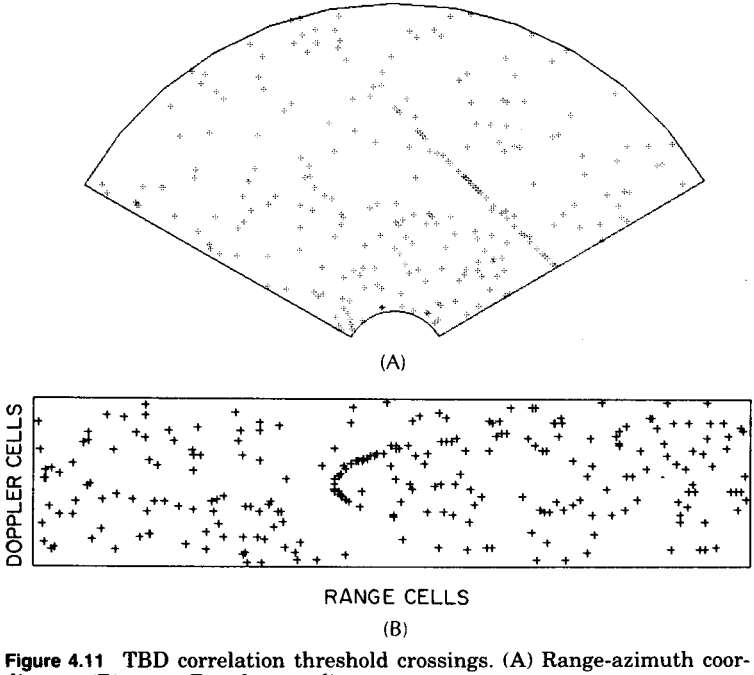

Figure 4.11 TBD correlation threshold crossings. (A) Range-azimuth coordinates; (B) range-Doppler coordinates.

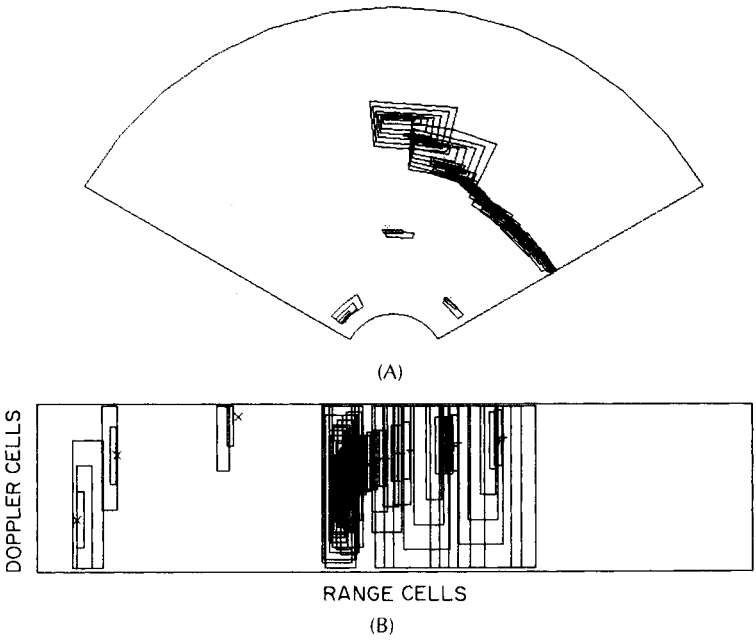

Figure 4.12 Formation of association windows. (A) Range-azimuth coordinates; (B) range-Doppler coordinates.

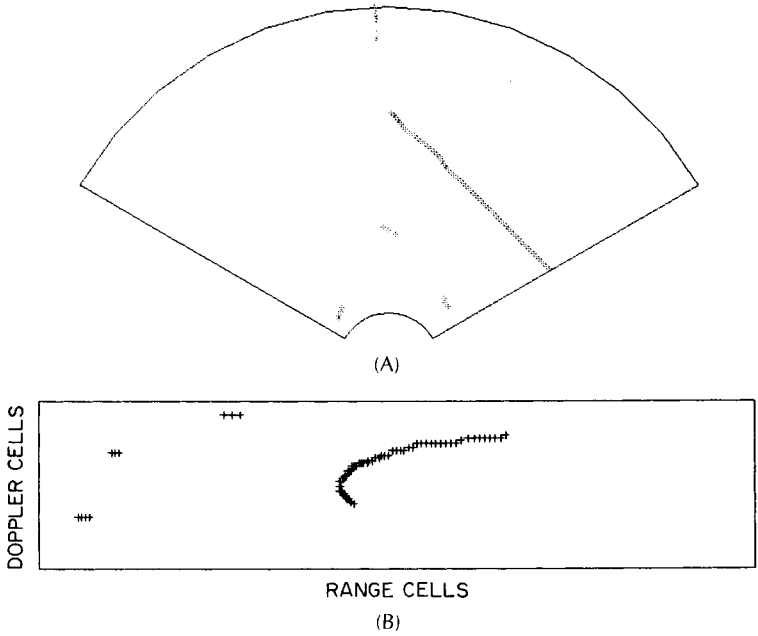

Figure 4.13 TBD correlation outputs. (A) Range-azimuth coordinates; (B) range-Doppler coordinates.

TABLE 4.2 Comparison of Integration Performance

Process	M	N	P_{fa}	P_d	SNR (dB)	ΔSNR (dB)
Single scan	1	1	1.0×10^{-7}	0.800	18.5	0.0
TBD-association	2	10	3.6×10^{-7}	0.271	10.1	8.4
TBD-correlation	2	10	1.9×10^{-6}	0.271	9.6	8.9
Coincidence	3	10	1.3×10^{-3}	0.381	7.7	10.8
Summation	. . . .	10	1.0×10^{-7}	0.037	5.9	12.6

output probability of false alarm (P_{fa}) of 10^{-7}. The table compares five processes in order of increasing SNR improvement (ΔSNR). For single-scan detection, the input probabilities of false alarm and detection p_d are equal to the output probabilities. For a Swerling 1 target, an SNR of 18.5 dB is required to achieve a P_D of 0.8. TBD association and correlation require 8.4 and 8.9 dB less SNR, using the optimum 10-scan logic. Correlation processing is superior to association processing because of the smaller window dimensions. Coincidence detection is nominally 2 dB better than TBD integration, but 2 dB worse than the noncoherent summation of target amplitudes. The calculations for both coincidence detection and noncoherent integration assume that the location of the target is known to within a single resolution cell. Thus, the corresponding performance measures represent the upper bounds on scan-to-scan integration improvement. Coincidence performance is quoted for 3-of-10 logic because, with no position uncertainty, 3-of-10 logic is superior to 2-of-10 logic. The noncoherent integration calculation uses Swerling 2 statistics, because the target is assumed to decorrelate from sample to sample.

Integrating over 10 scans, TBD is able to provide a significant increase in detection performance while allowing for the uncertainties of target motion and imposing only a relatively modest increase in signal processing. SNR improvements of 8.5 to 8.9 dB are equivalent to increasing the maximum range of a system by 60 to 70 percent. Alternatively, targets having an RCS nearly an order of magnitude smaller than normal can be detected to the original maximum range.

4.8 Adaptive Threshold Techniques

Melvin L. Belcher, Jr.

The use of hard limiters, sensitivity time control, and logarithmic amplifiers followed by the various forms of pulse width discrimination constitutes an attempt to adapt the radar to its environment by acting on the total signal prior to the threshold detector. A more robust alternative is to estimate the total signal input in a reference channel close to the time when a possible target signal arrives at the threshold.

Some parameter of the total signal that is measured over a period of time F and Doppler is then used to vary the threshold level by some statistical law (maximum *likelihood, etc.*).

This technique is not new; it is implied in the analysis of Marcum [461], in which he assumed that the noise level is measured prior to the determination of the threshold. The same procedure can be used for a general environment composed of noise, jamming, and clutter if the probability density function and power spectral density of the interference are known. The threshold is established as a function of the reference channel, which must contain a sufficient number of samples of the environment so that its output is an accurate measure of what will occur in the signal channel.

Constant false alarm rate detection processing

The input to the detection processor is generally the sampled range-gate/Doppler-filter outputs. A single-dwell detection processor is depicted in Fig. 4.14. Signal processing prior to this point emulates matched filtering subject to hardware implementation and sidelobe weighting constraints so as to maximize signal-to-noise ratio. Matched filtering provides appropriate signal processing for the detection and amplitude estimation of signals embedded in gaussian noise independent of the statistical criterion utilized in the detection processor [620].

The detector law operation at the input to the detection processor

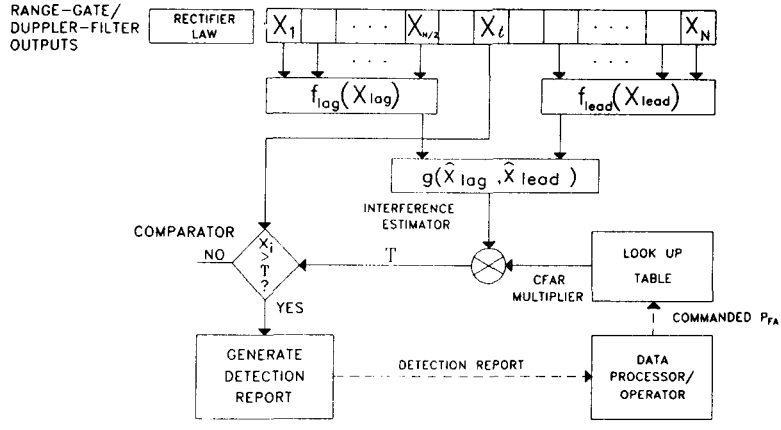

$f_\ell(\underline{X}_\ell)$ = STATISTICAL PARAMETER ESTIMATOR OF ℓth REFERENCE WINDOW SEGMENT

$g(\hat{X}_\ell, \hat{X}_m)$ = COMPOSITE STATISTICAL PARAMETER ESTIMATOR

Figure 4.14 Generalized CFAR processor ($P_D = 0.9$).

denotes the conversion of the IF or in-phase and quadrature baseband signal components into unipolar video. The video-converted samples are input to the detection-decision processor. Detection-decision processing consists of a binary decision at the output of each range-gate/Doppler-filter cell between two hypotheses: target-absent H_0, and target-plus-interference-present H_1. This decision is generally implemented by comparing the test sample magnitude x_i with a threshold value such that

$$\begin{aligned} x_i &< T \text{ implies } H_0 \\ &> T \text{ implies } H_1 \end{aligned}$$

Detection processors are generally designed to provide constant false alarm rate (CFAR) performance. The processor adjusts the detection threshold as a function of the local interference estimate based on the design false alarm probability and the CFAR algorithm. The actual short-term false alarm rate varies from that implied by the design value. CFAR thresholding prevents data processor or operator performance from being degraded by excessive return reports due to the combined effects of thermal noise, clutter returns, and other interference sources.

Each sampled range-gate/Doppler-filter output is termed a *cell;* the *test cell* denotes the output undergoing the detection decision test, X_t. Interference is estimated across a local area termed the *reference window,* which is centered around the test cell. The CFAR window may be implemented across range, Doppler, angle, time, or some combination of these measurement dimensions such that the associated interference samples can be assumed as generally homogeneous and representative of the test sample. Similarly, the extent of the reference window is generally constrained by the anticipated correlation interval of the background interference.

As indicated in Fig. 4.14, $f_{\text{lead}}(X_{\text{lead}})$ and $f_{\text{lag}}(X_{\text{lag}})$ are the interference estimation functions applied to the subwindows adjoining the test cell where X_l is the data-vector of samples composing the lth window region. The interference estimates from the two subwindows are combined to form the composite interference estimate via the $g_{(X_{\text{lead}}, X_{\text{lag}})}$ operation depicted in the figure. It is assumed for convenience that each subwindow is composed of $N/2$ samples and that $f_{\text{lead}(X)}$ and $f_{\text{lag}(X)}$ are identical estimation functions.

CFAR processors often utilize one-parameter processing where the assumed local interference probability density function within this region is characterized by a single statistical parameter, such as the mean. The associated detection threshold can be calculated by multiplying this interference estimate by a constant termed the *CFAR multiplier.*

The CFAR multiplier can be derived by following the approach of Neyman and Pearson and devising a likelihood test [230]. In short, this approach satisfies the CFAR criterion of maintaining a constant probability of false alarm while maximizing detection probability. Calculation of the CFAR multiplier presupposes a specific probability density function for the background interference as well as the desired probability of false alarm.

Characterization of the background as homogeneous denotes that each sample output possesses the same probability density function with identical statistical moments. The radar output cells are generally modeled as an ensemble of independent samples of the interference. In practice, range gates, Doppler filters, and beam positions overlap to suppress straddling losses so that significant intercell correlation exists. Intercell correlation reduces the number of independent samples available to estimate the local interference statistical parameter as described in Secs. 3.5 to 3.7.

Most operational CFAR processors employ some variation of *cell-averaging CFAR* (CA-CFAR or CA). CA-CFAR provides an unbiased minimum variance statistical estimate of homogeneous interference within the reference window. The detection threshold is calculated for a one-dimensional CA-CFAR window containing N samples as

$$T = k_{\text{ca}} \left[\sum_{i=1}^{N/2} x_i + \sum_{i=N/2}^{N} x_i \right]$$

Note that the $1/N$ factor has been incorporated into the CFAR multiplier. This implementation eliminates the real-time division that would be required to compute the mean.

The test cell should not be included in the local interference estimation. A strong target return present in the reference window would cause the local interference level to be overestimated and elevate the detection threshold. The summation should also omit the central L cells on each side of the test cell. These guard cells prevent a cell-straddling target return from contaminating the interference estimate.

The probability of detection for a single-pulse Swerling 1 return may be calculated as

$$P_D = \left[1 + \frac{P_{\text{fa}}^{-1/N} - 1}{1 + S/N} \right]^{-N}$$

where S/N is the average signal-to-noise ratio of the target.

CFAR techniques are often evaluated in terms of CFAR loss. CFAR loss is the incremental S/N required by a given CFAR threshold estimation scheme to achieve a specified detection probability over that required with known background interference. CFAR loss is effectively

the *S/N* margin required to accommodate the error imposed by the local interference estimation technique. Accordingly, CFAR loss increases with decreasing number of reference window samples since the variance of the interference estimate is inversely proportional to N. CFAR loss also increases with decreasing false alarm probability since the acceptable estimation error decreases.

The CFAR loss for a Swerling 1 target is plotted in Fig. 4.15 as a function of the number of independent reference cells for various false alarm probabilities. Note that CFAR loss can be kept below 1 dB at reasonable false alarm probabilities by choosing a reference window affording in excess of 32 samples. Nitzberg has noted that CFAR loss is roughly constant among the Swerling fluctuation models including the nonfluctuating target case [509].

Heterogeneous interference can be characterized somewhat empirically as exhibiting marked variation in statistical parameters within the CFAR reference window. In general, the interference PDF, as well as the mean power, can vary from cell to cell in a heterogeneous environment. In the context of this description, the interference is assumed to share a common PDF and to vary only in statistical moments unless otherwise noted.

The primary degradation effects due to heterogeneous interference are masking and clutter-edge false alarms. Target masking is due to the presence of strong interfering signals within the CFAR window that cause the interference to be overestimated so as to elevate the detection threshold above the optimum value. The target return is effectively masked since it is below the detection threshold even though the return may possess a substantial *S/N* relative to the interference in its cell. Masking can occur in multiple-target scenarios such as aircraft formations or as a consequence of a composite target return extending across multiple resolution cells.

Rickard and Dillard have derived analytical expressions to charac-

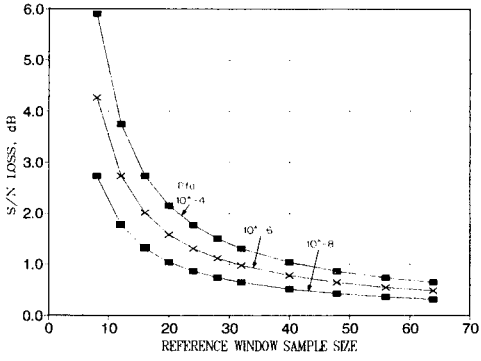

Figure 4.15 Adaptive detection or CFAR loss for Swerling 1 targets versus number of independent noise samples m to set threshold (P_D = 0.9).

terize the limiting detection probability cases for infinite target S/N with an interfering return located in the CA-CFAR reference window for all combinations of Swerling targets and interferers [259]. Ritchey has developed an expression to calculate S/N-dependent detection probability for a Swerling 1 target with reference cells contaminated by interfering Swerling 1 and nonfluctuating targets [598]. Figure 4.16 compares CA-CFAR detection performance as a function of average S/N for various interference cases. Note that a relatively modest average ratio of interfering signal to target return results in significantly degraded detection performance. Similar masking effects occur when the edge of an extended clutter region is located within the reference window.

In most applications, the system level impact of masking should be evaluated in terms of its impact on cumulative detection range [91]. *Cumulative detection range* is the range by which a radar system attains a specified cumulative probability of detection across multiple scans for a given target model, closing-rate and scan-period product, and

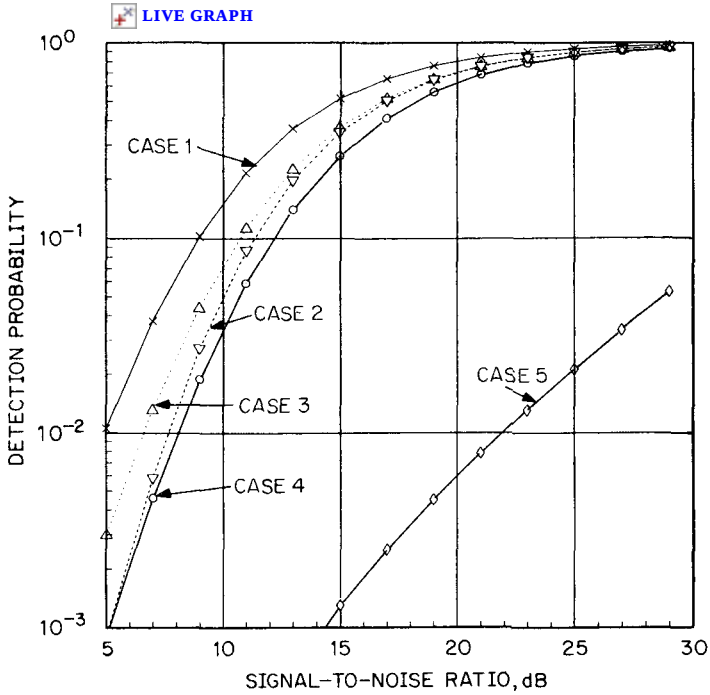

Figure 4.16 CA-CFAR detection performance with masking. Case 1: homogeneous interference; case 2: 1 nonfluctuating interferer with INR = 10 dB; case 3: 1 nonfluctuating interferer and 1 fluctuating interferer with INR = 10 dB; case 4: 2 nonfluctuating interferers with INR = 10 dB; case 5: 1 fluctuating interferer with INR = 30 dB.

environment scenario. Assessment of detection performance in heterogeneous interference environment requires consideration of scan-to-scan target and interference fluctuations as well as statistical characterization of extended clutter regions. Single-scan detection performance is important in scenarios such as those involving detection constrained by the radar horizon.

Clutter region transitions in the CA-CFAR reference window also elevate the false alarm probability beyond the design value. Specifically, the presence of relatively weak interference samples in the reference window taken outside the clutter field causes the detection threshold to be underestimated relative to a strong clutter return with the test cell. Moore and Lawrence noted that clutter region transition in interference power results in the false alarm probability increasing from a nominal value of 10^{-6} to 10^{-3} for CA processing with $N = 32$ [483].

Techniques for heterogeneous interference

A number of modifications have been proposed to enhance the robustness of CA-CFAR performance against heterogeneous interference by changing the detector law or incorporating an element of decision making into the interference estimation process. CFAR techniques designed to afford more robust performance in heterogeneous interference impose a larger CFAR loss than CA loss against homogeneous interference, assuming identical reference window sizes. This performance disadvantage is potentially offset by the corresponding capability to support larger reference windows without significant performance degradation. Robust CFAR processors may be designed with improved homogeneous interference performance by employing larger reference windows than could be tolerated by CA operation in a heterogeneous interference environment.

Greater-of-cell-averaging CFAR (GOCA-CFAR) uses the larger of the lead-window mean and lag-window mean as the local interference mean. This technique effectively suppresses false alarms at clutter edges while imposing an additional CFAR loss on the order of 0.1 to 0.3 dB [312]. However, GOCA degrades target-masking performance as the detection decision threshold is captured by a strong interferer in either window.

Trunk suggested the use of *smaller-of-cell-averaging CFAR* (SOCA-CFAR) to suppress target masking [701]. SOCA uses the lesser of the lead-window mean and lag-window mean as the local interference estimate. This technique is effective in preventing target masking if strong interference is limited to one of the two windows. However, the SOCA false alarm probability increases markedly at clutter edges. Hence, it appears unsuited for interference environments characterized

by relatively high interfering signal density or extended interference regions.

Moreover, this technique imposes a large homogeneous CFAR loss for small N [763]. A minimum window size of approximately 32 samples is required at typical false alarm rates to hold excess CFAR loss relative to CA to less than 1 dB.

The detection capability of all three CA-CFAR variations is illustrated in Fig. 4.17 for the case of a single interfering target in the reference window.

Under *log-cell-averaging CFAR* (LCA-CFAR), a logarithmic detector law is used prior to detection processing. This technique has been suggested to improve CFAR performance against heterogeneous interference [515]. The log detector output is processed via CA or one of the modified variants such as GOCA. However, the CFAR multiplier of Fig. 4.14 is replaced by a corresponding additive term k_{lca}. It can be shown that the corresponding interference estimate is equal to the product of the reference samples taken to the $1/N$ power.

Estimation of the interference from the reference window samples' ensemble product rather than the sum as in conventional CA reduces masking degradation. LCA imposes a larger loss than CA-CFAR. Hansen has derived the expression

$$N_{\log} = 1.65N_{\text{lin}} - 0.65$$

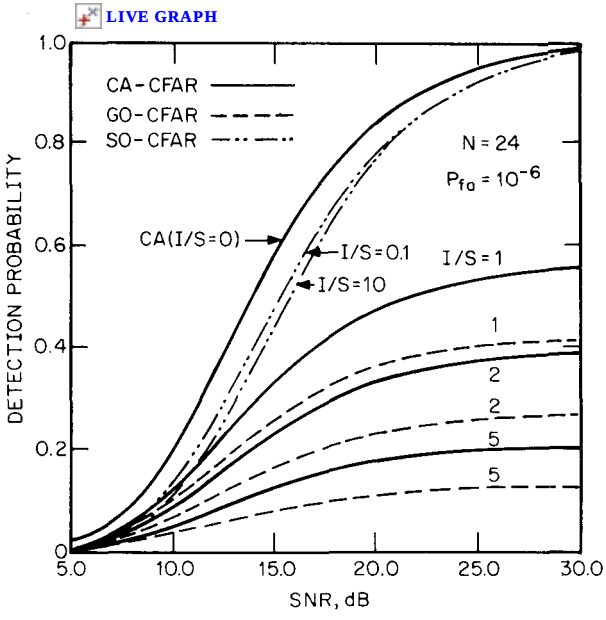

Figure 4.17 Detection performance of CA/GOCA/SOCA CFAR with one interferer. ([259] © *IEEE, 1988*)

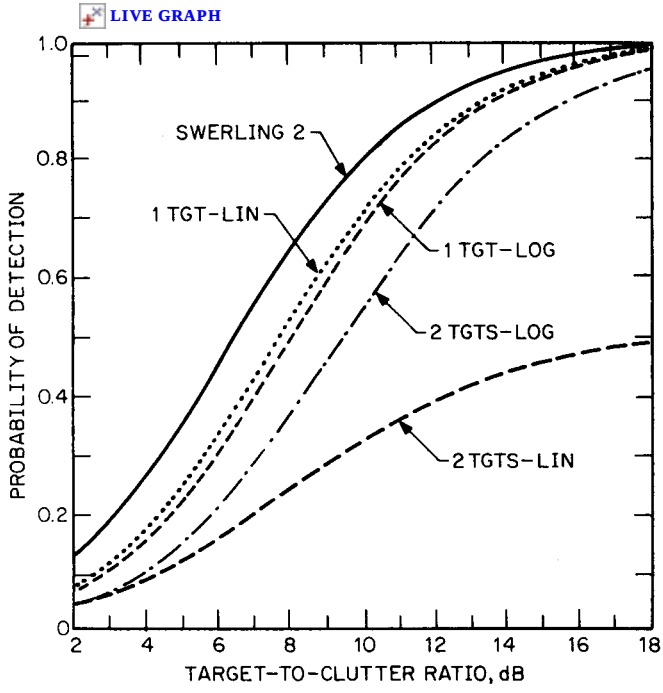

Figure 4.18 Detection probability versus SNR: L-CA-CFAR ($N = 8, P_{fa} = 10^{-3}$ 2-pulse noncoherent integration). ([*515*] © *IEEE, 1988*)

to define the number of LCA-CFAR samples N_{log} required to provide equivalent homogeneous interference CFAR performance to CA-CFAR with N_{lin} reference samples [311].

The relative advantage of CA over LCA dissipates with increasing degree of noncoherent integration and increasing reference window size. Detection performance for a design false alarm probability of 10^{-3}, a reference window size of 8 samples, two-pulse noncoherent integration, and a Swerling 2 target is depicted in Fig. 4.18. The one-target case corresponds to a single target embedded in homogeneous interference while the two-target case corresponds to the presence of an interfering target in the reference window.

Weber et al. have determined that LCA suffers worse clutter-edge false alarms than CA [759]. LCA emphasizes lower-power reference cells so as to underestimate the detection threshold when the test cell is near a clutter edge.

Ordered-statistic CFAR (OS-CFAR) has been proposed to mitigate masking degradation [616, 618]. In this case, the interference is estimated by rank ordering the reference window samples. The data set Z is derived by rank ordering the reference window samples X such that

$$Z_N > Z_{N-1} > \cdots > Z_k > \cdots > Z_1$$

The decision threshold is estimated as the product of the kth largest reference window sample, Z_k, and a CFAR multiplier. The CFAR multiplier is calculated as a function of k, N, and the design false alarm probability and is conditioned on the assumed interference probability density function.

Rohling has suggested that k be set to approximately $0.75N$ in order to provide acceptable performance in a heterogeneous environment while minimizing CFAR loss. Typically, OS-CFAR imposes 0.5 to 1 dB more homogeneous CFAR loss than CA. OS-CFAR loss varies with k for a given N with the detectability loss increasing significantly for small k. CFAR loss may be calculated as described by Levanon [430].

OS-CFAR mitigates target masking in cases in which the number of reference window cells contaminated by interfering signals r is less than $N - k$. The resulting lack of target masking can be perceived in the thresholding example of Fig. 4.19. Significant masking degradation occurs for r greater than $N - k$.

Some detectability loss occurs even if r is less than $N - k$; the number of reference samples used to estimate the test cell background interference is effectively reduced by r. Hence, the detection decision threshold is overestimated, resulting in a detectability loss and reduced false alarm probability.

Blake has calculated homogeneous CFAR losses of 0.71 and 0.48 dB, respectively, for OS-CFAR processing using $k = 54$ and $N = 64$, and CA-CFAR processors of equivalent reference window size; this calculation is conditioned on a design false alarm probability of 10^{-6} and an average S/N of 20 dB [72]. The detectability loss increases to 0.90 dB and 4.35 dB, respectively, for the same case with the addition of an equal-power, single interfering return located in the reference window.

Gandhi and Kassam have determined that the OS-CFAR false alarm probability can increase markedly at clutter transitions in which the test cell and one-half the reference window are contaminated [259].

Censored cell-averaging CFAR (CCA-CFAR), or *trimmed-mean CFAR*, has been suggested in an attempt to exploit the best characteristics of CA and OS [259, 598, 609, 763, 560]. Under this technique, the H largest and L smallest reference window samples are edited from the reference window prior to CA-CFAR estimation. The primary benefit in heterogeneous CFAR applications accrues from setting $L = 0$ and setting $H \geq$ the number of strong-interference-contaminated reference cells anticipated. Examination of Presley's and Ritchey's analyses suggests that H should be set to between $0.25N$ and $0.5N$ to

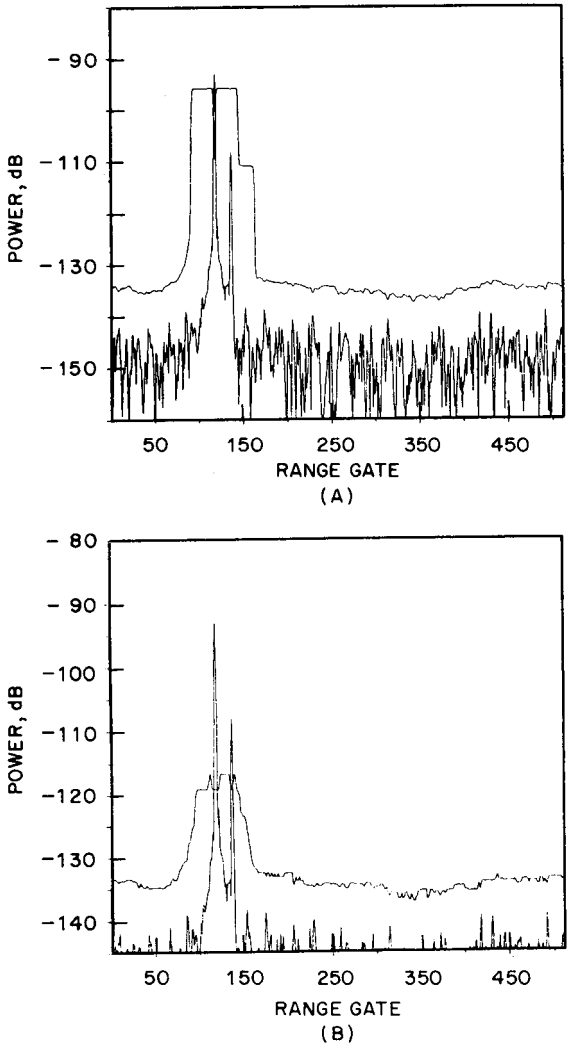

Figure 4.19 Multiple-target CFAR thresholding (average $P_{fa} = 10^{-6}$; 50-sample window). (A) CA-CFAR; (B) OS-CFAR. (*Courtesy L. Harkness*)

suppress masking effects and impose acceptable CFAR loss [91, 560]. Adapting Ritchey's definition of the CCA-CFAR threshold-estimation operation to the current notation yields

$$T_{\text{cca}} = K_{\text{cca}} \left[\sum_{i=1}^{N-H} Z_i + (N - H) Z_{H+1} \right]$$

Ritchey derived the second component of the sum so as to obtain an unbiased, minimum variance of the background interference, using $N - H$ samples.

The associated CFAR loss performance is illustrated in Fig. 4.20 for the cases of $l = 0$ through $l = 3$ Swerling type 1 interfering signals present in the reference window of 16 samples. The x-axis plots $N - H$. The solid curves were computed using an asymptotic approximation conditioned on the interfering signal-to-noise ratio approaching infinity. The dashed line for interference-to-noise ratio INR = 10 dB was calculated to demonstrate the accuracy of the asymptotic approximation. Ih comparison, the CA-CFAR loss is approximately 1.3 dB against homogeneous interference ($l = 0$).

As in the case of OS-CFAR, CCA performance deteriorates when the number of reference cells contaminated by strong interfering signals exceeds H. However, target-masking performance appears superior to OS for interfering signals numbering less than H since CCA provides a more accurate estimate of the nominal background interference. This relative advantage is typically on the order of 0.1 to 0.2 dB against homogeneous interference. The relative advantages of OS and CCA vary with the specific cases of interest.

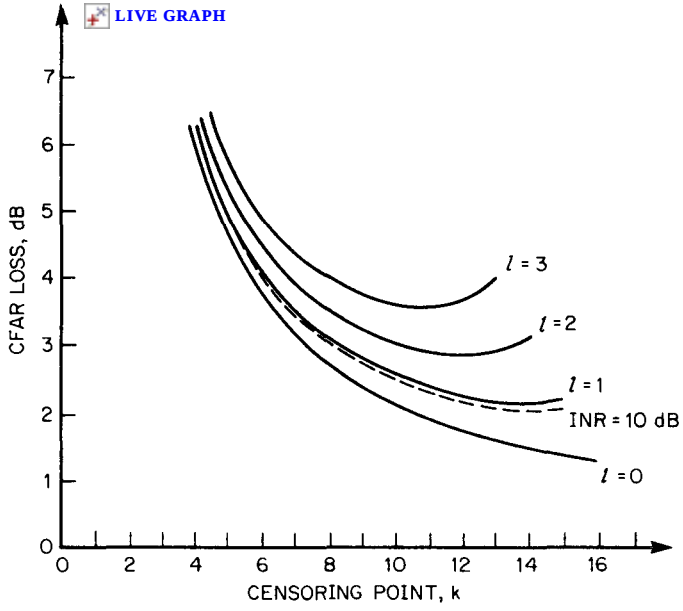

Figure 4.20 SNR loss of CCA-CFAR with fluctuating interferers for $P_d = 0.9$ and $P_{fa} = 10^{-4}$. Curves indicate l, the number of Swerling 1 interfering targets. Solid curves for INR approaching infinity. ([609] © *IEEE, 1986*)

The CCA false alarm rate increases at clutter edges. Ritchey and Hines have suggested dividing the reference window into leading and lagging components, performing separate CCA threshold estimation, and choosing the greater of the two to suppress clutter-edge false alarms [608].

Goldstein suggested the use of a two-parameter LCA-CFAR variation for automatic detection of targets embedded in log-normal or Weibull interference [277]. Weber and Haykin have developed a two-sample modification of OS-CFAR to accommodate two-parameter interference PDFs [23]. Two-parameter thresholding techniques generally result in increased CFAR loss. The performance of two-parameter CFAR techniques against heterogeneous interference has not been addressed in general form.

In principle, CFAR techniques that are insensitive to the interference PDF are an elegant solution to the problem of variation in interference probability density functions. These so-called distribution-free techniques (DF-CFAR) provide CFAR performance across a class of interference PDFs that include those of all anticipated interference sources [701, 35]. DF techniques typically impose significantly larger loss. The robustness of DF-CFAR effectively results in degraded detectability as these techniques do not exploit knowledge of the interference inherent in a known probability density function.

Rank-order techniques are the most widely utilized DF-CFAR implementation [580]. CFAR performance is provided across all continuous interference PDFs. Thresholding can be implemented by counting the number of times a given test cell exceeds a specified rank order threshold over a specified number of scans. Rank ordering DF techniques typically imposes losses on the order of 3 to 4 dB against homogeneous interference [182].

Adaptive detection summary

The heterogeneous interference environment encountered by most radar systems degrades conventional cell-averaging performance via masking and elevated clutter-edge false alarm probability. CFAR schemes employing some manner of rank ordering, such as ordered statistic or censored cell averaging, appear to mitigate these difficulties. The relative merits are driven by the particular environment scenarios specified. Distribution-free techniques appear attractive against interference environments characterized by significant probability density function variation at the cost of increased CFAR loss.

Signal processors in current radar systems are seldom designed to implement rank ordering at the high data rates required for detection processing. Hence, modified detector laws and decision-driven CA-

CFAR modifications are sometimes implemented to enhance performance against heterogeneous interference. Log-cell-averaging CFAR significantly mitigates masking degradation if the increased homogeneous CFAR loss and increased heterogeneous interference false alarm rate can be tolerated. Greater-of CFAR and smaller-of CFAR appear attractive under specialized circumstances.

Finn has also compared detection statistics of clutter echoes having the Rice distribution with those having the Rayleigh distribution. The Rice distribution is characterized by a coherent or steady component in addition to an incoherent, fluctuating component. This distribution is often attributed to the temporal fluctuation of ground clutter returns (but not to the spatial distribution). For the case in which the threshold has been mistakenly set on the assumption of a Rayleigh distribution, the threshold is set higher than need be; and the target detection and false alarm probabilities are considerably reduced. For example, if the threshold is set for $P_N = 10^{-8}$ on the basis of a Rayleigh-distributed sample of 30 cells and the actual signals have a ratio of the coherent to incoherent component of 2 to 1, the false alarm probability drops to 4×10^{-15}. This causes an additional loss of several decibels in target detectability above the value obtained if the correct distribution had been assumed. The opposite assumption can also be made, and an expected 2-to-1 ratio of coherent to incoherent component can be used to set the threshold. In this case there is a relatively minor increase in P_N from 10^{-8} to 3×10^{-5}.

As a final note on CFAR, the radar design community puts itself in a bad light in the eyes of management and customers by showing high CFAR losses in nonuniform clutter. They give the impression that if they were better designers they would not have such high values. The losses are primarily due to the nature of the environment and secondarily to the skill of the designer. While it is not the current standard, it would seem preferable to define *environmental loss* as the environment-induced loss and reserve the term *CFAR loss* for the inability to estimate the parameters of the distribution and optimally set the threshold.

4.9 Dynamic Range of Rayleigh Signals

The effectiveness of an adaptive technique using a "reference" channel is to some extent dependent on the dynamic range of the reference channel. A related design problem, one that is especially important in digital receivers, is that of choosing where to set the available dynamic range with respect to the mean or median levels of the input signals. A graph to aid in this determination is shown in Fig. 4.21 from Ward [748]. The left ordinate is the input signal voltage expressed in decibels,

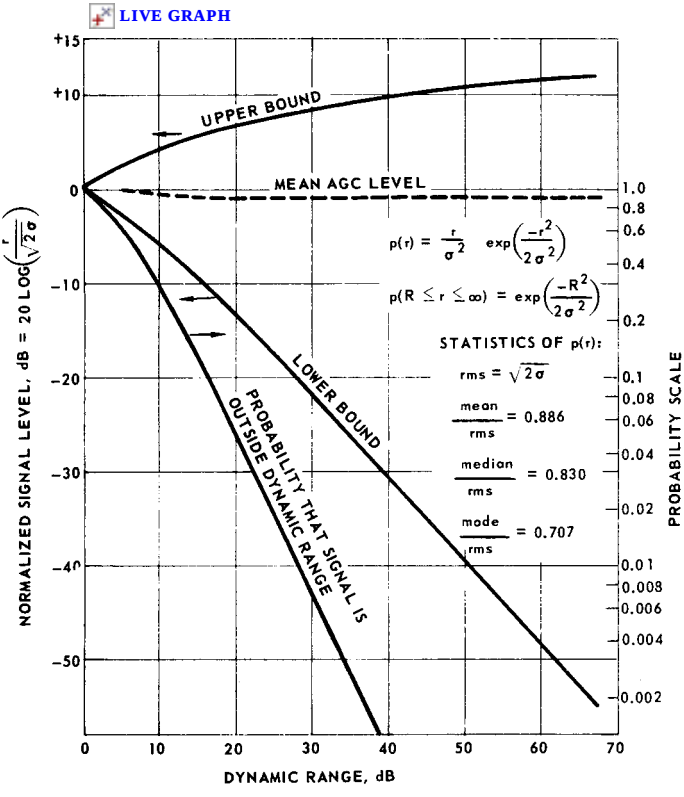

Figure 4.21 Dynamic range bounds for minimum probability of excluding a Rayleigh-distributed signal. (*From Ward [748]*)

and the abscissa is the dynamic range of the channel of interest. The probability that a signal will lie outside the dynamic range is shown as the right ordinate. The line marked "Mean AGC Level" is equal to the mean signal level for large dynamic ranges. The criterion of minimum probability of exceeding the dynamic range may not be optimum from the standpoint of detection, but it would seem reasonable to have a low probability that the peaks of the interference would exceed the available dynamic range.

4.10 Overall False Alarm Control

Previous sections discussed basic detection theory and the signal-to-noise ratios required for detection and the maintenance of a low false alarm probability. Initially, the assumption was that the noise was uncorrelated and had a constant mean value over time. The discussion was extended to include noise jamming and CFAR techniques to mea-

sure the mean value of the noise or jamming to allow threshold setting in a time-varying noise, jamming, or clutter environment.

It was noted that if the target is fluctuating, and especially when the clutter was spatially nonuniform, the threshold was required to be set far above the mean value of these interferences. Thus, a strong target echo was required, mandating high transmitter power and sophisticated processing. In recent years, and especially with the advent of fast and inexpensive digital processing, it has been found preferable to spread the false alarm control throughout the *system,* which is defined here to include the software that is not usually included in the definition of a radar.

This is illustrated in Fig. 4.22, which describes overall false alarm control in a surveillance radar such as a terminal or enroute air traffic control system. The blocks shown are one way of describing the flow of signals through a system. In this figure the emphasis is on the interfering signals rather than on the targets. The "Words per scan" row describes the bandwidth of the analog signal at the front end of the radar, the number of range gates after the signal is digitized (or combinations of range gates and Doppler filters), and finally the number of words that describe what are believed to be targets. The two lower rows describe the function of the block and the basis for discrimination of targets from interference.

The first block denotes the *sidelobe blanker* or *canceler.* It basically measures the interference entering the radar sidelobes, and an auxiliary broad-beam antenna. In the case of the blanker, it takes the ratio of the signals from a wide spatial angle to those entering the main antenna. If this ratio is high, it is assumed that it is a sidelobe interfering signal and blanks the main channel from declaring a mainlobe target at that location. The sidelobe canceler is more sophisticated in that it processes both antenna signals coherently, and effectively places a "null" in the mainlobe antenna pattern at the angular location of the interference. For this discussion the signal entering the next block is assumed to come from the mainlobe of the radar. The signal-processing block is the coherent signal-processing portion described in Chaps. 8 through 14. It is here that an attempt is made to separate targets from clutter, jamming, and any other interfering signal. Processing is in either the range or Doppler domain or both. At this output, assume that the sample rate is $3/\mu s$, and that in-phase and quadrature signals are detected to form 3×10^6 words.

The next boxes are the *CFAR* and *integration* functions in which thresholds to establish the false alarm rate are established. The exact configuration or order is not important for this discussion. The key point is that if the desired false alarm rate for the *system* is to be held to a few per 10-s scan, the threshold would have to be inordinately

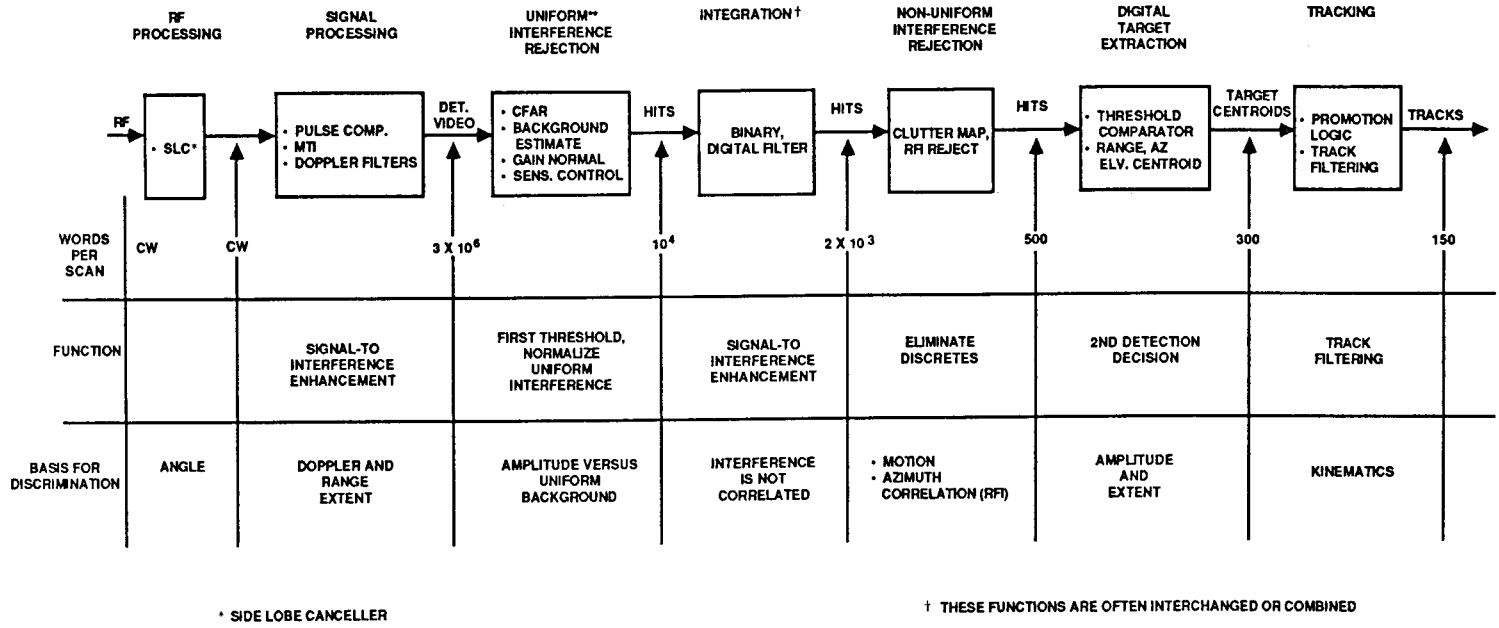

Figure 4.22 Surveillance radar false alarm management.

high above the mean (15dB?) to allow for large discrete clutter or other interference effects. In the figure it is shown that 2000 "hits" are allowed at this point, which might allow the threshold to be dropped by 10 dB in a discrete land clutter environment. Of this 2000, 1500 to 1800 may be cultural artifacts, moving vehicles, flocks of birds, etc.

The *clutter map block* (see Sec. 14.1) has previously stored the location of the fixed objects that leak through the signal processing, and will inhibit new detections at this location. The assumption here is that 1500 out of 2000 of the previous hits are rejected here. The *digital target extraction block* will then take hits on adjacent ranges or azimuths and attempt to decide whether there is one or more targets in an area. It will also reject a few other uncorrelated "targets." At this point there are perhaps 300 potential targets. They will be tracked for several scans to determine if they fit the allowable velocities of the desired targets. As an example, perhaps one-half of these are ground vehicles or targets currently being tracked, and the remaining ones are the 150 targets in the track file.

Chapter

5

Radar Targets

F. E. Nathanson

J. P. Reilly

5.1 General Scattering Properties—Simple Shapes

The radar range equation expresses the range at which a target may be detected with a given probability by a radar having a given set of parameters. This equation includes the target's *radar cross section* (RCS), which is a measure of the proportion of the incident energy reflected back to the radar.* This returned energy varies with a multitude of parameters such as transmitted wavelength, target geometry, orientation, and reflectivity.

The radar cross section of an object is proportional to the far-field ratio of reflected to incident power density, that is

$$\sigma = \frac{\text{power reflected back to receiver/unit solid angle}}{\text{incident power density}/4\pi}$$

Using this definition, consider the RCS of a perfectly conducting isotropic scatterer. The power intercepted by the radiator is the product

* A monostatic radar is assumed except in Sec. 5.10.

of the incident power density P_I and its geometric projected area A_I. The power of an isotropic scatterer is uniformly distributed over 4π steradians, in which case

$$\sigma_i = 4\pi \left[\frac{P_I A_I / 4\pi}{P_I} \right] = A_I \tag{5.1}$$

Thus, the RCS of such an isotropic reflector is its geometric projected area. The RCS of any reflector may be thought of as the projected area of an equivalent isotropic reflector which would return the same power per unit solid angle. A reflector that concentrates its reflected energy over a limited angular direction may have an RCS *for that direction* that exceeds its projected area. This indicates that, when specifying cross sections, one must also specify the aspect of the target. The RCS is also dependent on other parameters besides aspect angle.

The scattering properties of a metallic sphere serve to illustrate the nature of the RCS wavelength dependence [671, p. 41]. Three distinct regions of behavior for the RCS of a sphere of radius a are illustrated in Fig. 5.1. In the region for which $2\pi a/\lambda < 1$ (*Rayleigh* region) the RCS is proportional to λ^{-4}. As the wavelength is decreased beyond the point where $2\pi a/\lambda = 1$, the *Mie* or *resonance* region is entered where the RCS oscillates between ever diminishing values approaching the optical cross section. Finally, for very small λ the optical region is

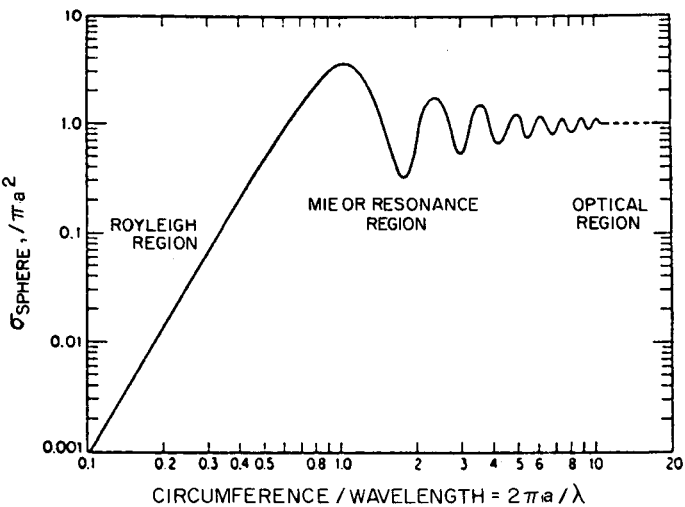

Figure 5.1 Behavior of the RCS (of a sphere) with wavelength *Rayleigh region:* λ large compared with dimensions; $\sigma \simeq \lambda^{-4}$. *Resonance or MIE region:* λ comparable to dimensions, σ oscillates with increasing λ; σ may be greater than physical area. *Optical region:* λ small compared with dimensions, surface and edge scattering occurs; $\sigma \rightarrow$ physical area.

entered where the fluctuations converge to the optical cross section πa^2. The following paragraphs give a basic description of scattering behavior for each region for perfectly conducting objects.

Rayleigh region

Although radar targets do not usually fall within the Rayleigh region (target dimensions smaller than the transmitted wavelength), other scatterers such as precipitation particles do. The wavelength dependence of the RCS for a sphere in this region is proportional to λ^{-4}, which also applies to most objects that have overall dimensions that are small compared with a wavelength. Siegel [346] shows that the critical parameter in determining RCS is the volume, slightly modified to account for the gross features of the shape. He finds that, for most bodies of revolution, the RCS at an aspect along the axis of symmetry is closely approximated by

$$\sigma = \frac{4}{\pi} k^4 V^2 F^2 \tag{5.2}$$

where $k = 2\pi/\lambda$, V is the volume of the scatterers in m^3, and F is a dimensionless factor that depends on the gross shape of the body. This shape factor may be neglected for spheroids except those of the very flat, oblate variety. Shape factors for other geometric shapes are also derived in Siegel's paper. This approach was found to lose accuracy as the scatterer became more flat; a flat surface has zero volume, but a nonzero cross section.

The RCS of any object in the Rayleigh region will be sensitive to polarization and aspect angle if one major dimension is small compared with another. This is discussed in the section on Circular Polarization.

Optical region [80, 340]

The optical region in which most radar targets of practical interest reside is so named because the ray techniques of geometric optics may be applied to the problem of RCS estimation. Any smooth, curved surface nearly normal to the incident field will give a specular return. In the optical region the RCS behavior with wavelength is monotonic, although the RCS does not necessarily converge to a constant value. The RCS behavior with wavelength may be classified for many simple objects in terms of the principal radii of curvature at the point where the normal to the surface is parallel to the direction of incidence: This is illustrated in Table 5.1. It is assumed that the objects are metallic and the dimensions of the shapes are large compared with the radar wavelength.

TABLE 5.1 Scattering Cross-Sections for Simple Shapes (Radius $a \gg \lambda$, Area $A \gg \lambda^2$

Variation with wavelength	Target/aspect	Radar cross section, σ
λ^{-2}	Flat surface of arbitrary shape and area A, normal	$\frac{4\pi A^2}{\lambda^2}$
	Triangular corner reflector with edge length a	$\frac{4\pi a^4}{3\lambda^2}$
λ^{-1}	Cylinder of length L and radius a, normal to axis	$\frac{2\pi a L^2}{\lambda}$
λ^0	Prolate spheroid with semimajor axis a and semiminor axis B	$\pi \frac{B^4}{a^2}$
	Paraboloid with apex radius of curvature ρ_0	$\pi\rho_0^2$
λ^1	Cylinder of length L and radius a (averaged over several lobes about an angle θ off normal)	$\frac{a\lambda}{2\pi\theta^2}$
λ^2	Infinite cone with half cone angle θ_0	$\frac{\lambda^2}{16\pi}\tan^4\theta_0$

For the flat plate perpendicular to the radar line of sight, the RCS can be considered to be the product of A (the area that is intercepting the radar energy) and $4\pi A^2/\lambda^2$ (the directive gain of the flat plate toward the radar). For a 1-m^2 flat plate at S-Band (0.1 m), the RCS is approximately 1200 m^2. Note that RCS increases as frequency squared. If the flat plate is tilted in one plane, this value is reduced by the sidelobe levels of a flat plate antenna aperture at the corresponding angles. For tilts of up to about 20°, the average RCS will still exceed 10^2 m^2. The cylinder acts like a one-dimensional antenna. For spheroids, the RCS is independent of wavelength, and is related to the physical cross-sectional area. The RCS of a sphere is about 1 m^2.

When the radar is looking into the point of an infinite cone or a cone with a half sphere at the opposite end from the point, the RCS is drastically reduced. The RCS of a cone with apex angle 33° is only about 2×10^{-6} m^2 (assuming no imperfections). Note the λ^2 dependence. This has been known for over 25 years, and is one reason why ballistic missile warheads were shaped in this general form.

The RCS of a flat plate is dramatically increased over the previously described shapes. A variation known as a *corner reflector* also augments the RCS as illustrated in Fig. 5.2. Its advantage is that the RCS is high over a broad range of angles as can be seen from simple optics. With a triangular corner reflector the mainlobe width is about 40°. Corner reflectors can be constructed from triangular or rectangular

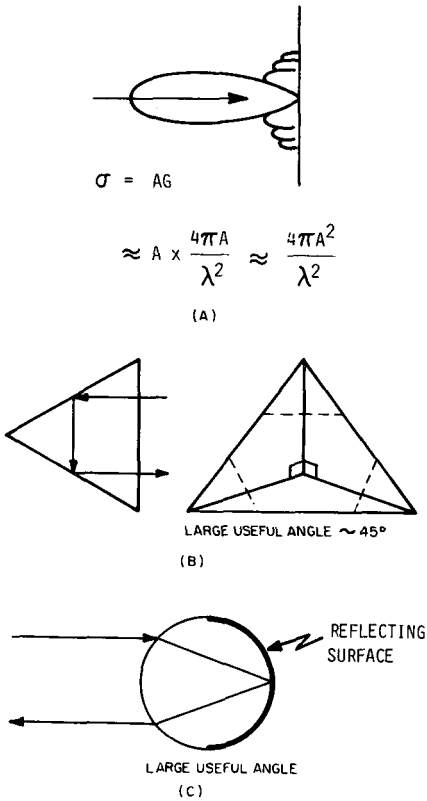

Figure 5.2 Targets with high reflectivity/unit area. (A) Flat plate; (B) triangular corner reflector; (C) Luneberg lens.

plates. A triangular corner reflector with improper angle alignment will degrade by 3 dB if all three edges deviate by 0.35λ or a single edge deviates by 0.7λ. The Luneberg lens is another variation of an augmented shape. The dielectric constant is graded along the radius such that the incoming rays are focused on the surface away from the radar, similarly to an optical lens. This surface often has a metal coating to reflect the energy. It is also possible to make a Luneberg lens with a single dielectric.

Corner reflectors and Luneberg lenses are often used for testing and calibration and on small boats that wish to be visible on marine radars.

The RCS of large, complex reflectors may often be approximated by breaking the body into individual reflectors and assuming that the parts do not interact. In this case the total RCS is just the vector sum of the individual cross sections

$$\sigma = |\Sigma_k \sqrt{\sigma_k} \exp(j4\pi d_k/\lambda)|^2 \tag{5.3}$$

where σ_k is the RCS of the kth scatterer and d_k is the distance between the kth scatterer and the receiver. This formula has an important application in estimating the RCS of an array of scatterers.

The greatest use of the optical approximation is the calculation of specular returns or their sidelobes. This method may fail when there is a surface singularity such as an edge or a shadow; in this case the wavelength dependence is generally of a lower order than for a specular return alone. Surface singularities cause second-order effects, including "creeping" or "traveling" waves, which may actually be the dominant source of reflections when specular returns are weak [646].

Resonance region

Approximate methods can provide a good estimate of the RCS when the characteristic size of the body is much smaller than the wavelength (Rayleigh region) or when it is much greater than the wavelength (optical region). In between lies a region where the geometry of the body is a critical factor, and neither the optical nor the Rayleigh methods can be easily applied to the problem of RCS estimation. Although a few techniques for RCS estimation in this region are available, no simple generalizations are possible. This subject is treated in several books [153, 673], and in short courses currently offered by Georgia Tech Research Institute.

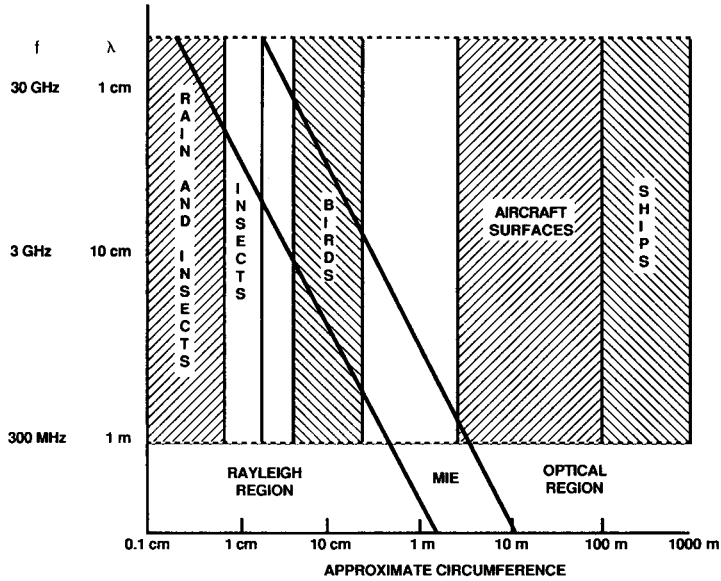

Figure 5.3 Sizes of typical radar targets relative to their wavelengths.

While Fig. 5.1 is accurate only for metallic objects, the general shape also applies to dielectrics. The relation of typical target RCS to the carrier frequency is illustrated in Fig. 5.3. The horizontal extent of each band illustrates the size range for objects often seen by radar. The slanted lines delineate the approximate reflectivity regions. Insects and raindrops are in the Rayleigh region for typical radar carrier frequencies. Their reflectivity increases with wavelength about as F^4. Birds are often in the resonance region. Large ones are a problem with L- and S-band surveillance radars. Aircraft, vehicles, and ships are large compared to most wavelengths, and even most of their parts are relatively large. Thus, these targets have relatively little frequency dependence.

5.2 Polarization Scattering Matrix

Consider a linearly polarized plane wave, propagating along the line of sight of the antenna, that is incident on a target. The incident field at the target can be resolved into components of electric field E_H^T and E_V^T along the H and V axes, respectively.* In general, the component of scattered electric field E^S resulting from the incident H component *only* has both H and V components. Expressed in terms of scattering coefficients, the H component of the scattered field is

$$E_H^S = a_{HH} E_H^T$$

and the V (orthogonal) component is

$$E_V^S = a_{HV} E_H^T$$

The first subscript in a_{HV} is for the transmitted component; the second, for receive. The total scattered energy is the vector sum of that due to E_H^S and E_V^S. When *both* components of incident field are present, the scattered field can be concisely stated in terms of the scattering matrix. (See [63, 262, 291, 449].)

$$\begin{pmatrix} E_H^S \\ \\ E_V^S \end{pmatrix} = \begin{pmatrix} a_{HH} & a_{HV} \\ \\ a_{VH} & a_{VV} \end{pmatrix} \begin{pmatrix} E_H^T \\ \\ E_V^T \end{pmatrix}$$

A similar polarization matrix exists for circular or elliptical polarization. Expressed in terms of right and left circularly polarized waves E_R and E_L,

* While the axes are arbitrary, this text uses only the more conventional horizontal H and vertical V axes (H or V polarization).

$$\begin{pmatrix} E_R^S \\ E_L^S \end{pmatrix} = \begin{pmatrix} a_{RR} & a_{RL} \\ a_{LR} & a_{LL} \end{pmatrix} \begin{pmatrix} E_R^T \\ E_L^T \end{pmatrix}$$

Circular polarization is illustrated in Fig. 5.4. If the reflector has circular symmetry about the line-of-sight axis, then the matrices have the properties

$$\begin{aligned} a_{HV} = a_{VH} = 0 \quad &\text{and} \quad a_{HH}, a_{VV} \neq 0 \\ a_{RR} = a_{LL} = 0 \quad &\text{and} \quad a_{RL}, a_{LR} \neq 0 \end{aligned} \tag{5.4}$$

and, for most cases, regardless of symmetry

$$a_{HV} = a_{VH}, a_{RL} = a_{LR} \tag{5.5}$$

One important consequence of these properties is that a radar using the same circularly polarized antenna for both transmission and reception receives little or no power from approximately spherical targets, such as raindrops, whereas the same transmit and receive linearly polarized antenna receives most of the energy. This property has been used to ascertain the ellipticity of raindrops and to reject weather clutter on both military and air traffic control radars. Both backscatter and attenuation vary with polarization for elliptical raindrops.

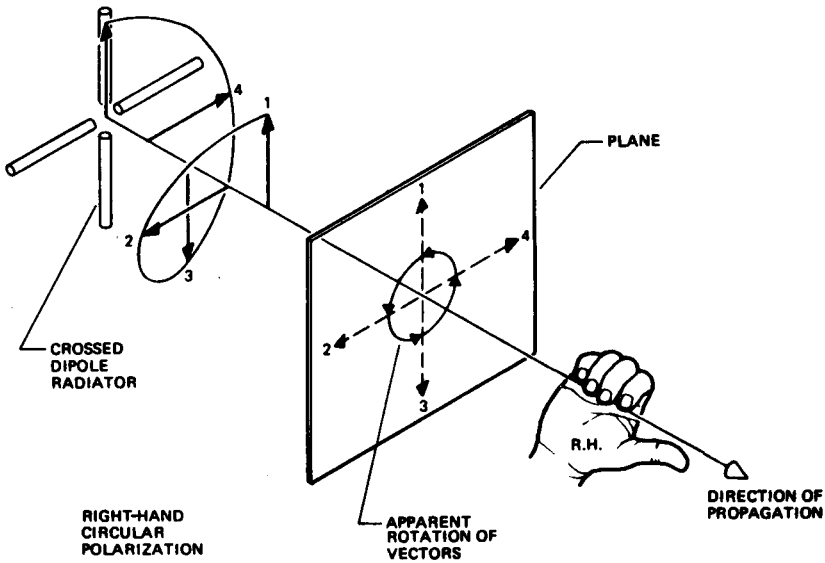

Figure 5.4 Field rotation of circular polarization. (*From Hill [337], Courtesy Watkins Johnson Co.*)

Circular polarization

When a radar transmits a circularly polarized electromagnetic wave, the receive aperture does not respond to the reflections from spherical objects if the transmit and receive apertures have the same "sense" of polarization. Reflections from complex scatters such as aircraft undergo a 2- to 6-dB "loss" in the process relative to linear polarization, but still appear in the receiver. This is addressed later in the section. It is perhaps appropriate first to discuss polarization properties of simple objects such as raindrops.

The reflectivity of spherical objects (e.g., small raindrops) depends on several factors. The primary factor currently under control of the radar designer is the ellipticity of the antenna polarization (or the departure from circularity). With circular antennas having pencil beams, values of 0.96 to 0.98 are reasonable. The following observations are important with circular polarization:

1. Large raindrops become elliptical. This occurs especially in thunderstorms and near the "bright band" or melting layer.
2. The attenuation of the horizontally polarized component of the radiation differs from that of the vertically polarized component, especially with larger drops. Thus, in the more distant parts of a storm, the attenuated waves become more elliptical, especially when the reflections occur from the closer parts of the storm.
3. Forward-scattered reflections from the ground have quite different strength for the horizontally and vertically polarized components, especially over seas, rivers, etc. Thus, the vector sum of the signal components including multipath is elliptically polarized when the forward-scattered reflection coefficient is high.

Ellipticity due to differential attenuation

Since larger raindrops are asymmetrical, the absorption coefficients differ for horizontally and vertically polarized components. Oguchi has calculated that for moderately heavy rain (12.5 mm/hr), the attenuation for spherical raindrops is about 10 dB/km each way at 4 GHz and 6.8 dB at 9 GHz. Thus, the differential attenuation between H and V polarization is 0.06 dB at 4 GHz and 0.8 dB at 9 GHz.

A receiver having the same-sense polarization would be effective in rejecting all but 1.5 percent of the 4-GHz echo, but would pass 20 percent of the 9-GHz echo. These values would apply to the echoes at the extreme range of the storm, with the vertically polarized component predominating. A good example of the effect of differential attenuation is given by the experiments of McCormick and Hendry, as shown in

TABLE 5.2 Circular Polarization Cancellation (dB) for Adjacent 0.5-km Range Gates
(Received Power Ratio for Opposite-sense Versus Same-sense Circular Polarization, dB)

Light rain								
32	32	30	28	30	32	29	27	25
31	31	30	28	30	32	29	27	26
32	31	30	28	30	32	29	27	26
31	32	30	29	31	32	29	27	26
Heavy rain								
19	18	15	14	12	10	8	6	5
19	19	15	14	12	10	8	6	4
18	19	15	14	12	10	7	5	3
19	18	15	14	13	10	7	5	2
Melting* layer								
25	25	25	24	23	10*	19*	29	29
27	26	26	25	24	10	19	29	29
27	27	27	26	24	9	19	28	28
26	26	26	26	23	9	19	27	28
Dry snow								
32	31	32	32	33	33	33	33	32
31	32	32	33	33	33	33	33	33
32	32	32	33	33	33	33	33	33
32	32	32	33	33	33	33	32	33

* SOURCE: From Hendry and McCormick [329].

Table 5.2. The numerical values in the table are the cancellation ratios in decibels. Range increases from left to right in 0.5-km increments and the rows represent time samples. The cancellation ratio is 19 dB at the near range, but only 2 to 5 dB at the distant range for heavy rain. This is at a relatively high carrier frequency of 16.5 kHz.

Polarization sensitivity of backscatter due to drop deformation

Large raindrops, hailstones, and water-coated ice particles near the melting layer are not spherical, and thus their reflection coefficients differ for the horizontally and vertically polarized components of circular polarization. The analysis of this effect has been performed by Oguchi and others and is fairly complicated. However, 2-mm-radius raindrops (moderate rain) falling at terminal velocity have an elliptical shape with a greater horizontal dimension and a minor-to-major axis ratio of about 0.8. Drops of 4-mm mean radius have a ratio of only 0.6. As might be expected, the differential backscatter can become quite large.

The experiments reported in Table 5.2 show that the measured cancellation ratio is often 10 dB poorer than theoretical for rainstorms, even at 5.5 GHz and below, where attenuation is not significant. The items in the table show the sharp reduction in the cancellation ratio at the melting layer (last two columns) due to the nonspherical shape of water-coated ice. The result of this effect is to have elliptically polarized echoes with the horizontal component predominating.

Ellipticity due to multipath

In many radar situations, especially those involving surface radars, the electromagnetic wave arriving at a rainstorm is the vector sum of the direct signal and the reflected signal from the surface of the earth (multipath). The lobing structure of the resultant pattern is quite familiar, but there is an additional factor with circular polarization. The reflection coefficient at grazing angles of 2 to 10° is considerably lower on the vertically polarized component, especially over seas, lakes, rivers, and marsh areas. Thus, the horizontally polarized component is canceled to a greater extent at some elevation angles, leaving the echoes from precipitations elliptically polarized with the *vertical component predominating*.

The overall effects on rain and targets from numerous sources are summarized in Table 5.3. The measurements at 9.35, 70, and 95 GHz were made on Florida storms by Richard, 1988 [595]. The average rejection ratio ranged from 20 dB at 9 GHz to 18 dB at 95 GHz. The primary use of polarization in meteorological radar is to determine the state of the hydrometeors. The ratio of the echoes on two orthogonal polarizations is a measure of the shape. Experiments have provided information from the ratio of the power on two polarizations. Further information is available from the full polarization matrix, but the overall benefit is not yet clear.

The echoes from chaff have the property of a higher horizontally polarized component. This is discussed in Chap. 6.

It is possible to improve the rejection of precipitation echoes, without implementing a full polarization matrix processor, by the use of an adaptive processor [502]. If circular polarization is transmitted and *both* senses of circular polarization are available in the receiver, the target echo will be divided between the two receive channels, but most of the precipitation will appear in the opposite sense channel. An implementation to improve the rain rejection is shown in Fig. 5.5.

The implementation is essentially that of an adaptive canceler. In simple terms, a time average is obtained of both the difference in amplitude and the difference in phase of the two channels. A portion of the signal in the larger channel (mostly rain) is scaled in amplitude to approximate the echoes in the smaller echo channel. The signals

TABLE 5.3 Reduction in Reflectivity Using Polarization Properties—Summary of Experimental Data

	Precipitation			Targets			
Wavelength	Type	Elevation, °	$\sigma_{RL/RR}$, dB	Type	Aspect, °	$\sigma_{HH/RR,VV/RR}$, dB $\sigma_{HH/LL,VV/LL}$, dB	$\sigma_{HH/HV}$, dB $\sigma_{VV/VH}$, dB
	Rain		22–30, 20	Birds			10
L, 24 cm	Wet snow		15	Comm. aircraft	−8 el., 0 az.	6–8, 1	9
				Land			7–8, 5
	Rain	< 10	18				
	Rain over sea	0–10 (av.)	20*				
S, 10 cm	Rain/marsh	0–10 (av.)	24*	Gen. aviat.	Nose(−/+25)	−1, −6	
	Rain/land	0–10 (av.)	27*	Gen. aviat.	Tail(−/+25)	−3, −6	
	Rain/desert	0–10 (av.)	34*				
				Land	−8 el.		6–10
				Vehicles	−3 el.		5–16
C, 5.6 cm	Rain	0–10	17	Trees	−3 el.		0–6
				Ships	−3 el.		−(2–8)
				Ships	−6 el.		3–15
	Thunderstorm		15	Aircraft	Nose/tail	(av.) 2.5	2.5–12
	Rain		26–28	Jet aircraft	Nose	4.5–6	10
X, 3.2 cm	Bright band	High	13–20	Ships	0 el.	6	
	Fine snow		26	Ships	−3–6 el.		7–15
	Rain	30	17–18	Jet/piston A/C	Nose/tail	3.5, 0–2	8–10
K, .86 cm	Bright band	30	5–11	Trees	−3 el.	2–4	4
	Dry snow	30	12–16	Vehicles	−3 el.		8–14

* Multipath limit.

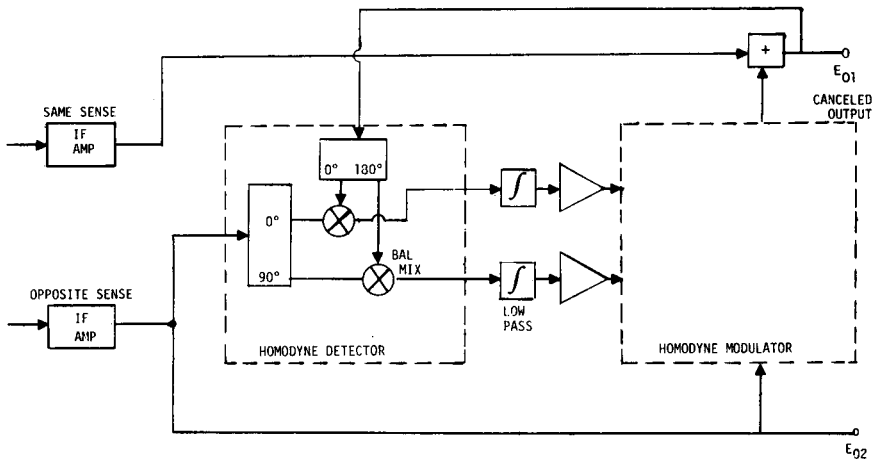

Figure 5.5 Circuitry for adaptive circular polarization (homodyne modulator = same circuitry as homodyne detector).

(rain) are subtracted to yield a "canceled" output in the target channel. Since the target echo is uncorrelated from channel to channel, it does not cancel. The time constant of the integrators should be at least 10 to 12 pulse durations. Time delays can be placed in the signal channels in order that the adapted elliptical polarization matches the location of the target. This is similar to time delays placed in CFAR circuits.

The circuitry is the same as that used in sidelobe cancelers for antennas. It appears that an additional 6- to 8-dB improvement can be obtained relative to a single circularly polarized channel system. The circuitry would also adapt to a single barrage noise jammer. The receiver effectively establishes the orthogonal polarization to any polarized long time duration signals.

A variation of this instrumentation was implemented by Fossi et al. [243]. With a combination of recorded jamming signals and simulation, they report an improvement of S/J of 12.2 dB.

Numerous experiments have been performed on the reduction of RCS of raindrop echoes with the use of "same-sense" circular polarization (σ_{RR} or σ_{LL}). In most of these radar experiments the reduction has been 15 to 30 dB where there are no terrain reflections. For surface radars and low-elevation angle beams (0 to 10°) the reduction is less [54]. The reduction in rain echoes by circular polarization appears to be almost constant through X-band, with poor results for heavier rains.

A good example of the radar reflectivity of small general aviation aircraft is the FAA experiments reported by Turnbull [716]. Measurements of full-size aircraft were made on a turntable at the RATSCAT facility at Holloman Air Force Base. In these and the following exper-

iments the pulse length was longer than the target. Two examples of RCS are shown in Figs. 5.6 and 5.7. Fig. 5.6 is the RCS versus aspect angle (horizontal plane) of a metal-skinned Cherokee 140 at S-band. Several things are noteworthy: (1) with linear polarization the average radar cross section in the nose aspect ($\pm 25°$) is of the order of 4 m^2; (2) in the region near broadside, there is an increase in RCS to over 100 m^2 due to the "cylindrical" fuselage; and (3) with same-sense circular polarization, the RCS is reduced about 6 dB. This aircraft has a relatively simple shape.

A similar set of results is shown for a Piper Super Cub, which has a fabric skin. The electromagnetic energy passes through the skin and sees the more complicated internal structure. This shows up most when comparing circular with linear polarization. With this aircraft, the RCS with CP is reduced by less than 3 dB.

The overall tests are summarized in Table 5.4, which includes data from L- through C-band. Note that there is not an obvious carrier-frequency dependence, even on these relatively small aircraft, or polarization-ratio dependence.

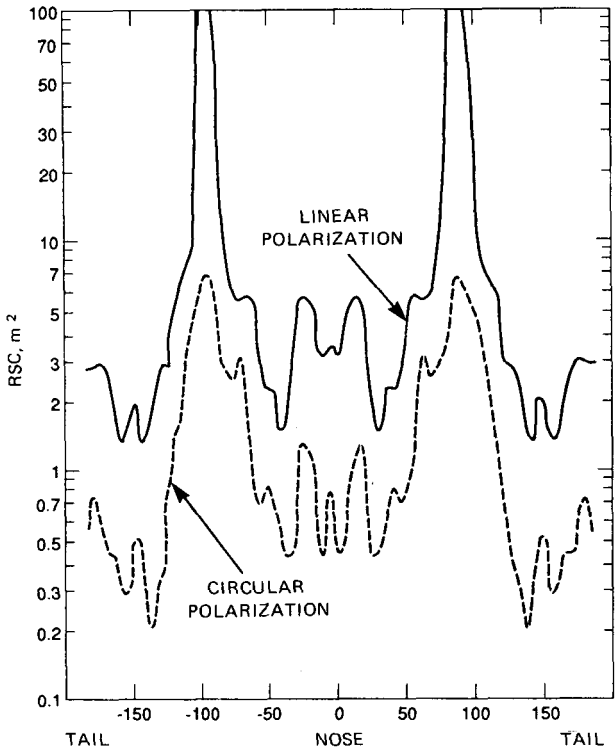

Figure 5.6 RCS of metal-skinned Cherokee measured at 2.8 GHz at RAT SCAT facility. (*From Turnbull* [*716*])

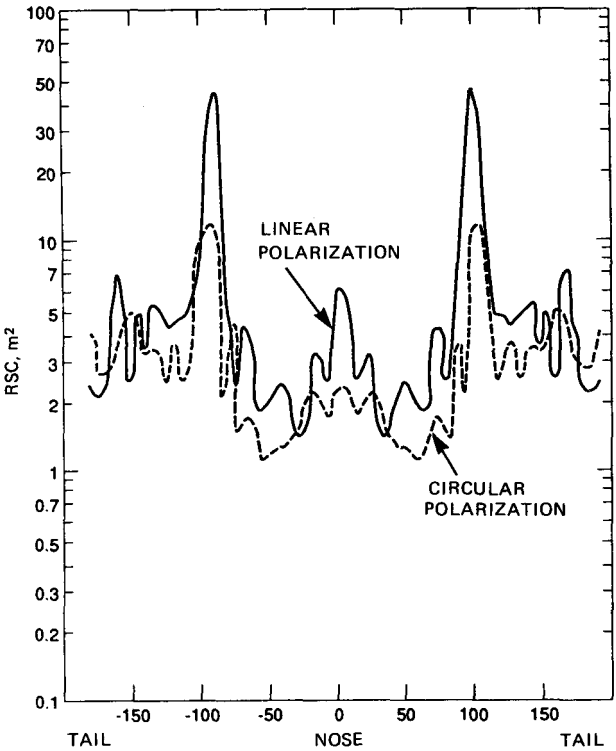

Figure 5.7 RCS of fabric-skinned Piper Super Cub measured at 2.8 GHz at Rat-Scat Facility. (*From Turnbull [716]*)

Unfortunately, the RCS of complex aircraft also reduces with same-sense circular polarization. Some typical values of the reduction in RCS with circular polarization below the values for linear polarization (σ_{HH} or σ_{VV}) are also shown in the table. One series of measurements of aircraft showed that $\sigma_{RR} \approx \sigma_{RL}$ and both were about 3 dB below σ_{HH} or σ_{VV} [262]. Most other experiments have shown a reduction in target RCS of about 5 dB for aircraft and even greater reductions for missiles and satellites.

There have been numerous examples of RCS measurements of airborne targets in the radar literature. The RCS for general aviation was illustrated in the previous section. Two other examples are given in Figs. 5.8 and 5.9 from a study by Follin et al. [241]. The first is for a Boeing 727-100C, which is typical of a moderate-size commercial passenger jet. While this figure is for measurements of a scale model, it was validated with measurements of the full version. The 0° observation angle is for nose measurements on horizontal polarization at a scaled L-band frequency. It was reported that the average RCS in a 10° region

TABLE 5.4 Radar Cross Sections of Small Aircraft ±25° from Nose or Tail—Horizontal Aspect Average over 10° (values in square meters)

	L-band (1.35)		S-band (2.8)		C-band (5.4)	
	Min*	Max†	Min	Max	Min	Max
Cherokee 140						
Nose—Vert.	0.9	6.0	3.0	5.5	~1.0	~5.0
—CP‡	0.11	0.8	0.4	1.4		
Tail—Vert.	0.7	1.7	1.3	2.9	~0.3	~6.0
—CP	0.3	0.6	0.3	0.7		
Cessna 150						
Nose—Vert.	0.7	3.8	0.5	5.0	~0.5	~4.0
—CP	0.5	1.3	0.9	3.0		
Tail—Vert	0.4	2.3	1.0	1.3	~0.5	~1.5
—CP	0.5	0.8	0.8	2.7		
Piper Super Cub						
Nose—Vert.	1.4	3.6	1.4	6.0	~1.5	~7.0
—CP	0.38	0.7	1.7	2.3		
Tail—Vert	4.2	10.0	2.1	7.0	~3.0	~5.5
—CP	1.2	2.5	2.2	4.8		

* Min—represents the lowest median cross section in a 10° region within ±25° of nose or tail.

† Max—represents the highest median cross section in a 10° region within ±25° of nose or tail.

‡ CP—circular polarization—same sense.

SOURCE: Adapted from Turnbull [716].

about the nose was 22 m^2, and the large specular return at 90° was about 3000 m^2. The target is obviously complex even at this relatively long wavelength. It appears from modeling that there are about 10 major scattering regions. Vertical polarization gave similar results. In the nose-on region, the distribution is approximately Rayleigh (chi-square of degree 2).

Fig. 5.9 shows full-size X-band measurements of a widely used Ryan drone that is the size of a large surface-to-surface missile. The nose-on cross section is about 2 m^2, but it falls below 1 m^2 at 30 to 70° aspects. Near nose-on, the distribution lies between the chi-square of degree 2 and degree 4, indicative of a slightly less complex target.

The foregoing measurements were for a pulse whose linear extent exceeds the radial target extent. If short pulses or wideband compressed pulses are used, the distributions will change as fewer scatterers are observed at one time. The RCS for short pulse systems will drop, as the mean RCS of the major scatterers must be less than the mean of the sum of all the scatterers. One set of measurements by Davies and Bromley [167] showed that the RCS of moderate-sized aircraft dropped by about 3 dB when the bandwidth of the signal (the inverse of the range resolution) increased from 10 to 80 MHz. Since 10 MHz corresponds to 50 ft, larger aircraft are already partially resolved. For large

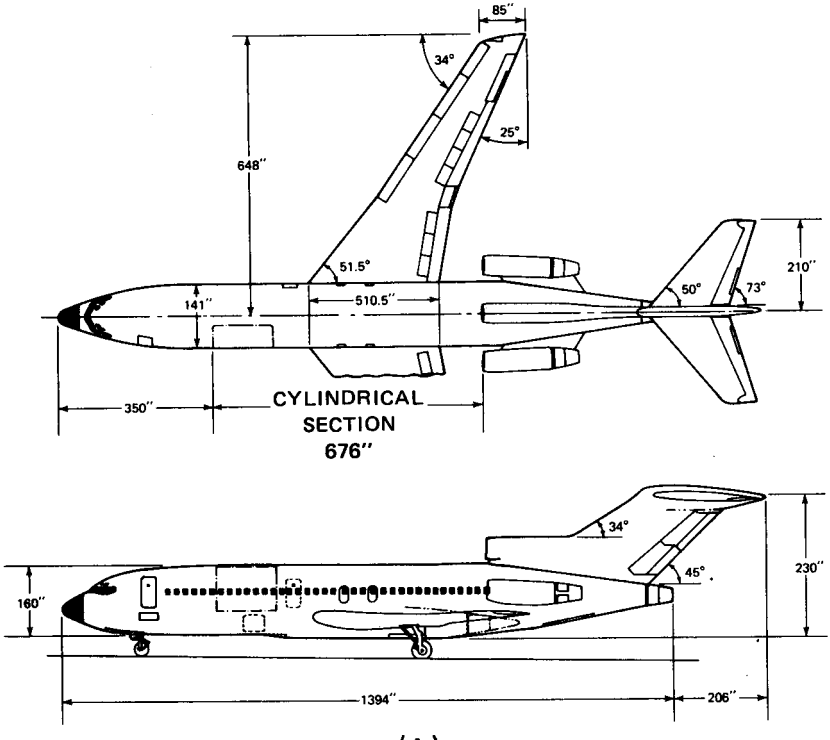

(A)

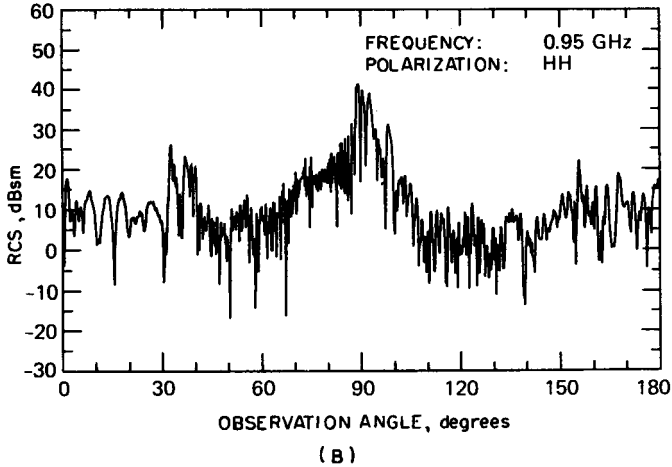

(B)

Figure 5.8 Boeing 727–100C aircraft. (A) Drawing of RCS model, with full-scale dimensions; (B) measured RCS. (*From Follin et al.* [*241*])

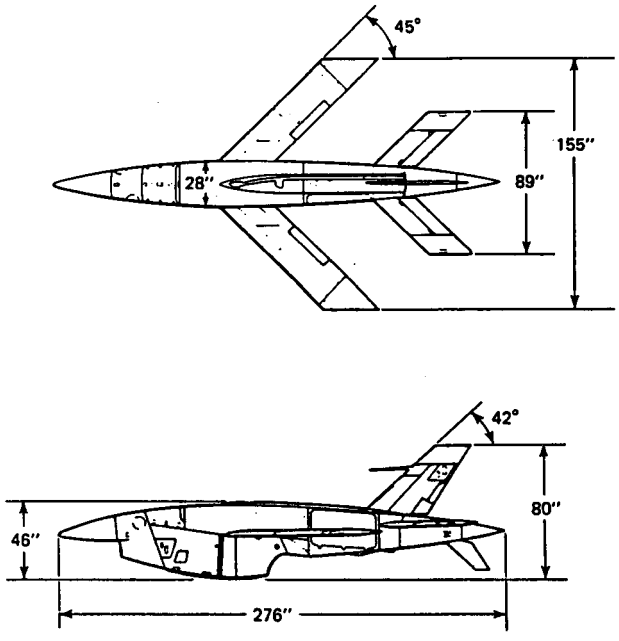

(A)

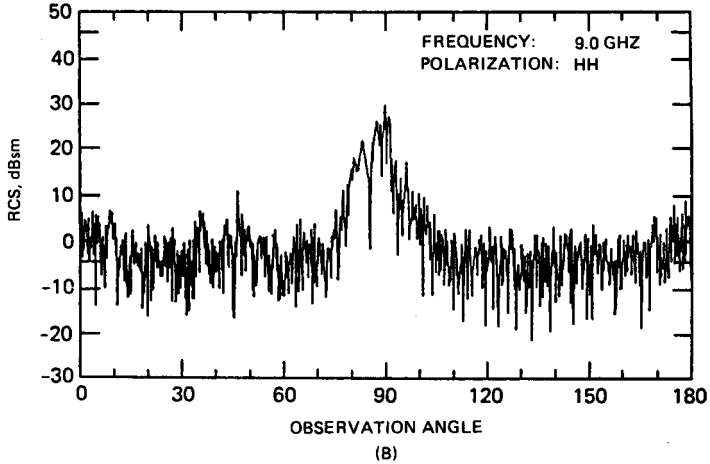

(B)

Figure 5.9 Teledyne Ryan drone. (A) Drawing; (B) measured RCS. (*From Follin et al.* [*241*])

aircraft, the drop in RCS is probably 6 to 8 dB when pulse durations drop from 1.0 μs to a few nanoseconds. Hence, surveillance radars tend to have longer pulses as opposed to tracking or identification applications.

TABLE 5.5 Summary of Rider's Results on Polarization*

Polarization mode	Aircraft, dB	Ground, dB	Rain, dB	Birds, dB
Linear reject	−9	−17	−20	−10
Circular accept	−1.3	−5.7	~0	0
reject	−0.6	−4.8	~−20	0

* The indicated values are relative to linear polarization.

Rider [599] observed a series of commercial aircraft with an L-band surveillance radar that was able to transmit either linear or circular polarization, and receive with the same- or opposite-sense polarization. While the same-sense and opposite-sense outputs were not made simultaneously, this should not significantly affect the results. Table 5.5 shows a summary of many measurements. The values in the table are mean values in decibels relative to same-sense linear polarization. The term *reject* applies to opposite-sense linear receive or same sense of circular polarization on receive.

In these experiments, there is little loss in the reflectivity of large aircraft when using circular polarization in the rain-reject mode. This conflicts with earlier experiments, which typically showed about 5-dB loss for the same-sense circular polarization. The moderately heavy cold frontal rain showed the expected 20-dB rejection with crossed linear or same-sense circular polarization. The results show a larger-than-expected rejection (17 dB) of the flat farmland in crossed linear polarization. The same-sense linear polarization reflectivity was $-28\text{dB m}^2/\text{m}^2$. If the results are general, the use of circular polarization on transmit and the ability to have both polarizations on receive would be valuable as a general mode. Air traffic control radars such as the ASR-9 and the ARSR-3 have circularly polarized transmit and either same-sense or opposite-sense circular polarization on receive as an option.

Rider [599], Poelman [555], and others have suggested that polarization diversity should improve detectability, as it is likely that the reflection from complex targets such as aircraft are mostly uncorrelated.

A similar technique for increasing the target-to-precipitation echo ratio is to use crossed linear polarizations (RCS is then σ_{HV} or σ_{VH}). While rain echoes are again reduced by 15 to 25 dB, the reduction in target RCS is generally greater than 7 dB [522].

5.3 Complex Targets—Backscatter and Distributions

Although it is possible to calculate the RCS of many geometrically simple shapes, most radar targets such as aircraft, ships, etc. are com-

plex. The RCS of complex targets can be computed in many cases by using the RCS of simple shapes. The most common procedure is to break the target into component parts and to combine them according to Eq. (5.3) [150, 149, 762]. This approach is usually used to determine the average RCS over an aspect-angle change of several degrees. Realistic complex structures such as large aircraft may exhibit 10- to 15-dB RCS fluctuations for aspect changes of a fraction of a degree [397]. Since the precise target aspect is generally unknown and time variant, the RCS is best described in statistical terms.

The statistical distribution of the RCS is of great importance in predicting detectability. For fluctuating targets, the detection probability of a single echo is roughly the probability that the target echo alone will cross a detection threshold; receiver noise primarily affects the false-alarm rate. This means that if the occurrence of a small RCS has a large probability, an unacceptably low detection probability can result for a given mean signal-to-noise ratio. A variety of RCS distribution models have been used; the choice depends on certain assumptions about the nature of the target. Table 5.6 summarizes the most widely used statistical RCS models (see Chap. 3), describes their applicability, and cites pertinent references.

Steady Target or Marcum model [461, 113]

The detection of a perfectly steady target echo in receiver noise was originally analyzed by Marcum. This *nonfluctuating* model is not realistic for real radar targets except in limited circumstances, such as when the target is a sphere or is motionless over the observation time.

Chi-square of degree 2*m* [368]

Specializations of the chi-square distribution encompass a large class of targets. The form of this distribution is given as item (2) in Table 5.6, in which $2m$ is the *degree of freedom*. As the degree becomes higher, fluctuations about the mean become more constrained, that is, the *steady* component becomes stronger. The ratio of the variance to the mean is equal to $m^{1/2}$. In the limit, as m becomes infinite, one has the steady-target case. Short-term statistics of aircraft RCS have been found to fall into various members of the chi-square family [585].

Swerling cases 1 and 2 (chi-square of degree 2) [689, 225]

The statistics of Swerling cases 1 and 2 are most often referred to as the *Rayleigh-power* or *exponential* distributions. Swerling case 2 sta-

TABLE 5.6 Statistical Models of Target Radar Cross Sections

Model	Density function of RCS, x	Applicability
(1) Marcum (*steady sinusoid* or *nonfluctuating target*)	One possible value	Perfectly steady reflector, e.g., spherical object or objects that are not rotating during the radar observation time [461, 225].
(2) Chi-square of degree $2m$ [Also Weinstock cases $(0.6 \leq 2m \leq 4.0)$]	$\frac{m}{\Gamma(m)\bar{x}}\left[\frac{mx}{\bar{x}}\right]^{m-1}\exp\left[-\frac{mx}{\bar{x}}\right]$	The distribution encompasses a class of target distributions (see items 3 and 4 below). Degree becomes higher as coherent component of target becomes greater [690, 762].
(3) Swerling cases 1 and 2 (*chi-square of degree 2, Rayleigh-power* and *exponential*)	$\frac{1}{\bar{x}}\exp\left(-\frac{x}{\bar{x}}\right)$ for $x \geq 0$	Random assembly of scatterers, no single one dominant. Applies to complex targets having numerous reflectors. Case 2 statistics apply when fluctuations are independent on a pulse-to-pulse basis. Case 1 applies to pulse-to-pulse dependence [689, 225].
(4) Swerling cases 3 and 4 (*chi-square of degree 4*)	$\frac{4x}{\bar{x}^2}\exp\left(-\frac{2x}{\bar{x}}\right)$ for $x \geq 0$	Has detection statistics nearly the same as when one large, steady reflection is combined with assembly of many small reflectors—RCS of large reflector same as sum of RCS of all the others. (See Rice distribution with $a = 1$.) Case 4 statistics apply when fluctuations are on pulse-to-pulse basis. Case 3 applies to pulse-to-pulse dependence [761, 225].

TABLE 5.6 Statistical Models of Target Radar Cross Sections (*Continued*)

Model	Density function of RCS, x	Applicability
(5) Rice (power)	$\frac{1}{\bar{x}}(1+a^2)\exp\left[-a^2-\frac{x}{\bar{x}}(1+a^2)\right]\cdot J_0[2ja\sqrt{1+a^2(x/\bar{x})}]$ for $x \geq 0$	One large reflector and an assembly of small reflectors. a^2 is the ratio of RCS of the large to the sum of all the rest. More exact for this condition than chi-square members, but fewer detection statistics have been published [397, 590, 638].
(6) Log-normal	$\frac{1}{xs\sqrt{2\pi}}\exp\left[-\frac{(\ln x-\overline{\ln x})^2}{2s^2}\right]$ for $x \geq 0$	Found to apply to many targets which have large mean-to-median ratios ρ – e.g., battleships, missiles, satellites, and aircraft near broadside aspects [322, 690].

NOTE: Detection statistics in varying amounts of completeness have been calculated for these target models in the literature cited. In all cases the interfering noise power is assumed to have an exponential probability density function (see item 3).

DEFINITIONS: x = RCS
$2m$ = degree of freedom
$\bar{x}$ = mean RCS
a^2 = ratio of RCS of large reflection to the sum of the small
J_0 = modified Bessel function
j = $\sqrt{-1}$
ρ = mean/median ratio
s = standard deviation of $\ln x$
$\overline{\ln x}$ = mean of distribution with $\ln x$ as the variable
$\Gamma(m)$ = gamma function with argument m

tistics apply when the RCS pulse samples are independent on a pulse-to-pulse basis (rapidly fluctuating). Case 1 statistics apply when the samples are correlated within a pulse group but are independent on a scan-to-scan basis (slowly fading). The pulse-to-pulse independence case is not applicable to most radar targets because of their narrow Doppler spectra (see Sec. 5.8). This assumption may be valid when pulse-to-pulse frequency diversity is used (see Sec. 5.9). The Rayleigh model applies to a random assembly of scatterers, no one of which is dominant. It is the most widely used of all distribution functions for modeling large complex targets [10, 63, 169, 490]. Experimental evidence suggests this model for complex targets such as large aircraft, whose aspects undergo large changes. However, it may not be appropriate when applied to a target that presents a limited range of aspects, such as a simple target viewed over a short period of time [541, 585].

Swerling cases 3 and 4 (chi-square of degree 4)

Case 4 statistics apply when there is pulse-to-pulse independence and case 3 statistics apply to scan-to-scan independence. Swerling assumed this model represented the class of targets having a large steady reflector and a number of randomly oriented small reflectors, although he did not attempt to justify the assumption on a physical basis. The exact distribution that fits this assumption was given by Rice.

Rice distribution

When an assembly of scatterers includes a steady reflector whose return is significant compared with the sum of all the others, the density function has the form of the Rice distribution (see [397, p. 560]) given by item (5) of Table 5.6, where a^2 is the ratio of the power from the large scatterers to the power from all the rest. When $a^2 \to 0$, this distribution converges to the Rayleigh density function, and when $a^2 \to \infty$, it converges to the steady-target case. Scholefield [638] compared the degree-4 chi-square case (Swerling 3 and 4) with the Rice distribution with $a^2 = 1$ (power from steady reflector equal to the power from the assembly). The detection statistics for the two agreed, except for small differences at the extremes of detection probability. The Rice distribution is an exact representation of the steady-plus-assembly reflector case.

Log-normal density function

The RCS distributions of some targets do not conform to any chi-square member. Some of these targets exhibit large values of RCS far more

frequently than would any member of the chi-square class. Examples of this class of targets are satellites, missiles, and ships, which often have large mean-to-median RCS ratios.* The RCS of these targets can frequently be closely represented by the log-normal density function [item (6) of Table 5.6], which arises when the logarithm of a variate is normally distributed. Swerling derived procedures for approximating this function with chi-square members [690]. The log-normal function was also studied by Heidbreder and Mitchell [322]. They postulated that the high tails of this density function arose in practice from large specular returns at a relatively few aspect angles. For conservative estimates of system performance, one should neglect these tails and resort to the Rayleigh assumption.

Discrete scatterer models

The RCS of a complex target can often be expressed as the combination of a number of discrete scattering centers. For a target composed of N discrete scatterers whose returns combine in a random-phase fashion, the RCS distribution converges to the exponential distribution (Swerling 1 and 2) if N is large enough. If N is relatively small, the RCS will deviate from the exponential model as analyzed by Castella and Reilly [114]. If each discrete scatterer is of equal magnitude, the RCS distribution is a delta function for $N = 1$, a beta function for $N = 2$, and for $N = 3$ follows a complete elliptic integral of the first kind. For $N > 3$, an analytic expression has not been obtained except for $N \to \infty$, in which case the exponential model applies. Results for various degrees of N obtained with Monte Carlo simulation show that with $N = 10$, the statistical model closely approximates the standard "many scatterer" case. With N as few as 5, the distribution is still reasonably close to that case.

Summary of statistical modeling

1. Modeling is basically a coarse procedure. In no case should an assumed statistical model be used for very precise calculations of system performance (i.e., performance at very high or at very low detection probabilities).

2. If only one parameter is to be used to describe a complex target, it should be the median RCS. Detection statistics should then be calculated by using the Rayleigh model (Swerling cases 1 and 2) having the same median value. The choice between the pulse-to-pulse or the

* The mean-to-mean ratio for the Rayleigh function is 1.44, and for the degree-4 chi-square is 1.18.

scan-to-scan independence assumption depends on the Doppler spectrum width of the echoes and whether frequency diversity is used.

3. If the tails of the actual RCS distribution function are known to be much higher than those for the chi-square members, an upper bound on system performance may be established by using the statistics for the log-normal distribution function. These statistics have been expressed in terms of the mean RCS and the mean-to-median ratio.

4. If the target is approaching the radar nose-on region, standard detection statistics should be used, and if a high detection probability is required before the target reaches a given range, cumulative detection statistics should be used.

5.4 Measured Aircraft and Missile RCS Distributions

While it is possible to measure aircraft RCS at a given aspect, the precise aspect in flight is unknown and time variant. A plot of the aircraft return versus time appears as a noiselike function, even when the *nominal* aspect of the aircraft is *constant*. Because of the uncertainties about the aspect, the RCS is usually best described statistically. Ordinarily, one assumes a Rayleigh distribution; this model has been suggested by experiments on large aircraft undergoing several angular degrees of aspect change. Unfortunately, this model does not apply to all aircraft and to all radar detection and tracking problems. A good portion of the uncertainty lies in the observation time used to obtain the RCS distribution.

In one series of experiments by NRL, RCS distributions were obtained for a variety of aircraft [10]. Flight paths were straight and level, and various aspect changes were observed by the radar. Data were recorded over 10-s intervals at P-, L-, S-, and X-bands. The Rayleigh model provided a good approximation to the distribution in many cases, although there were a large number of exceptions. The most consistent exceptions were for smaller aircraft and for all aircraft at broadside. Large, multiengine aircraft gave good Rayleigh approximations for aspect changes of only 1 or 2°. Small aircraft were often fit very poorly by this model, even when the aspect change was 8 to 9°. In most cases, deviations from the Rayleigh distribution tended toward higher-order chi-square functions. In these cases the Rayleigh assumption would tend to provide conservative estimates of detection ranges for detection probabilities greater than 50 percent.

In tests conducted by J. Whybrew at the Applied Physics Laboratory, RCS distributions at C-band were plotted for a variety of conditions and were compared with chi-square functions [585]. In all but a few cases good fits were made to some chi-square function between the 10-

and 90-percent points. For a small, two-engine Lear jet, chi-square approximations were obtained in the APL tests with degrees ranging from 1 to 37. About one-half the functions fell between degree 1.4 and 2.7. Occasionally, widely different distributions were obtained from one data segment to the next, even when the apparent azimuth aspects differed by only a degree or two. Figure 5.10 illustrates several measured density functions. In (A) and (B) the nominal aspects were similar, although the precise aspect was unknown since the "crab" angle of the aircraft was unknown. Part (A) is approximated by the Rayleigh functions and part (B) by the chi-square function of degree 22. In both cases the run length was 2.0 s, although the results were similar when the run was extended to 8 s. Parts (C) and (D) show density functions measured over 1 s. Part (C) has the appearance of the Rayleigh function, whereas part (D) does not resemble any known function. These distributions demonstrate the nonstationary character of the echoes.

The echoes from two Lear jets flying together approached the Rayleigh density functions more frequently than did those of the single jet, as illustrated by Fig. 5.11A. The ordinate is the degree of freedom of a chi-square function that best fits the data. The abscissa is the data run length T times the bandwidth of the spectrum σ_f^T measured over the same data segment. Bandwidth here is defined as the standard deviation of the airframe power spectral density function measured about the mean Doppler frequency. This figure demonstrates that the two aircraft could be represented by the Rayleigh function with more confidence than could the single aircraft. This behavior is expected, since the Rayleigh model is approached as the degree of complexity of the target increases. Fig. 5.11B summarizes density functions measured for other aircraft.

In general, as the product σ_f^T decreases, the estimated density function is expected to tend toward a model of higher degree of freedom. For example, if the measurement interval is so short that all the received pulses have the same value, the measured density function will consist of a single value. This corresponds to a chi-square function having infinite degrees of freedom. Although the tendency is not obvious from the figure, where numerous data runs are presented, it does appear in individual data segments that were broken into smaller intervals.

Table 5.7 lists some representative median RCS measurements for selected classes of targets and aspects. For most aircraft, the median RCS at nose aspect is smaller than that for other aspects, and this value can be used for conservative performance estimates. These are mostly measured with some interpolation. Some data are from scale models. No distinction is made in Table 5.7 between horizontal and

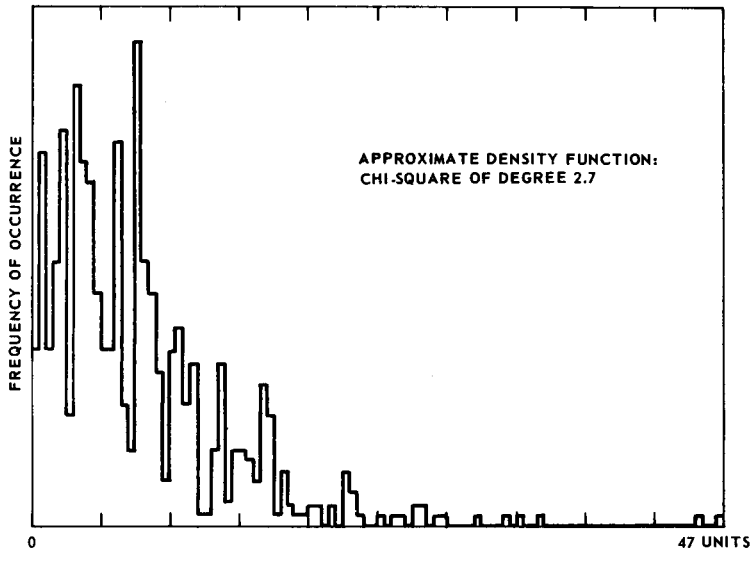

(A)

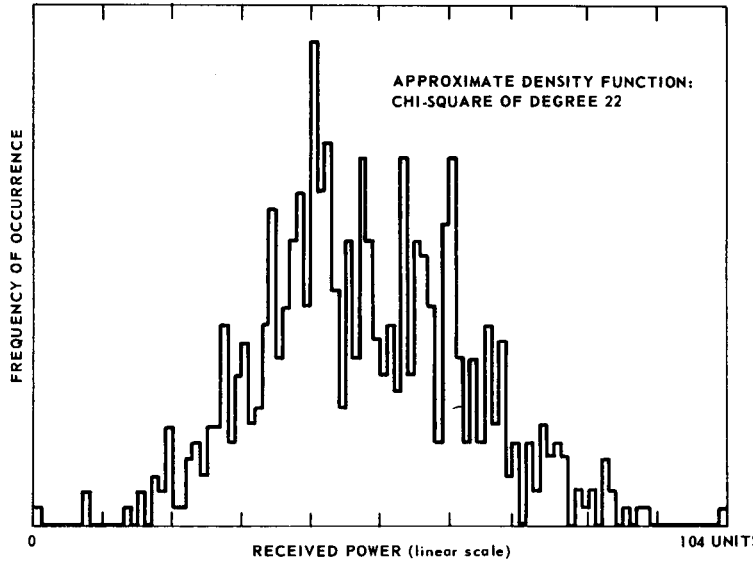

(B)

Figure 5.10 Probability density functions for small jet echoes. (A) Observation time 2 s, number of samples 624, aircraft aspect azimuth 0°, elevation 12°, range 17.5 nmi; (B) observation time 2 s, number of samples 624, aircraft aspect azimuth 10°, elevation 14°, range 17.0 nmi;

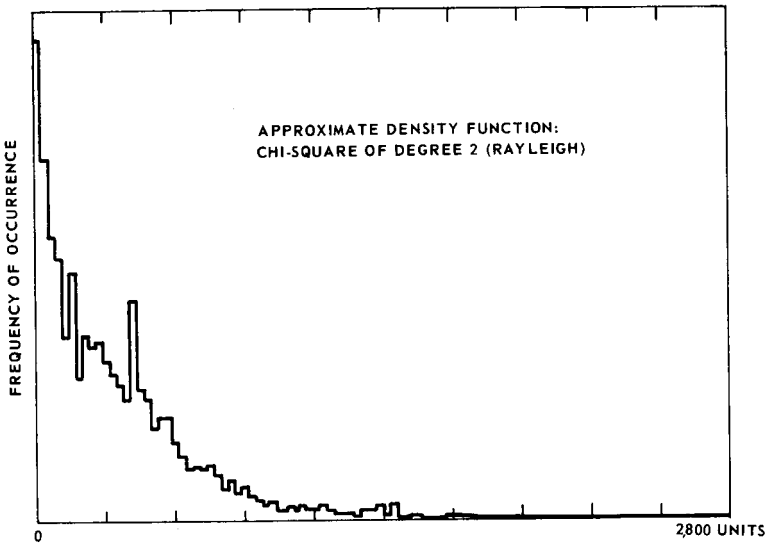

(C)

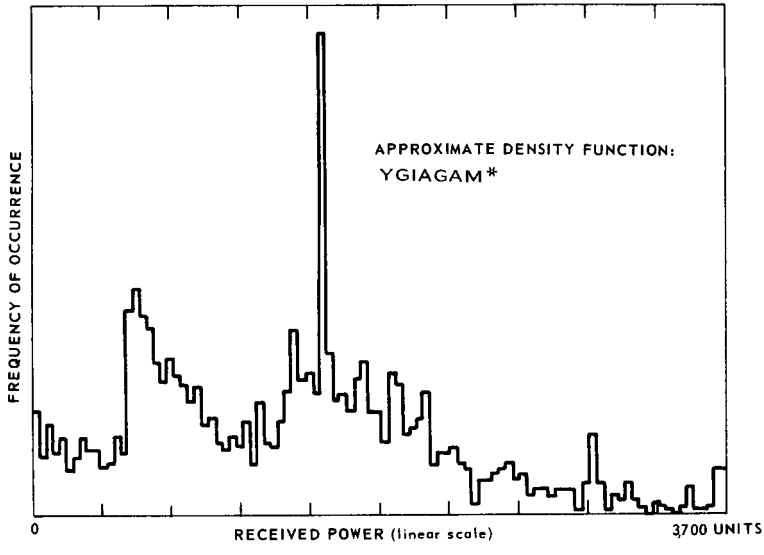

(D)

* YOUR GUESS IS AS GOOD AS MINE.

Figure 5.10 (*Continued*) (C) observation time 1 s, number of samples 2,500, aircraft aspect azimuth 37°, elevation 19°, range 8.5 nmi; (D) observation time 1 s, number of samples 2,500, aircraft aspect azimuth 72°, elevation 59°, range 4.9 nmi.

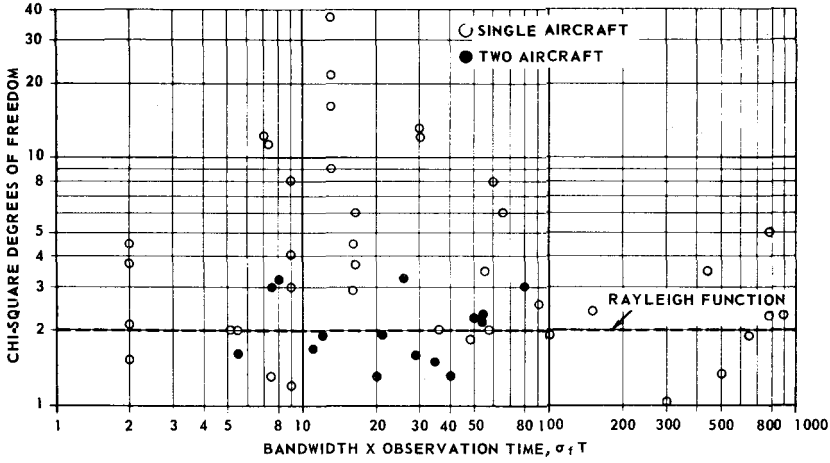

Figure 5.11 Chi-square representations of measured target RCS. (A) Observed RCS density functions for small jet aircraft; (B) observed RCS density functions for various aircraft. (*From Reilly [585], © IEEE 1969*)

vertical polarizations, since this makes little difference in the median RCS for most aspect regions.

5.5 Missile and Satellite Cross Sections

The RCS of missile and satellite targets generally falls into a class that is between a simple geometric shape and a complex target such as a large aircraft. The resulting distribution of RCS is neither that of a

TABLE 5.7 Targets—Median RCS, m^2

	Carrier frequency, GHz				
	1–2	3	5	10	17
Aircraft (Nose/Tail Avg.)					
Small propeller	2	3	2.5		
Small jet (Lear)	1	1.5	1	1.2	
T38-twin jet, F5	2	2–3	2	1–2/6*	
T39-Sabreliner	2.5		10/8	9	
F4, large fighter	5–8/5	4–20/10	4	4	
737, DC9, MD80	10	10	10	10	10
727, 707, DC8 type	22–40/15	40	30	30	
DC-10 type, 747	70	70	70	70	
Ryan drone				2/1	
Standing man (180 lb)	0.3	0.5	0.6	0.7	0.7
Automobiles	100	100	100	100	100
Ships—incoming ($\times 10^4$ m^2)					
4K tons	1.6	2.3	3.0	4.0	5.4
16K tons	13	18	24	32	43
Birds					
Sea birds	0.002	0.001–0.004	0.004		
Sparrow, starling, etc.	0.001	0.001	0.001	0.001	0.001

* Slash marks indicate different sets.

point reflector nor a random array of scatterers. This is pointed out by full-size X-band model measurements of a 54-in satellite* having spherical symmetry reported by Kennedy [394]. The cumulative distribution is shown in Fig. 5.12. Two sets of measurements are shown: a single frequency set, which shows a distribution that is more highly skewed than any of the Swerling models, and a frequency stepping set with each point being the average RCS from eight frequencies spread over 500 MHz. In both cases the mean-to-median ratio of RCS is about 10. Hence, the majority of RCS values are well below the *average*. However, the median and the decibel average dBsm (the absolute geometric mean) are similar.

With frequency agility the probability of both large and small RCS values decreases (see Sec. 5.9). Gaheen, McDonough, and Tice [255] compared the RCS distribution of the Tiros† and Nimbus satellites. These data are shown (Fig. 5.12) along with the unusual RCS distribution on a conical-shaped missile model. This model had a cone angle of 23.5°, a length of 150 in, and a diameter of 53 in at the tail. Note that frequency agility substantially reduces the number of RCS values below 0.01 m^2 for the missile target. On a single frequency, these data show that the median cross section of the cone-shaped missile is about

* Plus short stub antennas.

† The geometric cross-sectional area of the Tiros is about 3.4 m^2, or twice that of the 54-in satellite.

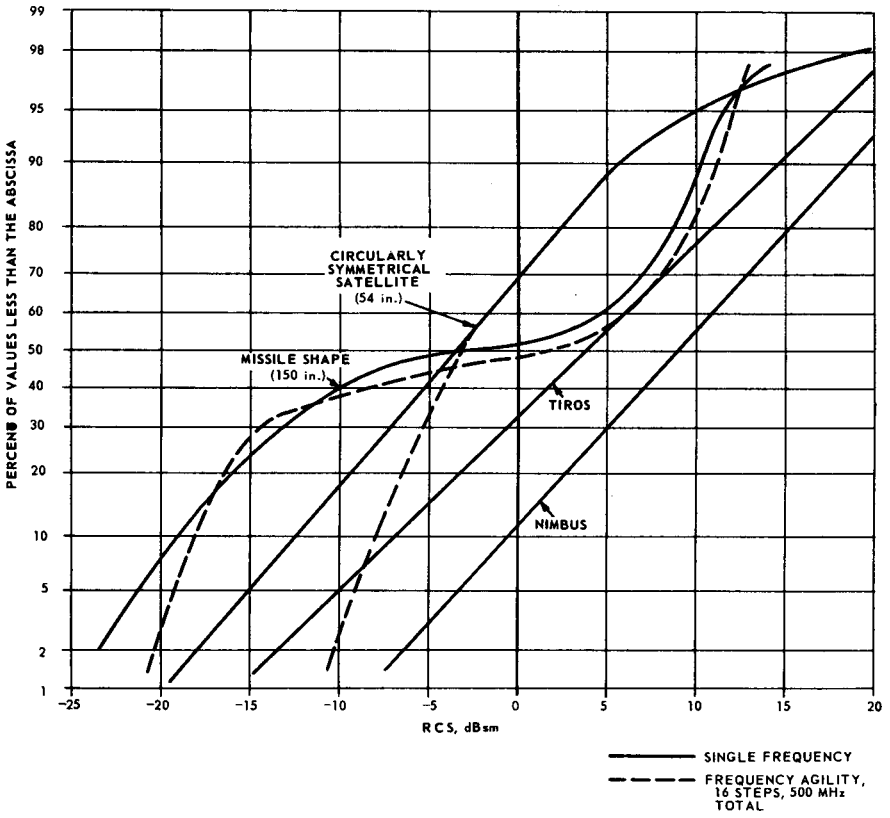

Figure 5.12 Cumulative distribution of satellite RCS average for all aspects. (*From the data of* [255])

1 m^2, while the 5-percent probability is about 20 dB less. Fig. 5.3 also suggests the log-normal distribution, which would appear as a straight line on this graph.

This satellite data should not be construed as being valid over a wide range of carrier frequencies. An indication of the frequency sensitivity of RCS of satellites is illustrated by a series of model measurements of the roughly 105-in Mercury space capsule reported by Mack and Gorr [457]. They show RCS values versus angle for simulated frequencies of 440 through 5600 MHz. Table 5.8 summarizes those data as percentiles exceeding a specified RCS. It can be seen that RCS values for the Mercury capsule do not have an obvious frequency dependence.

In the previous examples of satellite targets there was no attempt in the satellite design to reduce the RCS. However, in missile systems there is a considerable advantage in presenting a low RCS to a defending radar. For this reason there is a tendency to use radar-ab-

TABLE 5.8 Percentage of Aspect Angles That a Specified RCS Is Exceeded for the Mercury Capsule, Vertical Polarity

Frequency, MHz	$\sigma \geq 100$ m^2, %	$\sigma \geq 10$ m^2, %	$\sigma \geq 1$ m^2, %
440	0	28	70
933	35	69	98
1184	8	28	62
2800	7	47	96
5600	2	13	60

sorbing materials (RAM) or a low-RCS shape such as a wedge or a cone-sphere. The RCS is small for a cone-sphere over a broad range of carrier frequencies when observed near the pointed end of the cone. The RCS of this object is the vector sum of the reflections from the tip, the joint between the cone and the sphere, and a "creeping wave" [653, 658, 761]. A series of measurements and a theoretical curve are shown (Fig. 5.13), in which the nose-on cross section (in square wavelengths) is plotted as a function of the radius of the spherical portion (in wavelengths). The important points to note about this idealized target are that, neglecting the oscillations, RCS is proportional to λ^2 and the size of the object itself has little effect if the pulse length is greater than the target length.

5.6 Marine Targets

The radar backscatter from a ship cannot be uniquely predicted due to interference resulting from the forward-scattered electromagnetic waves. As an approximation, the received power at the radar can be written [397, 774]

$$P_r = \left[\frac{P_T G_T G_R \lambda^2 \sigma_t}{(4\pi)^3 R_t^4}\right]\left[16 \sin^4\left(\frac{2\pi h_a h_t}{\lambda R_t}\right)\right] \tag{5.6}$$

where σ_t = radar cross section in absence of reflections
h_a = antenna height
h_t = target height

The first term is the conventional free-space received power equation and the second term is a modifier that is periodic in elevation angle with a peak value of 16. This is the familiar lobing effect of surface radars that doubles the detection range at some elevations, but puts a null on targets that are situated on the surface of the water. There are several assumptions that must be explored before trying to evaluate the $\sin^4$ term in Eq. (5.6). The geometry can be illustrated by Fig. 5.14A. The modification of the field strength at the target is

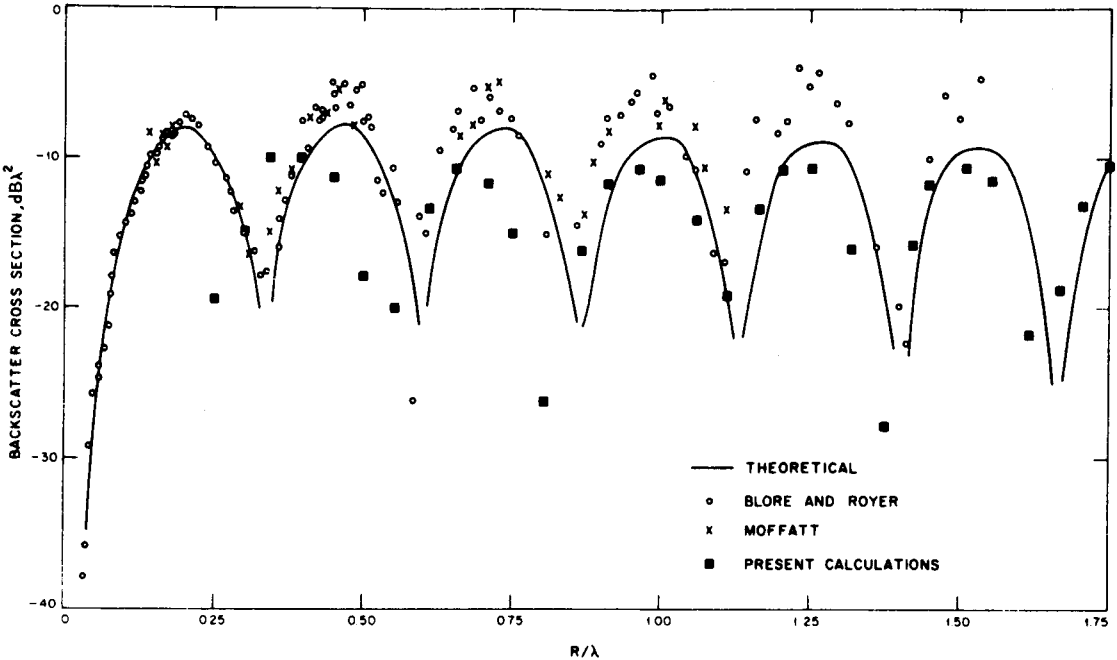

Figure 5.13 Experimental and theoretical nose-on cross section of a 15° half-angle pointed cone sphere. (*From Weiner [761]. Sources of data are given in the reference listed at the back of the book.*)

$$\eta = \frac{\text{field strength in the presence of the reflected wave}}{\text{field strength if the target were in free space}}$$

Any difference in the amplitude of the reflected wave compared with the direct wave is assumed to be due to the surface reflection coefficient being less than unity. Since the two path lengths are not exactly the same, the relative phase of the reflected wave differs. The total reflection coefficient R_s is thus a complex quantity and can be expressed as

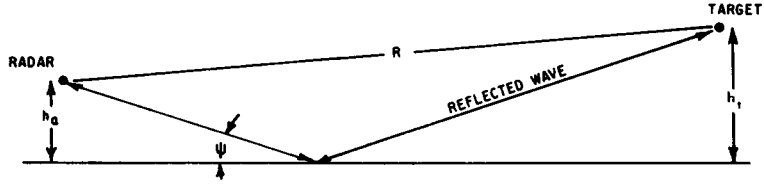

(A)

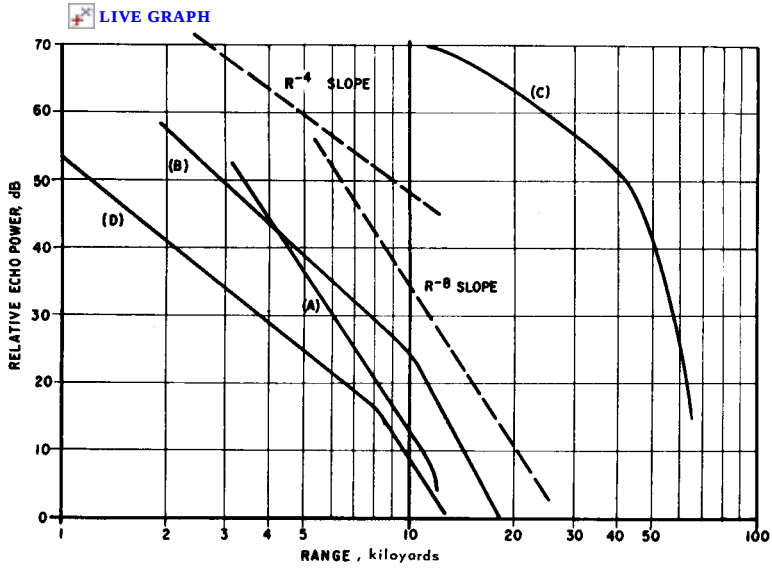

CURVE	h_a, ft	λ, cm	TARGET	REF.
(A)	470	150	SMALL SHIP	[774]
(B)	21	9.1	FREIGHTER	[397]
(C)	470	10	DESTROYER	[774]
(D)	60	3.2	40-ton TRAWLER	[174]

(B)

Figure 5.14 Geometry and measured relative echo power from ships. (A) Geometry for propagation above a flat surface; (B) relative echo power from ships.

$R_s = \rho \exp(j\Phi)$, where ρ is the real part of the reflected amplitude and Φ is the phase shift upon reflection (see Sec. 1.11).

It has been shown [774, 674] that for typical surface-radar calculation (target range $R_t >> h_a$ or h_t, and a flat surface with reflection coefficient of -1) the relative phase of the reflected wave with respect to the direct wave is

$$D = \frac{4\pi h_a h_t}{\lambda R_t} + \Phi$$

where D = difference in phase between direct and reflected paths (radians)
$\Phi = \pi$ for flat smooth sea

Section 1.12 on forward scatter shows that a reflection coefficient of -1 can be expected at low microwave frequencies ($\lambda > 30$ cm) and smooth seas. The relationship applies for grazing angles up to about 1° for both horizontal and vertical polarization. Assuming that the ship is a point reflector, making the small angle substitution in Eq. (5.6) yields

$$P_r = \frac{4\pi P_T G_T G_R \sigma_t (h_a h_t)^4}{\lambda^2 R_t^8} \tag{5.7}$$

Thus, received power from a ship may fall off as fast as R^{-8}, even without including the horizon effect.* Experimental verification of this is shown in Fig. 5.14B, which illustrates relative power received as a function of range. The location on the ordinate is arbitrary. The R^{-8} dependence near the horizon is obvious on curve A for the 150-cm radar. The transition from the R dependence (free space) to the R^{-8} dependence for the higher-frequency radars occurs approximately at $R = 4h_a h_t/\lambda$ and may be abrupt. Estimates of detection performance for various geometries and sea conditions can be obtained by using software such as EREPS [207] or TSC's Radar Workstation [571]. The difficult part of using the software is to enter a value for h_t, the effective target height, and the RCS of the ship, σ_t. Values for sea reflectivity are included in the software packages or you can insert values from Chap. 7. The following yields a good empirical fit for the vessel RCS in the absence of measured data.

The Naval Research Laboratory made carefully controlled measurements of the radar cross section of a number of naval vessels. Measurements were made at essentially grazing incidence at X-band, S-band, and L-band. An example is shown in Fig. 5.15, which gives the

* In Chap. 7 it is noted that the normalized backscatter from the sea itself σ_0 also falls off rapidly at low grazing angles.

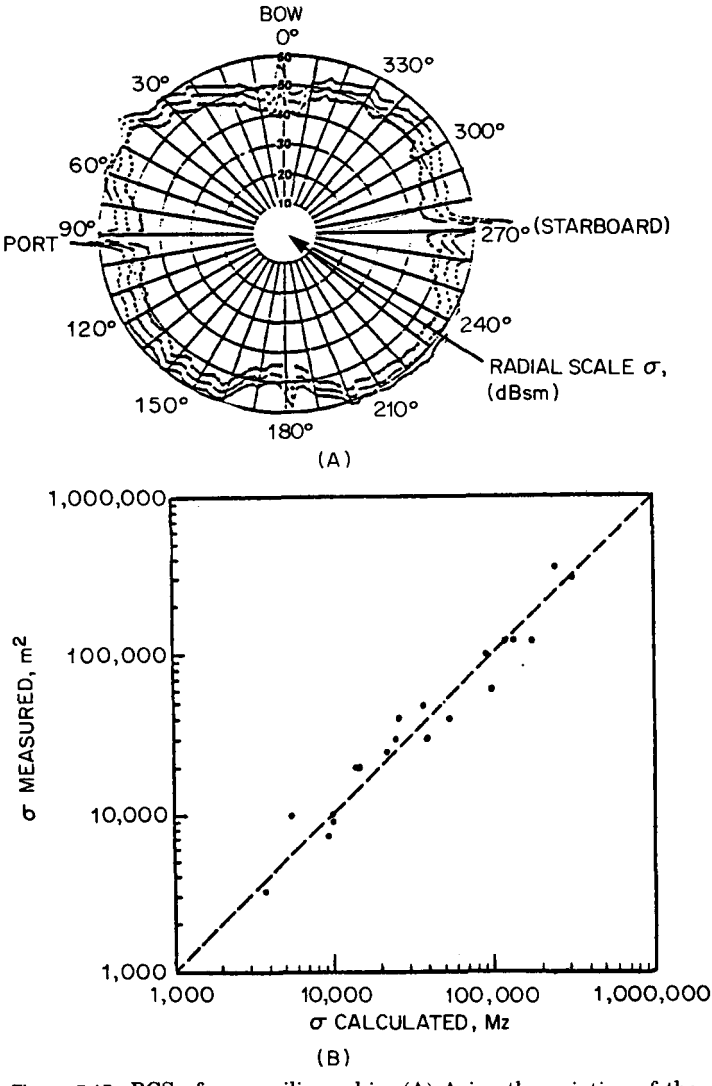

Figure 5.15 RCS of an auxiliary ship. (A) Azimuth variation of the radar cross section in 2° increments of a large naval auxiliary ship at X-band with horizontal polarization. The radial scale is the cross section measured in dB/m^2; the three curves correspond to the 20th, 50th, and 80th percentiles. (B) A comparison between the measured values of the cross section and those calculated from the empirical formula. (*From Skolnik in Eustace, H. F. (Ed.). The International Countermeasures Handbook, 3rd ed., pp. 278–279, 1977, 78. Courtesy Cardiff Publ. Co.*)

averaged values for the 20th, 50th, and 80th percentiles. When averages of the cross section were taken about the port and starboard bow and quarter aspects of the ships (omitting the peak at broadside), a simple empirical expression was obtained that permits the cross section to be

expressed in terms of the ship's displacement and the radar frequency. Such an expression for the 50th percentile is as follows:

$$\sigma = 52 f^{1/2} D^{3/2}$$

where σ = cross section, m^2
f = radar frequency, MHz
D = ship's (full load) displacement, kilotons

Similar expressions can be obtained to describe other percentiles. This expression holds for the microwave band over which the measurements were made and over the range of ship sizes examined (approximately 2000 to 17,000 tons). The above relation was used to estimate the RCS of various Russian ships. The results are summarized in Table 5.9.

As a result of the almost inseparable effects of sea reflection and the

TABLE 5.9 Estimated Soviet Ship RCS at 9 GHz

Ship/class	Displacement, tons	RCS, m^2
Carriers:		
Kuril class	40,000	1.2×10^6
Moskva class	18,000	3.7×10^5
Cruisers:		
Sverdlov class	19,200	4.1×10^5
Chapaev class	15,000	2.8×10^4
Kirov class	9,060	1.3×10^4
Kresta II class	7,500	1.0×10^4
Kynda class	6,000	7.2×10^4
Destroyers:		
Krivak and Kashin class	5,200	5.8×10^4
Kanin and Krupny	4,600	4.9×10^4
SAM Kotlin class	3,885	3.7×10^4
Tallin class	4,300	4.3×10^4
Frigates:		
Kola class	1,900	1.2×10^4
Riga class	1,600	9.9×10^3
Mirka I and II class	1,100	5.6×10^3
Petya I and II class	1,150	6.0×10^3
Corvettes:		
Grisha class	750	3.2×10^3
Poti class	650	3.2×10^3
Kronstadt class	380	1.1×10^3
FPBs:		
Osa I and II class	200	510
Komar	80	110

SOURCE: From Skolnik in Eustace, H. F. (ed.), *The International Countermeasures Handbook*, 3d ed., 1977–1978. Palo Alto: EW Communications, Inc., 1977, pp. 278–279.

cross section of the ship itself, only the measurements of ship cross section in the R^{-4} region are of general interest.

5.7 Miscellaneous Airborne Reflections and Clear Air Echoes

A modern high-power radar observes numerous reflections from various regions of the atmosphere. A radar that can detect a 1-m^2 RCS target at 200 nmi will also detect a 10^{-4}-m^2 object at 20 nmi unless specific techniques are used to inhibit detection of slowly moving, low-RCS objects at near range. In addition to echoes from aircraft, missiles, and precipitation, there are a variety of reflections that are not as easily explained. This section summarizes a few of the backscatter properties of some of the "phenomena" that appear on radar displays. The use of the term *phenomena* is to emphasize that, while many of the reflections are from discrete objects such as birds or insects, there are also numerous echoes from atmospheric anomalies including clear air layers at the tropopause [23], breaking gravitational waves [332], and *ring echoes* [671, p. 553].

The term *angel* has been used for many years to describe the radar reflections from a location in the atmosphere that does not contain a *known* discrete target. Many of these angels are undoubtedly due to the presence of small birds and insects. Table 5.10 provides a summary of the RCS of birds and insects at several carrier frequencies [269, 407, 38].

Because birds typically have dimensions comparable to a wavelength in the Mie region, the RCS is a strong and often oscillatory function

TABLE 5.10 Mean RCS of Birds and Insects*

	Size or length	Airspeed knots	Radar cross section, dBsm		
			UHF	S-	X-band
Duck	800 g	25–45	−13, −27	−30, −21*	−21
Gull	600–750 g	15–30		−30, −21*	
Pigeon	300–600 g	25–45	−30	−26,* −21	−28, −20*
Grackle	130 g		−40, −43	−25	−28
Starling	75 g	20–42		−30*	−31
Sparrow	25 g		−56	−28	−37
Hawkmoth	5 cm, 1.2 g	2.6	−74	−50	−39
Locust	2 × 0.4 cm				−30, −40
Honeybee	1.3 × 0.6 cm, 0.1 g	13	−72		−40 to −49
Dragonfly	3 cm	1.6	−72	−64	−50

* Averages over various aspects except when indicated by an asterisk, which denotes a broadside measurement.

of wavelength. This can be seen from the entries in the table in which the reported RCS at S-band (10 cm) is higher than at UHF (71 cm) or X-band (3.2 cm). It was also reported that the RCS distribution appears to follow a log-normal distribution with the mean-to-median ratio of about 2.5 for birds whose dimensions are greater than about four wavelengths, and a smaller ratio for smaller birds.

The RCS of a number of insects was also measured [420, 269]. Because these objects generally fall in the Rayleigh region, their RCS increases rapidly with increasing transmit frequency.

A single bird or insect is not a significant problem except when attempting to detect reduced cross section targets or projectiles. However, the numbers of birds in a resolution cell can be quite high. Barry [38] gave estimates as high as 200,000 birds populating a 10-mi radius from an air traffic control radar (ASR). Over 700 angels (collections of birds) were observed on one ASR with normal settings for the radar. These are typically within 15 mi of an ASR. The average RCS of the angels was 0.28 m^2 and varied from 0.005 to 2 m^2. Ground speeds were 10 to 59 knots and maximum height was 5000 to 6000 ft. With ASR radar parameters, the average was about 3 detectable angels per square mile at 2 to 4 nmi and 0.3 at 6 to 8 nmi.

Airspeeds of birds (Table 5.10) can be significant. These are not directly additive to wind speeds, especially with migrating birds. Airspeeds of the birds themselves tend to drop with tail winds and increase in head winds. Other studies have shown that the median ground speed of migratory birds is about 50 knots and that the median height is about 1000 ft. Some birds flew as high as 4000 ft. The RCS of birds displays a modulation due to the wingbeat. Typical modulation rates of 2 to 5 Hz are measured under daylight; nighttime measurements involving larger birds show wingbeats of as much as 10 to 12 Hz.

Although many radar reflections can be attributed to birds, insects, precipitation, etc., a number of other echoes cannot be easily identified. Many of these can be attributed to fluctuations in the refractive index of the atmosphere. Radar reflections have been reported from the region of the tropopause [23, 334]. This is a layer of air at an altitude of 8 to 16 km that delineates the separation between the troposphere and the stratosphere and is the region near which *clear air turbulence* (CAT) is often found to occur. Since CAT has a considerable adverse effect on jet aircraft, the possibility of detecting it by radar is currently receiving considerable attention. Clear air echoes were reported virtually every day of one six-week operation with a set of three large, high-powered radars at UHF, S- and X-bands. Some of the time they appear as "braided structures" that are attributed to breaking gravitational waves [332]. In another set of experiments, regions that showed clear air echoes were simultaneously probed with an aircraft and were found

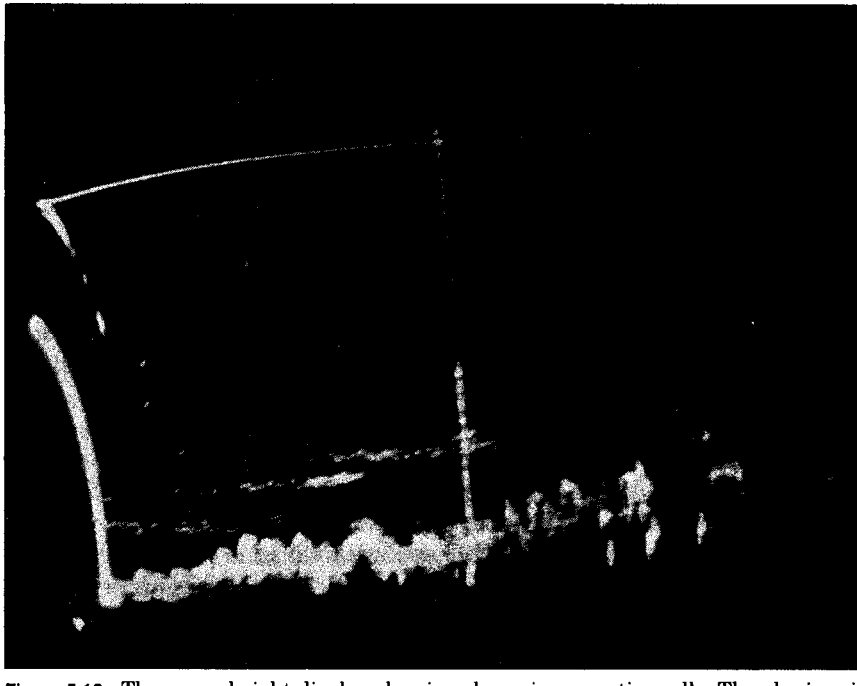

Figure 5.16 The range-height display showing clear air convective cells. The abscissa is range out to 20 mi, the ordinate is altitude with the nearly horizontal line the 20,000-ft Marker. Note also some layered echoes above the convective regions. (*From Katz [390]*)

to be turbulent [334]. An example of clear air echoes is shown in Fig. 5.16. An RHI display is shown with echoes that appear like braided structures (S-band radar). The sky was optically clear in these regions at the time of the photos.

There is also backscatter from the aurora in the polar regions, which is stronger at lower carrier frequencies. This is discussed briefly in Chap. 6.

Multifrequency radars can be used to distinguish between material particles, such as insects or clouds, and discontinuities in the atmosphere. It has been shown (see Chap. 6) that the reflectivity per unit volume η for particle diameters less than about 0.06λ is given by*

$$\eta = \pi^5 \lambda^{-4} |K|^2 \Sigma D^6 \tag{5.8}$$

where λ is the wavelength and D is the droplet diameter. The value of

* In Chap. 6 $\Sigma\sigma$ is used instead of η for the normalized volume reflectivity. The units of $\Sigma\sigma$ or η in this text are m^2/m^3 or m^{-1}.

$$K = \left| \frac{m^2 - 1}{m^2 + 2} \right|$$

where m is the complex refractive index. The equation for the reflectivity of a refractively turbulent medium can be approximated by [390]

$$\eta \approx \overline{(\Delta n)^2}\, L_e^{-2/3} \lambda^{-1/3} \tag{5.9}$$

where $\overline{(\Delta n)^2}$ is the mean-square refractice index fluctuation and L_e is related to the size of the turbulent eddies. The important difference between relations (5.8) and (5.9) is that echo particles like raindrops have a strong wavelength dependence while those from changes in refractivity are almost independent of wavelength. Thus, particulate matter or insects are seen primarily at the higher frequencies. Although the reflectivity η of the clear air echoes is only about 10^{-15} m^{-1}, they can be seen with high-powered radars at 10- to 20-km ranges.

There are many other reports of reflections from unidentified objects, many of which are caused by reflections resulting from anomalous propagation (ducting) in certain areas of the world. Air traffic control radars often develop tracks on atmospheric anomalies that do not appear to have been caused by ducting. These are often referred to as "angels" or as "worms" if they can be tracked. A good overall description of atmospheric echoes in the absence of precipitation is given in Chap. 11 of Doviak and Zrinć [187].

5.8 Spectra of Radar Cross-Section Fluctuations

The spectral width of the echoes from a complex target can have a considerable effect on the choice of radar processing technique and the specific parameters. In a Doppler tracking system (CW or pulse Doppler), it is desirable to reduce the Doppler filter bandwidth to the limits imposed by the fluctuations of the target echoes, the stability of the transmitter, and the Doppler shifts due to acceleration. Using this minimum Doppler bandwidth maximizes the signal-to-noise ratio and generally the signal-to-clutter ratio. To reduce the effect of target fading there should be additional postdetection (incoherent) integration of the outputs of the Doppler filters for a time duration greater than the correlation time of the target echoes.

Unfortunately, the relatively long correlation times of airborne targets means that in a tracking radar, the duration of a target fade may cause excessive range and angle errors. In a surveillance radar, the target cross section may remain in a null for the entire time the beam illuminates the target. This means that excessively long processing

times may be required to benefit from incoherent integration. One technique that offsets the need for long processing times is frequency agility, which is discussed in Sec. 5.9. Polarization agility also helps.

The benefit derived from incoherent integration is illustrated in Fig. 5.17, which shows the probability density function at the output of an incoherent integrator when the input signal was an aircraft echo [200]. Four integration times were examined: 10, 40, 160, and 640 ms. As the integration time increased, the probability of occurrence of a small RCS value was reduced. Fig. 5.18 shows how the ratio of the standard deviation of the RCS to its mean decreased with increasing integration time. The rate of reduction depends on the power spectral density of the echoes, as described in Secs. 3.6 and 3.7.

The spectra of RCS fluctuations of aircraft can be conveniently described in terms of three effects. First, the airframe spectrum is due to the relative motion between various scattering points. This relative

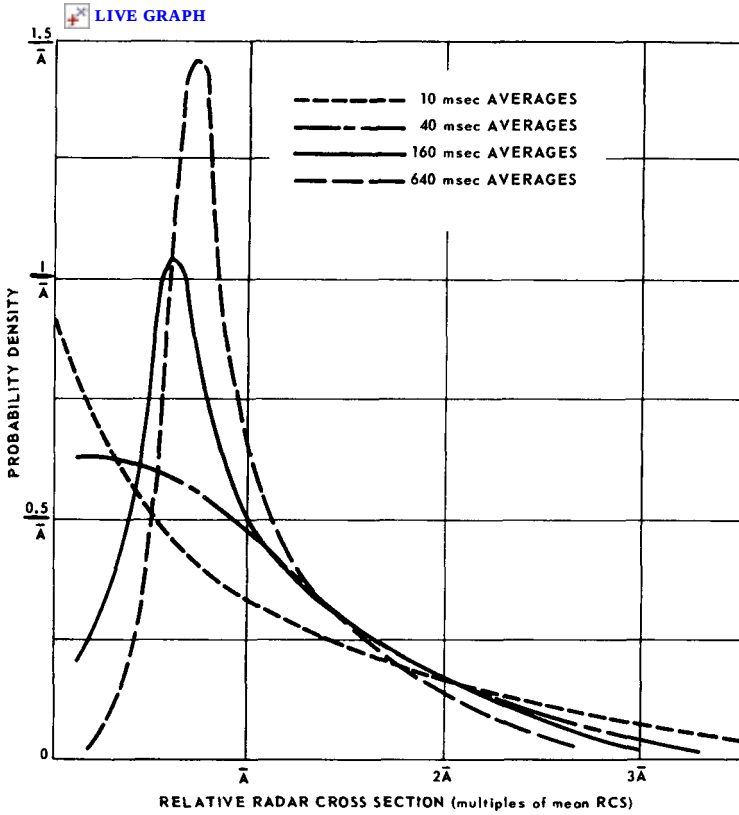

Figure 5.17 Probability density functions of X-band aircraft RCS (nose aspect). (*After Edrington* [*200*])

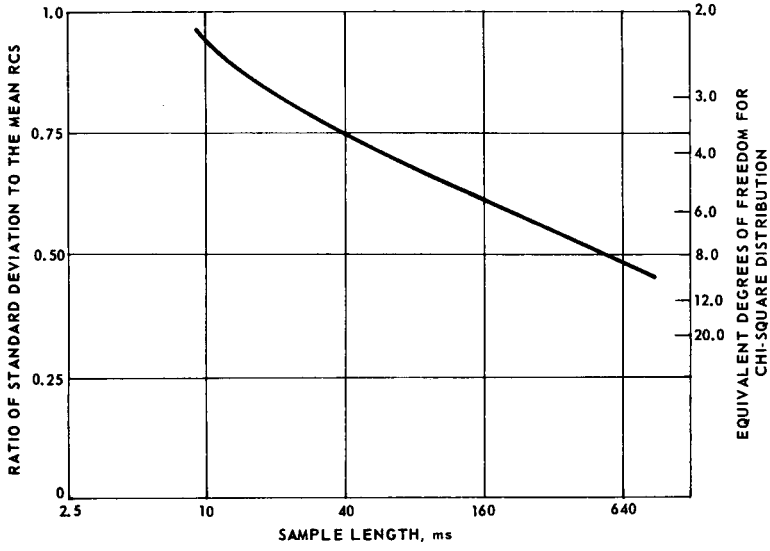

Figure 5.18 Relative standard deviation of aircraft RCS (nose aspect, X-band). (*After Edrington* [*200*])

motion occurs as the aircraft aspect changes. The resulting spectral width is proportional to the transmitted frequency. In a propeller aircraft, a second effect is caused by the amplitude modulation from the propellers. Returns from jet aircraft also contain modulation components at aspects that allow reflections from the interior of the engines. The spectral width from this component is not proportional to the transmit frequency but appears as amplitude modulation components about the airframe spectrum at multiples of the propeller rotation rate. The third effect is due to reflections from the rotating propeller or turbine blades themselves. At a given aspect the apparent center of reflection of a set of blades shifts back and forth in a periodic manner as the blades rotate. The radial component of this motion generates a spectrum typical of phase-modulation spectral energy. The phase modulation from a turbine echo is similar to a single sideband modulation with spectral lines dominating on one side of the airframe line.

The width of the airframe spectrum is expected to follow the relationship

$$\Delta f = K\left(\frac{L_0}{\lambda}\right)\left(\frac{\Delta\theta}{\Delta t}\right) \tag{5.10}$$

The constant factor K is a proportionality factor. The factor L_0/λ is a *characteristic* length of the target, such as wingspan or body length,

in wavelengths. The factor $\Delta\theta/\Delta t$ is a measure of the rate of change in target aspect. This could be a random fluctuation in aspect or a systematic change. The aspect change is due to random motion such as vibration, yaw, pitch and roll, and to systematic motion such as turning, maneuvering, or in a crossing flight. There is some indication that the length factor L_0 and the random component of $\Delta\theta/\Delta t$ are somewhat compensating. Larger aircraft have a smaller random motion due to their greater inertia. The systematic component of $\Delta\theta/\Delta t$ depends on the particular aircraft flight pattern. The work of Vogel [732] implies that, for a given $\Delta\theta/\Delta t$, the rate of signal fluctuation is proportional to L_0/λ. He used a model aircraft and simulated wavelengths of 26, 44, 96, and 160 cm. At all four wavelengths the envelope of the RCS-versus-azimuth plot was similar; however, the lobe structure detail depended on the wavelength. The number of lobes in the azimuth plot was very nearly $4L_0/\lambda$, where L_0 was taken to be the wingspan.

The three spectrum components are illustrated in Fig. 5.19 from Gardner [261]. In this example, the greatest density of energy is at the Doppler frequency of the airframe spectrum, although a greater percentage of the total energy resides at the propeller Doppler spectrum. The propeller lines appear about 8 dB below the airframe line, but their frequency extent is considerably greater. In other tests by Gardner, the propeller spectrum of a receding two-engine aircraft was most clearly defined between the aspects of 15 and 37° from the tail. In this aspect range the propeller lines were 8 to 10 dB below the airframe line. The propeller spectrum of an approaching two-engine aircraft was most clearly defined for aspects less than 18° from the nose. In these tests, the width, center frequency, and relative power of the propeller

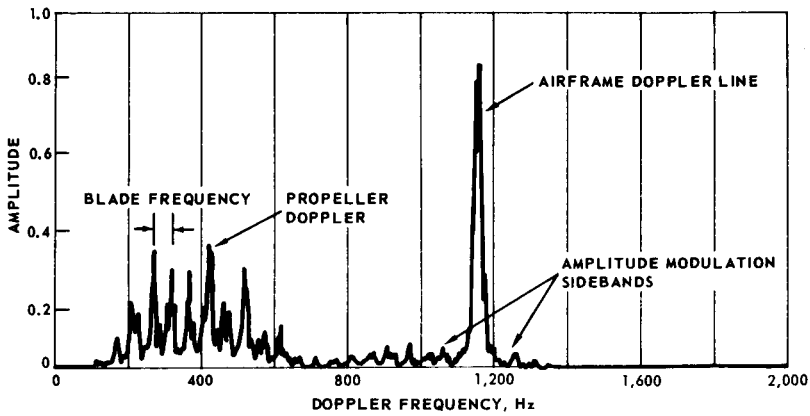

Figure 5.19 Doppler frequency spectrum of a propeller-driven aircraft (DC-7). (*From Gardner [261]*)

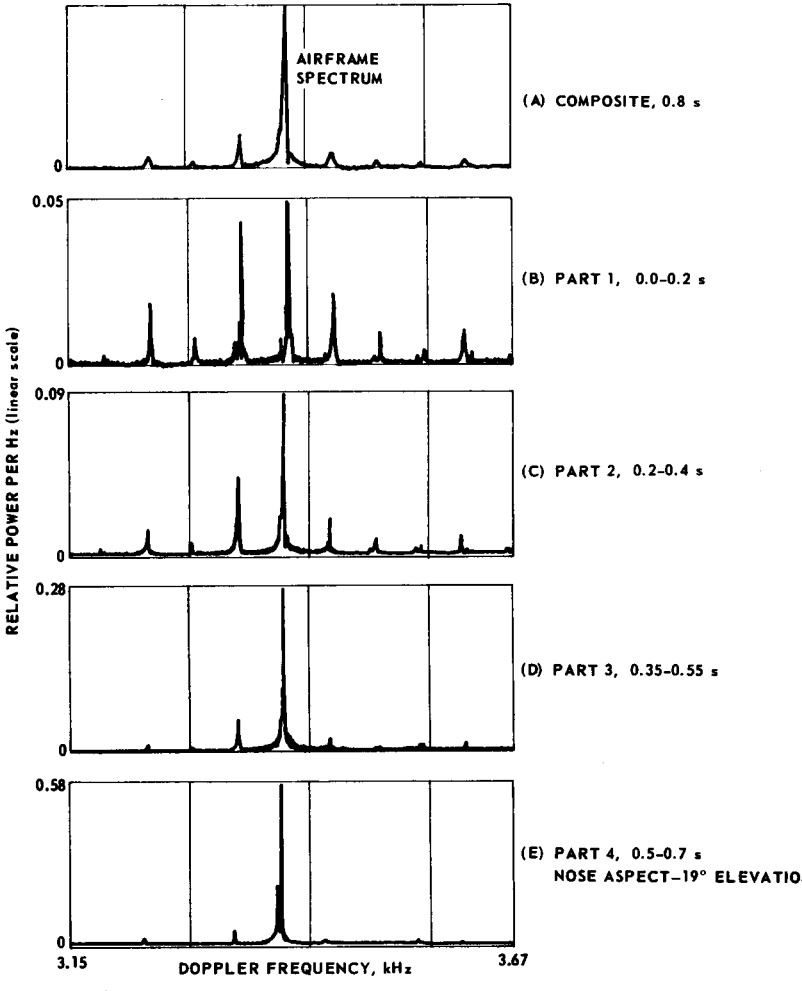

Figure 5.20 C-band spectra of T-28 aircraft showing propeller modulation.

spectrum varied with the aspect. For the aspects in which the propeller spectrum was strong, its 3-dB width varied from 200 to 1000 Hz.

The percentage of energy contained in the propeller spectrum is also time variant. Figure 5.20 shows the spectrum of a small T-28 single-engine aircraft at nose aspect. These spectra are taken from unpublished experiments performed at the Applied Physics Laboratory. Part A shows the spectrum as measured over an 0.8-s interval. Parts B through E show how the energy was partitioned over successive 0.2-s segments. (Notice that the vertical scale for each plot is different.) In this series of spectra, the total power in the propeller spectrum is

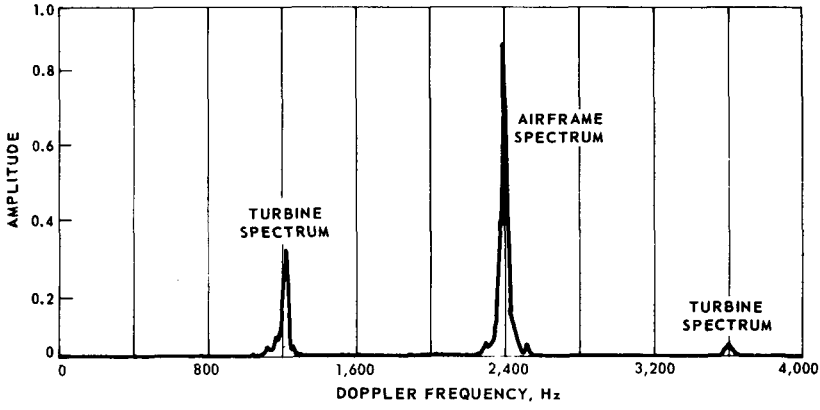

Figure 5.21 Doppler spectrum of an approaching single-engine turbojet fighter aircraft. (*From Gardner [261]*)

relatively constant, whereas the energy contained in the airframe spectrum varies from one 0.2-s segment to the next.*

The turbine spectrum present in jet aircraft echoes is illustrated in Fig. 5.21 from Gardner [261]. He detected the turbine spectrum at aspects up to 60° relative to the aircraft nose for a number of different aircraft. A lower sideband was observed at an average of about 5 dB below the aircraft line. An upper sideband was also observed, although it was very much weaker. Since the turbine echo energy is often considerable, it can easily be interpreted as a separate target at a different velocity. Hynes and Gardner observed turbine modulation components that were offset from the airframe line by the frequencies $\Delta f = nc$, where n is the compressor r/s and c is the number of compressor blades [355]. A general observation made was that the upper sidebands were much lower in amplitude than the lower sidebands.

The percentage of total energy outside the airframe spectrum was measured in a series of experiments using coherent C-band radar. Table 5.11 summarizes some preliminary findings. The percentages cited in this table refer, not only to the propeller and turbine lines, but also to any other components outside the airframe spectrum (e.g., vibration).

A few tests have been conducted from which the width of the airframe spectrum can be deduced. Table 5.11 summarizes measurements for which the aircraft has undergone small aspect rate changes (0 to 0.5°/s). Average spectrum widths are given in frequency units and in velocity units to remove the effects of the transmit frequency. The spectrum

* These illustrations have been normalized so that the maximum vertical deflection is constant.

TABLE 5.11 Percentage of Total Spectral Energy Outside of Main Airframe Spectral Line—Coherent Measurements

Aircraft	% energy outside of airframe spectrum			Aspect angle	No runs in av.
	Minimum	Average	Maximum		
T-28, small prop. aircraft	12	29	75	Nose	8
Lear jet, small two-engine	0	22	59	0–30°	6
Medium multiengine jet	4	11	17	Nose	7
Large four-engine jet, DC-8 or 707 size	17	28	38	Nose	3

width is seen to be relatively insensitive to the particular type of aircraft. This tends to support an assertion made earlier that the length of target and its random component of motion are somewhat compensating.

One example of the airframe spectrum for a small T-28 propeller aircraft is illustrated in Fig. 5.22. In this example the target flew a constant-altitude radial path. Its radial velocity decreased in 0.8 s because it was at a close range (3.5 nmi). The spectrum resolution is 7 Hz in A and 3.5 Hz in B through E. In the lower four plots there is a Doppler shift of the dominant spectral line of about 50 Hz. Relative strengths are shown at the upper left of each figure. The complex composite spectrum A is now easily explained. The spectral line on the left of A is the result of the response during interval B. The noisy response during period C is of relatively low amplitude and does not contribute a single line. The strong clean line in D contributes the central line of A, and the moderate amplitude line of E appears on the right of A. Thus, what at first appeared to be a wide fluctuation spectrum is probably due to target acceleration. This points out one of the difficulties in trying to relate coherent and incoherent spectrum measurements: acceleration results in spectral spreading in coherent, but not in incoherent, measurements. Another series of coherent spectrum measurements is shown in Fig. 5.23 for two small jets that were attempting to steadily maintain a wing-tip separation of 300 ft. Differences in their instantaneous velocities are evident. Because coherent spectrum measurements include the effects of acceleration, the spectrum widths so measured should be considered upper limits on the RCS fluctuation spectrum.

When the spectrum analysis is performed after envelope detection, it is no longer easy to separate the airframe spectrum from the other components. Part (B) of Table 5.12 summarizes some incoherent measurements made on jet aircraft. The spectrum width increases with the transmitted frequency and is roughly comparable to that for the

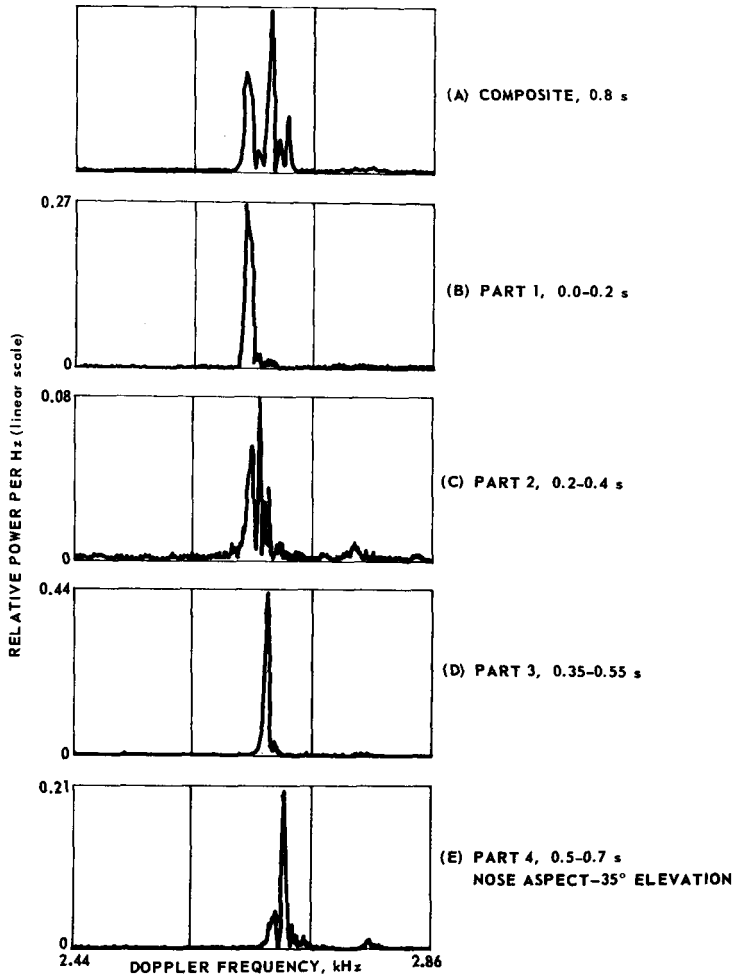

Figure 5.22 C-band power spectra of T-28 (propeller) aircraft.

airframe component of coherent measurements. It appears that the incoherent spectrum for jet aircraft is dominated by the airframe spectrum. The time required for independent sampling may be estimated by using the 3-dB width of the spectrum. For the gaussian spectrum, the standard deviation and the 3-dB width are related by $\sigma_f = 0.42\ \Delta f_{0.5}$. Using this relationship, along with the results of Sec. 3.7, the independence time is estimated by $T_I \approx 1/\Delta f_{0.5}$. This results in independence intervals ranging from 30 to 300 ms. Thus, unless polarization or frequency agility is used, the pulse-to-pulse independence assumption is not satisfied for most aircraft-detection radar problems.

The power spectrum of an aircraft or vehicle provides a signature of that class of target. Spectra from propeller or jet aircraft are easily

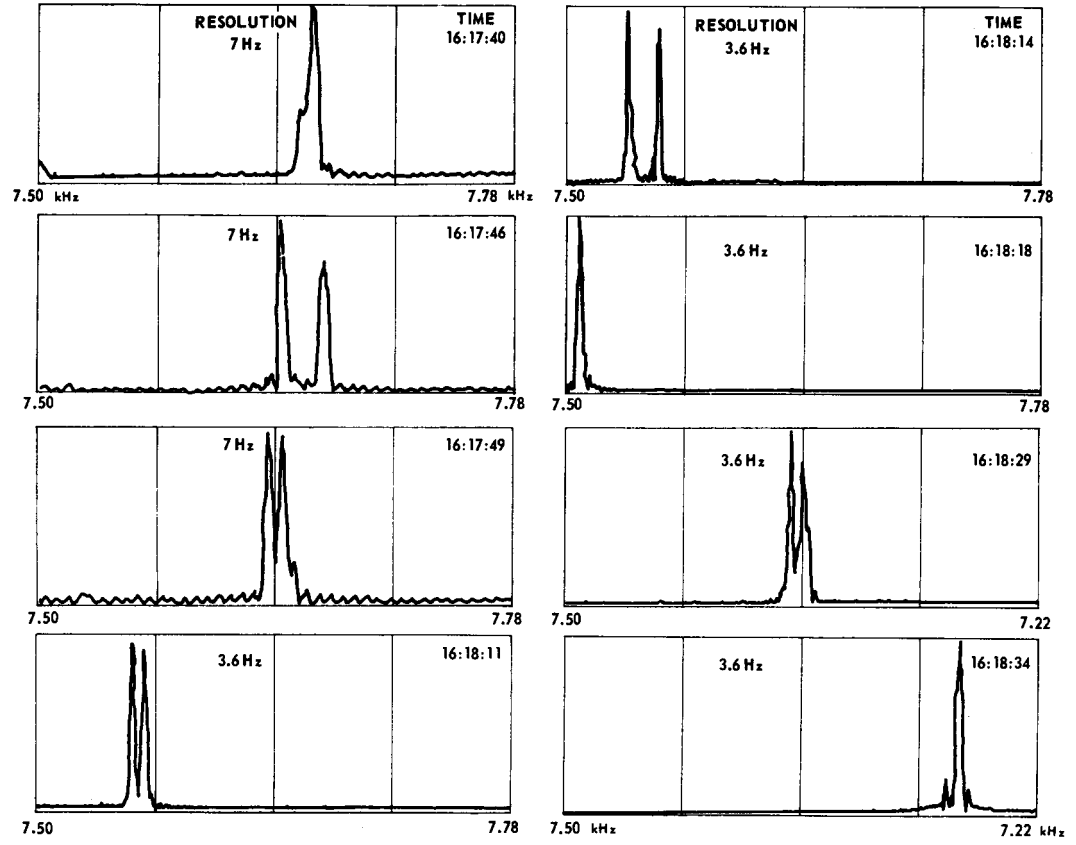

Figure 5.23 C-band spectrum of echoes from two jets—300-ft separation, radial flight.

TABLE 5.12 Airframe Spectrum Width for Nearly Constant Aspects

	Av. aspect angle, degrees	Transmit band	Record time, s	$\Delta f_{0.5}$ Av. 3-dB width		No runs in av.	Refs.
				Hz	m/s		
(A) Coherent measurements							
Small propeller plane	Nose	C	0.8	14	0.38	8	APL
Small two-engine jet	25–35	C	0.8	10	0.26	3	APL
Two-engine propeller	140–175						
	6–43	S	1.2	17.5	0.92	13	[261]
Four-engine propeller	135	S	5.2	7	0.37	1	[261]
Multiengine jet		S	5.2	15	0.8	1	[261]
		X	5.0	27	0.45	4	[261]
Small helicopter		C	0.8	69	1.8	4	APL
(B) Incoherent measurements*—jet aircraft							
Jet fighter	All	L	5	2.4	0.3	4	[10]
	All	S	5	3.7	0.2	6	
	All	X	5	6.2	0.1	3	
Jet	Nose	X	5	12.4	0.2	3	[201]
Three- and four-engine jets	Nose and Tail	K_a	24	28	0.13	9	
	Broadside	K_a	24	17	0.08	6	

* Spectrum width for incoherent measurements is defined as twice the distance along the frequency axes from the spectrum peak to the −3-dB point.

distinguished. In addition, each type of jet engine has a signature. These are often characterized by the *jet engine modulation* (JEM).

While there are few published results, some insight can be obtained by analysis and measurements on a helicopter reported by Fliss and Mensa [236]. They calculated the time history of a rotating blade such as a rotor, as illustrated in Fig. 5.24A. The simulated spectrum at different times corresponding to the position of the rotor is shown in Fig. 5.24B. Note the specular flash as the blade becomes perpendicular to the radar. The radial component of the tip is greatest at this time. Measured spectra on a rotating helicopter are shown in Fig. 5.25. The flash is quite clear, but the smaller tip signal is not apparent as in their other figures. Physical characteristics such as rotation rate, number of blades, and blade length can be inferred with proper implementation.

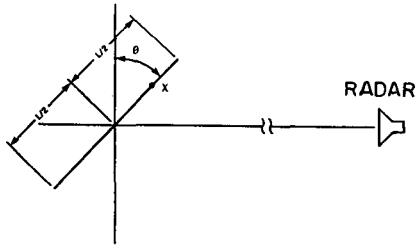

$$v(\theta) = K \int_{-L/2}^{L/2} \exp\left(-j4\,\pi \frac{\chi}{\lambda} \sin\theta\right) d\chi$$

(A)

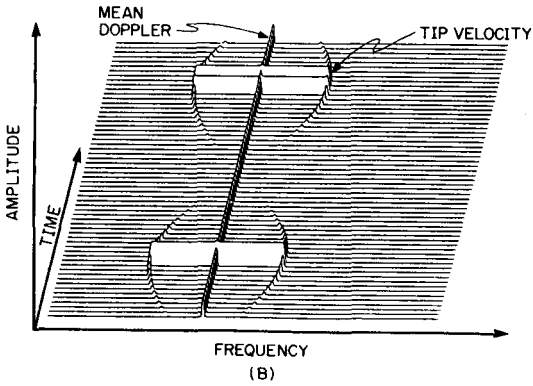

(B)

Figure 5.24 (A) Position and (B) simulated spectra of single rotor. (*From Fliss and Mensa [236], © IEEE, 1986*)

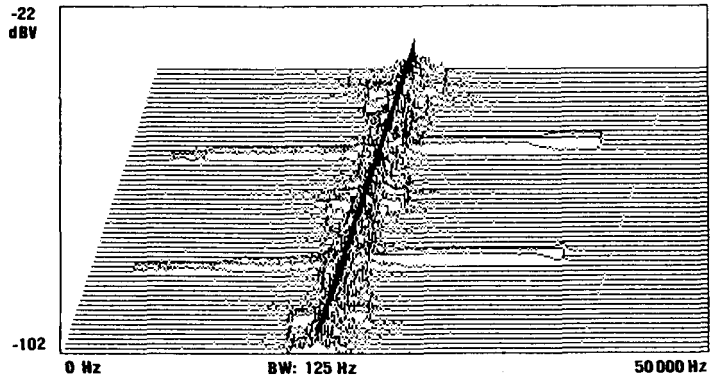

Figure 5.25 Measured helicopter spectra. (*From Fliss and Mensa [236], © IEEE, 1986*)

5.9 Frequency-Agility Effects on Target Detection and Tracking

A frequency agility or diversity radar transmits several pulses on different carrier frequencies during a single look at the target. The received signals are detected and either linearly integrated or otherwise combined with some logic technique. In detection and tracking radars frequency agility can

1. Deny enemies the possibility of concentrating all their jamming power at a single carrier frequency (spot jamming)
2. Reduce the probability that a target will have an aspect angle that gives a null in its RCS
3. Reduce range and angle tracking errors caused by finite target extent (glint) and multipath effects
4. Allow improvement in the target signal-to-clutter fluctuations (S/C) for incoherent pulse radars

The first item has been mentioned in Chap. 1 and in Gustafson and Ås [299]. The second and third benefits result from the modification of the RCS distribution and are discussed in this section. The fourth benefit will become obvious after a discussion of the effects of multiple-frequency transmissions on clutter echoes. Chapter 3 showed that the most difficult targets to detect with high probability were those whose echoes fluctuated slowly. (Swerling cases 1 and 3.) If such a target presents a null in cross section on a given pulse, its aspect may not change significantly to increase the RCS for successive transmit pulses during a single scan. The echo from a complex target is the vector summation of the reflections from every scatterer on the target, and

the phase of each scatterer's contribution is determined by the relative spacing of each reflecting point. If the maximum radial separation between scatterers is a large number of wavelengths, a fractional change in carrier frequency will drastically change the vector summation of the echo. Hence, the frequency-shifted echo may be decorrelated from that using the original wavelength. This will occur even if there is no change in target aspect. This is illustrated in Fig. 5.26 for the 54-in satellite target described in Sec. 5.5. The RCS is shown as a function of carrier frequency for a series of aspect angles near a null. The deep null at 85.7° aspect occurs only over a frequency span of about 40 MHz. A radar that transmits sufficiently different carrier frequencies in one scan can thus receive decorrelated echoes from a

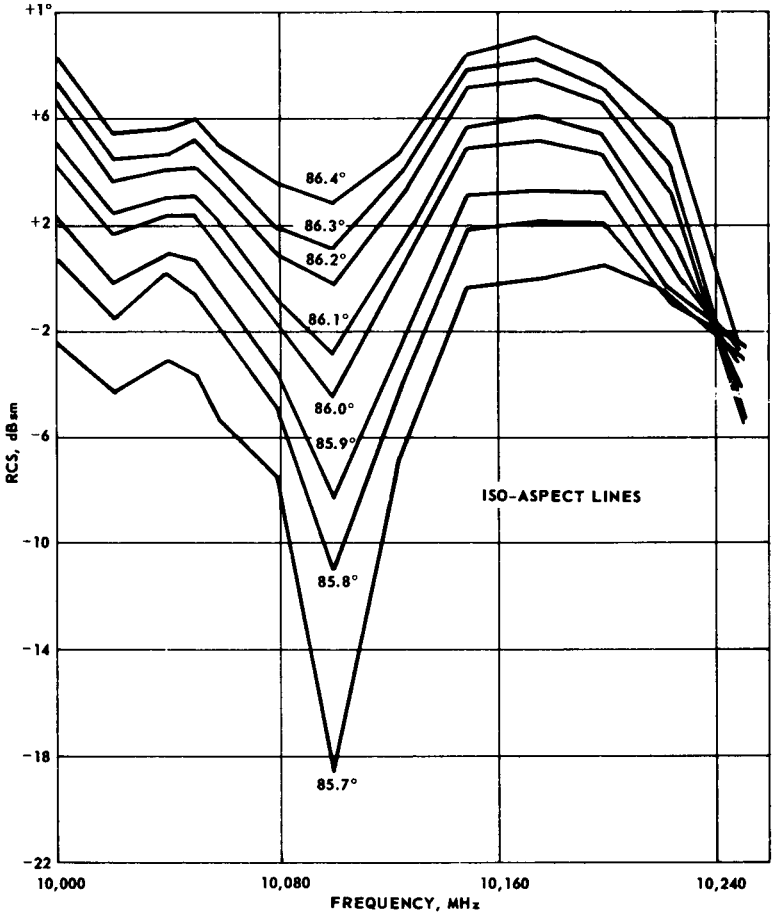

Figure 5.26 RCS versus frequency near a null for 54-in satellite (*After Kennedy* [*394*])

stationary target.* A target that is described as a Swerling case 1 for a single-frequency transmission becomes a case 2 target for a frequency agile radar, provided the frequency separation is sufficient. Similarly, a case 3 target becomes a case 4. If a high detection probability ($P_d \geq 0.9$) is desired, the case 2 or 4 target requires considerably less energy than the case 1 or 3 target for multiple-phase transmissions per scan because the probability of making a threshold decision during a signal null is greatly reduced. The next paragraphs give some analysis and experimental results on how much frequency shift is needed to decorrelate the target echoes and how greatly the detectability is improved.

Since there is no unique description of a complex target, the decorrelation of target echoes with frequency shifting can be described only for some idealized cases. Examples are a volume filled with a large number of scatterers (rain, chaff, etc.) or a number of reflection points distributed along a line target. Theoretical and experimental verification of the correlation coefficient for volume scatterers is given in Chaps. 6 and 7. For uniformly distributed reflecting points along a line target of length L, Birkemeier and Wallace [67] have shown that the correlation coefficient ρ of the square-law echoes is

$$\rho(\Delta f) = \frac{\sin^2[2\pi\Delta f(L \sin\theta)/c]}{[2\pi\Delta f(L \sin\theta)/c]^2} \tag{5.11}$$

where Δf = carrier frequency shift
$L \sin\theta$ = projection of target length onto radial dimension
c = velocity of light

This equation assumes that the pulse length $c\tau/2$ is greater than $L \sin\theta$. They also define a critical frequency shift Δf_c which yields the first zero of $\rho(\Delta f)$ and hence one definition of *decorrelation*

$$\Delta f_c = \frac{c}{2L \sin\theta} = \frac{c}{2L_0} = \frac{150 \text{ MHz}}{\text{length in meters}} \tag{5.12}$$

L_0 is defined as the effective radial extent of the scatterers. The term $c/2L_0$ can be seen to be the inverse of the radial target extent in radar time. Since $c \approx 3 \times 10^8$ m/s, the critical frequency shift is 150 MHz divided by the effective target length. Ray [578], using different criteria, suggests that 45 MHz/L_0 is sufficient for decorrelation with $\rho(\Delta f) = 0.5$. Gaheen, McDonough, and Tice [255] suggest that 75 MHz/L_0 is adequate (for a correlation coefficient of 0.4). Since most targets are

* The frequencies may be contiguous or separated by the interpulse period.

not a large collection of linearly distributed scatterers, these values may not completely result in decorrelated returns from a target at all aspects. However, they should be sufficient to fill in the deep nulls. The correlation function versus frequency shift for the satellite target is shown for three 10° aspect sectors in Fig. 5.27 from Kennedy [394]. In sector 1, where the cross section is quite small (0.5 m^2), there is considerable decorrelation of the received power with a frequency shift of $c/4L_0$. In sector 2, where the cross section is quite large (21 m^2), there is little decorrelation. In this region decorrelation is not essential or even desired since the reflections will be strong at all frequencies. By averaging eight frequencies spaced over a 250-MHz band, the nulls that were below -25 dB m^2 were enhanced by 17 dB. Those that were between -15 and -25 dB m^2 were enhanced by an average of 10 dB.

If the single-frequency target fluctuation model is known, the improvement in detectability for N pulses can be determined from the appropriate Swerling curves [461, 225]. Without frequency agility and with integration times that are short compared with the correlation time of the target echoes, case 1 or case 3 should be used. If the frequency shift of the agility radar is sufficient to decorrelate the target echoes, case 2 or 4 for N pulses integrated should be used. The improvement in detectability is the difference in (S/N) between the two sets. For partially decorrelated target echoes, N should be replaced with the number of independent target echoes N_i. This will give pessimistic answers since the noise fluctuation is further reduced by $N - N_i$ integrations. The improvement in detectability is illustrated in Fig. 5.28 [255] for the missile target studied by Kennedy and described in Sec. 5.5. The figure shows that the probability of the target echo exceeding any given small value x is improved drastically for 16 frequency increments, even for a total spread of 250 MHz. In this case $\Delta f \approx 16$ MHz, which is less than $\Delta f/4L_0$. Doubling the frequency spread gives only slight additional improvement because most of the gain comes from the first few independent samples.

Some experimental data have demonstrated the increase in detectability with frequency agility. The results of three sets of experiments on unidentified aircraft are summarized in Table 5.13. The first set at K_u band [378] gives the percentage of detections at various ranges for single frequency and for frequency stepping of 1 MHz per interpulse period. Both linear and logarithmic receivers were used. A somewhat unusual digital detection criterion makes it difficult to estimate the number of independent samples. The improvement in detectability was estimated from the observed detection range by

$$\Delta\left(\frac{S}{N}\right) \approx \left(\frac{\text{range with frequency agility}}{\text{range with single frequency}}\right)^4$$

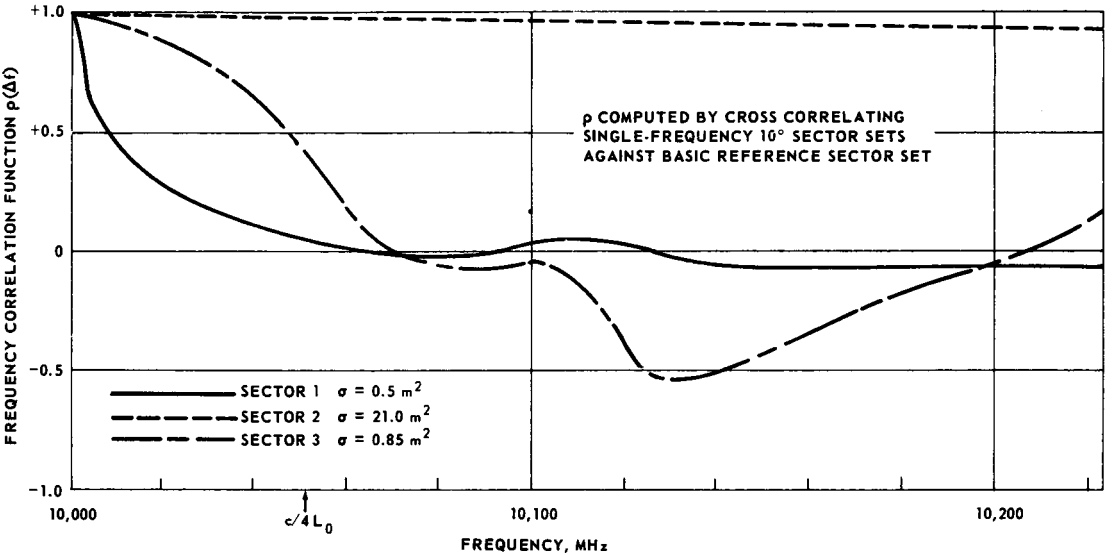

Figure 5.27 Normalized frequency correlation functions for 54-in satellite target (*After Kennedy* [*394*])

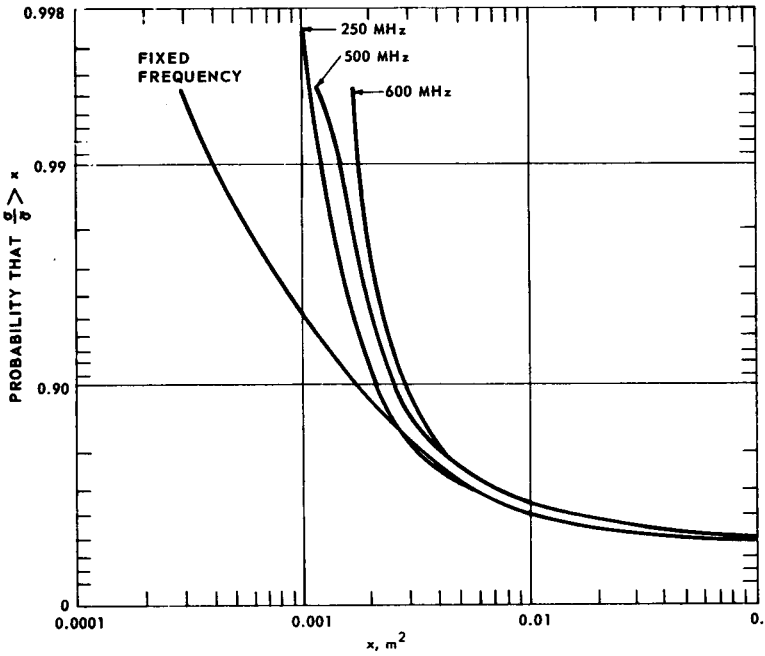

Figure 5.28 Missile target cross-sectional distribution versus bandwidth for 16 frequency increments (missile length = 150 in). (*After Gaheen et al.* [255])

Each detection included about 30 carrier frequencies spaced by 1 MHz. The unexpected detectability improvement at low detection probabilities is not explained.

The second set of measurements summarized in Table 5.13 is from a frequency-jumping search-radar test in Sweden [299]. The targets flew a controlled inbound course with a fixed-frequency or frequency-jumping track radar. Outbound targets had a 20-percent-greater tracking range to the first *dropout* in the frequency-jumping mode.

The third set of columns of Table 5.13 represents similar data for an unidentified aircraft reported by Waters [754]. The detected echoes on two carrier frequencies separated by 215 MHz were summed and compared with one of the channels. There were not enough tests to determine (S/N) improvement for the single-frequency transmission above $P_D \approx 80$ percent. Therefore the numbers in parentheses were estimated by extrapolating the single-frequency data at the lower values of P_D. A portion of the experimental improvement (1.5 to 2 dB) is accounted for by the postdetection of summation of two channels that would be obtained even if they had been on the same frequency.

Since in all tests the targets observed were not identified, it can only be conjectured from the data that their reflectivity distribution func-

TABLE 5.13 Experimental Results Showing Improved Target Detectability in dB with Frequency-Agility Transmission

Percentage detections	Boeing aircraft tests, 16.5 GHz increased sensitivity, ~30 pulses		Swedish tests		RRE tests, 2.8 GHz improvement with sum of two frequencies
	Δf = 1 MHz 1 pulse				
	Linear detector, dB	Log-amp, dB	Jet fighter	Small prop.	Δf = 215 MHz improvement in sum channel, dB
$P_d \approx$ 95–97	7.8	8.1	. . . .	. . . .	. . . .
95	6.4	7.2	. . . .	. . . .	(7)*
90	4.0	4.5	6.4	. . . .	(4)*
80	2.7	2.7	4.7	7.8	7.0
70	2.1	2.4	3.8	7.0	2.5
50	1.6	2.0	3.0	3.3	1.3
30	1.3	1.6	. . . .	1.8	1.2
10	1.2	1.4	. . . .	0.7	

* Experimental frequency agility compared with theoretical single frequency for Rayleigh fluctuating target.

SOURCE: Refs. 299, 378, and 754.

tions were between Swerling case 1 and case 3. In these studies the improvements for $P_D \geq 70$ percent are quite dramatic. Similar improvements are expected for satellite and missile targets. Improvements from frequency agility will be considerably less if the targets fluctuate during a single scan or if only the cumulative detection probability need be high (P_D per scan is low).

Figures 5.29A and 5.29B show frequency correlation functions measured by Gjessing and Hjelmstad [267, 268] for two small aircraft (Cessna 172 and F-16). The data appear to indicate several dominant reflectors plus a number of smaller ones. The dashed curve is a fit to the data which can be related to the effective length of the aircraft. The fit shows a close relation to the known length, and suggests that, in addition to the decorrelation of the aircraft echo with frequency that is needed to improve detectability, there is a simple means of size estimation by calculating the correlation function of the detected signals on each frequency. From their results, the "effective length" (ΔL) of these aircraft is perhaps one-half the actual length. They also showed that in accordance with the theory for nondispersive structures, there is a linear relationship between Doppler shift and carrier frequency. The oscillations of the measured correlation functions are related to

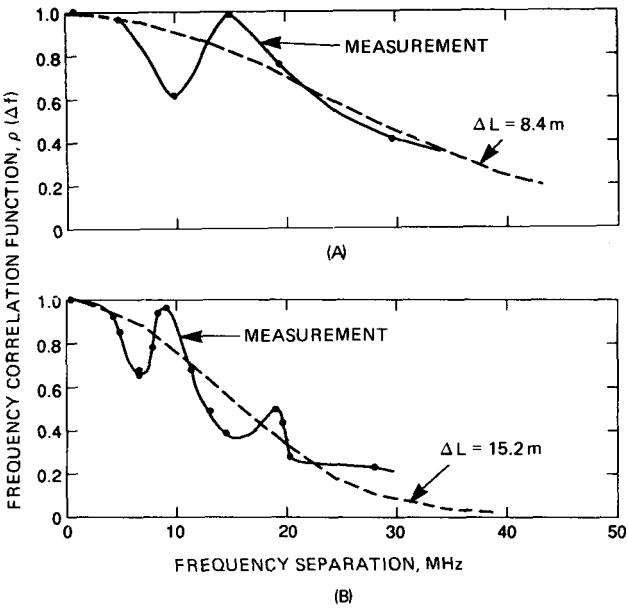

Figure 5.29 Frequency correlation functions. (A) Cessna 172 (L = 9 m); (B) F-16 (L = 16 m). Oscillations in measured values indicate a "thinned" distribution of scatterers. Broken line indicates a fit for dense arrangement of scatterers with Gaussian distribution. ΔL = Measured effective length. (*Adapted from Gjessing [268]*)

the number and placement of the dominant reflectors on the target. In another paper, Gjessing, [268] showed good agreement between theory and measurements on a 37.5-m cargo ship. He also showed that with his parameters, the echoes from sea clutter were mostly uncorrelated. He expanded on possibilities for target classification using Doppler, frequency agility, and polarization diversity as independent but complementary means of identifying an unknown target.

Figure 5.30 illustrates frequency correlation functions, $\rho(\Delta f)$, for targets consisting of assemblies of discrete scatterers of varying number [114]. One extreme case with $N = 2$ shows an oscillatory correlation pattern; a limiting case is for $N \rightarrow \infty$. When N is small, it is possible for $\rho(\Delta f)$ to achieve highly correlated values for sufficient frequency shift after a period of near-zero correlation. The frequency correlation pattern can provide information on the length of the target, as well as the radial separation of scattering centers. This information is a subset of what can be obtained in a coherent multifrequency system of the same bandwidth, but with a much simpler implementation (see Chap. 13).

Angle and range "glint" errors are also reduced with frequency agility, but it is more difficult to quantify the expected improvement. If the target can be represented by a line of scatterers perpendicular to the line of sight, there will be a *time-correlated* angle error signal for a single-frequency radar with the spectral energy of the error signal

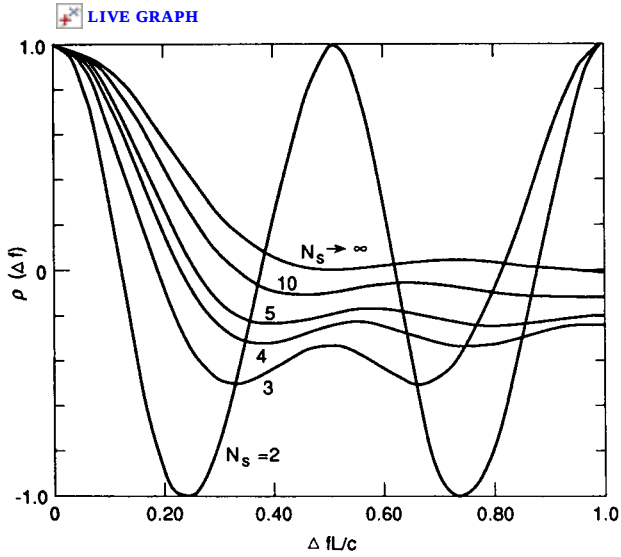

Figure 5.30 Frequency correlation functions for uniformly distributed discrete scatterers of varying number along a length L. (*From Castella and Reilly, 1987 [114]*)

concentrated near zero frequency.* Since the time constant of angle tracking loops is generally quite long, the angle error signals will follow the slowly varying phase front of the complex target echo. With several assumptions, as reported in [67, 490], the spectrum of the angle error signals for a target of linearly distributed scatterers can be written

$$W_u(f) = \frac{\overline{U^2}}{2f_m}\left(2 - \frac{3f}{f_m} + \frac{3f^2}{f_m^2} - \frac{f^3}{f_m^3}\right) \quad \text{for} \quad f \le 2f_m$$

$$= 0 \text{ elsewhere}$$

where $\overline{U^2}$ = mean-square value of perturbation signal $U(t)$
$f_m = f_0\Omega(L \cos \theta)/c$
f_0 = carrier frequency, Hz
Ω = rotation rate of line target about its center (small angles assumed)
$L \cos \theta = L_x$ = projection of target perpendicular to line of sight

The variance of $U(t)$ can be shown to be independent of Ω while the spectral width is proportional to Ω [67]. Frequency agility essentially spreads the *glint* spectral energy outside the angle-servo bandwidth. Another way of viewing this effect is that frequency agility allows a number of independent samples of the angle of arrival to be averaged within the passband of the angle servos [255]. Methods of analysis of the reduction in angle error variance are given in [67, 578]. Under certain conditions the maximum reduction in the angle error variance due to glint can equal the number of frequencies transmitted. This assumes that the separation between adjacent frequencies is greater than $c/2L_x$, where L_x is taken as the target projection perpendicular to the line of sight. Substantial glint reductions on both aircraft and ship targets have also been measured experimentally [299]. For the aircraft targets, the glint error signals up to 2 to 4 Hz were considerably reduced. With large ship targets the bearing errors were one-fourth to one-half as large with frequency-jumping as with single-frequency transmission. Range error fluctuations can also be reduced by frequency agility, which reduces the wander of the apparent *centroid of reflection*. For aircraft targets for which the length is comparable to the wingspan, the same amount of frequency shifting per pulse ($\approx c/2L_0$) improves detectability and reduces angle and range glint significantly.

This section has shown that in many cases frequency agility is desirable to modify target echoes and eliminate nulls in the RCS. It is

* Receiver noise is neglected in this discussion.

shown in Secs. 6.6 and 7.6 that frequency agility can also decorrelate distributed-clutter echoes. By integrating these echoes, the RCS is made to approach its mean value while the variance of the clutter is reduced. This improves the signal-to-clutter ratio just as incoherent integration improves the signal-to-noise ratio.

5.10 Bistatic Radar Cross Section of Targets

A bistatic radar's transmitting and receiving apertures are separated by a considerable distance. The major variation in a target's bistatic cross section is due to the difference in the respective angles to the target, with range differences playing only a second-order role. There is relatively little data on the bistatic reflectivity of most targets of interest because the range of geometries is quite large relative to monostatic geometries, and because of experimental difficulties. Most bistatic RCS models are derived from available monostatic data.

From theoretical considerations, computer models, and reported experiments, we can define three regions for bistatic target RCS as a function of the bistatic angle, B.

1. A quasi-monostatic region where the bistatic angle is sufficiently small such that there is little shadowing of one portion of the target and any retroreflectors such as corner reflectors have the same RCS as the monostatic case. Crispin and Siegel [148] also restricted this condition to perfectly conducting and relatively smooth targets.
2. A bistatic region with larger angles such that there is some shadowing. This would include conditions such as the reflections from the engines on the right side of an aircraft being shadowed by the fuselage when the receiver is viewing the aircraft from the left side.
3. The forward scatter or "forward-scatter enhancement region" near $B = 180°$.

Quasi-monostatic region

In the quasi-monostatic region, the *monostatic-bistatic equivalence theorem* is usually invoked. In this region the mean bistatic RCS is taken to be the mean monostatic RCS at the bisector angle. Monostatic RCS data or models are utilized while recognizing that there is considerable uncertainty. The equivalence theorem appears to be valid for small bistatic angles. The limits of "small" depend on the complexity of the target and the carrier wavelength. Consider the target to be receiving a plane wavefront from the transmitting antenna. It reradiates the energy as if the target were an irregular, but uniformly illuminated,

aperture. The angular width of the lobes that are reradiated is dependent on the ratio of the carrier wavelength to the effective dimension of this aperture in the direction of the receiver. In this case, *effective aperture* refers to the distance where significant scatterers occur. For small targets (in wavelengths), the quasi-monostatic region should be quite large. For point sources and spheres, the quasi-bistatic region extends to beyond $B = 90°$. This has been confirmed by calculations by Siegel et al. [148] and by measurements by Garbacz and Moffett [260] on spheres about one wavelength in diameter.

For moderately sized objects of perhaps 5 to 10 wavelengths, the equivalence theorem may hold for bistatic angles up to 6 to 12°. For large objects and small wavelengths, the region of validity may be only a few degrees. This is confirmed by measurements by Ewell and Zehner [214] on relatively large coastal freighters. The monostatic RCS of these ships at X-band is listed below:

The *Kansas*	24–31 dBsm
The *Hellenic Challenger*	33–38
The *Philippean Rizal*	29–36
The *Delaware Sun*	25–32

The bistatic RCS is shown in Fig. 5.31. Note that the bistatic values are within about 3 dB for $B < 5°$ and then fall off for the next 50°. This

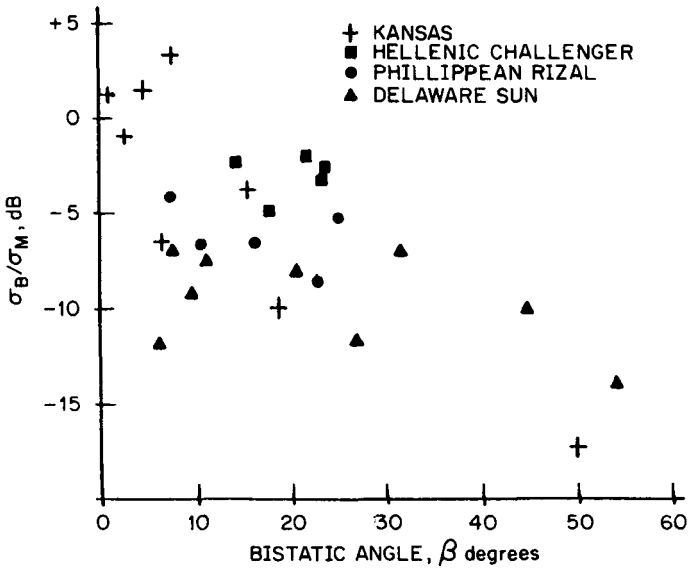

Figure 5.31 Ratio of bistatic RCS of ships to monostatic RCS. (*From Ewell and Zehner [214], © IEEE 1980*)

represents about as complex a target as will be encountered since the target size at X-band is over 1000 wavelengths. Willis [778] suggests that this region be restricted to $B < 5°$.

Bistatic region

In the region where shadowing and loss of retroreflectors are significant, the bistatic RCS is usually lower. The measurement on ships in Fig. 5.31 is one of the few data sets, but is probably representative of large complex targets. The calculated data on a 19-wavelength cylinder

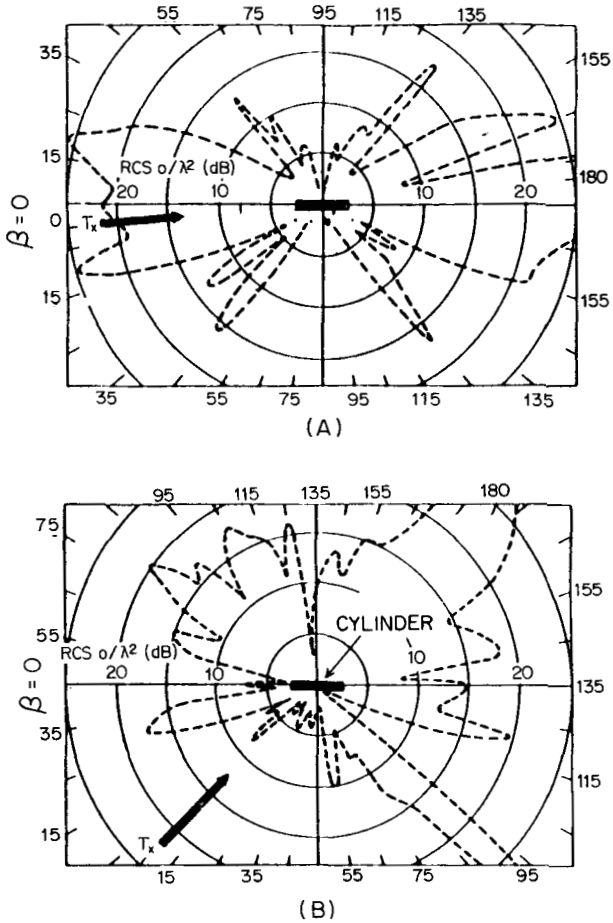

Figure 5.32 Calculated bistatic RCS, replotted as a function of bistatic angle β for a conducting cylinder (A) Near end-on; (B) 45° aspect; (C) broadside. (16 × 1.85 cm, 35 GHz, HH polarization). (*From Ewell and Zehner [214], © IEEE 1980*)

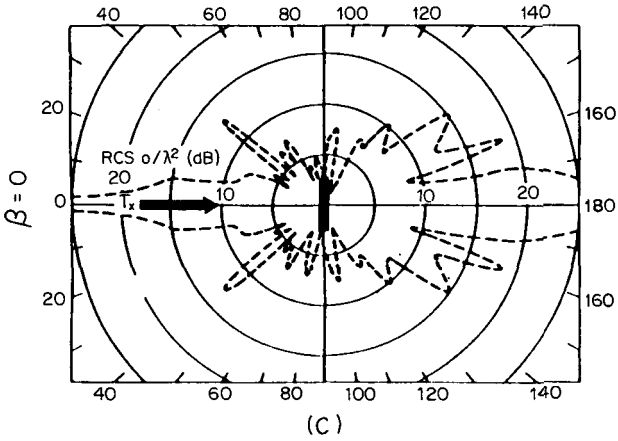

Figure 5.32 (*Continued*)

shown in Fig. 5.32 is an example of a simple but reasonably large target. If one reduces the backscatter from the nose, it could represent a small missile at L-band.

Without access to further data, one can only conjecture perhaps a 0.3-dB per degree falloff with bistatic angle from the ship data, with a maximum of perhaps 12 dB. In some target geometries, there will be an increase in RCS in this region. This will likely occur when the monostatic RCS is low as shown with the 45° aspect view of the cylinder. It is logical to predict that if radar-cross-section reduction techniques are used to reduce the "nose-on RCS" they will be less effective in the bistatic or forward-scatter regions.

Forward-scatter region

From an operational sense, the most important region for a bistatic radar is where the target is in a forward-scatter geometry. With the most common targets being aircraft, missiles, and ships in a nose-on aspect, there is a large specular reflection off the fuselage of an aircraft, the body of a missile, or the hull of a ship. In a near-nose aspect for the transmitter, the major forward reflections will be where $150 < B < 180°$. Siegel [655, 659] has shown that the maximum bistatic RCS in the forward-scatter region of a large, perfectly conducting body is $4\pi A^2/\lambda^2$ where A is the projected area. Note that this is the product of the intercepted area A and the gain of an aperture having area A.

In the forward direction, the RCS falls off from the value at $B = 180°$ depending on the size of the target. For a 3.2-wavelength sphere, the forward lobe is perhaps $\pm 10°$, while for a 0.38-wavelength sphere,

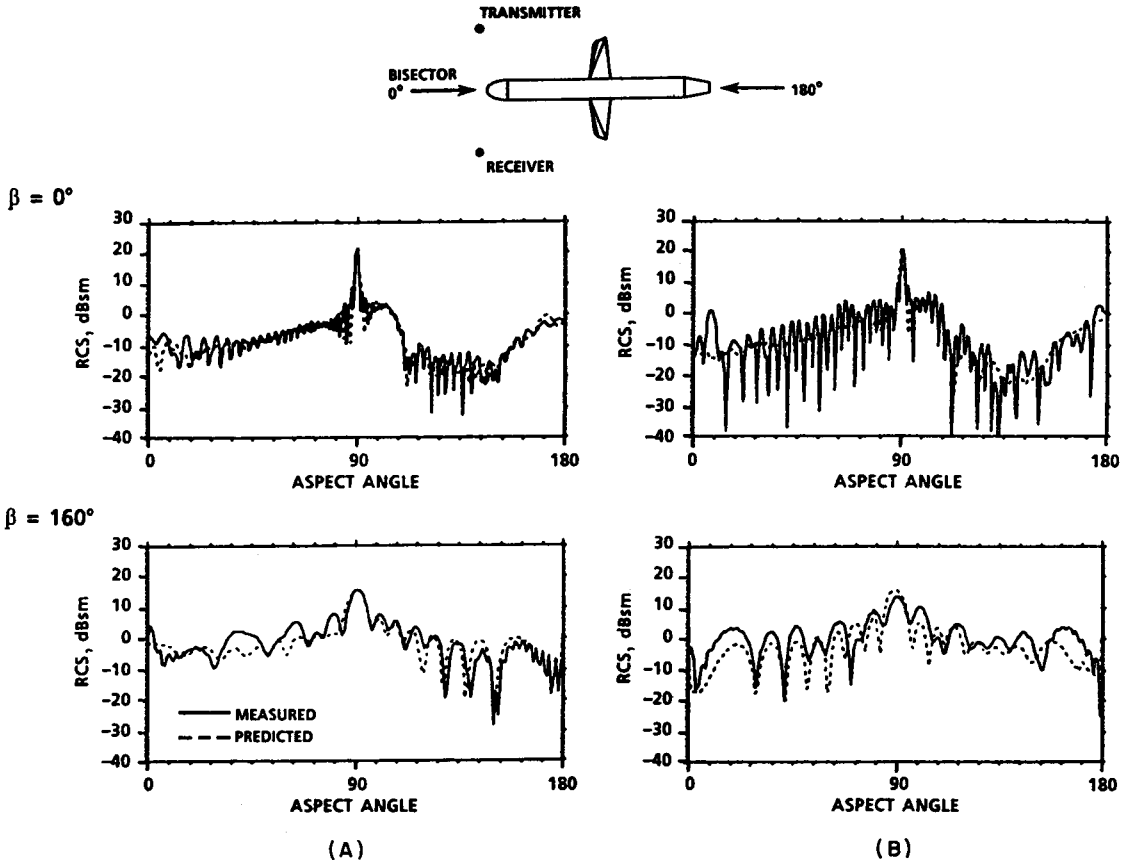

Figure 5.33 Bistatic RCS prediction of airborne platform shape using high-frequency technique, compared with measured data at 1250 MHz. (A) VV polarization; (B) HH polarization. (*From Chung-Chi Cha et al.* [*116*], © *IEEE 1988*)

the lobe width is about $\pm 60°$. Observe that, in Fig. 5.32 where the incident aspect is 45°, the monostatic RCS is relatively low as would be expected for a cylindrical target. Then note how large the RCS is in the forward region at 180° relative to the transmit energy. The lobe width is not shown, but is probably $\pm 6°$. The values in this region are quite large relative to most monostatic aspects. The fall off from this region as B decreases is likely to be similar to the fall off from monostatic geometry.

Data from measurements and modeling at L-band are summarized in Chung-Chi Cha et al. [116] for a missilelike shape that is 5 m long. Some results are shown in Fig. 5.33 with monostatic illumination and with a bistatic angle of 160°. With nose illumination and a 160° bistatic angle, the RCS is measurably higher. From another figure, when the bistatic angle is increased to 170°, the RCS is over 10 dB higher than the monostatic RCS. Figure 5.34 shows the results of the modeling technique versus carrier frequency for a bistatic angle of 10°. Note the inverse RCS relationship with frequency in the 0.2- to 3.0-GHz region for this relatively sleek body.

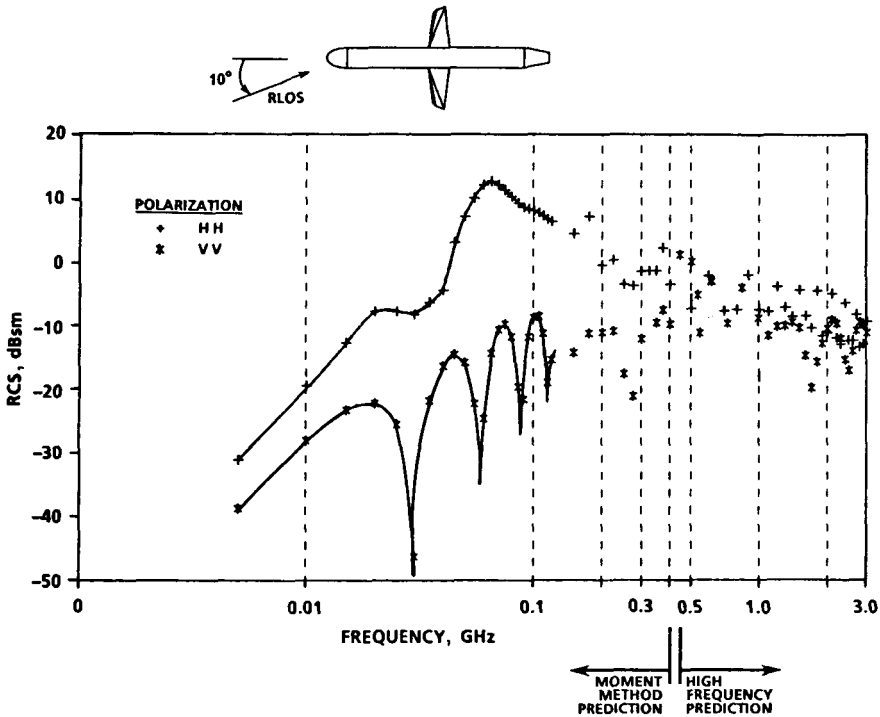

Figure 5.34 Bistatic data across frequency (target length = 5 m; lower curve is fuselage alone). (*From Chung-Chi Cha et al. [116], © IEEE 1988*)

Summary for large metallic targets

1. Use the equivalence theorem for $B < 5°$ for targets that are large and complex. Use it for targets that are only a few wavelengths long to $B = 10°$.
2. Use a value that decreases from the monostatic value at $5 - 10 < B < 90°$. The decrease from the forward-scatter region probably mirrors this.
3. The value near 180° is large and not easily estimated. If this geometry is possible, calculations or measurements are required.

For a more complete treatment see the Willis chapter in the *Radar Handbook* [778].

Chapter

6

Atmospheric Effects, Weather and Chaff

F. E. Nathanson

J. P. Reilly

Meteorological phenomena have two major effects on radar: the signals are attenuated by clouds, rain, snow, and the atmosphere itself; a relatively large signal is reflected from raindrops, hail, and snowflakes.* Attenuation becomes quite significant above X-band (9300 MHz), but backscatter from snow and rainfall generally dominates the detection and tracking problem at frequencies down to L-band (1300 MHz). To compound the problem, the backscatter spectrum from precipitation and chaff is broadened because of wind shear, vertical fall rates, and air turbulence, all of which limit the ability of Doppler processors to separate targets from clutter on the basis of their relative velocities. The backscatter coefficient of chaff dipoles is shown to have much less dependence on the carrier frequency than precipitation echoes, but both have similar amplitude and spectral distributions. The equations and numerical values in this chapter apply to monostatic radars with linear polarization.

* For general references see NASA Publications [361] [239] Atlas, "Advances in Radar Meteorology" [25], Battan, *Radar Meteorology* [48], and Doviak and Zrinc [187].

6.1 Standard Atmospheric Attenuation

Atmospheric attenuation has been treated by L. V. Blake and in NASA publications [239] [361]. Figure 6.1 from Blake shows the normal atmospheric attenuation through the entire troposphere. The attenuation for a horizontal beam at sea level as a function of range and frequency is shown in Fig. 6.2. Numerous other curves are given in the references. The attenuation coefficient per mile at sea level can be obtained from the slope of the curves near zero range in Fig. 6.2, or the zero altitude values in Fig. 6.3. The standard conditions refer to 15°C at the surface and 7.5 g/m^3 absolute humidity.

Figure 6.3 shows that standard atmosphere attenuation in dB/km falls off rapidly with altitude above sea level, especially at the higher microwave frequencies. At 10 km or above, attenuation can generally

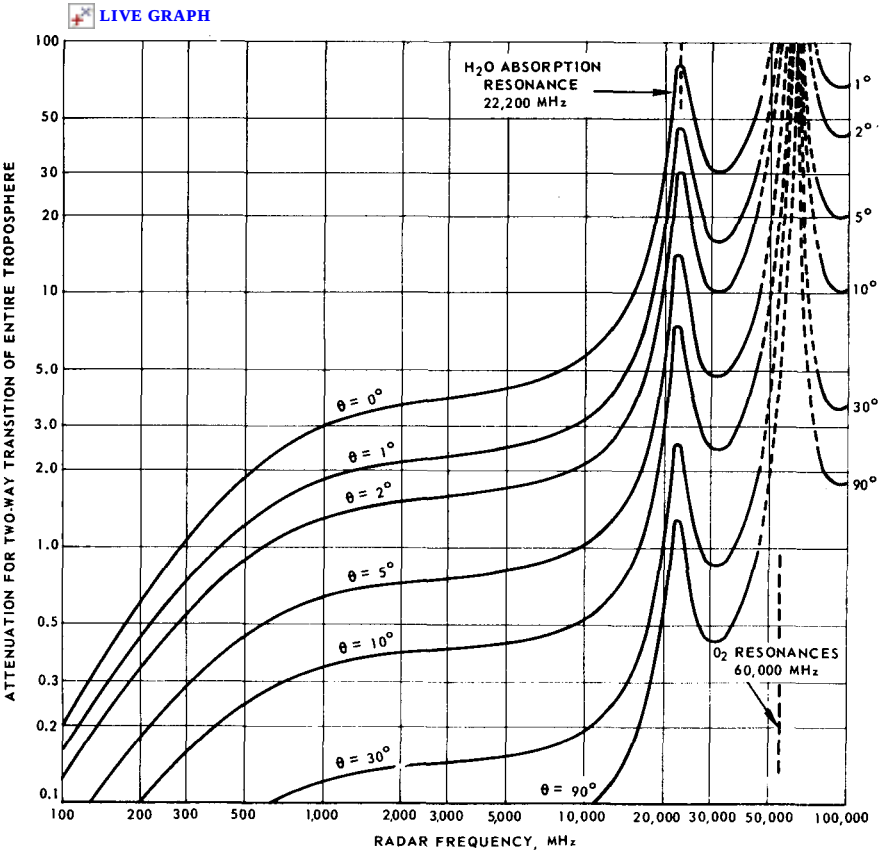

Figure 6.1 Radar attenuation for transversal of entire troposphere at various elevation angles. Applicable for targets outside the troposphere. Does not include ionospheric loss, which may be significant below 500 MHz in daytime. (*After Blake [75]*)

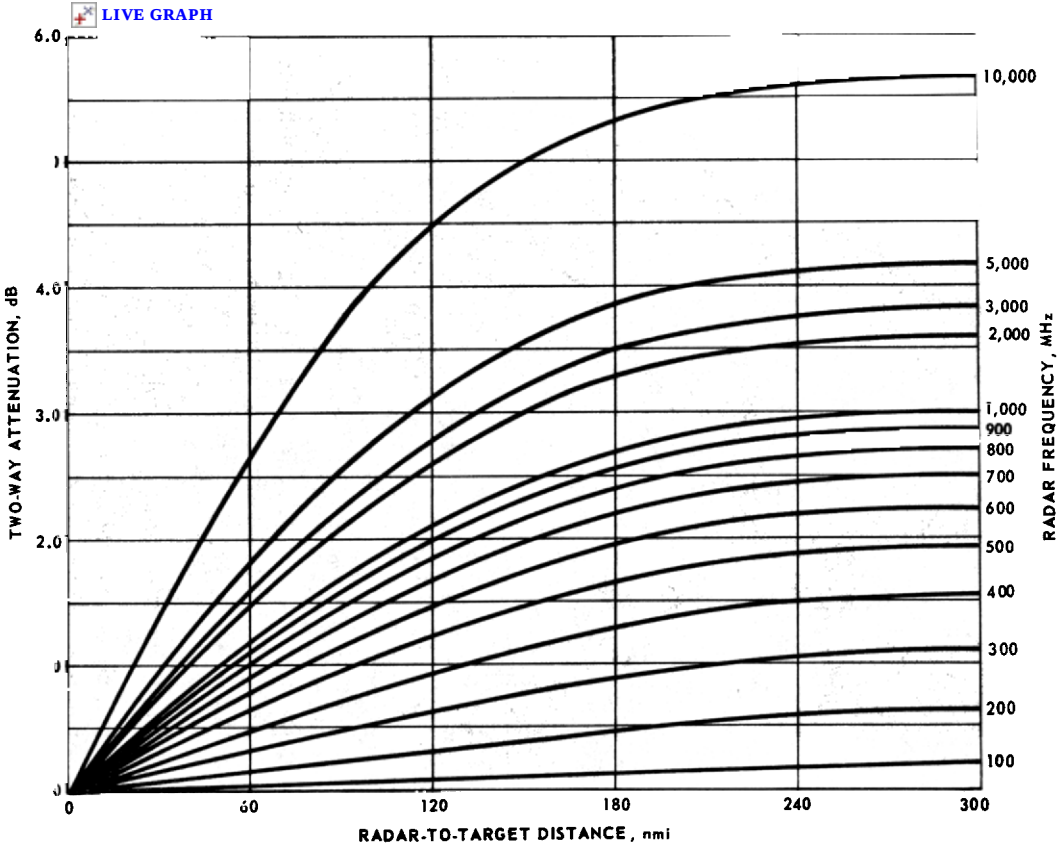

Figure 6.2 Radar atmospheric attenuation (0° ray elevation angle, 100–10,000 MHz). (*After Blake* [75])

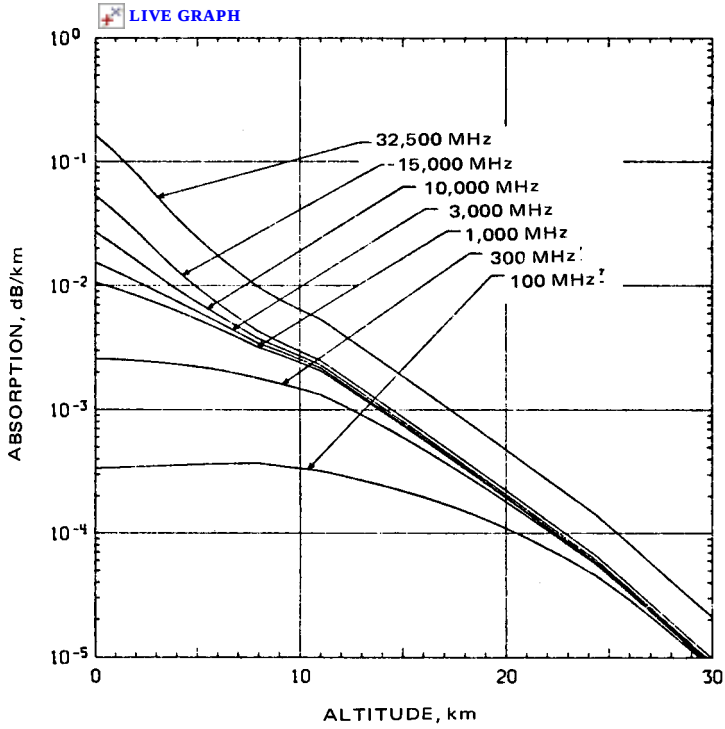

Figure 6.3 Variation of the total absorption coefficient in the standard atmosphere as a function of altitude for several frequencies. Includes oxygen and water vapor. (*From Blake* [*75*])

be neglected above 10-km altitude to at least 35 GHz. Values for higher carrier frequencies and other humidities can be found in Blood and Crane [78] and numerous other sources.

6.2 Precipitation Occurrence and Extent

Before exploring the impact of attenuation and reflectivity of meteorological scattterers, it is necessary to model their occurrence and extent. As with other natural phenomena, there is extreme variability in time and geographic location, as well as altitude, season, and other factors.

The common rainfall descriptors are:

Type	Rainfall rate, r in mm/h
Drizzle	0.25
Light rain	1.0
Moderate rain	4.0
Heavy rain	16.0
Excessive rain	>40.0

The National Weather Service defines the following levels for meteorological radars:

Level 1	1.52–6.09	mm/h
Level 2	6.09–25.9	mm/h
Level 3	25.9–53.1	mm/h
Level 4	53.1–114.3	mm/h
Level 5	114.3–180.3	mm/h
Level 6	180.3–	mm/h

In earlier times, radar specifications often indicated merely an "all-weather" capability. Specifications for modern target detection radars generally should define widespread rainfall rate as well as a high rainfall rate applying to a smaller area. In designing or evaluating a proposed system, one also requires an indication of the height profile of the rain and its spatial uniformity. For Doppler radars the wind velocity profile and local wind shear conditions are also required.

Statistical data on rainfall rate is summarized in Table 6.1 and Fig. 6.4. The table indicates that the probability of a rain exceeding 1 mm/h varies only from about 1.5 to 3.8 percent of the time from arid to wet areas. However, the probability of occurrence of greater than 20 mm/h varies by several hundred to one. It is shown in later chapters that design of air defense, air traffic control, or multimode airborne systems is quite different with anything near a 20-mm/h rainfall rate. It is also a question as to the "enemy's" ability to operate in such an environment. Military and civil surveillance radars usually specify widespread 1- to 4-mm/h rain and sometimes a storm of perhaps 16

TABLE 6.1 Instantaneous Rainfall Probability in Various Locations in the World, %

	Probability that indicated rainfall rate is exceeded, %			
	Light	Moderate		Heavy
	1	2	4	20 mm/h
Paris, France	1.6	0.74	0.22	0.001
Washington, D.C.	2.5	1.5	0.68	0.07
England (eastern)	2.4	1.5	0.65	0.004
Saigon, Vietnam	2.4	1.7	1.0	0.21
Turkey	1.5	0.7	0.25	0.01
Tokyo, Japan	3.2	2.0	1.2	0.24
Ceylon*	3.8	2.8	1.9	0.48
New Orleans	3.0	1.7	1.2	0.37
Worldwide average	1.6	1.0	0.47	

* Worst location noted.
Maximum altitude for radar purposes 25,000 ft (7.5 km).
Typical maximum altitude excluding thunderstorms 12,000 ft.
NOTE: See also [97, 119, 366].

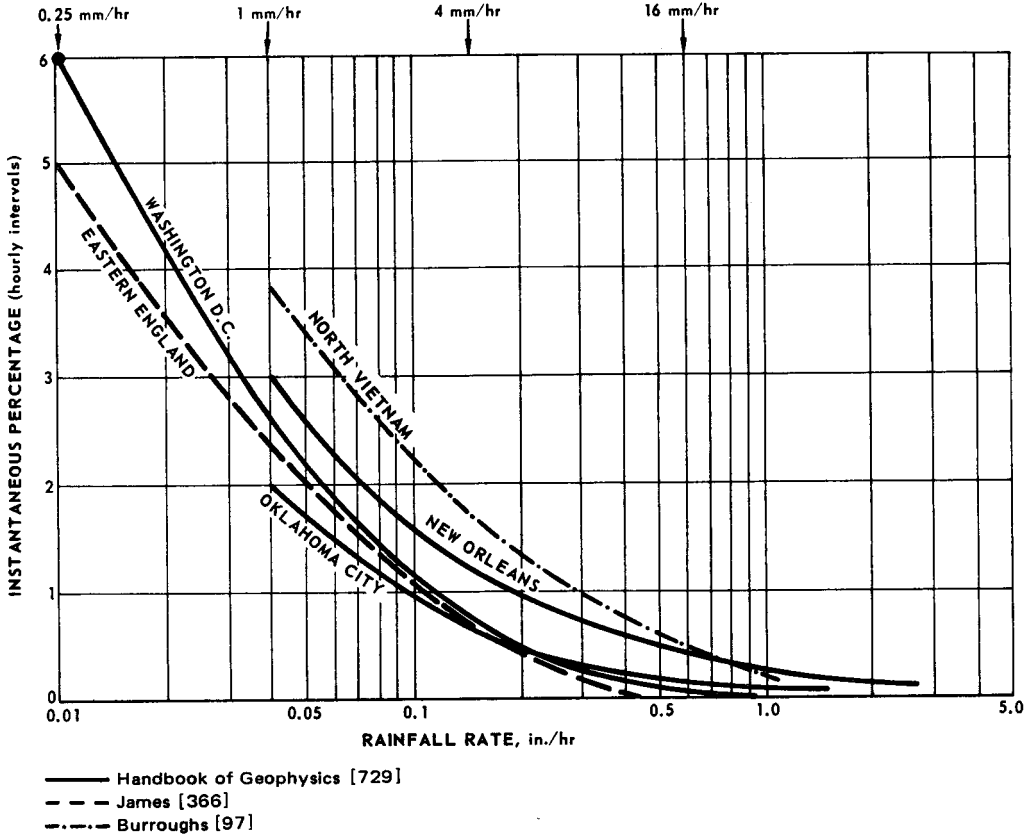

Figure 6.4 Percentage of time rainfall exceeds a given rate.

mm/h over a diameter of 10 to 20 km. Heavier storms have smaller diameters. Data on the diameter of storms vary widely with various models. James [366] suggested the following relationship.

$$\text{Diameter (statute miles)} = 25.9 - 14.7 \log r \qquad (6.1)$$

The foregoing relationship and others are illustrated in Fig. 6.5. The CCIR models that are widely used in communications have considerably smaller diameters. If this is a critical parameter, the designer should consult various studies in the Preprints of the Radar Meteorology Conferences, of the American Meteorological Society.

The variation of rainfall rate throughout the world is often taken into account in radar design. The examples shown earlier have evolved into worldwide climate regions to achieve some sort of standardization. The CCIR Rain Rate Climate Regions for the United States are shown on Fig. 6.6 with the point rain rate distributions on Fig. 6.7 [361]. These are appropriate for requirements for fixed site radars. The references [361, 81] also give worldwide models, which may be useful since rainfall

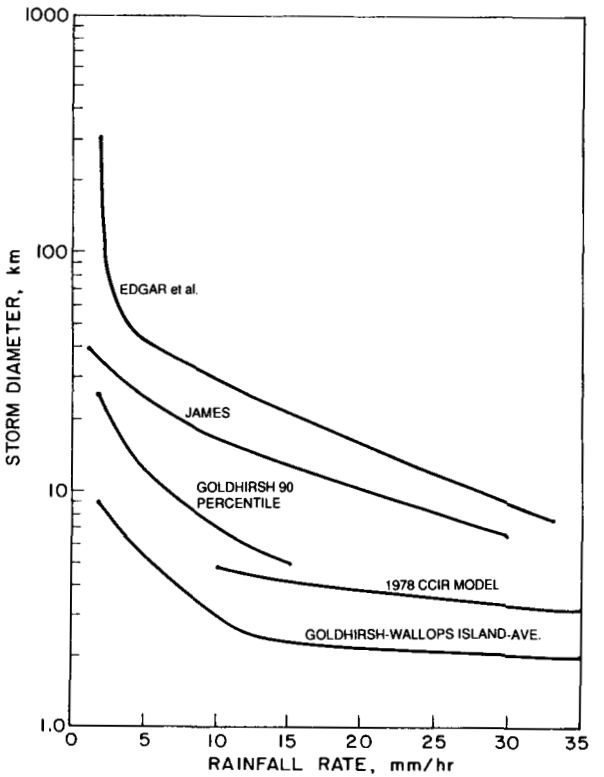

Figure 6.5 Reported diameter of rain storms versus rainfall rate.

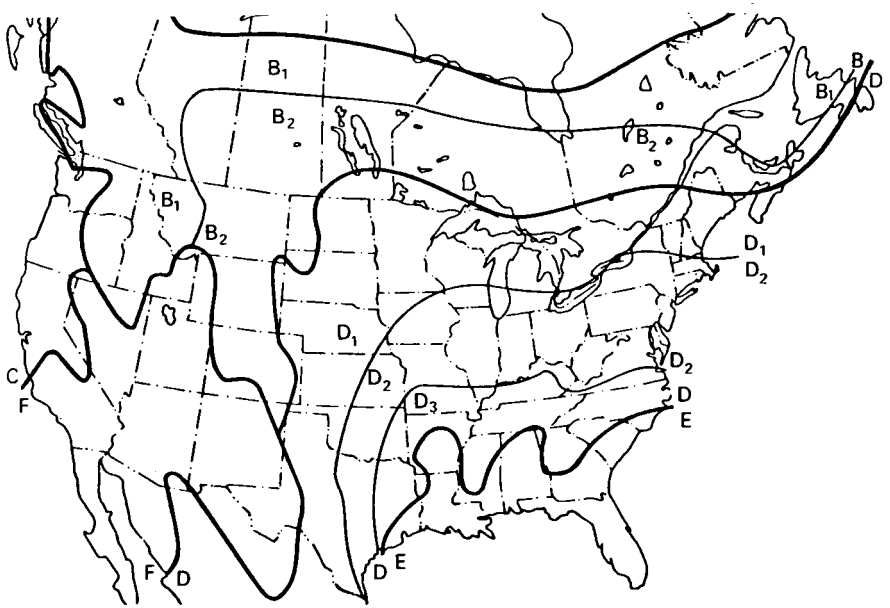

Figure 6.6 Rain rate climate regions for the continental U.S. and Southern Canada. ([361])

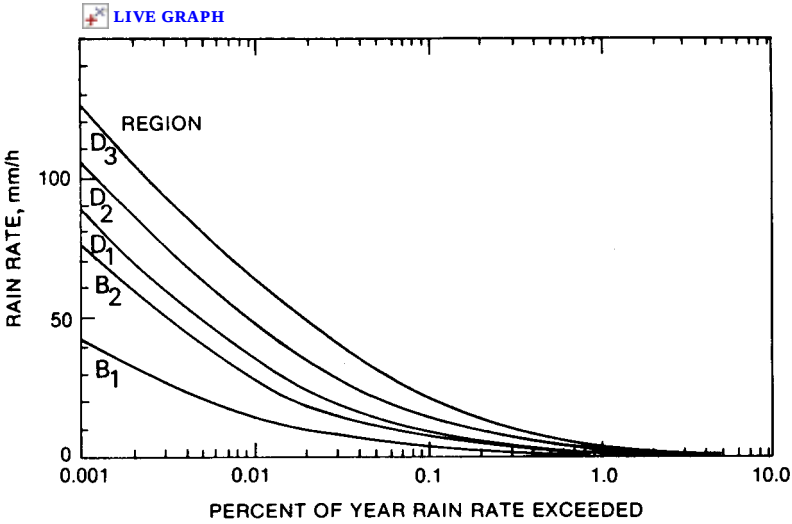

Figure 6.7 Point rain rate distributions as a function of percent of year exceeded. ([361])

varies considerably with geographic location. Europe has fewer heavy rains than southeast Asia, for example.

The height distribution of rain is also an important parameter when estimating attenuation and reflectivity. In general, rain reflectivity and attenuation decrease with height above the ground. One relationship for the falloff in intensity is $r/r_s = \exp(-0.2h^2)$ where r_s is the surface rainfall rate and h is height in kilometers [593]. In a second model the constant is 0.036. A third model from Fordon [242], for light to moderate summer mid-latitude rains, is illustrated in Fig. 6.8. Konrad [408] and Goldhirsh [275] made a number of measurements with well-instrumented radars. While the individual measurements gave rather erratic height profiles, the averaged median height profiles for summer storms are illustrated in Fig. 6.9. These represent reflectivity rather than water content. (The meaning of dBZ is explained later.) The effective height of the thunderheads is a variable, but the reflectivity often increases in the 2- to 6-km level. However, in many cases a specification of rain extending uniformly to a 4-km height is adequate. In some cases a linear falloff to about 6 km is added.

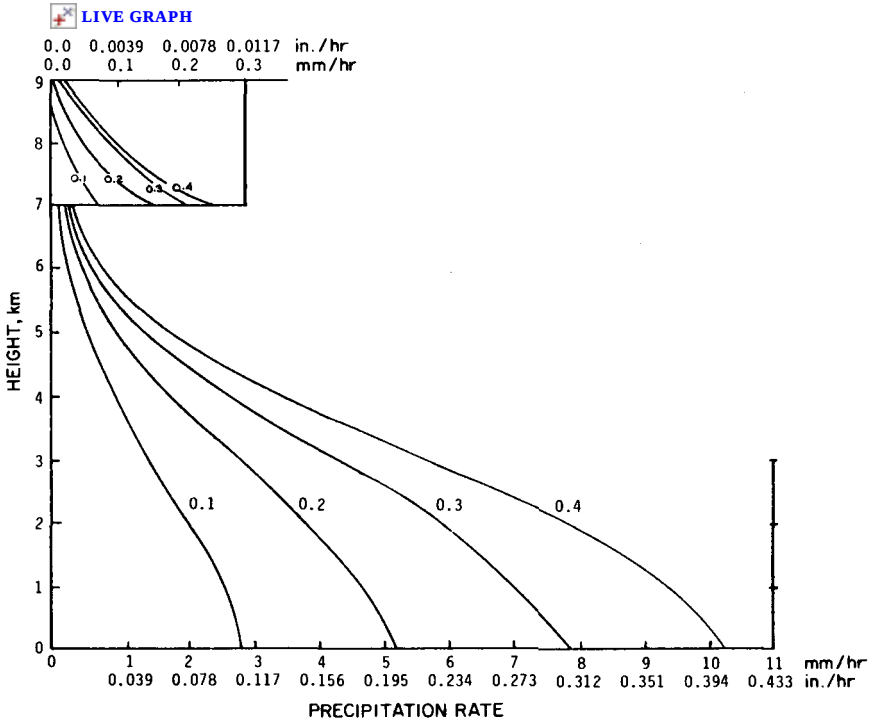

Figure 6.8 Estimated distribution of precipitation rate with height for summer rain in middle latitudes, for four values of estimated maximum updraft (specified in m/s by each curve). (*From Fordon [242]*)

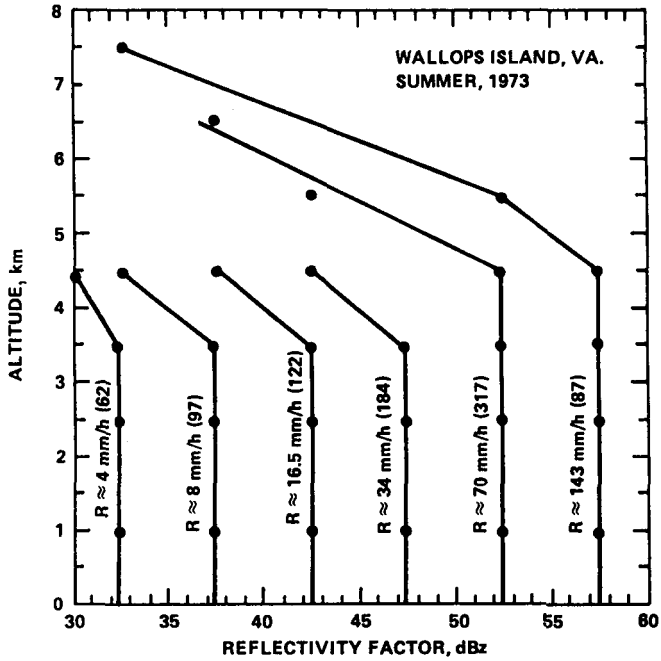

Figure 6.9 Median reflectivity factor profiles for given rain rates as measured at Wallops Island, VA, during summer of 1973. [361]

There are various overall models of rainstorms, but the one described in Table 6.2 is more descriptive of the physical processes. The left column is the height above the earth in 2000-ft increments. Starting from 22,000 feet, there are only ice crystals with 200 in a column 1 m^2 by 2000 ft high. They are small ($\approx$1.4 mm) and have low water content. As the crystals fall they start melting at 14,000 feet and there is a mixture of ice and water. By 10,000 feet there is only rain and water-coated ice spheres with a relatively large mean diameter and high water content. Near the surface, the precipitation consists only of waterdrops with a somewhat smaller diameter. The "bright band" effect with an increase in reflectivity at the melting layer is discussed in later sections.

6.3 Attenuation in Hydrometeors and Foliage

The attenuation by rain, snow, clouds, fog, and haze has been thoroughly studied and analyzed, in numerous experiments. The agreement between various theoretical models and experiments is good only if the model applies to the particular conditions of the experiments—especially in regard to liquid water content, the drop-size distributions,

TABLE 6.2 Rain Storm Model Versus Altitude

Height above earth's surface (1000 ft)	Rain			Ice crystals		
	Number of particles/m^2*	Mean diameter, mm	Water content, gm/m^3	Number of particles/m^2	Mean diameter, mm	Water content, gm/m^3
22				200	1.4	0.1
20				200	2.0	0.2
18				250	2.5	0.3
16				300	3.2	0.6
14	150	1.7	0.4	250	3.2	0.6
12	350	1.9	1.2	150	3.2	0.6
10	500	2.1	2.5			
8	550	2.0	2.2			
6	550	1.8	1.7			
4	550	1.8	1.7			
2	550	1.7	1.7			
0	300	1.4	0.4			

* In a column of 2-km height.

NOTE: surface rainfall = 5.8 mm/h.

TABLE 6.3 Typical Characteristics of Hydrometeors

	Typical base, m	Typical top, m	Density liquid, g/m	Diameter droplets, microns	Drops per m^3	Reflectivity Z_e, dB
Haze	0	1500	.001	0.1	10^8	
Fog (radiation)			.04	10	2×10^{11}	
(advection)	0	50	.15	20	4×10^{10}	
Fair weather cumulus	500	1000	.50	20	10^8	−30
Stratus (heavy)	500	1500	.3	10		−12
Cirrus	High		.17	170		14
Cumulus Congestus	1600	2000	.80	40		
Cumulonimbus			2.5	100		9
Rain (1mm/h)	0	4000	.06	310		26

SOURCE: After Refs. [720,266,504].

temperature, and spatial uniformity of the path. Attenuation in rain and snow are the primary concern in the higher microwave regions with clouds, fog, and haze becoming important at 35 GHz and up. Radar is increasingly being used in various forms of sensing as the attenuation in the optical regions is frequently excessive for most missions. A *general* description of various forms of hydrometeors with typical parameters is illustrated in Table 6.3. These are only representative cases—as fog can have a wide variety of visibilities; cumulus clouds come in various densities, etc. There is a wide range of drop sizes (the median or mode of the distributions shown here), number, and the density of the total liquid water. In later sections it is shown that the larger drop diameters dominate the reflectivity.

Attenuation in rain

The attenuation of electromagnetic waves in a uniform rain is usually significant above 2 GHz, and is proportional to the 2.3 to 2.8 power of frequency when the droplets are small compared with the wavelength. In this region the attenuation coefficient k is often expressed as

$$k = ar^b \text{ dB/km}$$

where r is rainfall rate in millimeters per hour and a and b are constants that depend on many variables, including frequency, polarization, and temperature.

There have been numerous measurements programs with many of the early ones summarized by Medhurst [471]. His summary showed that the measured attenuation was higher than the theoretical work of Gunn and East [298] especially at the lower rainfall rates. Since that time, it has been pointed out by Crane [145] that the "point"

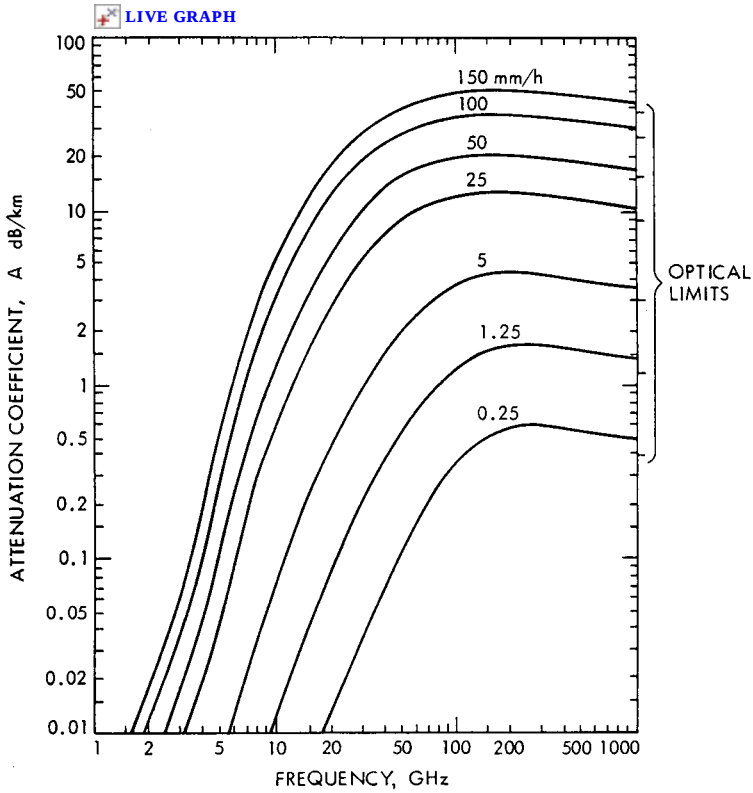

Figure 6.10 Attenuation coefficient as a function of rain rate and frequency. (*CCIR, 1986* [*361*] [*239*])

measurements tend to exceed the path average for low rainfall rates at lower precipitation levels. In addition, the humidity tends to be higher in rain. In the interest of standardization, it is suggested that the 1986 CCIR (International Telecommunications Union) model developed for communication systems be used, as there are many studies in the past 20 years that went into that model. It is shown in Fig. 6.10 and detailed constants on Table 6.4. The subscripts H and V correspond to horizontal and vertical polarization. The differences in these values lead to the elliptical polarization of attenuated signals described in the discussions on circular polarization in Chap. 5. In other, more detailed studies a values are lower and b values are higher for rainfall rates above about 30 mm/h.

Attenuation in clouds

The attenuation in clouds varies greatly due to the extreme variation in densities. The basic relationship is

TABLE 6.4 Specific Attentuation Coefficients*

Frequency, GHz	a_H	a_V	b_H	b_V
1	0.0000387	0.0000352	0.912	0.880
2	0.000154	0.000138	0.963	0.923
3	0.000650	0.000591	1.121	1.075
6	0.00175	0.00155	1.308	1.265
7	0.00301	0.00265	1.332	1.312
8	0.00454	0.00395	1.327	1.310
10	0.0101	0.00887	1.276	1.264
12	0.0188	0.0168	1.217	1.200
15	0.0367	0.0347	1.154	1.128
20	0.0751	0.0691	1.099	1.065
25	0.124	0.113	1.061	1.030
30	0.187	0.167	1.021	1.000
35	0.263	0.233	0.979	0.963
40	0.350	0.310	0.939	0.929
45	0.442	0.393	0.903	0.897
50	0.536	0.479	0.873	0.868
60	0.707	0.642	0.826	0.824
70	0.851	0.784	0.793	0.793
80	0.975	0.906	0.769	0.769
90	1.06	0.999	0.753	0.754
100	1.12	1.06	0.743	0.744
120	1.18	1.13	0.731	0.732
150	1.31	1.27	0.710	0.711
200	1.45	1.42	0.689	0.690
300	1.36	1.35	0.688	0.689
400	1.32	1.31	0.683	0.684

* Values for a and b at other frequencies can be obtained by interpolation using a logarithmic scale for a and frequency and a linear scale for b.
SOURCE: Ref. [361].

$$A = k_c D \text{ dB/km} \qquad \text{(one way)} \tag{6.2}$$

where k_c is the attenuation coefficient given in Fig. 6.11 and D is the liquid water density in gm/m^3 [681, p. 6–63].

The attenuation constant, A, is about 25 percent higher for saltwater clouds. Values of D generally fall in the range of 0.05 to 0.25 for stratiform or layered clouds and 0.3 to 1.3 for dense stratocumulus clouds, and averages about 2.5 for cumulonimbus (rain) clouds. For water clouds, A varies approximately as f^2, and for ice clouds, the attenuation is 1 to 3 orders of magnitude less and varies as f.

Attenuation in snow

Attenuation in dry snow is about 20 to 50 times less than in melted drops with the same fall rate in millimeters per hour. However, when the snow is melting, the attenuation can be even higher than rain. In

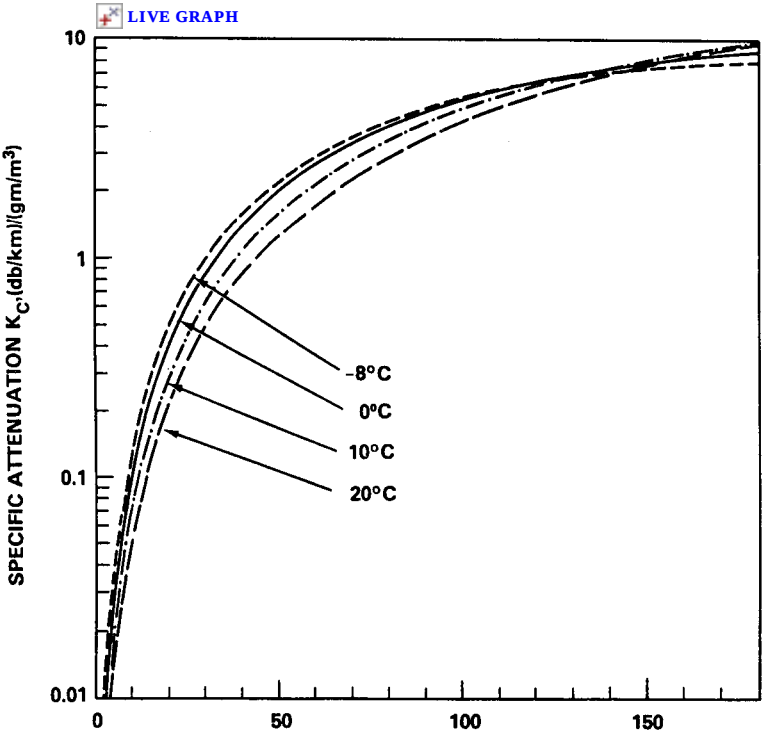

Figure 6.11 Attenuation coefficient K_c due to water droplets. (*From CCIR 1982 Rpt. 721–1*)

one model in a 0.3-km-thick melting layer, the attenuation was predicted to be 0.54 dB at 13.6 GHz, 3.7 dB at 35 GHz, 6.75 dB at 94 GHz, and 8.5 dB at 140 GHz [504].

Attenuation by fog, haze, and clouds

Attenuation by fog and haze is dependent on droplet size, density, and temperature. At millimeter wavelengths the drop-size distribution itself is not critical. As with rain there is a wide variety of densities. Haze droplets are the smallest, with sizes from 0.01 to 3 microns, and thus do not cause significant attenuation even at millimeter wavelengths.

Radiation fog that forms over land has droplet diameters of 5 to 35 microns and densities of about $2 \times 10^{11}/m^3$. *Advection* fog that forms over water has droplets of 7 to 65 microns and an average diameter of 20 microns, but lower densities of 0.4×10^{11} are observed. The advection fog is the type usually described in the literature [595, 286]. A table of the typical forms is shown as Table 6.3.

Richard [595] summarized the attenuation measurements at 20°C. He gives a value of 0.12 dB/km/gm/m^3 at 15 GHz, 0.55 at 35 GHz, 3.3 at 95 GHz and 7.0 at 150 GHz. An empirically derived relation for visibility (V) in kilometers as a function of liquid water content (M) in g/m^3 was given as

$$V = 0.024\,M^{-0.65} \qquad or \qquad M = (0.024/V)^{1.54}$$

A relationship for fog attenuation coefficient A_f (above 30 GHz), is [361]

$$A_f = -1.347 + 11.152/f + .06f - .022T \text{ dB/km/g/m}^3$$

where f is the frequency in GHz and T is in degrees centigrade.

Attenuation by foliage

The radar detection of personnel and land vehicles involves the major problems of clutter echoes from the terrain and cultural features, the attenuation resulting from natural or man-made obstacles and wooded areas, and forward-scatter phenomena. If the radar has sufficient sensitivity, the detection range can be computed with the land clutter reflectivity values of Chap. 7 and the equations of Chap. 2. To determine sensitivity, the attenuation due to foliage must be determined.

The wide diversity in the types and density of foliage makes the estimate of attenuation highly variable. Early studies were summarized by Saxton and Lane [633] at frequencies from 100 to 3000 MHz. They found that for either polarization the one-way attenuation by trees with leaves in that frequency region was given by

$$A = 0.25f^{\gamma} \text{ dB/m} \tag{6.3}$$

where f is the carrier frequency in GHz and $\gamma = 0.75$. This relationship and more recent ones are shown in Fig. 6.12. Recent experiments at Georgia Tech Research Institute [152, 777] confirmed the general dependence between 9 and 95 GHz, with a higher constant for summer conditions and dry foliage, and a lower constant for winter. However, the exponent, γ was only about 0.3. Other results with a lower constant have been reported [239, pp. 5–19].

There is greater confusion about the effect of the depth of the foliage and the related frequency dependence. This is summarized in Ulaby [720]. The CCIR report adopted the following relationship for communication calculations where the antennas are close to a grove of trees:

$$A = 0.2\,f^{0.3}d^{0.6} \text{ dB/m} \tag{6.4}$$

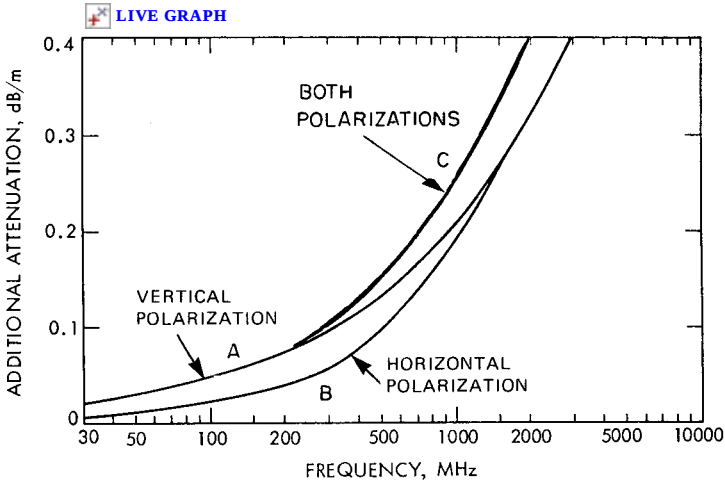

Figure 6.12 Attenuation in propagation through woodland. (*CCIR* 1986 [*239*]; *both polarizations* [*633*])

where d is the foliage depth in meters. It is not clear why the frequency exponent should be lower than in the earlier tests. In other experiments attenuation due to individual trees or a tree-lined road was 2 dB/m at 869 MHz and 2.8 dB/m at 1500 MHz [239]. Until a better model is obtained, Eq. 6.3 is as good as any for full foliage at low frequencies, but perhaps Eq. 6.4 is better above X-band.

Other sources of attenuation

There is attenuation of lower carrier frequency electromagnetic waves in the ionosphere. There are small losses due to water films on reflector antennas and significant loss from rain on radomes, especially older ones [39].

6.4 Backscatter Coefficient of Rain, Snow, and Clouds

The reflections from precipitation and chaff can constitute the major source of clutter on many radars. The reflections appear noiselike on any given pulse, but have some correlation from pulse to pulse. This section is devoted to the reflectivity statistics of these echoes.

The modeling or specification of this form of clutter is critical since few radars will see targets (especially aircraft) in the heaviest of storms, and there is as much difficulty in overspecification of the precipitation rate as there is in underspecification. The same holds true for chaff, and a specification of reflectivity has little meaning without an indication of the size and dynamics of the chaff cloud.

While the phenomena are quite different, rain and chaff appear statistically similar to a radar. The amplitude distributions are Rayleigh whether there are 10 or 10^6 raindrops or chaff dipoles in the radar volume. Both are excellent tracers of the horizontal winds, and while the fall rate of rain is higher (up to 9.6 m/s for large drops), this primarily affects vertically pointing radars.

The backscatter from precipitation particles can be represented by a random assembly of scatterers, no one of which has a dominant effect on the sum. The RCS of the random assembly may be derived by assuming that the relative phase of each scatterer's return is statistically independent of the others and is uniformly distributed between 0 and 2π. This is an example of the two-dimensional "random walk" problem in which each step is $\sqrt{\sigma_k}$. This, in turn, leads to the well-known *Rayleigh power* relation.

The relation for the volume reflectivity of rain, where the droplets are small compared to the radar wavelength (in the Rayleigh region), is

$$\Sigma\sigma = \eta = \pi^5 \lambda^{-4} |K|^2 \Sigma D^6 \text{ m}^{-1} \tag{6.5}$$

where λ = the carrier wavelength.
D = the droplet diameter.
K = related to the complex refraction index and is a fairly constant 0.9 over the microwave region for rain, and is about 0.2 for snow.

The units of $\Sigma\sigma$ or η for target detection radars are m^2 of equivalent radar cross section per m^3 volume or m^{-1}. At times η is given in other units and conversion must be made.*

While these units can be used for weather radars, the meteorological community uses Z for theoretical calculations of reflectivity, and Z_e is often used for empirical or experimental data. The term Z includes the wavelength dependency and is expressed in mm^6/m^3. It is usually expressed in the form

$$Z = ar^b \tag{6.6}$$

where r = rainfall rate in mm/h.

The most representative relationship used by radar and radar meteorology texts [671, 25, 48] is

$$Z = 200r^{1.6} \text{ (temperate latitudes) mm}^6/\text{m}^3 \tag{6.7}$$

* The $\Sigma\sigma$ merely states that the reflectivity is the vector sum of the reflected signals from each droplet.

An alternate relationship, proposed by Atlas [25], is $Z = 214r^{1.39}$. Measurements of Florida rains have fitted the equation $Z \approx 286r^{1.43}$ and in Indonesia $Z \approx 311r^{1.44}$ [494]. The lower values of the exponent in other experiments [25] generally correspond to microwave frequencies above X-band with drop size large with respect to 0.1 λ. Measurements at 35 GHz and higher place the exponent between 0.95 and 1.35; values for the constant term increase to almost 1000. Godard [270] suggests an exponent of 1.2 at 35 GHz.

The Z relationship is not in a useful form for radar system evaluation. A conversion factor to pulse radar received power, attributed to J. R. Probert-Jones [563], is

$$P_r = \frac{1.1 \times 10^{-23} P_t G_t G_r \theta\phi\tau Z L_a}{\lambda^2 R^2} \tag{6.8}$$

including the beam shape losses where in the units of the reference

P_t = transmitted pulse power, W.

P_r = received pulse power, W.

G_t, G_r = antenna gains, dimensionless.

θ,ϕ = one-way, half-power antenna beamwidths, degrees.

R = range to clutter cell, nmi.

λ = wavelength, cm.

τ = effective pulse duration, μs.

Z = reflectivity, mm^6/m^3 (Z is not wavelength dependent at low frequencies in the Rayleigh region).

L_a = atmospheric and rain attenuation, two way (a negative value in dB when this loss term is in the numerator).

The ratio of returned power from a target to the returned power from the clutter can then be derived from the classical radar equation (see Chap. 2 for a clearer description of loss terms).

$$\frac{P_{\text{tar}}}{P_{\text{rain}}} = \frac{K\lambda^4\sigma_t}{\theta\phi\tau Z R^2} \tag{6.9}$$

where K = constant (primarily to keep units consistent, ≈200 depending on antenna pattern and assuming 3 dB of beam shape loss on both target and clutter); it also includes the refractive index for rain.

σ_t = target cross section, m^2.

Since $[(\pi/4)\theta\phi\tau R^2]$ is the volume of the range cell (not in consistent units) and Z is the parameter generally used by radar meteorologists, it has been found that a more useful form for the radar target-detection criterion, where receiver noise power is small when compared with clutter power, is

$$R^2 = \frac{\sigma_t L}{(\pi/4)\phi\theta(c\tau/2)(S/C)\Sigma\sigma} = \frac{10^{10}\sigma_t L\lambda^4}{284(\pi/4)\phi\theta(S/C)Z\tau} \tag{6.10}$$

where beam shape losses for the target and the rain are assumed equal.

(S/C) = the signal-to-clutter ratio for a given probability of detection (S/C is $\approx$ 13 dB for a typical single-pulse surveillance radar with detection probability = 0.5 and false alarm probability $\approx 10^{-8}$).
θ,ϕ = one-way, half-power antenna beamwidths, radians.
$c\tau/2$ = effective pulse length, m.
σ_t = target cross section, m^2.
$\Sigma\sigma$ = backscatter coefficient, m^2/m^3, including wavelength effects.
L = processing losses appropriate to the rain backscatter case.
τ = pulse duration, s.
λ = wavelength, cm.
R = target range, m, assuming that the rain fills the volume of the range cell occupied by the target.

Table 6.5, derived from both theoretical and experimental data, gives $\Sigma\sigma$ versus frequency and type of precipitation. Interpolation between

TABLE 6.5 Reflectivity of Uniform Rain, η or $\Sigma\sigma$ m^2/m^3

		$\Sigma\sigma$, dB m^{-1} Transmit frequency, GHz						
Z (dB)	Radar band: Type	S 3.0	C 5.6	X 9.3	K_u 15.0	K_a 35	W 95	mm 140
−12	Heavy stratus clouds				−100	−85	−69	−62
14	Drizzle, 0.25 mm/h	−102	−91	−81	−71	−58	−45*	−50*
23	Light rain, 1 mm/h	− 92	−81.5	−72	−62	−49	−43*	−39*
32	Moderate rain, 4 mm/h	− 83	−72	−62	−53	−41	−38*	−38*
41	Heavy rain, 16 mm/h	− 73	−62	−53	−45	−33	−35*	−37*

* Approximate

NOTE: Recent experiments and theory have reduced the reflectivity at frequencies above 30 GHz relative to earlier predictions. Theoretical values at 35 and 95 GHz revised as per Crane and Burke and other considerations.

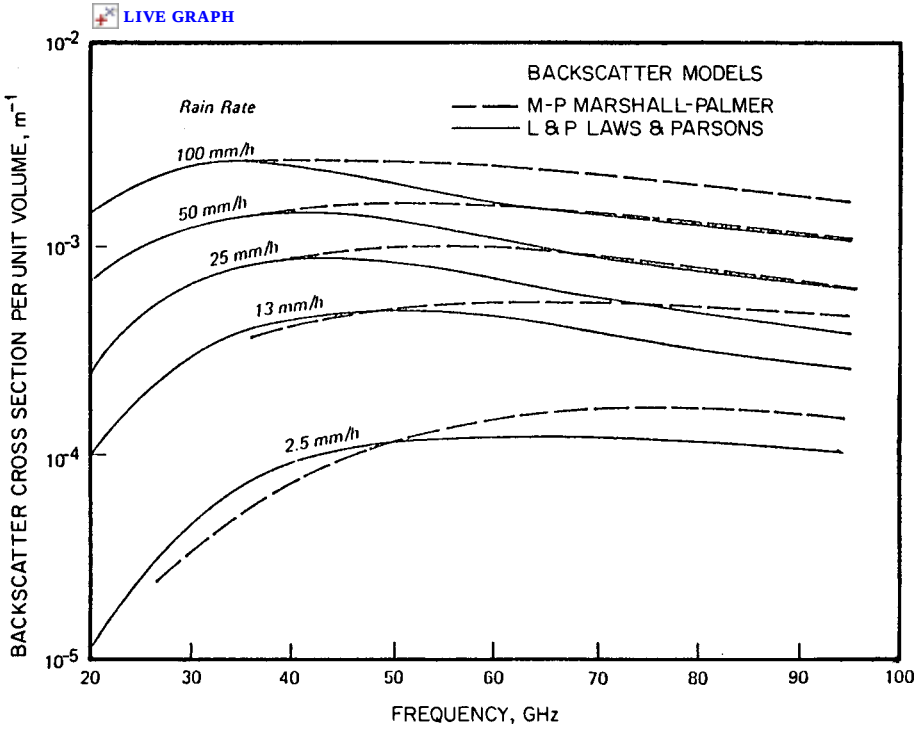

Figure 6.13 Reflectivity versus frequency for rain. (*Crane and Burke* [*146*])

radar bands on the table should be as λ^4 except for the highest frequencies and rainfall rates. Interpolation between the rainfall rates under the same restrictions should follow an $r^{1.6}$ law.

Values for reflectivity in the millimeter wave region, developed by Crane [146], are shown in Fig. 6.13. It shows two curves based on the two common drop size distributions. Since drop-size distributions vary considerably with location, temperature, etc., the reflectivity is more variable in the millimeter wave region (35 GHz up). The peak and then fall in reflectivity is due to the droplet circumferences reaching and then exceeding the wavelength. Richard [595] summarizes measurements in Florida rainstorms of the short, heavy shower type, and gives the following relationships for 2- to 100-mm/h rainfall rates. If average reflectivity from Eq. (6.6) is expressed in m^{-1}

Frequency	a	b
9.4 GHz	1.0×10^{-8}	1.52
35	2.2×10^{-5}	1.05
70	1.4×10^{-4}	0.59
95	8.9×10^{-5}	0.57

Note that the 70-GHz reflectivity is higher than both the 35 and 95 GHz for most of the rainfall-rate region. The 35- and 95-GHz data generally agree with Crane's curves. There is considerable uncertainty in this data set, which is discussed in Currie, 1988 [153].

Fog reflectivity is generally not significant, but some relations can be found in Gossard and Strauch [286, 288].

The $Z - r$ relationships reported for snow vary from $500r^{1.6}$ for ice crystals to $2000r^{2.0}$ for wet snowflakes, where r is the rate, but now refers to the water content of the melted snow in millimeters/hour. In converting the $Z - r$ relationship to backscatter power, the substantially lower refractive index (about one-fifth) of ice and snow reduces the backscatter power by a factor of 5 for a given value of Z. Battan [48] indicates that snow causes about twice the backscatter of rain of the same water content at 1 mm/h and 3 times the backscatter at 3 mm/h. A single set of measurements by the author gave the same (± 2 dB) backscatter at C-band for a uniform snow as would be calculated for a uniform 1 mm/h rain from Eqs. (6.7) and (6.8). The values of $\Sigma\sigma$ for stratus clouds in Table 6.5 are useful only as models since there is no uniform description of clouds. A series of measurements of the reflectivity for clouds has been reported in the U.S.S.R. and is abstracted in Table 6.6 [543]. The mean value of reflectivity, the variation, and the mode are given for several cloud types along with several vertical profiles. It should be noted that most of the values are higher than earlier estimates [671]. Reflectivity from rain clouds (Ns) is only about 3 dB below that of 1-mm/h rain at the freezing level.

Reflections from clear air

So-called "radar angels" and "anomalous echoes" are observed by radar operators on an almost regular basis. Because of their generally small radar cross section, they are normally limited to relatively short ranges on aircraft surveillance radar. The operator of these radars usually learns to recognize and discriminate against clutter returns. On the other hand, the modern generation of radars is becoming more concerned with quick reaction, automatic detection, and data processing of small radar cross-section targets, such as missiles, mortar or artillery shells, bullets, and small ground vehicles. In these systems, the high cross-section target and human recognition discriminants against sky clutter no longer exist. Furthermore, the great expense of these systems makes it increasingly important in early radar design and testing phases to be aware of the data processing and false alarm problems imposed by the natural environment.

Even in air traffic surveillance, radar angels may in fact present a much greater problem than is generally recognized, since there is no

TABLE 6.6 Reflectivity Statistics for Clouds

	Cirrus, Ci		Altocumulus, Ac, or Altostratus, As		Stratocumulus, Sc		Nimbostratus, Ns	
$\bar{Z}\left(\frac{mm^6}{m^3}\right)$	0.20		0.53		0.50		106.7	
σ_z (variation)	0.54		1.24		0.60		262.0	
Z_{mode}	0.05		0.05		0.50		50.0	
Z, dB below 1 mm/h rain	−30		−26		−26		−3	
Specific examples of vertical profiles	Height, m	$\bar{Z}$	Height, m	$\bar{Z}$	Height, m	$\bar{Z}$	Height, m	$\bar{Z}$*
	7460	0.11	4880	0.35	900	0.5	1250	3.4
	7820	0.09	5210	0.80	1150	0.43	1750	5.9
	8180	0.07	5540	1.16	1370	0.31	2250	9.0
	8540	0.07	5880	1.14	1600	0.31	2750	36.0
	8900	0.07	6250	0.58	1800	0.31	3200	272.5†
							3400	199.0
							3600	84.5
							3800	28.5
							4000	15.6
							4200	3.1
Peak cloud height, m	9000		6500		2000		4000	
Minimum cloud height, m	6900		4400		700		750	

* $\bar{Z}$ = 200 for 1 mm/h rain.
† Bright band, 0°C.
SOURCE: Ignatova, Petruskevskii, and Sal'man [543].

way of knowing how many small planes have been mistaken for a flock of birds, and vice versa. Even after an accident has occurred, it is probably impossible to trace the underlying cause to this type of occurrence.

Some years ago a Soviet MIG flown by a defecting pilot penetrated the U.S. air defenses and landed unhindered in Florida. This plane was spotted, briefly, on radar but went unreported. The radar operator was reported to have confessed that brief detections of this sort occur rather frequently. This is perhaps just a single example of an unrecognized but commonly occurring error. Surveillance radars in Florida often detect clear air echoes, and can track these echoes for minutes. The tracks have a "wiggly" character and are sometimes referred to as "worms."

It seems clear that several distinct types of sky clutter must be considered to model a nominal echo environment. Depending on radar characteristics, operation, and location, any of these may prove to be the most important. The first, and usually most important, is the large cross-section, discrete, "dot angels." They are generally attributed to birds and insects in the atmosphere, but may be due in part to other particles. They have grossly differing velocity, density, variation-in-activity, and wavelength characteristics. Actually, the small cross-section variety of discrete scatterers is more important in terms of a distributed phenomenon, since, in the cases of greatest concern, they occur in such density as to be unresolved by the radar resolution cell at all but very short ranges. A distributed meteorological backscatter phenomenon is included as a second distinct type of sky clutter, attributed to turbulent layers. A major cause has been shown to be the inhomogeneities in refractive index that result from turbulence. The radar reflectivity is proportional to the turbulent structure constant of refractive index (C_n^2). This is a complex subject and evaluation of its occurrence impact is described in Gossard [286], Strauch [288], and Doviak and Zrinć [187].

The difference between the frequency effects of particulate matter and refractive effects, is illustrated in Fig. 6.14. While values of C_n^2 exceeding $\Sigma\sigma = 10^{-12}$ have been reported for thin layers, even 10^{-14} or 10^{-15} is not very common. The changes in refractive index are also responsible for various ducting conditions. Ducting often causes radar rays to curve downward, and land and sea clutter that is normally beyond the horizon is clearly seen on ground-based surveillance radars. Ducting over the ocean is common and is described in Chap. 7.

Auroral clutter

In the Arctic regions there is significant reflectivity from the aurora, especially at low carrier frequencies. This clutter is primarily applicable

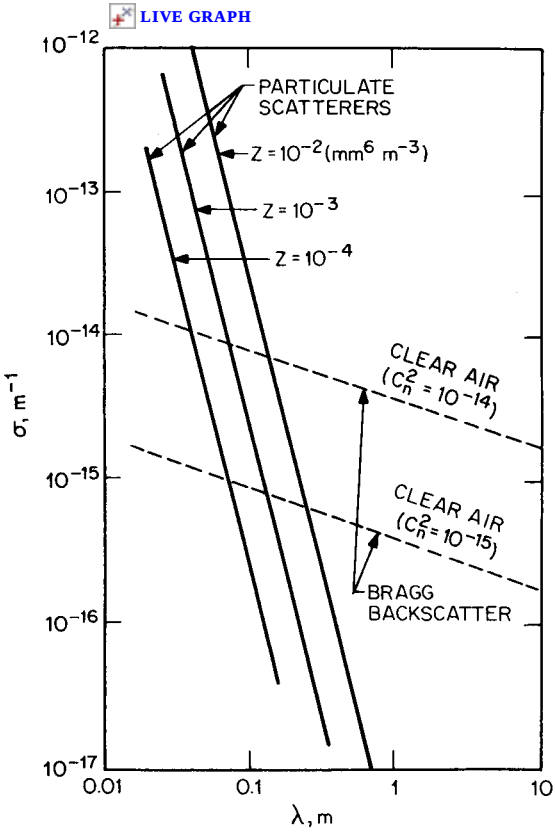

Figure 6.14 Backscattering cross section versus wavelength for particulate scatterers and for Bragg backscatter. The refractive index structure parameter C_n^2 is a measure of the turbulent fluctuations in n if the important scale ($\lambda/2$) lies within the inertial subrange of homogeneous isotropic turbulence. (*From Gossard and Strauch [286, 288]. Elsevier Science Publishers, 1983*)

to long-range radars since it exists as a layer at about 110 km above sea level. Reflectivity is highest at VHF frequencies and reduces to about $\Sigma\sigma = 10^{-9}$ at 400 MHz and 10^{-11} at 1.3 GHz. There is a Doppler shift of several hundred m/s.

6.5 Radar Precipitation Doppler Spectra

It is convenient to describe the Doppler spectra of radar signals returned from clouds or precipitation by four separate mechanisms (Atlas [25, p. 405] Doviak [187].

1. *Wind shear:* The change in wind speed with altitude results in a distribution of radial velocities over the vertical extent of the beam.

2. *Beam broadening:* The finite width of the radar beam causes a spread of radial velocity components of the wind when the radar is looking crosswind. There is a similar but smaller component in the vertical plane.
3. *Turbulence:* Small-scale fluctuating currents of the wind cause a radial velocity distribution centered at the mean wind velocity.
4. *Fall velocity distribution:* A spread in fall velocities of the reflecting particles results in a spread of velocity components along the beam. The maximum fall rate is about 9.6 m/s in the absence of downdrafts.

A fifth mechanism may be considered in a system using a rotating or moving antenna (see Chap. 9). This mechanism is independent of the characteristics of the precipitation itself and is not discussed in this chapter. If we assume that these mechanisms are independent, then the variance of the Doppler velocity spectrum σ_v^2 can be represented as the sum of the variances of each contributing factor*

$$\sigma_v^2 = \sigma_{\text{shear}}^2 + \sigma_{\text{beam}}^2 + \sigma_{\text{turb}}^2 + \sigma_{\text{fall}}^2 \tag{6.10}$$

Although independence is not strictly satisfied, Eq. (6.11) nevertheless provides a useful approximation. The spectrum width is given in velocity units, m/s; for most radar frequencies the spectra can be converted to frequency units through the Doppler equation. In practice a single Doppler spectrum may not look gaussian, but may appear like those illustrated in Fig. 6.15.

Wind shear

Although wind shear (the change in wind velocity with altitude) has long been known to meteorologists, its effect on precipitation spectra

---

* The power spectral density function of sea, land, or weather clutter is often described [34] by a gaussian spectrum having a stability or spectrum parameter a defined by

$$G(f) = G_0 e^{-af^2/f_0^2}$$

where $G(f)$ is the spectral density function of the clutter, f_0 is the transmitted frequency, a is the stability parameter (dimensionless), and G_0 is a constant that depends on the received average power. A more convenient expression for the power spectrum is given in terms of the frequency spectrum variance σ_f^2

$$G(f) = G_0 e^{-f^2/2\sigma_f^2}$$

Alternately, this equation can be expressed in terms of the velocity spectrum

$$G(v) = G_0 e^{-v^2/2\sigma_v^2}$$

The relationship between the spectrum variance and the parameter a is then

$$a = \frac{f_0^2}{2\sigma_f^2} = \frac{c^2}{8\sigma_v^2}$$

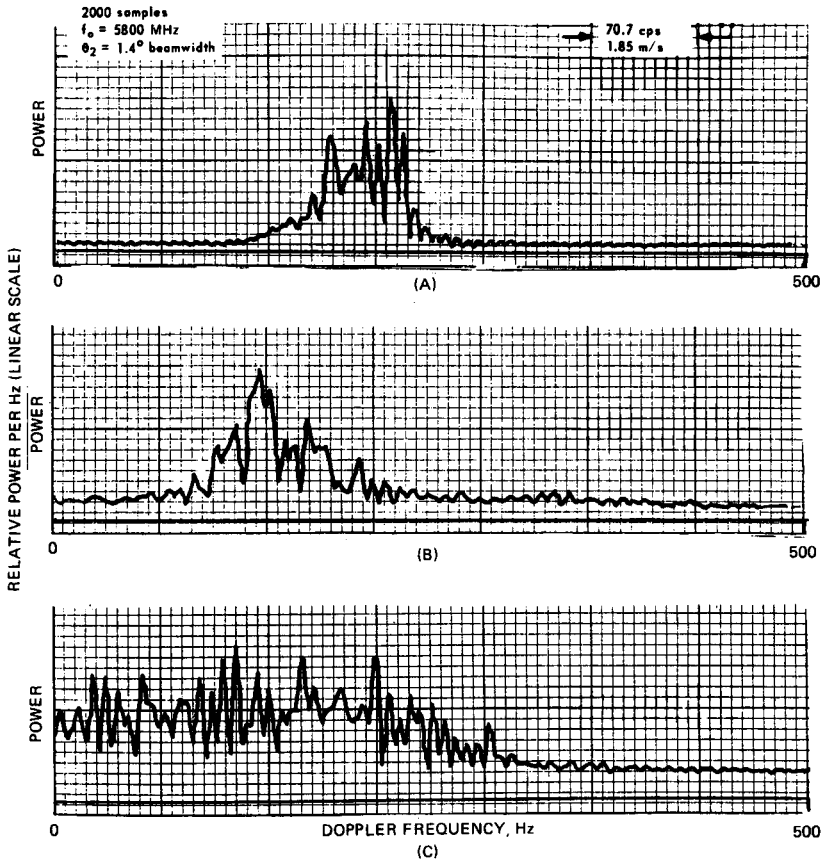

Figure 6.15 Sample power spectrum of rain echoes. (A) Range = 10 nmi; (B) range = 25 nmi; (C) range = 40 nmi.

is sometimes ignored. Wind shear can be the greatest factor contributing to the Doppler spectrum spread of precipitation echoes in a long-range, ground-based radar. The change in wind velocity with height is a worldwide and year-round condition. An altitude of maximum wind velocity is always present although it experiences seasonal changes in height and intensity. The change in wind velocity with height can often be approximated by a constant gradient. A representation of the wind shear effect is shown in Fig. 6.16.

For elevation angles of a few degrees, the difference in radial components at the half-power points of the beam is

$$\Delta V_r \approx |V_1 - V_2|$$

If we somewhat oversimplify and assume that the wind velocity gradient within the beam is constant, then for a gaussian antenna

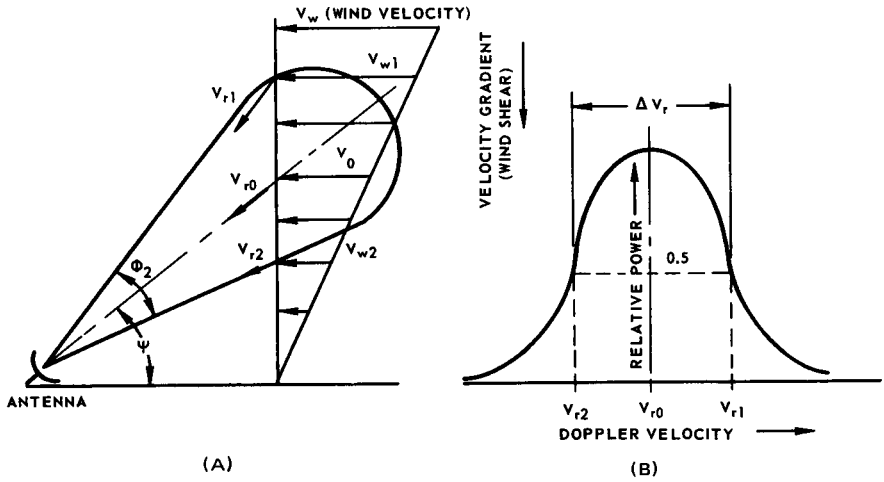

Figure 6.16 Effects of wind shear on the Doppler spectrum. (A) Physical picture (side view); (B) velocity spectrum.

pattern this velocity distribution will have a standard deviation that is related to the half-power width by

$$\sigma_{\text{shear}} = 0.42\,(\Delta V_r)$$

The difference between the normal wind shear and the small-scale gradients that are hazardous to aircraft is explained in Sec. 14.2. In terms of the wind speed gradient k this spectrum width is

$$\sigma_{\text{shear}} = 0.42\,kR\phi_2 \tag{6.12}$$

where k = the shear constant, i.e., velocity gradient, m/s/km, along the beam direction.
R = the slant range to clutter, km.
ϕ_2 = two-way, half-power antenna elevation beamwidth, rad.

For radar calculations the value $k = 5.7$ m/s/km is suggested for pencil-beam radars in the United States, pointing in the direction consistent with that of the primary high-altitude winds. Although this value may give excessive estimates of the average wind velocity, it is consistent with average values of shear observed for 0.5- to 2-km altitude thickness layers. For an arbitrary radar azimuth, a shear constant $k = 4.0$ m/s/km is more appropriate. There will be some direction in which the wind shear component is a minimum, although it may not be the crosswind at the beam center. Not only the wind speed but also the wind direction may change with height. As a result, in some instances the crosswind shear effect may be as great as the downwind effect. Figure 6.17 il-

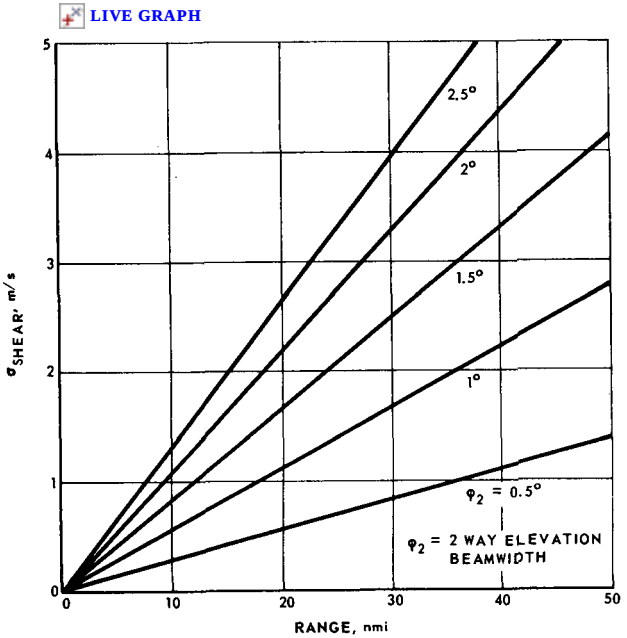

Figure 6.17 Spectrum width due to wind shear (average over 360° of azimuth).

lustrates the spectrum width due to wind shear as a function of range. The shear constant assumed is 4.0 m/s/km, which is an average over 360° azimuth. Statistics for wind speed gradients in the Eastern United States are given in Fig. 6.18.

Although Eq. (6.11) seems to indicate that the spectrum width can increase indefinitely, in practice the value of σ_{shear} is limited to about 6 m/s for beamwidths of 2.5° or less. This is partly because precipitation is limited at some altitude ceiling, such as 15,000 or 20,000 ft [501]. Beside the spectrum reduction due to the effects of a weather ceiling, the value of σ_{shear} at longer ranges is also limited when a strong *bright band* exists. Since the *bright band* echoes are of small elevation extent that gives 5 to 10 dB greater intensity than the rain echoes that are above or below it, this layer dominates the total clutter power, and tends to place an upper limit on the width of the spectrum. (See Sec. 6.7.)

If the elevation extent of the beam is large (> 2 km), such as with a "fan" elevation beam, or when observing distant weather, a somewhat more sophisticated model is required. The horizontal velocity gradient over 1-km altitude intervals exceeds the slope of the data in Fig. 6.18 due to the higher local gradients over 1-km intervals. This has led to a model in which the variance σ^2_{shear} increases with vertical extent rather than the standard deviation σ_s. This can be validated by looking

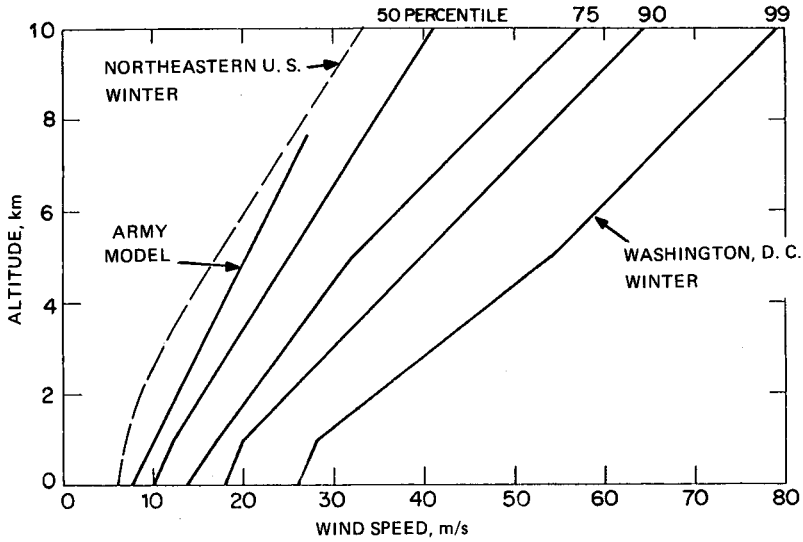

Figure 6.18 U.S. wind speeds in winter. (*Northeastern U.S. winter data from Handbook of Geophysics* [727])

at both U.S. data and the measurements of Jansenn and Van Der Spek [367] in the Netherlands. European winds and wind shear are somewhat less than in the United States. Their data for light rains were shown to have a gradient more like 4 m/s/km at shorter ranges and a lower total gradient at greater than 20 km with a 4° elevation beam. Their data show a more or less gaussian spectrum about 75 percent of the time with occasional double-peaked spectra.

There are other wind profile measurements that confirm a range of 4 to 7 m/s/km for 1-km extents. For a world-wide model, $\sigma_{shear} = 4$ m/s/km is suggested for small elevation extents and $\sigma^2_{shear} = 5$ m/s/km as a limit for larger vertical extents.

There is a fair amount of confusion about the terms wind shear and turbulence as used here and in radar meteorology texts, and the term as used by the aviation industry. In any case, tests reported by Labitt [418] with both aircraft sensors and weather radars show a high correlation of radar-reported turbulence (spectral width) and the "turbulence" in the aircraft. This is discussed further in Sec. 14.2, "Meteorological Radar."

Spectra caused by wind turbulence

Previous paragraphs have used the concept of a wind profile in terms of a mean velocity corresponding to a given altitude. Strictly speaking, because wind velocity is a nonstationary process, its mean cannot be defined without specifying the time over which the average is taken.

Fluctuations about the mean are then called turbulence, an unpredictable variation that must be described statistically. (For purposes of this chapter, the averaging time shall be understood to be on the order of 1 s.)

A number of experiments using radar measurements have shown that the turbulence spectrum width is nearly independent of height, and an average value of the spectrum standard deviations for altitudes up to 1.5 km is $\sigma_v \simeq 1.0$ m/s (although extreme values of 0.5 to 2.0 are also observed). For higher altitudes experiments indicate a lower value of $\sigma_v \simeq 0.6$ m/s [397, 614, 615, 675, 436, 501]. Additional data are given in Sec. 6.10 on chaff spectra.

Beam broadening

The spectrum component caused by beam broadening arises from the distribution of radial velocity components of a tangential wind blowing across a radar beam of nonzero width. The spectrum component will obviously have a zero mean and a standard deviation that may be derived in a manner analogous to the wind shear component.

$$\sigma_{\text{beam}} = 0.42\, V_0 \theta_2 \sin \beta \tag{6.13}$$

where θ_2 = the two-way, half-power antenna beamwidth in azimuth, rad.
V_0 = the wind velocity at beam center or, in airborne radar, the net radial velocity of the aircraft and the wind.
β = the azimuth angle relative to wind direction at beam center.

For most surface radar beamwidths (i.e., a few degrees) the beam-broadening component is quite small compared with the wind turbulence and wind shear components. For example, at a wind speed of 60 knots and a beamwidth of 2°, the maximum broadening component is 0.5 m/s. To calculate the mean wind speed as a function of height, the gradient 4.0 m/s/km is recommended with a minimum wind speed of 5 m/s at low altitudes.

Distribution of fall velocities

Because of the distribution of drop sizes in precipitation, a radar pointing vertically will observe a Doppler spread resulting from a distribution of precipitation fall velocities.* Lhermitte [435, pp. 25–28] states that the standard deviation of fall velocities for rain is approximately

* Fall velocities versus drop size are found in Medhurst [471] and are typically 4 to 6 m/s for light rains.

$$\sigma_{\text{fall}} \simeq 1.0 \text{ m/s (vertical velocity component)}$$

and is nearly independent of the rain intensity.* At elevation angle ψ the spread of radial fall velocities is

$$\sigma_{\text{fall}} = 1.0 \sin \psi \quad \text{m/s}$$

The mean fall velocity for heavier rains is ~9 m/s. For elevation angles of a few degrees, this component is insignificant when compared with the wind shear and turbulence components. For snow, $\sigma_{\text{fall}} \ll 1$ m/s regardless of the elevation angle.

Summary of precipitation spectrum components

From the previous discussion, the precipitation spectrum width may be computed by

$$\sigma_v = (\sigma_{\text{shear}}^2 + \sigma_{\text{turb}}^2 + \sigma_{\text{beam}}^2 + \sigma_{\text{fall}}^2)^{1/2} \quad \text{(m/s)}$$

where $\sigma_{\text{shear}} = 0.42\, kR\phi_2$ m/s ($\sigma_{\text{shear}} \leq 6.0$).
$\sigma_{\text{turb}} = 1.0$, m/s.
$\sigma_{\text{beam}} = 0.42\, V_0\, \theta_2 \sin \beta$, m/s.
$\sigma_{\text{fall}} = 1.0 \sin \psi$, m/s.
k = wind shear gradient, m/s/km (5.7 for along-wind direction or 4.0 averaged over 360° azimuth).
R = slant range, km.
θ_2, ϕ_2 = horizontal and vertical two-way beamwidths, rad.
β = azimuth relative to wind direction at beam center.
ψ = elevation angle.
V_0 = wind speed at beam center, m/s.

Mean velocity

The mean velocity may be of major significance in the operation and clutter-rejection properties of a radar because of its contribution to the spectral spreading already discussed. The mean Doppler offset may also be an important design parameter in a pulse Doppler or MTI processor. Wind speed at the surface varies greatly from day to day, and also with geographic location and season. Despite the statistical variability of surface winds, there is a general trend for the average wind velocity to increase with altitude up to some maximum value.

* There are often long *tails* on the low-frequency side of the Doppler spectrum due to the slow fall rate of the smaller drops.

For general radar evaluation purposes, it is reasonable to use a model having a mean surface wind velocity V_s and a maximum wind velocity V_m at an altitude h_m.

Values for V_m and h_m vary with location and season. Figure 6.18 illustrated typical profiles applicable to the winter season in the Northeastern United States. Above 25 km, the wind profile increases from its minimum upper altitude value to 37 m/s at an altitude of 40 km. A further example for the mid-Atlantic in January includes median winds of 15 m/s at the surface, 20 m/s at 3 km, and 40 m/s at 12 km. The same region in July would have similar winds aloft, but the mean surface wind would be closer to 10 m/s [727].

In addition to the change of velocity, a change in wind direction with altitude will exist. This is a manifestation of the wind shear phenomenon discussed earlier: It will result in a spectral spread when the radar resolution cell encompasses a large altitude extent. The variation in wind direction with altitude is termed a *veering angle* if the shift is clockwise, and a *backing angle* if it is counterclockwise. At latitudes above 20° N, all winds in the lower 1 km of the atmosphere typically have veering angles, and few examples of backing angles. Southerly surface winds veer more with height than do northerly winds. Above 1-km altitude, northerly winds display backing angles, and southerly winds continue to veer with height. In the lower 1-km "frictional layer" of the atmosphere, the average veering angle is 20 to 40°, with extreme values as high as 90°. At greater heights, winds either veer or back, but with approximately the same magnitude as in the frictional layer.

Experimental data

The previous discussion indicated that wind shear and wind turbulence are the primary contributors to the clutter spectrum of precipitation. At close ranges the turbulence effect should dominate ($\sigma_v \approx 0.6$ m/s or 1.0 for altitudes less than 3 km); and, as range is increased, a point should be reached where the spectrum increases linearly with range because of the wind shear effect. This relationship was verified in a series of experiments with a 5.2-cm radar having a two-way, half-power beamwidth of 1.4° [501]. Fig. 6.19 summarizes measurements of the range dependence of σ_v for this radar. The broadening effect with range is evident. The spectrum was found to be approximately centered at the radial wind speed component at the beam center. The measured spectral widths on some occasions were found to exceed 5 m/s at short ranges. Since the vertical extent of the radar beam is only about 1.6 km at 40 nmi, the square root relationship with elevation extent would also fit reasonably well. This condition was usually associated with very high wind shear gradients at low altitudes. The behavior of σ_v on

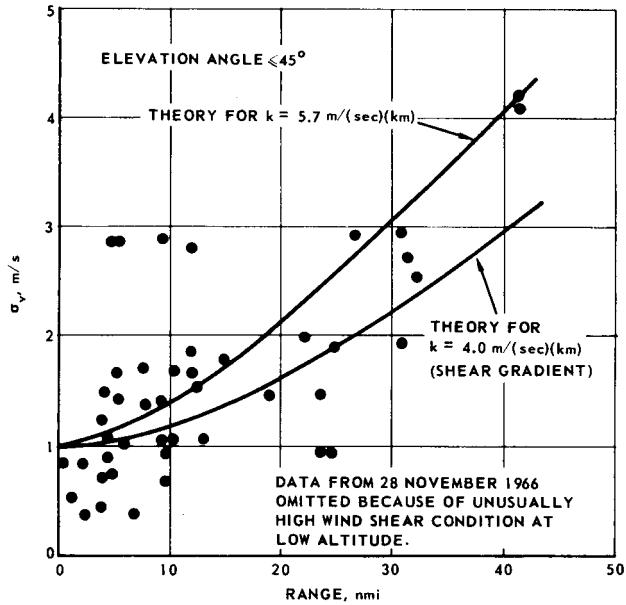

Figure 6.19 Spectrum standard deviation for rain echoes—composite graph from several tests (1.4° elevation beamwidth). (*From Nathanson & Reilly, IEEE [501]*)

one such day is shown in Fig. 6.20 (not included in Fig. 6.19); the wind velocity was 60 knots at 5000 ft on this day.

6.6 Frequency Correlation of Precipitation Echoes

In many radar applications it is desirable to get a good estimate of the mean value of rain or snow backscatter in as short a time as possible in order to establish a detection threshold. In addition, target detection

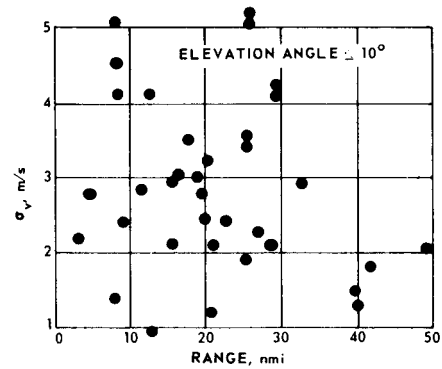

Figure 6.20 Spectrum standard deviation for rain on November 28, 1966—unusually high shear at low altitudes, e.g., 60 knots at 5000 ft.

is improved if the clutter echoes can be processed in such a way that the ratio of the variance to the mean of the processed return can be reduced. This goal can be met if the echoes from successive pulses are statistically independent and are detected and summed (incoherent integration). Unfortunately, the echoes from precipitation remain correlated for a number of milliseconds; however, the echoes can be made independent by shifting the carrier frequency from pulse to pulse by a frequency separation of at least the inverse of the pulse width.

This property of independence can be expressed by means of the *frequency correlation coefficient* which is defined as [463, 748]

$$\rho(\Delta f) = \frac{\overline{(I_0)(I)} - (\bar{I})^2}{\overline{I^2} - (\bar{I})^2} \tag{6.14}$$

where I_0 is the square of the signal amplitude at frequency f_0 and I is the square of the amplitude at $f_0 + \Delta f$. Many of the principles of frequency correlation for precipitation echoes follow the radar target characteristics discussed in Chap. 5. When the scattering volume contains many independent scatterers with more or less random positions, the normalized frequency correlation function of the echoes from multifrequency rectangular pulses can be written [395, 211]

$$\rho(\Delta f) = \left(\frac{\sin \pi\tau\Delta f}{\pi\tau\Delta f}\right)^2 \tag{6.15}$$

where τ = pulse duration.
Δf = the transmit frequency change.
$\rho(\Delta f)$ = the normalized correlation coefficient (correlation of the echoes from two pulses transmitted closely in time but separated in frequency by the increment Δf).

The $(\sin^2 x/x^2)$ function falls to zero at $\tau\Delta f = 1$ and remains less than 0.05 for $\tau\Delta f > 1$, i.e., the clutter echoes are uncorrelated for frequency shifts greater than $1/\tau$.

The result of an experiment to verify this relationship for rain is shown in Fig. 6.21 [501]. The frequency shift Δf in all cases was 500 kHz, the pulses were approximately rectangular and of durations between 0.4 and 3.2 μs, and the rainfall rate was high (20 mm/h). The elevation extent of the illuminated area was about 400 meters. The experimental results conform closely to the theory.

In conclusion, the signal-to-clutter ratio for spatially uniform clutter can be increased by frequency diversity and a postdetection integrator in the same way that the signal-to-receiver noise ratio is increased with postdetection integration. While it is shown in the next section

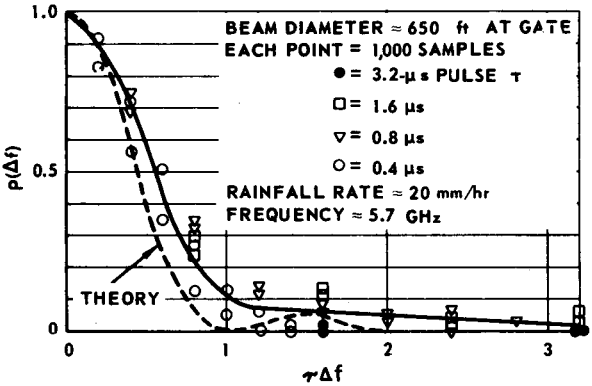

Figure 6.21 Correlation coefficient of rain echoes versus frequency shift-pulse length products (*From Nathanson & Reilly, IEEE [501]*)

that spatial uniformity is not the norm, there is probably a 5- to 8-dB benefit with proper CFAR circuits.

6.7 Spatial Uniformity of Rain Backscatter

In Chaps. 3 and 4 it was noted that many techniques for detection of targets in clutter were dependent on the clutter not only having a Rayleigh amplitude distribution and a short correlation time but also being spatially uniform. While there does not appear to be any quantitative description of the spatial uniformity of the mean backscatter, series of experiments conducted at the Applied Physics Laboratory have shown the wide variations in spatial characteristics with a C-band radar [501]. *Rain profiles* were taken by transmitting a pulse train and fixing a range gate at a selected minimum range R_0. The magnitudes of the amplitude of the echoes from 100 to 200 pulses were added and the sum stored in the digital computer. The range gate was then moved one-half to one pulse length, and the procedure repeated. This process, which took 10 to 60 s, was continued until the desired profile was obtained. Examples of these profiles are shown in Figs. 6.22 and 6.23. The ordinate is the summation of the amplitudes of all the samples at a given range multiplied by the range to compensate for the increase in beam volume and reduction in received power with range. The abscissa is the radial or slant range.

The tests were primarily on a series of thundershowers that were extensive, but obviously not uniform. The extent of the variation is indicated in Fig. 6.22A and B, which shows data that were taken only 2.25 min apart at an azimuth separation of only 2°. The extreme variations in reflectivity are quite apparent. Over 10 dB of variation were observed within 1 nmi (8 pulse lengths). The higher-intensity regions gave reflectivity values that would be predicted by Eq. (6.4) using the higher rainfall rates observed on a rain gauge (10 to 40 mm/h).

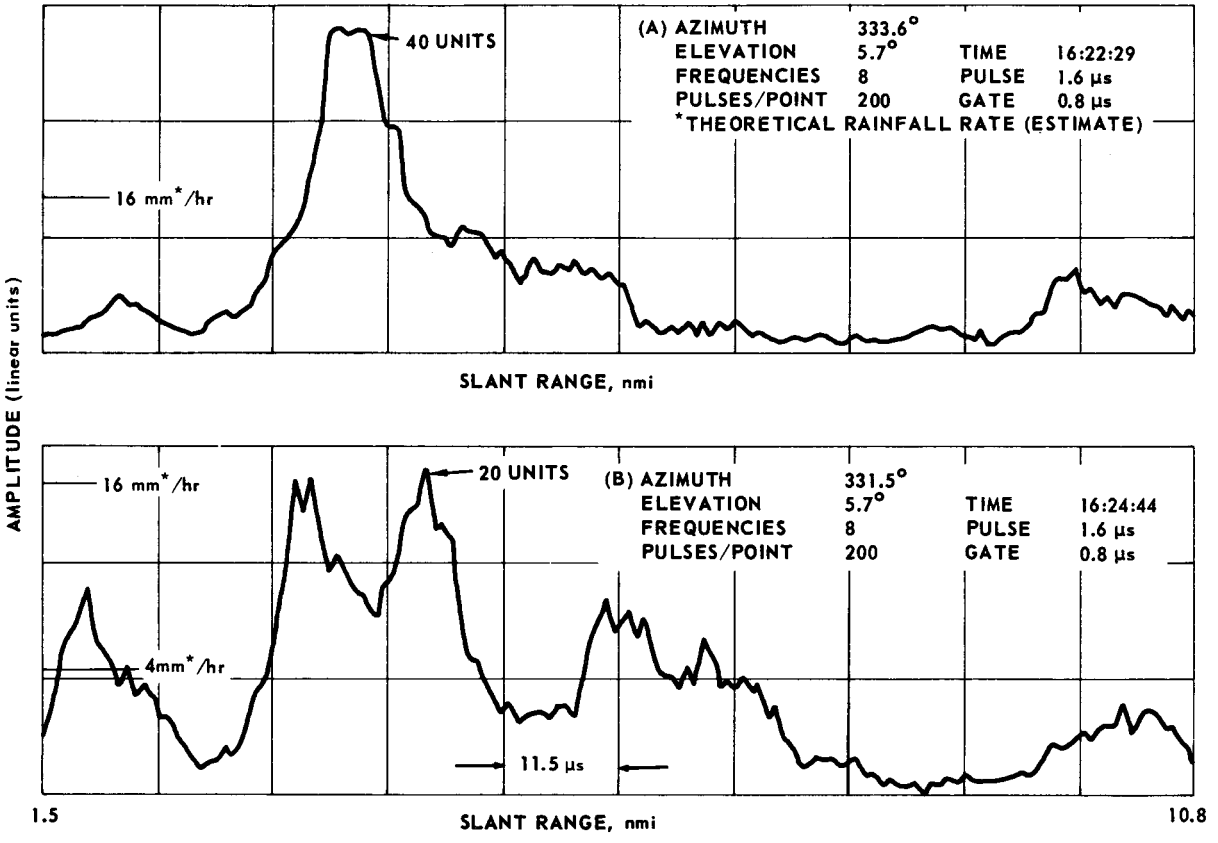

Figure 6.22 Summer storm rain—backscatter coefficient.

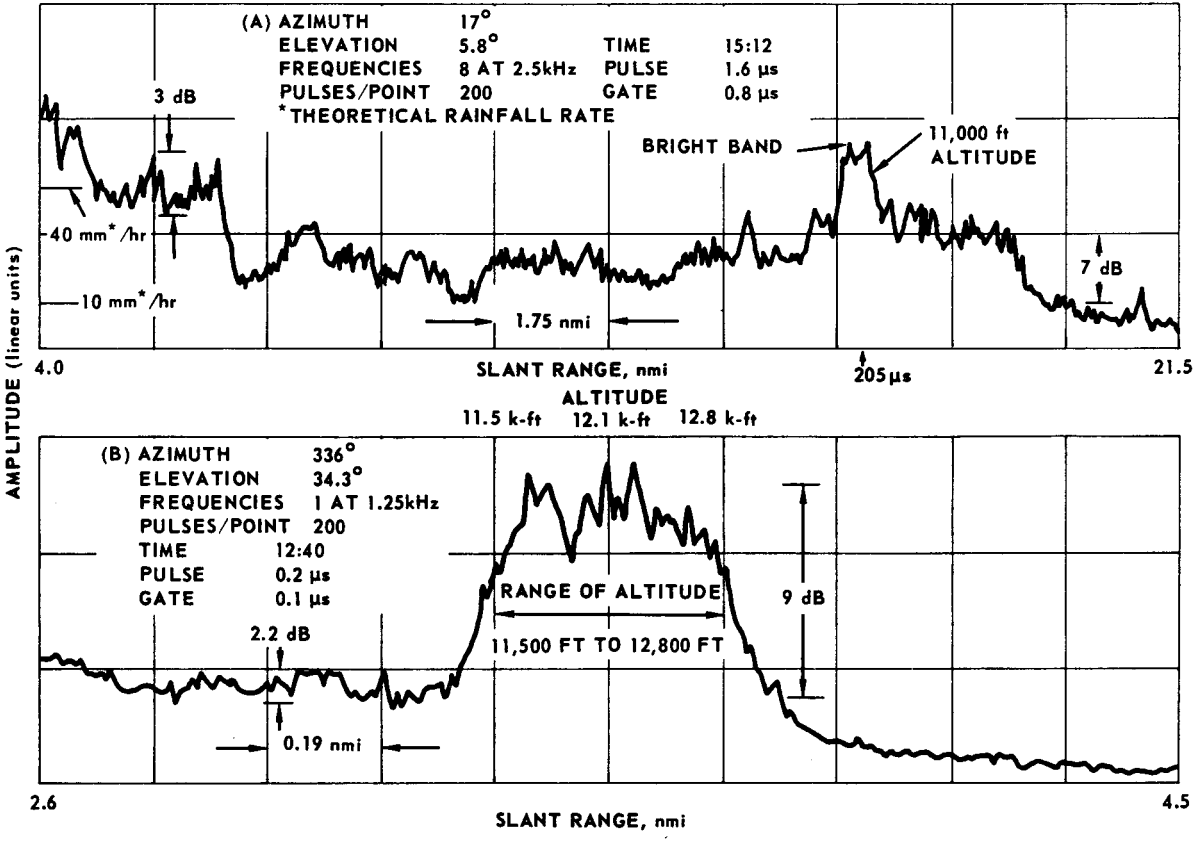

Figure 6.23 Heavy uniform rain—backscatter coefficient (with bright band).

An example of what could be considered a uniform rain gave rather consistent recordings of 16 to 40 mm/h for several hours. Radar profiles from this day are shown in Fig. 6.23. These two were chosen to illustrate the relatively uniform backscatter at lower altitudes and the apparent *bright-band* effect at the melting level.

With only a few exceptions the *uniform* rain appeared to be uniform at the lower elevation angles with about a ±2-dB peak-to-peak variation in backscatter coefficient over 1- to 2-nmi range intervals. The data in the figure and other data taken at about the same time indicate that spatial nonuniformities of less than 1 nmi in extent exceed any uncertainties in the measurements.

Unfortunately, the wide disparity of measurements on different days precluded postulating any model for the gross uniformity of rain clutter. Changes in the mean backscatter may be larger than ±10 dB in 10 nmi for showers, or as small as ±1 dB for the more uniform rains.

Similar runs were made on the uniformity of a snowstorm. The mean backscatter was more uniform than for any of the rain measurements.

An attempt was made to estimate the spatial extent of the major nonuniformities by computing the spatial correlation function of the *mean* backscatter. The sum of the magnitudes of the backscatter from the pulses at each range was corrected for the R^{-1} dependence and inserted into an autocorrelation program. The range displacement where the normalized autocorrelation drops to one-half its value of zero lag is thus a measure of the range extent of the variations of the mean backscatter. While the statistical sample was too small for a rigorous analysis, the *characteristic extent* of the nonuniformities (where $\rho = 0.5$) was 0.6 to 1.4 nmi in the showers. This value was 2 to 3 nmi for the uniform rain, including the bright-band effect, and in a snowstorm the extent was 1.4 to 1.9 nmi at 3° elevation. Data for stratus clouds indicate correlation distances of about 7 nmi. [504]

To determine how to set a threshold for target detection in storms or showers does require some model. Figure 6.24 further illustrates the complexity of the modeling problem. It is essentially a plan view of a New England shower region. Note the very high-intensity cores with diameters of 1 to 2 km dropping 20 dB in a comparable distance.

Sekine et al. [643] obtained spatial distributions for stormy conditions near Tokyo. The data fit the Weibull distribution quite well. The measured shape parameter, c, varied between 1.25 and 2.0 with an average of about 1.7 where 2.0 corresponds to the Rayleigh distribution. Lower values of c correspond to longer tails on the distribution. This in turn requires a 2 parameter or distribution-free CFAR, as described in Sec. 4.8, to maintain a constant false alarm rate. Ward [751] suggests modeling with the more complex K distribution, which also requires a sophisticated CFAR.

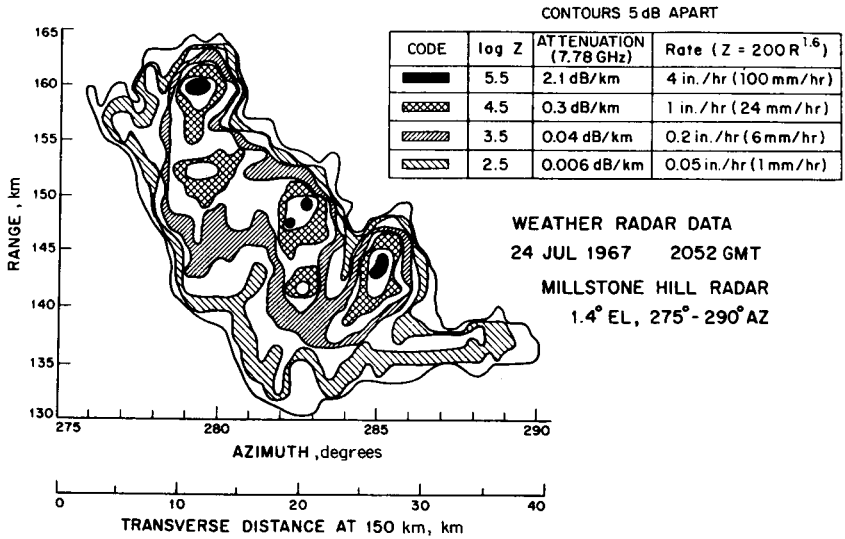

Figure 6.24 Weather radar map for New England showers. (*From CCIR, 1986* [*361*])

Physical explanation of the bright band

The various physical factors that influence reflectivity changes in the bright band are: (1) the change in the dielectric constant from that of ice to that of water, (2) the change in the fall velocity of precipitation particles through the melting layer, (3) coalescence or the combining of individual snow crystals into snowflakes or clusters of crystal, (4) shape effects, or deviations from the spherical shape in melting snow, and (5) growth of precipitation particles.

The first two physical factors are the basic cause of the bright band. After the snow falls below the melting level it acquires a coating of water which effectively changes its dielectric constant and causes an increase in reflectivity by a factor of about 5. This makes a peak of reflectivity at the bright band. By the time melting is completed, the fall velocity of the raindrops has increased to about 5 times that of the snowflakes. Due to the increased velocity the vertical spacing of the raindrops is 5 times as great as that of the snowflakes and hence the concentration of the number of raindrops becomes one-fifth that of the snow, thus tending to decrease the reflectivity. In the upper portion of the bright band, the increase in dielectric constant occurs without appreciable change in the fall velocity, while in the lower portion an increase in fall velocity occurs with little or no change in dielectric constant.

Coalescence is a more gradual process occurring both in the snow above the melting level and in the bright band. At low temperatures,

TABLE 6.7 Average Echo-Intensity Changes Due to Physical Factors Above and Below the Bright Band (BB)

Factor	Snow down to BB, dB	BB to rain below, dB
Dielectric	+4	+1
Fall velocity	−1.5	−5.5
Coalescence or breakup	+3	−1
Shape	+1.5	−1.5
Growth	0	+0.5
Total	+7	−6.5

below about −5°C, there is little tendency for coalescence to occur and snow mostly consists of single crystals. With increasing temperature, coalescence increases, possibly due to a greater cohesive property of the crystals. In the melting layer itself the snowflakes are frequently very large, sometimes as much as 3 to 4 in in diameter. Breakup of the large snowflakes into smaller raindrops may occur when melting is completed. Coalescence and breakup may be a highly variable factor.

In the melting layer, growth by condensation occurs due to the cooling effect of melting snow but in the absence of updrafts this effect is small and increases the reflectivity by about 12 percent. Table 6.7 shows estimated typical magnitudes of the various effects in the 2000-ft layers above and below the middle of the bright band (BB).

The bright-band thickness averages about 300 m, but can sometimes reach dimensions up to 1 km. The altitude of the bright band varies with latitude, climate, and season. An upper bright-band boundary may be assumed at the altitude (h_f) of the 0° isotherm. Reflectivity above the 0° isotherm diminishes at a rate of about 6.5 dB/km, up to the altitude of the tropopause (h_t). The altitude of the 0° isotherm is approximately related to latitude, ϕ, according to $h_f = 4$ km for latitudes up to about 36°, and $h_f = [4 - 0.75\ (\phi - 36°)]$ km for latitudes above 36°. The altitude of the tropopause, h_t, is approximately related to latitude according to $h_t = 17$ km for latitudes between 0 and 30°, and $h_t = 9$ km for latitudes between 30 and 90°. Between 30 and 90°, h_t may be approximately determined by linear interpolation of height versus latitude.

6.8 Tropospheric Refraction Effects

Radio waves propagated through a medium with a varying index of refraction undergo both refractive bending and retardation of their velocity of propagation. These phenomena give rise to angle and range errors when a target is being tracked by a surface radar. The angular error is caused by the bending of the radar beam such that the wavefront

reflected from a target appears to be coming from a direction other than the target's true angular position in space; the range error is due to the increase in time necessary to travel over the curved path as compared to the straight-line path between target and receiver and the variation in propagation velocity.

General practice has been to assume an atmospheric refractive index that decreases linearly with the height above the surface of the earth. The 4/3-earth-radius principle, based on this linear assumption, leads to errors at long ranges and low elevation angles. For the results in the following graphs, a negative-exponential model of the refractivity-height function (refractive index versus height above the earth's surface) is used. The model is $n(h) = 1 + 0.000313 \exp(-0.04385\ h)$, where h is altitude in thousands of feet and $n(h)$ is the refractive index. This model is based on a surface index of refractivity and is referred

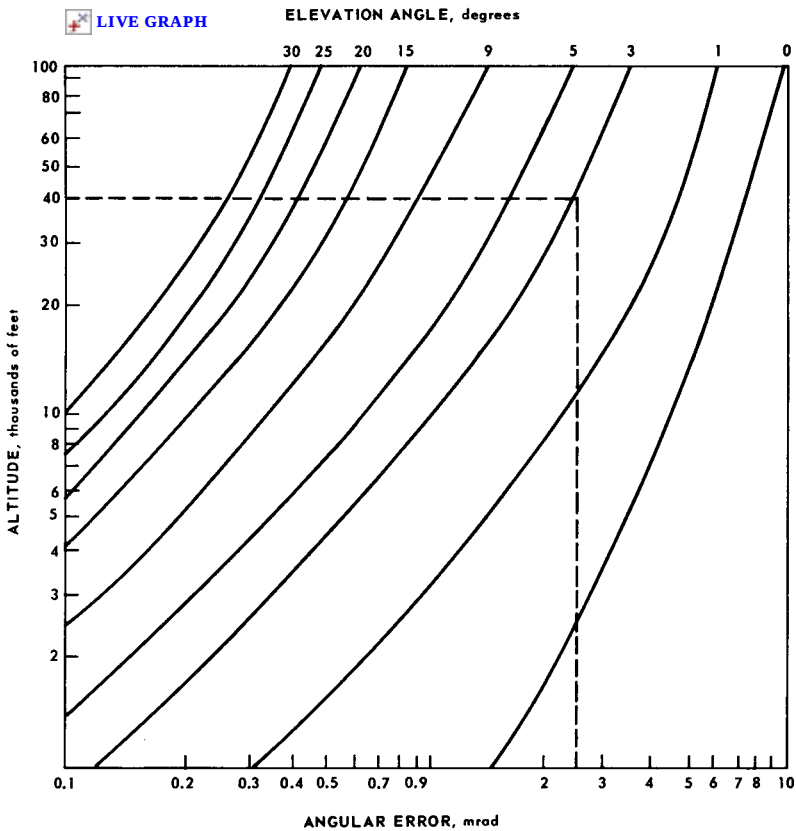

Figure 6.25 Target angular error due to refractive effect of earth's atmosphere (angular error is a function of target altitude and elevation angle). (*From Shannon,* Electronics [*648*])

to as the CRPL (National Bureau of Standards, Central Radio Propagation Laboratory) exponential reference atmosphere. Other values of the equivalent earth radius are described in Chap. 1.

The CRPL reference atmosphere was used to calculate the tropospheric angular and range errors presented graphically in Figs. 6.25 and 6.26. The angular error is the angle between the apparent ray path

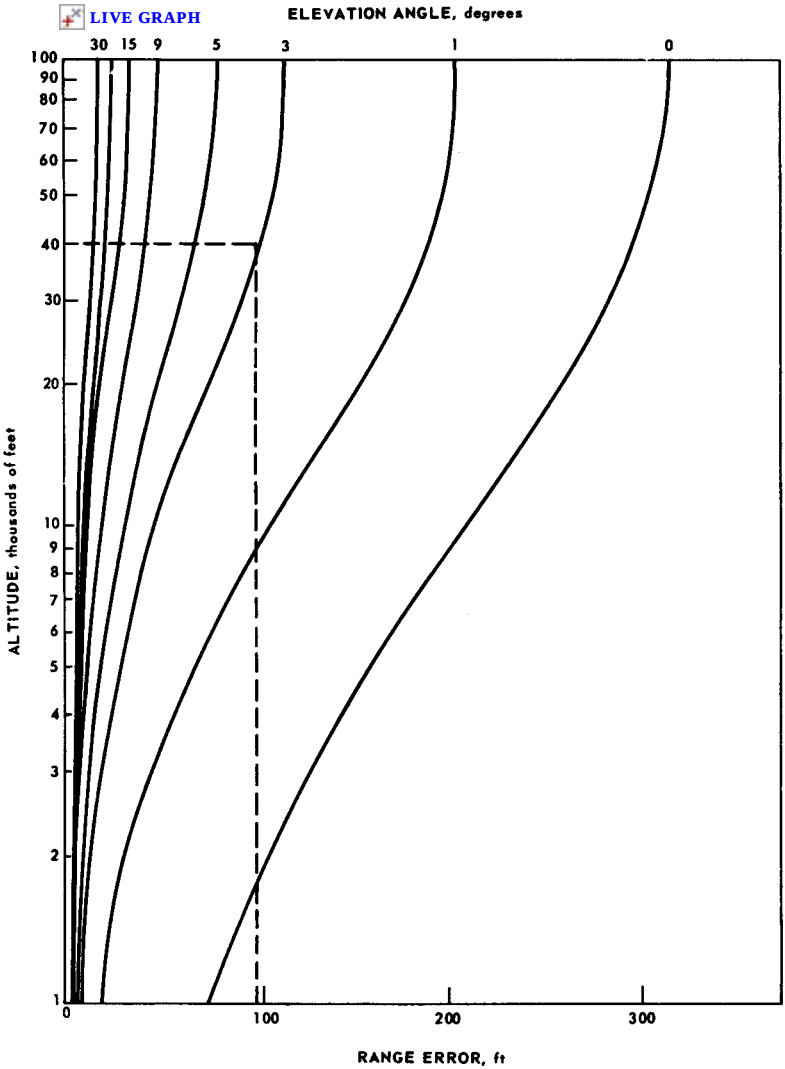

Figure 6.26 Target range error due to refractive effect of earth's atmosphere (range error is a function of target altitude and elevation angle). (*From Shannon,* Electronics [*648*])

to the target from the radar and the straight-line path from the radar to the target. The range error is the apparent increased range of the target caused by the wavefront traveling a curved path instead of a straight-line one. The range error as a function of the total path length is shown in Fig. 6.26 for a one-way path. For a two-way path the errors must be doubled. A radar several thousand feet above sea level would have less error. The NRL radar coverage diagram based on the CRPL exponential reference atmosphere is reproduced from Blake [75] as Fig. 6.27. Experimental data on refractivity have been reported by Nichols [507].

These range and elevation angle errors should be considered as known *bias* errors since their magnitudes are calculable. The uncertainty in their exact magnitudes (about 10 percent) from simplifying assumptions concerning the state of the atmosphere is partly from unknown bias errors and partly from "precision" errors. Contributing to the precision errors are the effects of irregularities in the troposphere. Barton [39, p. 489] gives some rms values of the fluctuation of range and angle in the troposphere as follows (see also Millman [476, p. 317ff]):

Type of weather	Δ range, ft	Δ angle, mrad
Heavy cumulus	2.0	0.7
Scattered cumulus	0.5	0.3
Small scattered cumulus	0.1	0.15
Clear moist air	0.02	0.07
Clear normal air	0.005	0.03
Clear dry air	0.001	0.015

The above bias error models are limited to surface-to-air paths and do not take into account meteorological conditions at the time of the measurement. In meteorological radar investigations and for cases in which true geometric target trajectories to the highest attainable degree of accuracy are desired, the reference atmosphere should not be used without modification. At the minimum it should be corrected on the basis of a directly or indirectly measured value of the refractive index at the radar location.

The radio refractive index of air

A summary of the state of knowledge of this parameter appears in Bean [49]. More recent data are in Blake [75], Ko [405], and the EREPS software [207]. Bean's conclusions, with some paraphrasing, are as follows:

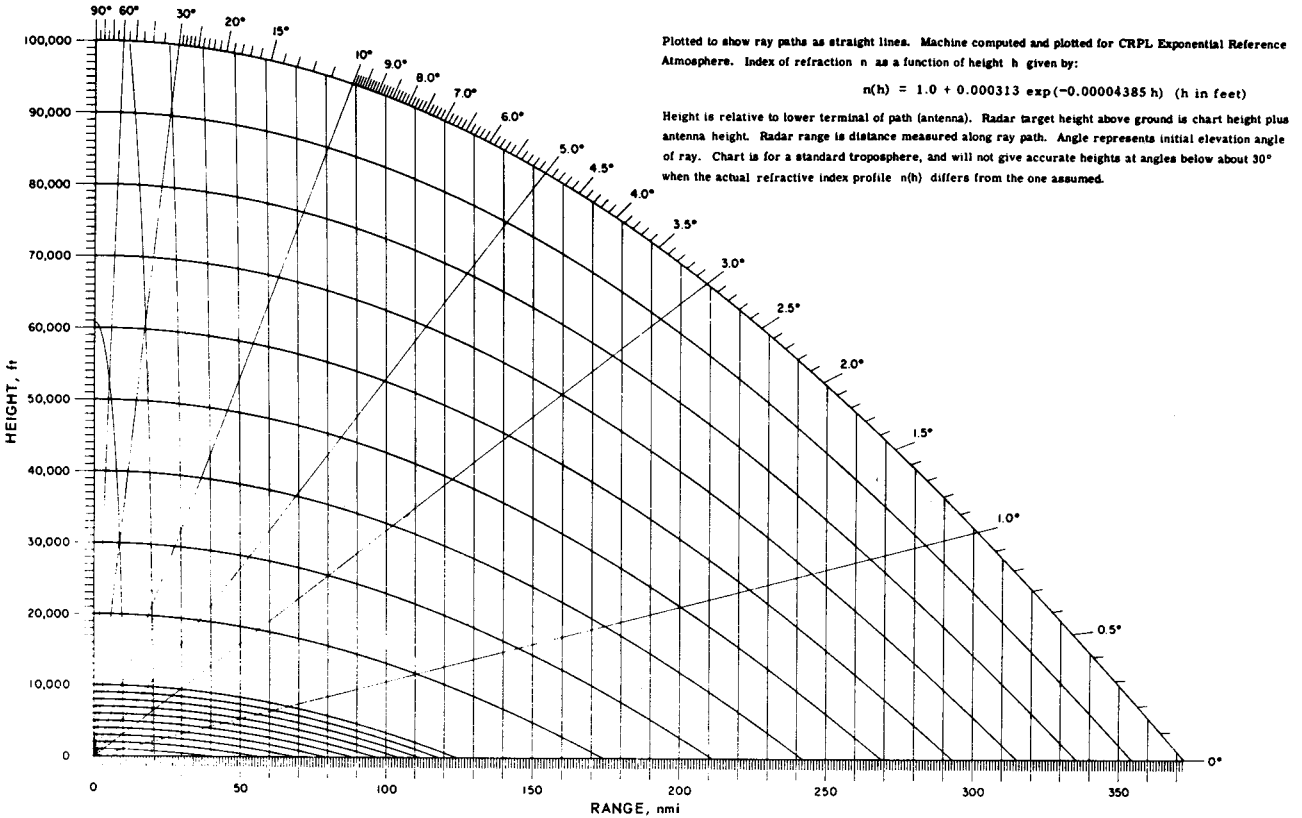

Figure 6.27 Earth radar coverage diagram. (*From Blake* [*75, 73*])

1. The differences in determined values of the constants in the expression for refractivity N (Bean's Eq. 10) are small compared with the errors from using the formula; i.e., the errors in using ordinary meteorological measurements (e.g., radiosondes) mask the errors caused by using published values of the constants.
2. The refractive index is effectively nondispersive for frequencies below, for example, 50 GHz. (N.B., ionospheric effects, multipath effects, and effects due to storm phenomena, which exhibit high coefficients of radiowave absorption, are not considered.)
3. The choice of atmospheric model for N depends on the location and application. World-wide statistics are given in the EREPS software.
4. The atmosphere, on the average, yields an exponential distribution of N with height.

Bean also indicates the divergence of a typical measured profile of N from the often assumed 4/3 earth profile. From his graphs it is evident that the 4/3 earth model has about the correct slope in the first kilometer above the earth's surface but decreases much too rapidly above that height. It is also seen that the observed refractivity distribution is more nearly an exponential function of height than a linear function as assumed by the effective earth's radius model. The exponential decrease of N with height is sufficiently regular to permit a first approximation of average N structure from surface conditions alone.

6.9 General Properties of Chaff

Fundamental relationships for chaff

Chaff (or *window*) is a form of electronic countermeasure that dates back to World War II. Lightweight inexpensive metallic or metal-coated fibers have high radar reflectivity per pound when their length is near one-half wavelength of the radar they are trying to confuse. The confusion can take one of several forms:

- A large cloud of dipoles dispersed in the atmosphere that shield aircraft or missiles either in or near the cloud
- A chaff "puff" that can emulate another aircraft or missile and cause false detections
- Packets of chaff that can also be used as track breakers in an attempt to force a track radar to track the chaff rather than the aircraft being tracked

The tactics of chaff use are complex but it is possible to model a basic chaff cloud and to detail its extent, reflectivity, and Doppler charac-

teristics. Chaff at frequencies below about 1 GHz is generally called "rope" and is either dispersed in small rolls or cut off a reel of wire or tape.

Chaff moves horizontally with the local winds as does rain. It is an excellent tracer of the winds such that the velocity spectrum is the same as the wind spectrum in the horizontal plane. For horizontally oriented radar beams the Doppler characteristics are almost identical to rain. At one time the U.S.S.R. completely covered Czechoslovakia with chaff and kept it "refreshed" for several days.

The chaff dipoles are designed to resonate at the frequencies of the radars that they are attempting to confuse. (Dipole length $\approx$ one-half radar wavelength.) Often the dipoles in a package are cut to different lengths to cover an entire radar band or several radar bands. The maximum backscatter cross section of a single dipole occurs when the dipole is oriented parallel to the E plane of the incident radiation and perpendicular to the direction of propagation. This gives a maximum radar cross section

$$\sigma_m = 0.857\,\lambda^2$$

Schlesinger [637] stated that if these dipoles are randomly oriented after dispersal into the atmosphere the overall cross section is approximately

$$\sigma = 0.18\,\lambda^2 N$$

where N is the total number of dipoles and σ is the resultant radar cross section. Other calculations give a constant of 0.14, which gives a value closer to experiments. He further calculates that if they were all cut from old style aluminum foil 0.001-in thick, $\lambda/2$ long, and 0.01-in wide the radar cross section is

$$\sigma \approx 3000\,W/f \quad \text{m}^2$$

where W is weight in pounds and f is transmit frequency in gigahertz. This would yield a 1000-m^2 cross section for a single pound of narrowband chaff at 3 GHz. (See also Cassedy and Fainberg [112] and Mack and Reiffen [458].)

The bandwidth of the resonant-length chaff is only about 10 to 15 percent of the center frequency as illustrated in Fig. 6.28; and if it is desired to cover the desired frequency range from 1 to 10 GHz with the 10-percent bandwidth assumption, a 1.0-lb package of broadband foil chaff would give a 60-m^2 radar cross section anywhere within the frequency range.

The modern form of chaff is aluminum-coated glass or mylar. At frequencies of 3 GHz or higher the diameter is about 0.001 inches. The

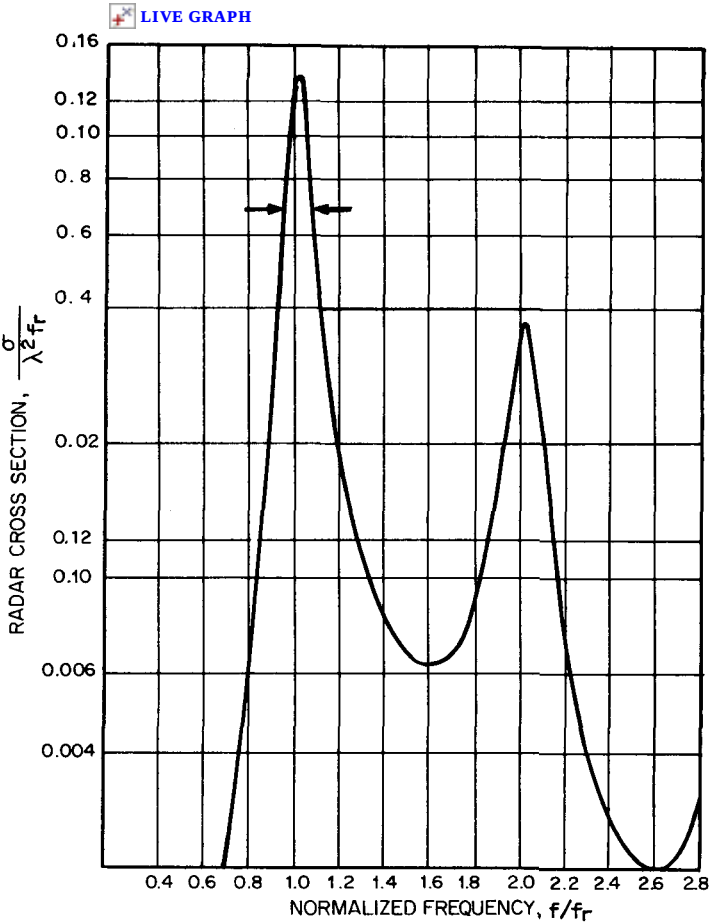

Figure 6.28 Frequency response of resonant chaff. (Chaff cross section in wavelengths; random orientation; A = length/diameter = 1000.) (*Courtesy: Lundy Electronics* [*454*])

radar properties of this type of chaff are illustrated in Fig. 6.29. Note that it theoretically takes only 800 dipoles to achieve an RCS of 1 m^2 at 3 GHz. In practice the foregoing values are not achieved due to several factors: (1) the thin aluminum coatings limit the conductivity, and (2) the effective number of dipoles is limited by clumping and "birdnesting." This is called the *disperson efficiency* and is on the order of 0.5 to 0.65. At 3 GHz, 1 lb of narrow-band chaff has an RCS of about 5000 m. Coverage from 1 to 10 GHz with larger-diameter (2 mil) dipoles below 3 GHz the RCS across the band still exceeds 100 m^2/lb. Peebles [537] has shown that the RCS remains high for moderately large bistatic angles.

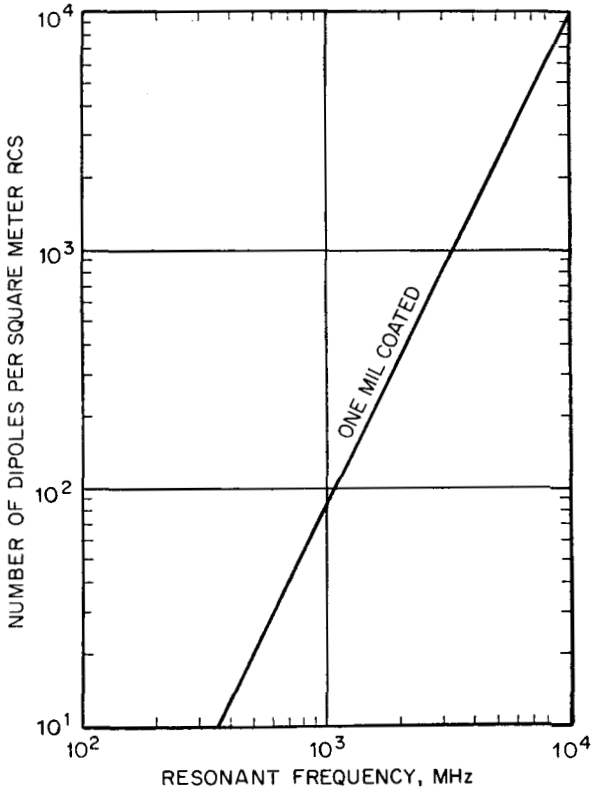

Figure 6.29 Theoretical number of chaff dipoles required per square meter of RCS at resonant frequency. (*Courtesy: Lundy Electronics* [*454*])

Modern chaff dispensers come in several varieties. In one form, dipoles are packaged into a plastic cylinder with a small explosive charge at one end. In one variety, 750,000 X-band, 250,000 C-band, and 250,000 S-band dipoles are packaged into a 6-in-long cylinder that weighs only about 6 oz. This is about 3 million dipoles per pound, and costs only a few dollars per package.

In another form illustrated in Fig. 6.30, the dipoles of desired length are laid out on a roll that is about 1 ft in diameter and has a chaff weight of 50 lb. Six rolls are placed in an aircraft pod with a total of 300 pounds per pod. To dispense the chaff, the rolls are rotated, and air is rammed into the nose of the pod, blowing the chaff out the rear of the pod. The dispensing rate is controlled by the rotation rate of the rolls.

At lower frequencies "rope" is used instead of chaff, and is made of wire—long filaments that may be twisted fibers or foil. One type,

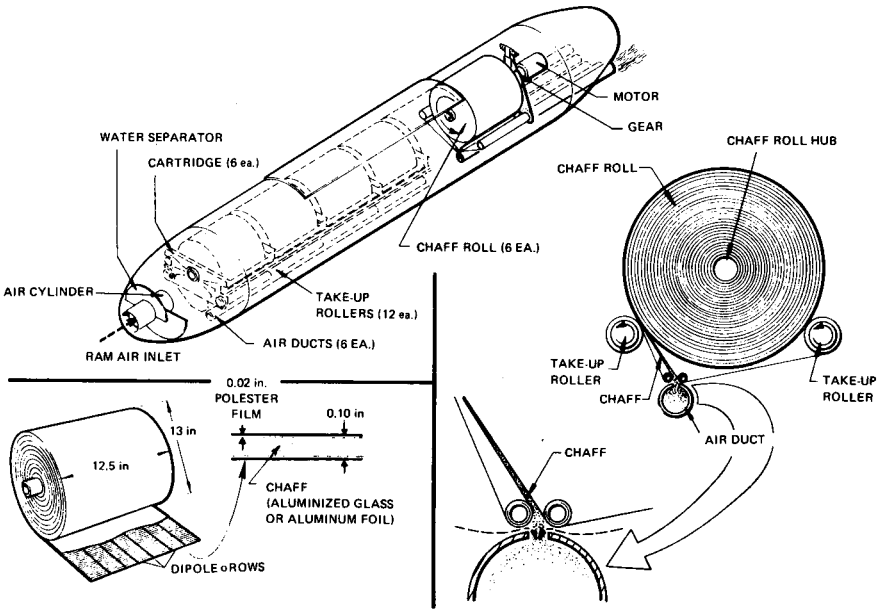

Figure 6.30 AN/ALE-38 chaff-dispensing system. (*From* Electronic Warfare, *vol. 4, no. 4, 1972. Courtesy Cardiff Publ. Co.*)

"stringball rope," is made of twisted fibers and is typically many meters long. It is characterized by its radar cross section per unit length. Although in a sense it is less efficient than dipoles, the λ^2 term in the RCS keeps the reflectivity at several hundred m^2/lb.

Fall rates for dipoles are dependent on construction. For coated fiberglass, it is less than 1 m/s.

Density of chaff

Obviously chaff can be dispensed at a wide variety of rates depending on the nature of the dispenser, the maximum chaff load of the aircraft, and the tactics. A typical system might be:

- Aircraft speed 600 knots or 10 nmi/min
- Broadband chaff of 200 m^2/lb (1 to 10 GHz)
- Drop rate of 10 lb/min or 1 lb/nmi
- Dispersion rate (horizontally) of 2.5 m/s (σ_v).

At some time between 10 and 100 min, depending on the wind conditions, the chaff will be dispersed to about 1 nmi in a horizontal plane and some fraction of a nautical mile in elevation. A convenient as-

sumption is that the chaff expands to a density of 1 lb/nmi^3 and has a reflectivity density of $\Sigma\sigma = 200$ m^2/nmi^3. Since there are 6.36 km^3 per nmi^3, this converts to about $\Sigma\sigma = 30$ m^2/km^3. If the aircraft flies a 75-nmi "racetrack" twice, with the second pass above or below the first by 1 nmi in elevation, the nominal cloud is 2 nmi by 2 nmi by 75 nmi in length. Three hundred pounds of chaff are dispersed in about 30 min.

The assumed density of chaff clouds is quite low, and the attenuation of electromagnetic waves is negligible. As a side issue, the U.S. and Canadian governments have made tests on the environmental implications of chaff drops. They found no problem.

6.10 Spectra of Chaff Echoes

The Doppler spectrum of chaff return can be split into four components in the same manner as for precipitation:

1. Wind shear due to finite height of the radar beam
2. Beam broadening due to finite width of the beam
3. Turbulence
4. Fall velocity distribution of the dipoles

In the case of precipitation it was shown that the wind shear and beam-broadening effects were caused by the variations in the horizontal motion of the droplets within the radar beam. This motion of the rain was shown to follow the horizontal wind speed very closely. Experiments by Pilie' et al. [552] have also shown that there is very high correlation between horizontal wind and chaff velocities at altitudes of from 5000 to 10,000 ft. Similar experiments showed the same high correlation at from 24,000- to 35,000-ft altitudes. It can be concluded that the calculation of the first two effects (due to wind shear) for chaff should be identical to that described for rain in Sec. 6.5.*

Because of the difficulty of separating the turbulent component from the shear components of the chaff spectrum, there is little information available on the spectrum of the chaff after dispersion. One fairly extensive set of data was reported by Smirnova [675] in 1965 in the U.S.S.R. Unfortunately his radar parameters were not included, but it was implied that the antenna beamwidths were about 0.7° and that the measurements were made looking almost exactly downwind. The altitudes observed were from about 1000 to 40,000 ft.

* The effects are identical if both the rain and chaff fill the radar beam. However, chaff does not usually have as much vertical extent.

Several conclusions can be reached by interpreting the available information:

1. The turbulence component σ_{turb} above 12,000 ft varies between 0.35 and 1.2 m/s with an average of about 0.7 m/s or somewhat less than the assumed value of 1.0 m/s for precipitation.
2. Below 12,000 ft, readings as high as 2 m/s have been recorded, but an average value from 1000 to 12,000 ft is close to the 1.0 m/s used for precipitation. The larger values may be partially due to the vertical fall velocity distribution [675].
3. An average of Smirnova's data on the turbulence velocity is included in Fig. 6.31. The lower-altitude tests (1500 to 13,000 ft) overlapped the high-altitude tests (8000 to 32,000 ft). Since there is not a significant correlation between wind velocity and turbulence it is as-

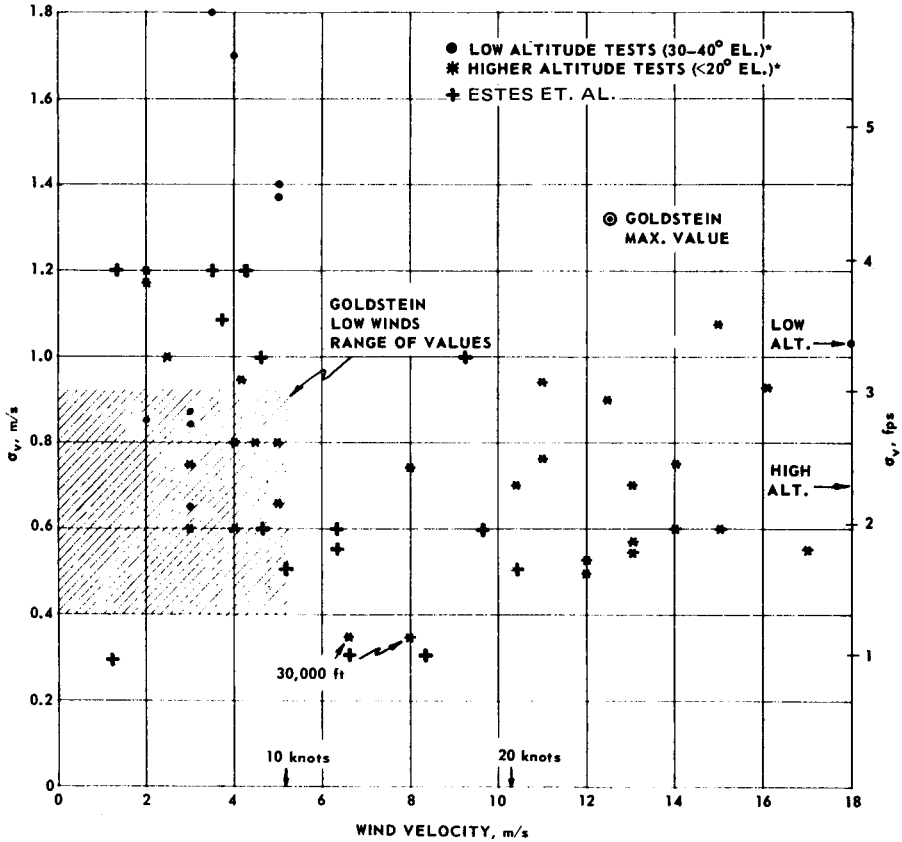

Figure 6.31 Turbulence σ_v of chaff versus wind velocity (*After Smirnova* [675], *Goldstein* [397], *and Estes et al.* [210]. © 1985 IEEE)

TABLE 6.8 Spectral Estimates for Mature Chaff

Run number	Radar	Chaff type*	R, km	BW, m/s	v_0, m/s	σ_v, m/s
M1	X-band	AGF/CR	5	0.8	9.9	0.6
M2	X-band	AGF/CR	6	0.8	10.8	0.5
M3	X-band	AGF/DC	6	0.8	−1.2	0.3
M4	X-band	AGF/DB	6	1.1	9.2	1.0
M5	X-band	AGF/CR	6	1.5	1.4	1.2
M6	X-band	AGF/CR	5	1.1	4.7	1.0
M7	X-band	AGF/CR	5	0.8	5.2	0.5
M8	X-band	AGF/DC	8	1.0	6.3	0.6
M9	X-band	AGF/DC	8	1.0	6.3	0.6
M10	X-band	AGF/DC	8	1.0	4.8	0.6
M11	UHF	AS/DB	13	1.5	3.9	1.1
M12	UHF	AS/DB	9	1.5	4.1	1.2
M13	UHF	AS/DB	12	1.5	3.3	1.2
M14	UHF	AGF/CR	19	0.6	6.5	0.3
M15	UHF	AGF/CR	31	0.6	8.5	0.3

* Chaff type code:

Type	*Code*
Dipole material	
Aluminum strips	AS
Aluminum-coated glass fibers	AGF
Dispensing method	
Continuously dispensed, roll	CR
Discrete unit, box	DB
Discrete unit, cartridge	DC

SOURCE: Ref. [210] © IEEE, 1985.

sumed that the horizontal turbulence component is roughly constant at 1.0 m/s for low altitudes and at about 0.7 m/s above 18,000 ft. These points are shown as arrows on the figure.

These data are only partially consistent with Goldstein's data (at $\lambda = 10$ cm) from World War II [397]; he estimated a standard deviation of 0.4 to 1.0 m/s* for low (< 10-knot) winds and 1.3 m/s for 25-knot winds. Barlow's [34] general value of 3.5 ft/s ($\approx$ 1 m/s) agrees more closely. Since the 0.4 m/s data point was for low winds and a different type of chaff, it can probably be disregarded. This leaves a range of σ_v between 0.6 and 1.3 m/s. Data from the more recent mature chaff measurements of Estes et al. [210] at both UHF and X-bands are included in Fig. 6.31 and shown in Table 6.8. The mean velocities varied between 1 and 11 m/s. Measurements were taken within a few minutes of dispersal. The data tend to confirm the low values for the turbulence component. They also presented data at 150 to 450 m behind the dis-

* The 0.4 m/s curve is for chaff dispensed from a blimp; this chaff had different aerodynamic properties than the chaff used to obtain the other values.

pensing aircraft and found spectral widths (σ_v) about double those of the clouds away from the influence of the aircraft.

The final component of the chaff spectra is the Doppler spread due to the variation in fall velocity of the dipoles. Chaff dipoles fall more slowly than do the large raindrops that dominate the backscatter from precipitation; dipoles have typical terminal velocities of 0.7 m/s as compared to about 6 m/s for 1 mm/h rain. Theoretical and experimental studies of the fall velocity chaff were made by Jiusto and Eadie [370], including metallized nylon cylinders 0.0035 in in diameter and 0.6 in long. The experimental work was in a small altitude chamber without air turbulence. The measured median terminal fall rate was about 0.6 m/s; σ_{fall} would be $\approx$ 1 m/s. The variation in the fall rate of the nylon cylinders was only a few tenths of 1 m/s. Thus, the range of vertical differential velocities is below 1 m/s ($\approx$ 0.5 m/s) at low altitudes. Further experimental data are available in Totty et al. [706].

The measured spectra for chaff and rain are similar enough so that separate computations are not needed except for two factors:

1. If the vertical dispersion of chaff at high altitudes is small, there will be less shear effect.
2. Chaff has a higher fall velocity at high altitude (over 25,000 ft) and a low terminal velocity $\approx$0.7 m/s; rain, on the other hand, has a higher terminal velocity than its *initial* condition (clouds).

The general equation for the total variance of the velocity spectrum for chaff is then

$$\sigma_v^2 = \sigma_{\text{shear}}^2 + \sigma_{\text{beam}}^2 + \sigma_{\text{turb}}^2 + \sigma_{\text{fall}}^2$$

where $\sigma_{\text{turb}} = 2.3$ ft/s ≈ 0.7 m/s.
$\sigma_{\text{fall}} = \sin \psi$ m/s.

It is emphasized in the chapters on processing that the mean velocity of chaff (and rain) is also important in many signal-processing techniques, especially MTI, and that the spectra described here are centered at the mean radial velocity of the volume cell containing the chaff.

Chapter

7

Sea and Land Backscatter

F. E. Nathanson
J. P. Reilly

7.1 Backscatter from the Sea—Monostatic

Backscatter from the surface of the sea limits the performance of radar surveillance and missile guidance for airborne, shipboard, and coastal early warning and defense systems. The following three sections provide models of the normalized radar power return from the sea as a function of frequency, polarization, grazing angle, and aspect with respect to the primary wind and sea condition. The statistics of these signals are given in Secs. 7.5, 7.6, and 7.7.

The general relationships between the wind and the surface conditions of the sea are given in Fig. 7.1. This figure defines *sea state* as well as would seem appropriate to subsequent discussions. Combined conditions at any given time or place may vary considerably from this chart because of the wind history or geographical factors. Note that *Beaufort sea state* [item (2) in the table] is not the same as the *hydrographic sea state* [item (6)]. The latter is appropriate for radar problems and is used in the following discussions.

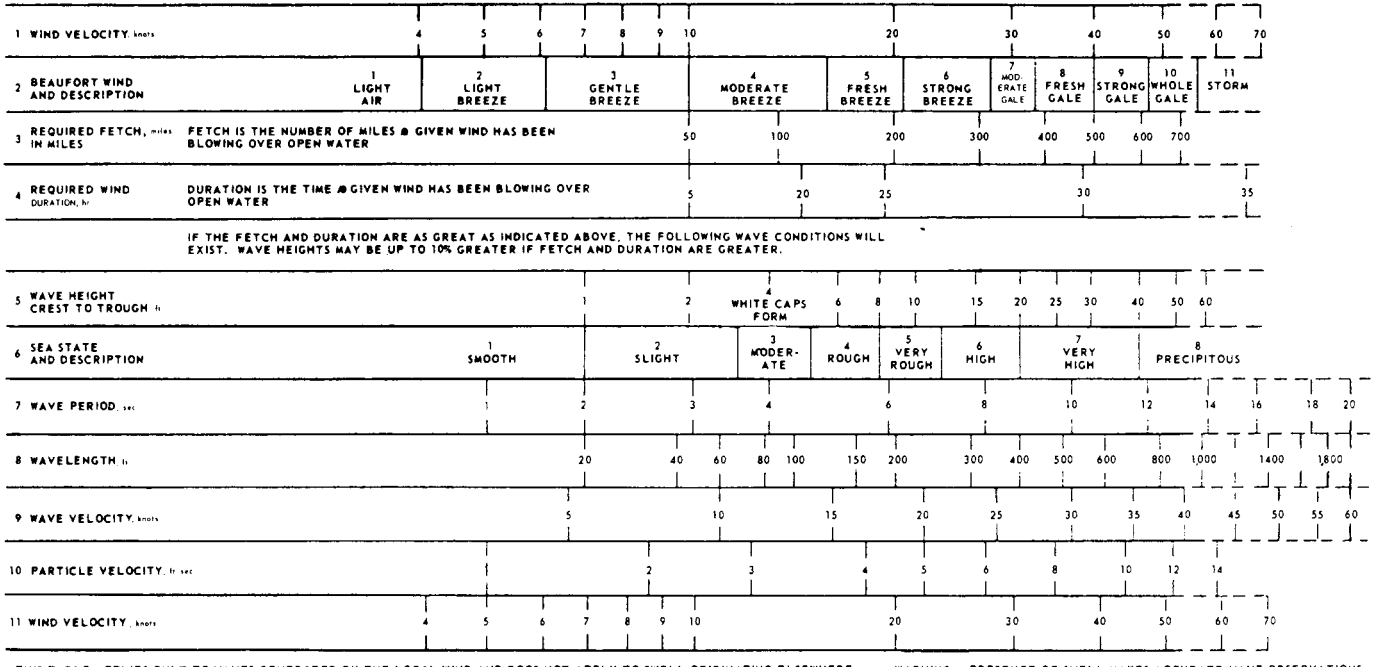

Figure 7.1 Wind waves at sea. (*From* Undersea Technology, *May 1964, p. 34 by permission of copyright owners Compass Publications, Inc.*)

To select radar parameters for operating near or on the sea, the relative probabilities of specific conditions of wind speed and sea state are needed. Severe storms degrade almost any radar system performance, but they rarely occur. Figure 7.2 gives worldwide probabilities of wind speed, derived by Long et al. [445] from the *U.S. Navy Marine*

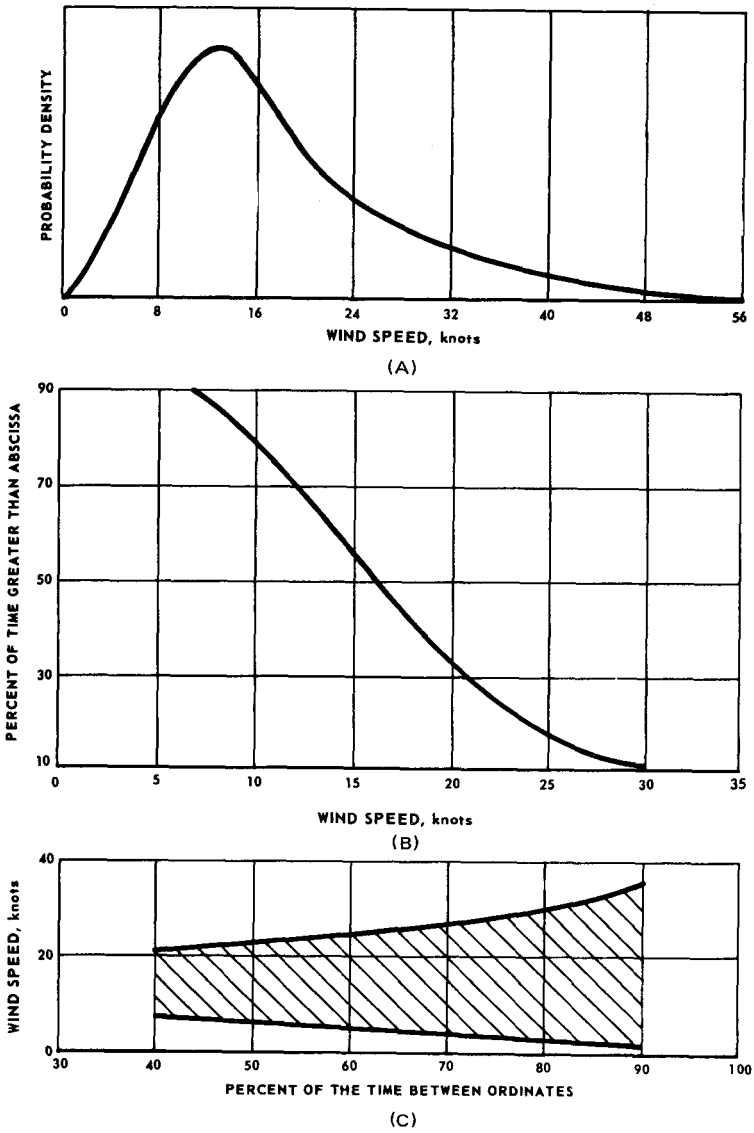

Figure 7.2 Surface wind speed statistics. (*From Long et al. [445]*)

Climatic World Atlases, 1957. Table 7.1 gives the relative frequency of occurrence of wave heights in specific regions of the oceans.

Description of the sea surface. The quantitative interpretation of radar scatter from the sea requires an appreciation of certain properties of ocean waves. A brief review is undertaken here of the ocean wave physics and characteristics. Also, common oceanographic nomenclature pertaining to ocean waves is defined and explained.

Sea state. This term is used here to refer to the state of the sea, or roughness, as determined by the heights of the largest waves present. Numbers have been assigned to sea states by the International Marines' Codes, and these are related to wave heights. They should not be confused with Beaufort (wind force) scale.

TABLE 7.1 Relative Frequency of Occurrence of Wave Heights in Specific Regions of the Oceans

Region	Percentage of time-significant wave height (ft) from					
	0–3	3–4	4–7	7–12	12–20	>20
North Atlantic between Newfoundland and England	20	20	20	15	10	15
Mid-equatorial Atlantic	20	30	25	15	5	5
South Atlantic at latitude of southern Argentina	10	20	20	20	15	10
North Pacific between latitude of Oregon and southern coast of Alaska	25	20	20	15	10	10
East-equatorial Pacific	25	35	25	10	5	5
West wind belt of South Pacific at latitude of southern Chile	5	20	20	20	15	15
North Indian Ocean during northeast monsoon season	55	25	10	5	0	0
North Indian Ocean during southwest monsoon season	15	15	25	20	15	10
Southern Indian Ocean between Madagascar and northern Australia	35	25	20	15	5	5
West wind belt of southern Indian Ocean between Cape of Good Hope and southern Australia	10	20	20	20	15	15
Averages over all regions	22	23	20	15	9	9

SOURCE: From Long et al. [445].

Significant wave height. This term is a common maritime descriptor referring to the average of the heights—from crest to trough—of the one-third highest waves; it is denoted $H_{1/3}$.

RMS wave (or roughness) height. This is a term describing root-mean-square height above the mean surface level—used in rough-surface scatter theories; it is denoted here by σ_h. While there is no exact general relationship between σ_h and $H_{1/3}$, a common approximation frequently used for wind waves is $H_{1/3} = 4\ \sigma_h$. Another approximation that is occasionally used is $H_{1/3} = 2.83\sigma_h$.

Average wave height. This is determined from rms wave height by $h_a = \sqrt{2\pi}\ \sigma_h$. Also related to significant wave height by $h_a = 1.6\ H_{1/3}$.

Length. The length or spatial period of a single ocean wave is the distance from one crest to another; it is denoted by L.

Period. Unless denoted otherwise, this refers to the length of time it takes two successive crests of a single wave to pass one point. It is denoted by T.

Spatial wavenumber. This is defined in terms of the length of an ocean wave as $K = 2\pi/L$.

Temporal wavenumber. This is the radian wavenumber given in terms of the period by $\omega = 2\pi/T$.

Fetch. This is the horizontal distance over which a nearly constant wind has been blowing. (It is also defined by its duration.)

Duration. This refers to the length of time during which a nearly constant wind has been blowing.

Wind waves. This refers to a system of ocean waves that is being, or has very recently been, aroused by winds blowing locally above that area of the ocean. Wind waves result in a random appearing ocean height profile.

Fully developed seas. This is an equilibrium sea state condition reached after sufficient duration and fetch at a given wind speed. The estimated duration and fetch versus wind speed required to produce fully developed seas is provided in Fig. 7.1.

Swell. When wind waves move out of the area in which they were originally excited by the winds, or after winds have ceased to blow, these waves change their shape and settle down to what is known as *swell*. Swell appears less random and more nearly sinusoidal, of great length, and with great width along the crestlines. The usual period of swell is from 6 to 16 s. Swell can arise from storm areas thousands of miles distant and can increase radar reflectivity.

Deep-water waves. When the water is sufficiently deep that the effect of the bottom on the propagation characteristics of the waves can be neglected, they are called *deep-water waves.* Generally, if the depth is greater than one-half the length of a given wave, the deep-water approximation is valid. Except near beaches, ocean waves are deep-water waves, and this assumption is utilized throughout this book.

Gravity waves. This term refers to waves in which the chief restoring force upon the perturbed water mass is gravity. Waves whose lengths L are greater than 1.73 cm are gravity waves, since gravity waves are the essence of sea state.

Capillary waves. This term refers to waves in which the chief restoring force acting on the perturbed water mass is surface tension (less than 1.73 cm in length).

7.2 Empirical Sea Backscatter Models for Low Grazing Angles

For surface clutter (sea, land, or ice) the term σ_0 is used to represent the normalized mean (or median) reflectivity from an area on the surface of the earth illuminated by a radar. In some references, the term σ° is used. The value is constant only for a given angle, carrier frequency, sea state, wind direction polarization, and even pulse length. To a first approximation the illuminated area is $A = R\theta_2\Delta R$ for small grazing angles (Ψ), narrow beamwidths and the peak antenna gain directed at the center of this clutter cell. R is the range from the radar to this cell, θ_2 is the two-way azimuth beamwidth, and ΔR is the range resolution given by $c\tau/2$ for noncoded pulses, or by the 3-dB resolution of a coded or compressed pulse. For better accuracy the effective pulse duration τ' from Chap. 2 may be used. There is at least a 3-dB standard deviation in almost all values of σ_0 whether they are experimental or theoretical. This uncertainty is expanded in later sections.

The clutter cross section in a resolution cell can be approximated by

$$\text{RCS} \approx R\theta_2\Delta R\sigma_0 \tag{7.1}$$

for small beamwidths and low grazing angles. Note that forward scatter is not explicitly taken into account, but is included in virtually all reported values of σ_0. The term is dimensionless and is called the *normalized radar reflectivity* and is most often presented as a mean value in decibels below 1-m^2 reflectivity per square meter of illuminated area.

Tables 7.2 through 7.8 are models primarily compiled from experimental data with some extrapolation and interpolation between data points. There are averages of the decibel values of upwind, downwind,

TABLE 7.2 Normalized Mean Sea Backscatter Coefficient σ_0 for Grazing Angle of 0.1°

		Reflection coefficient in dB below 1 m^2/m^2 at indicated carrier frequency, GHz						
Sea state	Pol.	UHF 0.5 GHz	L 1.25	S 3.0	C 5.6	X 9.3	K_u 17	K_a 35
0	V							
	H			90*	87*			
1	V			80*	72*	65*		
	H			80	75	71*		
2	V	90†	87*	75*	67	56		
	H	95†	90*	75*	67*	59*	48*	
3	V	88†	82*	75*	60*	51		47*
	H	90†	82*	68*	69*	53*		
4	V	85†	78*	67*	58*	48		45*
	H		74*	63*	60	48		
5	V	80†	70*	63*	55*	44		42*
	H		70†	63*	58*	42*		
6	V			56				
	H							

* 5-dB error not unlikely.
† 8-dB error not unlikely.
NOTE: Monostatic radar, 0.5- to 10-μs pulse.

TABLE 7.3 Normalized Mean Sea Backscatter Coefficient σ_0 for Grazing Angle of 0.3°

		Reflection coefficient in dB below 1 m^2/m^2 at indicated carrier frequency						
Sea state	Pol.	UHF 0.5 GHz	L 1.25	S 3.0	C 5.6	X 9.3	K_u 17	K_a 35
0	V		83†				63*	55†
	H			83*	79	74*		
1	V		78*	64*	60	58	54*	46†
	H			74	68	66*	58	
2	V	80†	73*	62*	55	52	52*	43†
	H	78*		66*	60	56*	53*	
3	V	78†	70*	58*	50*	45	47*	40*
	H		68*	60*	50	46	42*	
4	V	75†	65	57*		43	44*	38
	H			55*		42	39*	
5	V	73†	64*	52*		39	39	35*
	H		64*	52*	44*	39	38*	
6	V					34	37*	31*
	H			46*		34	37*	

* 5-dB error not unlikely.
† 8-dB error not unlikely.
NOTE: Monostatic radar, 0.5- to 10-μs pulse.

TABLE 7.4 Normalized Mean Sea Backscatter Coefficient σ_0 for Grazing Angle of 1.0°

		Reflection coefficient in dB below 1 m^2/m^2 at indicated carrier frequency						
Sea state	Pol.	UHF 0.5 GHz	L 1.25	S 3.0	C 5.6	X 9.3	K_u 17	K_a/w 35/94
0	V		68*			60*	60*	60*
	H	86*	80*	75*	70*	60*	60*	60*
1	V	70*	65*	56	53	50	50*	48*
	H	84*	73*	66	56	51	48*	48*
2	V	63*	58*	53	47	44	42	40*
	H	82*	65*	55	48	46	41	38*
3	V	58*	54*	48	43	39	37	34
	H	73*	60*	48	43	40	37	36
4	V	58*	45	42	39	37	35	32
	H	63*	56*	45	39	36	34	34*
5	V		43	38	35	33	34	31
	H	60*	50*	42	36	34	34	
6	V			33		31*	32	
	H			41		32*	32	

* 5-dB error not unlikely.
NOTE: Monostatic radar, 0.5- to 10-μs pulse.

TABLE 7.5 Normalized Mean Sea Backscatter Coefficient σ_0 for Grazing Angle of 3.0°

		Reflection coefficient in dB below 1 m^2/m^2 at indicated carrier frequency						
Sea state	Pol.	UHF 0.5 GHz	L 1.25	S 3.0	C 5.6	X 9.3	K_u 17	K_a/w 35/94
0	V				60*	<56*	50*	48*
	H	75*	72*	68*	63*	<58*		53
1	V	60*	53*	52	49	45	41*	41
	H	70*	62*	59	54	50	45*	43*
2	V	53	50	49	45	41	39	37
	H	66*	59	53	48	43	38	40
3	V	43*	43*	43	40	38	36	34
	H	61*	55*	46	42	39	35	37
4	V	38*	38	38	36	35	33	31
	H	54*	48*	41	38	35	32*	32
5	V	40*	38	35	35	33	31*	30*
	H	53	46	40	36	33	30*	
6	V					28	28	
	H			37		30	28	

* 4-dB error not unlikely.
NOTE: Monostatic radar, 0.5- to 10-μs pulse.

TABLE 7.6 Normalized Mean Sea Backscatter Coefficient σ_0 for Grazing Angle of 10°

		Reflection coefficient in dB below 1 m^2/m^2 at indicated carrier frequency						
Sea state	Pol.	UHF 0.5 GHz	L 1.25	S 3.0	C 5.6	X 9.3	K_u 17	K_a/w 35/94
0	V		45*		44*	<47*	<45*	44*
	H		60*			<56*		
1	V	38	39	40	41	42	40	38
	H		56*		53	51		
2	V	35*	37	38	39	36	34	33
	H	54*	53	51	48	43	37	36*
3	V	34*	34	34	34	32	31	31
	H	50	48	46	40	37	32	31
4	V	32*	31	31*	32	29	28	29
	H	48*	45	40	36	34	29	29
5	V	30	30	28	28	25	23	26*
	H	46	43	38	36	30	26	27*
6	V	30*	29	28	27*	22*	18*	
	H	44*	40*	37	35*	27*	24*	

* 4-dB error not unlikely.
NOTE: Monostatic radar, 0.5- to 10-μs pulse.

TABLE 7.7 Normalized Mean Sea Backscatter Coefficient σ_0 for Grazing Angle of 30°

		Reflection coefficient in dB below 1 m^2/m^2 at indicated carrier frequency						
Sea state	Pol.	UHF 0.5 GHz	L 1.25	S 3.0	C 5.6	X 9.3	K_u 17	K_a/w 35/94
0	V		42*	42*	42*	37*	33*	
	H		50*	50*	50*	48*	45*	
1	V	38*	38*	40	42	36	31*	35*
	H		46*		48	44*	38*	
2	V	30	31	32*	34	32	26*	30
	H	42	41	40	42	38*	35*	35*
3	V	28	30	29	28	26	23	23*
	H	40*	39	38	37	34	28	29*
4	V	28	28	27	25	24	22	22
	H	38*	37	37	35	29	21	21
5	V	28	24*	23	22	22	18	20*
	H	35	34*	32	30	26	18	20*
6	V	25*	23*	22*	21*	17	15	
	H	33*	32*	30*	29*	21*	16	

* 5-dB error not unlikely.
NOTE: Monostatic radar, 0.5- to 10-μs pulse.

TABLE 7.8 Normalized Mean Sea Backscatter Coefficient σ_0 for Grazing Angle of 60°

Sea state	Pol.	Reflection coefficient in dB below 1 m^2/m^2 at indicated carrier frequency						
		UHF 0.5 GHz	L 1.25	S 3.0	C 5.6	X 9.3	K_u 17	K_a 35
0	V	32	33	34	26*	23	22*	
	H	32	32	32	27*	25*	22*	26*
1	V	23*	22	24	24	24	20*	24*
	H	22	24	25	26	24	20	
2	V	20*	21	21	23	18	18*	19*
	H	22	21	21	22	23	18*	
3	V	18*	18*	19	18*	16*	14	14*
	H	21	20	20	20	21	16*	16*
4	V	14*	15* 8	15* 6	15* 4	14*	11 9	10
	H	21*	18* 10	17* 8	16* 7	15*	12* 11	12*
5	V	18*	15*	15	15	13*	11*	4
	H	21*	18*	17	17	14	10*	
6	V	18*	17*	15*	14*	11*	10*	
	H	20*	19*	17*	16*	12*	10	

* 3-dB error not unlikely.
NOTE: Monostatic radar, 0.5- to 10-μs pulse.

and crosswind where available. They are adjusted from incidence angle (from the vertical) or depression angle to the grazing angle ψ, which is the angle of the ray to the local horizontal of the radar cell (often called the *clutter cell*). Note that the remote sensing community uses incident angle rather than grazing angle. Median values were adjusted to mean values where practical. Occasionally data have been modified where the author believes it to be an error (such as with early NRL X-band data).

A smooth curve cannot be drawn through all the points and some data points deviate from a smooth fit. The reason for this presentation is that new data can be easily entered or modifications can be made. The original data set (1968) comprised about 25 references and was in the first printing of the first edition of this book (1969). This has often been used as a standard model. However, it was updated in later printings (after about 1974), but was not labeled as such. A few extra data points helped fill out the tables. Further revisions were distributed in 1983 and 1987 in short courses and government reports, but not published openly. Many helpful associates supplied data points from tests that were never published. This version (1990) is the result of about 60 experiments, but still contains many uncertainities especially at low carrier frequencies and low grazing angles.

The author now believes that two effects made the earlier low-grazing angle data higher than a true mean. First, the early data was generally from less sensitive radars and sometimes the experimenters reported only points at which the echoes were above normal due to unknown increases in wind speed, wave heights, or ducting. Second, the frequent occurrence of ducting increases σ_0 as was pointed out by Dyer [195, 196], Eaves and Reedy [197, p. 330], and Reilly and Dockery [583]. Propagation effects are discussed in Sec. 7.8. Changes in excess of 10 dB at 0.1-degree grazing are not uncommon.

If the tables are to be used to specify conditions for detection of low-flying aircraft, missiles, ships, periscopes, etc., the possibility that some of the entries may be biased on the high side would only lead to conservative calculations of radar performance—these radars would encounter ducting at least some of the time and must still detect the targets. Perhaps upwind values should be used for conservative specifications. For remote sensing, global mean values may be more appropriate. The new tables reflect some lower values of σ_0 at low grazing angles as represented by newer experiments, but still may be biased higher by ducting conditions. Some values are still higher than models such as the one developed by Georgia Tech [346]. The tables do not sort the short pulse or spiky sea clutter problem, discussed later.

Some of the entries in the 35-GHz column also include the 94-GHz band. The few sets of data available at these frequencies either do not indicate a pattern as to which frequency has higher or lower values, or even a clear polarization difference (see Rivers [610], Dyer [196], and Wetzel in Skolnik [673, p. 13.12]). At millimeter waves, higher wind speeds, especially at low grazing angles, involve attentuation due to the spray that reduces the measured reflectivity. This could be part of the reason why Sittrop reported X-band reflectivity as being higher than the K_u-band values for wind speeds in excess of 30 knots and 0.5- to 2-° grazing [668, 669, 670]. This factor is in addition to assumptions about Bragg resonance.

The tables do not provide data at the HF frequencies (3 to 30 MHz) which are a highly specialized area of radar. HF reflectivity characteristics are complicated by the fact that the wavelength of the gravity waves is sometimes comparable to the electromagnetic wavelength. However, it appears clear that at low grazing angles the reduction in σ_0 going from 3 to 0.5 GHz does not continue to 0.05 GHz. It is not clear where σ_0 increases again, but for grazing angles below 10°, σ_0 increases to a maximum of about -27 dB at low grazing angles for vertical polarization in the upwind/downwind direction. The physical process is complex and the Doppler spectrum is double peaked. For further information see Headrick in the *Radar Handbook* [673] and [445, 301, 11, 121, 681].

In general, the tabulated values table are for:

1. An average of the upwind, crosswind, and downwind values where available.
2. Pulse lengths in the 0.5- to 5-μs region, with echoes having approximately Rayleigh distributions since they span multiple waves.

Data points not conforming to these assumptions have been crudely adjusted to conform. An asterisk is shown where data are questionable or where there is a severe conflict, leading to an expected error as indicated. Multipath factors are included.

The following ground rules have been observed and used for extrapolation and interpolation, involving grazing angles up to 30°

1. For a given entry on the table, the return from vertical polarization will equal or exceed that from horizontal and the deviation will increase at lower sea states, lower depression angles, and lower transmit frequencies. The polarization differences do not appear to apply to high sea states and above 15 GHz.
2. The backscatter increases with grazing angle from 0 to 20° as θ^n, where n may be as high as 3 for low angles, low sea states, and low frequencies. The value of n decreases in the tables toward the lower right-hand corner (high frequencies and sea states), where it approaches 0.
3. The backscatter coefficient at low grazing angles almost always increases with transmit frequency as f^m for horizontal polarization to at least 15 GHz where m may be as high as 3 below 2 GHz for a very low grazing angle (less than 1°) and seas below state 3. As the angle, sea state, or transmit frequency exceeds these values, the exponent drops toward 0.
4. The backscatter increases with sea state by as much as 10 dB/sea state for low seas and low frequencies, but reduces to a smaller change at higher sea states and frequencies. Earlier studies by NRL (1965–1970) indicates a "saturation" at about sea state 4 for C- and X-band, but more recent studies by NASA at K_u-band and Raytheon (for General Dynamics) indicate that σ_0 continues to increase significantly up to 30 to 40-ft wave heights.
5. Sea state 0 arbitrarily corresponds to a significant wave height less than 0.25 ft and winds less than 4 knots.
6. Ducting conditions often increase σ_0 at low grazing angles (see Sec. 7.8).

7.3 Sea Clutter Near Vertical Incidence

The reflectivity at vertical incidence is of importance in remote-sensing and in airborne radars where the *altitude line* echo enters the sidelobes of a sensitive airborne radar. Reflectivity is quite high for calm seas at 0° incidence (90° grazing), since the radar is looking downward onto a mirror-like flat plate with some curvature due to the spherical nature of the ocean surface. Thus, like a flat metallic plate, the ocean surface will have a gain factor and σ_0 will exceed unity. Unfortunately, the beamwidth of most measurement radars is relatively large and the earth's curvature must be taken into account. In addition, even 2 to 4° errors in knowing the vertical will yield significant errors. Thus, vertical incidence σ_0 data varies from +10 to 26 dB for calm seas for either polarization. Values of +15 to 20 dB for X- or K_u band are appropriate for typical calm seas and small beamwidths. Note that with wavelengths of 2 to 3 cm, the sea would have to be extremely calm to emulate a flat plate. However, tank measurements by Uliana et al. [721] at 94 GHz yield σ_0 as high as +26 dB for light winds. For calm seas at lower carrier frequencies σ_0 probably increases to above 20 dB until the carrier frequency is low enough that the waves penetrate the sea. Early measurements reported about +16 dB at 400 MHz. See Daley [158], Moore's and Wetzel's chapters in the *Radar Handbook* [673] and the Ulaby et al. volumes [720].

As the seas get rougher the surface is no longer like a mirror, and the reflected echoes will be deflected away from the vertical. The reflectivity will drop 5 to 7 dB for sea state 5 at X- or K_u band for either polarization. As the incidence angle decreases from the vertical, a point is reached at which there is little dependence on roughness, polarization, or carrier frequency. This occurs at about 11 to 15° incidence angle and estimates average about $\sigma_0 = +8$ dB for narrow-beam radars from 1 to 15 GHz, with some lower values nearer to 0 dB reported in earlier experiments.

This *high grazing angle* (80 to 90°) region is thus characterized by rougher seas directing energy away from the radar rather than toward it. There is a considerable base of data in the previously cited references and the large volume of NASA material based on the SEASAT program and airborne scatterometer flights. At depression angles of 60 to 70° the sea-state dependence reverses and for sea states of 4 or less, the magnitude of σ_0 increases as sea state increases. Near vertical incidence, there is little dependence on wind or wave direction.

The region of grazing angles between 10 and 60° is often called the plateau region as there is only a mild angle dependence. With an elevated radar, the power density on the surface is proportional to the sine of the grazing angle. Many years ago a term γ was introduced as

a reflectivity term (for land or sea) that is independent of grazing angle. It is called the *constant* γ *model;* it represents a good fit to much of the data, and is still in use today.

$$\sigma_0 = \gamma \sin \Psi$$

It is a valid approximation for angle ranges $3° < \Psi < 60°$ but is sometimes used beyond that. There is an extensive set of experiments at X- and K_a band by Masuko [464] with comparison to a considerable data base from the remote sensing world.

At the low angles, Barton [39] and others suggest that the sin Ψ relationship is valid to the critical angle $\Psi_c = \lambda/4\pi\sigma_h$ where σ_h is the rms surface deviation from the average height. Below Ψ_c the propagation factor plays a dominant role, but the numerous theories do not fit the data well as ducting and shadowing play a major role for very low grazing angles.

7.4 Polarization and Wind-Direction Effects on Reflectivity

The polarization of the electromagnetic wave of the radar has a complex and not well understood effect on reflectivity. In a perhaps oversimplified description, the reflecting parts of the wave structure react differently to horizontally and vertically polarized signals. For low to moderate grazing angles and lower sea states, the echo from vertically polarized radars is heavily dependent on the gravity wave, while the echoes from horizontally polarized radars are more dependent on the smaller (<1.7 cm) capillary waves. The signals on each polarization are to a certain extent independent. It will be shown in later sections that the Doppler shift is higher for horizontal polarization. In addition, if the pulse length in distance units is less than or comparable to the distance between ocean waves (especially when looking upwind or downwind) the amplitude and spatial distributions depend on polarization. It has been shown that there is a degree of clustering of the echoes on the polarization sphere (see Chap. 5). With a dual polarized radar this may lead to better discrimination of specific targets, but it is not clear that it is operationally significant in general target-detection radars.

For typical moderate- to long-pulse radars Tables 7.2 through 7.8 show that the *mean* reflectivity is somewhat higher on vertical than on horizontal polarizations. This is even more clear when looking at results of specific experimenters such as Daley [157, 158, 159] and Long [444] plus many papers in the remote-sensing world. Note that the ratio of vertically polarized echoes, denoted σ^0_{VV}, to horizontally polar-

ized ones denoted σ^0_{HH} appear to be highest in the range of 0.3 to 30°, and for lower carrier frequencies.

The early results led to the use of horizontal polarization for aircraft and ship surveillance. This was the appropriate choice until the pulse lengths were shortened (or pulse compression was used), and the adverse statistics of high-resolution, horizontally polarized sea echoes negated the improvement from the smaller resolution cell. The polarization choice is discussed in the section on short-pulse radar.

There were attempts to improve target detection in sea clutter by cross-polarized linear polarizations. The reflectivity is 5 to 15 dB lower for σ^0_{HV} or σ^0_{VH}, where the first subscript refers to the transmit polarization and the second subscript to the receive polarization. One experiment is illustrated in Fig. 7.3. However, most target echoes are also reduced by 5 to 15 dB. Same-sense circular polarization reduces the echo by a few dB relative to vertical polarization [444], but again there does not seem to be a significant effect on system design. Unless there are advances in some form of adaptive polarization, crossed polarization does not appear fruitful for target detection. In remote sensing radars, polarization alternatives can be used to provide a signature of the sea surface.

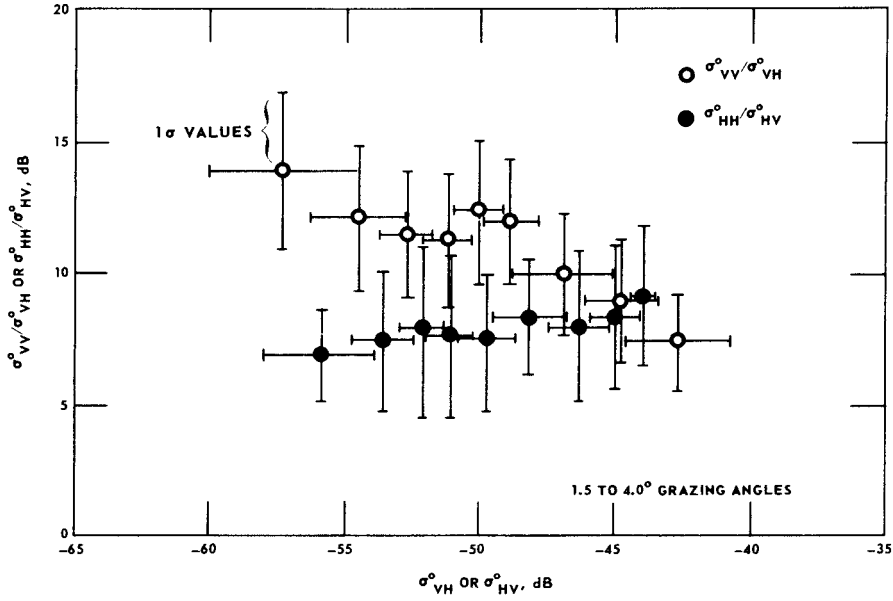

Figure 7.3 A comparison of σ_0 at 6.3 GHz for various polarizations and a wide variety of sea states. (*From Long* [*449*])

Reflectivity versus wind direction

At most grazing angles (except near the vertical), the azimuth angle between the electromagnetic rays and the wind direction or ocean wave propagation direction is significant. At any given time there may be some difference between the instantaneous wind vector and the direction of the average waves. The wave direction is dependent on the wind vector history and other factors. Radar observations in the *upwind* direction generally yield the highest backscatter. Backscatter from the *downwind* direction is somewhat lower and *crosswind* backscatter is the lowest. This can be explained by the angle of the surfaces of a breaking wave in which the reflecting slopes for an upwind look are the most vertical. A typical upwind/crosswind ratio is 6 dB, but higher values are possible [464]. The wind direction effect vanishes for very low grazing angles, diminishes at high sea states, and vanishes near vertical incidence. Some NRL data is shown in Fig. 7.4.

7.5 Spectrum of Sea Clutter Echoes

Relationship between sea clutter bandwidth and sea state for low grazing angles

The Doppler spectrum of sea backscatter is more complex than what was previously believed. One explanation for the frequency spread of signals returned from sea clutter is that the distribution of radial velocities of the scatterers causes a distribution of Doppler frequencies. These scatterers may be either individual wavelets, wind-blown spray and foam at higher sea states, gravity waves and swell, or any combination of these. When the spread of the velocity distribution increases, such as when the surface of the sea becomes more agitated, the clutter spectrum also broadens.

The width of the velocity spectrum σ_v may be related to the width of the Doppler spectrum σ_f by the familiar expression

$$\sigma_v = \frac{\lambda}{2}\sigma_f \tag{7.2}$$

where λ is the transmitted wavelength. Spectrum measurements are expressed in velocity rather than frequency units so that the results of investigations at various frequencies can be compared.

If the scattering mechanism is the same for all wavelengths, then multiplication of the Doppler spread by $\lambda/2$ should make spectrum measurements (expressed in velocity units) at different frequencies independent of frequency. Experimental observations from a number of different investigators are illustrated in Figs. 7.5 and 7.6. The carrier

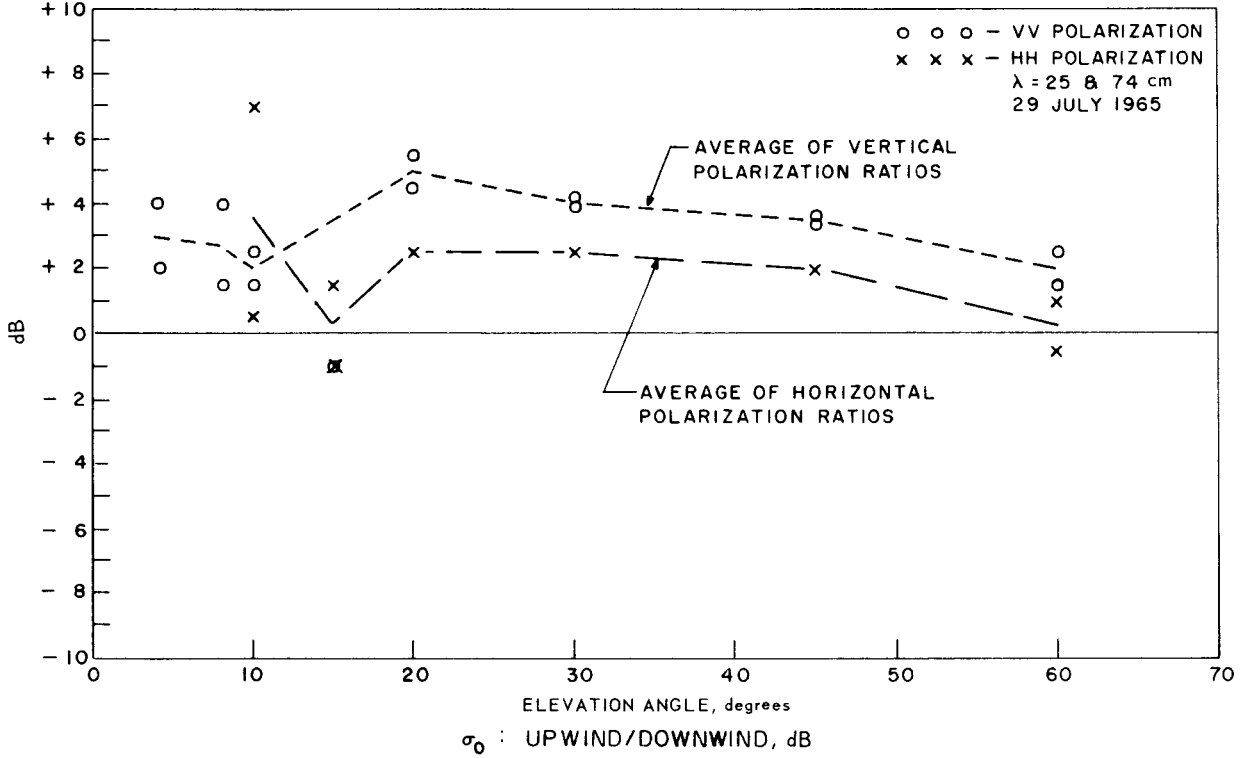

Figure 7.4 Upwind/downwind sea backscatter ratio at P- and L-bands. (*From Daley* [*156*])

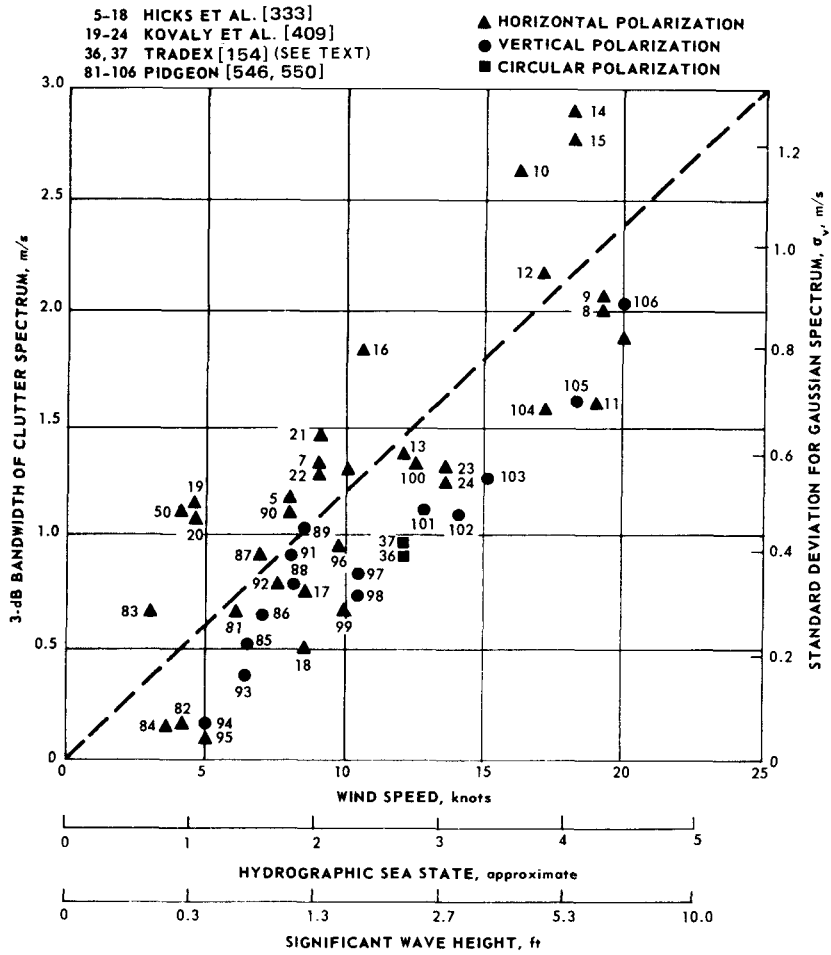

Figure 7.5 Variation of bandwidth for coherently detected sea clutter signals.

frequencies used ranged from 220 MHz to 9.5 GHz. (Most measurements were made at the higher frequencies.) Figure 7.5 presents the data of early experimenters who analyzed the clutter spectrum prior to envelope detection, whereas Fig. 7.6 presents data of those who analyzed the spectrum after envelope detection. These figures show the spectrum half-power width as a function of wind speed. Sea agitation is also shown in terms of hydrographic sea state since this seemed to be a most simple and convenient expression. In some cases the investigators did not specify the wind speed, but gave some other indication such as sea state or wave height. In these cases a value for wind speed was deduced. Newer data were not plotted, but follow the

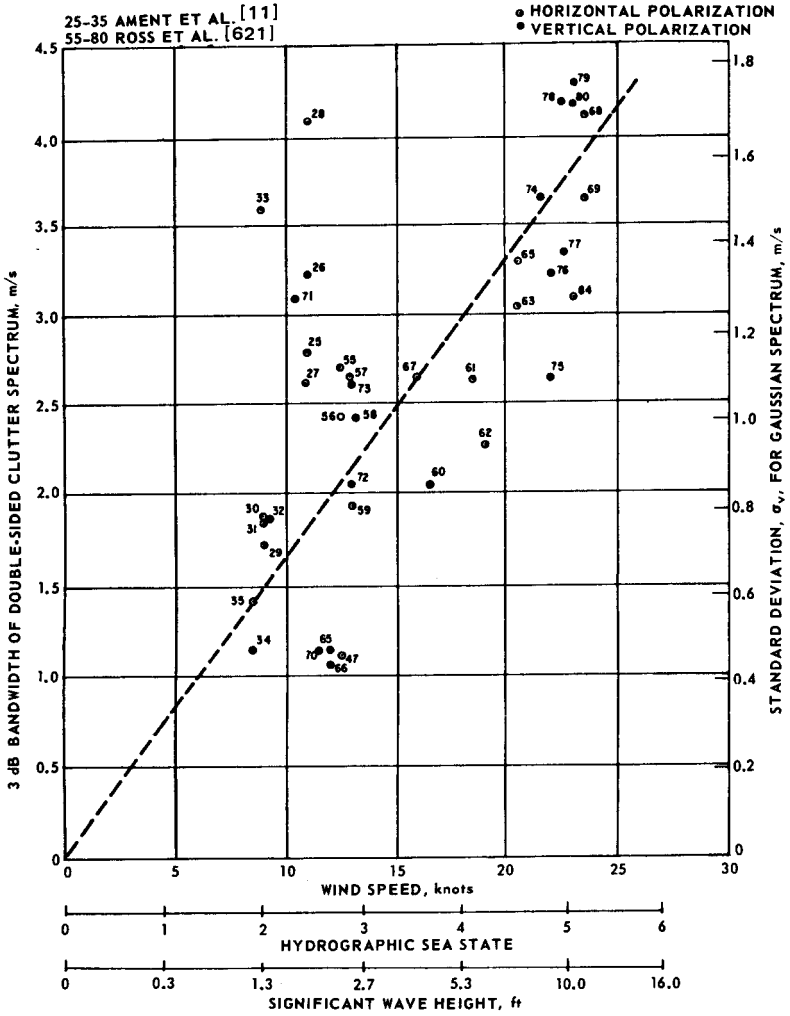

Figure 7.6 Variation of bandwidth for envelope-detected sea clutter signals.

same trend. Since in theory the spectra of coherently detected and envelope-detected signals differ, the two analyses must be treated separately. Tails of the distributions are discussed separately.

For purposes of this section a coherently detected signal may be thought of as one whose spectral properties are examined before envelope detection. The spectrum bandwidth, when predetection analysis is used, is defined as the half-power width of the double-sided spectrum. Figure 7.5 shows an almost linear dependence of bandwidth on wind speed or sea state. Alternately, the spectrum width may be given in

terms of its standard deviation σ_v. For a hypothetical gaussian-shaped spectrum the relationship between the standard deviation and the half-power width ΔV is

$$\begin{aligned} \sigma_v &= 0.42\,\Delta V \text{ in velocity units} \\ \sigma_f &= 0.42\,\Delta f \text{ in frequency units, Hz} \end{aligned} \tag{7.3}$$

In this section, bandwidth Δf for envelope-detected signals is defined as twice the width from the spectrum peak to the half-power point. A plot of postdetection spectrum bandwidth to corresponding values of wind speed is shown in Fig. 7.6. Although the scatter of points is larger than for the coherently detected signals, notice that for a given value of wind speed the envelope-detected bandwidth is larger than the coherently detected bandwidth. If we accept the interpretation that the Doppler spectrum (predetection spectrum) is caused by the random motion of independent scatterers, then the video spectrum (postdetection spectrum) is caused by the velocity difference distribution of the scatterers. Thus, the second central moments of the two spectra can be related; the variance of the video spectrum being twice that of the Doppler spectrum. This result can be arrived at by expressing the video spectrum as the convolution of the Doppler spectrum with itself.* The variances of the two spectrum representations are related by

$$\sigma^2_{\text{video}} = 2\sigma^2_{\text{Doppler}} \tag{7.4}$$

When the Doppler spectrum is gaussian, the video spectrum is also gaussian. Therefore, the half-power width of the video spectrum should also be greater by the factor $\sqrt{2}$. Comparing Figs. 7.5 and 7.6, we see that this relationship is indicated.

The data shown in Fig. 7.5 indicate that σ_v is about 10 percent of the wind velocity and the 3-dB width is about 25 percent of the wind velocity. Henry [330], using a 50-m resolution pulse, reports similar values at X-band (vertical polarization) with two components in the main part of the spectrum and a much smaller third component near the wind speeds of 20 to 24 knots. The crosswind spectrum width is somewhat narrower.

Sittrop [669] uses a somewhat more complex relationship for σ_v versus windspeed at low grazing angles, but the data is in general agreement with Fig. 7.5. Both polarizations were measured. At X-band, the upwind/crosswind ratio of the bandwidth is higher than unity at low winds but lower than unity at winds above about 20 knots. At K_u band there is a negligible ratio.

* This result is for a square-law detection process. See Davenport and Root [163, pp. 251–257].

Sittrop also reports a significant low-frequency spectral component of a few tenths of a hertz at X-band. It amounts to about 25 percent of the total power and is attributed to swell. In addition, the total spectral bandwidth is significantly greater for 0.12-μs pulses relative to 0.5.

Pidgeon [550], Curry [154], Kovaly [409], Hicks [333], and NRL investigators [3] reported small differences in spectral width versus wind direction. These earlier experiments tended to use longer pulses and longer observation times. Attempts to derive differences in upwind, downwind, and crosswind spectral widths proved inconclusive. At this time for general sea clutter modeling for target detection, it seems appropriate to assume that spectral width is independent of wind direction.

As with studies of the effect of wind direction, the measurements of the effect of polarization using longer pulse durations are not conclusive. Early data by Pidgeon [550] plus newer data by Sittrop [669] show small dependencies with vertical or horizontal polarization. Data obtained by Nohara et al. [512] show minor differences for 1-μs pulses, but the tails of the spectrum on horizontal polarization are considerably longer than for vertical. With circular polarization it is shown that the *mean* Doppler is different for H and V polarization, and the spectral width includes both components. Curry's results [154] tend to verify this.

As has been stated, there are multiple components to the sea backscatter, especially at low grazing angle. Even the observation time of the experiment plays a significant role. Figure 7.7 pictorially shows the video and coherent spectrum that can be interpreted in many different ways:

1. A long-term measurement (many seconds) in which the waves are accelerating or decelerating.
2. Three gravity waves at different velocities.

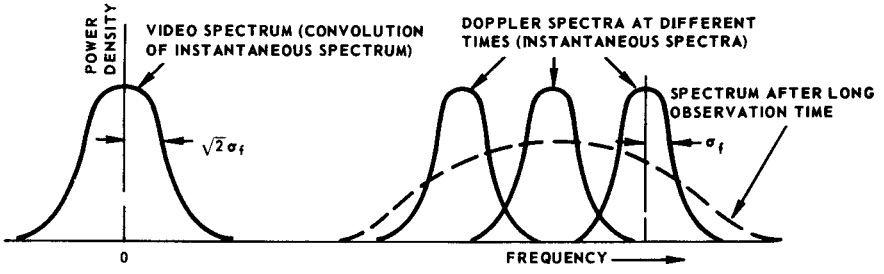

Figure 7.7 Video spectrum and Doppler spectra showing the effects of observation time.

3. A *swell* component, a gravity wave component, a *capillary wave* component, and possibly a wind-driven-*spray* component. The spray may account for the *tail* in the spectrum reported by recent observers at X-band and above.

These may be different with different polarizations. As an example, consider a long-term measurement in which the short-term internal turbulent motion spectral width is σ_f. Since the group is assumed to have slow motion as a body, the instantaneous spectrum slowly shifts the position of its peak value. Measurements made after a period of observation long enough to include these slow variations would have a variance equal to the sum of the variances for the instantaneous spectrum and the slow variation, i.e., the Doppler spectrum has the variance

$$\sigma_{\text{dl}}^2 = \sigma_{\text{di}}^2 + \sigma_g^2 \tag{7.5}$$

where σ_{dl}^2 is the variance of the Doppler spectrum for a long observation time, σ_{di}^2 is the variance of the instantaneous Doppler spectrum, and σ_g^2 is the variance due to the group velocity for the total observation time. The variance of the video spectrum, however, is independent of σ_g^2, i.e., Eq. (7.5) still applies.

$$\sigma_{\text{video}}^2 = 2\sigma_{\text{di}}^2 \tag{7.6}$$

Eqs. (7.5) and (7.6) may be combined to relate the long-term Doppler spectrum and the video spectrum

$$\sigma_{\text{video}} = \sqrt{2}\,(\sigma_{\text{dl}}^2 - \sigma_g^2)^{1/2} \tag{7.7}$$

Mean value of Doppler shift

As implied in the discussion on the spectral width, there are numerous components that go into the mean value of the Doppler shift. Figure 7.8 illustrates that the mean velocity of the scatterers is related to the wind direction by a cosine factor. These measurements were made by Pidgeon with a 5.8-GHz surface radar. Note that there is a slightly lower-peak Doppler shift with the shorter pulse. A summary of Pidgeon's data at other wind speeds is shown in Fig. 7.9. The grazing angles were 0.1 to 10°. Note that the Doppler shift is significantly higher on horizontal polarization. Other data are 10 to 20 percent higher but confirm this trend.

Baker [28] notes the higher Doppler shift in the upwind/downwind direction for a surface X-band radar. He reports about a 3-m/s shift for *H* polarization, and about 2.5 m/s for *V* polarization for sea state 3 to

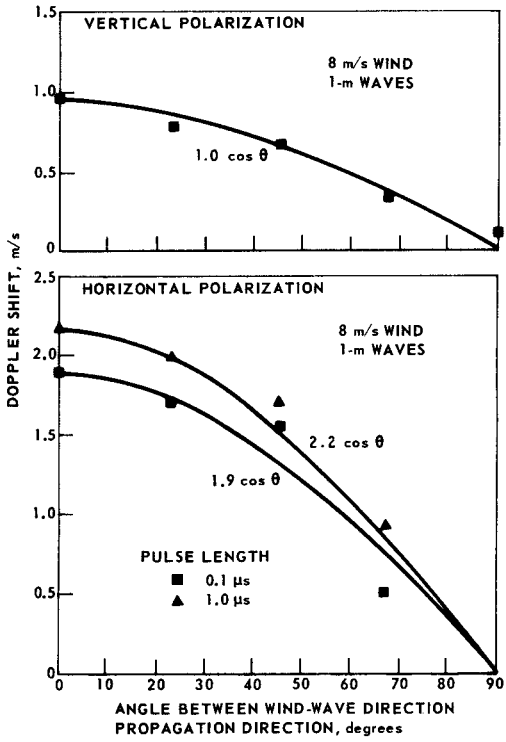

Figure 7.8 Mean Doppler shift of sea echoes at various angles from the wind direction. (*After Pidgeon [550]*)

4, but his waves were riding on an unknown velocity swell. For sea state 1, the average Doppler shift was 1 m/s for H polarization, and 0.7 m/s for V polarization. He used a short, 4.2-m pulse and his spectra are double peaked.

7.6 Spatial and Frequency Correlation of Sea Clutter

The spatial correlation of sea clutter is defined as the cross correlation between the signals returned from two separate patches of the sea in the radial dimension. The time interval separating the measurement of these two signals is assumed to be so small that there is negligible time decorrelation. At 5.7 GHz, Pidgeon [546] noted that the separation necessary to achieve independence was about the distance corresponding to a pulse length. Figure 7.10 illustrates the spatial correlation function versus radial displacement in units of pulse length. Included in Fig. 7.10 are spatial correlation functions replotted from several sources. The pulse length dependence is evident at UHF, S-band, and C-band. Further measurements are required to determine better if the

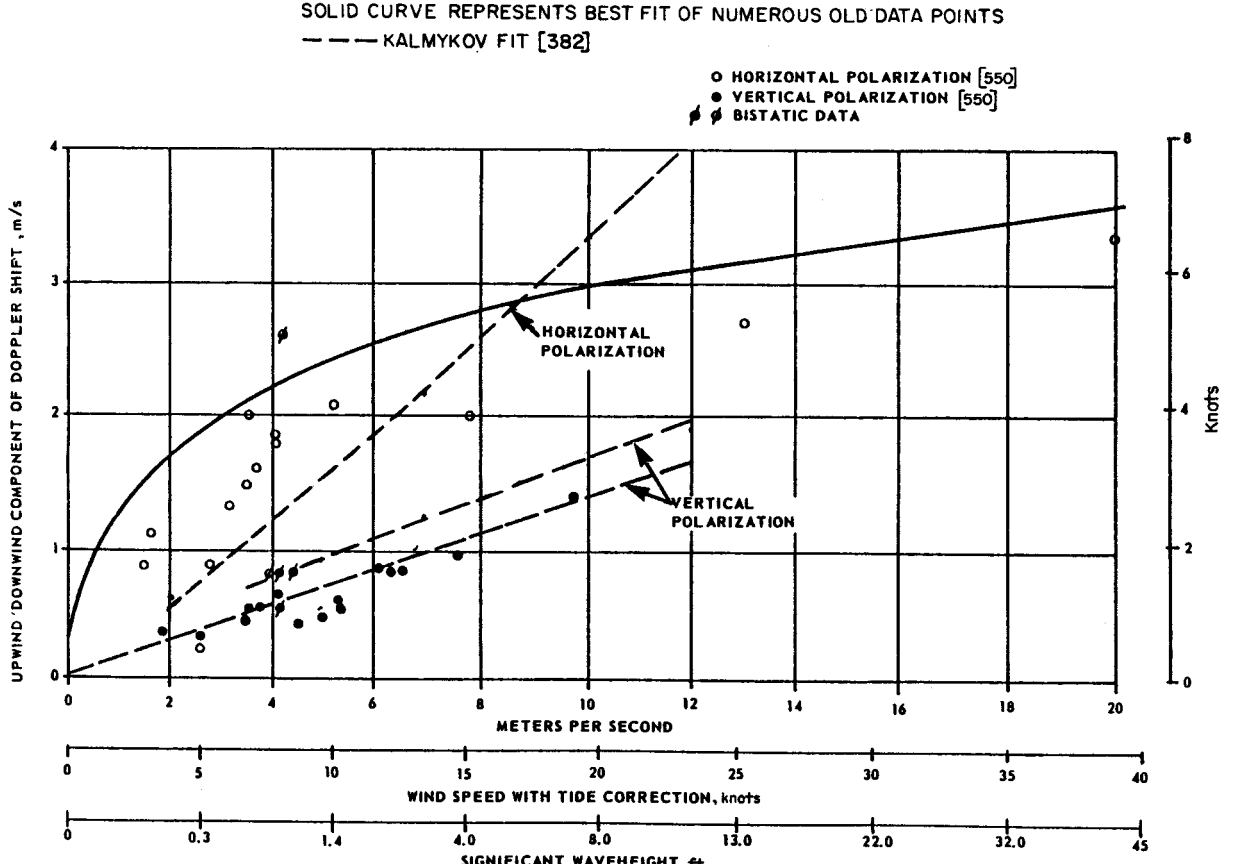

Figure 7.9 Mean Doppler shift for sea clutter. (*From Pidgeon* [550], *Kalmykov* [382], *and older data*)

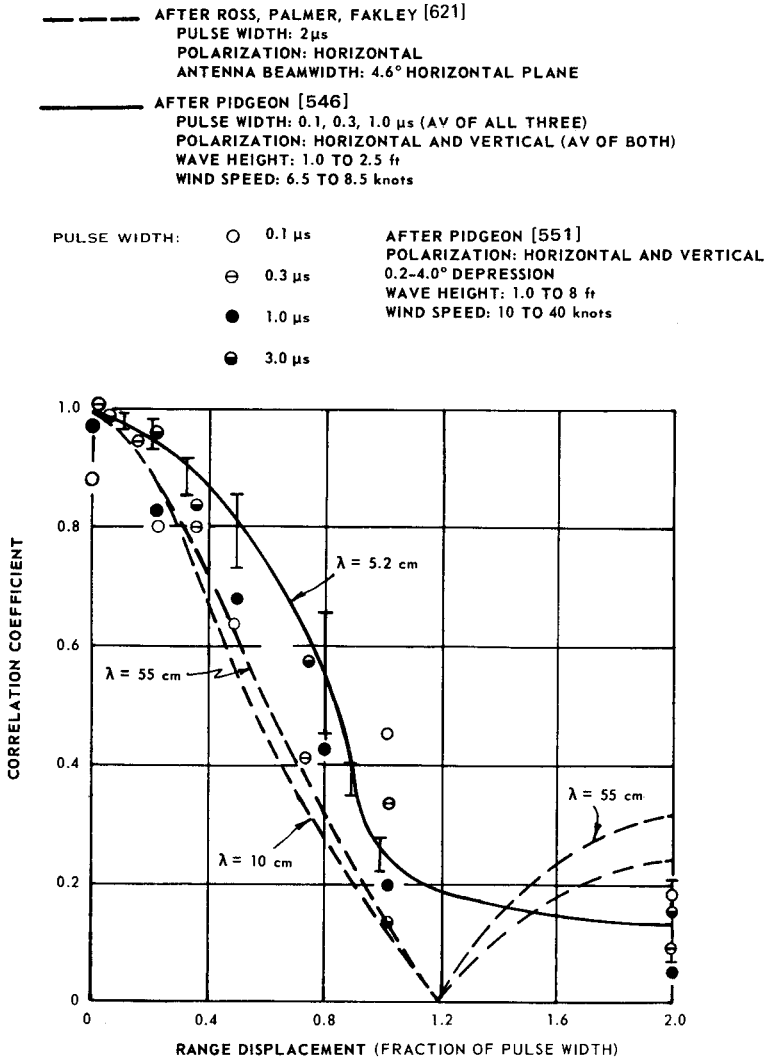

Figure 7.10 Spatial correlation of radar sea return.

returns are partially decorrelated in range for very short pulses (<0.1 μs) and narrow beamwidths, in which case the sea echo is resolved into individual waves (see Sec. 7.7).

In the measurement of the mean backscatter σ_0 from the sea, the number of independent clutter samples determines the accuracy of the estimated mean value of the backscatter. It has been shown in Sec. 7.5 that the sea return from a given cell is correlated for a period of many milliseconds and that to achieve accuracies of about 1 dB in the

estimation of the mean requires measurement times in excess of 1 s for a stationary radar. Airborne radar measurements of clutter acquire the necessary independent samples averaging over space. Carrier frequency is a third *dimension* for averaging clutter returns.

The frequency correlation of clutter is also of great importance for the detection of low-flying aircraft or surface targets by a stationary radar. It is shown in Chap. 3 that incoherent integration can improve the detectability of target returns in the presence of sea clutter if the sea-clutter return is decorrelated from pulse to pulse.

Following the same approach as was described in Sec. 6.6 for precipitation echoes, it has been shown by Goldstein [278], Kerr [397], and Wallace [744] that for a large collection of independent scatterers the correlation coefficient of the intensity of the radar echoes from a rectangular transmit pulse can be expressed as

$$\rho = \left(\frac{\sin \pi\tau\Delta f}{\pi\tau\Delta f} \right)^2 \tag{7.8}$$

where τ = pulse duration
Δf = transmit frequency change
ρ = correlation coefficient

The correlation coefficient falls rapidly to zero at $\tau\Delta f = 1$ and remains near zero for $\tau\Delta f \geq 1$.

The return from the sea for small beamwidths and pulse lengths does not contain as large a number of scatterers as does an extensive rain; however, it would appear to contain a sufficient number to cause partial independence when the frequency separation exceeds the inverse of the pulse length. If the waves are resolved, the correlation function may take other forms, as described by Voles [736].

An experimental program to determine the correlation coefficient of sea returns with frequency was performed by the Defense Research Laboratory of the University of Texas (Pidgeon [551, 546]). The experiments were performed primarily at C-band (5.7 GHz) with both horizontal and vertical polarization and with a 2.5°, two-way beamwidth.

Figure 7.11 is a composite of the correlation coefficient versus $\tau\Delta f$ for the data. The upper curve is for the *infinite* collection of small scatterers. The experimental points for $\tau\Delta f \ll 1$ are less than unity due to the slight time decorrelation for the signals with small frequency separations. The solid-line data represent points taken at about 10° grazing angle, wind speeds of 3 to 9 knots, and wave heights of ½ to 2½ ft (Pidgeon [546]). The correlation coefficients at $\tau\Delta f > 1$ for pulse lengths of 0.1, 0.3, and 1.0 μs are all below 0.2, which indicates that

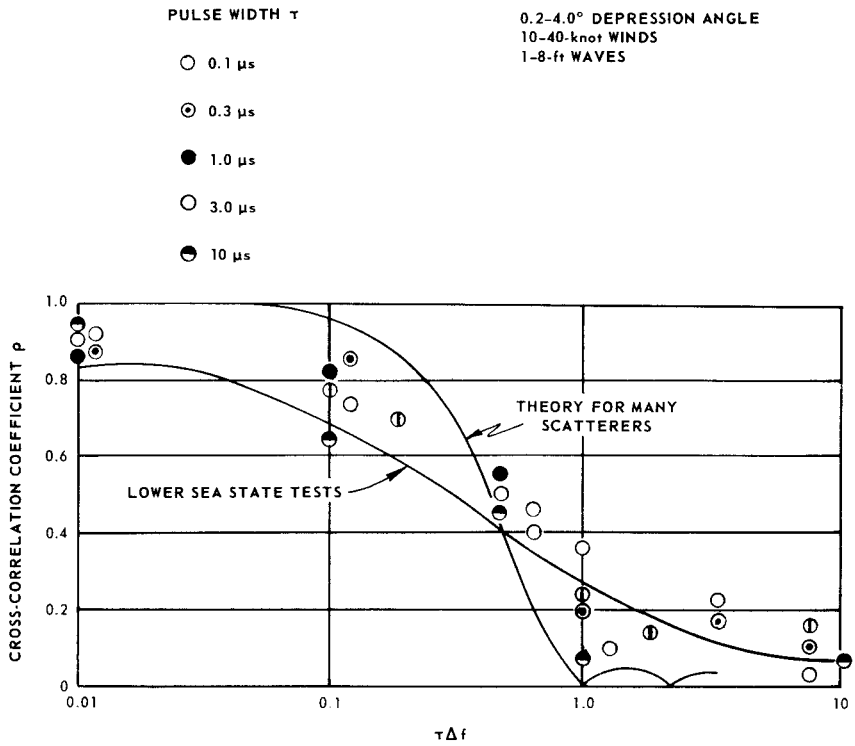

Figure 7.11 Frequency correlation of radar sea return at C-band as a function of pulse length times frequency shift (vertical and horizontal polarizations). (*After Pidgeon* [*546, 551*])

the return is essentially decorrelated. The individual points are from higher sea-state tests. Lind [438] also showed decorrelation results.

Figure 7.12 shows only the data points for the 0.1-μs pulse transmissions at lower sea states; this was done in order to determine whether the *spiky* clutter described in Sec. 7.7 is more correlated with frequency. Although the spread in the computed correlation coefficient is somewhat greater for horizontal polarization, the echoes seem decorrelated at $\tau\Delta f \geq 1$; however, the mean backscatter power that is common to all frequencies for the 5-s computation period was subtracted before the correlation coefficient was computed.* Thus an echo from an individual wave that persists for the entire measurement period would be taken out of the data, and sea-clutter spikes are often correlated for 5 to 10 s. As in any attempt to describe the correlation

* The correlation process describes only deviations from the echo in the region of interest.

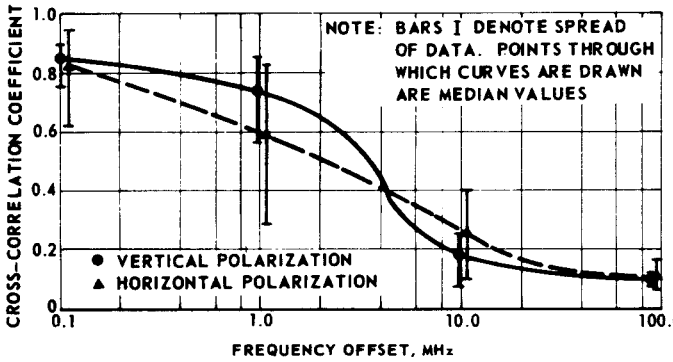

Figure 7.12 Frequency correlation of radar sea return (pulse length = 0.1 μs, C-band).

properties of a nonstationary process, care must be taken to ensure that the measurement is applicable to the type of radar processor that is under consideration. Typical reported data show 6- to 8-dB improvement with frequency agility and postdetection integration.

7.7 Short-Pulse Sea Clutter Echoes or Spikes

It is well known that the amplitude statistics of sea and land clutter deviate from the Rayleigh distribution for short pulses, narrow beamwidths, and low grazing angles. The tails of the distribution extend further from the mean value than would be expected from a *large* number of random scatterers. It is not difficult to visualize the resolution of ocean waves, since the individual waves often have a spatial period of over 200 ft ($\tau = 0.4$ μs). This is important in high-resolution or high-pulse compression ratio radar systems where a threshold detector is set at some arbitrary value above the mean value of the receiver noise or clutter. Numerous descriptions of spiky clutter have been reported, especially for horizontal polarization sea return. Partly because of the difficulty of recording sea clutter echoes from short-pulse radars, it is difficult to confirm a specific power distribution function for short sea clutter echoes. The early measurements with an 8-ns, X-band, 0.9° beamwidth radar reported by Conlon [135] and Myers [496] of NRL suggest a log-normal distribution. This distribution, which was introduced for certain targets (satellites, birds, etc.), appears as a gaussian distribution when σ_0 *in decibels* is plotted on probability paper. The ratio of the standard deviation to the mean value of σ_0 is one parameter of interest since it is equal to unity for the Rayleigh distribution. Conlon's data show that value to be between 1.5 and 2.1 for

short-pulse, vertically polarized sea backscatter at ranges of 450 to 2500 yards from a surface radar. The horizontally polarized echoes had a standard deviation-to-mean ratio of from 6.0 to in excess of 14.0 under the same conditions. In some data runs the echo that occurred 2 percent of the time exceeded the median echo by 20 dB. For vertical polarization this value was only 8 to 10 dB; and for a Rayleigh distribution, 7 dB would be expected. The more highly skewed distributions occurred at about sea state 2.

Measurements made by Pidgeon [551] with a C-band surface radar cover the range of pulse lengths between 0.03 and 10.0 μs with a horizontal beamwidth of about 3°. A-scope returns from the shorter pulse transmissions are shown in Fig. 7.13. The echoes were quite spiky with the effect being more pronounced with the 30-ns pulses.

An attempt to determine the change in distribution with pulse length is shown as Fig. 7.14. Since the complete distributions from Pidgeon's data are not available, only the ratio of the standard deviation to the mean is shown. An estimate of this parameter is also shown from the NRL data. This parameter is unity for a Rayleigh distribution. Pidgeon's tests were at C-band with a 2.5° beamwidth, and the NRL tests were at X-band with a 0.9° beamwidth. The lines drawn through the average values are merely to indicate the trend toward a highly skewed

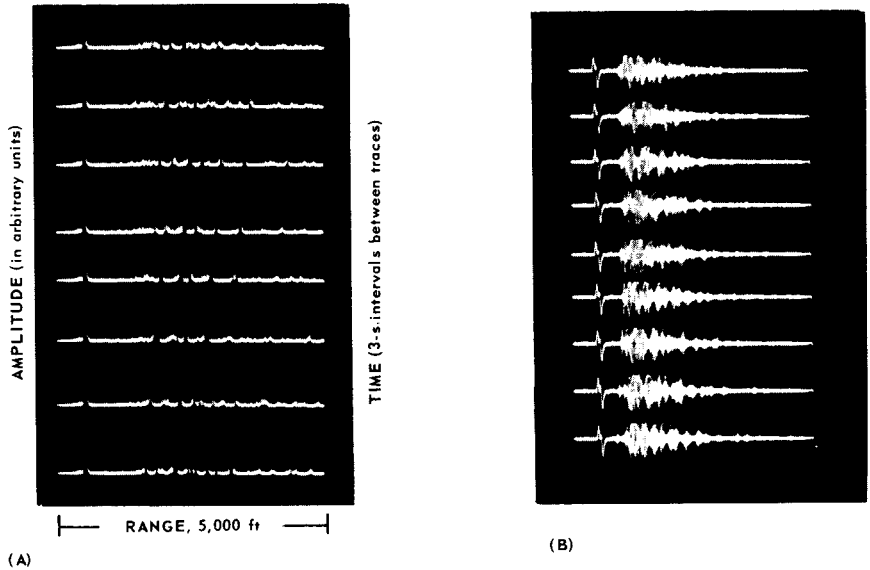

Figure 7.13 A scope returns from sea clutter at C-band (sea state = 5, trace length = 5000 ft, about 3 s between traces). (A) 30-ns pulse-detected video; (B) 100-ns pulse-bipolar video.

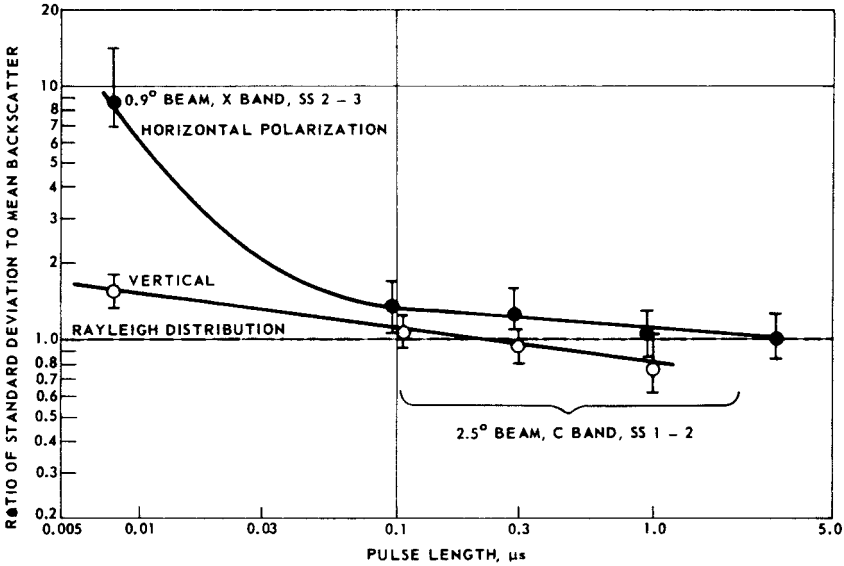

Figure 7.14 Distribution of short-pulse sea backscatter σ_0, standard-deviation-to-mean ratio.

distribution at short pulse lengths, especially with horizontal polarization.

In recent years many experiments to refine the sea spike distribution have been reported [708], [610], [751], [28], [330], [447], and [141]. There is not a clear pattern at this time except that for radars looking for small aircraft, missiles, and ships above the sea at low grazing angles (< 6 to $10°$) there will be major problems due to sea spikes. The degree of the problem depends on the wind speed, radar pulse width, polarization, and to a lesser extent the carrier frequency. A useful pictorial from Hansen and Cavaleri [308] is shown in Fig. 7.15. The surface radar was at X-band and they observed a sea state 3. The abscissa is time and the ordinate is RCS in m^2. The upper four traces are for vertical polarization. The spiky nature of the sea backscatter is obvious. Note that with a 10-to-1 reduction in pulse width there is less average clutter, but the peaks do not drop significantly from 10 m^2. The lower four traces are for horizontal polarization. It can be visualized that the average RCS is lower for H than for V, but that the spikes, while fewer in number, are comparable in RCS. Thus while the product of σ_0 and the cell area drops with reduced pulse duration, the RCS of the spikes drops considerably less.

To determine the false alarm performance, it must be determined how far the threshold must be raised above the mean to achieve a given P_f. The data of Bishop [68, 69] with a surface radar for 270- and 70-

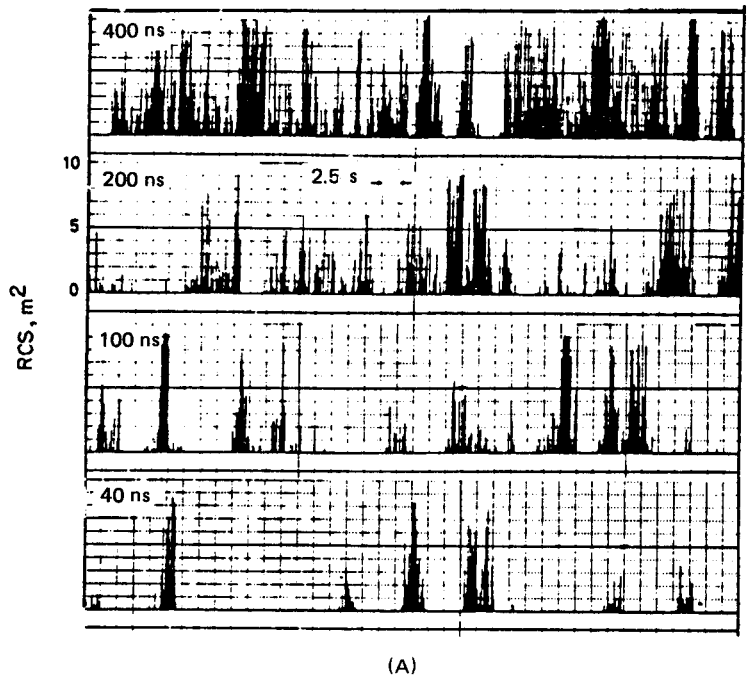

Figure 7.15 Pulse-to-pulse amplitude of scatter for sea state 3, with pulse widths from 400 to 40 ns (scales: 1 m^2 per division and 2.5 s per major division). (A) Vertical polarization; (B) horizonal polarization. (*From Hansen and Cavaleri* [*308*])

μs pulses provide information to $P_f = 10^{-5}$. At X-band for vertical polarization and 270-μs pulses the threshold must be 11 to 21 dB above the mean for vertical polarization and 17 to 22 dB above the mean for horizontal polarization. For 70-ns pulses the thresholds must be 12 to 18 dB for V and 21 to 22 dB for H. Compare these to the threshold values for receiver noise (~11 dB) given in Chap. 3.

Ryan [629] presents data for an X-band airborne radar observing sea clutter at grazing angles of 0.3 to 2.0°. One set of data provides information at P_f of 10^{-3} and 10^{-4} for 200-ns and 30-ns pulses at horizontal polarization. For the 200-ns pulse upwind the threshold is 10 dB at 2°, 14 dB at 1°, 13 dB at 0.5°, and 12 dB at 0.3°. For the 30-ns pulse the threshold was 20 dB at 2°, 10 dB at 1°, and 20 dB at 0.5°. In contrast with the Hansen and Cavaleri data, there were many spikes of over 20 dBsm.

A number of empirical models for the statistical distribution of sea clutter have been considered at various times besides the "classical" Rayleigh power, including the Weibull, the log-normal, and the K-distributions. Each of these models represents an attempt to describe the often non-Rayleigh appearance of sea echo. Much of the confusion concerning models stems from a failure to distinguish between a *temporal distribution* applying to series of measurements at a single resolution cell, and a *spatial distribution* applying to samples from spatially distinct cells. The temporal distribution is often reasonably described as a Rayleigh power distribution if the cell contains even a few discrete scatterers. Even a single sea spike exhibits a fluctuating echo, despite the appearance of a single physical entity that endures some several seconds. However, if the short-term mean power in a resolution cell is sampled from one cell to another, the distribution of the means will itself be a statistical variable. This leads to the concept of a *compound distribution,* in which the mean of a Rayleigh distribution is itself a random variable. This arises from the fact that the sea is not truly homogeneous, especially at low grazing angles, but rather has reflectivity related to wave and swell patterns, wind patterns, shadowing from wave structures, and statistical variations of wave structure. The degree of heterogeneity depends on the size of the illuminated area, among other factors.

A model that is mathematically convenient is the Weibull distribution; its density function $p(x)$ and cumulative distribution $P(x)$ are given by the following two equations

$$p(x) = \frac{\ln 2}{ax} = \left(\frac{x}{x_m}\right)^{1/a} \exp\left[-\ln 2 \left(\frac{x}{x_m}\right)^{1/a}\right] \tag{7.9}$$

$$P(x) = 1 - \exp\left[-\ln 2 \left(\frac{x}{x_m}\right)^{1/a}\right] \tag{7.10}$$

where x_m is the median value of reflectivity, and a is a slope parameter affecting the skewness of the distribution. The mean and median of a Weibull distribution are related by

$$\frac{\bar{x}}{x_m} = \frac{\Gamma(1 + a)}{(\ln 2)^a} \tag{7.11}$$

where $\bar{x}$ is the wide-area mean reflectivity across a large number of resolution cells (i.e., the parameter σ_0 that has been treated elsewhere in this chapter), and Γ is the gamma function. As the a-parameter increases above unity, the distribution becomes increasingly skewed, and increasingly narrow as a is less than unity. With $a = 0$, a single-valued delta function is obtained. When $a = 1$, Eq. (7.9) is identical to the Rayleigh power form; with $a = \frac{1}{2}$, the Rayleigh voltage form is obtained. Sometimes the Weibull slope parameter is given in reciprocal form as $c = 1/a$. The existence of two conventions is often a source of confusion. The Weibull distribution is plotted in Sec. 7.13.

7.8 Sea Clutter under Ducting Conditions*

Despite attempts to account for the relevant parameters in empirical models (for example, [583, 669, 670, 346]), calculated predictions of clutter power can deviate significantly from measurements and among various models. A significant source of variability may be traced to the atmospheric conditions that affect low-altitude radar propagation. The present discussion considers two models: one has been developed at the Georgia Institute of Technology [346] ("GIT" model); a second draws from the reflectivity data tabulated in this chapter, data from Barton [43], as well as features of the GIT model ["HYB" (hybrid) model]. A mathematical description of the GIT model is given at the end of this section; the HYB model is described in Ref. [583].

Differences among various models are most apparent at grazing angles ψ below a few degrees. At small angles, reflectivity in the GIT model varies approximately as ψ; the relationship is closer to ψ^2 in the HYB model, as well as that of Sittrop [669, 670]. A small grazing angle dependence of ψ^4 is predicted from theoretical interference effects, a discussion of which may be found in references [583, 444, 532]. Some measurements conforming to a ψ^4 law have been reported [392]. On the other hand, a ψ^2 dependence is evident in various empirical models, including the HYB model. One hypothesis is that the measured data used to adjust empirical parameters in the GIT model were collected during standard, nonducting propagation conditions [583]. Measurements used in the HYB model are thought to reflect a more diverse

* Portions of this section have been adapted from [583].

set of conditions, including ducting. Considering the prevalence of ducting conditions in ocean propagation (see Sec. 1.10), this hypothesis appears reasonable.

The small-angle behavior in the foregoing discussion is expected below a transitional angle that is proportional to the ratio λ/h_e, where λ is the radar wavelength, and h_e is the equivalent scattering height of the sea waves [444, 346, 680]. When average backscatter is plotted against range, one expects that beyond a *transitional range,* clutter ought to fall off as R^{-7} or R^{-5} for grazing angle relationships of ψ^4 or ψ^2, respectively. For ranges less than the transitional value, one expects an R^{-3} dependency, assuming that $\sigma_0 \sim \psi^{-1}$ for angles above a few degrees.

The clutter power range laws in the foregoing description are expected to occur in nonducting propagation conditions, such as the standard $\frac{4}{3}$ earth atmosphere. However, significant deviations from these ideal range laws are often observed in experimental data. For example, range law exponents as low as -4 have been observed in the region where -7 is expected under the standard atmosphere assumption [195]. Although clutter measurements have historically had many uncertainties with respect to the measurement conditions, the presence of ducting or near-ducting (super refraction) conditions is the probable cause of high clutter levels at longer ranges. Indeed, certain clutter reflectivity data presented by Dyer [195], applying to a period when ducting was present, can be fitted to the grazing angle relationship $\psi^{1.4}$. Measurements from the same area, but made later in the day when ducting was absent, provided a grazing angle fit of about $\psi^{3.8}$.

At this point, it is useful to differentiate between the geometrical grazing angle that a straight line from the antenna makes with the surface tangent at a given range, and the angle that the incident energy makes with the same surface tangent at that range. The former angle can be calculated from geometry and is the angle used in the grazing angle relationships already mentioned. The latter definition, however, is the one that should be used to drive empirical models of reflectivity. In standard atmosphere-type conditions, the two definitions agree when an adjustment is made to the earth radius used in the geometrical calculations. In more complicated refractive conditions, the direction of propagation at the surface is substantially modified and cannot be determined from geometry alone. An example of this phenomenon has been demonstrated for evaporation ducts in Fig. 1.10. Thus, without independent knowledge of the propagation characteristics, one cannot deduce a grazing angle law from clutter power measurements based on the apparent range law.

Due to the sensitivity of clutter reflectivity to ψ, it is desirable to account for distortions of the grazing angle in some way. It is also reasonable to expect that sea returns will respond to the propagation

factor applicable to near-surface altitudes. Accordingly, a method that incorporates both grazing angle and propagation factor effects is desirable. One method is to assume that the GIT reflectivity calculations apply to a standard atmosphere condition [583], to remove the $\frac{4}{3}$ earth propagation factor from the reflectivity values, and to substitute the propagation factor for the specific propagation condition of interest. This result is an adjusted reflectivity σ_{op}:

$$\sigma_0'(\psi) = \frac{\sigma_0(\psi)}{F_s^4(\psi)} \tag{7.12}$$

$$\sigma_{op}(\psi_p) = \sigma_0'(\psi_p)\, F_p^4(\psi_p). \tag{7.13}$$

where $\sigma_0(\psi)$ is the reflectivity determined from the GIT model evaluated at the grazing angle ψ, and $F_s^4(\psi)$ is the propagation factor for the $\frac{4}{3}$ earth model, evaluated at a range corresponding to the grazing angle ψ. In Eq. (7.13), $F_p^4(\psi_p)$ is the propagation factor for ducted propagation, evaluated at a range where the grazing angle is ψ_p; the latter can be determined by optical ray-trace data, such as shown in Fig. 1.10. Beyond the limiting range, we assume that the grazing angle is equal to the asymptotic values noted at the limiting range. $\sigma_{op}(\psi_p)$ accounts for variations in both the grazing angle and the propagation factor. There are a number of methods for determining the propagation factor. The method used here is based on the *electromagnetic parabolic equation* (EMPE) model, which provides a complete solution of a parabolic approximation to the Helmholtz wave equation [184, 405].

The propagation factor is customarily evaluated at a specific height above the sea surface. An equivalent height for clutter is approximately $0.6h_a$, where h_a is the average wave height [680, 444]. The reflectivity calculation indicated by Eqs. (7.12) and (7.13) involves the ratio F_p^4/F_s^4, which causes the resulting answer to be relatively insensitive to the precise height that is assumed for the clutter. The calculation method indicated in the foregoing has been referred to as the *reflectivity and propagation* (REPROP) method.

Figures 7.16 and 7.17 illustrate reflectivity values that are generated by using the REPROP method. The antenna height is assumed to be 23 m, and the polarization is vertical. Each figure includes separate plots for average wave heights of $h_a = 0.25$, 1.25, and 2.5 m. The figures also list approximate sea states S. The results of the HYB model (upper curve), and the unmodified GIT model (lower curves labeled $h_d = 0$) are included for comparison.

Received clutter power

The rate of falloff of clutter power may be conveniently examined by calculating a normalized power (P_{cn})

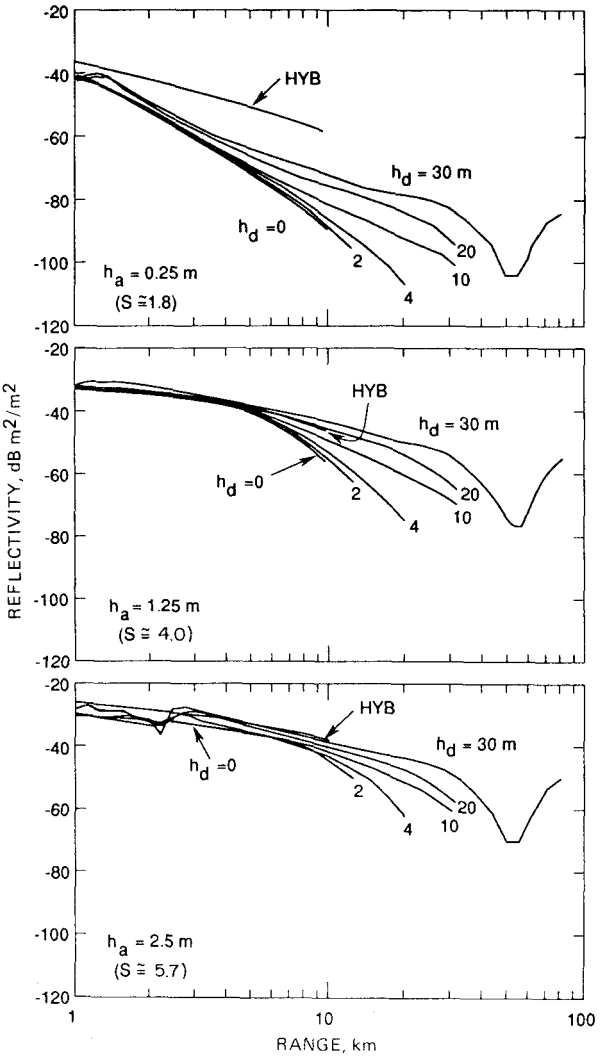

Figure 7.16 Reflectivity at 9 GHz calculated by reflectivity and propagation method. (*From Reilly and Dockery, 1990 [583]*)

$$P_{cn} = P_c/P_c(\text{ref}) \tag{7.14}$$

where P_c is the absolute clutter power, and $P_c(\text{ref})$ is that determined under some reference set of conditions. The normalization by $P_c(\text{ref})$ makes P_{cn} independent of radar specific variables (such as transmit power and antenna gain). For the comparisons presented in this section, the reference condition is defined as the received clutter power in a $\frac{4}{3}$ earth atmosphere, and at a range of 10 km.

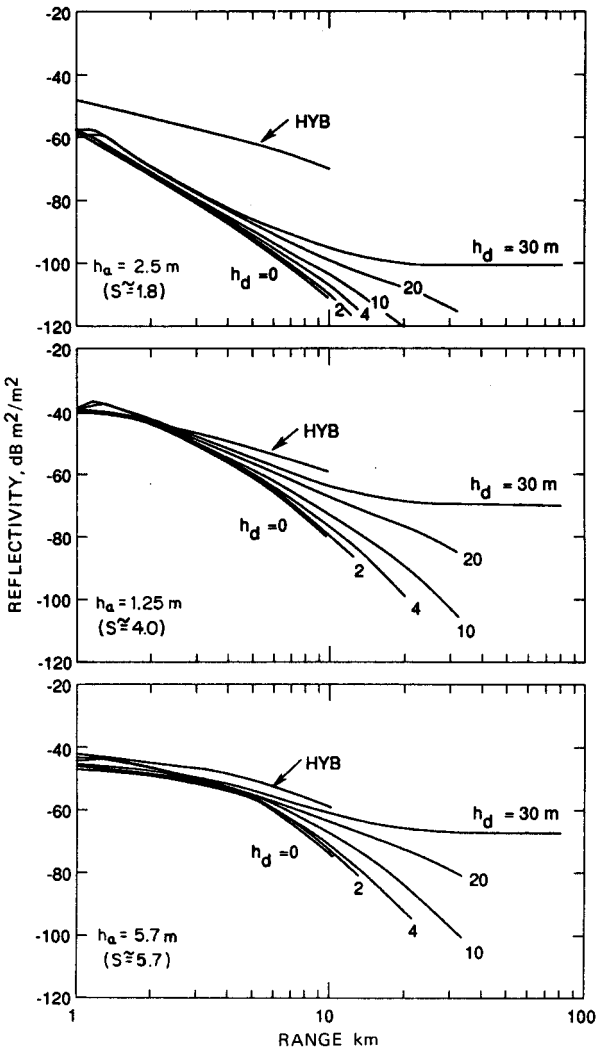

Figure 7.17 Reflectivity at 3 GHz calculated by reflectivity and propagation method. (*From Reilly and Dockery, 1990 [583]*)

The ratio given by Eq. (7.14) may be expressed alternatively as:

$$P_{cn}(R) = \frac{\sigma_{op}(R,\psi_d)}{\sigma_{op}(\text{ref})\, R^3/R_{\text{ref}}^3} \tag{7.15}$$

where $\sigma_{op}(R,\psi_d)$ = the REPROP reflectivity determined at range R.
$\sigma_{op}(\text{ref})$ = the same variable corresponding to the reference condition (4/3 earth and R = 10 km).
R_{ref} = the reference range (10 km).

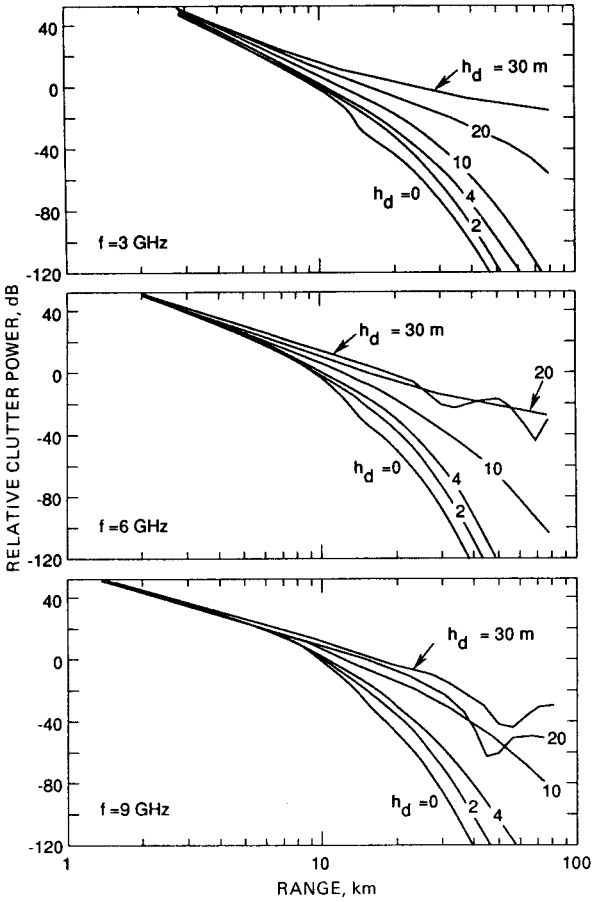

Figure 7.18 Relative clutter power calculated by reflectivity and propagation method (h_a = 1.25 [S = 4.0]). (*From Reilly and Dockery, 1990* [*583*])

Figure 7.18 illustrates the range dependence of P_{cn} for the REPROP method at frequencies of 3, 6, and 9 GHz. Individual curves are shown for the $\frac{4}{3}$ earth atmosphere and for duct heights of 2, 4, 10, 20, and 30 m. The oscillations that are seen at the higher frequencies and duct heights are due to multimode interference effects which arise because the larger ducts support more than one waveguide mode. The depths of the nulls are not accurately represented due to the relatively coarse range steps used in the calculations (20 steps per decade, equally spaced on a logarithmic scale). Calculations using the REPROP model have been compared with experimental S-band data [183]. The refractive conditions during these tests varied substantially with range, but the model performed quite well.

GIT reflectivity model

The following equations express the sea reflectivity model developed by the Georgia Institute of Technology [346]. Except for changes in notation, the equations are as given in the cited reference. The model is expected to be applicable during standard atmosphere propagation conditions.

A. Frequency range = 1 to 10 GHz

Reflectivity equations

$$\sigma_0(H) = 10 \log (3.9 \times 10^{-6} \lambda \psi^{0.4} G_a G_u G_w)$$

$$\sigma_0(V) = \begin{cases} \sigma_0(H) - 1.05 \ln (h_a + 0.015) + 1.09 \ln (\lambda) \\ \qquad + 1.27 \ln (\psi + 0.0001) + 9.70 & \text{(3 to 10 GHz)} \\ \\ \sigma_0(H) - 1.73 \ln (h_a + 0.015) + 3.76 \ln (\lambda) \\ \qquad + 2.46 \ln (\psi + 0.0001) + 22.2 & \text{(below 3 GHz)} \end{cases}$$

where $\sigma_0(H)$ and $\sigma_0(V)$ are the reflectivities evaluated at H and V polarizations, respectively.

Adjustment factors

$$G_a = \frac{a^4}{1 + a^4}$$

$$G_u = \exp [0.2 \cos \phi (1 - 2.8\psi)(\lambda + 0.015)^{-0.4}]$$

$$G_w = \left[\frac{1.94 V_w}{(1 + V_w/15.4)} \right]^q$$

Definitions for adjustment factors

$$q = \frac{1.1}{(\lambda + 0.015)^{0.4}}$$

$$a = \frac{(14.4 \lambda + 5.5) \psi h_a}{\lambda}$$

B. Frequency range = 10 to 100 GHz

Reflectivity equations

$$\sigma_0(H) = 10 \log (5.78 \times 10^{-6} \psi^{0.547} G_a G_u G_w)$$

$$\sigma_0(V) = \sigma_0(H) - 1.38 \ln (h_a) + 3.43 \ln (\lambda) + 1.31 \ln (\psi) + 18.55$$

Adjustment factors

$$G_a = \frac{a^4}{1 + a^4}$$

$$G_u = \exp\left[0.25 \cos\phi\,(1 - 2.8\psi)\,\lambda^{-0.33}\right]$$

$$G_w = \left[\frac{1.94\,V_w}{(1 + V_w/15.4)}\right]^q$$

Definitions for adjustment factors

$$q = 1.93\,\lambda^{-0.04}$$

$$a = \frac{(14.4\,\lambda + 5.5)\,\psi\,h_a}{\lambda}$$

C. *Units and symbols*

$\sigma_0(H)$, $\sigma_0(V)$ = reflectivity for H and V polarization, dB · m^2/m^2

h_a = average wave height, m ($h_a \cong 4.52 \times 10^{-3}\,V_w^{2.5}$)

λ = radar wavelength, m

ψ = grazing angle, rad

V_w = wind velocity, m/s

ϕ = look direction relative to wind direction, rad

7.9 Short-Range Clutter*

In a low-prf system (range unambiguous), reflections from ranges beyond that of the target add to the total received. The relative amount of clutter power returned from distant ranges depends critically on the propagation conditions. Commonly encountered evaporation ducts, for instance, enhance clutter returns from ranges well beyond the "standard atmosphere" horizon [583].

In a high-prf system (Doppler unambiguous), the interpulse period may be shorter than the round-trip delay to the maximum required target-detection range, and clutter returned from ranges shorter than that of the target may fold onto the target's reflection. Any pulse repetition interval shorter than the round-trip delay to the target is subject to short-range clutter interference. In such cases, antenna beam shape effects can have a major influence on the degree of clutter interference, and propagation effects are less important.

The effects of antenna design on short-range surface clutter have been analyzed in [584]. Some highlights of that study are mentioned here. In accordance with practice in many modern systems, the horizon

* Portions of this section have been adapted from [584].

search function is assumed to be separate from a volume search function. A single row of horizon search beams has been assumed.

Received surface clutter is given by an integral along a constant range contour (Fig. 7.19). The amount of clutter power from a given clutter element varies with the corresponding antenna coordinates in accordance with

$$P_c \propto \int f_t^2(\alpha,\theta) f_r^2(\alpha,\theta) \sigma_0 \, d\theta \tag{7.16}$$

where P_c = received clutter power
α and θ = azimuth and elevation angles with respect to antenna boresight
f_t^2 and f_r^2 = antenna power pattern factors (transmit and receive), defined such that $f_t^2(0) = f_r^2(0) = 1$
σ_0 = clutter reflectivity

For homogeneous surface clutter, σ_0 is assumed to be constant over the equal-range contour, so that factor may be factored out of the integral sign. In that case it is convenient to describe an integrated antenna pattern as:

$$f(\alpha) = \int_{-\pi/2}^{\pi/2} f_t^2(\alpha,\theta) f_r^2(\alpha,\theta) \, d\theta \tag{7.17}$$

where it is assumed that the backlobes of the antenna pattern may be ignored. Equation (7.17) defines an effective antenna pattern for the integrated clutter along an equal-range contour corresponding to a depression angle α. This function replaces a conventional antenna pat-

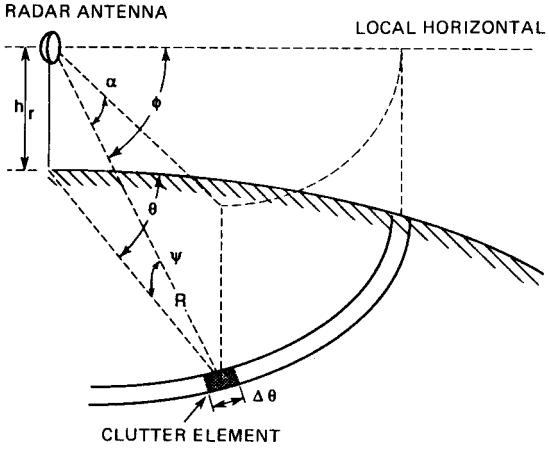

Figure 7.19 Geometric relationships for surface clutter.

tern factor requiring two angular variables, α and θ. Equation (7.17) may be expressed in normalized form as:

$$f_n(\alpha) = \frac{f(\alpha)}{f(0)} \tag{7.18}$$

By definition, $f_n(0) = 1$. Clutter power follows the relationship

$$P_c \propto \sigma_0 f_n(\alpha) \tag{7.19}$$

This expression is convenient for clutter calculations inasmuch as only one angular variate is needed for the antenna pattern.

The clutter received from a particular range depends on the three-dimensional antenna pattern. Clearly, we can reduce sidelobes at the expense of widening the main beam by using appropriate illumination tapering functions. However, the optimum strategy for aperture illumination is not immediately apparent. Short-range clutter performance was investigated for various illumination strategies. Other assumptions made with respect to radar parameters are: (1) single-row horizon search pattern, (2) constant horizon search time, (3) constant P_d for a horizon target, and (4) coherent integration within a beam. It is necessary to adjust the transmitted power in order to satisfy these assumptions when varying the antenna illumination function or "upspot" angle. The term *upspot* refers to the deviation from a horizontal elevation used in the horizon search process.

A number of antenna functions were considered in this study, as outlined in Table 7.9. The cases represented in the table involve variations in the aperture illumination; the aperture size was held constant such that $d/\lambda = 39.3$. The symbol "U" refers to uniform illumination; the symbol "T" refers to a Taylor-weighted pattern, with the designated sidelobe (SL) level. Mathematical expressions for the antenna patterns are given by Milligan [475]. The values listed under ATL refer to the amplitude taper loss as tabulated by Milligan; b_2 is the 6-dB width of the two-way beam; b_t refers to the 3-dB beamwidth of the transmit pattern (1.5° in this case). The last two columns of Table 7.9 list power factors that indicate the increase in transmitter power needed to maintain the same horizon detectability as a system with uniform antenna illumination on both transmit and receive (case 0). As used here, *detectability* means detection probability as limited by receiver noise. With zero upspot angle, the power factor is given by the decibel sum of the ATL term, and a beamwidth factor 10 log $b_2/b_{2,0}$, where $b_{2,0}$ is the two-way beamwidth for case 0. The beamwidth adjustment accounts for the fact that coherent integration gain is inversely related to beamwidth. With antenna upspot, the power factor includes the additional loss in *S/N* ratio resulting from the fact that a horizon target is no longer in the peak of the antenna pattern.

TABLE 7.9 Antenna Patterns Used in Analysis: Constant Aperture, Variable Illumination; d/λ = 39.3

Case	Pattern		ATL, dB			b_2(6 dB), °	Power factor*	
	Transmit	Receive	Transmit	Receive	2-Way		u_p = 0°, dB	$u_p = b_t/2$, dB
0	U	U	0	0	0	1.5	0	6.00
1	U	T, SL = 45	0	1.60	1.60	1.65	1.19	6.09
2	T, SL = 25	T, SL = 45	0.28	1.60	1.88	1.71	1.31	5.90
3	T, SL = 35	T, SL = 45	0.86	1.60	2.46	1.81	1.64	5.73
4	T, SL = 45	T, SL = 45	1.60	1.60	3.20	1.90	2.17	5.88

* *Power factor* indicates the relative transmitted power increase needed to maintain the same horizon detectability as case 0 with zero upspot angle.

An implicit assumption used in evaluating the influence of the antenna pattern on the target echo is that the effects of surface multipath do not vary greatly with changes in the antenna pattern and upspot. One condition justifying such an assumption is that the elevation (or depression) angles of direct and surface multipath rays do not differ greatly as compared with the antenna beamwidth. The assumption would also be applicable whenever the surface is sufficiently rough that the forward scatter reflection coefficient is small. With the stated assumption, the change in a horizon target's power would directly follow the antenna pattern along the horizon pointing direction.

Figure 7.20 illustrates relative clutter power as a function of range for each of the antenna illumination functions identified in Table 7.9. The vertical axis in Fig. 7.20 gives the decibel equivalent of a normalized *C/N* ratio:

$$\frac{C}{N} = kp_n(\alpha)\sigma_0 P R^{-3} \tag{7.20}$$

where k includes the various terms in the radar range equation; P = power adjustment for constant horizon detectability as previously discussed; and P = decibel value indicated by the two final columns in Table 7.9. The plots shown in Fig. 7.20 use $k = 10^3$ and R is in kilometers. The upper part of Fig. 7.20 applies to an antenna pointing angle aligned along the local horizontal; the lower part of the figure applies to an elevation-pointing angle (upspot) of 0.75°, which, in this example, is equal to the 3-dB beamwidth of the uniformly illuminated one-way pattern. The maximum clutter power without upspot occurs at a range between 1 and 2 km. In a range-ambiguous search system, the clutter peak would represent the limitation on the achievable signal-to-clutter ratio. Consequently, variations in radar operating parameters leading to a reduction of the clutter peak would translate into corresponding signal-to-clutter gains. This statement is generally true, almost without regard to the range at which the clutter peak occurs.

As a general rule, the clutter peak with 0° upspot increases as we proceed from case 0 to case 4. With upspot added, the clutter peak is reduced significantly. Under case 0, the maximum clutter peak with upspot occurs at about 0.8 km, and is associated with the first sidelobe of the transmit pattern. With the upspot condition, case 1 has the minimum clutter peak among the five cases examined here. The case 1 antenna pattern is preferable from several points of view: it has the lowest clutter peak with upspot; it has sidelobes that are far superior to case 0; and it has the most narrow two-way beamwidth next to case 0.

Figure 7.21 displays the effects of upspot angle on the *S/C* ratio (upper

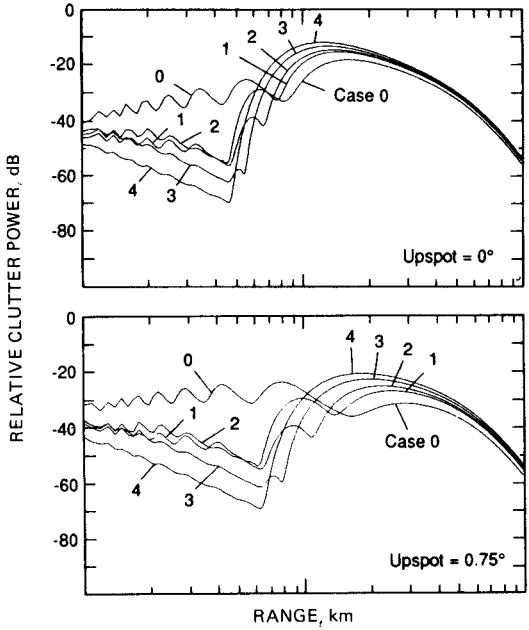

Figure 7.20 Normalized sea clutter power in horizon search for various illuminations (X band, $D/\lambda = 39.3$). Power adjustment maintains equal horizon detectability across cases. (*From Reilly,* [*584*])

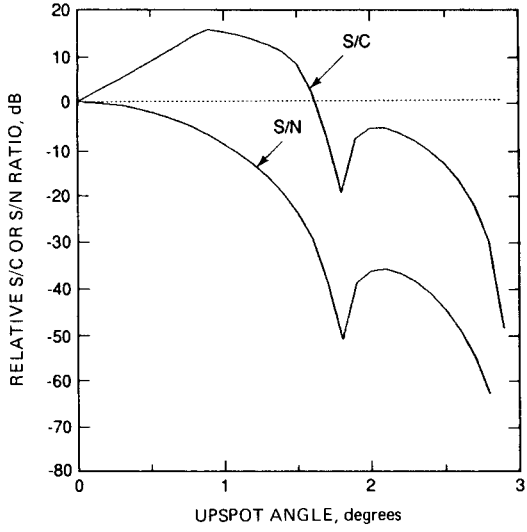

Figure 7.21 Variation of S/C and S/N ratios with upspot angle in horizon search for aperture illumination case 1. Clutter is defined by its maximum value with respect to range. (*From Reilly* [*584*])

curve) and the *S/N* ratio (lower curve) for the case 1 illumination function. It is assumed here that the target is situated on the horizon at the peak of the antenna beam, such that the *S/N* ratio versus upspot is defined by the antenna beam pattern. The clutter power is assumed to correspond to the peak of the profile displayed in the case 1 curves of Fig. 7.20. The upper curve shows that the *S/C* ratio continues to increase with upspot to a maximum angle of 0.9°. At that point, the *S/C* ratio curve abruptly ceases to increase because the point of maximum clutter power shifts from the mainlobe to the first sidelobe. That effect can be understood by referring to Fig. 7.20. Under the upspot condition of 0.75°, the peak clutter occurs from mainlobe returns at a range of about 2.5 km; the clutter at a range of 1 km due to the first sidelobe of the transmit pattern is slightly below that from the main beam. With a slight additional increase in upspot angle ($> 0.9°$), the mainlobe clutter falls below that from the first side, and the range of maximum clutter shifts abruptly from 2.5 to 1 km.

Figure 7.21 shows that the increase in *S/C* ratio with upspot angle occurs at a much faster rate than the loss of *S/N* ratio. If one is willing to accept a modest loss in *S/N* ratio, a correspondingly larger benefit in *S/C* ratio can be gained. For example, at an upspot angle of 0.6°, the *S/N* ratio loss is 3 dB, but the *S/C* gain is 10.4 dB. In order to recover the *S/N* ratio loss, it would be necessary to increase transmitter power by 3 dB, all other things being equal.

7.10 Backscatter from Various Terrain Types

The next sections describe the characteristics of surface clutter. In the detection of small, low-altitude aircraft, missiles, and surface targets, radar backscatter from various land and cultural features creates a more severe problem than does the backscatter from the seas. This is because land and cultural features generally have a higher reflectivity at low grazing angles than does the sea surface. This effect is mitigated somewhat in the case of airborne targets, since the Doppler shift and spectrum width of land returns are small compared with those due to aircraft velocities. MTI techniques on stationary or slowly moving radars can have high clutter rejection ratios for most land objects (Chap. 9). The discussion in the next sections applies primarily to monostatic target-detection radars.

It is difficult to give an adequate statistical distribution of the backscatter characteristics of land for the following reasons:

1. The statistical nature of the return from a given area cannot be related to the type of land as easily as the relatively convenient use

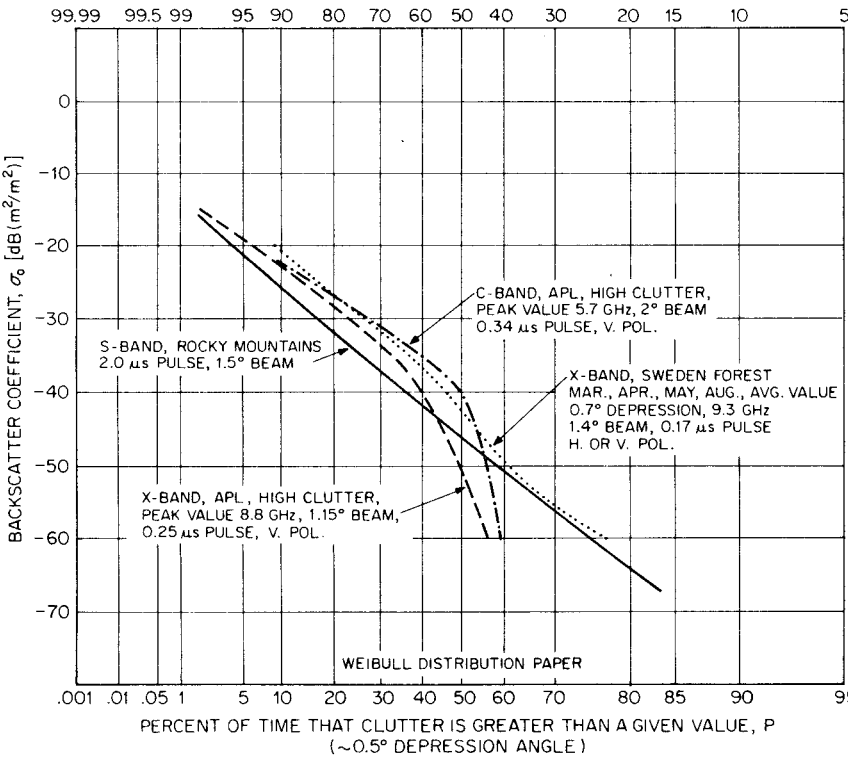

Figure 7.22 Land clutter backscatter distributions from surface radars.

of sea state descriptions. (Note that even the sea-state description at any time is highly subjective.)

2. The land backscatter amplitude distribution at low grazing angles does not usually conform to the Rayleigh distribution because of the *shadowing* from hills, buildings, trees, etc. Even land that is considered flat will roll by a degree or two.
3. The moisture content of the soil, or snow cover, can alter the backscatter coefficient.
4. The derivation of a mean (σ_0) or median value (σ_m) differs between land and airborne measurements. The fixed radar sites essentially perform a time average of a given clutter cell while an airborne measurement performs a spatial average.

Figure 7.22 gives several cumulative distribution functions of σ_0 from land-based radars.* Two of the radars were operated at the Applied

* The pattern factor effects are included in σ_0.

Physics Laboratory in Maryland for the detection of low-flying aircraft. Both of the profiles shown are for an azimuth angle where the clutter return extended for several miles. The terrain consisted of rolling countryside with patches of 30-ft-high trees and a number of small houses. The approximate peak values of the time fluctuation were plotted rather than the temporal average. The third distribution is from a Swedish forest area [232] with a radar of similar parameters to the X-band radar at APL. While the maximum values of σ_0 for these two areas are similar, the median values of the backscatter coefficient for the two APL radars differ by about 11 dB for the same terrain. This is undoubtedly due to the shadowing effect, which almost completely obscures close to 50 percent of the terrain. The median values from these two experiments would seem to indicate a strong frequency dependence, but that is not generally the case. The Swedish data in Fig. 7.22 from Linell [441] do not have as marked a shadowing effect as do the APL data, probably because the radar used by Linell was located atop a 100-ft waterworks tower. The APL radars are approximately 50 ft above the local terrain. A fourth cumulative distribution is shown for a mountainous area.

The low-angle backscatter measurements reported by about 50 investigators are crudely summarized in Tables 7.10 through 7.14. Various general classifications of terrain are arranged on the chart in order of increasing backscatter coefficient at low depression angles. The values of σ_0 for each frequency are the average of horizontal and vertical polarizations unless otherwise stated. The values for σ_0 are approximate since some experimenters reported distributions from which σ_0 had to be approximated. The results can be considered seasonal averages since the return from vegetation and forests varies by more than 9 dB, depending on the amount of foliage [232]. This same reference shows that the terrain backscatter was about 6 dB lower than the lowest seasonal average when there was a 4-in snow cover at depression angles of about 1°.

The term S in Tables 7.10 through 7.14 is an initial attempt to define the statistics of the backscatter coefficient for a pulse radar, where S is the dB difference between the median and the 84th percentile value of the cumulative distribution. Its significance is explained later. While not included in these tables, σ_m refers to the median value and σ_{84} refers to the value of the backscatter coefficient that is *not* exceeded in 84 percent of the range cells. The difference between these values S has been found to be as high as 20 dB. The use of the mean rather than the median may be mathematically less satisfying, but in observing experimental data the medians vary so dramatically depending on the siting, pulse duration masking, etc., that it is not clear how to average and construct a model. The median is less than noise in many data sets. The mean values are much better behaved. Thus, this model

TABLE 7.10 Radar Land Reflectivity σ_0, Grazing Angle = 0 to 1.5°*

When there is a value for σ_0 | S, a non-Rayleigh distribution is indicated:

	Carrier frequency											
	L-band 1–2		S 2–4		C 4–8		X 8–12		K_u 12–18		K_a band 31–36	
	σ_0	S	σ_0	S	σ_0	S	σ_0	S	σ_0	S	σ_0	S
Desert—relatively flat	45†		46†		40†		40†	8				
Farmland—rural	36†	10	34†	10	33†	8	33	13	23†	13	18†	
Heavy woods, jungle, rolling terrain	28†	8	28†	13†	27†	13†	26	13		13	21†	
Urban	25†	10†	23†		21†		20†	>13				

* σ_0 in dB below 1 m^2/m^2, S in dB from 50th to 84th percentile.
† 5-dB error not unlikely.

TABLE 7.11 Radar Land Reflectivity σ_0, Grazing Angle = 3°*

Non-Rayleigh Distribution:
σ_0 | S

	Carrier frequency											
	L-band 1–2		S 2–4		C 4–8		X 8–12		K_u 12–18		K_a band 31–36	
	σ_0	S	σ_0	S	σ_0	S	σ_0	S	σ_0	S	σ_0	S
Desert—relatively flat	43†		38†		35†		32†		30			
Farmland—rural	32†		31†		30		28	8	25†	8	18	
Heavy woods, jungle, rolling terrain	24†		25†		25		24†	8	24†	8	19	
Urban	20†		19†		19†		18		12†			

* σ_0 in dB below 1 m^2/m^2, S in dB from 50th to 84th percentile.
† 5-dB error not unlikely.

TABLE 7.12 Radar Land Reflectivity σ_0, Grazing Angle = 10°*

	Carrier frequency					
	L-band 1–2	S 2–4	C 4–8	X 8–12	K_u 12–18	K_a band 31–36
	σ_0 | S	σ_0 | S	σ_0 | S	σ_0 | S	σ_0 | S	σ_0 | S
Desert—relatively flat	38†	36†	33†	30	28	25†
Farmland—rural	30†	28†	26†	26	22	18†
Heavy woods, jungle, rolling terrain	26†	24†	23†	23	20	19†
Urban	18†	18†	18†	16†		

* σ_0 in dB below 1 m^2/m^2, S in dB from 50th to 84th percentile.
† 5-dB error not unlikely.

TABLE 7.13 Radar Land Reflectivity σ_0, Grazing Angle = 30°*

	Carrier frequency					
	L-band 1–2	S 2–4	C 4–8	X 8–12	K_u 12–18	K_a band 31–36
	σ_0 | S	σ_0 | S	σ_0 | S	σ_0 | S	σ_0 | S	σ_0 | S
Desert—relatively flat	28	25	23	21	19	18
Farmland—rural	20†	18	16	16	16	15
Heavy woods, jungle, rolling terrain	18	16	16	14†	14†	12†
Urban	15†	13†	11	10		

* σ_0 in dB below 1 m^2/m^2, S in dB from 50th to 84th percentile.
† 5-dB error not unlikely.

TABLE 7.14 Radar Land Reflectivity σ_0, Grazing Angle = 60°*

	Carrier frequency					
	L-band 1–2	S 2–4	C 4–8	X 8–12	K_u 12–18	K_a band 31–36
	σ_0 | S	σ_0 | S	σ_0 | S	σ_0 | S	σ_0 | S	σ_0 | S
Desert—relatively flat	21†	17	16	14†	13†	13†
Farmland—rural	15	16	15	14	13	13
Heavy woods, jungle, rolling terrain	19†	15†	15	14	12	11
Urban	12†	11†	10†	10†		

* σ_0 in dB below 1 m^2/m^2, S in dB from 50th to 84th percentile.
† 5-dB error not unlikely.

better represents those areas where there is less masking and hence there is a land-clutter problem, especially for radars observing low grazing angles. If there is no value for S, the data appear to fit a Rayleigh distribution. In Secs. 7.7 and 7.13 there are equations and graphs for Weibull and log-normal distributions.

In a surface pulse radar with narrow beams and short pulse lengths (<1 μs), the value of $\sigma_m + S$ should be used for low false-alarm probability ($<10^{-2}$) systems; but, depending on the false-alarm criteria, $\sigma_m + 2S$ or $\sigma_m + 3S$ may be more appropriate.* As the depression angle of the radar increases, the shadowing effect diminishes and the backscatter conforms more closely to the Rayleigh distribution (see Sec. 7.7). When there is a vertical bar in a box it means that the distribution deviates considerably from the Rayleigh assumption. The following statements are tentative, but their general trends are indicative of low depression angles and homogeneous terrain:

1. The mean backscatter coefficient increases somewhat with frequency for most terrain types but usually not faster than linear with transmit frequency. The frequency effect on return from urban areas is quite small.
2. The mean backscatter coefficient increases about linearly with grazing angles from 1 to 10°. In some cases a reduced value is found at 3 to 5°.
3. There are polarization differences on individual measurements, but there is not a strong general effect. The tables represent an average.
4. In cultivated areas, soil moisture and snow cover have a strong effect.
5. As the pulse duration decreases from 1 μs, σ_m decreases and S increases, especially at low grazing angles. The mean value, σ_0, changes very little.

In general the data base is good up to K_a band for surface radars ($\psi < 2°$) and airborne radars ($\psi > 3°$) for low mountains, farmland, and wooded areas. There is sufficient data at 1.3 to 15 GHz to provide good estimates of cities and deserts. In these cases, the uncertainty in knowing the type of terrain probably exceeds the experimental errors (~3 dB). Data from 0 to 1.5° grazing is combined since it is extremely difficult to know true grazing angles, as almost all terrain rolls a degree or two. An illustration of the general trend versus frequency and angle is shown in Fig. 7.23. The data points in the tables are believed to be more accurate.

The available data at K_a band for deserts, farmland, and some wooded areas that show that reflectivity varies little with frequency for $\psi =$

* σ_m would have to be derived from the graphs in Sec. 7.7 and 7.13.

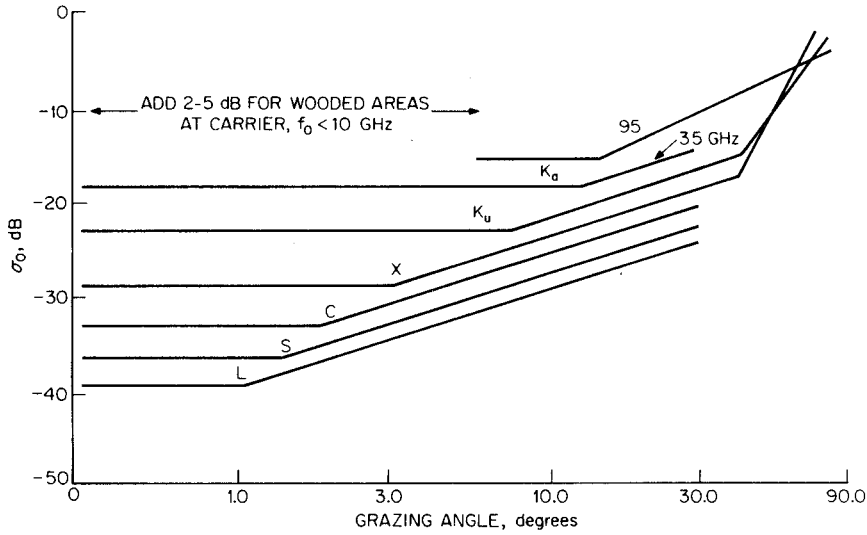

Figure 7.23 Reflectivity values for typical rural land clutter (mean values).

10° and 30°. However, the sparse data at $\psi = 0$ to 3° indicate a significant frequency dependence ($\sigma_0 \approx f^2$) for farms and wooded areas; further experimental data are required to determine this apparent frequency dependency.

Polarization dependencies have been neglected since an obvious trend cannot be found. On the average, the reflectivity on horizontal polarization is a few dB lower for $\psi = 0$ to 3°. This may be due to the preponderance of vertical scatterers (crops, trees, buildings) at these angles. At $\psi = 10°$, the echoes on horizontal polarization seem to exceed vertical by about 2 dB, but this trend disappears at $\psi = 30°$. At this point other system considerations such as target cross sections, tracking, and rain rejection with circular polarization should dominate the choice of polarization.

Surface reflectivity from ice and snow

The values of σ_0 for ice and snow are surprisingly complex. They depend on the liquid water content of the snow, and whether the ice is new or multiyear. Summaries are available in Ulaby [720] Volume III, Onstott [524], Moore et al. [484], and Currie and Brown [153] at millimeter waves. With Arctic ice there is some increase with carrier frequency at mid grazing angles. For ice fields at 10° grazing angles, typical values of σ_0 are -25 to -35 at X-band and increase to -15 to -25 at 30° grazing angle. For millimeter wave radars, at a 10 to 15° grazing angle, σ_0 from snow-covered terrain varies from -10 to -20 dB at 35 or 95

GHz with the higher values for refrozen snow and lower values as liquid water content increases. The values for $\psi = 30°$ are about 5 dB higher and σ_0 is approximately 0 dB for $\psi = 60$ to 90°. Data are included in Currie [153] and Hayes [319].

7.11 Composite Terrain at Low Grazing Angles

The description of land clutter return has been divided into types of terrain having backscatter coefficients that differ by a spread of about 15 dB between cities and cultivated land. If a surface radar is placed near a city a composite terrain return will be obtained. An example of this placement is shown in Fig. 7.24 [176]. The radar used to obtain these data was located near Huntsville, Alabama; the survey was made with an L-band radar using a 3-μs pulse and a 1.8° azimuth beamwidth. The figure was drawn for 241 of the returns from the strongest *cells;* the Huntsville city area gave the group of higher values of σ_0, and the hilly countryside showed another distribution centered around $\sigma_0 = -40$ dB. It appears from the report that over 2000 cells were observed, but that about 90 percent of the cells were masked by the terrain and hence gave negligible return. The median value σ_m cannot be determined, and even the 84-percent value is probably indeterminate. Boothe [83] later fit this type of data to a Weibull distribution. The false alarm probability for a simple search radar, owing to clutter returns at this location, is determined by the relatively few large clutter cells unless a *clutter mapping* system is used to inhibit the returns from the city area. This is discussed in Chap. 14.

The histogram shown is appropriate only for the pulse length and beamwidth used. A decrease in either parameter will yield an even greater percentage of masked cells. The number of cells with substantial returns will increase, and the σ_0 of those cells containing strong reflectors will also increase. On the other hand, the percentage of cells with strong reflectors will decrease as the strong targets are resolved out.

Descriptive data on the increased shadowing effect at low depression angles and the seasonal variations of backscatter are included in the previously cited Swedish experiments [232]. Spatial distributions are available for depression angles of 0.4 to 5.0° (Table 7.15). At any given month, or for the all-season average, the median value of the backscatter coefficient σ_m decreases very rapidly for decreasing depression angles. This is a stronger effect than would normally be expected for *rough* surfaces (especially for the pine and fir forest); however, the variable S increases rapidly with decreasing depression angle. Thus, the clutter power in a given direction is concentrated in the peak signals

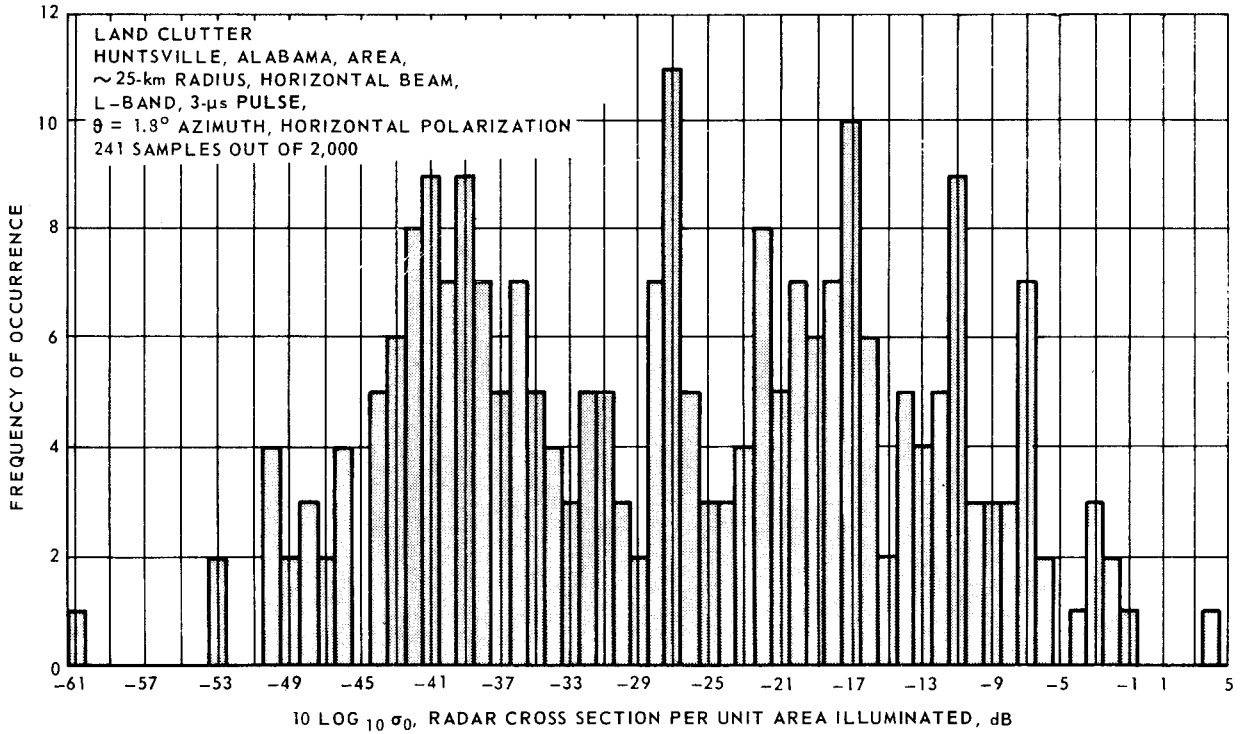

Figure 7.24 Histogram of occurrence of σ_0. (*After Holliday* [*342*])

TABLE 7.15 Summary of Swedish Land-Clutter Experiments*

Depression angle, °	March (snow)		April		May		August		November		Average	
	σ_m	S	σ_m	S	σ_m	S	σ_m	S	σ_m	S	$\bar{\sigma}_m$	$\bar{S}$
Normalized backscatter from cultivated flat land, dB												
5.0	−39	7	−30.2	5	−26.3	4.7	−23	4.6	−26.3	4.7	−26.4	4.8
2.5	−50.5	13	−38.2	10.7	−38.2	7.7	−30	6.5	−32.5	7.5	−35	8.1
1.25	−53.5	16.5	−48	14.2	−46.5	11.8	−38.5	10.5	−41	12.3	−43	13.7
0.4			<-50	>20								
Backscatter from pine and fir forest, dB												
0.7	−43.5	18	43.5	18	−43.5	18	−43.5	18	−36	15	−41.6	17.2
0.5					−49	~18					−49	~18
0.4					−56	~19					−56	~19

* σ_m = median backscatter coefficient, dB; $\bar{\sigma}_m$ = average σ_m, dB, for April to November; $\bar{S}$ = average standard deviation for April to November. Radar parameters: antenna height = 100 ft, wavelength = 3.2 cm, pulse length = 0.17 μs, azimuth beamwidth = 1.4°. Horizontal polarization = vertical polarization.

SOURCE: From Linell [441].

with negligible contribution from the shadowed areas. The use of σ_m and S (in decibels) allows calculation for the total clutter power received by a system if the spatial distribution is log-normal or Weibull. The seasonal variation for the cultivated land backscatter is also interesting. A distinct minimum is shown for the snow cover in March and a peak return for the crops in August.

In a series of tests by the Naval Research Laboratory over various parts of the United States at from 5 to 9° depression angles, S was about 6 dB at 5°, and 5 dB at 9° for either polarization at X-band [97, 149]. The value of σ_m was -21 to -29 dB except near the city of Nashville, where σ_m increased to about -12 dB.

Polarization effects

Polarization dependencies have been neglected in Tables 7.10 to 7.13 since an obvious trend cannot be found. For large terrain areas, the reflectivity on horizontal polarization is a few decibels lower for $\psi = 1$ and 3°. This may be due to the preponderance of vertical scatterers (crops, trees, buildings) at these angles. At $\psi = 10°$, the echoes on horizontal polarization sometimes exceed vertical by about 2 dB, but this trend disappears at $\psi = 30°$. For remote sensing, the differences in polarization are significant for an area with a specific crop or group of trees or state of irrigation or azimuthal angle with respect to rows of crops. For target-detection radar models a clear pattern is not evident. At this point other system considerations such as target cross sections, tracking, and rain rejection (with circular polarization) should dominate the choice of polarization.

There have been a number of efforts to determine if the use of crossed linear polarization (*HV* or *VH*) can aid in detection. There is some evidence that polarization ratios (*VV/VH*, etc.) can be of some assistance in detecting vehicles or aircraft if there are long integration times. However, attempts to use cross polarization are usually negated by the reduction in RCS of aircraft or vehicles by about 10 dB (see Chap. 5). The cross-polarized reflectivity (σ_{VH} or σ_{HV}) of fields, woods, villages is 5 to 15 dB lower than same sense reflectivity (σ_{VV} or σ_{HH}). The use of the full polarization matrix or adaptive polarization shows more promise, but it is too early to draw conclusions [771].

A question often asked about land clutter is how much subclutter visibility or improvement factor is needed to detect a low-flying aircraft. The difficulty of giving a simple answer to this question is illustrated in Fig. 7.25, which shows what is essentially an A-scope trace of a surface radar. Here, however, the ordinate is the integrated amplitude of the clutter echoes from many transmitted pulses. The abscissa is range from the radar. The data were taken in Howard County, Mary-

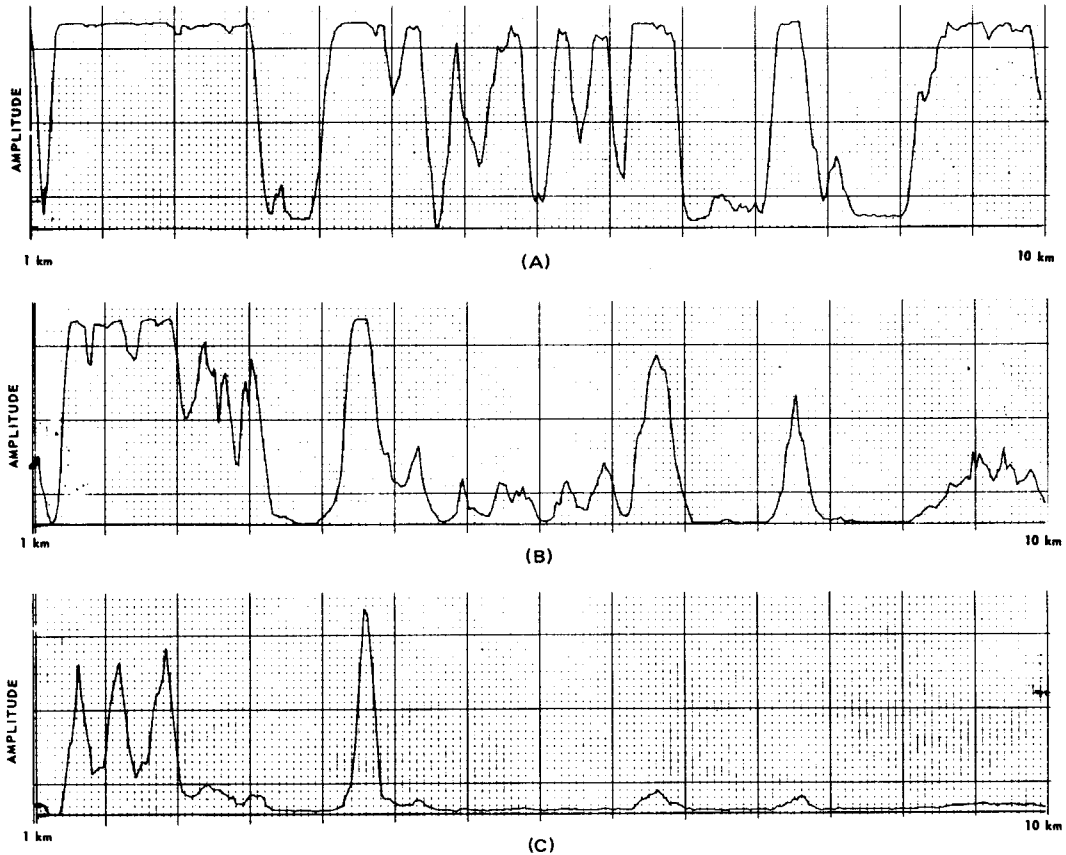

Figure 7.25 Land clutter profiles (0.8-μs pulse, effect of clutter attenuation). (A) 10 − dB attenuation; (B) 30-dB attenuation; (C) 50-dB attenuation.

land with a 1.4°, two-way beamwidth, 10-kW C-band radar with vertical polarization. No STC was used. To obtain the traces, 10, 30, and 50 dB of attenuation were successively inserted ahead of the receiver. This allows determination of the effects of different amounts of clutter attenuation without having to construct a processor that actually discriminates between signal and clutter. In trace *a,* with 10 dB of attenuation, the system was saturated for most of the trace. There is effectively 30 dB of *clutter attenuation* in trace *b* and 50 dB in trace *c*. Thus, even with 30 to 50 dB of *clutter attenuation,* some land echoes are seen on the output display.

A second question of interest is how much is target detection improved if the pulse width is reduced or if pulse compression is used. The upper trace of Fig. 7.26 shows how the land clutter looks if the pulse length is 3.2 μs. The same region as in Fig. 7.25 was observed with 10 dB of attentuation prior to the receiver. It is virtually impossible to detect a target at any time under these conditions. In *b* the pulse length was reduced to 0.8 μs with the same peak power and in *c* the pulse length is 0.2 μs. While the 16-to-1 reduction in the pulse length does not materially reduce the large reflectors, the chance of seeing a target between the high-clutter regions is considerably improved. Although the reflectivity in the location where these traces were taken is high, there is little masking. The cumulative distributions of σ_0 for the three pulse widths in this region are shown in Fig. 7.27. It can be seen on the lower right of the curves that the percentage masking is more pronounced for the shorter pulses and that the strong reflectors (water towers, etc.) give higher peak values of σ_0 with shorter pulses.

It can be concluded that land clutter echoes are rarely uniform in space, nor do they have a Rayleigh distribution, and that the relatively simple range equations for a clutter-limited radar in Chap. 2 must be used with care. A more reasonable detection criterion would be based on the percentage of the area of interest in which a low-flying target can be detected. This is the so-called *intervisibility* criterion.

7.12 Composite Terrain at Mid-Angles

The backscatter from composite terrain at 8 to 70° grazing angles does not have a strong shadowing effect and is less sensitive to polarization and transmit frequency. To a first approximation the angle dependence can be removed by using the parameter γ, which is defined as

$$\gamma = \frac{\sigma_0}{\sin \psi}$$

where ψ is the grazing angle and γ is usually expressed in $dB(m^2/m^2)$. Numerous sources, for example [185], have shown that γ is almost

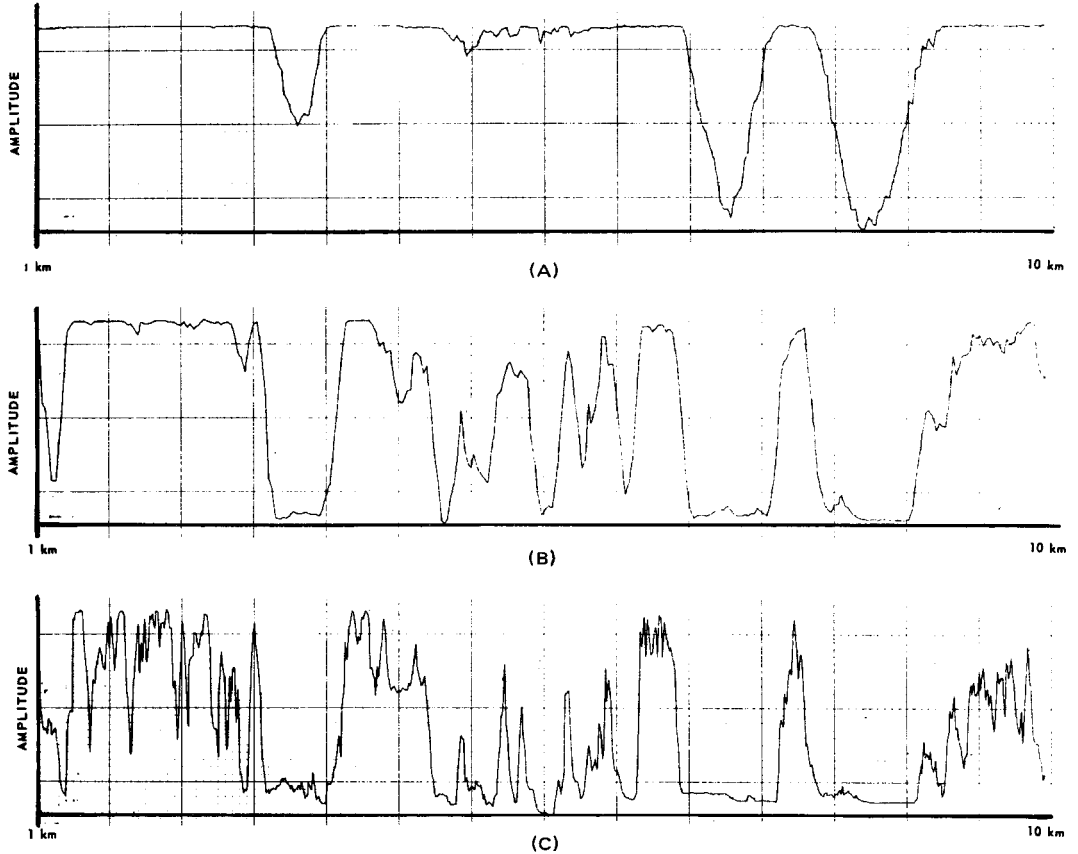

Figure 7.26 Land clutter profiles for heavy clutter area—effect of pulse length. (A) 3.2-μs pulse; (B) 0.8-μs pulse; (C) 0.2-μs pulse.

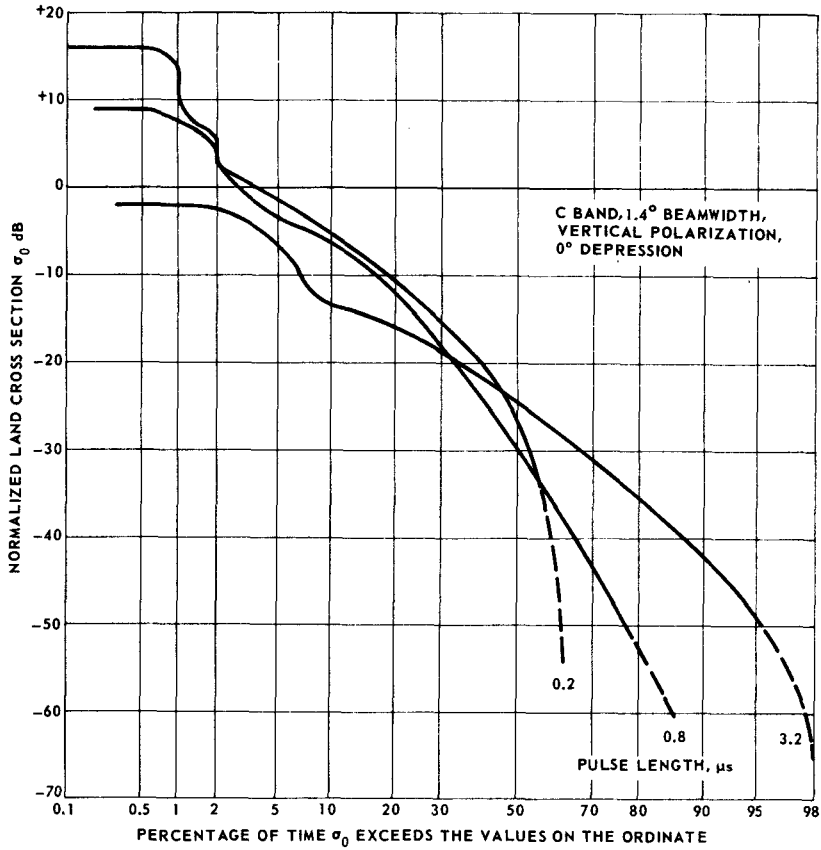

Figure 7.27 Cumulative distribution of land cross section σ_0 for high clutter azimuth.

independent of ψ, neglecting backscatter from essentially smooth surfaces such as deserts and roads. A convenient summary for all frequencies (400 to 35,000 MHz) and all polarizations for grazing angles of 6 to 70° is

$$\gamma_{\max} \approx -3 \text{ dB}$$

$$\gamma_m = \gamma_{\text{median}} \approx -14 \text{ dB}$$

$$\gamma_{\min} \approx -29 \text{ dB}$$

In this oversimplification, $\gamma_{\max}$ is a maximum of various experiments rather than a peak signal in time. Similarly, γ_m and $\gamma_{\min}$ are *averages* of the reported medians and minimum values. The maximum values are dominated by the echoes from urban areas. Above 65° grazing angle

γ_m (and σ_0) increases rapidly to a value of 0 to 15 dB(m^2/m^2) at vertical incidence.

There are numerous reports* on the values of γ and σ_0 for various terrain types and frequencies, but the spread in the reported data precludes as detailed a summary as was given in the case of sea clutter. A heavily averaged (in decibels) chart of γ_m and γ_{max} for several frequencies and gross terrain classifications is given in Table 7.16. It shows that for rough terrain (woods, hills, and cities) there is not an obvious frequency dependence; for roads and desert areas, γ increases slightly less than linearly versus frequency. On the other hand there is a strong dependence on the type of terrain (roughness) especially at the lower microwave frequencies. The value of γ_{max} is an indication of the decibel average of the maximum values reported by each experiment rather than an indication of the maximum expected return.

Barton [39] accepts the overall median of -14 dB, and suggests -5 dB for mountains, -10 dB for wooded hills, -15 dB for farmland and -20 dB for flatland. These values are consistent with the table.

The trend with frequency shown on the table continues to 95 GHz. Currie [152] gives data to indicate a γ of -8 dB at 95 GHz for grass, crops, and deciduous trees. Thus, it is preferable to use some frequency correction for γ rather than a single value. Since the overall averages cited were heavily based on X-band data, there should be a correction factor for general terrain (excluding deserts and cities) on a base frequency $f_0 = 10$ GHz. It is suggested that, when expressed in decibels

$$\gamma = \gamma_{avg} + 5 \log \left(\frac{f}{f_0} \right)$$

For example, $\gamma_{avg} = -14$ dB, then γ is calculated to be -9 dB at 100 GHz and -18.5 dB at 1.3 GHz.

The references indicate no obvious polarization dependence. The spatial probability density functions seem to conform more closely to the Rayleigh law than they do for low grazing angles. The temporal distribution functions result from a combination of a fixed and a fluctuating component, with the ratio depending on the terrain type.

Reflectivity at vertical incidence

As with sea clutter, land reflectivity is highest at vertical incidence and falls off rapidly as the incidence angle departs from 90°. Water areas may be +15 dB; roadways and runways may be +11 dB; sub-

* See [6, 57, 123, 142, 165, 175, 178, 209, 240, 289, 297, 368, 388, 387, 389, 391, 395, 444, 480, 531, 532, 587, 650, 696].

TABLE 7.16 Averaged Land-Clutter Return $\gamma = \sigma_0/\sin\psi$, ψ = 15 to 70° Grazing, in Decibels Below 1 m^2/m^2*

Terrain type	Av. of median γ, dB	Carrier frequency, GHz											
		UHF 0.50		L 1.25		S 3.0		X 9.0		K_u 17		K_a 35	
		γ_m	γ_{max}	γ_m	γ_{max}	γ_m	γ_{max}	γ_m	γ_{max}	γ_m	γ_{max}	γ_m	γ_{max}
Deserts and roads	25	37	30	32	28	28	22	23	10	23	17	22	15
Cultivated land	22	32	18	. . .	. . .	. . .	10	18	10	19	10	16	5
Open woods	16	22	12	15	8	17	10	15	10	15	8	14	5
Wooded hills	14	16	. . .	. . .	. . .	. . .	. . .	13	6	15	8	13	. . .
Cities	11	6	−2†	11	4	15	5	12	3	. . .	. . .	. . .	. . .

* Data taken from incoherent, monostatic radars, with pulse width ≈ 3 μs.
† 2 dB above 1 m^2/m^2.

urban areas and cities near 0 dB. Ice is also about 0 dB. Where there are woods, vegetation, and grass there is two-way absorption and σ_0 may drop to -10 dB at the higher frequencies. Skylab observations over the entire North American Continent (K_u band, summer) show an average of $+3$ dB. Moisture in the earth has more effect at lower carrier frequencies ([673] Chap. 12) as the waves penetrate the earth.

Frequency agility

As with precipitation and sea clutter there is a benefit to using frequency-agile transmission and postdetection processing if the cell contains distributed clutter. Surface-radar experiments of wooded terrain are illustrated in Fig. 7.28 [264, 586]. They show that sufficient decorrelation occurs for $\tau\Delta f$ between 1 and 2. This may not be the case if only 1 or 2 discrete scatterers dominate in a resolution cell. The decorrelation depends on whether the discrete is a point scatterer or a line scatterer that is not exactly perpendicular to the radar. It is suggested that $\tau\Delta f$ be at least 2 for satisfactory frequency-agility performance in land clutter.

7.13 Composite Terrain—Spatial and Temporal Distributions

In the design or evaluation of radars to detect and track targets in a land clutter background, there are two key distributions that determine

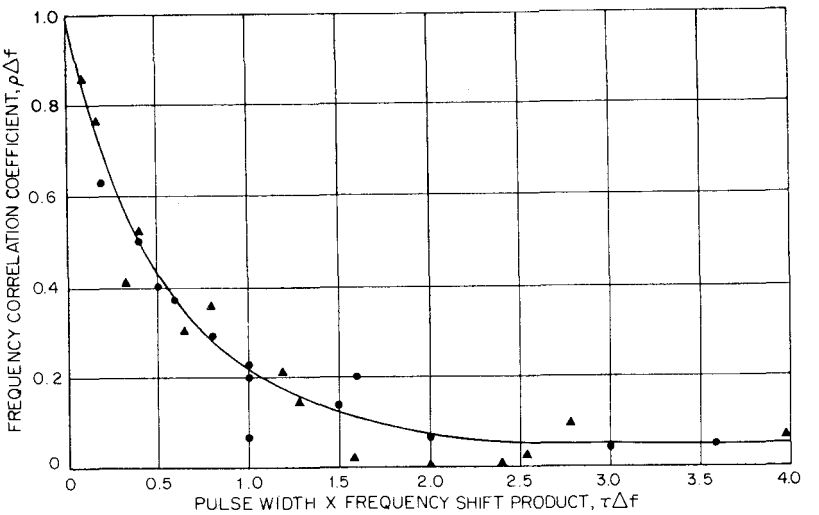

Figure 7.28 Frequency correlation function of land returns—wooded terrain, C-Band.

design parameters and performance. The first is the amplitude and fluctuation properties of the echoes from a single resolution cell. If the cell contains many distributed scatterers, one amplitude distribution will be Rayleigh (exponential power distribution). The spectrum depends on the *relative* motion of the scatterers from pulse to pulse. If a portion of the scatterers do not move in the observation period, there will be a Rice distribution (see Chap. 3), which has a dc component as well as a fluctuating one. The form of the temporal distribution affects the design of CW, MTI, pulse Doppler, and MTD processors as described in Chaps. 9, 11, and 14. These temporal statistics are discussed later in this section.

The spatial distribution describes the variation of mean power across spatial resolution cells. Figures 7.25 and 7.26 illustrated this since the temporal fluctuation at each cell was heavily averaged before display. The spatial statistics affect where the target-detection threshold is to be set relative to some estimate of one or more parameters of the distribution. This is the CFAR problem of Chap. 4. If the distributions have a large *tail* as indicated by a large value of S (Tables 7.10, 7.11) for grazing angles of 0 to 3° the thresholds must be set quite high to avoid false alarms due to clutter.

Composite terrain distributions

Terrain echoes fluctuate over a very wide dynamic range, making it difficult to process signals within the linear range of a receiver. This is one of the reasons why the average RCS is difficult to accurately determine. The median RCS, on the other hand, is often easier to measure because receiver nonlinearities are less troublesome.

For an essentially homogeneous echoing area, σ_0 and σ_m are expected to be equal within a few decibels. Distributions lie somewhere between the Rayleigh and the log-normal distributions. As has been considered the case for many years, it is a reasonable first approximation for land and sea echo to be assumed Rayleigh in character at higher grazing angles with moderately long pulses [444]. Depending on various radar parameters and the terrain, large amplitude peaks occur more often than is predicted by that distribution, but usually less often than is predicted by the log-normal distribution.

For a Rayleigh distribution,

$$10 \log_{10} \left(\frac{\sigma_0}{\sigma_m} \right) = 1.6 \text{ dB}.$$

In other words, if a distribution is perfectly Rayleigh in character, the average RCS exceeds the median by 1.6 dB. The Rayleigh distribution is shown as a member of the Weibull family in Fig. 7.29.

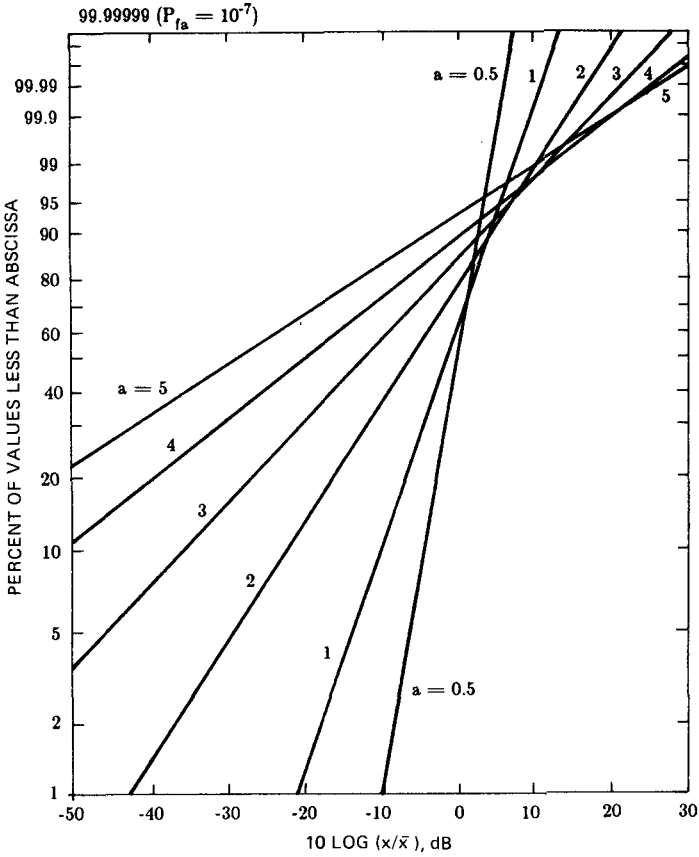

Figure 7.29 Weibull cumulative distribution functions normalized to mean values. Slope parameter $a = 1$ is the Rayleigh power function, and $a = 0.5$ is the Rayleigh voltage function.

Although the Rayleigh model is a reasonable one to use for moderately long pulses and relatively steep grazing angles, especially for homogeneous terrain [444], it is often found that the distribution of land clutter possesses much longer tails than would be predicted by a Rayleigh assumption. In an attempt to characterize experimental data, various other distributions have been used, the log-normal distribution being one of these. In the log-normal model, the decibel value of clutter power (or of reflectivity) is taken to be normally distributed. Just as with a standard normal function, the log-normal distribution is characterized by two parameters, such as the mean and standard deviation, or the mean and mean-to-median ratio. The standard deviation of the log-normal function is indicated as S when the random variable is

expressed in decibel units: the mean $\pm S$ is coincident with the 16th and 84th cumulative percentiles.

For a log-normal distribution,

$$10 \log_{10} \left(\frac{\bar{\sigma}}{\sigma_m} \right) = 0.115 \, [S^2(\text{dB})]$$

where $[S^2(\text{dB})]$ is the variance and $S(\text{dB})$ is the standard deviation of a distribution for which power levels are expressed in decibels. The log-normal distribution is illustrated in Fig. 7.30. If S is 7 dB, the threshold must be 10 dB higher than for the Rayleigh at the 0.9999 probability ($P_f = 10^{-4}$).

For a gaussian distribution, two standard deviations centered about the median contain 68 percent of the data points. For a Rayleigh distribution, there are approximately 11 dB between these points (two standard deviations).

Unfortunately, the log-normal distribution predicts extremely high values at the 10^{-5} and 10^{-6} probability points. If a radar cell is 0.1 km in range and 1 km in azimuth the area is 10^5 m^2. If $\sigma_0 = -20$ dB the mean RCS is 30 dBsm. If S is 8 dB the RCS at $P_f = 0.9999$ is 52

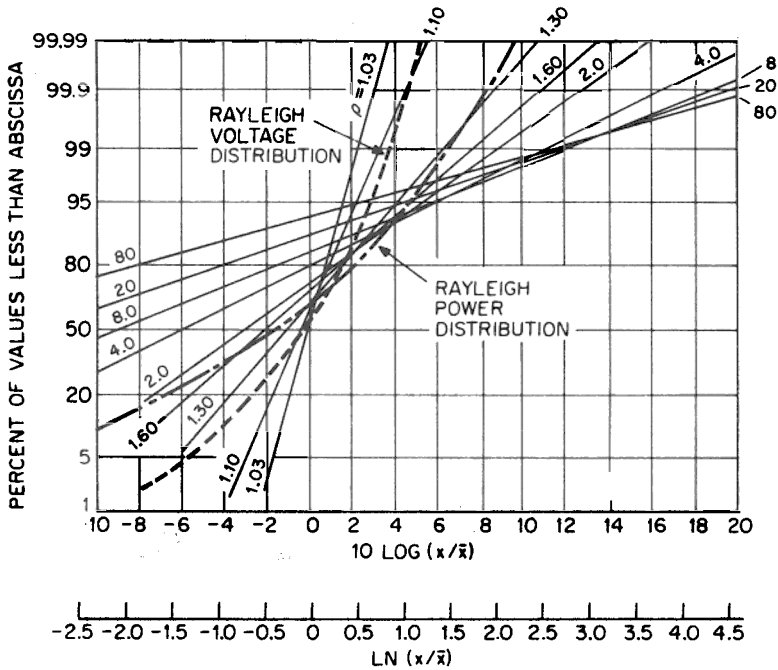

Figure 7.30 Log normal cumulative distribution function, normalized to mean value. The parameter ρ is the mean-to-median ratio.

dBsm. This is not unreasonable but at $P_f = 10^{-5}$ or 10^{-6} unreasonable values would be predicted. For this reason the Weibull family is becoming more commonly used as the tails are not as severe.

High values of S were reported in Table 7.15 by Linell in Sweden, from ships looking at terrain on the east and west coasts of the United States and in Puerto Rico. Other examples are given in the following figures.

Figure 7.31 shows the spread parameter S for 0.1 to 6.0° grazing

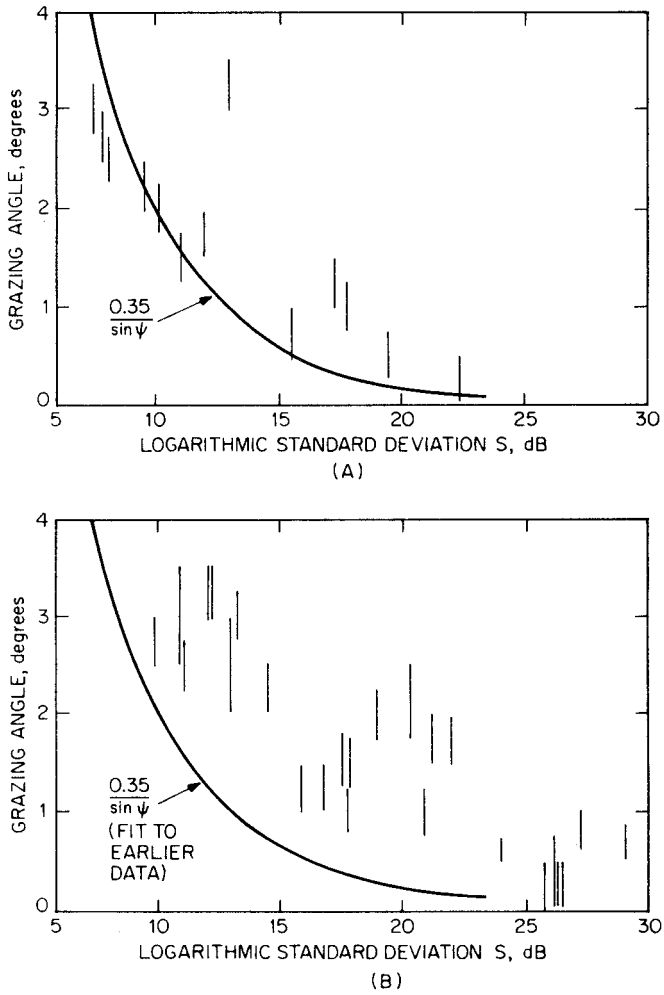

Figure 7.31 Standard deviation of log-normal distribution versus depression angle (X-band, horizontal polarization). Solid line is fit to many data sets. (A) Dunes (vertical bars; (B) mixed terrain (trees, fields, houses).

TABLE 7.17 Reflectivity of Large Discrete Land Echoes at a Rural Site

Type of scatterer	Grazing angle, °	Temporal median, dBsm	Temporal peak, dBsm
Three autos	2.0	42	47
Metal roof building	3.5	43	45
House	3.5	44	46
Mobile home	4.0	42	46
30-ft hill	4.5	38	40
Rural building	4.5	40	41
Hospital	5.2	40	45
Mobile home	5.9	40	42
Metal-roof barn (40 ft)	6.7	43	49
Small-business district	10.5	42	48
3 metal sheds	11.2	42	44
House (aluminum siding)	11.4	41	44

angles from 10 experimenters plus measurements in the Netherlands.* Note the sharp increase S at the lower grazing angles. The solid lines were derived from a fit to other 10 sources of data, reduced by the author. An attempt to relate S to the cell area was unsuccessful.

Land-clutter discretes

The often cited tails of the spatial distributions of land areas sometimes result from natural formations but more often are from nearly vertical cultural features when seen by surface radars, aerostat radars, or long-range airborne surveillance radars. They consist of buildings, houses, powerlines, pylons, lighting poles, tracks, autos, billboards, etc. Even in less developed countries there are numerous structures made of corrugated metal, oil drums, old vehicles, ships, etc. McEvoy [467] measured a number of these in western Massachusetts (rural with smaller towns) with an S-band, horizontally polarized radar with a 2° azimuth beamwidth and a 0.4-μs pulse. These are similar parameters to an air surveillance radar (ASR). A summary of the *median* reflectivity of the larger discretes is shown in Table 7.17 in dBsm. They exceed 40 dBsm and fluctuate to near 50 dBsm. The author has observed water towers in excess of 50 dBsm in similar surroundings. To see a 1-dBsm target in such a clutter background generally requires clutter attenuation in excess of 55 dB.

The industry is now accepting a given density of discretes as part of a radar specification. Typical numbers include one 30-dBsm discrete

* See also: de Loor G. P., A. A. Jurriens, and H. Gravenstein, "The Radar Backscatter from Selected Agricultural Crops," *IEEE Trans.* vol. GE-12, no. 2, pp. 70–77, April 1974.

per nmi^2 for an airport area, to perhaps 10/nmi^2 in a moderately sized city. Lacomme [419] suggests an average urban area of 0.8/nmi^2 at 40 dBsm and 0.8/nmi^2 for 50 dBsm. For a city he suggests 17/nmi^2 at 40 dBsm and 0.3 nmi at 50 dBsm. These values appear to be modeled around an X-band radar with a 0.4 μs pulse.

A recent FAA specification [206] for an L-band surveillance radar includes 500 autos of 10 dBsm in the coverage area plus 50 to 200 discretes in specified areas. Of these, 10 percent exceed 30 dBsm, 5 percent exceed 40 dBsm, 2 percent exceed 50 dBsm, and 1 percent exceed 60 dBsm.

Rigden [43, pp. 227–232] made land measurements with a high-resolution (100 MHz), C-band surface radar, and reported that 18 percent of the clutter cells exceeded 1 dBsm and less than 1 percent exceeded 10 dBsm. At the 10-dBsm level the extent of each "point clutter" was less than 40 ns.

Spectrum of land clutter

The fluctuation spectrum of echoes is primarily from vegetated terrain and arises from the relative motion of the vegetation moving about in the wind. As the wind speed increases, the motion increases and the spectrum width is almost directly proportional to the transmitted frequency, at least in the 1- to 10-cm range of wavelengths. Figure 7.32 displays the spectrum width as a function of wind speed as determined from the data of many different sources. The transmitted wavelength varied from 1.25 to 9.2 cm. An estimated fit to the data is shown by the solid line. From the lower right corner, the dashed line represents the 90th percentile value for most data sets. Polarization does not seem to be a significant factor. The standard deviation of the clutter spectra (σ_v) in velocity units was determined by estimating the best fit to the gaussian shape, noting its standard deviation, and converting it to velocity units through the Doppler equation. The data of Fishbein et al. [233] is included in Fig. 7.32. One data set is illustrated in Fig. 7.33, which shows large high-frequency tails in the power spectrum and approximated $P(f) = 1/[1 + (f/f_c)^3]$. The relatively thorough U.S.S.R. Forest Measurements by Kapitanov et al. [383] are also included in Fig. 7.32. Their measured spectra show tails with an exponent of 3.2 to 4.0 to about the −40-dB level; the average is 3.7. In presenting these data, no distinction is made between those spectra resulting from coherent and those from square-law detection. There is a steady (dc) component superimposed on these fluctuations. The ratio of the power in steady component (dc) to that in fluctuating component (ac) is also shown in Fig. 7.32. This is the solid line decreasing from top right. The value can be used to fit the Rice distribution if desired. When calculating

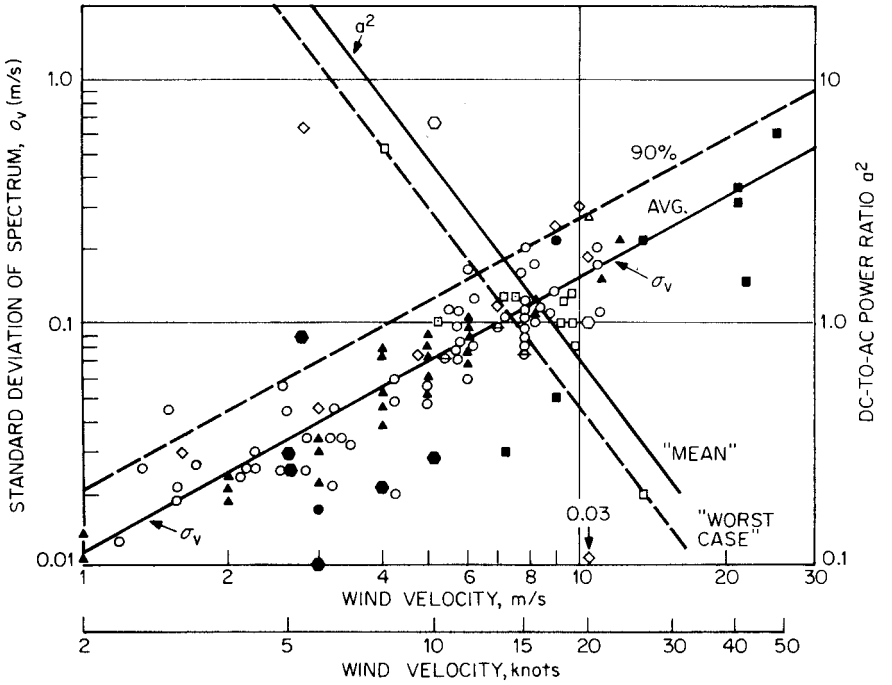

Figure 7.32 Spectrum width for land clutter, wooded terrain (fixed antenna). a^2 is ratio of dc-to-ac component of signal. (*Solid triangles are U.S.S.R. data* [*383*].)

MTI system performance, the dc and ac terms should be considered separately.

It is believed that the dc component is composed of the tree trunks reflections, large branches, and the surrounding terrain itself, while the ac component results from the leaves and smaller branches. As the wind increases, a greater proportion of the branches and trunks are set into motion. Even the relatively simple single MTI canceler will eliminate most of the dc component as long as the transmitter is stable and the dynamic range is not exceeded. The longer tails are more difficult to eliminate, and there may be little improvement from additional stages of MTI. If cancelations of greater than 30 dB are desired, the details of the spectral shape should be included in the analysis.

A case can be made for three contributions to the spectrum. A relatively strong dc component would be due to reflections from terrain, tree trunks, and for major tree branches. A fluctuating but smaller-amplitude component can be traced to smaller branches plus power lines etc. A third-higher frequency group would be from leaves, vehicles, vibrations, blower fans, wind-blown debris, moving people, birds, etc.

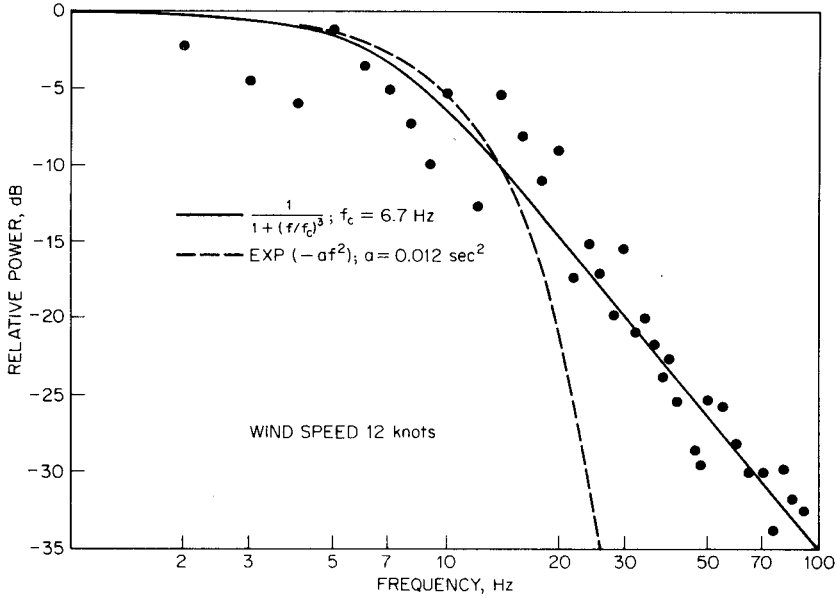

Figure 7.33 Approximations of the clutter spectra obtained with an X-band radar. (*From Fishbein et al.* [233])

As clutter rejection in the 60- to 80-dB range is being required, this third group needs better definition.

Simkins et al. [663] prepared three models for L-band surface radars that include both a dc component and a fluctuating one. He presents relationships for mountains, hills, and valleys. The broadest spectra are for the valleys, where an inverse f^3 relationship is suggested.

7.14 Bistatic Sea and Land Clutter

There are little data on bistatic land and sea clutter, some of which is included here. Since the primary usage of bistatic configurations is where the transmitter is on the surface and the receiver is a missile seeker more or less in the vertical plane above the transmitter, the primary concern is with a low-grazing-angle transmission and a somewhat larger (but less than 90°) receive grazing angle. Barton [46] has suggested the following approximation to the bistatic reflectivity:

$$\sigma_{0b} = [\sigma_{0t} F_t^4 \sigma \text{ or } F_r^4]^{1/2}$$

where σ_{0b} = bistatic reflectivity
σ_{0t} = monostatic reflectivity as seen by sensor at transmitter location

σ_{0r} = monostatic reflectivity as seen by sensor at receiver location

F_t^4 and F_r^4 = two-way propagation factors from reflecting area to transmitter and receiver, respectively

Note that σ_{0t} and σ_{0r} are evaluated at their respective grazing angles.

If ψ is greater than a few degrees, the value of F_r^4 approaches unity and

$$\sigma_{0b} = (\sigma_{0t} F_t^4 \sigma_{0r})^{1/2} \qquad \text{for } \psi_r > \text{critical angle}$$

If the constant gamma relationship holds,

$$\sigma_{0b} = \gamma F_t^2 [(\sin \psi_t)(\sin \psi_r)]^{1/2}$$

This implies that the bistatic reflectivity can be estimated from the reflectivity at the geometric mean of the transmit and receive angles.

This section indicates that, because of the definition of σ_0 and its use in the radar equation, the bistatic value σ_{0b} may be higher than σ_0 if $\psi_t >> \psi_r$ at low grazing angles and σ_{0b} may be lower than σ_0 if $\psi_t > 60°$.

Consider that at least for the pulse-limited case, σ_0 is defined as the reflectivity per unit *surface area* rather than in the plane perpendicular to the centerline of the radar beam. As such, the monostatic σ_0 increases with ψ even for rough surfaces since the transmitter power density on the surface increases with ψ_t. This led to the development of the term γ where $\gamma \sin \psi = \sigma_0$. For rough surfaces γ is close to a constant for $3° < \psi < 60°$.

Consider the diagram in Fig. 7.34. Assume that these ellipses are the "footprints" of a transmit and a receive beam of the same beamwidth, and that the radar is pulse limited by a pulse of duration τ. The longer ellipse A is from the lower ψ and the shorter ellipse B is from the higher ψ. Note that if the transmitter is higher and illuminates area B, and the receiver observes A, the power density on the surface will be higher than for the reverse case. Even assuming omnidirectional

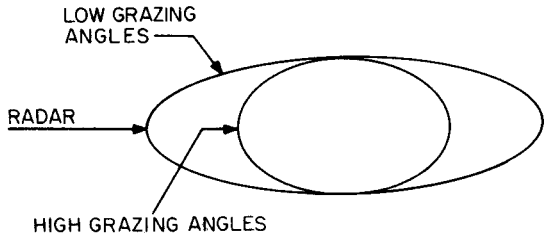

Figure 7.34 Surface illumination.

scattering, σ_0 will be greater when the transmit grazing angle is higher. This is true even if the radar cell is limited to $c\tau/2$ in range extent. Thus, since σ_0 (monostatic) increases with ψ by its definition, σ_{0b} should be determined from the transmit angle up to near the specular region, as illustrated in Fig. 7.34.

The first conclusion is that one must not arbitrarily invoke reciprocity. Other tentative conclusions state that for vertical incidence transmitters (i.e., geosynchronous or orbiting satellites) one cannot use $\psi_t = 90°$ to obtain σ_{0b} since specular scattering dominates unless ψ_R is very close to 90°. For $60° < \psi_R < 89°$, σ_0 should be somewhere between σ_0 for 60° and σ_0 for 90°.

Measured bistatic characteristics—sea and land

Experimental programs designed to study the bistatic sea cross section have been reported by Pidgeon [547, 548] and Domville [185]. Both authors reached similar conclusions from their findings. A list of experiments is contained in Willis in the *Radar Handbook* [673].

The bistatic cross section was measured from very small transmitter depression angles (0.2°) to vertical incidence. The case in which the transmitter depression angle is less than 10° is of particular importance as illustrated in Fig. 7.35; Pidgeon found no cross-section dependence on receiver depression angles ranging from 10 to 90°. Domville reports the same findings in similar situations for receiver depression angles ranging from 6 to 30°. They found the cross section to be dependent on transmitter depression angle, and follows within the same order of magnitude the values predicted by monostatic models. Since the bistatic cross section almost agrees with monostatic models with the same depression angle, while the bistatic receiver angle is independently varied, Pidgeon concluded that the cross section depends only on the transmitter angle.

Polarization dependence was also studied with greater bistatic cross sections obtained with vertical polarization. Cross sections from crossed polarization were 10 to 15 dB lower than from vertical polarization for transmitter depression angles below 1°. This difference was only 5 to 8 dB for transmitter angles greater than 3°.

Ewell and Zehner [214] reported bistatic sea clutter with an X-band, 0.2 μs radar. The transmitter and receiver were on the surface and the azimuth angle was varied. Azimuthal bistatic RCS fell rapidly with similar results for both polarizations. The drop was about 5° db at 20°–30° out of plane to about 20 db for 45° out of plane.

The British General Electric Co. studies of bistatic cross sections were classified into three main categories according to terrain type—

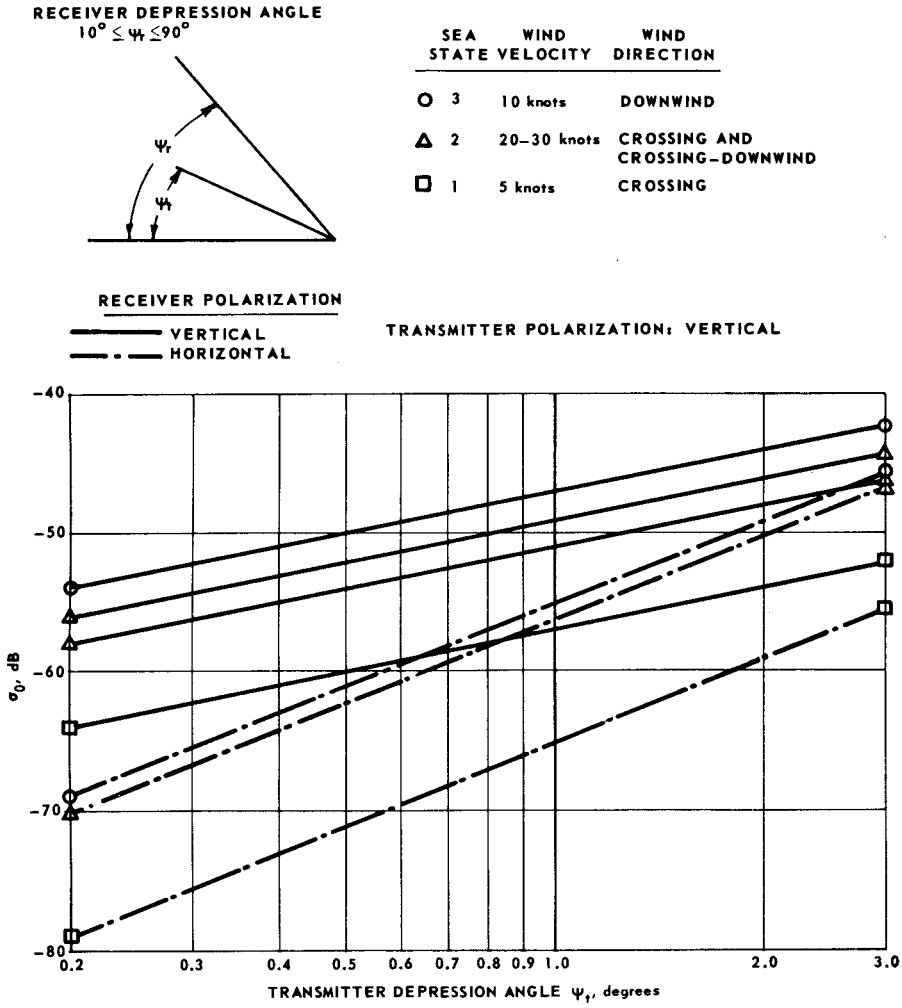

Figure 7.35 Bistatic cross section (C-band). (*After Pidgeon* [548])

forest, urban, and rural. Forward reflection and backscatter measurement results were made at large and small receiver depression angles using a CW X-band radar. The large-angle backscatter measurements are similar to those of Blackwell and Rogers [71]. Forward reflection coefficients measurements were made using two aircraft. A CW transponder was carried in one aircraft and served as the actual transmitter. The receiver and transmitter were carried 3 mi astern in another airplane. Small-angle measurements were made by placing the transmitter 4 to 10 ft above the local terrain and flying the receiver over the transmitter along the illuminated track. The general intent of such

measurements was to obtain an overall picture covering a wide range of conditions. Much information from different sources was grouped into the three categories and included in the results.

Two important results are shown in Fig. 7.36. First, the bistatic cross section is shown to remain constant for receiver depression angles greater than 5°. Domville also reported this conclusion for receiver angles between 6 and 40°. No statistical variation with azimuth angle was reported. These facts support an isotropic scattering model for forest terrain. Note also the monostatic data collected by Goodyear and Philco. If all the RRE data were plotted according to transmitter depression angle, these points would group between 1/2 and 2°. Note that the monostatic curves extrapolate to this point group. Since the curves indicate a strong transmitter angle dependence and little receiver angle dependence, monostatic measurements may be used as a good first approximation to bistatic situations.

Blackwell and Rogers [71] concluded their study on a dry coniferous forest with a vertically polarized CW X-band radar. The receiver was carried in one aircraft and was steered toward a transponder placed 20 ft above the ground. Runs were made at either 500 or 1000 ft. The transmitter, equipped with a wide-beam antenna, was carried in a second aircraft 2 mi astern the receiver. For receiver depression angles greater than 5°, accuracy of 4 dB is reported; for less than 5°, the illuminated ellipse about the transponder becomes extremely large, destroying terrain homogeneity and causing excessive shadowing. A summary for rural land is illustrated in Fig. 7.37 (replotted by Willis [673]). The conical shape about vertical incidence is general for all terrain types, but the extent of the ridge in the forward quadrant about the specular angle is indicative of the isotropic nature of the terrain.

Domville [185] also made some measurements on a semidesert in Libya. The terrain surface was primarily sand and stones with plants 0.1 to 0.5 m high. A rainstorm did not alter the results. The transmitter, as in other tests, was only a few meters above the ground.

Virtually no change in bistatic reflectivity was noted for considerable changes in receiver angle. No data were given for the forward region, but with lower values for the bistatic angle, the reflectivity was -40 dB. With a single azimuth shift of 15°, he reported a decrease of about 0.3 dB per degree of azimuth shift relative to the plane of incidence. Horizontal and vertical polarization yielded similar results, with cross polarization down by about 7 dB.

It was noted that with his system, a Land Rover exceeded the terrain echo by almost 10 dB. However, a herd of camels exceeded the clutter by only 5 dB. The number of humps was not recorded.

Lorti [450] reported some additional tests including those by Johnson and Fey at 95 GHz with both transmitter and receiver on the ground. The falloff rate versus azimuth angle was about 0.1 dB per degree.

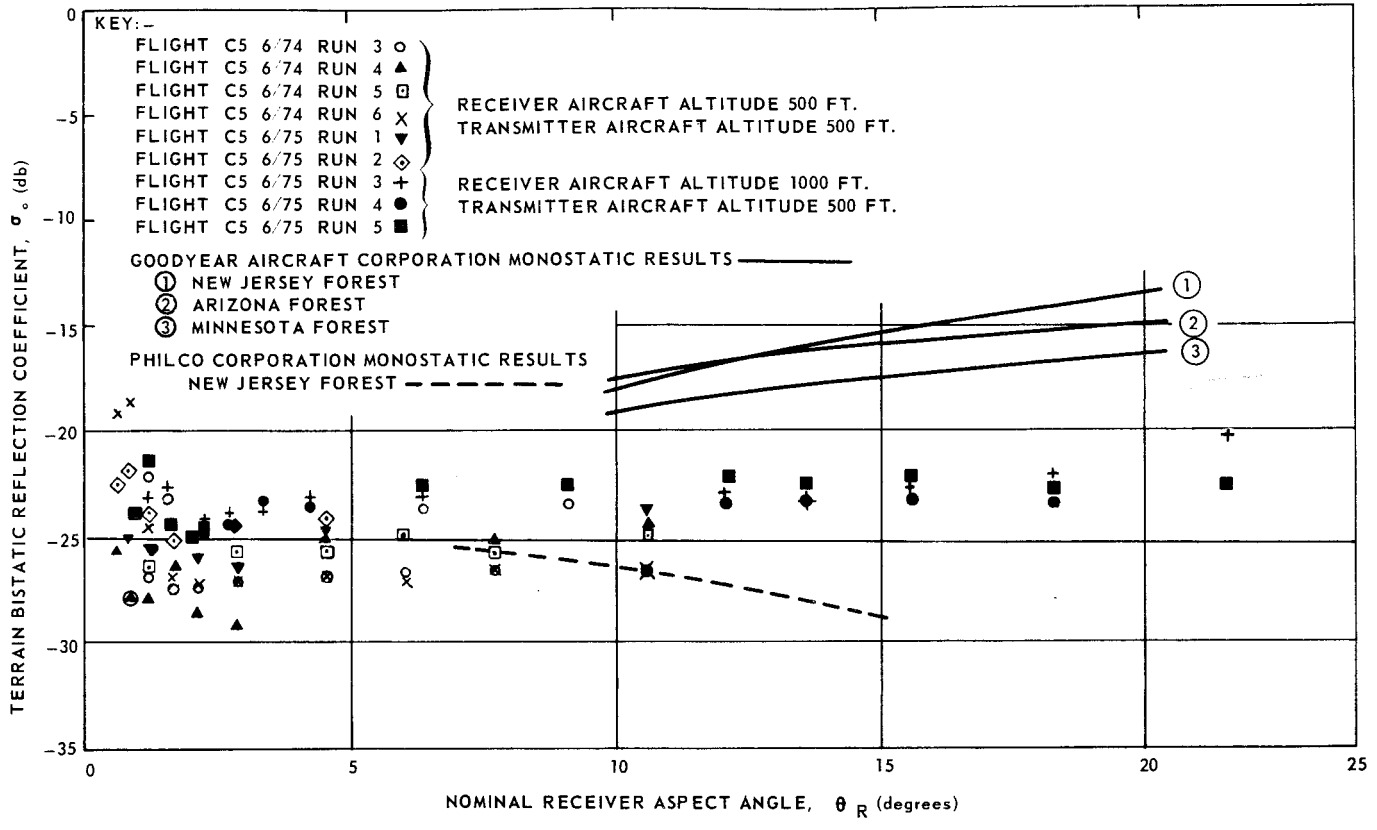

Figure 7.36 Mean terrain bistatic reflection coefficient variation with nominal receiver aspect angle for near grazing illumination (X band).

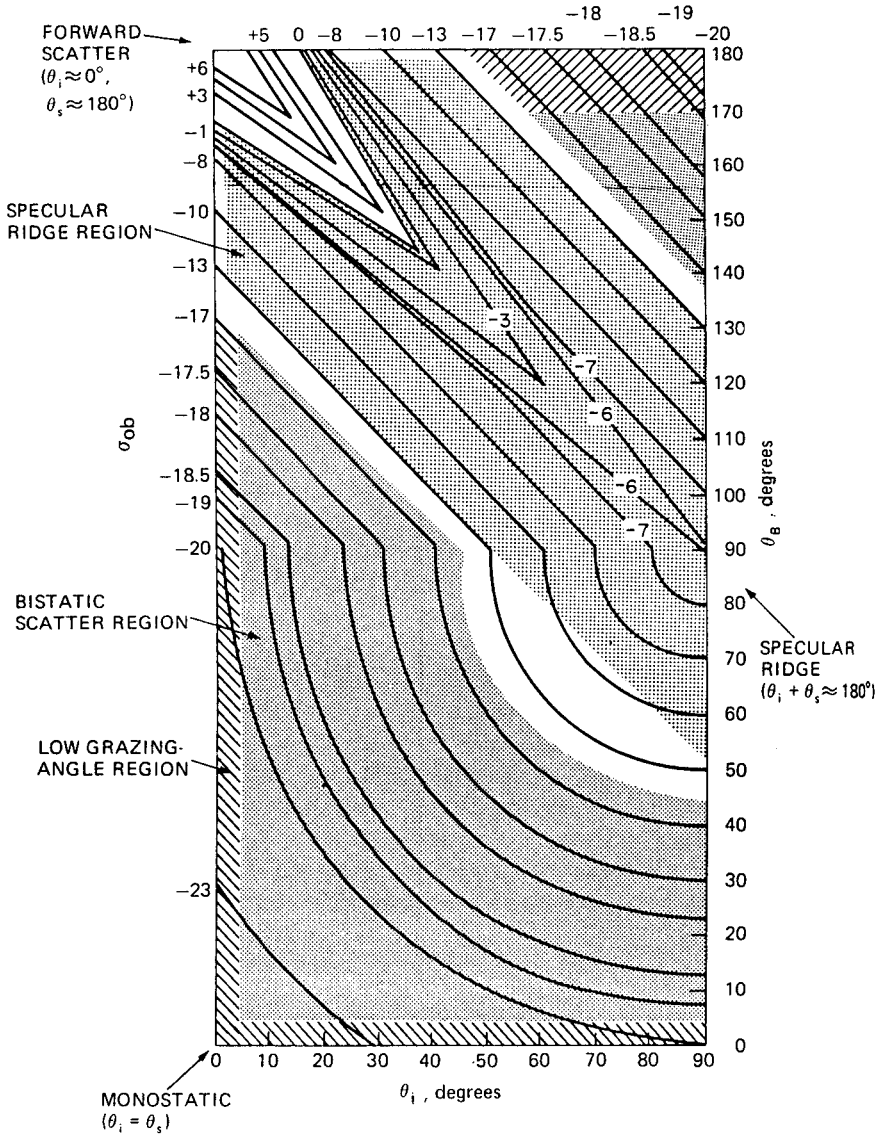

Figure 7.37 X-band, vertically polarized bistatic reflectivity, σ_{0b}, in-plane ($\phi = 180°$). (*Data summary for rural land [185]*)

Forward region

The best data on the forward region in land are again the data of Domville [185]. Figure 7.37 shows the specular ridge from the forward scatter where the incident grazing angle is near zero and the receiver is near 180°, to where both angles are 90°. As in the case of man-made targets, the reflectivity is quite high.

In summary, there are angles at which the clutter backscatter is low relative to monostatic. The commonly encountered targets may or may not have high reflectivities at these angles, depending partially on whether there has been a deliberate attempt to reduce the monostatic RCS. See Willis in the *Radar Handbook* [673] for their use in system analysis.

Chapter

8

Signal-Processing Concepts and Waveform Design

The first seven chapters explored the concepts of detection, display, and target and clutter reflectivity that are common to many forms of radar processing. With proper interpretation these concepts are applicable to the various waveforms and signal processors to be discussed in the following seven chapters.

This chapter includes some of the general principles of waveform and processor design. The choice of transmit waveform and of the corresponding receiver configurations involves two separable design problems. The waveform must be chosen to optimize performance in some total environment. The limitations are generally external to the radar though restrictions may be imposed by the type of transmitter or antenna. The currently accepted belief that there is no universal waveform is not surprising in light of the wide variety of waveforms used for electrical communication, a subject that has had over 100 years of intensive study. On the other hand, the inability to find a *best* waveform is not an excuse for failure to search for *locally optimum* waveforms for specific radar tasks and environments.

The design of the radar processors (the hardware) is somewhat separable since there are generally two or more ways to design a near-optimum processor for a given waveform. Cost, complexity, and reliability rather than physical realizability are generally the bounds on

processor design. Practical signal processors with less than a 2-dB deviation from maximum efficiency have been constructed for virtually all waveforms.

This chapter introduces the subject of waveform design with the now standard range-Doppler ambiguity function description of Woodward [779] that was derived in the early 1950s. The ambiguity function discussion in Sec. 8.3 contains only a summary of the results pertinent to the descriptions of the specific waveforms and processors of later chapters. Detailed descriptions of the general properties of various general waveform classes and their ambiguity functions can be found in many excellent references such as Siebert [654], Skolnik [671], Cook and Bernfeld [136, 64], Spafford [678, 677], Fowle [246], and Rihaczek [602]. A detailed tutorial definition and description of the radar ambiguity function and many of its properties can be found in Sinsky's Chap. 7 of [94]. These expand the pioneering work of Woodward.

Despite their wide study, a knowledge of ambiguity functions has not generally been a substitute for learning specific waveforms and processors. This is primarily due to several limitations in the *general* descriptions of the ambiguity function. While with modern computers it is not difficult to derive the ambiguity function for a specific waveform, it is not generally possible to derive a specific waveform by starting with an ambiguity function. There are exceptions to this for a specific class of waveforms (i.e., FM, phase-coded waveforms, pulse trains). Also, the range dependence of various clutter and target echoes complicates the basic relationships of the foregoing references if the target and clutter are not at the same distance from the radar. Finally, a thorough and bounded description of the target and clutter environments is required for unique selection of appropriate waveforms. It is hoped that the descriptions of specific targets and clutter in Chaps. 5, 6, and 7 in conjunction with an analytical description of the environment (see Sec. 8.3) will remove some of this limitation.

8.1 Radar Requirements as We Approach the Year 2000

While the radar technology was advancing rapidly in the late 1970s and 1980s, several transients were injected into what had been a slow evolution in radar system requirements. Both designers and users long recognized that better reliability and maintainability were needed, and that these were achievable. It was also recognized that the development of jammers was advancing rapidly throughout the world, although at no greater pace than had been predicted in the early 1960s.

The first and most severe transient was the realization that reduced cross section or "STEALTH" aircraft and missiles would be flying in

quantity in the mid-1990 era. The techniques of reducing radar cross section by shaping were well known 20 years ago in the radar community and especially in the ballistic missile defense world. Radar-absorbing materials (RAM) were also widely available, but not practical for use on high-speed aircraft or missiles. Their importance did not influence the major procurements until about the time of President Carter's announcement of the STEALTH aircraft. It is not known whether technology advances led to his announcement, or whether the funding then became available to develop the technology. In any case, the military radar procurements of the early 1990s are calling for radar target reflectivity (RCS) of 1 to 3 orders of magnitude smaller than those of today.

Another transient was the Falklands war, and the realization that even non-STEALTH missiles such as the Exocet could take advantage of the multipath null over water to elude radar detection. This moderately small target flying low over the ocean had an important effect on subsequent radar specifications.

Finally, the antiradiation missile (ARM), which passively homes on radar (or communication) emissions, was becoming an inventory item and not the "new" tactic that it was in Vietnam. These transients and the resulting changes in radar design are illustrated in Fig. 8.1.

The most straightforward radar improvement is the low-sidelobe antenna that is not included in the figure. For a small loss in gain, there is benefit in several areas. The logistics of placing an electronic jammer or an ARM consistently in the main beam of a radar is a difficult task. Thus, the tactical limitations require that the ARM operate in the sidelobe emissions of the threatened radar. In the ECM case, a 20-dB reduction in the average sidelobe level is equivalent to a factor of 100 reduction in the received jammer power. In the ARM case, the mathematics are not so trivial, since the task of the ARM signal processor is to detect the 100-times-lower radiation level in the presence of all the emitters in the frequency band. While it is well known that a 20-dB reduction in target cross section requires a 20-dB increase in radar power-aperture product or receiver sensitivity, it is not as well known what lengths must be taken to operate in an environment of clutter and false targets. The current generation of surveillance radar systems achieves satisfactory clutter improvement factors (I) of 45 to 55 dB for ground-based systems, and perhaps 10 to 20 dB more for airborne systems where there is no close-in clutter. The limitations of these systems include

1. Transmitter amplitude stability.
2. Transmitter phase stability.
3. Pulse width stability.

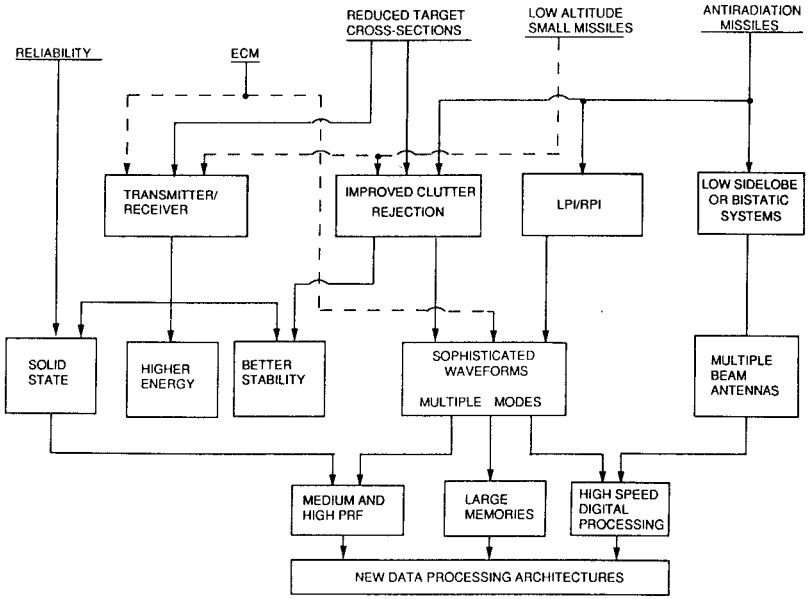

Figure 8.1 Effect of new radar threats.

4. Pulse timing jitter.
5. Analog-to-digital converter dynamic range.
6. Signal-processor dynamic range.

These are in addition to the environmental limitations and the theoretical limitations in filter design. A 20-dB overall improvement may require 20-dB upgrades to two of the above items and perhaps 12- to 15-dB improvement to the others. These will be part of the major challenges of new system design.

If the foregoing improvements are achieved, a new world of clutter emerges that was never before a major concern. The better current surveillance radars currently see numerous vehicles if they are designed to detect helicopters or crossing targets. In certain aspect angles, autos and trucks have radar reflectivities of 1000 to 10,000 dBsm or 10^5 to 10^6 times the reflectivity of reduced RCS targets. It is often impossible to separate these 65-mi/h vehicles from small "targets" at over 130 mi/h. Check your physics to see that the top of the spokes of the wheels are moving at twice the speed of the vehicle.

Referring again to Fig. 8.1, a 20-dB reduction in RCS, or the equivalent in a small missile flying low over the oceans, requires an equivalent increase in transmitter energy or receiver sensitivity in the absence of jamming. With jamming, it all must come from transmitter

energy. The same 20-dB improvement must be made in the ability to reject clutter. In addition to specific waveforms and processors to achieve this, the transmitter stability must often improve by 20 dB.

The requirement for higher reliability (on the left of Fig. 8.1) is leading to solid-state transmitters. This often conflicts with the requirement for greater total energy, which is often easier to obtain from tubes at the higher microwave frequencies. In addition, solid-state transmitters like to work with high duty factors. In general, high duty factor is obtained by higher PRFs, which often require more complex signal processing also. For a monostatic radar, the antiradiation missile is best countered by low-probability-of-intercept (LPI) or reduced-probability-of-intercept (RPI) waveforms wherein the energy is spread out in both time and frequency. This also leads to more sophisticated waveforms. With monostatic radars, multiple receive beams are desirable, while they are almost mandatory with bistatic systems. Thus the new "threats" almost always drive to more sophisticated waveforms. Since the environments often vary, depending on where the radar is looking, multiple waveforms are common and multimade radars are becoming common. Thus, large digital memories and higher-speed processing circuitry are needed. Fortunately these tools are now available to the radar designer. The new signal processors are quite impressive.

All these advances need an advanced data-processing architecture to select the optimum waveform for a given environment and to reconfigure the signal processor to match the waveform.

8.2 Matched Filters

In the earlier discussions of signal detectability and the corresponding radar range equations in Chaps. 1 through 4, it was emphasized that the signal-to-noise ratio should be maximized. The receiver transfer characteristic that achieves this end for white noise was derived by North [514] and is called the *matched filter* for the transmit waveform (see [714; 671, Sec. 9; 136, Chap. 2].

If the transmit waveform is represented by $u(t)$, its Fourier transform is

$$F(\omega) = \int_{-\infty}^{\infty} \exp(-j\omega t)u(t)\,dt$$

If the receiver transfer function is $H(\omega)$, the output signal of the receiver prior to envelope detection is

$$g(t) = \int_{-\infty}^{\infty} [\exp(j\omega t)]F(\omega)H(\omega)\,df \tag{8.1}$$

Let $g(t_0)$ be the maximum value of $g(t)$. The power spectrum of the noise at the filter output is

$$G(\omega) = \frac{N_0}{2}|H(\omega)|^2 \tag{8.2}$$

where $N_0/2$ = the noise spectral density in watts/hertz at the filter input. The factor one-half occurs because both negative and positive frequencies are used in the analysis, and the usual definition of noise density considers only positive frequencies. The average noise output power is then

$$N = \frac{N_0}{2}\int_{-\infty}^{\infty}|H(\omega)|^2\,df$$

The energy of the input signal can be written

$$E = \int_{-\infty}^{\infty}u^2(t)\,\mathrm{dt} = \int_{-\infty}^{\infty}|F(\omega)|^2\,df \tag{8.3}$$

An optimum radar detector must maximize the ratio of peak signal power to mean noise power at its output.

$$\frac{|g(t_0)|^2}{N} = \frac{\left|\int_{-\infty}^{\infty}F(\omega)H(\omega)\exp(j\omega t_0)\,df\right|^2}{\frac{N_0}{2}\int_{-\infty}^{\infty}|H(\omega)|^2\,df} \tag{8.4}$$

The receiver transfer function, $H(\omega)$, which maximizes this ratio, can be found by use of Schwarz' inequality. The resulting filter is known as the matched filter.

$$\left|\int_{-\infty}^{\infty}x(\omega)y(\omega)\,dw\right|^2 \le \int_{-\infty}^{\infty}|x(\omega)|^2\,d\omega\int_{-\infty}^{\infty}|y(\omega)|^2\,d\omega \tag{8.5}$$

From this inequality, it follows immediately that

$$\frac{|g(t_0)|^2}{N} \le \frac{2E}{N_0}$$

The maximum output signal-to-noise ratio occurs when the equality holds. The ratio is equal to unity only if

$$H(\omega) = KF^*(\omega)\exp(-j\omega t_0) \tag{8.6}$$

where the asterisk denotes the complex conjugate, t_0 is the time delay to make the filter physically realizable, and K is a gain constant. As a result the peak signal-to-noise power ratio is

$$\frac{\hat{S}}{N} = \frac{2E}{N_0} = \frac{2 \text{ (signal energy)}}{\text{noise power density}}$$

It should be noted that $\hat{S}$ is the peak *instantaneous* signal power and N is the mean noise power. If the output signal is a pulse of sine wave, it is conventional to define the output signal-to-noise ratio as the mean signal power at t_0 divided by the mean noise power, so that for the optimum filter given by (8.6) we have $S/N = E/N_0$. Since there has been no specification of the waveform represented by $u(t)$, the output signal-to-noise ratio is independent of the shape or complex modulation of the waveform as long as the noise is white. In later sections, it is shown that the *optimum* filter for detecting targets in strong clutter signals may not be the matched filter if the clutter location or spectrum is known. The impulse response function $h(t)$ of the filter described by Eq. (8.6) is

$$h(t) = K_2 u^*(t_0 - t) \tag{8.7}$$

In other words, the impulse response is a delayed time *image* or time inverse of the input waveform multiplied by a simple gain constant. Since the output of a filter is the convolution of the input signal and the impulse response, the matched filter output $g_0(t)$ can be expressed as

$$g_0(t) = \frac{1}{T}\int_{-T/2}^{T/2} f(\tau) f(\tau + t_0 - t)\, d\tau$$

Thus, in the absence of noise, the waveform is a time-shifted replica of the autocorrelation of the input signal.

If the interfering noise is gaussian and does not have a flat spectrum (is not white), but can be described by a power density spectrum $N(\omega)$, then the general optimum filter can be described by [264, 136].

$$H_0(\omega) = \frac{KF^*(\omega) \exp(-j\omega t_0)}{N(\omega)} \tag{8.8}$$

Under these conditions the matched filter also maximizes the probability of detection for a given false alarm rate.

The matched-filter output being the autocorrelation function of the transmit waveform is a general result. This indicates that the matched

filter may also be implemented as a cross correlator between the echo from a point target and a time-delayed and Doppler-shifted replica of the transmit signal. This is illustrated in later chapters.

It might seem that the matched filter might be difficult to realize. This is not the case for many common waveforms since it is general practice to construct a filter that yields within 1 dB of the sensitivity of the matched filter. Thus, the assumption that a matched filter is used is the basis of the range equations of Chap. 2. If compromises are made, the loss in sensitivity should be included in those equations.

As an example, consider the rectangular pulse of duration τ. The transfer function of the matched filter is the complex conjugate function of the spectrum of the signal [Eq. (8.6)]. Since the gain constant K and the time delay t_0 are of little importance, $H(\omega) = F^*(\omega)$. Thus, for a rectangular video pulse, the magnitude of the filter gain is

$$|H(\omega)| = K\tau \left| \frac{\sin \omega\tau/2}{\omega\tau/2} \right| \tag{8.9}$$

Figure 8.2A shows a surprisingly simple matched filter with the response function of Eq. (8.9). When the rectangular video pulse is inserted into the filter, there is a linear rise at the output for time τ and then a linear fall to zero as shown on the right of Fig. 8.3. This is, of course, the autocorrelation function of the pulse neglecting time delays, losses, and gain terms.

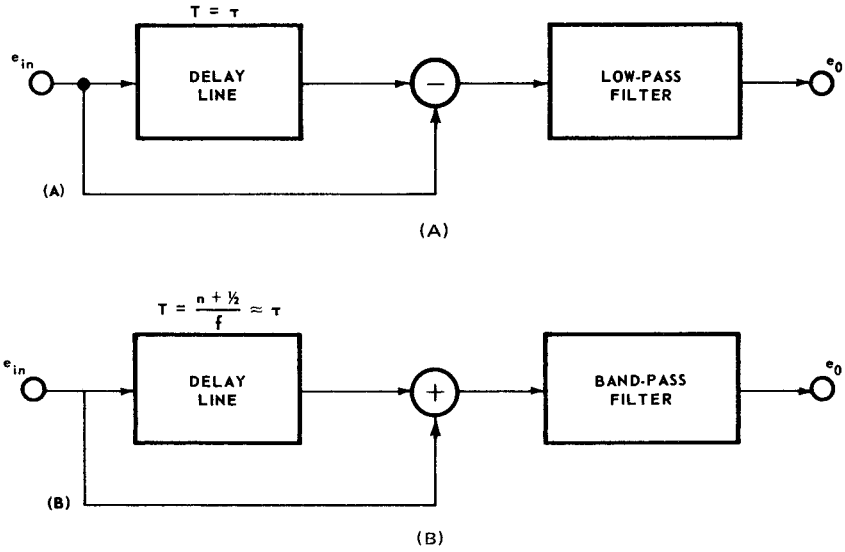

Figure 8.2 Matched filter for rectangular pulse duration τ. (A) Bipolar video (two required); (B) IF pulse (carrier frequency = f).

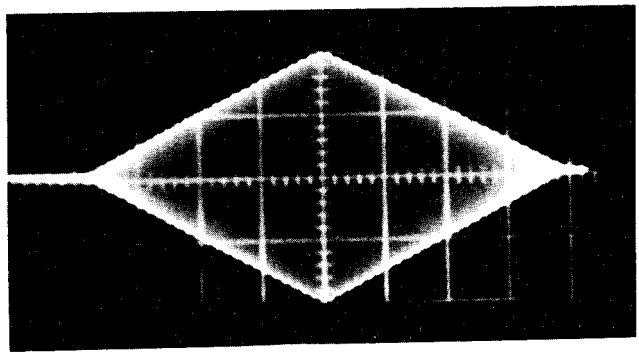

(A)

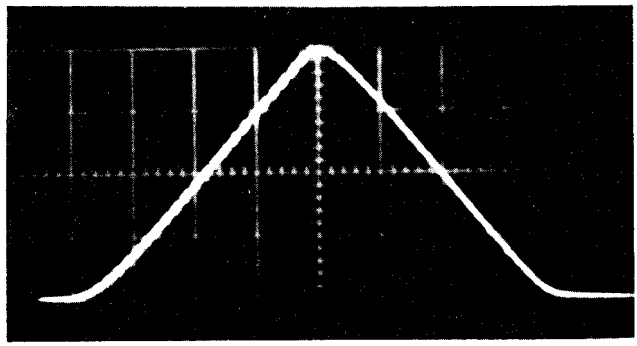

(B)

Figure 8.3 Filter responses for rectangular input pulse (sweep speed = 1 μs/cm, pulse length = 4 μs). (A) Matched-filter IF response for strong signal (IF = 3.16 MHz); (B) matched-filter detected video for strong signal. (*Courtesy of S.A. Taylor* [697])

Since pulsed radar signals are modulations of an RF carrier, the single video pulse is not a sufficient representation of the signal unless a *homodyne* or I = Q system with two quadrature channels and two matched filters is implemented when the receiver conversion is made from RF or IF to video signals.

Unless quadrature channels are instrumented, the maximum detection efficiency is obtained with bandpass filters at RF or IF. The matched filter for a rectangular pulsed sinusoid is shown as Fig. 8.2B. The filter must have a high Q and the length of delay line must be exactly an odd half cycle of the period of the carrier. If τ is large compared with a period of the carrier, the peak output of the filter will be within a few percent of the theoretical maximum [613]. It should

also be noted that the impulse responses of both of the IF and video filters are the time images of the waveforms to which they are matched.

An experimental result with the IF matched filter is shown in the top photo of Fig. 8.3. The S/N out of this filter was 0.9 dB (0.88 dB theoretical) higher than with a single-tuned bandpass filter having the optimum bandwidth of $0.4/\tau$. The matched filter for a rectangular pulse is not as widely used as would be expected since the sin x/x response makes the receiver susceptible to out-of-band interference. A filter with a more rapid falloff has a loss of less than 0.5 dB. For similar reasons, trapezoidal rather than rectangular pulses are used to reduce interference between radars.

It should be noted that maximizing predetection S/N maximizes detectability in noise only if the system is linear (a square-law or higher-order detector will often increase the output S/N but will not enhance detectability [740, pp. 117; 328]. As stated previously, S/N in this book refers to a predetection power ratio unless stated otherwise.

The previous discussions showed that S/N in a matched filter receiver is independent of the transmitted waveform. Until about 1950, power amplifier transmitters were not generally available, and most transmitted waveforms were either CW or sine wave pulses. The advent of practical power amplifier chains led to an interest in the transmission of pulses with complex modulation and *pulse compression* systems. The primary object of pulse compression was to transmit high energy with a long pulse and simultaneously to obtain resolution corresponding to a short pulse.

8.3 The Radar Ambiguity Function

The study of radar waveforms would be quite simple if there were not a relative radial velocity between the radar, target, and the environmental interference (clutter). However, when there is a significant Doppler shift, the reflections from even a point target are no longer replicas of the transmitted waveform. As a result, when there is relative motion the output of the *stationary target,* or zero Doppler, matched filter is not the autocorrelation function of the transmit waveform. In addition, the response from a second target or clutter at a slightly different range may appear at the matched-filter output when the desired target response is at its peak value. This overlap of signals occurs when the time extent of the waveform is greater than the differential time delay between the targets. As a result a special set of mathematical functions has evolved to allow interpretation of the output of a signal processor either when there is a target with a significant radial velocity or when multiple targets are present. These functions are called time-frequency autocorrelation functions or ambiguity functions and are based on the

text by Woodward [779]. A concise definition of the radar ambiguity function, suggested by Sinsky [666] and accepted by the IEEE [356] resolves an inconsistency in the sign convention of this function. This revised convention is used in this edition.

The radar ambiguity function quantitatively describes the interference to a reference target caused by a range- and Doppler-shifted second target of equal cross section when using a matched-filter receiver as defined in (8.6). The radar ambiguity function is defined [92] as the response of the matched-filter radar receiver to a target displaced in range delay τ and Doppler frequency ν from a reference target. The response is measured at the instant in time when the reference target is at its maximum value.

The ambiguity function is therefore closely related to the matched-filtered output waveform. In fact it is simply the squared magnitude of the time-reversed matched-filter response. The matched-filtered output due to a Doppler-shifted echo is

$$g(t) = \int u(x)u^*(x - t) \exp(j2\pi\nu x)\, dx \tag{8.10}$$

The time-reversed matched-filter response, also referred to as the correlation function of $u(x)$, is obtained from (8.10) by substituting $-\tau$ for t^*

$$\chi_u(\tau,\nu) = g(-\tau,\nu) = \int u(x)u^*(x + \tau) \exp(j2\pi\nu x)\, dx \tag{8.11}$$

The radar ambiguity function is defined as the squared magnitude of this correlation function.

$$\psi_u(\tau,\nu) = |\chi_u(\tau,\nu)|^2 \tag{8.12}$$

In practice plots of the correlation function magnitude $|\chi_u(\tau,\nu)|$ are referred to as ambiguity diagrams (preferable as three-dimensional representations). In this notation $\tau = 0$ and $\nu = 0$ correspond to the time delay and Doppler displacement of the target of interest; i.e., the ambiguity diagram origin is centered on the target location in the range Doppler plane or range Doppler space.

For the case of matched-filter reception, the origin of the ambiguity function may be thought of as the output of the matched filter that is tuned in time delay and frequency shift to the signal reflected from an

---

* All integrals without limits are assumed to have either infinite limits or for at least the entire radar observation interval. Since there is no consistency in the notation for these functions, the symbols of many of the references have been altered to make this text more self-consistent. While the symbol ϕ is often used for Doppler shift, it is used here for elevation angle, etc.

idealized point source target. In this case τ becomes the time delay relative to the target position, and ν becomes the Doppler relative to the target Doppler [18]. The filter responses far from the desired target location are undesirable if other targets or clutter may appear at these locations. The ambiguity response at $\psi_u(\tau,0)$ is then the filter response to reflections at a different range but at the same Doppler as the target at the same point in time where the reference target is at its maximum; i.e., $\tau = 0$. Also $\psi_u(0,\nu)$ is the ambiguity response to a reflection at the same range as the target but with other Doppler shifts.

By the use of Parseval's theorem, the ambiguity function can also be written

$$|\chi_u(\tau,\nu)|^2 = \left| \int F(f - \nu)F^*(f) \exp [-j2\pi f\tau] \, df \right|^2 \tag{8.13}$$

where $F(f)$ is the Fourier transform of the wave form $u(t)$. It is assumed that the received echoes are mixed with the transmit carrier frequency, and the only frequency variable of interest is the Doppler shift. An important inequality is

$$\psi_u(\tau,\nu) \leq \psi_u(0, 0) \tag{8.14}$$

that is, the ambiguity function is a maximum at the origin. There are many other relationships in the literature that are important for specific studies [562, 602]. The following are general assumptions implied in the development of the ambiguity function and its application in this text [678]:

1. Point targets are assumed. This allows the usual convention of normalizing the peak signal power P_s to unity at the origin of the ambiguity function

$$P_s = \psi_u(0, 0)$$

2. Target acceleration is assumed to be negligible.

$$a \ll \frac{\lambda}{T_d^2} \tag{8.15}$$

where a = target acceleration
λ = carrier wavelength
T_d = the signal duration

See Kelly and Wisner [393] for extensions to accelerating targets.

3. Mismatch of the envelope of the target echo and the transmit waveform due to high relative velocities is negligible or

$$\frac{2v}{c} \ll \frac{1}{BT_d} \tag{8.16}$$

where v = the radial target velocity relative to the radar
c = velocity of light
B = the signal bandwidth

(See Remley [588] for the effect when this constraint is violated.)

4. All signals are narrow band such that the term *Doppler shift* is meaningful. This can be expressed as $B \ll f_0$, where f_0 is the carrier frequency. Rihaczek [602] shows that this is not a very severe restriction.
5. There is a small percentage difference in the range from the radar to the various targets in the region of interest of the ambiguity diagram. This widely used simplification is a poor approximation for CW radar or pulse-train transmissions when the target of interest is distant from the radar and clutter or undesired targets are close to the radar. Analytic expressions to account for the range dependence are found in Chaps. 9, 10, and 11.

There are several other properties that simplify the use of the ambiguity function. It is convenient to normalize the signal $u(t)$ to unit energy

$$\int |u(t)|^2 \, dt = 1 \tag{8.17}$$

It is also useful to define a cross-ambiguity function $\psi_{uv}(\tau,\nu)$ for use when the receiver filter is mismatched to the transmit waveform [684, 683, 678]

$$\psi_{uv}(\tau,\nu) = |\chi_{uv}(\tau,\nu)|^2 = \left| \int u(t) v^*(t + \tau) \exp [j2\pi\nu t] dt \right|^2 \tag{8.18}$$

where the subscript u refers to the waveform properties and the subscript v refers to the mismatched filter. Then, with point targets and the customary signal normalization

$$\int\int \psi_u(\tau,\nu) \, d\tau d\nu = \int\int \psi_{uv}(\tau,\nu) \, d\tau d\nu = 1 \tag{8.19}$$

This important relation states that the total volume of the ambiguity function for all waveforms and filters is constant over the prescribed τ and ν space and must be less than unity over any finite region. Equation (8.19) is especially important in clutter and multiple-target

environments. The undesired portions of the ambiguity function (the range and Doppler ambiguities away from the origin) can be rearranged and hopefully placed in a region that is of little importance (i.e., at Doppler frequencies that are higher than expected from any target of interest). It will be shown that this can be accomplished if the approximate range and Doppler separation of targets and clutter are known.

Before expanding on the further properties of ambiguity functions for various waveforms, it seems worthwhile to pause and illustrate the derivation of the ambiguity function for a linear FM pulse (chirp). This particular derivation is an abstract of an analysis by P. J. Luke with a sign change to conform to the current standard.

Ambiguity function for linear FM pulse

Consider a signal represented in Woodward's notation as follows:

$$s(t) = \text{rect}\left(\frac{t}{\tau'}\right) \exp[j2\pi\,(f_0 t + \tfrac{1}{2} k t^2)] \tag{8.20}$$

where $\text{rect}\,(Z) = 1 \quad \text{if} \quad |Z| < \tfrac{1}{2}$
$= 0 \quad \text{if} \quad |Z| > \tfrac{1}{2}$

τ' is then the pulse length, and $f_0 + kt$ is the instantaneous frequency. This can be rewritten in the form $s(t) = u(t) \exp[j2\pi f_0 t]$, and $u(t) = \text{rect}(t/\tau') \exp[j\pi k t^2]$ is the complex envelope function.

The time-frequency autocorrelation function is computed from Eq. (8.11). As previously stated, it is customary to normalize the signal to unit energy. In the present case this is accomplished by dividing $u(t)$ by $\sqrt{\tau'}$. Substituting in Eq. (8.11), one obtains

$$\chi_u(\tau,\nu) = \frac{e^{-j\pi k\tau^2}}{\tau'} \int_{-\infty}^{\infty} \text{rect}\left(\frac{t}{\tau'}\right) \text{rect}\left(\frac{t+\tau}{\tau'}\right) \exp\left[-j2\pi\,(k\tau - \nu)t\right] dt \tag{8.21}$$

For $0 \le \tau \le \tau'$ the limits of integration are $-\tau'/2$ and $(\tau'/2) - \tau$, since the integrand is zero outside this range. Thus for $0 \le \tau \le \tau'$, one can obtain

$$\chi(\tau,\nu) = e^{j\pi\nu\tau} \frac{\sin[\pi\,(k\tau - \nu)(\tau' - \tau)]}{\pi(k\tau - \nu)\,\tau'} \tag{8.22}$$

For $-\tau' \le \tau \le 0$, the limits are $-\tau'/2 - \tau$ and $\tau'/2$, and

$$\chi(\tau,\nu) = e^{j\pi\nu\tau} \frac{\sin[\pi(k\tau - \nu)(\tau' - |\tau|)]}{\pi(k\tau - \nu)\tau'} \text{rect}\left(\frac{\tau}{2\tau'}\right) \tag{8.23}$$

which is valid for all τ.

The time-autocorrelation function may be obtained from Eq. (8.23) by setting $\nu = 0$; thus

$$\chi(\tau,0) = \frac{\sin[\pi k\tau\tau'(1 - |\tau|/\tau')]}{\pi k\tau\tau'} \operatorname{rect}\left(\frac{\tau}{2\tau'}\right) \tag{8.24}$$

The right side of Eq. (8.24) resembles the expression usually given for the compressed pulse $(\sin\pi k\tau\tau')/\pi k\tau\tau'$ which is actually the response of an ideal lossless delay equalizer. The differences are the factor rect $(\tau/2\tau')$, which makes the true matched-filter output zero for $|\tau| > \tau'$, and the argument of the sine function, which in Eq. (8.24) contains an additional factor $(1 - |\tau|/\tau')$.

The zeros of Eq. (8.24) occur at those values of τ for which $k\tau(\tau' - |\tau|)$ is an integer. Since this is a quadratic expression in τ, the zeros are not uniformly spaced. The values of τ for which Eq. (8.24) has zeros are given by

$$|\tau| = \tfrac{1}{2}\tau'\left[1 \pm \sqrt{1 - \frac{4n}{D}}\right] \tag{8.25}$$

where $D = k(\tau')^2$ is the compression ratio. Note that the maximum integer n is less than or equal to one-fourth the compression ratio.

Simple pulse ambiguity function

The ambiguity function for a simple rectangular pulse is

$$\psi(\tau,\nu) = \left[\frac{\sin^2\pi\nu(\tau' - |\tau|)}{(\pi\nu\tau')^2}\right] \operatorname{rect}\left(\frac{\tau}{2\tau'}\right) \tag{8.26}$$

where τ' is the pulse duration. (This notation is used where pulse length might be confused with the time delay variable τ.) The function rect is the pulse function defined by Woodward [Eq. (8.20)]. The ambiguity function is normalized so that $\psi(0, 0) = 1$.

The linear FM chirp pulse in which the frequency varies at the rate k Hz/s has the normalized ambiguity function expressed in Eq. (8.23).

Comparison of Eqs. (8.23) and (8.26) shows that the only difference is that ν in Eq. (8.26) is replaced by $\nu - k\tau$ in Eq. (8.23). The result is that the surface represented by Eq. (8.23) may be obtained from that represented by Eq. (8.26) by translating every point (τ,ν) to the point $(\tau, \nu - k\tau)$. Such a translation is a *shear* of the function parallel to the ν axis (see Figs. 8.4 and 8.5). A cross section of the surface at constant τ is unaltered in shape or size but is shifted in the ν direction by an

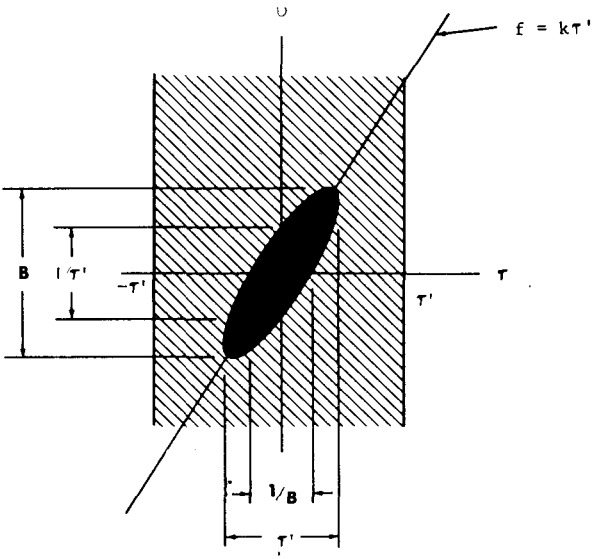

Figure 8.4 Ambiguity diagram for frequency-modulated pulse of sine wave.

amount proportional to τ. On the other hand, a cross section of the simple pulse ambiguity function at constant ν corresponds to a cross section of the FM ambiguity function along a line in the (τ,ν) plane having slope k with respect to the τ axis. These two cross sections have the same shape and for any given τ have the same amplitude, but the second is stretched relative to the first by the factor $\sqrt{1 + k^2}$. A more detailed figure is shown in Chap. 13.

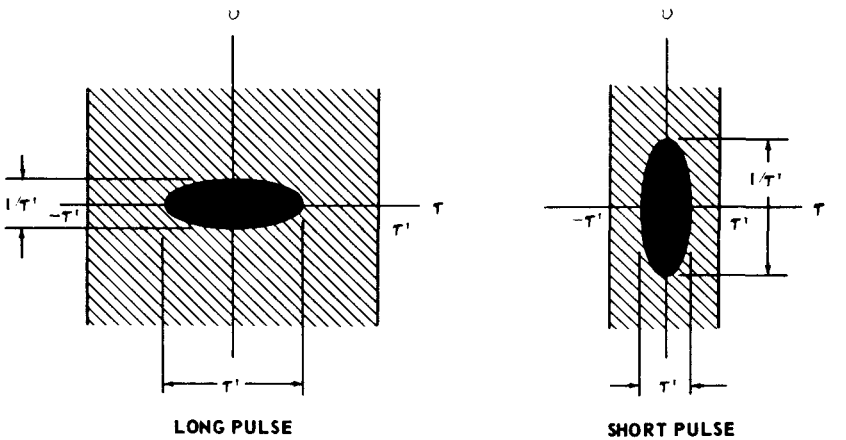

Figure 8.5 Two-dimensional ambiguity diagram for a single pulse of sine wave. (*After Siebert, IRE* [654])

A *top view* of the ambiguity diagrams for the FM pulse of bandwidth $B = k\tau'$ and for the single pulse of duration τ' is shown in Figs. 8.4 and 8.5. The dark areas generally represent the regions where the ambiguity function is above an arbitrary level (say 3 dB). The hatched areas represent the regions where $\psi(\tau,\nu)$ has a smaller but nonzero value. The hatched areas are often called the sidelobes of the ambiguity function.

Other waveforms

Ambiguity diagrams for many other common radar waveforms can be found in the literature [136; 677; 671, Sec. 10]. The coherent pulse-train waveform is generated by sampling a sinusoidal carrier with N pulses of duration τ'. The interpulse period (constant in this case) is T, and the time duration of the train is T_d as shown in Fig. 8.6A. The frequently illustrated ambiguity diagram for $N = 5$ is shown as Fig. 8.6B. The majority of volume of the ambiguity diagram can be seen to be distributed into a number of small area spikes that are periodic in range delay τ and Doppler ν. The hatched areas are called the Doppler ridges and are shown in more detail in Chap. 11. Note that there is a clear area of $T - 2\tau'$ between the ridges in the range dimension (as long as $T \gg 2\tau'$). If the undesired echoes can be placed in this region by choice of T and τ', they will not yield any response at the receiver output when the desired target is observed. The undesired echoes are then completely *resolved* from the target. The popularity of pulse-train or burst waveforms and pulse Doppler processors for multiple-target environments results from this interference-free region and the small area of the central lobe of the ambiguity function. It can be shown that there is no waveform that has a single isolated spike ambiguity diagram [597].

Relation to accuracy

The area and shape of the central lobe of the ambiguity function are directly related to the accuracy that target-range (time-delay) or target-radial velocity (Doppler shift) can be measured. The relations for range accuracy when velocity is known or Doppler velocity accuracy when range is known were given in Sec. 1.8. It can be shown that for a given S/N the range uncertainty is proportional to the extent of the central lobe on the time axis and the Doppler uncertainty is proportional to the extent of the central lobe on the Doppler axis [779, 671, 654, 244]. However, if both range and Doppler are unknown, there is a limit to the combined measurement of both. This is sometimes called the *radar uncertainty relation*. Rihaczek [568], based on the works of Gabor and Helstrom, showed that

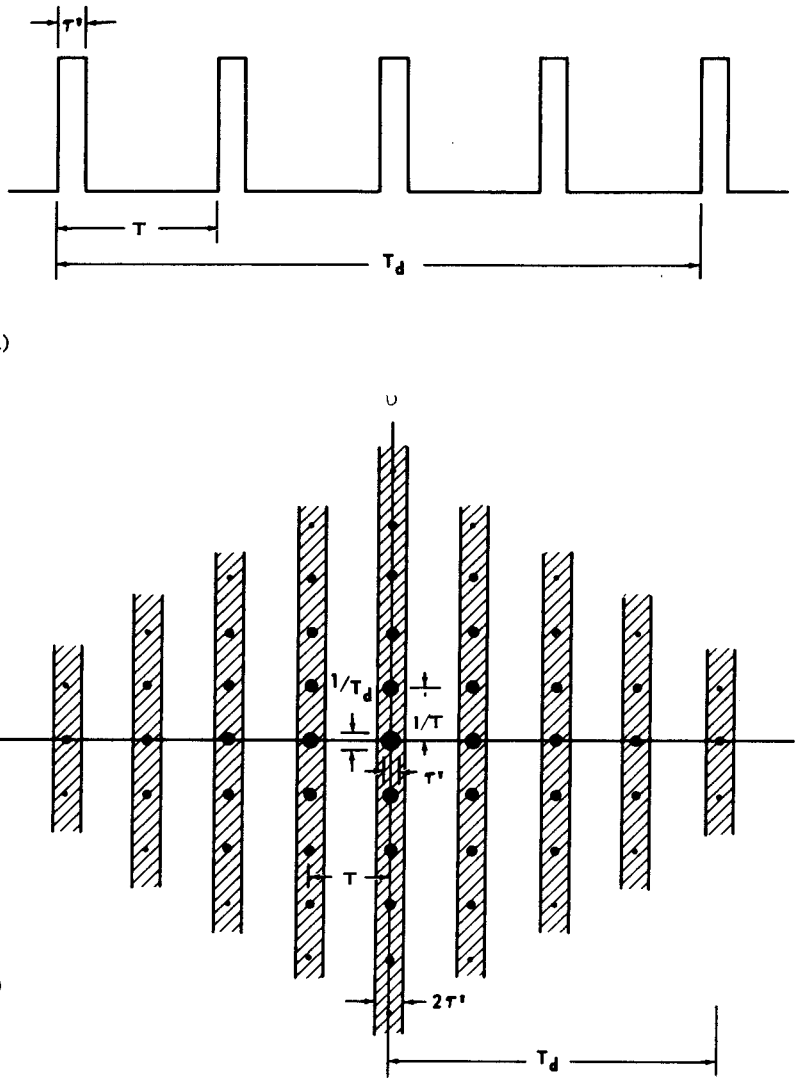

Figure 8.6 Ambiguity diagram for a pulse-train consisting of five pulses. (A) Waveform; (B) ambiguity diagram for (A). (*After Siebert* [*654*])

$$\beta^2 t_e^2 - \alpha^2 \geq \pi^2$$

$$\sigma_\tau = \frac{1}{\beta(2E/N_0)^{1/2}(1 - \alpha^2/\beta^2 t_e^2)^{1/2}} \tag{8.27}$$

$$\sigma_\nu = \frac{1}{t_e(2E/N_0)^{1/2}(1 - \alpha^2/\beta^2 t_e^2)^{1/2}} \tag{8.28}$$

Combining the above relationships

$$\sigma_\tau \sigma_\nu \leq \frac{1}{\beta t_e (2E/N_0)} \left[1 + \frac{\alpha^2}{\pi^2} \right] \tag{8.29}$$

where, as defined in Sec. 1.8, σ_τ and σ_ν are the rms range and Doppler uncertainties, β is the rms signal bandwidth, and t_e is the effective time duration of the waveform.* The term α is a phase constant that measures the linear FM content of the signal [603]. A high FM content can be shown to increase the uncertainty in simultaneous measurement of range and velocity. Unless $2E/N_0$ *or* S/N is extremely large, it is difficult to tell where the target is on the diagonal ridge of the FM ambiguity function. The resolution measurement properties of the linear FM waveform have been further clarified in a later paper by Rihaczek [605].

If there is no linear FM as in a uniformly spaced single-frequency pulse train or other amplitude-modulated waveforms ($\alpha \approx 0$), the uncertainty decreases as the time-bandwidth product $\beta\tau_e$ is increased. As in clutter rejection or countermeasures immunity, the time-bandwidth product is a useful measurement of the *quality* of a waveform.

8.4 The Radar Environmental Diagram (With J. Patrick Reilly)

The ambiguity diagram has been used as a tool for evaluating the choice of waveform in specific environments. It has proven quite successful for suggesting specific waveforms for resolving multiple targets in range or range rate and in certain highly specific clutter environments. With a surveillance radar system, which may simultaneously encounter several types of clutter with various spectral characteristics at unspecified locations, the ambiguity diagram alone is generally insufficient to make the choice of waveform. "In the extreme case, all signals (waveforms) are equally good (or bad) as long as they are not compared against a specific radar environment" [136, p. 70].

Chapters 6 and 7 have shown that different types of clutter have considerably different spectral, spatial, and amplitude distributions. Since the power reflected from land areas, sea surfaces, chaff, and precipitation often is far in excess of that from the target, it is necessary to choose the transmit waveform on the basis of these distributions. Fortunately, there are inevitably some bounds on the location, velocity,

* Fowle, Kelly, and Sheehan [244] derived similar relationships in terms of frequency-time correlation with somewhat different definitions for effective bandwidth and time duration. They also included a discussion of the effect of rotation of the axes of the ambiguity function on accuracy.

and intensity of clutter. The environmental diagram shown in Fig. 8.7 is a pictorial representation of a *"clutter threat"* or *"clutter model"* [503]. It can also be used to help suggest the appropriate waveform for a particular class of radars. The diagram in this form is useful for an air traffic control or air defense surveillance radar located at a coastal site.

The limits on the radial velocity of various types of clutter are given on the ordinate, while the range extent is indicated along the abscissa. In this example the scale is broken to allow all four major types of clutter to be presented simultaneously. Land clutter is shown extending from the origin to 10 km in range to represent the radar horizon for the particular location. The vertical extent of the bar is the standard deviation of the velocity spectrum for land clutter echoes from a wooded area with a 20-knot surface wind.* Density of the cross-hatching or shading can represent the reflectivity of the clutter of interest. Land clutter is shown as a solid bar to indicate that it generally has the highest reflectivity of any form of clutter seen by a surface-surveillance radar.

Sea clutter is modeled on the figure for a state 4 sea as a relatively intense type of clutter with a spectrum standard deviation of 1.0 m/s. It is shown centered at 3.4 m/s mean velocity. This is a reasonable value when looking directly into the wind or waves. On the other hand, the mean velocity may be zero when looking crosswind. The range of mean velocities $\pm V_0$ is given by the vertical dashed line to indicate that the cross-hatched region can be centered anywhere between ± 3.4 m/s. The cross-hatching is more dense near the radar to show that the reflectivity near the radar is higher than at the lower grazing angles near the horizon. It becomes obvious that these models are derived on a statistical basis. Whoever specifies a clutter threat model essentially defines under what conditions the radar system must meet full specifications. While there is a finite probability of sea state 7 occurring, it would be costly to expect full performance in that environment.

Figure 8.7 also models the clutter threat for a rainstorm that may occur 5 to 10 percent of the time. Mean velocities of 28 m/s are not uncommon at moderate altitudes. As was the case for sea clutter, crosswind values of the mean velocity of precipitation clutter drop to zero. The increase in the spectral width with range shows the combined effect of wind shear and the increasing vertical extent of the antenna beam at longer ranges. The standard deviation of the spectrum can be obtained from Chap. 6 when the beamwidth is known. Similarly, the mean radial velocity V_0 can be approximated by a linear increase with the height of the beam center or with slant range.

* The mean velocity of the trees V_0 is obviously zero.

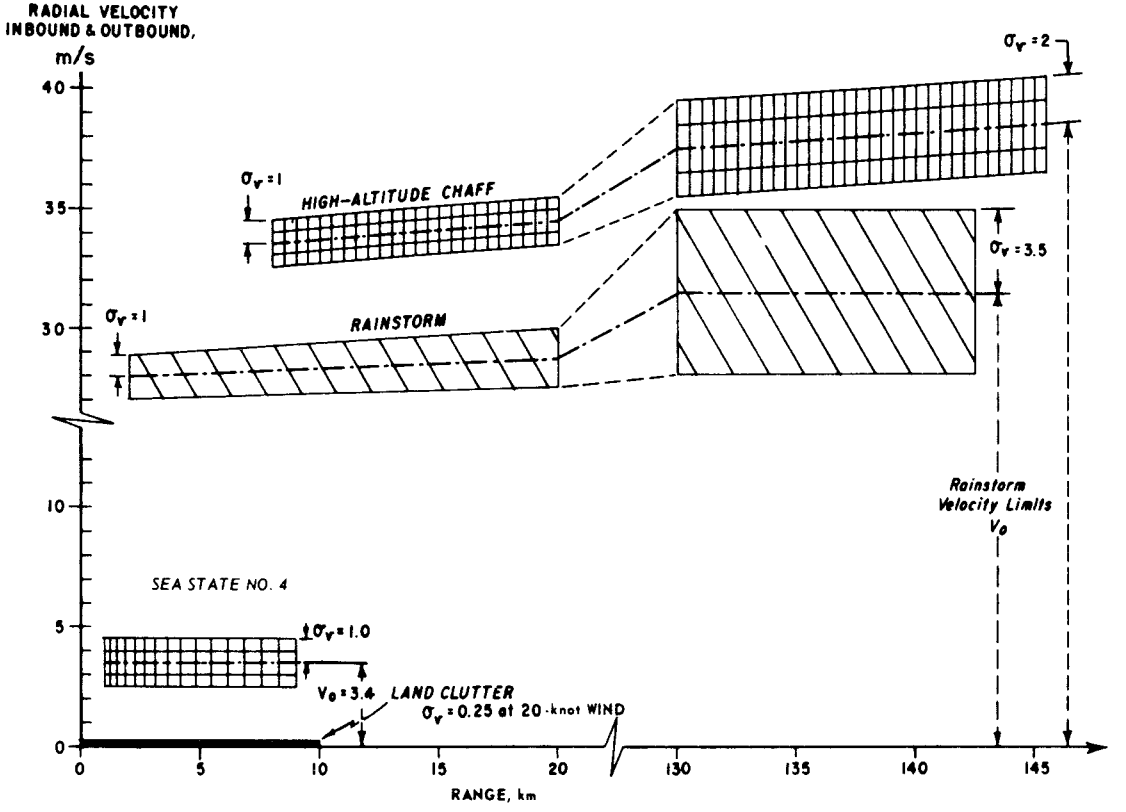

Figure 8.7 Environmental diagram for air defense radar.

Finally, a high-altitude chaff corridor is illustrated in the same format. At all altitudes chaff moves at the velocity of the prevailing winds. Since the vertical extent of a chaff corridor is usually less than that of a rainstorm, the standard deviation of the spectrum usually has a lower value at long ranges than for rainstorms.

In all of the examples given, the spectral width has been expressed in meters per second and must be multiplied by $2/\lambda$ to convert to Doppler frequency. The relationship between the physical motion of the clutter scatters and the spectral width has been found to conform to the Doppler equation throughout most of the microwave region of interest.

The cross-hatching for rain and chaff is shown in the figure to have lower density in the shear regions, indicating that the power spectral density of the echoes is lower for a given reflectivity than for signals with a narrow spectral width.* It should be noted that normalized reflectivity per unit frequency rather than received power spectral density is indicated by the cross-hatching.

Target-threat models can also be superimposed on this diagram, with the origin of the figure representing the radar location. This technique of presentation, sometimes called an *R-V* diagram, has been used to show the range and velocity bounds on a ballistic target with impact points near the radar site.

In its simplest form, the environmental diagram gives a pictorial description of the clutter and should aid the radar system designer by giving the numerical limits of the clutter characteristics for his design. If the carrier frequency is defined, the ordinate can be converted to hertz. If the radar performance in severe clutter is also desired (e.g., higher sea states, wind speeds, etc.) a second environmental diagram can be drawn.

Just as the ambiguity diagram is not a panacea for choosing waveforms in a multiple-target environment, the environmental diagram does not suggest a unique waveform for maximum clutter rejection although it may suggest certain desirable characteristics of the waveform or the processing technique. For example, if land echoes are the only clutter threat, a waveform and receiver response function with a *notch* or null at zero velocity, such as one obtains with a moving target indicator (MTI), is obviously desirable. For other types of clutter the MTI (see Chap. 9) technique must be modified. It is well known that MTI systems designed for land use do not work very well on ships since the location of the MTI notch may be in error by the mean Doppler of

* This is important in CW or pulse Doppler systems that may have a Doppler filter bandwidth that is narrower than the clutter spectrum.

the sea clutter V_0 relative to ship's motion. *Clutter-locked* systems, in which the ship's (or aircraft's) velocity and V_0 are removed by compensating for the relative mean velocity of the clutter, have considerably improved the performance that can be obtained on moving platforms.

If rain and chaff are part of the clutter threat, the required width of the notch and the mean compensating frequency are often excessive especially at the higher carrier frequencies; and other signal processing techniques must be used.

Since the axes of both the ambiguity and environmental diagrams can be drawn to the same scale, they can be superimposed to reveal range Doppler regions where clutter energy will be received. Preferably, the ambiguity diagram (AD) should be a transparent overlay, as its origin represents the expected target range and velocity. This location may occur over a large part of the environmental diagram (ED). The clutter outputs of a matched-filter receiver will then appear with the range Doppler characteristics defined by the intersections of the nonzero portions of the two diagrams. High clutter outputs will correspond to superposition of the dense areas on both diagrams, while the occurrence of either one alone will not yield a clutter output. In evaluating a search system, the origin of the AD must be successively located on the ED at all target range and velocities within the specified threat model. An intersection of a high sidelobe on an AD with a low-density rainstorm is obviously less serious than an intersection with high-density (large σ_0) land clutter.

The diagonal ridge on the AD for a linear FM search-radar waveform will obviously intersect with the rainstorm or chaff returns at some locations. The clutter output is then proportional to the *width* of the ridge. Since the width of the ridge (say at the 3-dB points) is inversely proportional to the time-bandwidth product or pulse compression ratio, the clutter output is minimized for high compression ratios.

With a stationary radar and a CW waveform (Chap. 10), there is no intersection of the narrow horizontal ambiguity ridge and the clutter regions on the ED for targets with radial velocities of greater than ± 40 m/s. Thus, if target detection is not required in the Doppler region corresponding to less than ± 40 m/s, the theoretical clutter output of narrow-band Doppler receiver filters is zero. As a result, the theoretical clutter rejection of a CW radar system is infinite. In practice, however, while the receiver output contains no high Doppler frequency clutter, the front end of the receiver often becomes saturated since it receives all of the clutter energy. CW system performance is generally limited by transmitter noise on the clutter echo, spillover signals, and the intermodulation products of all the clutter signals. Some special properties of ambiguity functions were addressed in the first edition [498].

8.5 Optimum Waveforms for Detection in Clutter

All of the waveforms discussed in Chaps. 9 through 14 are optimum for some particular clutter or ECM environment within the constraints of cost and complexity. The very short sinusoidal pulse waveform has a thin, vertical ridge ambiguity diagram. This thin ridge has a small common area with the distributed clutter regions of the environmental diagram. Similarly, a simple CW waveform may be the optimum for a surface radar if the targets of interest have a radial velocity in excess of 40 m/s. The purpose of this section is to briefly refer to some of the numerous studies of optimization for clutter environments.

Optimization when the relative Doppler shift is zero or unknown

The design of optimum processors for detecting signals in clutter has been approached from several directions [17, 1, 136, 535]. Urkowitz [722; 671, Sec. 12.4] considered the form of the optimum receiver when the interference was entirely clutter and the target may have the same radial velocity as the clutter. For stationary clutter, the received power spectrum is identical to the power spectrum of the transmitted signal. That is, $N(\omega) = |F(\omega)|^2 = F(\omega)F^*(\omega)$. Then, from Eq. (8.8) and neglecting time delay the *optimum* clutter filter transfer function can be written

$$H_{\text{opt}}(\omega) = \frac{K}{F(\omega)} \tag{8.30}$$

where $F(\omega)$ is the Fourier transform of the received signal and K is a constant. Since this filter would have an infinitely wide total bandpass, the analysis emphasized the more practical band-limited case. In this latter case, the improvement I in signal-to-clutter ratio S/C was found to be proportional to the receiver bandwidth in the absence of receiver noise. In the usual case when noise is present, it has been shown by Manasse [460], Rihaczek [606], Brookner [95], Urkowitz [725], and others that increasing the signal bandwidth and using a matched filter is a better solution than merely increasing bandwidth when there is no Doppler separation of targets and clutter or when the separation is unknown.

In Manasse's study it was assumed that the clutter consisted of a large, randomly distributed ensemble of very small independent point scatterers. He showed that the transfer function of the optimum filter when noise is present is given by

$$H(f) = \frac{F^*(f)}{(N_0/2) + k|F(f)|^2} \tag{8.31}$$

where $N_0/2$ = the (additive) receiver noise spectral density
k = *a constant*
$|F(f)|^2$ = the energy spectrum of the received signal

Manasse also showed that the single-pulse optimum signal-to-total interference ratio can be expressed as

$$\left(\frac{S}{N+C}\right) = A^2 \int \frac{|F(f)|^2}{N_0/2 + k|F(f)|^2}\, df \tag{8.32}$$

The constants A and k are determined by the nature of the target and clutter echoes and the geometry. Two important conclusions were drawn for the single pulse case from the relationship of Eq. (8.31).

1. When no clutter is present $S/(N + C)$ depends only on signal energy-to-noise density as shown by matched-filter theory.
2. When noise is negligible $N_0 = 0$ or when clutter is dominant $C \gg N$, $(S/N + C)_{\text{opt}}$ depends only on effective system bandwidth and does not depend on transmitted pulse energy (i.e., the Urkowitz [722] result).

It was also shown that when the spectrum of the pulse is flat as with a rectangular envelope linear FM or chirp pulse, a further improvement is obtained.

Rihaczek [606] expanded the work of Urkowitz, Manasse, and others and showed that for negligible differential velocity between the target and clutter the matched filter is nearly the optimum filter whenever the clutter-to-noise ratio is less than 5. He also studied the case when there is a differential Doppler ν_0 between target and clutter. In that case the bracketed term in the denominator of Eq. (8.32) is replaced by $|F(f - \nu_0)|^2$. The optimum waveform is then obtained when $F(f)F(f - \nu_0) = 0$ for $F(f) \neq 0$. This is essentially stating that the ambiguity function of the signal should have no volume at those portions of the time-frequency plane where the Doppler shift is ν_0.

Analytical and numerical results of this type were also obtained by Brookner [95] who emphasized that the existence of an optimum filter is dependent on the presence of nulls in the signal spectrum. A knowledge of the target-clutter Doppler is extremely important in taking advantage of the nulls. Westerfield, Prager, and Stewart [767] presented a study of waveform optimization for the noise-free case but where the target has a Doppler shift and the clutter has a spectral spread. Using the ambiguity function, they show that the spectrum of the transmit signal should either be much narrower or much wider than the clutter spectral spread.

This discussion has neglected the analyses of the multiple-target environment in the preceding references. The reduction of close-in (proximal) range or Doppler *sidelobes* of the ambiguity diagram for a given waveform is reserved for later chapters.

Optimization based on relative Doppler shift

The previous analyses emphasized the optimization for waveforms that were constrained to a single envelope and the target-to-clutter differential was not known. There has also been a considerable effort in optimizing performance in clutter when there is known to be a significant Doppler shift. The best known example is the MTI processor (Chap. 9) where a null in the spectrum of the received echo is placed at the mean Doppler velocity of the clutter. It is shown that rejection of clutter signals having finite spectral width is improved as the number of cancellation stages is increased. Thus, the optimum *waveform* becomes the coherent pulse burst or pulse train (Chap. 11), and the MTI processor is a clutter-rejection filter rather than a matched filter. However, it will be shown that when target velocity is unknown, increasing the number of pulses (the total energy) does not improve the signal-to-noise ratio when the MTI processor alone is used. Thus, a further optimization is to cascade an MTI clutter-rejection filter with a matched filter for the pulse train (see Kroszezynski [416] and Kaiteris and Rubin [380]). This is now called the MTD (Chap. 14).

The optimization of pulse-train waveforms and processors has been studied in a number of excellent references [17, 171, 380, 589, 601, 626, 628, 678].

Many of the specific cases are examined in Chaps. 11 and 14. However, it is worthwhile at this time to point out a pitfall in using the basic ambiguity function to compute the performance of a long pulse-train waveform in an extended clutter environment (i.e., *uniform* rain). This results from the general assumption given in Sec. 8.2 that the echo from a given scatter at any location in the time-frequency plane of the ambiguity diagram yields the same power at the receiver. With this assumption the range dependence $P_R \sim 1/R_n$ is neglected. It can be seen from the data in Chaps. 5 through 7 that the value of the exponent n is 4 for point targets, 2 for uniform volume scatterers and 3 to 4 for surface clutter. The range-law dependence can severely degrade the performance obtained from long-duration waveforms when distant targets must compete with *ambiguous* close-in clutter.

While it would be nice to give a new set of guidelines for general waveform design when the environment is not well defined, I will suggest only two that have been inferred but not stated explicitly.

1. The time duration of the waveform should be either very much greater than or much less than the time delay to the target when the target is at a range where detection is mandatory.
2. The spectral spread of the transmit waveform should be either very much greater than that of the clutter or very much narrower than that of the clutter. However, the minimum spectral spread should not be much less than the spectral width of the target echo.
3. Complex environments are resulting in radars with multiple modes, preferably with adaptive selection of waveforms and filter shapes.

While much has been learned from Woodward's ambiguity diagram, it seems fitting to close with a timely quotation by Woodward made about 14 years after his book was published [780].

> *A Futility Theorem*
>
> There is continued speculation on the subject of ambiguity clearance. Like slums, ambiguity has a way of appearing on one place as fast as it is made to disappear in another. That it must be conserved is completely accepted but the thought remains that ambiguity might be segregated in some unwanted part of the *t-f* (time-frequency) plane where it will cease to be a practical embarrassment.

He then proceeded to dispose of "grandiose clearance schemes."

8.6 Desirability of Range Doppler Ambiguity

It can be seen from the discussion in this chapter and in Chaps. 9 through 14 that there are common waveforms that yield a wide variety of ambiguity function shapes. The contours of the mainlobe (at 3 dB down from the peak) may be circular or elliptical with either large or small enclosed areas. The major axis of the elliptical shapes may be parallel to the range axis as with a CW transmission or parallel to the Doppler axis as with a short-pulse transmission. As was shown in Sec. 8.2, it may be a diagonal ridge with the rotation angle controlled by the change of carrier frequency per unit time. The contours of the mainlobe of the ambiguity function may also have relatively small area by displacing some of the total volume to other regions of the ambiguity plane. This may be achieved with pulse-train waveforms (Chap. 11) or *noiselike* phase-coded waveforms (Chap. 12). It is shown in later chapters that the relative location of the target and the clutter or false target regions on the ambiguity plane may be the dominant factor in the choice of waveform. This section points out some general hardware considerations that also affect the choice of waveform class and hence the ambiguity function shape.

The area of the ambiguity plane that is of interest for this discussion is a rectangle with dimensions determined by the maximum target range R_m and the maximum target Doppler frequency $\pm f_{dm}$ (assuming equal positive and negative maximum radial velocities). This may be called the range Doppler coverage area. Let the 3-dB contour of the central lobe of a thumbtack-type ambiguity function have a small area determined by $1/T_d$ in Doppler where T_d is the effective coherent transmission time and by $c/2B$ in range where c is the velocity of light and B is the effective or rms transmission bandwidth. Then the number of range Doppler *cells* to be examined n for a target is approximately the ratio of the area of the target *rectangle* to the mainlobe *rectangle* of the ambiguity diagram of the waveform. With a consistent definition of T_d and B this can be expressed as

$$n \approx \frac{4R_m f_{dm} BT_d}{c} \tag{8.33}$$

This relation merely states that the use of thumbtack-type ambiguity functions with large time-bandwidth products BT_d requires that many range Doppler cells be examined for the existence of a target. In most waveform-receiver combinations the range cells appear sequentially at the receiver output. Thus, it is necessary to examine $2T_d f_{dm}$ Doppler channels per range cell to determine the presence of a target. For example if the waveform has a duration of 0.1 ms and the maximum target Doppler f_{dm} is $\pm$ 50 kHz, approximately 10 Doppler channels must be instrumented. If the required transmission bandwidth B for clutter reduction, target resolution, or accuracy is 2 MHz and the maximum range coverage R_m is 164 nmi ($2R_M/c$ = 2.0 ms), these Doppler channels must be examined for 4000 range cells.

In one sense this thumbtack ambiguity resulting from the use of a *noiselike* waveform is optimum if unambiguous target location in both range and velocity are required. However, the price of instrumenting the 10 Doppler channels per range gate may in some cases be exorbitant compared with the total radar cost. It is possible to reduce the hardware complexity if some ambiguity in target location in range and Doppler is permissible. For example, the transmission bandwidth requirement may be needed for clutter reduction only, and, from a system standpoint, exact determination of range or velocity is superfluous. In this case a waveform with a range Doppler ambiguity such as linear FM (chirp) may be adequate. The central lobe of the linear FM ambiguity function contains about $2T_dB$ resolution cells although many of these are generally outside the target range Doppler coverage. Then the output of the single channel FM matched filter can be said to contain simultaneous observations of a larger portion of the range Doppler coverage than with a noiselike transmission.

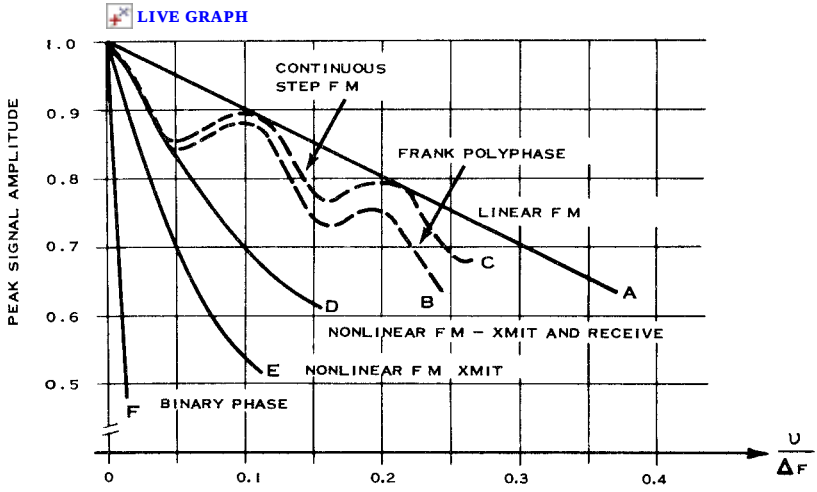

Figure 8.8 Signal amplitude versus normalized Doppler shift for waveforms with different degrees of range-Doppler coupling.

Various types of waveforms have different tolerance to Doppler shifts or *range Doppler coupling factors* [136, Chap. 9; 604, 526]. Some examples are shown in Fig. 8.8. The ordinate is the moving-target echo amplitude at the output of the receiver normalized to the stationary-target output amplitude. The abscissa is the normalized Doppler shift ($\nu/\Delta f$). With the parameters of the foregoing example, the frequency deviation of the waveform Δf is 2 MHz and the maximum Doppler shift is 50 kHz. Then the maximum normalized Doppler shift is defined as $f_{dm}/\Delta f$ or 0.025 in this case. The assumption for this figure is that there is only a single Doppler channel implemented to reduce hardware cost while accepting the loss in signal-to-noise ratio. If the reduction in amplitude is slight at f_{dm}, the hardware saving may be justified. The waveforms studied, the time-bandwidth product of the examples, and the references for the data in this text and elsewhere are

1. Linear FM or chirp $T_dB = 100$, Chap. 13 ([136, Chap. 9]).
2. Frank polyphase code $T_dB = 100$, Chap. 12 [136].
3. Contiguous step FM $T_dB = 100$, Chap. 13 [136].
4. Nonlinear FM with Taylor spectrum weighting on transmit and receive $T_dB = 50$, Chap. 13 [526].
5. Nonlinear FM with Taylor spectrum weighting on transmit $T_dB = 50$ [526].
6. Binary phase code $T_dB = 63$, Chap. 12.
7. Linear FM with Taylor weighting on receive $T_dB = 50$ [526].

It can be seen from Fig. 8.8 that the linear FM waveform has the most tolerance to Doppler shift. At $\nu/\Delta f = 0.025$ there is a negligible signal loss and the 10 Doppler channels need not be implemented. However, there is considerable ambiguity in the simultaneous determination of range and velocity. This ambiguity is the price paid for a single-channel receiver. It can also be seen that the contiguous step FM (stepped chirp), the Frank polyphase codes, and the particular nonlinear FM on transmit and receive used in the example also yield less than 1-dB signal loss at $f_d/\Delta f = 0.025$. The binary phase-code waveform with $TB = 63$ yields very poor performance at a normalized Doppler shift of 0.025 unless the appropriate Doppler channels are implemented. The curves of Fig. 8.8 are only appropriate for the time-bandwidths specified.

There is another factor to be considered when multiple targets may be encountered. The time (range) sidelobes increase when there is a significant Doppler shift. Waveform and receiver filter combinations that have small ambiguities on the range axis, $[|\chi(\tau,0)| \ll |\chi(0,0)|]$ often have substantial ambiguity (sidelobes) for $f_d \geq \frac{1}{2} T_d$. This can be seen from Fig. 8.9. The nonlinear FM transmit waveform E that had about a 2-dB signal loss at $\nu/\Delta f = 0.025$ has about -9-dB peak range sidelobes. On the other hand the linear FM waveform with Taylor weighting on receive maintains a -33-dB range sidelobe level.

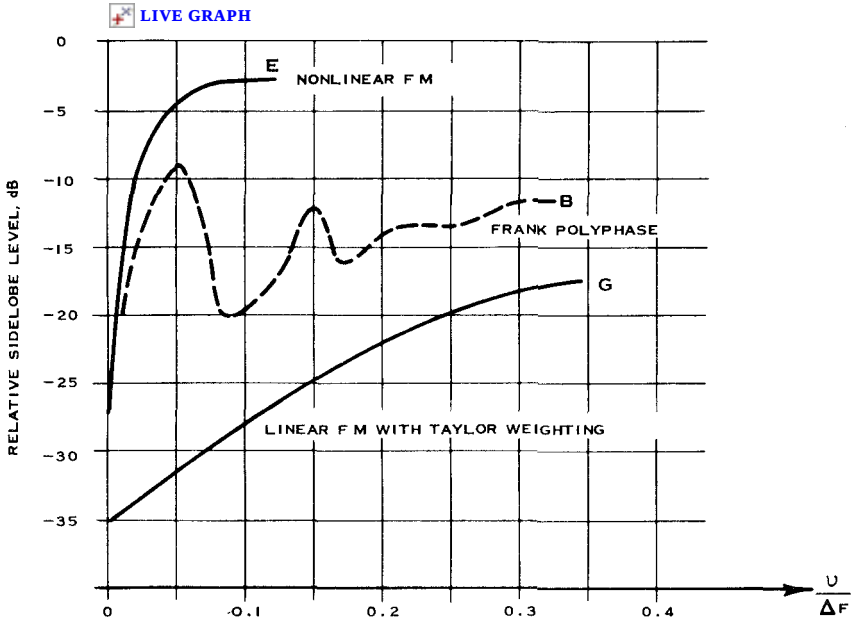

Figure 8.9 Ratio of mainlobe to sidelobe peak of ambiguity function versus normalized Doppler shift for waveforms with high FM content. [*136, 526*]

In a similar manner the pulse-train waveforms with their "bed of nails" ambiguity functions may have more than one peak in the range-Doppler coverage. The adverse effect of these ambiguous peaks with extended clutter is discussed in Chap. 11. When clutter is not a problem, the ambiguities in range or Doppler may be tolerable and result in simpler hardware. The parameters of many current pulse Doppler systems deliberately have ambiguities in one coordinate of the ambiguity plane to achieve accuracy or resolution in the orthogonal coordinate.

The essential point of this section is that when ambiguities in the range Doppler coverage can be tolerated there may be considerable hardware savings. This is perhaps the primary reason for the continuing popularity of chirp systems in current radars. Alternately, ambiguity in certain regions of the range Doppler coverage can be traded for accuracy or resolution in range or Doppler as with pulse-train waveforms.

8.7 Classes of Waveforms

In subsequent chapters the various waveforms and their properties are addressed. There are numerous options and the designer or evaluator must determine which is appropriate to the task. The family of the widely used radar waveforms is summarized in Fig. 8.10 (polari-

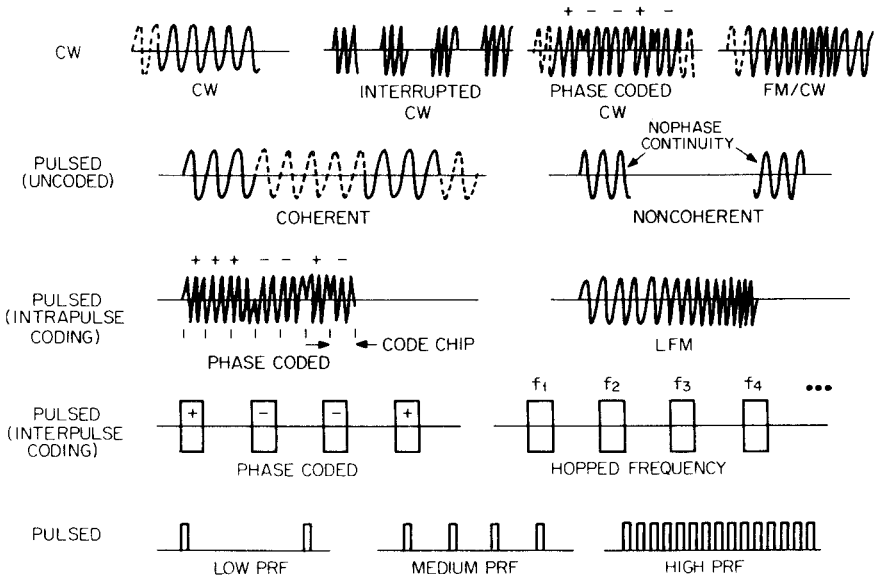

Figure 8.10 A partial listing of the family of radar waveforms. (*Courtesy of Technology Service Corporation*)

zation and impulse radars are not included). The first row is the continuous wave or CW types. They are most appropriate where determining velocity is the major goal, such as in traffic radars where Doppler resolution of targets and clutter is critical and determining range is less critical, and in shorter-range systems. The pulsed waveforms may be coded or uncoded. They may be coded within a pulse (*pulse compression*) or from pulse to pulse. Finally, the pulsed systems are typically denoted by *low PRF* where range is unambiguous but Doppler may be ambiguous; *medium PRF* where both range and Doppler are likely to be ambiguous; and *high PRF* where range is ambiguous but Doppler is not. Pulsed systems are obviously used where range resolution and accuracy are desired, and if high clutter rejection is desired, there is coherency from pulse to pulse.

The coherent pulse-train waveform is almost always required for surveillance radars where some ranging is desired and high clutter rejection (>35 dB) is necessary. Figure 8.11 illustrates terminology commonly used to describe pulse-train waveforms. While there is no standard, this terminology is utilized in almost all of this book and in many others. In newly designed systems it is common to implement 10 or more possible waveforms for ground-based surveillance and track-while-scan systems, while airborne fire control systems may have 25 or more.

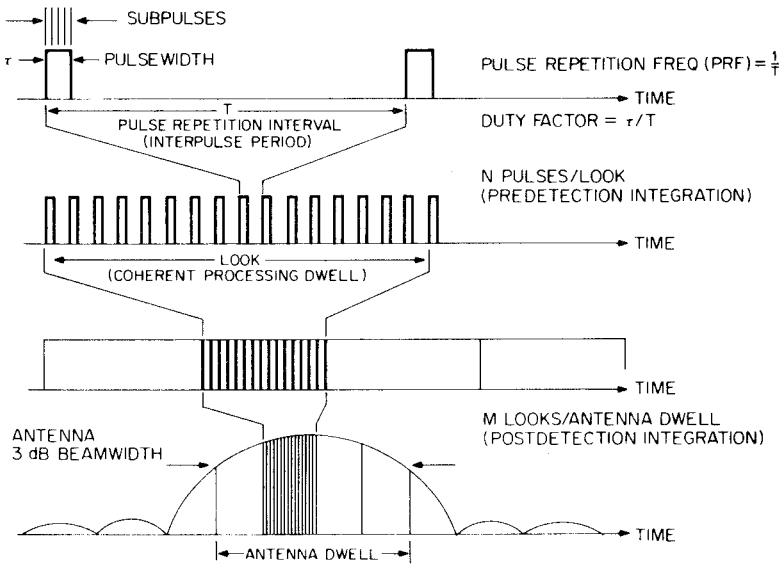

Figure 8.11 Pulse train radar waveform terminology. (*Courtesy of Technology Service Corporation*)

Classically, high PRF waveforms were used for airborne fire control. The systems worked well for closing intercepts with high Doppler. When there is a crossing target or tail chase, medium PRF appears to be the waveform of choice, with some sacrifice in maximum range. Low PRF has not been as successful due to inability to keep the clutter notches located at the surface clutter Doppler when implemented on a high speed platform that induces clutter spreading.

To evolve or evaluate a complex system it is necessary to examine the pulse-train properties and losses from Chaps. 9, 11, and 14 and also the coding within a pulse described in Chaps. 12 and 13.

8.8 Digital Representation of Signals

The understanding of digital signal processing is greatly enhanced if digitized signals are represented by complex numbers: in this representation, for example, a single-frequency sine wave signal is depicted as a rotating phasor. In addition to a certain mathematical convenience, however, there are practical equipment advantages to using complex signal representations. In terms of implementation, complex signals are derived by separating real signals into in-phase (I) and quadrature (Q) components. Some of the advantages which accrue from the use of I-Q processing become apparent in subsequent sections.

Figure 8.12 shows the method by which I and Q channels are derived from a single-channel input signal. The signal is a single-frequency sine wave frequency $\omega_0 + \omega_1$, with an amplitude A and an arbitrary phase angle Φ_0 at $t = 0$. In this example it is assumed that ω_0 represents the I-F center frequency. An oscillator provides coherent I and Q reference sources given by $2 \cos \omega_0 t$ and $-2 \sin \omega_0 t$, respectively. After the signal is mixed with the I and Q reference sources, the products are low-pass filtered to retain the difference in frequency terms. This results in the signal being split into in-phase and quadrature components, which are given by

$$\mathrm{I} = A \cos (\omega_1 t + \Phi_0)$$
$$\mathrm{Q} = A \sin (\omega_1 t + \Phi_0)$$

This pair of signals can then be thought of as a complex signal $\mathrm{I} + j\mathrm{Q}$. If the I and Q channels are now sampled and the analog samples converted to a sequence of digital numbers, x_k in the I channel and y_k in the Q channel, the resultant sample pairs can be considered to be complex digital words $A_k = x_k + jy_k = |A_k| \exp (j\Phi_k)$. In this form, the successive sample pairs can be thought of as a sequence of digitized phasors with magnitudes $|A_k|$ and successive phase angles Φ_k. In the foregoing example of a single sine wave input signal

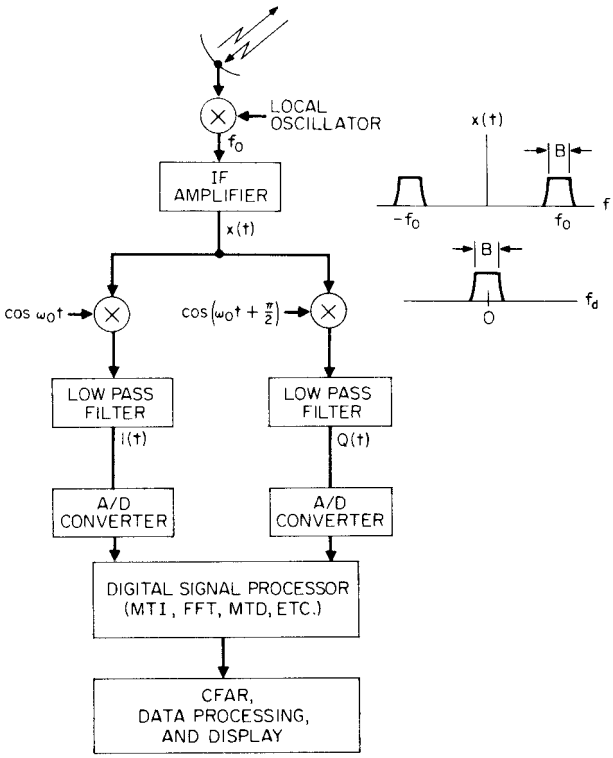

Figure 8.12 Introduction of digital processing into radar system.

$$x_k = A \cos(\omega_1 t_k + \Phi_0)$$
$$y_k = A \sin(\omega_1 t_k + \Phi_0)$$
$$|A_k| = A$$
$$\Phi_k = \omega_1 t_k + \Phi_0$$

where t_k = the successive sampling times

The complex digitized signal can be thought of as a sequence of rotating phasors of constant amplitude A, which rotate through a phase angle $\Delta\Phi_1$ between successive samples. In Doppler radar, this represents the target moving toward or away from the radar by a fraction of a wavelength. The amount of phase shift $\Delta\Phi_1$ depends on the frequency of the input signal f_1. This signal representation is shown in Fig. 8.13 in which a counterclockwise rotation is chosen as the positive direction.

If the input signal has a Fourier amplitude spectrum with handwidth B, then after mixing with the I-Q reference and low pass filtering, the

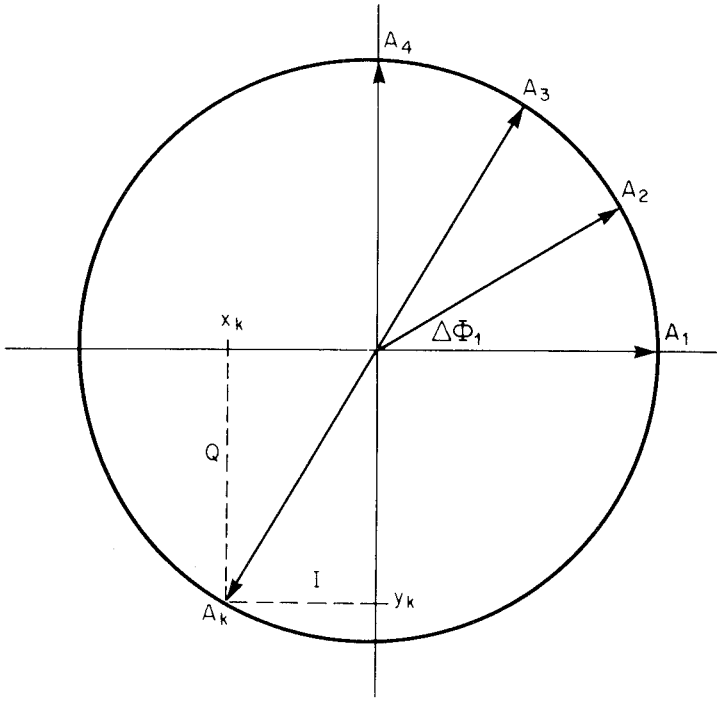

Figure 8.13 Rotating phasor representation of a complex digital signal.

amplitude spectra at the input to the I and Q channel converters will be positioned at zero frequency as illustrated in Fig. 8.12.

In a signal channel processing system, shifting a signal spectrum down in frequency makes it impossible to separate positive and negative frequency components. This is the spectral foldover phenomenon. When both in-phase and quadrature channels are utilized, however, the spectrum may be treated as if such spectral foldover does not occur. Although foldover does occur in each channel, the 90° phase relationship between the two channels makes it possible to recover the original undistorted spectrum if the channels are properly processed.

The lack of foldover is one of the advantages of I-Q processing. As a practical matter, although two A/D converters are required for I-Q processing, each can operate at half the speed required in a single-channel processor. The sampling theorem requires that the A/D in each channel sample the signal at rate $f_s = 2f_{\max} = B$ samples/s. (Note that one always wants to keep the maximum video frequency as low as possible in order to use the slowest speed and hence cheapest A/D possible.)

There is a small loss for not having continuous sampling. If one knew

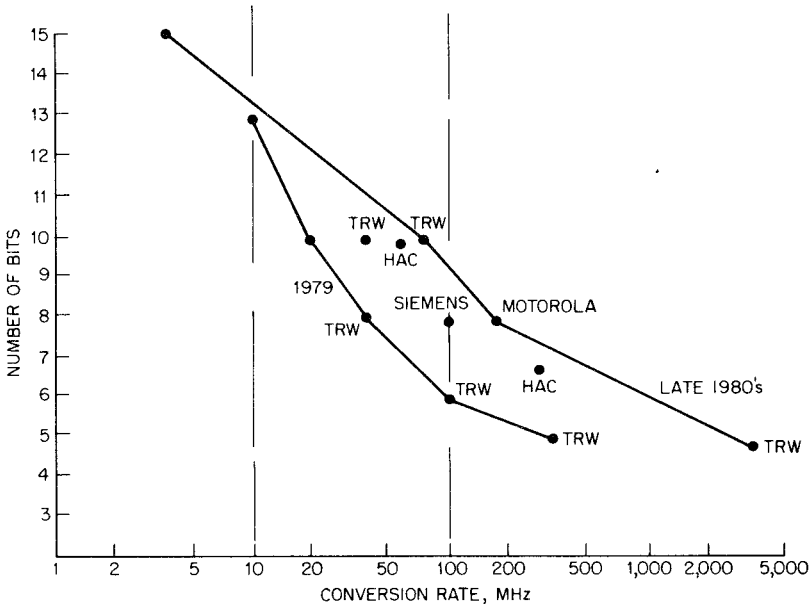

Figure 8.14 Analog-to-digital converter technology.

the exact time of the peak of the matched-filter output, sensitivity could be improved by about 0.6 dB at low false-alarm probabilities. Since target range is unknown prior to detection, this is an unreasonable goal. Most of the 0.6 dB can be gained with sampling at $2B$ samples/s.

Note that the total number of samples collected in T seconds will be $2BT$ for the single-channel system. For the dual-channel (I-Q) system, the number of samples collected in T seconds will be BT for each channel. Hence the total number will be $2BT$ for this case also, as one would expect if the sampling theorem requirements are to be met.

As with all microelectronic circuitry, the technology of A/D converters is advancing rapidly. However there is high cost and complexity in using the state-of-the-art technology. In the past, the newest devices were inaccurate in the lowest bits, and often had undesired transients. It is preferable to design for a speed slower by a factor of 2 to 4 than what is possible. Alternately, two slower-speed A/Ds can be used, with each sampling every other range gate. Figure 8.14 illustrates the technology of the late 1980s. The problems of centering high-dynamic-range signals in the A/Ds and the potential losses are discussed with respect to MTI in Chap. 9 and with respect to pulse Doppler processors in Chap. 14.

Chapter

9

Moving Target Indicators (MTI)

J. Patrick Reilly

MTI systems comprise the most widely used class of radar processors for detecting moving targets in a background of clutter. Clutter is distinguished from receiver noise by its relatively narrow, low-frequency spectrum, which implies that these echoes are correlated from one sample to the next. Because of this property it is possible to reduce the effects of clutter with filters that reject energy at clutter frequencies but pass the Doppler-shifted echoes from targets having higher velocities than the clutter. A processor that distinguishes moving targets from clutter by virtue of the differences in their spectra is called a moving target indicator or simply MTI. The simplest MTI processor, the single delay-line canceler, subtracts two successive echoes from the same location; reflections from stationary objects cancel, while those from moving targets produce fluctuating signals. When an MTI processor is cascaded or combined with a pulse Doppler processor, it is usually referred to as a *moving target detector* (MTD). Principles of MTD processing are discussed in Chap. 14.

MTI processors built around delay-line cancelers have been used since World War II. Early systems were primarily limited by system

instabilities such as oscillator incoherence. Subsequent equipment refinements have in many cases shifted the main source of limitation from equipment instabilities to the characteristics of the clutter itself.

MTI canceler systems maximize signal-to-clutter ratios only for highly correlated interference. It should be understood that, to maximize the signal-to-noise ratio, the radar system must also contain a matched filter for the individual pulses. It is also assumed that the clutter-to-noise ratio is large. It is meaningless to speak of clutter power being reduced to levels that are below the basic thermal noise limitation.

Several basic types of MTI processors have been implemented. One distinction between them is the type of information processed in the returned signals, that is, whether the phase, the amplitude, or both phase and amplitude are processed. Systems that use only phase or amplitude do not match the performance of those systems that use both phase and amplitude. Virtually all modern systems use quadrature channel processing, which is equivalent to amplitude and phase processing (see Sec. 9.3). Nevertheless, it is worth discussing other types of MTI processors since many of these are still in use.

9.1 MTI Configurations

Phase-processing MTI

The main elements of the phase-processing MTI system are illustrated in Fig. 9.1. Because the system must distinguish moving targets from stationary clutter by virtue of the target's Doppler frequency, the phase coherence within the system itself must be held within close tolerances. This coherence is provided by a *stable local oscillator* (STALO) and a *coherent oscillator* (COHO) that establishes the intermediate frequency. The STALO translates the signal from the transmitted RF to an intermediate frequency. The COHO provides a reference signal for coherent detection of the received echo. In the simplest processor this phase-detected signal is processed in a delay-line canceler that forms the difference between two signals separated in time by the interpulse period. One branch of the canceler circuit in an analog system contains a *bandpass equalizer,* whose function is to match the frequency response of the delay-line branch. The operation of the MTI system when both signal and clutter are present is analyzed by considering their separate effects. This is a valid approach only if the system is linear. The addition of a limiter (shown as an option in Fig. 9.1) affects the signal-to-clutter ratios as discussed in Sec. 9.4.

Consider the operation of the canceler in response to an echo from a target at a particular range R_0. The signal presented to the canceler is

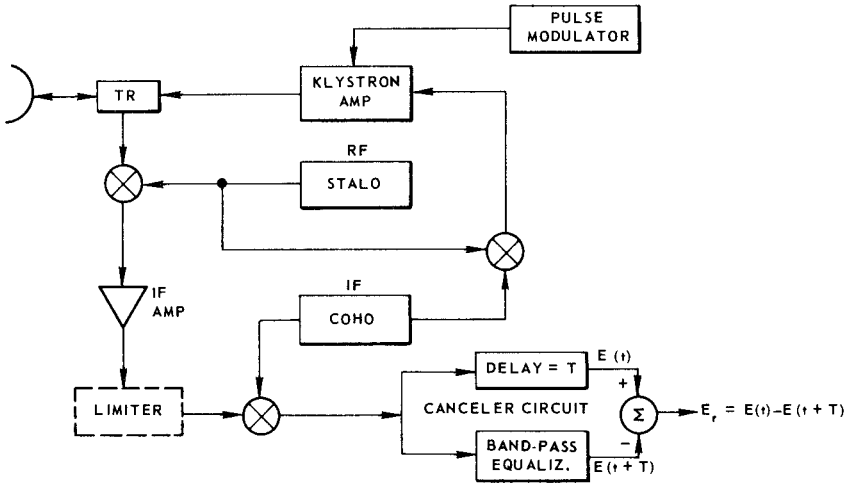

Figure 9.1 Phase-processing MTI system.

$$E_1 = E \sin (2\pi f_d t + \varphi_0)$$

where φ_0 = the phase shift due to range = $4\pi R_0/\lambda$ (relative to that of the reference oscillator)
E = the amplitude of uncanceled signal
f_d = the Doppler frequency

The signal at an interpulse period later is

$$E_2 = E \sin [2\pi f_d(t + 1/f_r) + \varphi_0]$$

where $1/f_r = T$ is the pulse repetition time. The signal output E_r from the canceler is

$$E_r = E_1 - E_2 = -2E \sin \left(\frac{\pi f_d}{f_r}\right) \cos \left[2\pi f_d \left(t + \frac{1}{2f_r}\right) + \varphi_0\right] \quad (9.1)$$

One assumption implicit in this formulation is that each branch of the canceler has unity power gain. In later analyses this same assumption is made when considering clutter alone. No loss of generality is incurred when calculating signal-to-clutter ratios since the gain cancels in the ratio. As Eq. (9.1) indicates, the difference voltage is a sine wave at the Doppler frequency whose amplitude depends on the relationship between the Doppler frequency and the pulse repetition frequency. The solid line of Fig. 9.2 describes the gain of the canceler circuit as a function of Doppler frequency. In this figure S_0 and S_i represent the peak output and input signal power. Notice that certain

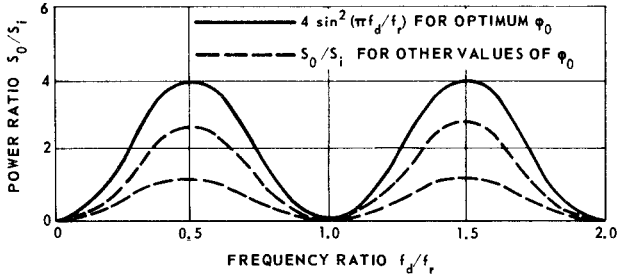

Figure 9.2 Power response of single-delay processor.

Doppler frequencies exist for which the output is zero. They occur whenever

$$f_{d\ \text{blind}} = nf_r \qquad n \text{ an integer} \tag{9.2}$$

The corresponding *blind speeds* are

$$V_{d\ \text{blind}} = \frac{\lambda}{2} nf_r \qquad n \text{ an integer} \tag{9.3}$$

As explained in Sec. 9.5, the signal power gain equals 2 when averaged uniformly over all values of f_d/f_r.

The MTI systems under consideration are pulsed systems. Therefore, a target's signal does not have the appearance of a continuous sinusoid at the Doppler frequency; rather the MTI output for a target echo can be considered to consist of a sample of the voltage E_r [Eq. (9.1)]. The value of the difference signal depends on the phase φ_0. As illustrated by the dashed curves of Fig. 9.2, *blind phases* exist in addition to the blind speeds. These phase nulls may be eliminated with quadrature processing. The loss resulting from blind phases is not as serious a problem as the loss caused by blind speeds if there are many transmit pulses per beamwidth. However, the loss associated with using only a single quadrature channel can be significant compared with dual-channel performance [505]. For example, the penalty associated with single-channel operation without postdetection integration is 4.4 dB at $P_d = 0.5$, and 10.7 dB at $P_d = 0.9$, with $P_{\text{fa}} = 10^{-6}$. This loss drops with integration—with a Swerling case 2 target, the loss is about 2.5 dB for two integrations, and drops slowly to 1.5 dB for infinite N; with a Swerling case 1 target, the loss can be estimated by assuming that the single-channel system has one-half the number of pulses as a dual-channel system [764]. The radar designer may be willing to accept the additional loss in order to conserve hardware.

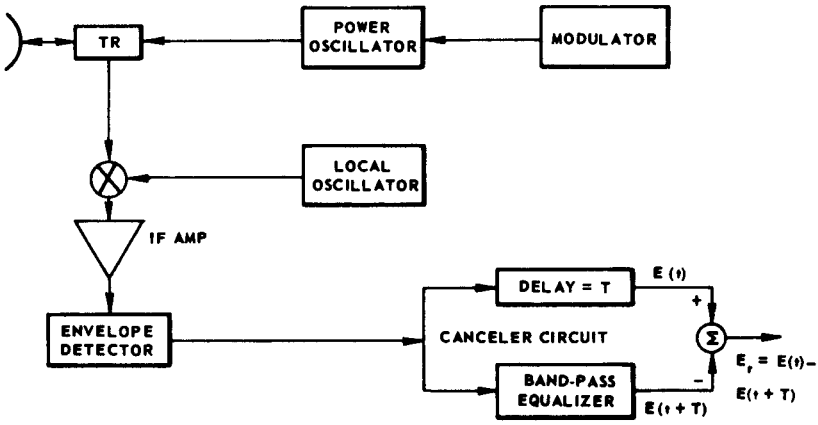

Figure 9.3 Envelope-processing MTI system.

Amplitude-processing MTI

The amplitude-processing or, more correctly, *envelope-processing* MTI, diagrammed in Fig. 9.3, is one example of what is termed a *noncoherent* system in other literature. An advantage of this system is that the local oscillator need not be as stable as in other systems. A disadvantage of this system is, paradoxically, that clutter must be present in relatively large amounts to detect moving targets. This can be understood by referring to the phasor diagram of Fig. 9.4. This figure shows that the amplitude of the voltage $E_s(t)$ presented to the canceler varies because of the Doppler phase change of the target echo. The amplitude difference indicated in the figure is the output of a canceler circuit that takes

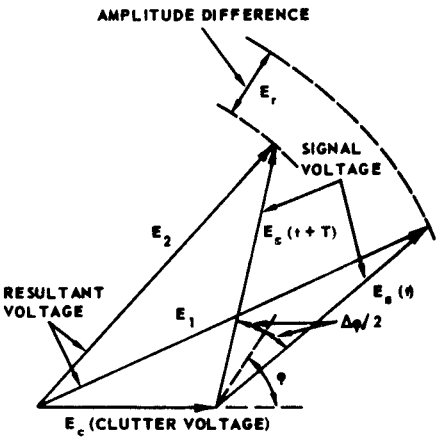

Figure 9.4 Phasor diagram of signal and clutter.

successive amplitude differences. Of course, if no clutter were present, the envelope of the signal would remain constant on a pulse-to-pulse basis. Thus, the canceler output would consist only of receiver noise for targets in the absence of clutter.

The amplitude-processing MTI also possesses blind speeds and blind phases that depend on target range and Doppler frequency. Referring to the phasor diagram of Fig. 9.4, the resultant voltage amplitude may be expressed in terms of the signal and clutter amplitude by using the law of cosines

$$E_1^2 = E_c^2 + E_s^2 - 2E_cE_s \cos\left(\varphi - \frac{\Delta\varphi}{2}\right)$$

At a time later by the interpulse time, the target echo is assumed to have changed phase by the amount $\Delta\varphi$, and the amplitude can be written

$$E_2^2 = E_c^2 + E_s^2 - 2E_cE_s \cos\left(\varphi + \frac{\Delta\varphi}{2}\right)$$

where E_c, E_s = clutter and signal voltage, respectively
E_1, E_2 = magnitude of signal-plus-clutter voltage for the second pulse
φ = average phase of the signal relative to the clutter
$\Delta\varphi$ = relative phase change of signal during the interpulse period

If the detector prior to the canceler is a square-law device, the canceler circuit will form the difference between E_1^2 and E_2^2. Thus, the signal output is given by

$$E_r = E_1^2 - E_2^2 = 4E_cE_s (\sin\varphi)\left(\sin\frac{\Delta\varphi}{2}\right)$$

and, since $\Delta\varphi = 2\pi f_d/f_r$

$$E_r = 4E_cE_s \left(sin\frac{\pi f_d}{f_r}\right)(\sin\varphi) \tag{9.4}$$

Equation (9.4) demonstrates that, just as in the phase-processing MTI system, both blind speeds and blind phases exist and that the power output for a target's signal depends on the presence of clutter.

The performance of a noncoherent MTI will generally be significantly below that of a coherent quadrature processor, as noted in Sec. 9.4. Nevertheless, there may be valid reasons for implementing a nonco-

herent processor, such as when MTI processing is to be added to an existing noncoherent system. One such system was implemented for surface vessel detection against a background of sea clutter [113]. Noncoherent MTI processing has also been used in weather radars with significant land returns, where land clutter remains constant from pulse to pulse, but weather plus land echoes fluctuate from pulse to pulse.

Quadrature-channel- (vector) processing MTI

It was shown that a phase-processing MTI is subject to blind phases in addition to blind speeds. The worst condition of a blind phase, as suggested by Eq. (9.1), would be where the PRF is at a multiple of the Doppler frequency, and the phase of the signal is at a null of the sinusoidal time response. In that case, each sample of the signal would have a zero value, even though the signal might be at an optimum velocity with respect to blind speeds. Problems due to blind phases are obviated with a quadrature channel processor, such as the one illustrated in Fig. 9.5. The illustration includes a number of features that

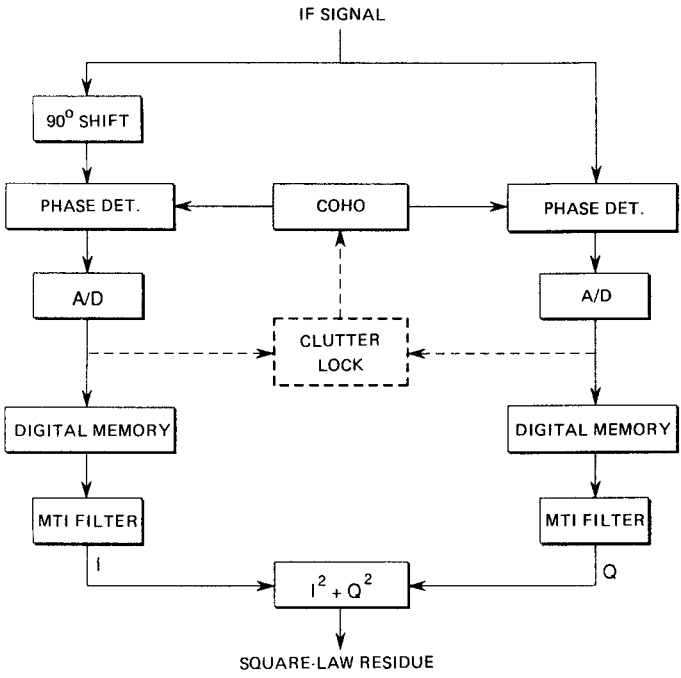

Figure 9.5 Quadrature channel MTI processor; features shown include digital implementation, clutter locking, and square-law detection.

are discussed presently, such as a digital implementation and a clutter-locking circuit. For the moment, ignore these new features and concentrate on the quadrature aspect of the diagram.

The quadrature processor has two channels, identical with the exception of a 90° phase shifter included in one channel. The output of the two channels would be as indicated by Eq. (9.1), except that the cosine multiplier indicated for one channel would be a sine term in the other channel. The two channel outputs are indicated as I (in-phase) and Q (quadrature); the vector sum calculated by $(I^2 + Q^2)^{1/2}$ would always result in the magnitude given by the initial term in Eq. (9.1), irrespective of the phase ϕ_0. Because of the similarity with vector arithmetic, the quadrature processor is sometimes referred to as a *vector processor*. The quadrature processor would have a frequency response indicated by the solid curve of Fig. 9.2.

Figure 9.5 shows the processor as using a square-law detector. One might prefer a linear-law detector to reduce dynamic range requirements. In a digital system, a linear-law detector can be closely approximated by the greater of $|I| + \frac{1}{2}|Q|$, or $|Q| + \frac{1}{2}|I|$. Currently available digital processors can perform the square-law calculation on a single chip.

The availability of high-speed A/D converters makes a digital implementation of an MTI feasible in modern systems. The digital implementation allows significant flexibility in the design and operation of the MTI processor. For instance, it is easy to adapt the MTI filter characteristics to the environment and target. A digital system, however, also imposes certain constraints on the maximum MTI performance due to A/D quantization and dynamic range limitations. These issues are covered in Secs. 9.3 and 14.4.

Clutter-locking MTI

The presence of a mean velocity component of clutter can drastically affect MTI performance as demonstrated in a succeeding section. This mean velocity component can originate either from the average motion of the clutter itself or from the motion of the radar platform (as in a moving ship or aircraft). It is desirable to remove the average clutter frequency from the radar signal. One method for doing this uses the *clutter-locking* feature that is included in Fig. 9.5. An implementation of the technique is shown in Fig. 9.6. In this example, the average interpulse phase change is measured in a phase comparator and averaged over several range bins, thus providing an estimate of the average clutter velocity. The average velocity is compensated for with a phase shifter placed in one branch of the canceler circuit. The response

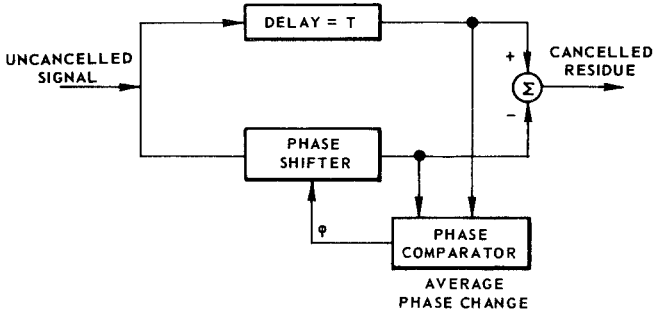

Figure 9.6 Example of clutter-locking circuit.

of this canceler would follow that shown in Fig. 9.2 except that the frequency axis would be offset such that the null normally at zero velocity would occur at a frequency corresponding to the mean clutter velocity.

Since the phase-averaging process involves a finite number of samples, the mean velocity at the range of interest can only be estimated. Section 9.2 discusses losses associated with the averaging process. If a strong target were present in one of the range cells, its Doppler frequency could contaminate the estimate of the clutter velocity. This potential problem could be mitigated if the interpulse phase change were averaged over a sufficient number of range cells. It may also be desirable to have an adaptive technique whereby the clutter-locking circuits can be bypassed when the clutter power is small. If more than one type of clutter were present (for example, precipitation and land or sea clutter) and if there were a wide disparity in their mean velocities, a simple clutter-locking technique would not be effective. This problem could be solved with higher-order cancelers, in which response nulls can be selectively placed at more than one frequency.

Multiple cancelers

Multiple delay-line cancelers provide greater clutter rejection than the single-canceler circuits described previously. One form of multiple canceler is composed of cascaded sections of single-canceler circuits (Fig. 9.7). The configuration using n cascaded sections is equivalent to the weighted sum of the $n + 1$ pulses.

It is easily verified that, for an n-stage canceler, the weighting that gives an operation equivalent to the cascaded canceler follows the binomial coefficients of $(1 - x)^n$. By forming successive differences as in Eq. (9.1), the peak target power response for an n-stage canceler is obtained [581].

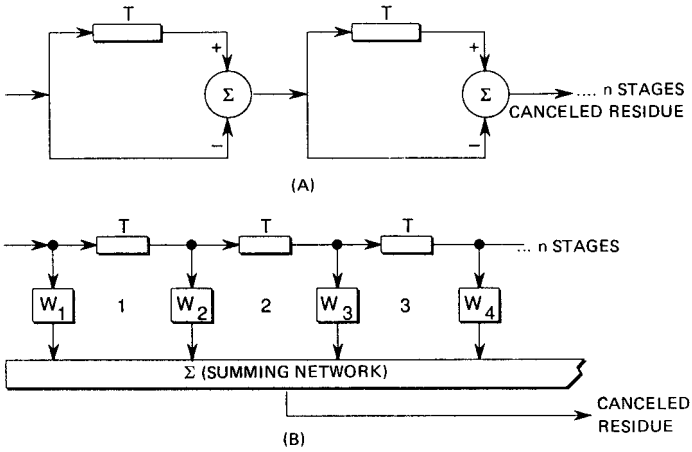

Figure 9.7 Multiple delay-line cancelers. (A) Cascaded canceler sections; (B) weighted summer.

$$\left(\frac{S_0}{S_i}\right)_n = 2^{2n} \sin^{2n}\left(\frac{\pi f_d}{f_r}\right) \tag{9.5}$$

This equation shows that the blind speeds are independent of the number of canceler stages. The signal power gain when averaged over all possible target Doppler frequencies for an n-stage canceler is

$$\begin{aligned}
\left(\frac{\overline{S}_0}{S_i}\right)_1 &= 2 = 3 \text{ dB} \\
\left(\frac{\overline{S}_0}{S_i}\right)_2 &= 6 = 7.8 \text{ dB} \\
\left(\frac{\overline{S}_0}{S_i}\right)_3 &= 20 = 13 \text{ dB} \\
&\vdots \\
\left(\frac{\overline{S}_0}{S_i}\right)_n &= 1 + n^2 + \left[\frac{n(n-1)}{2!}\right]^2 + \left[\frac{n(n-1)(n-2)}{3!}\right]^2 + \cdots 1
\end{aligned} \tag{9.6}$$

If combined phase and amplitude processing (vector or IF processing) were not used, the multiple canceler would experience a 3-dB loss in performance because of the blind phases, as explained for the single canceler.

One disadvantage of the cascaded-section canceler is that, because

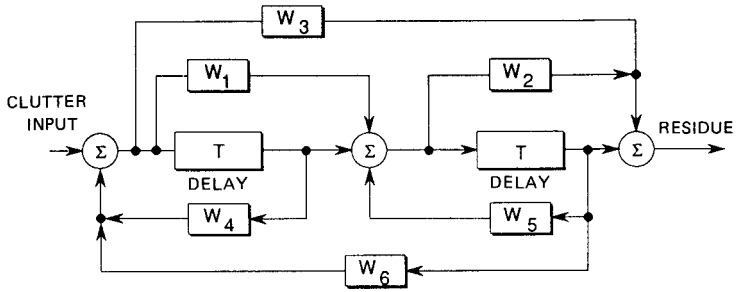

Figure 9.8 General two-delay filter using feedback and feedforward techniques.

of the $\sin^{2n}$ response, the rejection of target signals near the blind frequencies becomes more severe as n is increased. It is possible to obtain other MTI response curves with multiple-canceler systems using various feedback and feed-forward circuits as illustrated in Fig. 9.8 [671, pp. 132–135; 63, Chap. 3; 723; 769]. The advantage of the feedback system is that the clutter notch may be shaped along with a very flat signal response between blind speeds. The disadvantage is that this response is only for a steady-state condition; this requires that a number of pulses be processed before the steady-state condition is met. It is thus more appropriate for systems with rotating antennas rather than phased arrays.

The quadrature processor is frequently analyzed with complex notation, where the real and imaginary parts apply to the I and Q channels respectively. The most general form of canceler uses complex weights $W_k = a_k + i\,b_k$, where i is the complex operator, and a_k and b_k are the weights applied to the I and Q channels respectively. The velocity response with general complex weights and target Doppler frequency, is given by the following expression:

$$\left(\frac{S_0}{S_i}\right) = \sum_{k=1}^{n} \sum_{j=1}^{n} e^{i(k-j)2\pi f_d T} W_k W_j^* \tag{9.7}$$

where n = number of weights
f_d = target-Doppler frequency
T = interpulse period
W^* = the complex conjugate of W

Equation (9.7) is a more general form of Eq. (9.5). When the response is averaged over all Doppler frequencies, the following expression is obtained:

$$\left(\frac{\overline{S_0}}{S_i}\right) = \sum_{k=1}^{n} |W_k|^2 \tag{9.8}$$

Equation (9.8) is identical to Eq. (9.6) when binomial weights are used. When the weights in the two quadrature channels are equal, Eq. (9.8) indicates that the quadrature processor has 3 dB more gain than a single-channel processor. Similarly, the clutter power also has a 3-dB gain enhancement. The advantage of the two-channel system comes not strictly from power gain, but rather from the improvement in signal statistics at the processor output, i.e., the elimination of blind phases.

Staggered PRF systems

The blind speeds inherent in the previously described MTI processors can pose serious limitations on target detection. The use of a varied pulse repetition frequency provides a technique for extending the first blind speed (see [247, 538]). For a system that has two repetition intervals available, T_1 and T_2, the three-pulse canceler may form the successive differences

$$E_r = [E(t) - E(t + T_1)] - [E(t + T_1) - E(t + T_1 + T_2)]$$

This is equivalent to the weighted sum

$$E_r = E(t) - 2E(t + T_1) + E(t + T_1 + T_2) \tag{9.9}$$

Using similar techniques, it is possible to process combinations of more than two pulses by forming their weighted sum, as in Fig. 9.7. When staggering is used weights other than binomial may be more desirable, as pointed out in Sec. 9.2.

Consider the two-period (three-pulse) system that has the ratio of interpulse spacing $T_1/T_2 = a/b$ (a and b are integers). The first true blind speed occurs at the frequency that satisfies the following equation:

$$\left(f_d\right)_{\text{blind}} = \frac{a}{T_1} = \frac{b}{T_2} \tag{9.10}$$

As the stagger ratio T_1/T_2 is increased, the depth of the nulls between the blind speeds in the response characteristics is increased as shown in Fig. 9.9.

The improvement factor is traditionally used as an index of MTI performance. An alternate index might be formulated in terms of the percent of Doppler space exceeding some design value of I [415]. Such an index would be valuable for characterizing the improvements with PRF staggering. This is described in Sec. 14.4.

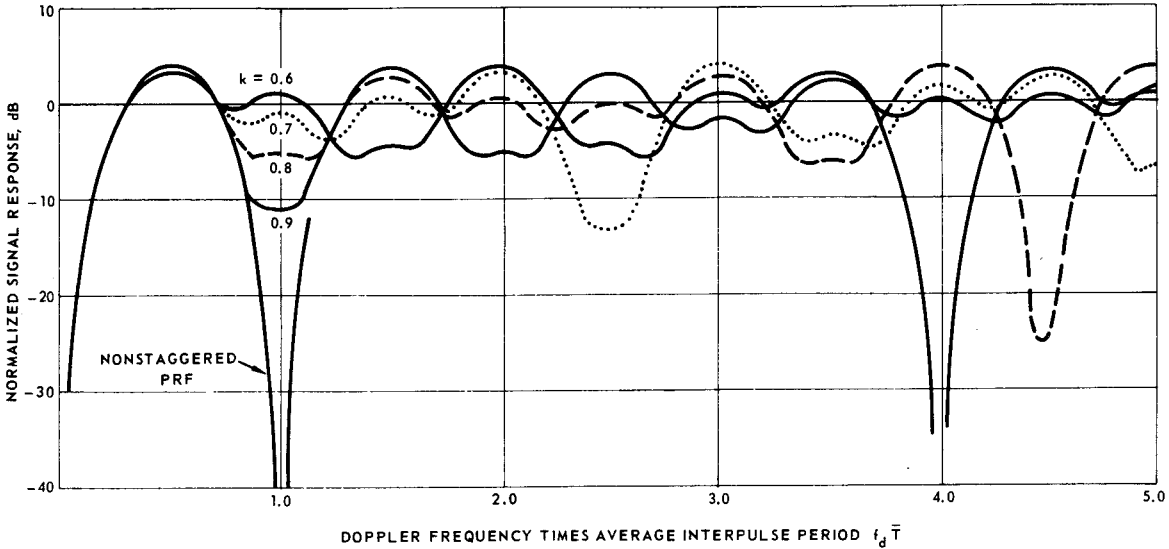

Figure 9.9 Response curves for three-pulse staggered canceler (k = stagger ratio).

9.2 Limitations on MTI Performance—Clutter Fluctuations

MTI improvement factor

This section introduces two quantities that provide a measure of MTI performance,* *clutter attenuation* (CA), and system improvement factor I. Clutter attenuation is defined as the ratio of input clutter power C_i to output clutter power C_0.

$$\text{CA} = \frac{C_i}{C_0} \tag{9.11}$$

The system improvement factor is defined as the signal-to-clutter ratio at the output of the MTI system compared with that at the input, where the signal is understood as that averaged uniformly over all radial velocities, i.e.,

$$I = \frac{\overline{S}_0/C_0}{S_i/C_i} \tag{9.12}$$

which can be expressed as

$$I = \frac{\overline{S}_0}{S_i}\,\text{CA} \tag{9.13}$$

The following paragraphs show how the improvement factor is limited by the environment, the system configuration, and the radar parameters. These limitations are discussed individually and then, in Sec. 9.7, are related to the radar equations of Chap. 2.

Early MTI systems were limited primarily by the instabilities of the radar itself; however, subsequent developments in hardware have often shifted the main cause of limitation to the statistical properties of the clutter. The role of the clutter statistics can be appreciated from the following analysis.

Consider the residue signal from a single canceler

$$E_r(t) = E(t) - E(t + T)$$

where T = the interpulse time. Because of the noiselike appearance of clutter, it is not possible to predict the residue at any given time;

* MTI performance was at times measured in terms of *subclutter visibility*. There does not appear to be a standardized definition of this term; consequently, it is not invoked as a measure of MTI performance.

instead, the residue power must be averaged over the ensemble of canceled signals.

$$\overline{E_r^2(t)} = \overline{[E(t) - E(t + T)]^2}$$

For stationary statistics this average is

$$\overline{E_r^2(t)} = \overline{2E^2(t)} - 2R(T) \tag{9.14}$$

where $R(T)$ = the autocorrelation function of the clutter evaluated at $\tau = T$. The autocorrelation function may be expressed in terms of the normalized correlation function

$$\rho(\tau) = \frac{R(\tau)}{\overline{E^2(t)}}$$

By recognizing that $\overline{E^2(t)}/\overline{E_r^2(t)} = \text{CA}$, Eq. (9.14) can be expressed as

$$\text{CA} = \frac{1}{2[1 - \rho(T)]} \tag{9.15}$$

The improvement factor follows from Eq. (9.15)

$$I_1 = \frac{1}{1 - \rho(T)} \tag{9.16}$$

This result shows that the improvement factor depends only on the correlation function of the clutter signal evaluated at a single point—the interpulse time. A parallel development yields the expression for the double canceler

$$I_2 = \frac{1}{1 - \frac{4}{3}\rho(T) + \frac{1}{3}\rho(2T)} \tag{9.17}$$

The MTI improvement factor can be more generally expressed in terms of arbitrary parameters regarding the number of pulses processed, the weights, and target Doppler. The following equation is an extension of the foregoing in terms of complex notation:

$$I = \frac{(S_0/S_i)}{\sum_{k=1}^{n} \sum_{j=1}^{n} W_k W_j^* \rho[(k - j)T]} \tag{9.18}$$

The numerator represents the signal gain as defined by Eq. (9.7) for a specific Doppler frequency, or by Eq. (9.8) if the signal gain is to be

averaged over all Doppler frequencies. The denominator represents the clutter gain (attenuation). It is easily verified that the general equation reduces to the specific forms of Eqs. (9.16) and (9.17) when applied to two- and three-pulse cancelers with binomial weights. The improvement factor defined by Eq. (9.18) is not restricted to MTI processors, but is equally valid for other coherent processors, including Doppler filter banks. For applications with multiple filters, the complex weights would be separately chosen for each filter, and the improvement factor would apply to that particular filter. In evaluating Eq. (9.18), use $\rho(T) = \rho(-T)$, and $\rho(0) = 1$. Equation (9.18) readily accommodates the specification of a mean frequency component in the clutter spectrum. For a clutter process having a mean clutter frequency of f_c, the correlation coefficient is given by

$$\rho(T) = \rho_0(T)\, e^{i2\pi f_c T} \tag{9.19}$$

where $\rho_0(T)$ = the correlation coefficient with zero mean Doppler.

Equation (9.18) provides a general expression for the MTI improvement factor. Applied expressions may be determined by specifying the MTI weights and the clutter correlation coefficients. It is customary to assume binomial weights—unless otherwise stated, that will be the assumption in this chapter. The correlation coefficients are customarily evaluated assuming a gaussian spectrum, which leads to a gaussian correlation function. However, a gaussian shape is not universally accepted for clutter spectra (see Secs. 7.5, 7.13). Indeed, some experimental data for sea clutter indicate spectra with multiple peaks. Furthermore, spectra for rain clutter are sometimes thought to possess longer tails than the gaussian function would indicate. In that case, a gaussian assumption might lead to somewhat optimistic predictions of clutter performance. This subject has not been well documented. Unless otherwise stated, a gaussian assumption is used in this chapter. It does provide a reasonable fit to experimental data in some cases, and it is easy to manipulate mathematically. But the reader should be aware that other, more pessimistic, assumptions can be made. Assuming a gaussian spectrum and binomial MTI weights, the improvement factor can be expressed as* [581]

$$I_1 = \frac{1}{1 - \exp[-2(2\pi\sigma_v/\lambda f_r)^2] \cos 4\pi\, V_0/\lambda f_r}$$

$$I_2 = \frac{3}{3 - 4\exp[-2(2\pi\sigma_v/\lambda f_r)^2] \cos 4\pi\, V_0/\lambda f_r + \exp[-2(4\pi\sigma_v/\lambda f_r)^2] \cos 8\pi\, V_0/\lambda f_r} \tag{9.20}$$

* When $V_0 = 0$, the resulting expression is identical with that normally encountered in the literature.

where σ_l = the standard deviation of clutter spectrum, m/s
V_0 = the mean value of clutter spectrum, m/s
λ = the radar wavelength, m
f_r = the pulse repetition frequency, s^{-1}

Expressions for higher-order cancelers are derived in [581]. At this point we may verify that the signal-to-noise ratio is not affected by the MTI processor. The improvement factor is evaluated for wideband noise from Eqs. (9.15) and (9.16) using $\rho(T) = 0$. The result is that the improvement in signal-to-noise power is unity, i.e., the average signal-to-noise ratio is not improved over that of a single pulse.

For usable MTI operation (e.g., for $I_1 > 10$ dB) the arguments of the exponential and cosine functions in Eqs. (9.20) are much less than unity. Therefore, a good approximation may be obtained by taking the first two terms of the Taylor series for e^{-x} and $\cos x$, giving

$$I_1 \cong \frac{\lambda^2 f_r^2}{8\pi^2(\sigma_v^2 + V_0^2)} \tag{9.21}$$

The expression for the double canceler may be obtained by taking the first three terms of the Taylor series. For $V_0 = 0$, the result is

$$I_2 \cong \frac{\lambda^4 f_r^4}{128\pi^4 \sigma_v^4} \tag{9.22}$$

Evaluation of improvement factor

Figure 9.10 illustrates the improvement factor limitation for binomial canceler systems when $V_0 = 0$. These curves apply to either clutter-locking systems or those that receive clutter of zero mean Doppler. The reduction in improvement factor due to a nonzero mean clutter Doppler is illustrated in Fig. 9.11, which shows the loss (in decibels) from a system where $V_0 = 0$. The loss is seen to depend on the ratio V_0/σ_v.*

Equation (9.20) can also be evaluated with values of σ_v and V_0 that correspond to the experimental values of clutter. For example, Fig. 9.12 shows the limitations on the single-canceler clutter improvement factor imposed by the spectrum of sea clutter as a function of sea state. Particular values of σ_v and V_0 may be obtained from the models of Chap. 7.† It is evident that the presence of a mean Doppler component of sea clutter has a considerable effect on the improvement factor.

---

* Figure 9.11 accurately describes the loss in the linear regions of Fig. 9.10. The nonlinear regions are, of course, most unsatisfactory for MTI performance because of the poor improvement factor.

† The worst case values of V_0 and σ_v for horizontal polarization are shown. (See Reilly [581] and Nathanson and Reilly [503].)

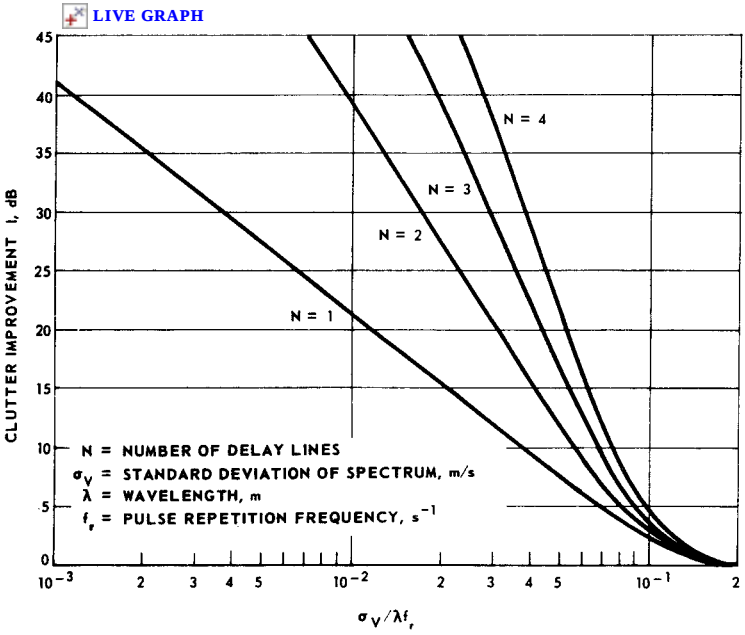

Figure 9.10 Improvement factor for delay-line canceler as limited by clutter spectrum ($V_0 = 0$, binomial weighted MTI).

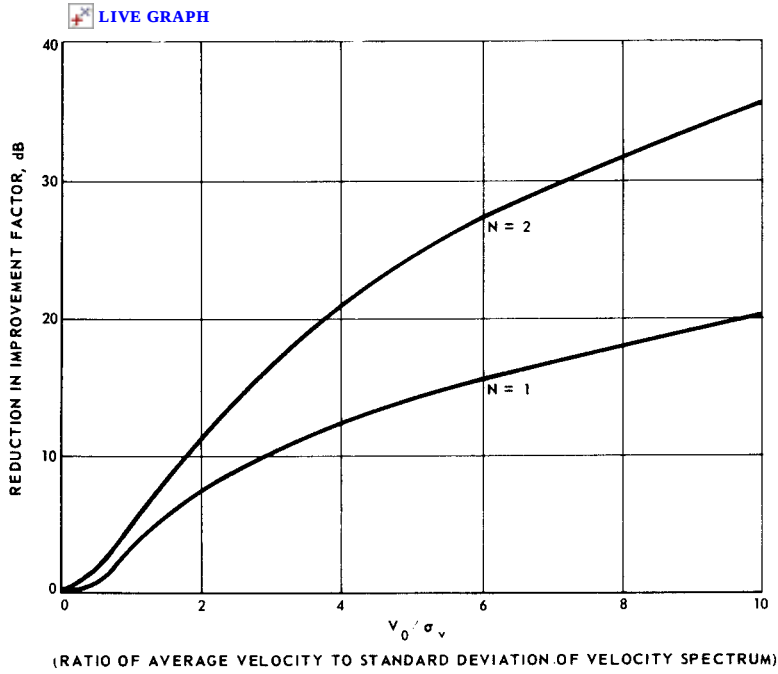

Figure 9.11 Reduction in improvement factor due to an average velocity component of the clutter spectrum (N = number of delay lines, binomial weighted MTI).

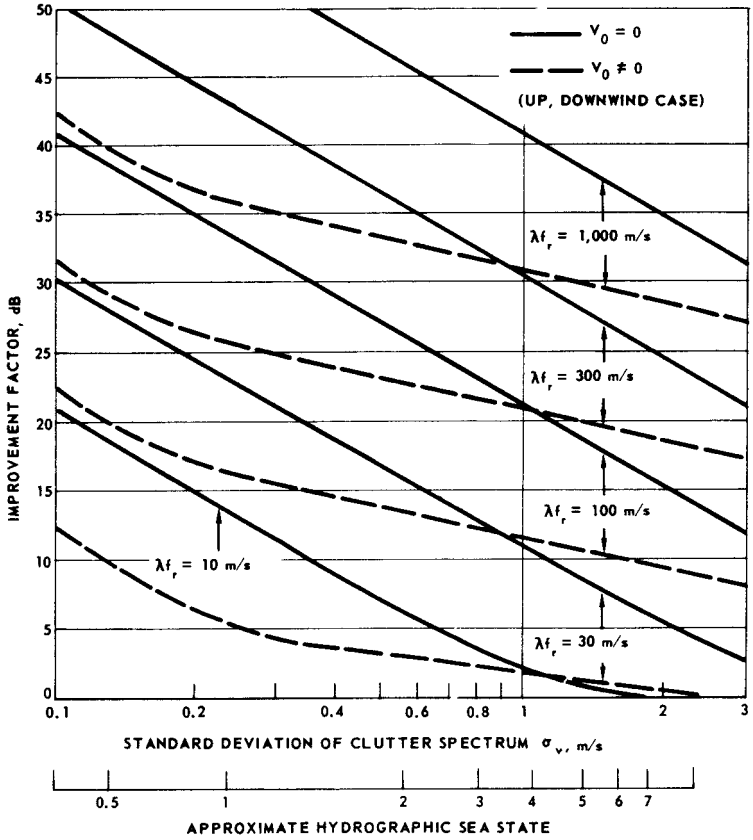

Figure 9.12 Limitation of single-canceler improvement factor by sea clutter (horizontal polarization).

For most radars the clutter improvement factor for precipitation is a function of range. This is so because the spectrum width of precipitation clutter is a function of range (because of the wind shear effect described in Chap. 6). Figure 9.13 illustrates an example of the improvement factor limitation for precipitation clutter when clutter locking is used. This figure represents the limitation when the radar is pointing in the up- or downwind direction, which is when the shear effect is most severe. Figure 9.14 shows the degradation that results when the mean velocity is not compensated for. These curves are drawn for a specific elevation angle since the shear-versus-range relationship is a function of angle and beamwidth.

Errors in estimating mean clutter velocity

The preceding section demonstrated that the mean velocity component of clutter can seriously degrade MTI performance. One system that

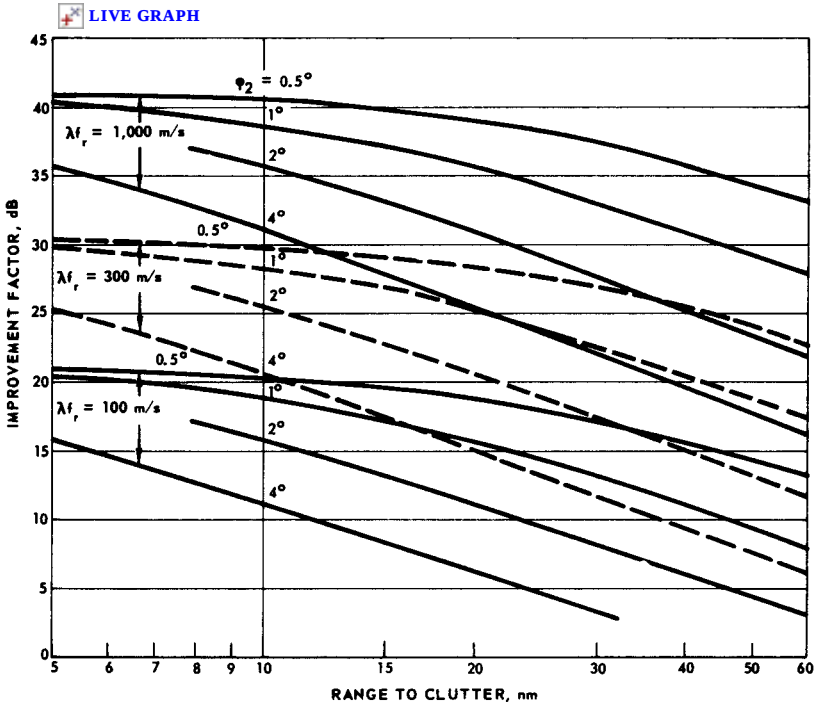

Figure 9.13 Single-canceler improvement factor as limited by precipitation clutter (clutter-locked, radar looking up-/downwind, wind shear (k) = 5.7 m/sec/km, typical of Eastern U.S.).

compensates for the mean velocity component is a clutter-locking system (Fig. 9.6) in which the mean clutter frequency is determined by averaging the phase differences between the returns from two pulses over several range intervals. Since the averaging process involves a finite number of samples, the mean velocity at the range of interest can only be estimated, i.e., the estimate of the mean will exhibit a statistical fluctuation.

The average Doppler frequency of a band-limited process may be estimated from interpulse phase differences through

$$\bar{f} \cong \frac{2\pi}{NT} \sum_{i}^{N} \Delta\varphi_i \tag{9.23}$$

where $\Delta\varphi$ = the interpluse phase difference
T = the interpulse time
N = the number of independent measures of $\Delta\varphi$

Voles [737] has demonstrated that interpulse phase differences provide rather poor estimates of the mean frequency, and a significant number

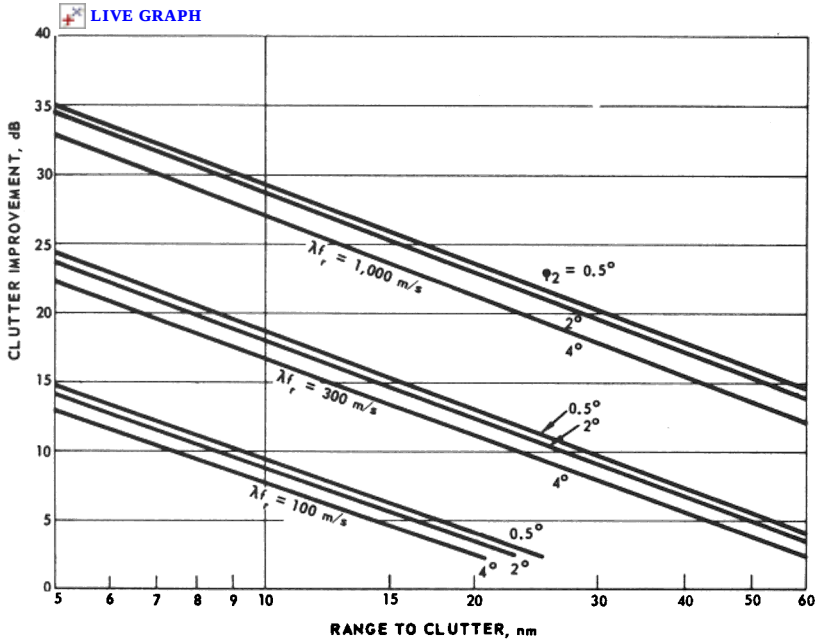

Figure 9.14 Single-canceler clutter improvement as limited by precipitation (no clutter locking, radar looking up-/downwind, elevation angle = 2°, two-way elevation beamwidth = ϕ_2).

of samples may be needed to achieve acceptable accuracy. Figure 9.15 illustrates the loss in single and double MTI cancelers due to averaging the interpulse phase shift over a finite number of pulses. It is assumed that N independent samples are obtained, such as by forming phase differences across N range bins, and that the spectral characteristics are the same in each bin. The losses are expressed relative to a system with a gaussian spectrum having zero mean Doppler. As noted in the figure, the number of samples needed to keep the loss within some prescribed limit is a function of the maximum improvement factor attained with a perfect estimate of the mean Doppler. To keep the loss within some prescribed limit is a function of the maximum improvement factor attained with a perfect estimate of the mean Doppler. To keep the loss within one or two dB, some tens of range bins may be needed in the averaging process, the precise number depending on the order of the canceler and the attainable improvement factor. Additional losses associated with including the target's signal in the average, or with a mean Doppler that varies with range, can impose additional limitations beyond those represented in Fig. 9.15.

The technique of shifting by the average in Eq. (9.23) is not optimum when the clutter spectrum is multimodal, such as when more than one

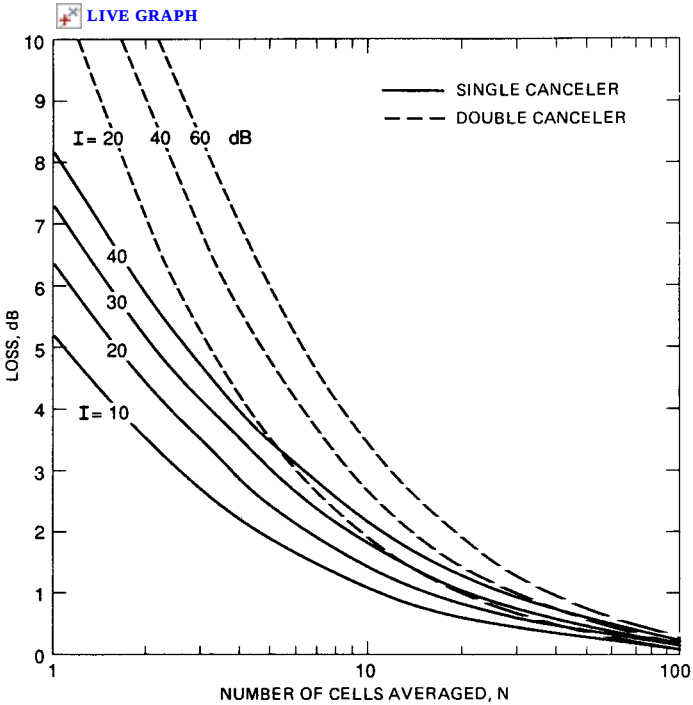

Figure 9.15 Clutter-locking loss in single and double MTI cancelers due to averaging the interpulse phase shift over N range cells. Curve parameters indicate improvement factor with perfect velocity compensation (*From Voles [737]*)

type of clutter is simultaneously present [203, 734]. Other techniques for clutter locking have been studied [733, 734, 735, 737] including a digital implementation suitable for weather clutter environments [651].

Limitations on staggered PRF systems

The blind speeds inherent in MTI operation pose a serious limitation to target detection. Section 9.1 described a staggered PRF system that increases the first blind speed. One disadvantage of the staggered PRF system is that, as the difference in interpulse times is increased, the clutter attenuation decreases (when the pulses are weighted binomially). To illustrate this point, consider a three-pulse canceler using staggered PRF. The improvement factor for the staggered system I_s is derived in a manner parallel to that used to derive Eq. (9.17), resulting in

$$I_s = \frac{1}{1 - \frac{2}{3}[\rho(T_1) + \rho(T_2)] + \frac{1}{3}\rho(T_1 + T_2)} \tag{9.24}$$

The improvement factor for the staggered system can be compared with that for a double-canceler system with interpulse time $T = (T_1 + T_2)/2$ by using Eq. (9.17) in the form

$$I_2 = \frac{1}{1 - \frac{4}{3}\rho[(T_1 + T_2)/2] + \frac{1}{3}\rho(T_1 + T_2)} \tag{9.25}$$

Equation (9.24) can be expressed in terms of the stagger ratio

$$I_s = \frac{1}{1 - \frac{2}{3}[\rho(T_1) + \rho(kT_1)] + \frac{1}{3}\rho[T_1(1 + k)]} \tag{9.26}$$

where $k = T_2/T_1$.

Using the gaussian function for the spectrum of clutter, the autocorrelation function is also gaussian and may be expanded into a Taylor series.*

$$\rho(\tau) = \exp\left[\frac{-\tau^2}{2\sigma_\tau^2}\right] = 1 - \frac{\tau^2}{2\sigma_\tau^2} + \frac{\tau^4}{8\sigma_\tau^4} \cdots$$

Using the first three Taylor series terms in Eqs. (9.25) and (9.26) results in the ratio

$$\frac{I_2}{I_s} \cong \frac{4\sigma_\tau^2}{3T^2}\frac{(1 - k)^2}{(1 + k)^2} + \frac{16}{(1 + k)^4}\left[k^2 - \frac{(1 - k)^4}{12}\right] \tag{9.27}$$

where $T = (T_1 + T_2)/2$
$k = T_2/T_1$
I_2 = the improvement factor without staggering
I_s = the improvement factor with staggering

Figure 9.16 illustrates this ratio with the abscissa in terms of I_2 rather than σ_τ^2/T^2. This figure demonstrates that, as the stagger ratio departs from unity, the clutter attenuation is decreased toward the performance of the single canceler. While the losses associated with staggered waveforms may be substantial when binomial weights are used, they may be largely recovered by using alternative weights, as discussed in the following.

* For a gaussian spectrum $\sigma_\tau = 1/2\pi\sigma_f = \lambda/4\pi\sigma_t$. The first few terms of the Taylor series are adequate except for small cancellation ratios.

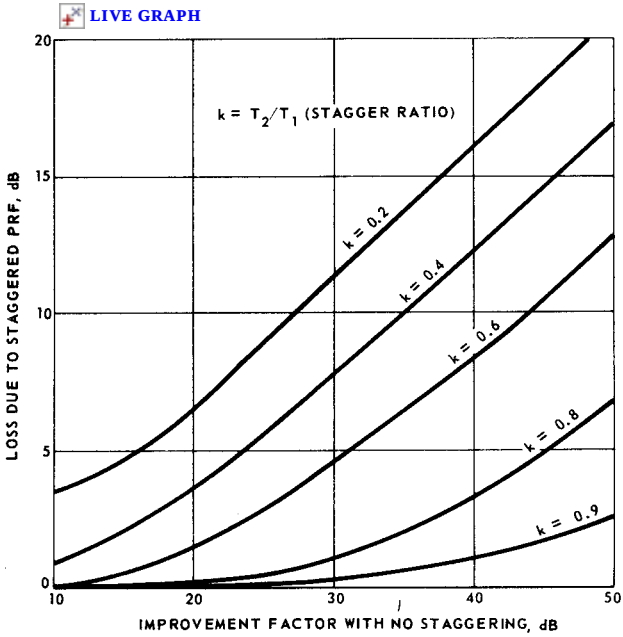

Figure 9.16 Improvement factor loss with staggered PRF system using binomial weights. (The period of the unstaggered canceler is the same as the average period of the staggered system.)

Alternative MTI weights

Binomial weights used in conventional MTI processors are not necessarily optimum. Optimum weighting schemes have been studied by several authors. Capon, for example, studied weights that maximize the average clutter improvement with unknown target-Doppler frequency [107]. The resulting weights are real quantities. The conventional processor with two pulses ($W_1 = 1, W_2 = -1$) is already optimum. The solution for higher-order cancelers depends on the pulse-to-pulse clutter correlation. With highly correlated clutter, the optimum three-pulse canceler weights are nearly the binomial values [107, 416, 740]. By maximizing the improvement factor defined according to Eq. (9.12), we do not guarantee that P_d is also maximized. Nevertheless, for coherent MTI processing, the weights that maximize either I or P_d are virtually identical [412].

Ares studied the weights that optimize the improvement factor for a particular target Doppler frequency, where the interpulse periods are fixed [18]. The resulting weights are complex, i.e., the pulses must be amplitude weighted and phase shifted. The exact weights depend on the target-Doppler frequency and on the clutter correlation coeffi-

cients. With this type of processor, and assuming a gaussian clutter correlation function, a three-pulse canceler may be improved by about 1.8 dB relative to a processor with binomial weights, and a four-pulse canceler by about 3 dB.

Ares also derived weights that are real and independent of the clutter correlation and target velocity. These weights are called *maximally flat* because of the shape of the ambiguity function, in which the first $n - 2$ derivatives are zero. If we consider the first of n weights equal to unity, the other weights are determined by solving the set of equations:

$$\begin{aligned} W_1 &= 1 \\ W_2 + W_3 + \cdots W_n &= -1 \\ W_2 S_2 + W_3 S_3 + \cdots W_n S_n &= 0 \\ &\vdots \\ W_2 S_2^{n-2} + W_3 S_3^{n-2} + \cdots W_n S_n^{n-2} &= 0 \end{aligned} \tag{9.28}$$

where S_i is the time delay between the first and i_{th} pulses. For example, if the interpulse periods are $T_1, T_2, \ldots T_{n-1}$, then $S_1 = 0$, $S_2 = T_1$, $S_3 = T_1 + T_2$, etc. When no staggering is used, $T_1 = T_2 \ldots$ etc., and the solution reduces to the binomial weights. For three pulses with staggering, the maximally flat weights are:

$$W_1 = 1, W_2 = -\frac{T_1 + T_2}{T_2}, W_3 = \frac{T_1}{T_2}$$

The maximally flat solution for four pulses is:

$$\begin{aligned} W_1 &= 1 \\ W_2 &= -\frac{(T_1 + T_2)(T_1 + T_2 + T_3)}{T_2(T_2 + T_3)} \\ W_3 &= \frac{T_1(T_1 + T_2 + T_3)}{T_2 T_3} \\ W_4 &= -\frac{T_1(T_1 + T_2)}{T_3(T_2 + T_3)} \end{aligned}$$

The signal response curve using these weights is only slightly altered from that using binomial weights. The main advantage is that the improvement factor losses caused by staggering (Fig. 9.16) can be recovered. Thus, the velocity response function and the clutter notch may be shaped almost independently: the response function is determined

by the interpulse staggering; the clutter notch is determined by the weights.

9.3 Digital MTI Limitations

When a signal is quantized, its exact value is uncertain; that is, it appears as though additional *quantization* noise was added to the system. Clutter cannot be canceled to a level below this basic noise limitation. The abrupt clipping imposed on a signal as it exceeds the saturation level causes a signal distortion. This results in additional frequency components which pass through the MTI system. These two effects are analyzed separately in the following. Additional losses are associated with finite sampling in the range domain (see Chap. 4).

Quantization errors

Signal and clutter may not be analyzed separately in a nonlinear process such as quantization. The *signal* must be defined as the incremental increase in output power when a signal is present at the input compared to that when it is not. Using this definition, the signal-to-clutter ratio at the output of the digital MTI processor (Fig. 9.5) is

$$\frac{P_{s0}}{P_{c0}} = \frac{\overline{[(E_1 + C_1 + \epsilon_1) - (E_2 + C_2 + \epsilon_2)]^2} - \overline{[(C_1 + \epsilon_3) - (C_2 + \epsilon_4)]^2}}{[(C_1 + \epsilon_3) - (C_2 + \epsilon_4)]^2} \tag{9.29}$$

where P_{s0}, P_{c0} = output signal and clutter power, respectively
E_1, E_2 = input signal voltage for the first and second pulse
C_1, C_2 = input clutter voltage for the first and second pulse
ϵ_1, ϵ_2 = quantization errors when signal and clutter are present
ϵ_3, ϵ_4 = quantization errors when only clutter is present

This equation may be considerably simplified by making some assumptions concerning independence:

$$\overline{(E_1 - E_2)(C_1 - C_2)} = \overline{(E_1 - E_2)(\epsilon_1 - \epsilon_2)} = \overline{(C_1 - C_2)(\epsilon_1 - \epsilon_2)} = \overline{(C_1 - C_2)(\epsilon_3 - \epsilon_4)} = 0$$

Defining σ_ϵ^2 as the variance of the quantization error results in

$$\frac{P_{s0}}{P_{c0}} = \frac{\overline{(E_1 - E_2)^2} - \overline{2(\epsilon_1\epsilon_2 - \epsilon_3\epsilon_4)}}{\overline{(C_1 - C_2)^2} + 2\sigma_\epsilon^2 - \overline{2\epsilon_3\epsilon_4}} \tag{9.30}$$

Defining ρ_ϵ as the correlation coefficient of the quantization error for clutter alone and $\rho_{\epsilon s}$ as that when both clutter and signal are present, Eq. (9.30) becomes

$$\frac{P_{s0}}{P_{c0}} = \frac{\overline{E_0^2} + 2\sigma_\epsilon^2[\rho_\epsilon(T) - \rho_{\epsilon s}(T)]}{2\{P_{ic} - \overline{C_1 C_2} + \sigma_\epsilon^2[1 - \rho_\epsilon(T)]\}} \tag{9.31}$$

where $\overline{E_0^2} = \overline{(E_1 - E_2)^2}$

P_{ic} = the input clutter power

T = the interpulse time

The improvement factor is obtained by dividing Eq. (9.31) by the input signal-to-clutter power ratio. Using the fact that the average signal gain for the single canceler is 2, the improvement factor is then

$$I_1 = \frac{1 + (\sigma_\epsilon^2/E^2)[\rho_\epsilon(T) - \rho_{\epsilon s}(T)]}{1 - \rho(T) + (\sigma_\epsilon^2/P_{ic})[1 - \rho_\epsilon(T)]} \tag{9.32}$$

where $\rho(T)$ is the correlation coefficient of the clutter signal. Eq. (9.32) illustrates that the quantization error correlation $\rho_\epsilon(T)$ has a *quieting* effect on the noise power caused by σ_ϵ^2. However, except for clutter having an interpulse correlation coefficient unusually close to unity or for quantization levels approaching the rms value of the clutter signals, $\rho_\epsilon(T)$ is very small as illustrted by Fig. 9.17 [88]. Neglecting the correlation factor ρ_ϵ,

$$I_1 \cong \frac{1}{1 - \rho(T) + \sigma_\epsilon^2/P_{ic}} \tag{9.33}$$

This analysis may be extended to include the double canceler. The details are quite similar to the steps used to analyze the single canceler except that there are considerably more terms to contend with. The result is

$$I_2 = \frac{1 + \dfrac{\sigma_\epsilon^2}{E^2}\left\{\dfrac{4}{3}[\rho_\epsilon(T) - \rho_{\epsilon s}(T)] - \dfrac{1}{3}[\rho_\epsilon(2T) - \rho_{\epsilon s}(2T)]\right\}}{1 - \dfrac{4}{3}\rho(T) + \dfrac{1}{3}\rho(2T) - \dfrac{\sigma_\epsilon^2}{P_{ic}}\left[\dfrac{4}{3}\rho_\epsilon(T) - \dfrac{1}{3}\rho_\epsilon(2T)\right] + \dfrac{\sigma_\epsilon^2}{P_{ic}}} \tag{9.34}$$

Again, neglecting the quieting effects of the quantization correlation results in

$$I_2 \cong \frac{1}{1 - \dfrac{4}{3}\rho(T) + \dfrac{1}{3}\rho(2T) + (\sigma_\epsilon^2/P_{ic})} \tag{9.35}$$

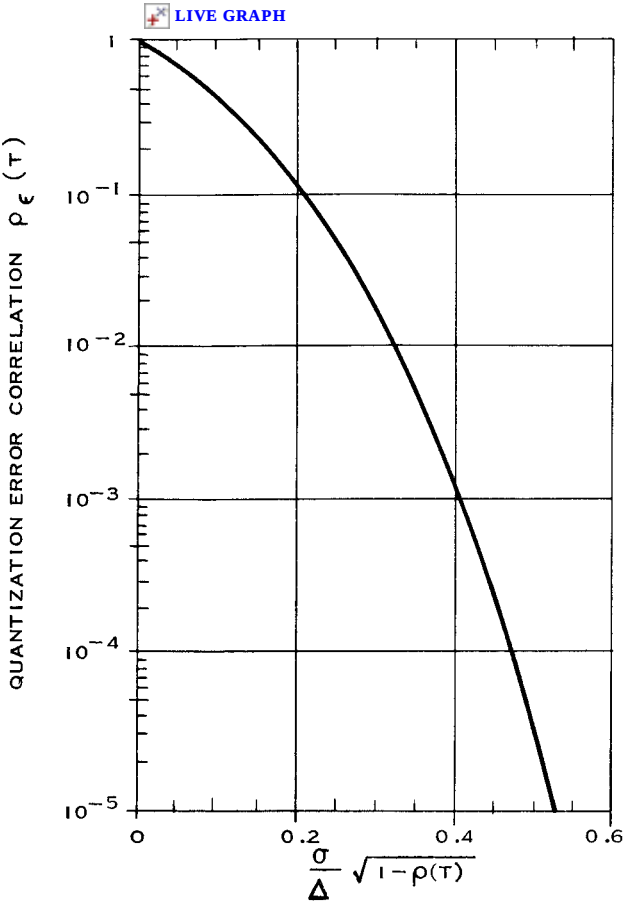

Figure 9.17 Quantization error correlation coefficient (Δ = quantization increment, σ = rms amplitude before quantization, $\rho(T)$ = correlation coefficient of input signal). (*From Brennan and Reed, IEEE* [88])

Eqs. (9.34) and (9.35) differ from the standard MTI equation only by the factor involving the quantization error, which is an additional limitation on the improvement factor. For correlations approaching unity, the maximum possible improvement is given by

$$I_1 = I_2 = \frac{P_{ic}}{\sigma_\epsilon^2} \qquad \text{limitation due to quantization errors} \qquad (9.36)$$

The quantization error may be expressed in terms of the number of bits of quantization by assuming a uniform error distribution which yields

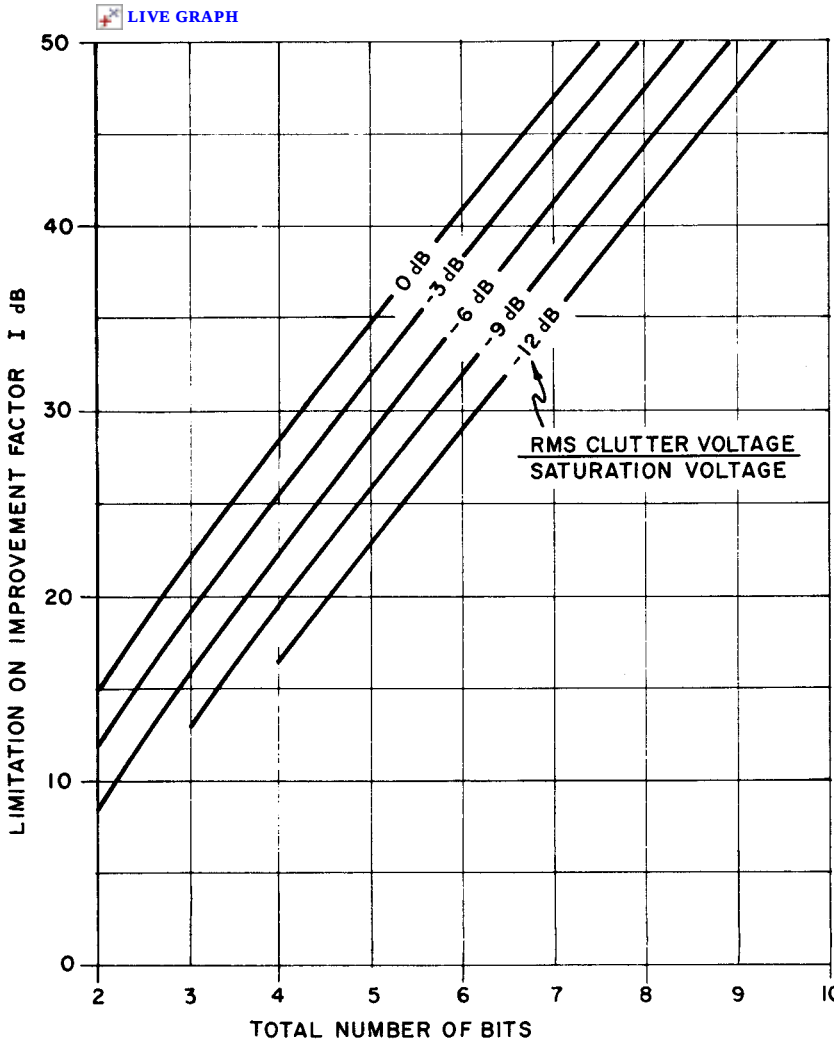

Figure 9.18 Improvement factor limitation imposed by quantization errors (nonredundant zero).

$$\sigma_\epsilon^2 = \frac{E_m^2}{12(2^{n-1} - 1/2)^2} \tag{9.37}$$

where n is the number of bits (including sign bit) and E_m is the saturation voltage of the digital register. Substituting into Eq. (9.36),

$$I_1 = I_2 = \frac{P_{ic}}{E_m^2} 12(2^{n-1} - 1/2)^2 \tag{9.38}$$

This limitation on improvement factor, illustrated in Fig. 9.18, applies when the signal is less than E_m. For greater signals, the effects of

clipping must be considered. For a given number of quantization levels, their spacing can be optimized for best canceler performance [704]. The optimum setting is a function of the input clutter power and the clutter correlation.

Losses due to clipping

Clipping occurs when the quantized signal exceeds the saturation level of the register, which results in a broadening of its spectrum and a narrowing of its correlation function. The value of the correlation coefficient after clipping is desired since this quantity can be used to define MTI performance through Eqs. (9.16) and (9.17).

The expression for the nonlinear transformation of an autocorrelation function has been derived in a number of places, but it is difficult to evaluate for the most general case when both signal and clutter are present. However, when the signal-to-clutter ratio at the input of the MTI processor approaches zero, the equations are greatly simplified. The expression for the correlation function of gaussian distributed noise alone is given by Van Vleck [728]:

$$R_0(T) = \rho_i(T)\left[\operatorname{erf}\left(\frac{b}{\sqrt{2}}\right)\right]^2 + \frac{2}{\pi}\sum_{n=3,5,\cdots}\frac{\rho_i(T)}{n!}\left[H_{n-2}(b)\exp\left(\frac{-b^2}{2}\right)\right]^2 \tag{9.39}$$

and the desired correlation coefficient is

$$\rho_0(T) = \frac{R_0(T)}{R_0(0)}$$

where $\rho_i(T)$, $\rho_0(T)$ = input (before clipping) and output (after clipping) correlation coefficients
$\operatorname{erf}(x)$ = the error function
b = clipping level divided by rms clutter voltage
$H_n(x)$ = Hermite polynomial of degree n

Two extreme cases are readily evaluated

$$\begin{aligned} \rho_0(T) &= \rho_i(T) && \text{for } b \to \infty \\ \rho_0(T) &\frac{2}{\pi}\sin^{-1}[\rho_i(T)] && \text{for } b \to 0 \end{aligned} \tag{9.40}$$

Intermediate cases have been evaluated on a digital computer by including Hermite polynomials up to the degree 6000 in the summation. Results are presented in Fig. 9.19 in terms of the clutter improvement

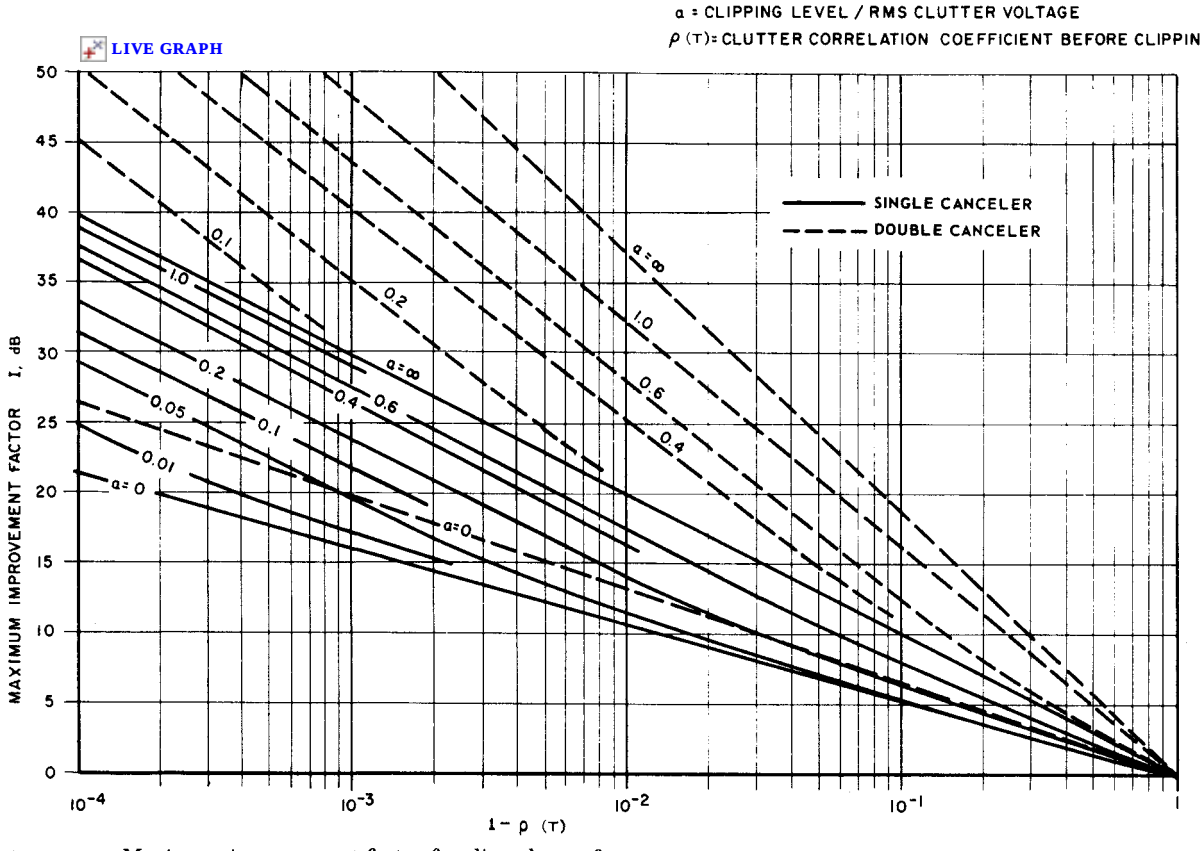

Figure 9.19 Maximum improvement factor for clipped waveforms.

factor for the single and double canceler. These curves illustrate the improvement factor through the MTI canceler alone and do not show any additional losses in signal-to-clutter ratio which occur in the *A/D* conversion process. When clipping is severe, two results are noteworthy: MTI performance is considerably degraded, and the difference in performance between the single and the double canceler is much smaller than that for a linear system.

One should interpret these results with caution. The improvement factor has been evaluated in terms of the improvement in output signal-to-clutter power ratio, and is not necessarily coincident with the gain in detectability. The distinction arises because the nonlinear process involves a modification of the statistical distribution of the clutter residues (see Sec. 9.4 for a further explanation of this distinction). Note that the statistical distribution for small clipping levels differs markedly from that for large clipping levels.

9.4 Noncoherent and Nonlinear Processes

MTI followed by postdetection integration

If there is more than one MTI output in each beam position, the quadrature processor shown in Fig. 9.5 may be further refined with the addition of a postdetection integrator. In this case, successive residues represented by $I^2 + Q^2$ (or some other power-law variant) would be summed at the MTI output. The combination of MTI filtering and postdetection integration has the property that when the clutter is highly turbulent, i.e., has small pulse-to-pulse correlation, the MTI performance is poor, but the postdetection integration process gives additional improvement. On the other hand, when the clutter is highly correlated, the MTI performance is good and the integration process is relatively ineffective. The performance of the combined processor may be understood by examining the correlation coefficient of the MTI residue:

$$R_r(kT) = \overline{[E(t) - E(t + T)][E(t + kT) - E(t + T + kT)]} \quad (9.41)$$

where R_r = the correlation function (not normalized) of the MTI residue
$f(t)$ = the input clutter signal
T = the interpulse period

By carrying out this operation and normalizing, the residue correlation coefficient ρ_r may be expressed in terms of the input clutter correlation ρ by*

* This is essentially a special case of an analysis by Urkowitz [724].

$$\rho_r(nT) = \frac{2\rho(nT) - \rho[(n+1)T] - \rho[(n-1)T]}{2[1 - \rho(T)]} \tag{9.42}$$

When the residue signal is squared, the result is a signal having a dc component plus a fluctuating component. The correlation coefficient of the fluctuating component $\rho_s(kT)$ is given by [161, Chap. 12]

$$\rho_s(kT) = \rho_r^2(kT) \tag{9.43}$$

Recall from Chap. 3 that the reduction in noise variance with integration of dependent samples may be evaluated in terms of the correlation coefficients of the samples. By using the expression for $\rho_s(kT)$ in conjunction with Eq. (3.10), one may determine the reduction in noise variance as expressed by the equivalent number of independent samples. The result for the MTI integration process previously described is (see also [303]):

$$N_I = N^2 \left[\sum_{k=-(N-1)}^{N-1} \{N - |k|\} \rho_r^2(kT) \right]^{-1} \tag{9.44}$$

The result of the MTI integration process is shown in Fig. 9.20. The solid lines show the reduction in clutter fluctuation power for a single canceler and for the integrator as a function of the standard deviation of a gaussian clutter spectrum. The gain for the combined processor is approximately given by their decibel sum. The combined processing gain for higher-order cancelers has also been evaluated in a manner similar to the preceding. The results are almost identical to those for the single canceler, except for the asymptotic behavior as $\sigma_v/\lambda f_r \to 1$.

As the clutter correlation approaches zero (the right-hand axis of Fig. 9.20), it becomes equivalent to wideband receiver noise. The detectability improvement of a combined processor with uncorrelated inputs falls short of the gain that would be obtained with noncoherent integration of the same number of pulses; the loss ranges from 1 dB for a two-pulse canceler to 2.5 dB for a five-pulse canceler [712]. The loss occurs because the MTI residues are correlated, even though the input may be noiselike.

The results indicated by Fig. 9.20 are indicative of the potential gain in a combined MTI and postdetection processor, but may not exactly represent the gain in target detectability because the statistical distribution function of the target plus noise has not been accounted for.

IF limiting

Because of the extremely wide dynamic range of clutter power relative to receiver noise, some form of clutter limiting will inevitably be present. The quantization process in a digital MTI requires clipping at a level

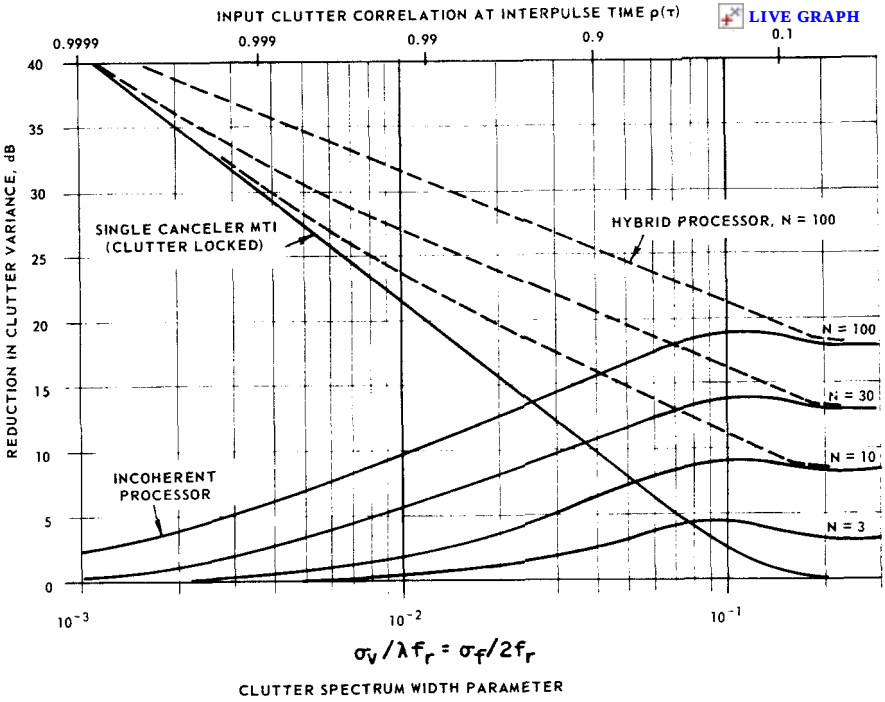

Figure 9.20 Clutter performance improvement for MTI followed by postdetection integration of N residues.

dictated by the digital dynamic range. Clipping was shown to result in significant losses relative to an ideal linear MTI system (Fig. 9.19). Another form of limiting takes place at the IF frequency prior to quadrature detection (refer to Fig. 9.1). The difference between IF limiting and quadrature clipping is represented in Fig. 9.21 as a limit in the I/Q domain. With IF limiting, the clutter vector is constrained to a circle; with quadrature clipping, the vector is confined to a square. In either case, the abrupt transition from a linear to a limited signal results in a broadening of the clutter spectrum, and consequently a reduction in the achievable improvement factor.

Ward and Shrader [750] evaluated the losses due to IF limiting using transformed clutter correlation coefficients, in a manner similar to the development described in Sec. 9.3 for quadrature clipping. Figure 9.22 illustrates the maximum improvement factor for different levels of limiting in two- and three-pulse cancelers using binomial weights. The variable a is the ratio of the limit voltage to the rms input clutter voltage. On this scale, $a = 0$ indicates "hard" limiting, and $a = \infty$ indicates an ideal linear system. With hard limiting, much of the advantage of higher-order cancelers is lost. As the limit level is allowed

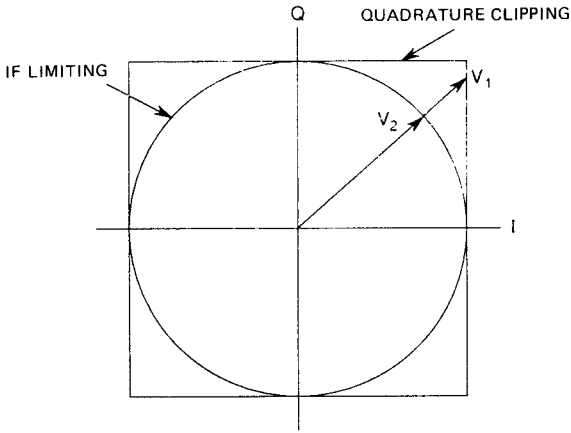

Figure 9.21 Representation of signal limiting in the I/Q domain. Quadrature clipping confines a signal (V_1) to a square; IF limiting confines a signal (V_2) to a circle.

to increase, the achievable improvement factors rise significantly. For example, with $a = 1$, the maximum value of I is only modestly degraded relative to an ideal system with $a = \infty$; the degradation is about 0.5 dB, 2 dB, and 6 dB in two-, three-, and four-pulse MTIs, respectively. The above analysis of MTI limiting has been extended to include the effects of receiver noise [290] as well as the signal [468].

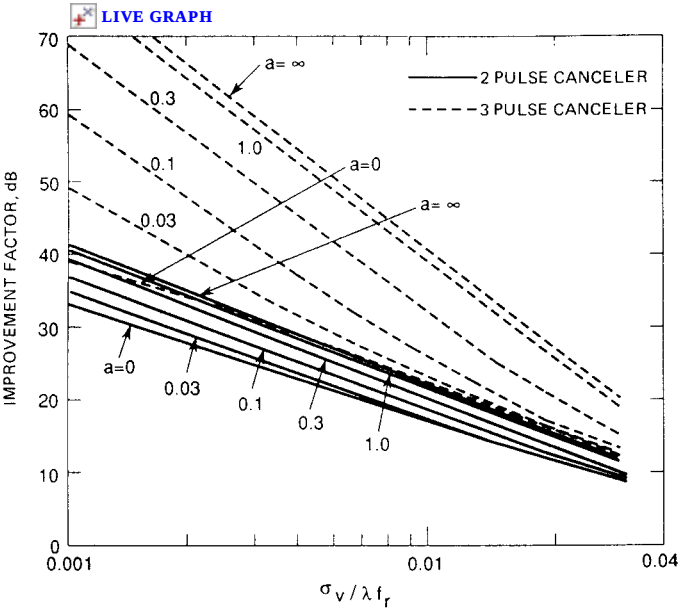

Figure 9.22 Maximum achievable MTI improvement due to IF limiting in three- and four-pulse cancelers. a defines limit voltage divided by rms clutter voltage (*From Ward & Shrader [75], © IEEE, 1968*)

The losses associated with IF limiting (Fig. 9.22) are not as severe as those for quadrature clipping (Fig. 9.19). This result is due to the fact that clutter phase changes cause abrupt discontinuities with quadrature clipping but not with IF limiting, as suggested by the vector limit diagram of Fig. 9.20. Therefore, the spectral spreading with IF limiting is less severe than with quadrature clipping. Consequently, a digital MTI system may perform better if a limiter is included at IF, such that there is less clipping in the quantization process [783].

The preceding analysis has used the conventional improvement factor as an index of MTI performance. There is some intuitive appeal in the notion that the reduction in interference power is a meaningful index of performance. However, the use of a power-related index for nonlinear processes should be made with caution, as shown in the next section.

Performance index for nonlinear or noncoherent processes—amplitude-processing MTI

The improvement in signal-to-clutter power is customarily used as an index of MTI performance. For linear MTI processes, such as general weighted summer of Fig. 9.7, this directly translates into an equivalent improvement in target detectability. Such is not always the case when the clutter signal is subjected to a nonlinear or noncoherent transformation prior to the MTI or filtering process. Although the power definition of I is often more tractable mathematically for noncoherent processes [205, 414], its relationship to detectability improvement is not always apparent.

Two possible definitions of an *improvement factor* were suggested by Bath and Castella [47]:

$$I_{\text{power}} = \frac{(S_0/S_i)}{(C_0/C_i)} = \frac{(S_0/C_0)}{(S_i/C_i)} \tag{9.45}$$

$$I_{\text{detection}} = \frac{(S_i/C_i)_{D,1}}{(S_i/C_i)_{D,n}} \tag{9.46}$$

where S_0, S_i, C_0 and C_i refer to the signal and clutter power at the output and input of the MTI processor, $(S_i/C_i)_{D,1}$ is the input S/C ratio needed to achieve some stated level of detection with one pulse, and $(S_i/C_i)_{D,n}$ is the input S/C ratio needed for the same level of detection after processing n pulses in an MTI filter. The first expression is the

conventional definition of the MTI improvement factor, and is based only on a power ratio, without regard to detection performance. The second definition is based on detectability. When n samples of a gaussian clutter process are coherently combined in a general weighted summer (Fig. 9.7), the two definitions are the same. However, when the samples are first subjected to a nonlinear or noncoherent transformation, such as with the noncoherent MTI shown in Fig. 9.3, the two definitions can be very different.

The equality of the two definitions for a linear, coherent processor follows from the fact that a linear combination of gaussian samples remains gaussian, but with modified standard deviation. If a nonlinearity or noncoherent transformation occurs prior to the MTI filtering process, the statistical distribution of residues becomes altered, and a simple power calculation does not necessarily correspond to the same detectability gain. The distinction can be very significant as illustrated in Fig. 9.23. The figure compares a two-pulse noncoherent amplitude MTI having a square-law envelope detector (as in Fig. 9.3), with a coherent MTI (as in Fig. 9.5). The two solid lines represent the improvement factor calculated using a detectability criterion [Eq. (9.46)]. For a correlation coefficient of $\rho = 0$ (wideband noise), the noncoherent MTI performs below the coherent system by about 10 dB; for larger ρ where MTI filtering is effective, the difference is closer to 13 dB. The broken line indicates the improvement factor using a power ratio calculation for the noncoherent MTI according to Eq. (9.45). From the power ratio definition, one might conclude that the noncoherent pro-

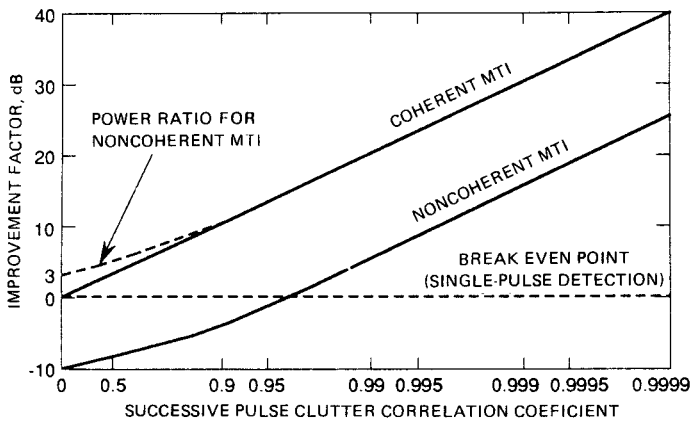

Figure 9.23 Comparison of the improvement factors of two-pulse coherent and noncoherent MTIs ($P_D = 0.5$; $P_{fa} = 10^{-6}$ averaged over all Dopplers). Solid lines apply to detectability definition of improvement factor; broken curve applies to power ratio definition. (*From Bath & Castella [47], © IEEE, 1984*)

cessor is superior to the coherent processor for small values of ρ, and that it converges to the performance of the coherent processor for larger ρ. But from a detectability viewpoint, this conclusion would clearly be erroneous.

With a three-pulse canceler the detectability improvement for a square-law noncoherent processor is typically 20 dB below that for a coherent MTI; with a four-pulse canceler, the noncoherent MTI loss is about 25 dB. Bath and Castella also show that the performance of the noncoherent MTI depends on the power law of the detector and the input S/C ratio. The maximum attainable P_d with a linear-law detector is 0.66, even for large S/C ratios at the radar input. With higher-order detector laws, P_d approaching 1.0 is attainable with sufficiently large S/C ratios.

9.5 Ambiguous-Range Clutter

For radar processors employing multiple pulses in each beam position, a limitation on target detection may be imposed by clutter foldover, i.e., reflections from ranges other than that of the target itself. In a low PRF system (range unambiguous), reflections from ranges beyond the target add to the total clutter power interferences. The relative amount of clutter power returned from distant ranges depends critically on the propagation conditions. Commonly encountered evaporation ducts, for instance, enhance surface-clutter returns from ranges well beyond the "standard atmosphere" horizon [583].

Returns from the first ambiguous range are customarily called *second-time-around clutter;* returns from the next interval are called *third-time-around clutter,* etc. Returns from ambiguous ranges can severely limit the achievable clutter improvement in environments where the clutter is extensive in range. This limitation results from the fact that ambiguous-range returns do not receive the full set of processor weights, thus seriously compromising the MTI rejection characteristic.

The effects of ambiguous-range clutter can be easily illustrated in a two-pulse MTI system. Consider the residue power from a reference range, R_0, at which a target's detection must be tested.

$$\overline{E_r^2(t)} = \overline{\{E_0(t) - [E_0(t + T) + E_1(t)]\}^2} \tag{9.47}$$

where $E_r(t)$ = the residue signal, $E_0(t)$ and $E_0(t + T)$ are the clutter returns from the first and second pulses at range R_0; $E_1(t)$ is the second-time-around clutter from the first ambiguous range $R_1 = (R_0 + r_u)$, r_u is the unambiguous range given by $CT/2$, and T is the interpulse interval. The bar over the expression indicates the statistical average. Equation (9.47) may be alternatively expressed as

$$\overline{E_r^2(t)} = \overline{\{[E_0(t) - E_0(t + T)]^2} - \overline{2E_1(t)[E_0(t) - E_0(t + T)]} + \overline{R_i^2(t)}\} \quad (9.48)$$

The first term is the residue signal in the absence of second-time-around clutter. The middle term vanishes because $\overline{E_0 E_1} = 0$ (the returns from ranges R_0 and $(R_0 + r_u)$ are independent). Equation (9.48) may be conveniently expressed as

$$\overline{E_r^2(t)} = \overline{E_0^2}[2 - 2\rho_0(T) + k_1] \quad (9.49)$$

where k_1 = the ratio of clutter power at the target range to that at the first ambiguous range, i.e.,

$$k_1 = \overline{E_1^2}/\overline{E_0^2} \quad (9.50)$$

The clutter improvement factor is given by the ratio of signal gain to clutter gain (or reduction), expressed by

$$I = \frac{\overline{S_0}/S_i}{\overline{E_r^2}/\overline{E_0^2}} \quad (9.51)$$

Following standard conventions, the signal gain term in the numerator is typically averaged over all Doppler frequencies. For the two-pulse canceler, $\overline{S_0}/S_i = 2$, and Eq. (9.51) may be expressed as

$$I = \left[1 - \rho_0(T) + \frac{k_1}{2}\right]^{-1} \quad (9.52)$$

where $\rho_0(T)$ = the correlation coefficient of the returns from the target range. The limitation on the improvement factor imposed by the second-time-around clutter may be evaluated by assuming that the clutter is perfectly correlated at the detection range, i.e., $\rho_0(T) = 1$, in which case

$$I_{\max} = \frac{2}{k_1} \quad (9.53)$$

For a three-pulse canceler, the returned signal includes contributions from both first and second ambiguous ranges. The residue power with binomial weights is given by

$$\overline{E_r^2} = \overline{\{E_0(t) - 2[E_0(t + T) + E_1(t)] + [E_0(t + 2T) + E_1(t + T) + E_2(t)]\}^2} \quad (9.54)$$

With manipulations similar to those used for the two-pulse canceler analysis,

$$I = \left[1 - \frac{4}{3}\rho_0(T) + \frac{1}{3}\rho_0(2T) - \frac{2}{3}k_1\,\rho_1(T) + \frac{5}{6}k_1 + \frac{1}{6}k_2\right]^{-1} \tag{9.55}$$

The first three terms in the brackets give the double-canceler improvement factor in the absence of clutter foldover; the additional terms are the contributions from first and second ambiguous interval clutter. The maximum improvement factor is again obtained for perfect correlation, i.e., $\rho(T) = \rho(2T) = 1$, so that

$$I_{\max} = \frac{6}{k_1 + k_2} \tag{9.56}$$

where $k_2 = \overline{f_2^2}/\overline{f_0^2}$, which represents the relative amount of clutter power reflected from the second ambiguous range ($R_0 + 2r_u$). If the first-interval clutter is dominant ($k_1 >> k_2$), then, comparing Eqs. (9.53) and (9.56) shows that the binomial three-pulse canceler has a limitation that is better than the two-pulse canceler only by a factor of 3 (5 dB).

The limitation from clutter foldover in a general n-pulse processor with arbitrary weights, W_i, is

$$I_{\max} = \sum_1^n W_i^2 \left[k_0\left(\sum_1^n W_i\right)^2 + k_1\left(\sum_2^n W_i\right)^2 + k_2\left(\sum_3^n W_i\right)^2 + \cdots k_{n-1}\,W_n^2\right]^{-1} \tag{9.57}$$

The first summation term in the foregoing expression represents the general signal gain in the numerator of Eq. (9.50), and the terms in brackets represent the denominator. By definition, $k_0 \equiv 1$. Equation (9.57) is based on the assumption that $\rho(T) = 1$ for all T; consequently, the expression gives the maximum possible value of I.

Equation (9.57) suggests that only the clutter at the unambiguous range R_0 receives the benefit of all n weights. Subsequent ambiguous-range returns are processed with fewer of the weights and therefore receive relatively little cancellation. For example, the first weight W_1 is absent from the returns at the first ambiguous range ($R_0 + r_u$), with the result that the cancellation of those returns is significantly compromised.

The cancellation of ambiguous-range returns can be improved by using *fill pulses*, i.e., pulses that are transmitted but given zero weight in the receiver processor. The benefit of fill pulses can be illustrated in the three-pulse canceler, in which the weights are $W_1 = 0$, $W_2 = 1$, $W_3 = -1$. In this example, the first pulse is a fill pulse, and the other two are combined as in a two-pulse canceler. The maximum improvement factor according to Eq. (9.57) is:

$$I_{\max} = \frac{2}{k_2} \tag{9.58}$$

This expression may be compared with Eq. (9.56), which is the corresponding limitation of a three-pulse canceler without a fill pulse. Consider, for example, $k_1 = 10^{-2}$ (−20 dB), and $k_2 = 10^{-4}$ (−40 dB). The three-pulse canceler in this example would have a maximum improvement factor of 27.7 dB, but with a fill pulse, the limitation would be 43.0 dB.

The limitation from ambiguous-range clutter is illustrated in the following for rain and for sea clutter under various conditions of evaporation ducts.

In volume clutter that fills the radar beam, the returned power is inversely proportional to the square of range, such that

$$k_i = \frac{R_0^2}{(R_0 + ir_u)^2} \tag{9.59}$$

From Eq. (9.58) the maximum improvement factor in a two-pulse canceler is

$$I_{\max} = \frac{2(R_0 + r_u)^2}{R_0^2} \tag{9.60}$$

It is interesting to note that beyond one-half the unambiguous range ($R_0 \geq 0.5\, r_u$), the maximum clutter improvement factor for the single canceler is only 12.5 dB.

Equation (9.60) is pessimistic in that it uses the assumption that the clutter completely fills the beam at the first ambiguous range. If a maximum altitude for rain (or chaff) is assumed, the ambiguous range echoes only partially fill the beam. Equation (9.60) can then be rewritten

$$I_{\max} = \frac{2(R_0 + r_u)^2}{R_0^2\, \Delta F_1} \tag{9.61}$$

where ΔF_1 = the fraction of the beam volume that is filled by clutter at a range $R_0 + r_u$.

A similar expression for a three-pulse canceler without fill pulses can be expressed from Eq. (9.56) as

$$I_{\max} = 6 \left[\frac{\Delta F_1\, R_0^2}{(R_0 + r_u)^2} + \frac{\Delta F_2\, R_0^2}{(R_0 + 2r_u)^2} \right]^{-1} \tag{9.62}$$

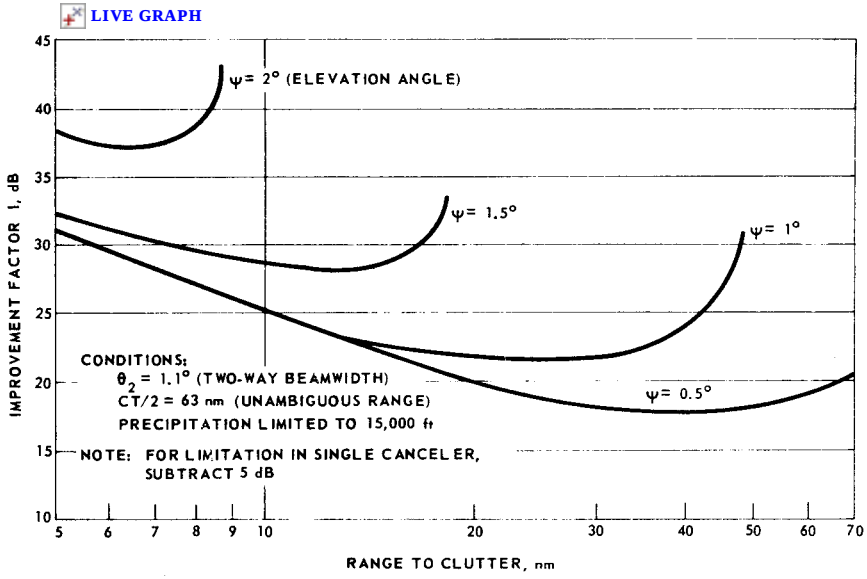

Figure 9.24 Limitation on improvement factor due to second-time-around clutter for double canceler MTI.

The first term in the brackets generally dominates the second. As noted previously, the maximum improvement factor of the three-pulse canceler is only 5 dB above that for the two-pulse canceler.

The effect of ambiguous-range clutter from rain is illustrated in Fig. 9.24 for a surface radar with a 1.1°, two-way beamwidth. The unambiguous range is 63 nmi. The term, ΔF_1, has been estimated from a $^4/_3$ earth chart, with uniform rain up to an altitude of 15,000 ft. The increase in I at longer ranges is the result of the majority of the beam being above the rain at the ambiguous range. Some clutter, however, may remain in the sidelobes of the antenna. This analysis does not treat the problem of sidelobe clutter.

Figure 9.25 illustrates the improvement factor limitation imposed by ambiguous range sea clutter in a three-pulse MTI canceler [582]. Values for k_1 and k_2 for use in Eq. (9.56) have been derived for sea clutter under evaporation ducting conditions [583]. In this example, the radar is at S-band, and the unambiguous range is either 20 or 30 km. Corresponding limitations in a two-pulse canceler may be closely approximated by subtracting 5 db from the values shown in the figure.

The limitations due to ambiguous range foldover depend critically on the radar PRF, the processor weights, and the profile of clutter power versus range. In our sea clutter example, ambiguous range clutter was not particularly serious, unless the unambiguous range interval was relatively short, and the duct height was relatively large. It would,

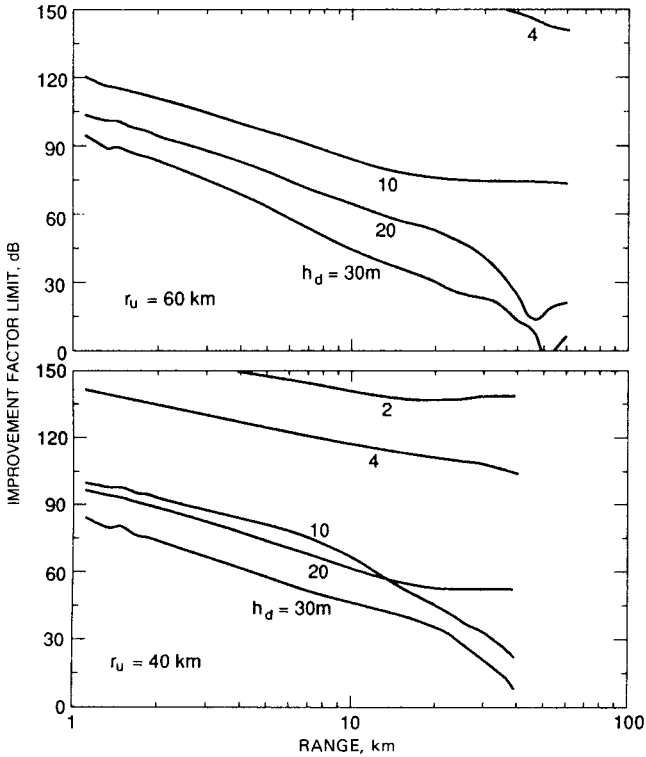

Figure 9.25 Improvement factor limitation due to ambiguous-range clutter in three-pulse binomial canceler; X-band; h_d refers to evaporation duct height (m); r_u refers to unambiguous range interval (km).

however, be possible to construct examples of surface clutter in which the limitations imposed by distant clutter were more serious. For example, land returns from a distant coast could provide significant returns, particularly if a propagation duct were present.

As a general rule of thumb, the required number of fill pulses is equal to the ambiguous range interval at which efficient clutter cancellation is needed. If ambiguous-range clutter is not significant, then fill pulses are not needed; if it is desirable to cancel clutter at the first ambiguous-range interval, then one fill pulse is needed, etc.

To illustrate the potential advantages of fill pulse processing, consider the preceding rain clutter example. For a receiver gate centered at 20 nmi and for rain filling the beam at the ambiguous ranges, the relative power factors from Eq. (9.59) are $k_1 = 0.057$, and $k_2 = 0.011$. However, the rain altitude limitation of 15,000 ft places the rain outside the radar beam at the second ambiguous range (188 nmi) with the

result that $k_2 = 0$, regardless of the elevation angle. Thus, in this example, the three-pulse improvement factor limitation without filling [Eq. (9.56)] is 20.2 dB; but with single-pulse filling [Eq. (9.58)], is theoretically infinite, i.e., is limited by factors other than ambiguous range reflections.

The benefits of fill processing are realized only if the pulse train uses a constant interpulse interval so that ambiguous clutter is sampled at the same range on each successive receiver sample. If, however, interpulse staggering is used, the ambiguous ranges would not necessarily be the same on each sample. As a result, clutter beyond the unambiguous range would not receive the benefits of MTI cancellation.

These observations suggest the use of adaptive strategies if the radar system can alter its repetition interval and pulse weights. In an ideal system, the number of pulses, their weights, and the repetition interval would be adaptable to the magnitude and fluctuation spectrum of the clutter at the target location, as well as the magnitude and characteristics of clutter at distant ranges.

9.6 Airborne MTI

Airborne radars are sometimes used for long-range surveillance of air targets. In such systems, surface clutter may be a serious source of interference that often requires the use of some sort of MTI filtering. Airborne MTI (AMTI) systems pose special technical challenges and limitations that are generally not of concern in fixed or ship-borne radars. Figure 9.26 illustrates some features of an AMTI radar. An aircraft is assumed to have a platform velocity V_p. The corresponding clutter Doppler velocity, V_c, will depend on the scan angle coordinates according to

$$V_c = V_p \cos \theta \cos \alpha \tag{9.63}$$

where θ and α are the azimuth and depression angles with respect to the velocity vector of the aircraft (level flight assumed). This leads to lines of constant Doppler frequency called *isodops* that form hyperbolas on the earth's surface (using a flat-earth analogy). For surveillance of distant targets, $\alpha \approx 0°$, and V_c varies as $\cos \theta$. Another feature emphasized in the figure is that the illuminated areas on two successive pulses at the same range and angle do not precisely overlap. These features impose unique requirements and limitations in the AMTI system.

One obvious requirement of the AMTI system is the need for clutter-locking measures to compensate for a significant Doppler offset. Such compensation must vary with the scan angle. One of the early clutter-

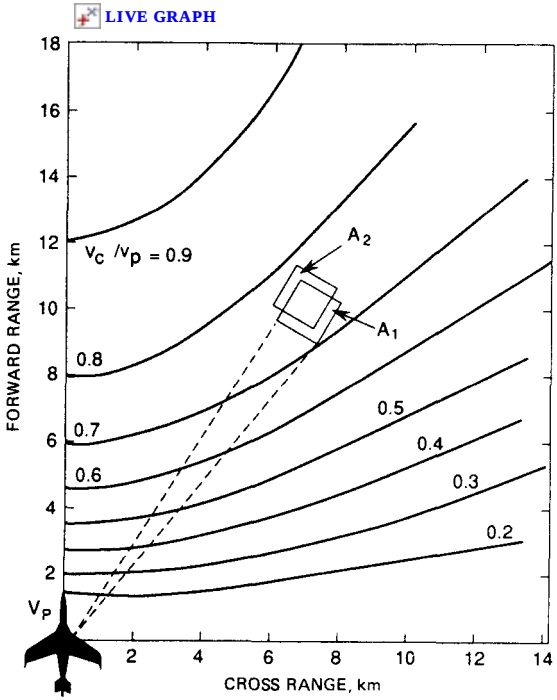

Figure 9.26 Clutter characteristics seen by airborne radar. Curves represent "isodops," having constant mean Doppler frequency, expressed as a fraction of platform velocity, V_p. A_1 and A_2 represent illuminated areas on two successive pulses at same range and azimuth relative to platform. Distance scale applies to platform altitude of 6 km.

locking techniques became known as the TACCAR system ("time averaged clutter coherent airborne radar"), a description of which has been presented by Shrader [653]. Later methods for clutter locking are referred to in Secs. 9.1 and 9.2.

The isodop lines become more closely spaced as the scan angle varies from zero to 90°. Consequently, the spectral spread increases as the viewing direction moves toward broadside. The azimuth dependence of spectral spreading is roughly given by the derivative of Eq. (9.63) with respect to azimuth (assuming $\alpha \approx 0$ for distant ranges). The velocity spread with respect to an antenna angular increment of $d\theta$ is thereby given by:

$$dV_c = V_p \sin\theta \, d\theta \tag{9.64}$$

The equation suggests that the clutter velocity spread is a minimum when viewing straight ahead and is maximum at broadside angles. An

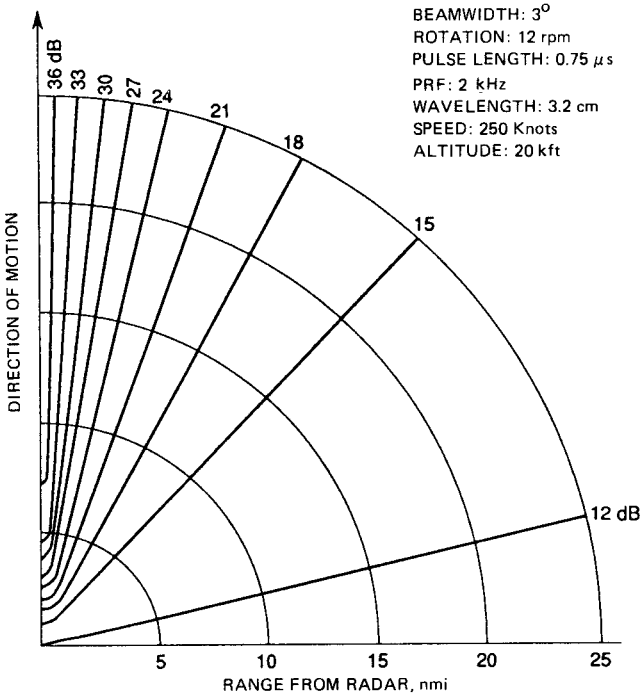

Figure 9.27 Contours of equal MTI improvement factor for Airborne MTI. Contours are symmetric in all four quadrants. (*Adapted from Dickey* [*178*])

explicit form for the clutter spectrum in an airborne radar is given in Sec. 10.5. It follows that, with perfect clutter locking, the achievable MTI improvement factor will be maximum at zero azimuth and will decrease toward broadside azimuth angles. Figure 9.27 [178] illustrates the theoretical performance of an AMTI at X-band. In this example, the clutter improvement I varies from 36 dB at zero degrees to less than 12 dB at broadside.

The antenna sidelobes can impose a significant limitation in an AMTI. This statement can be appreciated with reference to Fig. 9.26, which suggests that the three-dimensional antenna pattern will encounter Doppler frequencies from zero to the full platform velocity. often the Doppler spread will exceed the PRF, and will completely fill the target Doppler coverage. In such cases, the improvement factor limitation imposed by antenna sidelobes can be roughtly approximated as the ratio of integrated power in the antenna pattern to the integrated power in the sidelobes. Because of the relationship between the sidelobes and clutter Doppler, AMTI performance can be improved with antenna aperture weighting procedures [13].

The effects of platform motion on AMTI performance depend on platform velocity, antenna depression and azimuth angles, antenna pattern, pulse width, wavelength, and altitude [178, 221, 264, 325]. One limitation arises from the fact that, for a constant range and azimuth with respect to the aircraft, the illuminated area is slightly displaced from one pulse to the next, resulting in a loss of correlation of the signal returned from the two pulses. For a shift only in range (applicable to 0° azimuth), the correlation of the I- or Q-channel signal versus range displacement for a uniform distribution of scatterers is

$$\rho(nT) = \frac{\Delta R - nV_pT}{\Delta R} \qquad \text{for } 0 \le nV_pT \le \Delta R \tag{9.65}$$

where ΔR = the range resolution. To illustrate the potential limitation, consider a system with an interpulse period of 2 ms, a range resolution of 75 m (τ = 0.5 μs), and a platform velocity of 150 m/s (291 kn). Equation (9.65), along with Eqs. (9.16) and (9.17), indicates a limitation of 21.8 dB for a two-pulse canceler, and 23.5 dB for a three-pulse canceler. Even a modest range shift can impose a significant limitation on the AMTI. Its effects can be mitigated in a phased array or multiple-feed dish antenna by shifting its phase center between transmitted pulses. This configuration is called a *displaced phase center antenna* (DPCA) [673, Chap. 16].

9.7 System Limitations

The MTI improvement is limited by those factors that reduce the correlation of the clutter. In previous sections we examined the effects of decorrelation imposed by the fluctuating structure of the clutter scatterers. Other sources of decorrelation can be traced to instabilities and motion of the radar itself. Several of the sources are considered in this section.

Phase errors

Phase instabilities in the demodulation process result in fluctuations in the clutter signal. The residue due to a phase change $\Delta\varphi$ at the IF frequency may be expressed by

$$\begin{aligned} E_r &= E_1 - E_2 \\ &= E\cos(\omega_{IF}t + \varphi_0) - E\cos[\omega_{IF}(t + T) + \varphi_0 + \Delta\varphi] \end{aligned}$$

where E = the magnitude of the uncanceled signal
$\Delta\varphi$ = the phase error over the interpulse period

IF = the intermediate frequency
T = the pulse repetition period

This equation may be reduced to

$$\frac{E_r}{E} \cong 2 \sin \frac{\Delta\varphi}{2} \sin \left(\omega_{IF} t + \varphi_0 + \frac{\Delta\varphi}{2} \right)$$

The ensemble average of the magnitude of E_r^2/E^2 is recognized as the reciprocal of the clutter attenuation factor. For small values, $\sin \Delta\varphi \cong \Delta\varphi$, which results in

$$\frac{1}{\text{CA}} = \frac{\overline{|E_r|^2}}{\overline{E^2}} = \overline{\Delta\varphi^2} \qquad \text{for the single canceler} \tag{9.66}$$

Using Eq. (9.11), the improvement ratio as limited by phase instability is

$$I_1 = \frac{2}{\overline{\Delta\varphi^2}} \qquad \text{limitation due to phase instability} \tag{9.67}$$

Equation (9.67) expresses the clutter improvement limitations due to phase instabilities that can arise from transmitter STALO or COHO variations in a single-canceler system.

A similar analysis of the double-canceler system requires some assumptions concerning the correlation of phase instabilities. The forms of the three pulses at the input of the double canceler are

$$E_1 = E \cos (\omega_{IF} t + \varphi_0)$$

$$E_2 = E \cos [\omega_{IF}(t + T) + \varphi_0 + \Delta\varphi_1]$$

$$E_3 = E \cos [\omega_{IF}(t + 2T) + \varphi_0 + \Delta\varphi_1 + \Delta\varphi_2]$$

where $\Delta\varphi_1$, $\Delta\varphi_2$ = respective phase errors in radians during the first and second interpulse periods. The normalized residue is

$$\frac{1}{\text{CA}_2} = \frac{\overline{|E_1 - 2E_2 + E_3|^2}}{\overline{E^2}} \frac{\overline{|E_{r2}|^2}}{\overline{E^2}}$$

Two special cases of E_{r2} are of interest. In the first case, the phase errors from one pulse to the next are assumed equal (as in an oscillator with constant or slow drift). In this case the peak residue for small $\Delta\varphi$ gives

$$\frac{1}{\text{CA}_2} = \frac{\overline{|E_{r2}|^2}}{\overline{E^2}} \cong \overline{\Delta\varphi^4} \qquad (\text{for } \Delta\varphi_1 = \Delta\varphi_2)$$

In the second case, the phase errors from one pulse to the next are assumed statistically independent, that is, $\overline{\Delta\varphi_1\Delta\varphi_2} = 0$. In this case the peak residue is

$$\frac{1}{CA_2} \cong 2\overline{\Delta\varphi^2} \qquad \text{for } \overline{\Delta\varphi_1\Delta\varphi_2} \cong 0$$

The improvement ratio limitation for the double canceler is

$$\left.\begin{aligned} I_2 &= \frac{6}{\overline{\Delta\varphi^4}} \qquad \text{for } \Delta\varphi_1 = \Delta\varphi_2 \\ I_2 &= \frac{3}{\overline{\Delta\varphi^2}} \qquad \text{for } \Delta\varphi_1 \text{ independent of } \Delta\varphi_2 \end{aligned}\right\} \text{limitation due to phase instability} \tag{9.68, 9.69}$$

For phase errors that are only partially correlated, the solution for I_2 lies between the values corresponding to Eqs. (9.68) and (9.69). An analysis of systematic instabilities is given by Barton [45].

Timing jitter

Timing jitter results in variations in the transmit interpulse time or in the receiver sampling time. The effects on MTI performance can be understood through the following approximate analysis. Consider two echoes returned from a stationary target where the interpulse delay time fluctuates about the nominal value T. The output of the canceler would consist of two spikes of width equal to the difference between the timing errors for the two pulses ϵ_1 and ϵ_2 as illustrated in Fig. 9.28. Prior to threshold detection, the pulses are assumed to be passed through a low-pass filter whose bandwidth is approximately $1/\tau$ and rectified. The peak value of the residue out of such a filter is approximately

$$E_r = \frac{E(\epsilon_1 - \epsilon_2)}{\tau}$$

where ϵ_1, ϵ_2 = the timing errors for the first and second pulses.

The normalized residue power averaged over the ensemble for the two pulses is

$$\frac{\overline{E_r^2}}{\overline{E^2}} = \frac{2\overline{(\epsilon_1 - \epsilon_2)^2}}{\tau^2}$$

which, for independent ϵ_1, ϵ_2, is

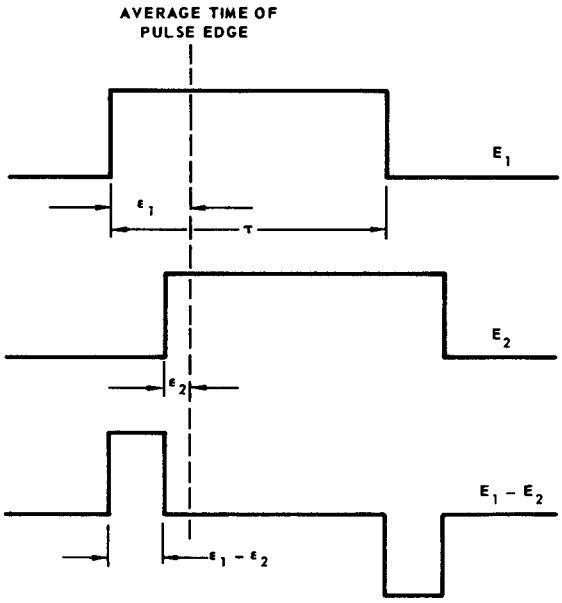

Figure 9.28 Illustration of pulse-to-pulse timing jitter.

$$\frac{1}{\text{CA}_1} = \frac{\overline{E_r^2}}{\overline{E^2}} = \frac{4\sigma_\epsilon^2}{\tau^2} \quad \text{for the single canceler}$$

where σ_ϵ^2 = the variance of the leading time of the pulse.

Using a similar procedure, the residue from the double canceler for the two impulses reduces to [581]

$$\frac{1}{\text{CA}_2} \leq \frac{12\sigma_\epsilon^2}{\tau^2}$$

Taking the equality for the more pessimistic value, the improvement ratio, as limited by pulse jitter for either a single or double canceler, can be expressed as

$$I_1 = I_2 = \frac{\tau^2}{2\sigma_\epsilon^2} \qquad \text{limitation due to timing jitter} \tag{9.70}$$

A more rigorous analysis of timing jitter has been carried out by Liu [442] in terms of arbitrary MTI weights and spatial distribution of clutter. For conventional MTI and clutter assumptions, the improvement factor for both two- and three-pulse cancelers can be expressed as

$$I \cong \frac{d^2}{(\sigma_{\epsilon 1}^2 + \sigma_{\epsilon 2}^2)} \tag{9.71}$$

where $\sigma_{\epsilon 1}^2$ and $\sigma_{\epsilon 2}^2$ are the rms values of the transmitter and receiver sampling jitter respectively, and d is the rms value of the transmitted pulse (equal to 0.58τ for a square pulse of width τ). It can be seen in this expression that the effects of transmitter and receiver sampling timing jitter are identical.

Another cause of cancellation residue that is quite similar to pulse position jitter results from variations in pulse width. Since a pulse width variation of δ produces a single spike of the same width, the improvement factor can be immediately written by comparison with that for pulse jitter

$$I_1 = I_2 = \frac{\tau^2}{\sigma_\delta^2} \qquad \begin{matrix}\text{limitation due to pulse} \\ \text{width variations}\end{matrix} \tag{9.72}$$

where σ_δ^2 = the variance of the pulse width.

Amplitude instabilities

Another source of canceler residue can arise from pulse-to-pulse fluctuations in transmitted power or in signal gain. The residue from two pulses of different amplitudes is

$$E_r = \Delta E_1 - \Delta E_2$$

where ΔE_1, ΔE_2 = the voltage variations about a mean value for the two pulses. The normalized residue power is expressed in terms of the relative amplitude fluctuation as

$$\frac{\overline{E_r^2}}{E^2} = \frac{\overline{(\Delta E_1 - \Delta E_2)^2}}{E^2}$$

which, for independent fluctuations, becomes

$$\frac{1}{\mathrm{CA}_1} = \frac{\overline{E_r^2}}{E_2} = \frac{2\sigma_E^2}{E^2} \qquad \text{for the single canceler}$$

The normalized residue for the double canceler is

$$\frac{\overline{E_{r2}^2}}{E^2} = \frac{\overline{(\Delta E_1 - 2\Delta E_2 + \Delta E_3)^2}}{E^2}$$

Again assuming independent fluctuations,

$$\frac{1}{\mathrm{CA}_2} = \frac{\overline{E_{r2}^2}}{E^2} = \frac{6\sigma_E^2}{E^2} \qquad \text{for the double canceler}$$

The clutter improvement ratios follow from Eq. (9.13).

$$I_1 = I_2 = \frac{E^2}{\sigma_E^2} \qquad \text{limitation due to amplitude fluctuation} \tag{9.73}$$

Antenna scanning limitations

It was shown in Sec. 9.6 that the translational motion of the antenna can impose a significant limitation on the achievable improvement factor because of the degradation of the pulse-to-pulse clutter correlation. Another important cause of clutter decorrelation is related to the angular motion of the antenna in a mechanically scanned system. Because of the antenna rotation, the radar does not receive echoes from the identical patch of scatterers from one pulse to the next, which causes a loss of correlation. Of course in an electronically scanned system, the antenna coordinates would remain fixed during an MTI dwell, and this limitation would not exist. The effects of antenna scanning can be analyzed by approximating a two-way antenna pattern as a gaussian function

$$G(\theta) = G_0 \exp\left(-\theta^2/2\sigma_{\theta 2}^2\right) \tag{9.74}$$

where $\sigma_{\theta 2}$ = the equivalent two-way standard deviation of the antenna power pattern (radians) and G_0 is the on-axis antenna power gain factor. The voltage of the echo from an elemental reflector would also have a gaussian time function as the antenna scans the patch of reflectors. The voltage from any individual scatterer would then vary with time as

$$E(t) = K \exp\left(-t^2/2\sigma^2\right) \tag{9.75}$$

where $\sigma = \sqrt{2}\sigma_{\theta 2}/\alpha$ is the standard deviation of the time function
α = the rotation rate of the antenna, rad/s
K = a scaling factor

When many independent scatterers are present, numerous responses, each having the form of Eq. (9.75), are superimposed. The resulting spectrum retains the shape of the individual spectra, but the scaling factor K is increased.

The power spectral density function of the return is obtained by taking the squared magnitude of the Fourier transform of $E(t)$, which is

$$G(\omega) = G_0 \exp(-\omega^2/2\sigma_\omega^2)$$

where $\sigma_\omega = (\alpha/2\sigma_{\theta 2})$, rad/s
ω = the radian frequency variable
σ_ω = the standard deviation of the spectrum, rad/s

The spectrum standard deviation due to scanning is expressed in hertz by dividing σ_ω by 2π. Furthermore, the standard deviation of the antenna pattern $\sigma_{\theta 2}$ may be replaced by an equivalent expression for the two-way, half-power azimuth beamwidth θ_2, which for a gaussian pattern is related by $\theta_2 \cong 2.36\ \sigma_{\theta 2}$. The result of these substitutions is

$$\sigma_s = \frac{\alpha}{5.35\ \theta_2} \text{ Hz} \tag{9.76}$$

where σ_s is the spectrum width induced by antenna scanning, Hz, and θ_2 is the two-way horizontal beamwidth, rad.

The effect of the scanning spectrum spreading σ_s can be more readily compared to that of clutter motion σ_v by converting σ_s in Eq. (9.76) to equivalent velocity units through the Doppler equation

$$\sigma_s = \frac{\alpha\lambda}{10.7\ \theta_2} \text{ m/s} \tag{9.77}$$

with λ in meters and α in rad/s.

Figure 9.29 shows σ_s for various beamwidths and rates of scanning.

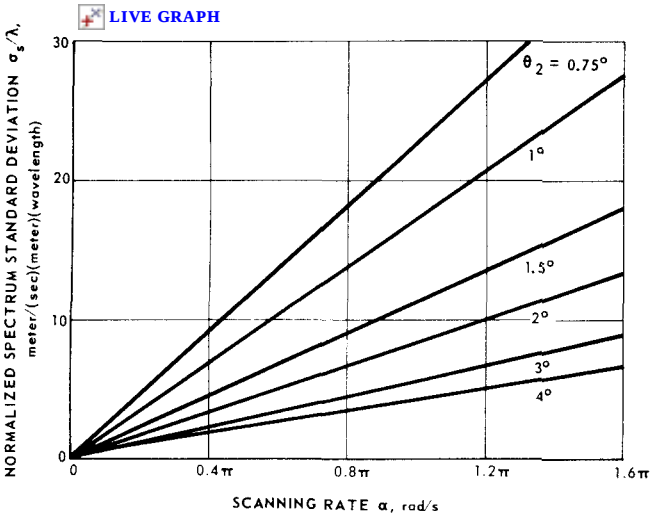

Figure 9.29 Normalized spectrum width due to antenna scanning (two-way half-power horizontal beamwidth = θ_2).

To determine the MTI performance limitation caused by antenna scanning, the value of σ_s may be used along with Fig. 9.10 to obtain a value of the improvement factor. The result is nearly identical when the more realistic sin θ/θ pattern is assumed [295]. The limitation due to antenna scanning can be significant but can often be eliminated by using an electronically scanned antenna.

MTI system improvement factor

In the previous paragraphs we discussed factors that limit the clutter improvement ability of MTI radars. These individual limitations may be combined to give the system clutter improvement. To obtain the system improvement, recall that the clutter improvement is defined in terms of the residue power at the output of the canceler. If each source of residue power is independent, then the total residue power $\overline{E_{rt}^2}$ is simply the sum of the separate causes $\overline{E_{ri}^2}$, that is

$$\overline{E_{rt}^2} = \overline{E_{ra}^2} + \overline{E_{rb}^2} + \overline{E_{rc}^2} + \cdots \overline{E_{ri}^2}$$

Then, the total system improvement ratio I_T may be calculated from

$$I_T = \frac{\overline{S}_0}{S_i} \text{CA} = \frac{\overline{S}_0 \, \overline{E^2}}{S_i \overline{E_{rt}^2}}$$

It is evident from the preceding equation that the system improvement ratio can be determined from the individual ratios by

$$\frac{1}{I_T} = \frac{1}{(I)_a} + \frac{1}{(I)_b} + \frac{1}{(I)_c} + \cdots \tag{9.78}$$

where I_T is the total system improvement factor (power ratio) and $(I)_i$ is the improvement as limited by the ith cause.

To illustrate the relative importance of the various limitations, consider a radar that has the following parameters:

λ = 50 cm (transmitted wavelength)
f_r = 0.6 kHz (pulse repetition frequency)
τ = 3 μs (pulse width)
$\varphi_2 = \theta_2$ = 1.5° (two-way vertical and horizontal beamwidth, respectively)
α = 0.4π rad/s (antenna scanning rate—12 r/min)
N = 2 (number of cascaded cancelers)

The type of cancellation scheme is a quadrature canceler. Assume the system instabilities are as follows:

σ_ϵ = 20 ns (timing jitter)
σ_δ = 15 ns (pulse-to-pulse width variation)
$\Delta\varphi$ = 10 mrad (pulse-to-pulse independence) (rms phase instability at the canceler frequency)
σ_E/E = 0.005 (amplitude instability pulse-to-pulse variation)

Let the source of clutter be precipitation at 50 nmi and the wind shear gradient be 4 m/(s)(km) where $\psi = 2°$ (elevation angle). The precipitation is assumed to exist up to 15,000-ft altitude. Table 9.1 lists the clutter improvement limitation due to each individual cause. The additional loss due to the mean velocity component is given when no clutter locking is used or, alternately, when clutter locking is provided on the basis of eight samples of interpulse phase change. The table shows that the overall system improvement is 13.8 dB when clutter locking is not used or 24.6 dB when it is used. In this example, the primary limitation is due to motion of the clutter.

TABLE 9.1 System Limitations for Example MTI

Source of limitation	I_2, dB	Determined by
I. Clutter motion		
1. Spectrum width $\sigma_v = (\sigma^2_{\text{shear}} + \sigma^2_{\text{turb}})^{1/2} = 4.2$ m/s	34	σ_{shear} and σ_{turb} from Chap. 6
2. Antenna scanning ($\sigma_s = 2.3$ m/s)	44	I_2 from Fig. 9.10 σ_s from Fig. 9.38
3. Total σ_v (Root sum square of 1 and 2) = 4.7 m/s	31.5	I_2 from Fig. 9.10
4. Additional loss due to mean velocity component		V_0 from Chap. 6 Loss from Fig. 9.11
(a) No clutter locking ($V_0/\sigma_v = 3.2$) Loss = 17 dB		V_0 from Chap. 6 Loss from Fig. 9.11
(b) With clutter locking ($n = 8$) Loss = 3 dB		Loss from Fig. 9.15
5. Total limitation due to motion		
(a) No clutter locking	14.5	Item 3 less item 4a
(b) With clutter locking	28.5	Item 3 less item 4b
II. Timing jitter	40	Eq. (9.67)
III. Pulse width variation	46	Eq. (9.69)
IV. Phase instability	45	Eq. (9.66)
V. Amplitude instability	46	Eq. (9.70)
VI. Second-time-around clutter	—*	Eq. (9.59)
VII. Total system improvement factor		
1. No clutter locking	13.8	Eq. (9.75) items I–VI
2. With clutter locking	24.6	Eq. (9.75) items I–VI

* In this example, the radar beam is completely out of the clutter of the first ambiguous range. Therefore, second-time-around clutter causes no limitation. (Altitude is determined with the aid of a 4/3 earth chart.)

Range equations for MTI systems

The clutter improvement factor describes the ability of the MTI system to improve the signal-to-clutter ratio; however, this factor may not always be directly used to compare the performance of two different systems since they could have the same clutter improvement even though one had a lower signal-to-clutter ratio to start with. The detection range in clutter, on the other hand, provides a basis for system evaluation and comparison. The following paragraphs develop expressions for the detection range for MTI radars.

MTI detection range for targets in volume clutter

Equation (9.21) approximated the clutter improvement factor for a single canceler. The values of σ_v and V_0 for precipitation may be related to range as discussed in Chap. 6. The following presents some of the environmental factors described in that section in a form that will be useful for the present discussion.

Chapter 6 showed that the spectrum variance for precipitation clutter σ_v^2 is due primarily to the effects of wind shear and turbulence, that is, $\sigma_v^2 = \sigma_{\text{shear}}^2$ can be approximated

$$\sigma_{\text{shear}} \approx 0.42\, k\Delta h = 0.42\, kR\varphi_2 \tag{9.79}$$

where Δh is the altitude spread of the radar beam, m; k is the component of wind velocity gradient in the direction of the radar beam, m/(s)(m) (for the up- or downwind case a typical value for the eastern United States is $k \cong 5.7$ m/(s)(km); φ_2 is the vertical half-power beamwidth—two-way path, rad; R is the range to clutter, m; and σ_{shear} is in m/s. The clutter improvement factor may be related to range by combining Eqs. (9.21) and (9.79). For $V_0 = 0$ this is

$$I_1 \cong \frac{\lambda^2 f_r^2}{8\pi^2(\sigma_{\text{turb}}^2 + 0.18\, k^2R^2\varphi_2^2)} \tag{9.80}$$

Chapter 2 developed the expression for detection range in volume clutter. Assuming that the required signal-to-clutter ratio in the MTI system may be decreased by an amount equal to the clutter improvement factor,* the range equation becomes†

* This assumption does not account for the effect that the velocity response characteristics of the canceler have on the detection probabilities. For a treatment of this topic, see Wainstein and Zubakov [740, Sec. 42].

† The additional loss due to the mean velocity component V_0 may be included in the loss factor L.

$$R^2 = \frac{4(\ln 2)\sigma_T L I_1}{\pi\theta_2\varphi_2(c\tau/2)(S/C)\Sigma\sigma_i} \tag{9.81}$$

where the value of I_1 is given by Eq. (9.80), which suggests two special cases. In one case the shear effect is dominant (as when the radar looks up- or downwind at distant ranges); in the other case the turbulence effect is dominant (as when the radar looks crosswind or for short ranges).* For the shear-dominant case, Eq. (9.81) becomes

$$R^4 = \frac{2.8(\ln 2)\lambda^2 f_r^2 \sigma_T L}{\pi^3 k^2 \theta_2^3 (c\tau/2)(S/C)\Sigma\sigma_i} \qquad (\sigma^2_{\text{shear}} \gg \sigma^2_{\text{turb}}) \tag{9.82}$$

This range equation is seen to depend on the product λf_r; (S/C) refers to the signal-to-clutter ratio at the input to the detector for a given P_D.

In the turbulence-limited case Eq. (9.81) becomes

$$R^2 = \frac{(\ln 2)\lambda^2 f_r^2 \sigma_T L}{2\pi^3\theta_2\varphi_2(c\tau/2)(S/C)\Sigma\sigma_i\sigma^2_{\text{turb}}} \qquad (\sigma^2_{\text{turb}} \gg \sigma^2_{\text{shear}}) \tag{9.83}$$

MTI detection range for targets in area clutter

Chapter 2 developed the expression for the detection range of targets in area clutter. Again assuming that the required signal-to-clutter ratio may be reduced by an amount equal to the clutter improvement ratio, the detection range expressions of Chap. 2 become

$$R^2 = \frac{\lambda^2 f_r^2 (\sin\psi)\sigma_T L}{2\pi^3\theta_2\varphi_2(S/C)\sigma_0(\sigma_v^2 + V_0^2)} \qquad \tan\psi > \frac{\varphi_2 R}{c\tau/2} \tag{9.84}$$

$$R = \frac{\lambda^2 f_r^2 (\cos\psi)\sigma_T L}{8\pi^2\theta_2(S/C)(c\tau/2)\sigma_0(\sigma_v^2 + V_0^2)} \qquad \tan\psi < \frac{\varphi_2 R}{c\tau/2} \tag{9.85}$$

Equations (9.82) to (9.85) show that the power law of the single-canceler range equation may vary between 1 and 4, depending on the condition of clutter. The maximum range in precipitation or in sea clutter may be calculated in the crosswind case by using a zero mean clutter velocity, and in the up- or downwind case by using V_0 from

* Another example of the turbulence-limited condition is for a chaff cloud that has a small vertical extent.

Chap. 6. As a result, the range coverage for MTI systems can be described by an elliptical pattern.

The previous range equations have been developed for the single-canceler system. The corresponding equations for the double-canceler can, using the clutter improvement factor I_2, be developed in a similar manner.

Chapter

10

Environmental Limitations of CW Radars

The continuous wave (CW) radar is frequently used for detection and tracking of moving targets.* In its simplest form a single sinusoid is transmitted, and the received signals are mixed with the transmitted carrier frequency. The existence of moving targets is determined from the *beat note* or Doppler frequency shift f_d.

$$f_d = \frac{2v}{\lambda} \tag{10.1}$$

where v is the radial velocity difference between the target and the radar (positive for closing geometries) and λ is the carrier wavelength. The advantage of this technique is its simplicity.

As with virtually all radar waveforms, the angle of arrival of the target echoes can be determined with multiple receive apertures or with monopulse receivers. On the other hand, there is no target-range determination or resolution except with special geometries that occur with lunar or planetary observation radars. If range resolution is re-

* For general references see Saunders in Skolnik [673], Povejsil et al. [557], and Vinitskiy [731].

quired, the transmit waveform must be modulated. Frequency modulation is discussed in Sec. 10.2 and Chap. 13, and binary-phase modulation is discussed in Chap. 12.

Since the CW receiver responds to echoes from all ranges, it is generally necessary to separate the *leakage* or *spillover* from the transmitter and signals from close-in clutter. This is usually accomplished by filtering out received signals at the carrier frequency and at the Doppler frequency of the clutter. An alternate technique is to pulse the transmitter at a rate higher than twice the expected Doppler frequency. This technique is called interrupted CW or ICW to distinguish it from *pulse Doppler* or range-gated processors. ICW is discussed in Secs. 10.2 and 10.4, and pulse-Doppler processors are discussed in Chap. 11.

Rather than delve into the wide variety of CW or FM-CW receivers that are described in the literature (671, Chap. 3; 508; 732), this chapter emphasizes the clutter limitations of CW radars. The equations and graphs of Secs. 10.3 through 10.5, combined with the clutter backscatter coefficients of Chaps. 6 and 7, should lead to quantitative computation of the detection performance of CW radars. It is shown that even if the spillover of the transmit signal into the receiver can be reduced to a tolerable level, clutter signals will exist that are far in excess of the minimum detectable signal (MDS).

10.1 Transmitter Spillover and Noise Limitations

Perhaps the primary design problem in CW radar is transmitter/receiver isolation. Because both are operating simultaneously, the receiver must reject the transmit signals and operate on the received ones. This direct coupling between the transmitter and receiver, variously called *leakage, spillover,* and *feedthrough,* can easily obscure target echoes. As an example, if the radar transmits 1 kW (60 dBm) of continuous power and the minimum detectable signal (MDS) is -130 dBm, there must be in excess of 190 dB of isolation at the target Doppler frequency. About 20 to 40 dB of this can be obtained with ferrite circulators between the transmitter and receiver of a single-aperture system. If separate or polarized apertures can be utilized, 70 to 120 dB of isolation are obtainable.* When the geometry permits, such as in space tracking or planetary observation radars, the antennas can be widely separated or on opposite sides of a mountain to achieve even greater isolation. In addition to this isolation, additional rejection can be obtained with circuitry that samples the transmit signal and effectively *subtracts* a portion of it from the spillover signals. These spe-

* Only 20 to 30 dB by polarization alone.

cialized techniques can achieve additional isolation exceeding 60 dB [314; 518].

Even with these techniques the spillover signal power can exceed the MDS by 90 dB and cause severe dynamic range problems in the receiver. The problem often does not arise from the spillover alone, but from the AM and FM noise sidebands of the transmitter leakage that appear in Doppler passband of the target. A high-quality CW transmitter may have AM noise sidebands that are 90 to 120 dB below the carrier in a 1-kHz bandwidth, and FM noise sidebands 70 to 95 dB below the carrier in the same bandwidth. These sidebands will either raise the MDS or appear as spurious false targets. Noise sideband limitations are discussed in [574; 271; 272; 314; 731, Chap. 2] and are only briefly summarized here. Transmitter noise will also appear on all clutter signals.

The permissible transmitter noise levels can in general be handled separately for AM and FM noise. However, there is no single parameter that can be specified that describes the transmitter stability requirements. The simplest requirement to consider is that of spurious signals separated from the carrier frequency (or the main beam clutter frequency for an airborne radar) by at least a Doppler shift $\Delta f_{\min}$. These signals could be interpreted as a target. As might be expected, the lower the value of $\Delta f_{\min}$ the more stringent are the transmitter stability requirements. For maximum sensitivity, the spurious signals in the Doppler filter of interest must be below the noise level in that filter. For example, if the spillover (or clutter) is 80 dB above the rms noise, a sideband rejection ratio requirement R of 86 dB on the AM and FM noise independently will ensure that, in the worst case of in-phase AM and FM components, the resultant signal will no more than equal the noise level [272]. First, consider the AM noise component. If M is the fractional amplitude modulation, there are two sidebands of amplitude $1/2M$. The maximum allowable value of M for a given AM sideband rejection ratio R_{AM} is

$$M_{\max} = 2R_{\text{AM}}^{1/2} \tag{10.2}$$

For noise sidebands due to frequency modulation, the relationship is not as simple. In most cases the modulating frequency f_m is below $\Delta f_{\min}$ and the higher-order sidebands must be calculated from the Bessel coefficients. Graphs are available in [272, Fig. 3.2] for calculating the maximum deviation for a given modulating frequency f_m and sideband rejection ratio R. For single sinusoidal frequency modulation and a very small index of modulation

$$\frac{P_c}{P_{\text{SB}}} = \left(\frac{f_m}{\Delta f_{\text{rms}}}\right)^2 = 20 \log \left(\frac{f_m}{\Delta f_{\text{rms}}}\right) \text{ in dB} \tag{10.3}$$

where P_c is the carrier and P_{SB} is the total power in both sidebands. Δf_{rms} is generally defined for a 1-kHz bandwidth as the rms deviation of a single sinusoidal frequency modulation at the center of a 1-kHz bandwidth that would equal the rms deviation of the total frequency modulation of the actual signal contained in the whole 1-kHz band [574].

The configuration of the receive signal processor also influences the sensitivity of AM and FM noise if limiting is used to achieve a constant false-alarm rate (CFAR). Raduziner and Gillespie [574] have shown that limiting at IF, prior to Doppler filtering, has a different effect on AM and FM noise on clutter echoes than does a synchronous detection or homodyne receiver followed by a high-pass filter, remodulation to IF, and then limiting before Doppler filtering. When clutter-limited, the homodyne system will tend to reduce the effect of FM components resulting from a single sinusoid or low-index complex frequency modulation entering the receiver from stationary clutter echoes. (There is some controversy on this subject.)

10.2 CW, FM-CW, and ICW Transmissions

CW

It was shown in Sec. 8.3 on the environmental diagram that the Doppler spectra of clutter echoes as seen by a stationary radar are often disjoint from the spectra of aircraft or missile echoes. As a result, there can be complete resolution of moving-target echoes from clutter. Thus, in theory the clutter rejection or improvement factor I is infinite. In practice, transmitter noise or receiver saturation is the limiting factor on target detectability. With an airborne CW radar the target spectrum may or may not overlap the clutter spectrum depending on the geometry and closing velocities as discussed in Sec. 10.6.

The detection range of a CW radar can be written from Eq. (2.6) as

$$R^4 = \frac{\overline{P}_T G_T L_T A_e L_R L_p L_a L_s \sigma_t}{(4\pi)^2 K T_s b (S/N)} \tag{10.4}$$

These terms are the same as those defined in Sec. 2.1 with the exception that the average transmit power $\overline{P}_T$ is used rather than the peak power P_T, and the Doppler filter or *speedgate* bandwidth b is used for the noise bandwidth. This equation is obtained by making use of the general theorem given in Chaps. 1 and 8, which states that detectability depends on the transmitted energy and not on the details of the transmit waveform (see also [136, Chap. 6]). The only modification to Eq. (10.4) that is necessary for CW radar computations concerns the requirement

for a matched filter. For a sine-wave CW transmission and a stationary reflector, this would call for a zero-bandwidth receiver. In practice, the filter bandwidth b must encompass at least the target spectral width due to fluctuation, target acceleration, antenna scanning modulation, time on target, and any frequency uncertainties in the receiver local oscillators, filters, etc. In current radars the filters generally have wider bandwidth than the absolute minimum, but there is a partial compensation for the loss in detectability with the use of postdetection filtering or integration. Typically, (S/N) for a CW radar must be at least 6 dB, rather than the 13-dB value required for detecting steady targets with pulse radars.

If the CW transmission is truncated at time T_d as shown on Fig. 10.1*A*, a closer approximation can be made to a matched filter, but spillover and clutter problems are aggravated. The effect of truncation is to give all the spillover signals a $\sin^2(\pi f_d T_d)/(\pi f_d T_d)^2$ spectrum. Even if the product of the Doppler shift and the dwell time $f_d T_d$ is large, clutter signals that are often 50 to 100 dB above the target echo will have spectral components at f_d that are well above the noise in the filter bandwidth b. This effect is expanded on in Chap. 11 on pulse Doppler and burst waveforms.

FM-CW

While it is possible to truncate a CW transmission at a time T_d and estimate range to some fraction of $cT_d/2$, pulsed CW transmission for greater than 1 ms has found little application except for planetary observation radars. By far the most common technique for determining target range is to frequency modulate a continuous transmission (FM-CW). The modulation waveform may be a linear sawtooth, a triangle, or a simple sine wave. These modulations have the effect of broadening the spectrum of the transmit waveform and thus enhancing the ability to determine range.

If the modulation waveform is a linear sawtooth, the time-frequency relationships will be as in Fig. 10.2. A carrier frequency f_0 is modulated at a rate $\dot{f}_0$ and transmitted. The echo from a target at range R will occur after a time $T_t = 2R/c$ as shown in Fig. 10.2A. The received signal is mixed with the transmit signal and the difference or beat frequency f_b is extracted. If the target is stationary,

$$f_b = f_r = \dot{f}_0 T_t = \frac{2R}{c} \dot{f}_0 \tag{10.5}$$

where f_r is the beat frequency due only to the target range ([354, Sec. 3.3]). The beat note has a constant frequency except near the turn-

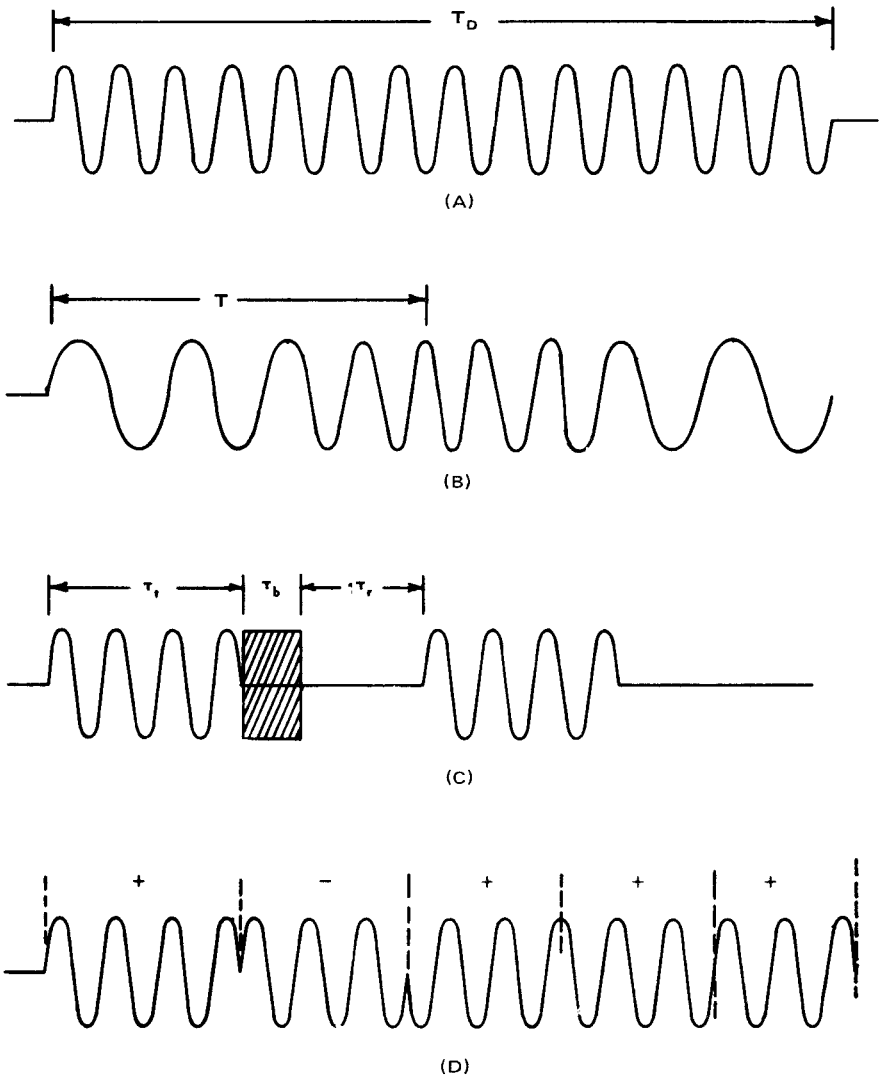

Figure 10.1 Waveforms for the general class of CW radar. (A) Continuous sine wave CW; (B) frequency modulated CW; (C) interrupted CW; (D) binary phase-coded CW.

around region of the sawtooth. If the carrier is modulated at a rate f_m with a frequency deviation Δf, the range of a target can be determined from

$$R_0 = \frac{cf_r}{4f_m\Delta f} \tag{10.6}$$

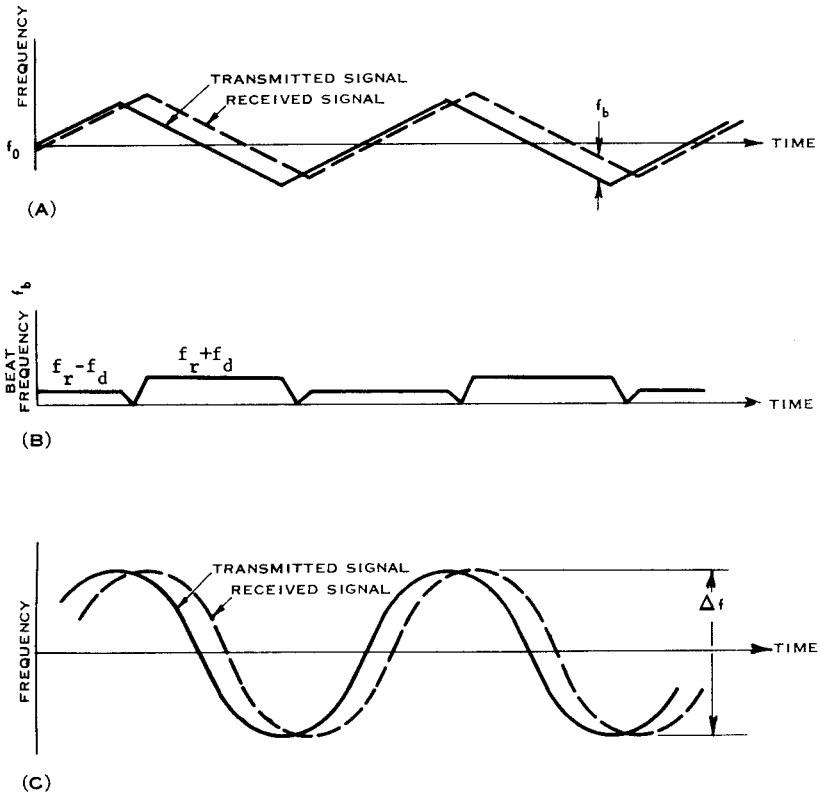

Figure 10.2 Frequency time relationships in FM-CW radar when the received signal is shifted in frequency by the Doppler effect. (A) Transmitted (solid curve) and echo (dashed curve) for triangular modulation; (B) beat frequency for triangular modulation; (C) transmitted and received signals for sine-wave modulation. (*After Skolnik [671]*)

If the target has a radial velocity v, the echoes will have a Doppler shift $f_d = 2v/\lambda$. Then, the beat frequency waveform appears as in Fig. 10.2B. The range frequency f_r can be determined from the average beat frequency [671]

$$f_r = \frac{1}{2}[f_b\,(\text{up-slope}) - f_b\,(\text{down-slope})] \tag{10.7}$$

The inverse of the frequency deviation can be considered analogous to an *effective* pulse length in pulse radar, while the modulating frequency is analogous to the PRF [557].

If the carrier is sinusoidally modulated with a voltage waveform

$$e_t = E_T \sin\left(2\pi f_0 t + \frac{\Delta f}{2f}\sin 2\pi f_m t\right) \tag{10.8}$$

the received signal from a target at range R, when mixed with the carrier frequency, will yield a difference frequency voltage waveform [671, p. 89; 557]

$$e_b = kE_T E_r[\sin 2\pi f_0 T_t + \pi \Delta f T_t \cos(2\pi f_m t - \pi f_m T_t)] \tag{10.9}$$

where k = a constant of proportionality
E_r = the received voltage from the target
$T_t f_m \ll 1$

The transmit and received waveforms are shown as Fig. 10.2C.

If the argument of Eq. (10.9) is differentiated with respect to time, the average beat frequency $\bar{f}_b$ over one-half a modulating cycle can be approximated by letting $\cos \pi f_m T_t \approx 1$. Then [671, p. 90]

$$\bar{f}_b = \frac{4Rf_m \Delta f}{c} = f_r \tag{10.10}$$

The total spectrum of a carrier that is frequency modulated by a sine wave consists of a series of spectral lines that can be described by Bessel functions of the first kind and order 0, 1, 2, 3, etc. A reduction in spillover signals and close-in reflections can be obtained by the use of filters that pass only certain harmonics of the modulating frequency. For example, extraction of only those received frequencies near $3f_m$ will result in considerable spillover rejection at a penalty of 4 to 10 dB in signal-to-receiver noise power. The detection of targets up to a given range can be optimized by proper choice of the modulating frequency f_m and extraction of the receive signal components corresponding to the desired order of the Bessel function $J_n(f)$. It should be emphasized that frequency modulation will also smear the clutter spectrum over a wide range of frequencies. This may or may not be desirable depending on the total clutter power-to-signal ratio and the clutter location.

Target range can also be determined by phase modulation of the carrier. The most common waveform consists of simple binary phase modulation (0 to 180° phase shift) as illustrated in Fig. 10.1D. This technique is described in Chap. 12.

Interrupted CW (ICW)

When a single antenna must be used for both transmitting and receiving, it is often impractical to achieve the desired isolation between the final transmitter stage and the receiver. To alleviate this problem

and to eliminate the close-in clutter backscatter, the transmitter is often turned on or *pulsed* at a high rate for 10 to 60 percent of the total time. During this time τ_t and for a short *blanking period* $\tau_b$the receiver is switched off to eliminate transients, spillover, and close-in clutter. The remainder τ_r of the interpulse period is used for reception of the target echoes. The timing is shown diagrammatically in Fig. 10.1C. Then the interpulse period T can be written as

$$T = \tau_t + \tau_b + \tau_r \tag{10.11}$$

then

$$d_t = \frac{\tau_t}{T} < 1 \qquad d_r = \frac{\tau_r}{T} < 1 \qquad d_b = \frac{\tau_b}{T} < 1$$

where d_t and d_r are the transmit and receive duty factors and d_b is the blanking duty factor.

It is assumed that the receiver has a single range gate and that the PRF = $1/T$ is greater than twice the highest target-Doppler frequency. This type of transmission is often called *pulse Doppler* in airborne radar systems but is referred to in this text as interrupted CW or ICW to distinguish it from the multiple range-gate systems discussed in Chap. 11 on pulse Doppler and burst waveforms.

Since the echo from a distant target with unknown range can enter the receiver no more than $100\,d_r$ percent of the time, there is an average loss in received signal power. This is generally referred to as *eclipsing* of the target echoes. One of the primary problems in the choice of an ICW waveform is to optimize the proportion of the interpulse period T devoted to τ_t, τ_b, and τ_r. Three types of optimization have been studied in which it is assumed that the target range is much greater than $cT/2$:

1. The transmitter is peak-power-limited and it is desired to maximize the target signal-to-noise ratio S/N averaged over all possible target ranges for a given blanking time τ_b.
2. The transmitter is average-power-limited such that a large value of d_t will necessitate a reduction in peak transmit power. The optimization is again for maximum average S/N for a given blanking time τ_b.
3. The system sensitivity is limited by close-in clutter, and it is desirable to increase τ_b to blank out the close-in clutter. This optimization will maximize the signal-to-clutter ratio for a given amount of degradation in S/N.

The optimization of the average signal-to-noise ratio is not the

same as the optimization of detection probability [271]. If the target is eclipsed during any given observation time, the loss in detectability is infinite. To alleviate this situation, the PRF is often switched between two or three values during the time the antenna moves one beamwidth.

Peak-power-limited case

For the peak-power-limited radar, Walcoff [741] has shown that the average receive power from the target can be written

$$\overline{P}_r \approx \frac{2}{3}\tau_r^3 + (1 - 2\tau_r - \tau_b)\tau_r^2 \qquad \text{for } \tau_t > \tau_r \tag{10.12}$$

$$\approx \frac{2}{3}\tau_t^3 + (1 - 2\tau_t - \tau_b)\tau_t^2 \qquad \text{for } \tau_t < \tau_r \tag{10.13}$$

Assuming that the receiver noise during the period τ_r is the limiting factor on detectability, the receiver noise power N can be written

$$N = KT_s b d_r \tag{10.14}$$

where K = Boltzmann's constant
T_s = system noise temperature as defined in Eq. (2.3)
b = Doppler filter noise bandwidth
d_r = receiver duty ratio

By calculating $\overline{P}$ and N for various values of τ_b, it was found that the optimum ratio of τ_t/τ_r was 1.67 for all values of d_b. The normalized signal-to-noise ratio is shown in Fig. 10.3 as a function of d_t for several values of d_b. Since the minimum value of d_b is a function of the antenna, receiver layout, and spillover problems, it can generally be estimated prior to the choice of τ_t and τ_r. Once τ_b can be approximated, the other terms can be determined by letting $\tau_t/\tau_r = 1.67$.

Average-power-limited case

A second case of importance is when the transmitter average power is limited. This case also applies to preliminary design studies since transmitter cost for high-duty ratio systems is more dependent on average than peak power. Walcoff [741] has also calculated the average return power for this case.

$$\overline{P}_r \approx \frac{2\tau_r^3}{3\tau_t} + (1 - 2\tau_r - \tau_b)\frac{\tau_r^2}{\tau_t} \qquad \tau_t > \tau_r \tag{10.15}$$

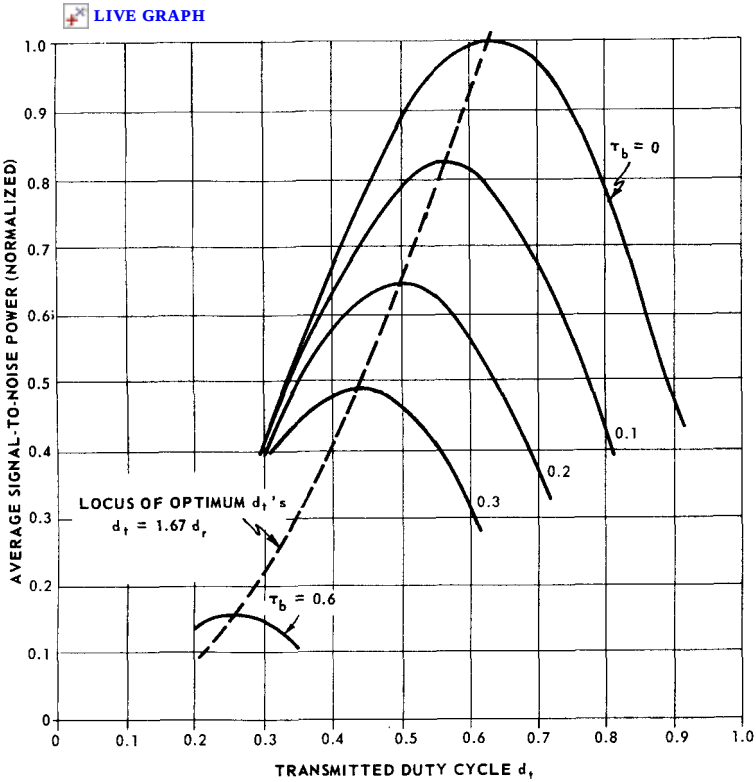

Figure 10.3 Signal-to-noise ratio in the receiver gate as a function of duty cycle and receiver blanking time. Peak-power-limited case. (*After Walcoff* [*741*])

$$\approx \frac{2}{3}\tau_t^2 + (1 - 2\tau_t - \tau_b)\tau_t \qquad \tau_t < \tau_r \tag{10.16}$$

The receiver noise power is the same as expressed in Eq. (10.14). The optimization of S/N leads to $\tau_t = \tau_r$ for all values of τ_b. In this case there is less loss in S/N than for the peak-power-limited cases when τ_b is large, since the peak power can be increased indefinitely as τ_b is increased. One method of selecting τ_b is to draw graphs of clutter-to-signal power ratio P_c/P_s versus range, shown in Figs. 10.5 through 10.7. From these graphs the location of the maximum clutter regions can be determined. Often τ_b can be extended in order to gate out much of this clutter at the price of a moderate reduction in receiver duty factor.

Clutter-limited case

The clutter-limited case is difficult to evaluate in closed form. When the clutter is primarily the reflections from uniform rain close to the

radar, the blanking period (in distance units) must be at least equal to the extent of the antenna near field to significantly reduce the clutter power. Thus,

$$\frac{c\tau_b}{2} > \frac{D^2}{\lambda} \tag{10.17}$$

where D is the antenna diameter and λ is the carrier wavelength. This is necessary since only one-half the clutter power is returned from the near field of a single-aperture CW system.

If the clutter is primarily due to sea or land clutter, the choice of τ_b that maximizes S/C is strongly dependent on antenna height, main beam elevation angle, antenna sidelobes, and the potential use of a *clutter fence.*

10.3 Rain Clutter Power for Separate Transmit and Receive Antennas

This section considers the backscatter power from a uniform rain surrounding a two-aperture CW radar.* The radar has separate circular transmit and receive antennas that are collimated (parallel beams) on some distant target. It is assumed that the near fields (Fresnel regions) of the two antennas do not overlap and that the total backscatter from the rain is primarily due to the overlap of the far field patterns of the antennas as shown in Fig. 10.4. Further assumptions for this section are

1. The antennas have the same-sense linear polarization and uniform phase excitation.
2. Both apertures are large compared with a wavelength, and small angle approximations can be made.
3. The rain is uniform everywhere.
4. Direct spillover and multiple scattering are negligible.

Wild [773] considered the total clutter power in the receiver for separate, equal-diameter coplanar antennas. For uniformly illuminated apertures and neglecting attenuation, the relative backscatter power P_R/P_T can be approximated by

$$\frac{P_R}{P_T} = 0.022 \frac{\lambda \Sigma \sigma}{\alpha} \qquad \text{uniform illumination} \tag{10.18}$$

* An analysis for a single-aperture CW system can be found in Nathanson, *Radar Design Principles,* first edition (New York: McGraw-Hill, 1969).

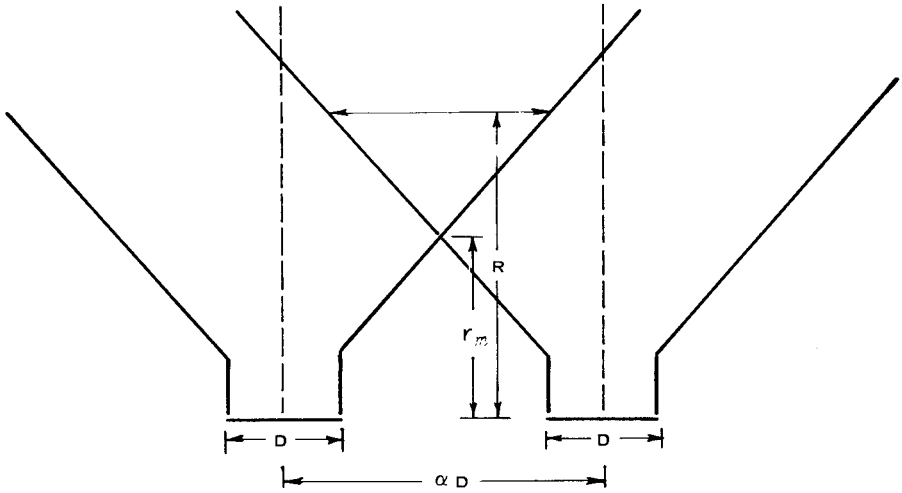

Figure 10.4 Antenna beam geometry for separate apertures of equal diameter D.

where λ = carrier wavelength, m
$\Sigma\sigma$ = volume reflectivity, m^2/m^3
α = center-to-center spacing in antenna diameters as illustrated in Fig. 10.4, $\alpha \geq 1$

For uniform illumination (first sidelobe 17.5 dB down from the mainlobe), about 93 percent of the total power is from the overlapping regions of the main beams. The region where the mainlobe of one antenna intercepts the first sidelobe of the other contributes 4 percent. The remaining sidelobe contributions are about 3 percent.

The range dependence of the clutter is shown in Fig. 10.5. The ordinate is the incremental relative backscatter and the abscissa is an arbitrary normalized range in units of the minimum range where the beams overlap r_m.

$$r_m \approx \frac{\alpha D/2}{3.8\lambda/\pi D} = \frac{\alpha D^2}{2.44\lambda} \tag{10.19}$$

where D is the diameter of the uniformly illuminated apertures, and r_m is slightly less than the transition range nr_0 between the near and far fields.

Three curves are shown on the graph. Curve (A) is the contribution of the mainlobes, (B) includes the addition of the mainlobe to first sidelobe power, and (C) is the total power (in increments of R/r_m). From these curves the spectrum of the transmit FM noise which is received with the rain clutter can be derived. In addition curve (C) can be used

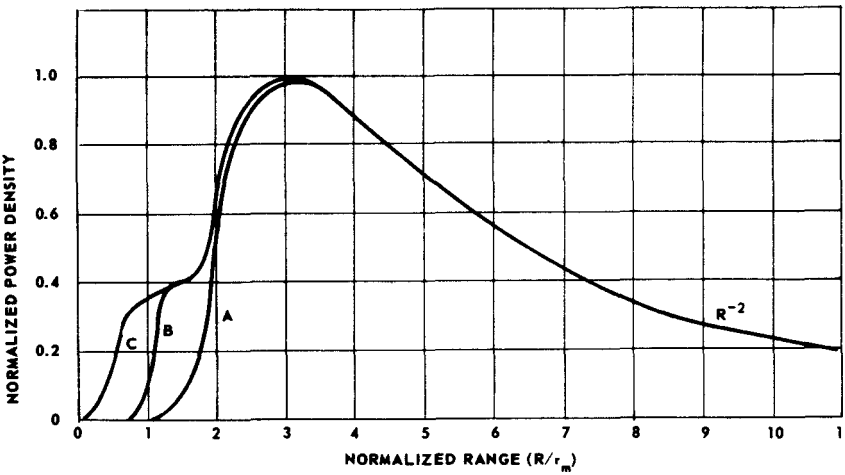

Figure 10.5 Range dependence of echo for two antenna CW radars in uniform rain. (A) Mainlobe contribution; (B) mainlobe plus first sidelobe; (C) total CW echo range power density. (*Courtesy of Wild* [773])

to estimate the total clutter power by integrating only for the range increments where the receiver is on.

At carrier frequencies above 10 GHz and rainfall rates above 16 mm/h, the attenuation of the distant rain clutter signals may become significant. By expressing the two-way attenuation coefficient (from Chap. 6) in units of dB/r_m, Eq. (10.18) can be multiplied by an empirical attenuation factor to yield the relative backscatter for heavy rainfall

$$\frac{P_R}{P_T} = 0.022\,(0.27)^{a^{0.64}}\,\frac{\lambda\Sigma\sigma}{\alpha} \tag{10.20}$$

where a is two-way rainfall attenuation in dB/r_m and is valid for $0 \leq a \leq 3$. Attenuation can be neglected for $a \leq 0.2$ with less than 1-dB error unless the FM noise on distant clutter is important.

Wild [773] also made hand calculations for amplitude-tapered apertures with a $[b + (1 - K^2)^n]$ distribution for $b = \frac{1}{2}$, $n = 2$ where K is the radial distance from the center of the aperture [305, p. 66]. This results in first sidelobes 26.5 dB below the peak gain. In this case 99 percent of the reflected power comes from the main beam intersection. Neglecting attenuation, the relative rain backscatter power can be approximated for equally sized apertures.

$$\frac{P_R}{P_T} = \frac{0.023\lambda\Sigma\sigma}{\alpha} \qquad \text{tapered illumination} \tag{10.21}$$

A limited number of calculations were also made for unequal circular apertures with uniform illumination. With a few tenths of a decibel error, Eq. (10.18) can be modified as

$$\frac{P_R}{P_T} = \frac{0.056\mu\lambda\Sigma\sigma}{\alpha(2.7)^{\mu}} \qquad \text{unequal apertures} \tag{10.22}$$

where N = the ratio of the larger aperture diameter to the smaller aperture diameter

Then $0 \leq \mu \leq 1$. Sidelobe contributions should yield only a slight increase in the relative backscatter.

The only widely reported experiments on the backscatter from two-antenna CW radars is the work of Kiely [400]. As with the single-aperture experiments, there is considerable disparity with the theory, even when the rainfall attenuation is estimated. The theory predicts higher relative backscatter than the experiments with the separated antennas.

10.4 Sea and Land Clutter Power for Surface Antennas

While the computation of the magnitude and spectrum of sea and land clutter echoes from an airborne antenna can be approximated by the relationships of Sec. 10.5, it is difficult to present simple relationships for the clutter echoes from a surface radar. This is a result of the clutter echoes being a highly sensitive function of the sidelobe structure of the antenna. One successful method of computation inserts the best estimate of the antenna pattern into a digital computer along with an analytic function for the clutter backscatter as a function of depression angle $\sigma_0(\Psi)$. The clutter response from a large number of small areas on the surface is then integrated. The numerical results given in this section are the result of such a procedure. The emphasis is on the effect of beamwidth, sidelobe structure, and elevation of the centerline of the beam above the horizontal. The results are applicable to a CW, interrupted CW (ICW), or pulsed radar.

In order to give physical significance to the results, a number of assumptions have been made.

1. The target is in all cases a 5-m^2 aircraft or missile at 50 nmi from the radar.
2. The radar is vertically polarized at 60 ft above a flat earth and has an average CW power of 1 kW or an ICW peak power of 5 kW.
3. The frequencies of interest are C-band (λ = 6 cm) or X-band (λ = 3 cm).

4. The mean sea or land clutter reflectivity can be represented by $\sigma_0(\Psi) = \gamma \sin \Psi$ for $0.001 < \Psi < 0.1$ rad where γ is a constant, independent of Ψ. This gives a better approximation to the reflectivity than would a constant value for σ_0, although the values in Chap. 7 are even better. For the computations $\gamma = -28$ dB, which roughly corresponds to the reflectivity from a sea state 3 at C-band, a sea state 2 at X-band, or very flat terrain at either band.
5. Forward-scatter effects have been neglected. This should not be a major factor at C- or X-band
6. Antenna spillover has been neglected.
7. The computation is performed in range increments of 1.2 μs (0.1 nmi) and in azimuth increments of 0.004 rad. Clutter at azimuth angles beyond 20° did not influence the results.
8. Two basic antenna types are considered. The first is a small symmetrical antenna with a 3° beamwidth with −20-dB first sidelobes and −30 dB for the next few sidelobes. The second is a measured pattern of a higher-quality antenna with a 1.8° beamwidth at C-band, −30-dB first sidelobes, and the next sidelobes falling off rapidly. This latter antenna pattern is scaled for X-band transmission and also for a 3.6° beamwidth.

Two systems are considered; the first is a pure CW system, and the second is an ICW system with 1.2-μs transmit time, 2.0-μs clutter decay time, and 1.8-μs receive time. The pulse repetition frequency is thus 200 kHz.

It may be well to collect the approximate equations for the return signals to get a feeling for effects such as transmit frequency. The clutter return can be written for main beam illumination (neglecting loss terms).

$$P_c = \frac{P_T G_T G_R \lambda^2 (\sigma_0 A)}{(4\pi)^3 R_c^4} \tag{10.23}$$

where A = illuminated area
σ_0 = reflection coefficient = $\gamma \sin \Psi \approx \gamma h / R_c$ (Secs. 7.2, 7.11)
h = antenna height above the surface
R_c = range to center of clutter element
but $A = R_c \theta (c\tau/2)$ for small θ and low grazing angles
θ = two-way azimuth beamwidth, rad
τ = pulse duration or range-gate duration

Reducing the equation, one obtains

$$P_c = \frac{P_T G_T G_R \lambda^2 \gamma h \theta (c\tau/2)}{(4\pi)^3 R_c^4} \qquad \text{main beam} \tag{10.24}$$

The return from a target of cross section σ_t and at range R_T is

$$P_s = \frac{P_T G_T G_R \lambda^2 \sigma_t}{(4\pi)^3 R_T^4}$$

and the received clutter-to-signal ratio is

$$\frac{P_c}{P_s} = \frac{\gamma h c \tau}{2\sigma_t} \left[\frac{R_T}{R_c}\right]^4$$

By using γ rather than σ_0 the range term drops out of the equation for targets in the clutter. A small antenna height would seem to be advantageous, but it reduces the radar horizon and delays initial *acquisition* of targets.

The results to follow were computed using typical antenna patterns and calculated antenna gains at the target and clutter locations. Some typical results are presented in Fig. 10.6 and Table 10.1. Figure 10.6 illustrates the clutter-to-signal power ratio as a function of clutter range R_c for the 1.8° beamwidth, high-quality circular antenna with elevation of the antenna centerline in milliradians as a parameter. The point at which the main beam hits the clutter is the "hump" at the center of the graph. The smaller hump at the left is due to the first-sidelobe clutter power. The total clutter power for a CW transmission (the area under the curves) is also indicated along with the beam elevation. It can be seen that elevating the beam reduces the clutter signal much faster than the target signal, although the signal-to-receiver noise power ratio is reduced. The total clutter signal for the ICW transmission is obtained by integrating at only those delay times when the receiver is on (1.8 μs every 4.0 μs). In this case there is a 5.5-dB loss *on the average* in target signal from the CW case for 0° elevation due to the receive duty factor of 36 percent. Results with several other antenna configurations are shown in Table 10.1. The first column gives the antenna type and frequency. The second column is the beam elevation in milliradians (17 mrad = 1°). The third column is the received clutter power P_c for $\gamma = -28$ dB. This factor is important to determine if there is receiver saturation. For rough seas, add 10 dB to P_c and P_c/P_s, and for typical wooded or hilly terrain, add 20 dB. The clutter-to-signal power is given for both the CW and ICW cases. The sensitivity loss column accounts for the reduced power density on the horizon as a result of elevating the beam and the 36-percent receiver duty factor of the ICW system.

It can be seen that a reduction of the beamwidth by a factor of 4 reduces the clutter-to-signal ratio by about 20 dB, and elevating the beam by about two-thirds of a beamwidth achieves a similar reduction. The ICW mode is advantageous only with the elevated beam with the nine-tenths beamwidth.

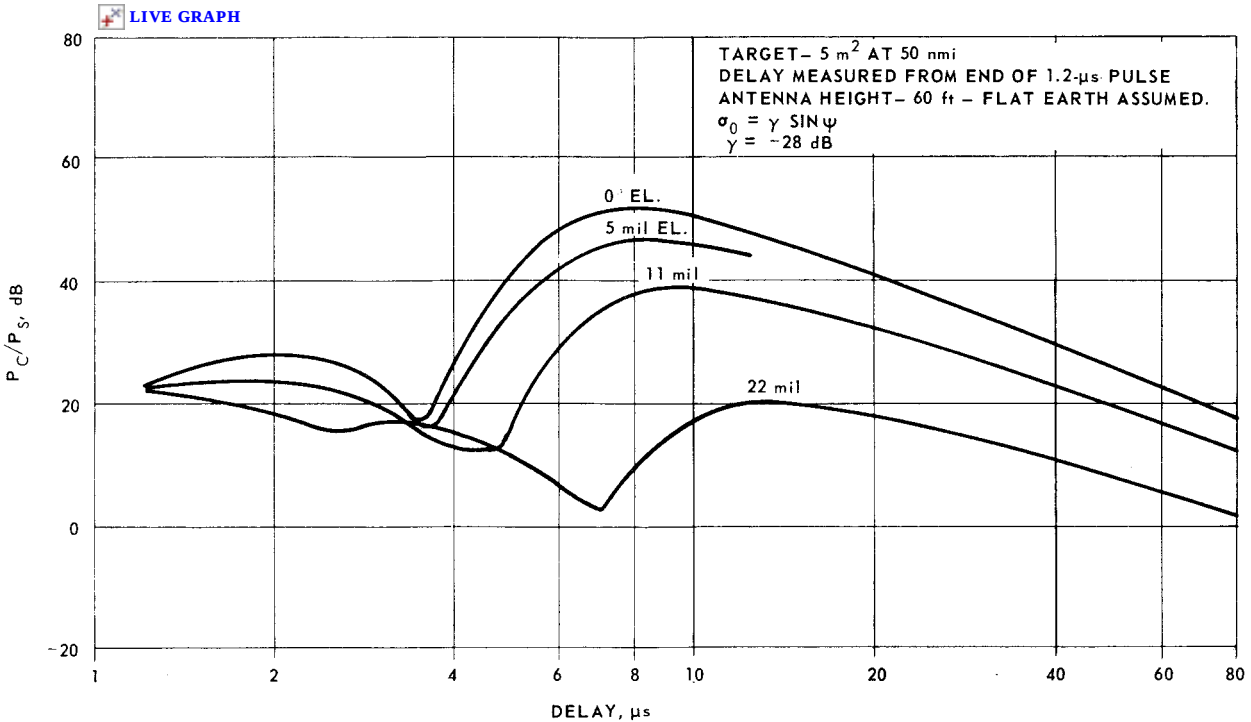

Figure 10.6 Ratio of clutter power to target echo power per 1.2 μs of range delay (1.8° beamwidth). The total clutter power for a CW system is −52 dBm for 0° beam elevation, −58 dBm for 5-mil elevation, −62 dBm for 11-mil elevation, −79 dBm for 22-mil elevation.

TABLE 10.1 Clutter-to-Signal Ratios for Various Antennas for h = 20m, 5-m² Target at 50 nmi, $\gamma = -28$

Antenna size, frequency, and beamwidth	Elevation angle, °	CW transmission			ICW transmission	
		P_c dBm	P_c/P_s, dB	Sensitivity loss, dB	P_c/P_s, dB	Sensitivity loss, dB
8-ft X-band		−58	47	0	47	5.5
High-quality		−70	37	—	37	—
$\theta = 0.9°$		−85	28	7.5	22	13.0
8-ft C-band		−52	60	0		
High-quality		−58	54	—		
1.8°		−62	51	—		
		−79	41	7.5		
2-ft X-band		−58	73	0		
High-quality	22	−68	64	—		
3.6°	44	−85	53	7.5		
2.5-ft X-band Low-quality 3.0°	0	—	82	—		

It can be seen from the values of total clutter power that considerable Doppler filtering is required even for the moderate environment that was assumed. The clutter problem does not vanish even if the centerline of the antenna beam is two to three beamwidths above the horizon. This is illustrated in Fig. 10.7 for the two antennas previously discussed. The total clutter power exceeds the target echo, but the problem is far less severe for high-gain antennas with low sidelobes. These values can be compared with pulse system calculations in Chap. 7.

10.5 Clutter Spectrum for Airborne Radars

Since the primary purpose of a CW radar is the detection and tracking of targets on the basis of their velocity separation from clutter, it is useful to calculate the Doppler spectrum of these clutter echoes. If the radar is stationary, the relationships of Chaps. 6 and 7 should suffice, although it may be necessary to include a computation of the spectra of antenna sidelobe echoes. The Doppler spectrum at an airborne receiver is dominated by the platform motion.

This section gives the equations to compute this spectrum by assuming that the antenna is circularly symmetrical with a beamwidth of less than 0.25 rad. In addition, the clutter is assumed to be homogeneous with a negligible mean velocity compared with the platform motion. The analysis applies to a CW or ICW radar where the target and clutter are many times the unambiguous range.

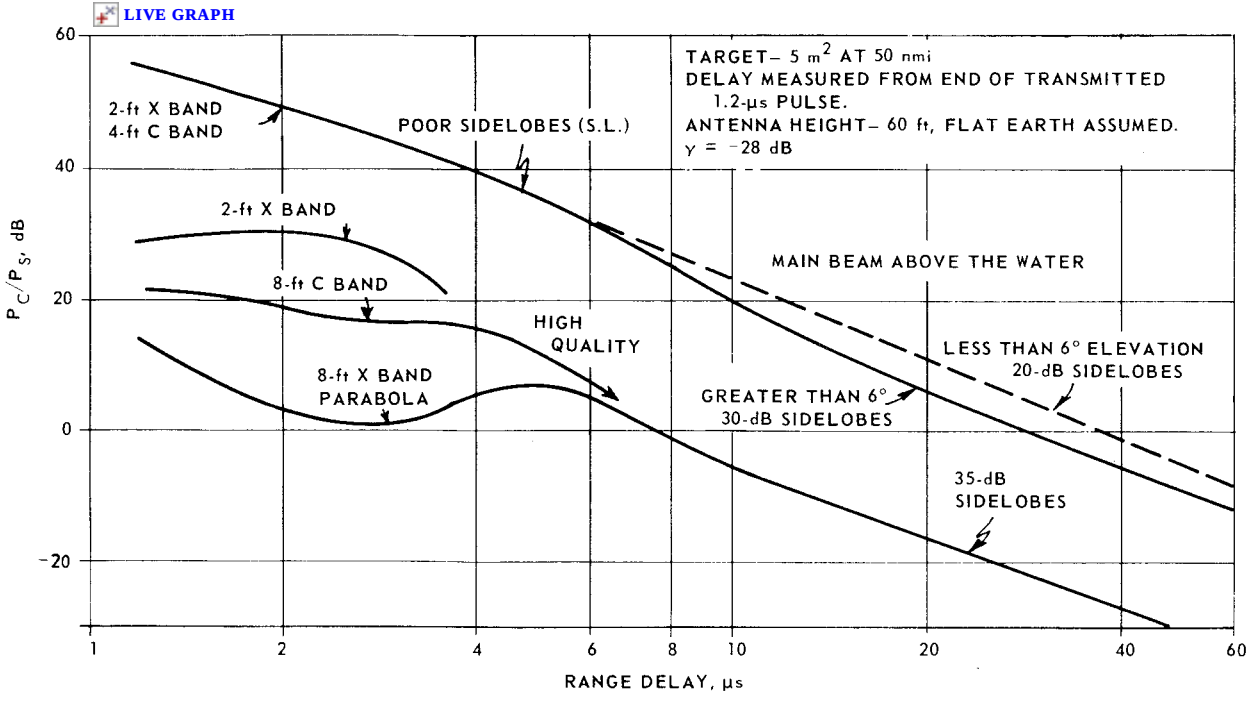

Figure 10.7 Ratio of sidelobe clutter power to target power for antenna beam elevation angles of 2–3 beamwidths and targets in the main beam.

Following the procedures of Farrell and Taylor [221], the computation of the spectrum is divided into an antenna mainlobe computation and one or more sidelobe computations. They computed that, outside the first sidelobe, the sidelobe clutter spectrum is essentially flat. This occurs because there is no special correspondence between a particular sidelobe and a region on the surface of the earth. While this simplifying assumption is used in the equations of this section, Helgöstam and Ronnerstam [325] and Biernson and Jacobs [66, Fig. B.1] give more detailed spectral shapes for the first few sidelobes.

The geometry is shown in Fig. 10.8. The airborne radar at height h is moving at a velocity V in the Y-Z plane. The dive angle ζ arises in later discussions. The hyperbolas shown in the X-Y plane are the contours of constant Doppler or *isodops*. The Doppler frequency f_d of the echoes from the center of the main beam is then [221]

$$f_d = \frac{61V \cos \Lambda}{\lambda} \tag{10.25}$$

where V = the platform velocity, ft/s
λ = the RF wavelength
Λ = the angle, rad, between the antenna axis and the radar platform velocity vector if $0 < \Lambda < \pi$

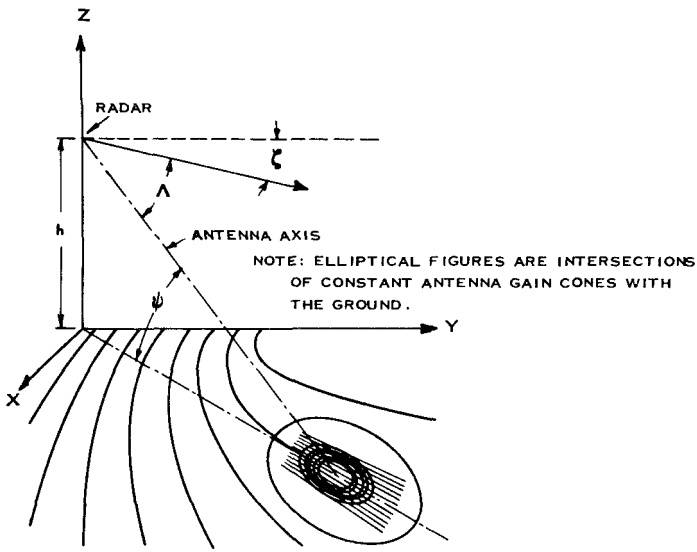

Figure 10.8 Antenna geometry for airborne radar observing surface clutter. (*After Farrell and Taylor, IEEE* [221])

If both V and λ are in meters, the constant is equal to 2. The maximum spectral density in watts/hertz at this center frequency, neglecting radar loss terms L, is

$$W_m(f_d) = \frac{10^{-8}\hat{P}_T d_t G_0^2 \lambda^3 \theta_1 \sin \Psi \sigma_0(\Psi)}{h^2 V \sin \Lambda} \tag{10.26}$$

where d_t = transmit duty factor ($\hat{P}_T d = \bar{P}$ for CW radar)
G_0 = peak antenna gain ($G_T = G_R$)
θ_1 = one-way half-power beamwidth, rad
Ψ = depression angle from the horizontal
$\sigma_0(\Psi)$ = normalized backscatter coefficient at angle Ψ
h = antenna height above surface, ft

The shape of the main beam clutter spectrum is

$$W_m(f_d \pm \Delta f) = W_m(f_d) \operatorname{erfc}\left[\frac{0.0387\lambda \Delta f}{V\theta_1 \sin \Lambda}\right] \text{W/Hz} \tag{10.27}$$

where erfc = the complement of the error function.

These expressions were obtained [221] assuming that

1. The earth is flat. Determination of $\sigma_0(\Psi)$ from Chap. 7 at the true grazing angle rather than the depression angle will make this a better approximation.
2. The antenna main beam has a gaussian shape.
3. The reflection coefficient σ_0 is a constant over the main-beam illuminated area.
4. The range R to various points in the illuminated area is essentially constant.
5. The angle from the velocity vector to the line of sight Λ is greater than the angle from the center of the beam to the first null. If this is not the case, the spectrum of the clutter will most likely be disjoint from an inbound target.

The main beam clutter-to-signal power ratio can be calculated by dividing the product of Eq. (10.27) and the Doppler filter bandwidth b by the target echo power.

The sidelobe clutter-to-noise ratio was also derived by Farrell and Taylor [221]. Assuming a flat Doppler spectrum in the sidelobe regions,

$$\frac{P_{cn}}{P_s} = \frac{4.3 \times 10^{12} \hat{P}_T d_t^2 G_0^2 g^2 \lambda^3 \sigma_0 \cos \zeta}{\bar{F} h^2 V} \qquad \text{for} \qquad \zeta \leq 45° \tag{10.28}$$

where P_{cn} = the clutter power in the nth *isodop* or nth Doppler channel
ζ = the dive angle from the horizontal of the aircraft or missile, positive downwards, rad
$\overline{F}$ = receiver noise figure, power ratio
g = the normalized sidelobe power gain [if the sidelobes (one-way) are 30 dB below the main beam $g^2 = 10^{-6}$; also $G_0 g$ is the absolute sidelobe gain]

Clutter spectral densities for ICW transmission are given in [325, Figs. 2 and 3]. MTI performance is described in Sec. 9.6.

Even if the target echo is well above the clutter, or if the clutter and target echo spectra are disjoint, there is always a possibility that a Doppler filter will "lock up" on the main beam clutter. This problem is often alleviated by looking at the highest Doppler frequencies first if only inbound targets are of interest. An alternate procedure is to determine the spectral width of the echo, since in general the clutter has a broader spectrum than the target. This latter method is sometimes called a *coherency check*.

Chapter

11

Pulse Doppler and Burst Waveforms

11.1 Terminology and General Assumptions

It is now generally accepted that the use of a pulse-train waveform is virtually a necessity to detect small airborne targets in a land clutter background.* The processing can take the form of the classical pulse Doppler described here, a sophisticated MTI (Chap. 9), or a *moving target detector* (MTD) (Chap. 14).

A pulse Doppler radar combines the range-discrimination capability of pulse radar with the frequency discrimination capability of CW radar by using a coherent pulse train, i.e., a train of pulses that are samples of a single unmodulated sine wave. For a fixed repetition rate, the spectrum consists of a set of lines with spacing equal to the repetition frequency. When a coherent pulse train is reflected by a moving object, the lines of the spectrum are Doppler frequency shifted an amount proportional to the object's radial velocity. When a number of objects with different velocities are present, the resultant echo is a superpo-

* For general references see Resnick [589], Rihaczek [606, 601, 603], Galejs [257], Morris [487].

sition of a corresponding number of pulse trains, each with its own Doppler shift. A range gate is used to select only those pulse trains coincident in time (within a pulse width) with the pulse-train echoes from the target. A narrow-band filter following the range gate often selects only a single spectral line corresponding to a particular Doppler shift, thus attenuating all those trains that pass the range gate but do not have the proper Doppler shift.

Burst waveforms may be considered a special case of pulse Doppler, with an implied range of 8 to 32 pulses per antenna beam position. This distinction is somewhat related to radar function, with the truly continuous transmission of pulses (pulse Doppler) being more appropriate to tracking systems with long *dwell* times on the target. The burst waveforms are better suited to surveillance or acquisition systems, as the parameters are chosen for compatibility with time restrictions inherent in three-dimensional surveillance radars.

Therefore, the term *pulse Doppler* is used to describe systems with essentially continuous transmission of pulses, and the terms *burst waveform* or *pulse train* to describe transmissions of finite extent. A *pulse Doppler receiver* is considered one that extracts the energy in a single PRF line of the spectrum, while a *comb filter receiver* extracts the energy in all the spectral lines. With proper design, the performance of both types of receivers should be equivalent.

The use of the term *burst waveform* also implies removal of three restrictions generally attributed to pulse Doppler processes.

1. A burst waveform need not have all the pulses radiated at the same power level, and the processor may have amplitude or phase weighting on a pulse-by-pulse basis.
2. A processor for burst waveforms need not have a physical range gate but may have its gating defined by the time of arrival of the processor output at a threshold.
3. A burst waveform need not have all the pulses on the same carrier frequency.*

In this section several assumptions are made about the waveform and the target being observed.

1. The target velocity is not high enough so that its echo passes out of the range gate during the coherent integration time.†

* The burst waveform with each pulse at a different carrier frequency or with only a few pulses per frequency is discussed in Chap. 13.

† If this is not the case, see Rihaczek [604] who discusses the errors involved and methods of compensation.

2. The target is not accelerating or decelerating by an amount sufficient to spread the Doppler echoes beyond the response of a single Doppler filter (see Chap. 5).
3. The carrier frequency is much greater than the spectral width of an individual pulse. This is not a general requirement.
4. The change in phase versus time due to target radial velocity is negligible during a single pulse.

It is to be noted that *pulse Doppler* in this book is also differentiated from multiple-pulse MTI or other multiple-pulse coherent systems that do not require that a range gate precede the Doppler filtering. It is also assumed that an attempt is made to make the receiver a matched filter to the pulse train. Deviations from these assumptions are handled as efficiency factors L_s rather than by defining separate techniques.

The pulse Doppler waveform consists of a train of pulses that are constant-amplitude samples of a coherent carrier frequency. For convenience in definitions, the minimum number of pulses N is 8 and the duty cycle low enough to separate this technique from *interrupted* CW, which has no range gating other than to prevent the receiver from saturating on the transmitted signal leakage or from close-in clutter returns (see Chap. 10).

The pulse Doppler technique shares many of the potential advantages of CW, pulse, and MTI systems, but suffers some of the limitations of each. Some of the advantages include:

1. The ability to measure range and velocity unambiguously over a predetermined region of the ambiguity plane in the presence of multiple targets
2. The ability to reject unwanted echoes in either Doppler or range domains or in both; higher surface-clutter rejection than other processors
3. Coherent rather than incoherent integration of the returns from many pulses with the attendant reduction in the required (S/N) or (S/C) per pulse
4. Less sensitivity than MTI systems to the mean velocity and spectral width of the unwanted clutter if the target velocity is separated from the center of the clutter spectrum by $> 1/T_d$, where T_d is the coherent integration time
5. Much greater *spillover** rejection and often greater *close-in* clutter rejection than with CW systems

* Leakage of signals directly from transmitter to receiver.

The limitations cannot as easily be categorized but are intimately tied to the choice of such parameters as carrier frequency, PRF, pulse width, and filter bandwidth. The only truly general limitation is that pulse Doppler receiver circuitry is usually more complex than that found in pulse, CW, or simple MTI receiver systems. Pulse Doppler also requires a transmitter with a pulsed-power amplifier chain or at least a pulsed transmitter in which the phase of each transmission is stored in some manner. This can be construed as a limitation of most coherent systems.

11.2 Range-Doppler Limitations

In the discussion on MTI systems, it was generally assumed that the interpulse period was greater than the required unambiguous range. If the resulting *blind speeds* presented a serious limitation, a staggered or dual PRF system was suggested. Ambiguous ranges were only considered if second-time-around clutter echoes *folded* into the range interval of interest. In most current search radars the time per beam position has been sufficient to allow long interpulse periods and still retain three or more pulses per beam position. With the advent of large phased arrays with long detection ranges and narrow antenna beams, the time per beam position is considerably reduced. Since the pulse Doppler technique implies many pulses per beamwidth, the range-ambiguity problem becomes difficult to avoid. These are called medium or high PRF.

The ambiguity problem is more acute in search systems for air defense where the PRF and pulse length must be chosen to accommodate a broad span of target ranges and radial velocities. The carrier frequency and PRF determine the Doppler ambiguities (blind speeds) from the usual Doppler equation

$$f_d = \frac{2v}{\lambda} = \frac{2vf_0}{c}$$

where f_d = the Doppler frequency shift
λ = the transmit wavelength = c/f_0
v = the echo radial velocity

For an unambiguous velocity response it is required that

$$f_d < \frac{\text{PRF}}{2} = \frac{1}{2T}$$

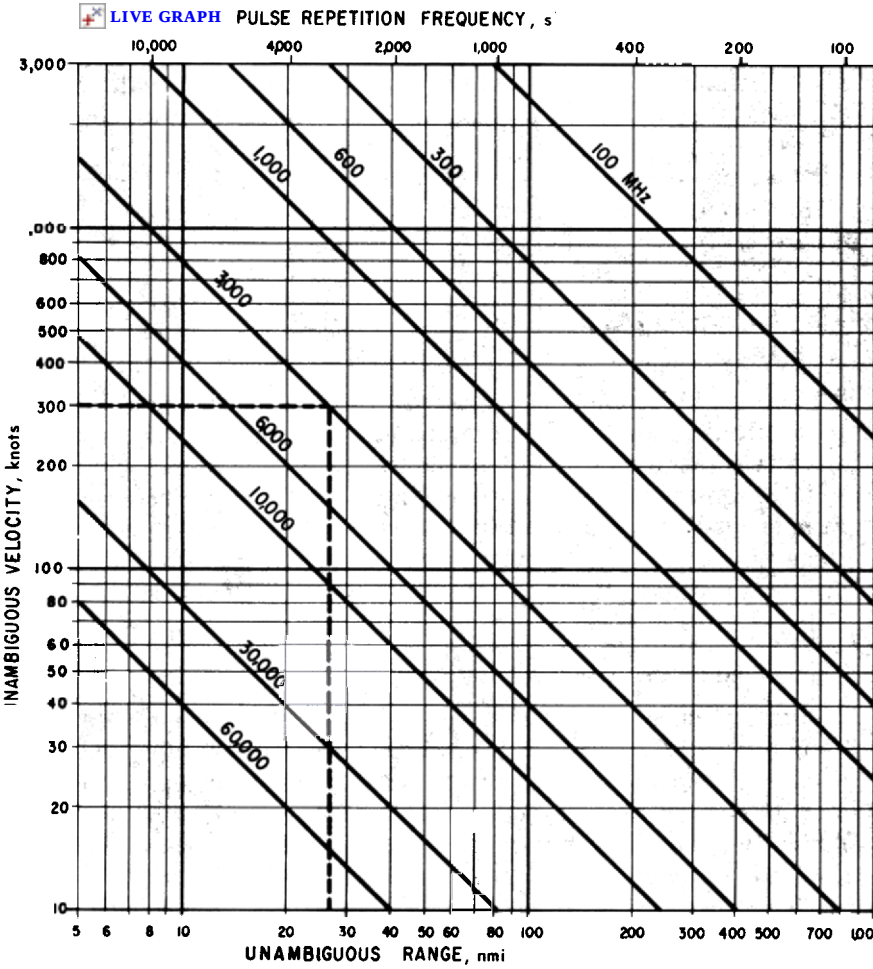

Figure 11.1 Unambiguous velocity versus unambiguous range.

where T = the interpulse period. For an unambiguous-range response, $R_{max} \leq (c/2)(T - \tau')$ where τ' is the pulse duration.* The solution of both of these inequalities is shown in Fig. 11.1. The graph can be entered at the desired maximum unambiguous velocity with a horizontal line to the carrier-frequency line. The projection of this intersection to the abscissa gives the maximum unambiguous range and the related pulse repetition frequency. Alternately, the desired maximum range or PRF

* In this chapter τ' is used for pulse length where it might be confused with the time displacement variable τ.

can be entered on the abscissa to determine the unambiguous velocity. The example shows that for ±300-kn velocity coverage at S-band (3000 MHz), the unambiguous range is less than 27 nmi. For a finite number of pulses, the width of the spectral lines will slightly reduce these values.

It becomes obvious that for many short-wavelength applications, unambiguous operation is impractical and parameters should be chosen by careful study of the ambiguity diagram.

11.3 Ambiguity Diagrams for Single-Carrier Pulse Trains

The ambiguity function described in Chap. 8 has appeared in many forms. It has proven useful in interpreting the performance resulting from the transmission of finite pulse trains in either multiple-target or clutter environments. In studies of the ambiguity function or diagram, it must be emphasized that the peak of the function is centered at the range and Doppler of the target. Clutter and interference are then assumed to have the differential range and Doppler shifts.

Constant interpulse period

The uniform pulse train consisting of N rectangular pulses of duration τ' and interpulse period T is the simplest and most widely used pulse Doppler waveform. Its great utility is based on the complete absence of time ambiguities in the region between the transmit pulses.* The ambiguity diagram of this waveform for $N = 9$ is shown in Fig. 11.2 (see Resnick [589]). The central response is labeled $\psi(0, 0)$, and the velocity response near the range axis where $\tau = 0$ is of the form for $\omega = 2\pi v \ll 1/T$

$$\psi(0,\omega) \approx \frac{\sin^2(N\omega T/2)}{N^2 \sin^2(\omega T/2)} \approx |\chi(0,\omega)|^2 \tag{11.1}$$

The range response on the Doppler axis $\omega = 0$ is the square of the autocorrelation function of the individual rectangular pulses repeated at intervals of T. For a finite pulse train, the *envelope* of the range-ambiguity peaks of period T decreases as $(N - |K|)^2/N^2$, with K representing integer values of the interpulse period over $-(N - 1) \leq K \leq (N - 1)$.

* If all the targets in the environment are located within the unambiguous range $c(T - 2\tau')/2$ and are separated by at least $2\tau'$, there can be infinite resolution of their echoes. See Chap. 8 for terminology.

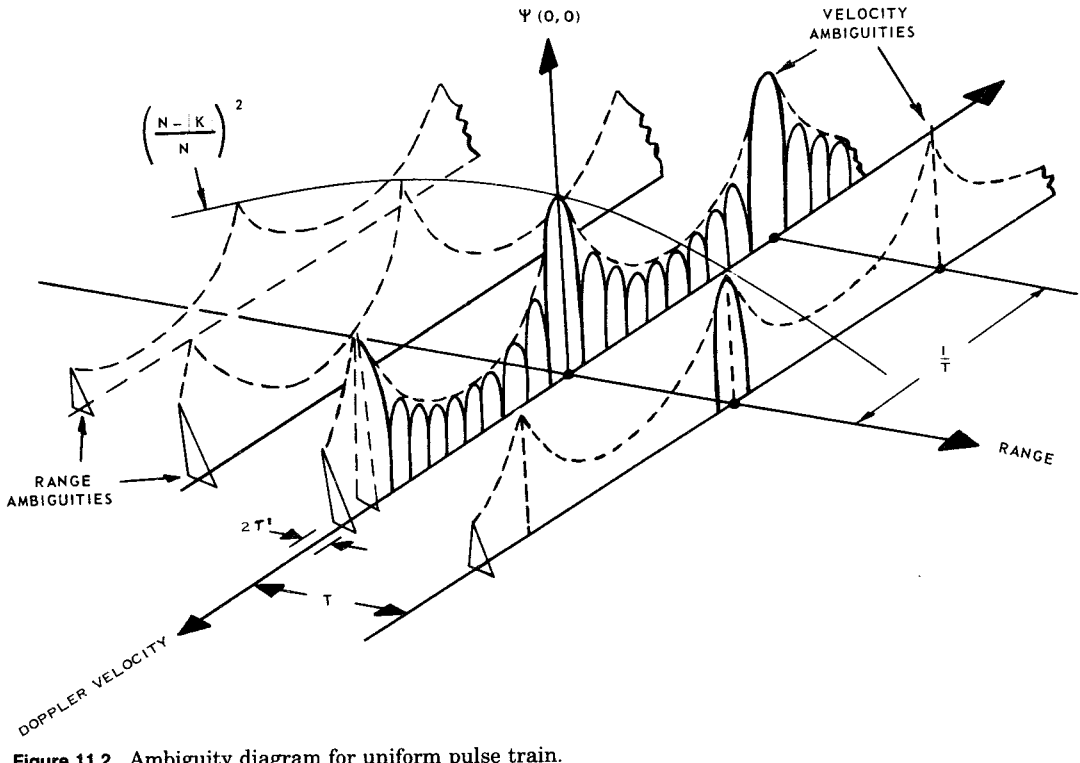

Figure 11.2 Ambiguity diagram for uniform pulse train.

TABLE 11.1 Ratio of Target Response to Doppler-Shifted Interference for Uniform Pulse Spacing Without Weighting Function

Number of pulses	Average Doppler response, dB*		
N	$0.1/T$, $0.9/T$	$0.3/T$, $0.7/T$	$0.5/T$
8	.....	19.1	21.0
12	15.4	22.5	24.6
16	16.5	24.7	27.0
20	18.1	27.3	29.0
24	20.2	29.0	30.6
32	23.0	31.5	33.1

* The values in this table can be interpreted as the average improvement in clutter-to-signal ratio for *point* clutter at the target range but separated in Doppler frequency. This illustrates the interference rejection of the matched-filter receiver for a uniform pulse train.

Since the range response can be zero for a large portion of the unambiguous range if τ'/T is small, the primary regions of interest are the ridges parallel to the velocity axis. If the number of pulses is large, the sinusoidal sidelobes rapidly decrease from the values on the range axis and at multiples of $1/T$. The Doppler response envelope is minimum at $1/2T$, where the *peak* sidelobe is roughly equal to $1/N$ times the peak in amplitude of $1/N^2$ in power. *Average* values of the sidelobe power response at other regions along the Doppler axis are given in Table 11.1 for various values of N and at various percentages of the unambiguous Doppler frequency.

Staggered pulse trains

Since in the time frequency plane of the ambiguity diagram the area between range ambiguities has identically zero sidelobes, the uniformly spaced pulse train provides maximum freedom from extended clutter echoes. When the target is relatively small and the clutter is widely distributed or the interfering targets are large, this would be the best burst waveform to use if N could be made sufficiently large. Amplitude and phase tapering can be used to reduce the Doppler sidelobes, and each individual pulse can be modulated to increase range resolution. These variations are discussed in later sections.

The main difficulty with the uniform pulse burst is that large range ambiguities will be *close-in* unless the PRF is low, and Doppler ambiguities will be *close-in* unless the PRF is high. The nonuniform burst provides maximum freedom from *significant* ambiguities and is most useful where the interfering targets are all of approximately the same cross section as the desired target. A small mainlobe volume of the ambiguity function is desirable, as in other pulse trains.

To construct a suitable waveform, the interpulse period should be varied so that a maximum number of time sidelobe locations are gen-

erated. This requires an *almost uniform* stagger in multiples of the pulse width. Time axis sidelobes in the autocorrelation function are not allowed to overlap, and hence no sidelobe has an amplitude greater than $1/N$. The term *magic stagger* has been applied to this type of pulse train. In terms of the ambiguity surface $\psi(\tau,\omega)$ for this type of waveform, Resnick [589, p. 29] has shown that

$$\frac{\psi(0, 0)}{N^2} \geq \psi(\tau, 0) \qquad \text{for} \qquad |\tau| \geq \tau' \tag{11.2}$$

In other words, the central spike of the ambiguity function is at least N^2 greater than any zero Doppler time sidelobe in the region outside twice the pulse width. He also showed that this inequality holds for all Doppler. For the foregoing type of burst, when the number of pulses N exceeds a *few dozen,* it is desirable that the average PRF be high enough so that the first Doppler ambiguity at $f_d = 1/T$ is at a higher frequency than the highest Doppler frequency of interest to minimize Doppler ambiguities at the target range. The ambiguity function for the Resnick-type waveform is shown in Fig. 11.3. The apparent periodicity for the Doppler response at zero range offset is somewhat misleading as is explained subsequently. Resnick also showed that

$$\int_{-\infty}^{\infty} \int_{K\Delta-\tau'}^{K\Delta+\tau'} |\theta(\tau, \omega)|^2 \, d\tau \frac{d\omega}{2\pi} = \frac{1}{N^2} \tag{11.3}$$

where $\theta(\tau, \omega)$ = the signal correlation function [see Eq. (8.10)]
Δ = the minimum interpulse period
K = integer used to define discrete periods of the ambiguity surface

Since a sidelobe of the autocorrelation function is produced by each of the N pulses with the $N - 1$ other pulses, the total volume contained in these sidelobes is

$$\int_{-\infty}^{\infty} \int_{-\infty}^{\infty} |\theta(\tau, \omega)|^2 \, d\tau \frac{d\omega}{2\pi} = 1 - \frac{1}{N} \qquad \textit{for} \qquad |\tau| > \tau' \tag{11.4}$$

and the remainder of the volume is along the Doppler axis within the strip ($\tau' \geq \tau \geq -\tau'$).

Since the pulse train consists of small deviations from a uniform pulse train, the close-in spectrum (near the range axis) resembles the $\sin NX/\sin X$ shape of the uniform pulse train. In that region, the clutter or interference rejection is comparable to the uniform pulse train. Thus, this waveform merits use where major range ambiguities cannot be tolerated, and the maximum expected target-Doppler velocities are

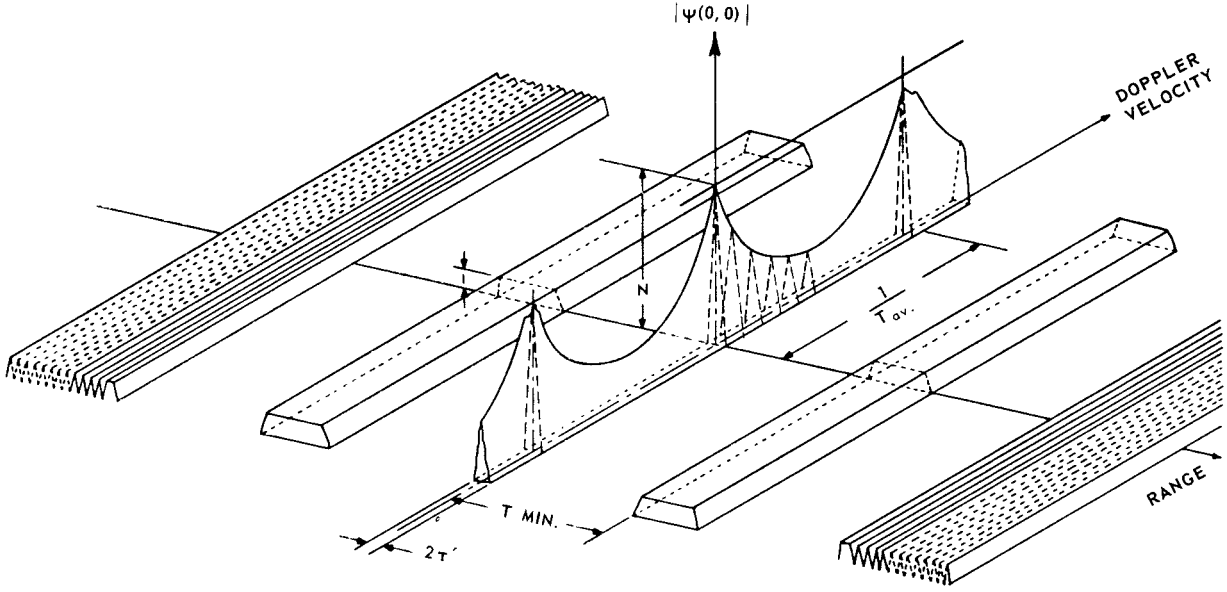

Figure 11.3 Envelope of the correlation function for a nonuniformly spaced pulse train of N pulses. (*After Resnick* [*589*])

within the first few ambiguous regions. This is illustrated in Fig. 11.4 for a 32-pulse train where $\Delta = 55\,\tau'$ and total duration is $3346\,\tau'$. The abscissa is the normalized Doppler frequency in units of T_{av}^{-1} where T_{av} is the average interpulse period.

Nonuniformly spaced pulse trains having a moderately low sidelobe level will be generated when the sequence of interpulse spacings is

$$\Delta_i = \Delta + \tau'[X + iq] \text{ modulo } (N - 1)$$

where $i = 0, 1, 2, \ldots, N - 2$
N = the number of pulses in the train ($N - 1$ is a prime number)
X, q = positive integers such that $N - 1 > q > 0$ (choose $q \approx (N - 1)/2$, but not $N/2$ or $(N - 2)/2$) and $N - 1 > X \geq 0$.

The duration of the train will be

$$T_d = (N - 1)\left[\Delta + \tau'\left(\frac{N-2}{2}\right)\right]$$

The minimum interpulse spacing Δ, which is also the distance to the first time sidelobe, can be as low as

$$\Delta \approx \frac{N^{3/2}\,\tau'}{4}$$

and the duration-bandwidth product of the pulse burst can then be expected to be

$$T_d B \approx \frac{T_d}{\tau'} \approx \frac{N^{5/2}}{4}$$

For a pulse train with 32 pulses the maximum sidelobe level will be 30 dB down and the minimum $T_d B \approx 1450$. It can be seen that, as the number of pulses becomes large ($N > 100$), the length of the pulse train may become excessive. The duty factor may be lower than desired for target detectability or full transmitter utilization. Several of the Resnick trains are illustrated in Table 11.2. Since the sidelobes are fairly high, this waveform is not widely used.

The second-order statistical properties of the target ensemble will undoubtedly limit the maximum duration of the waveform. Further, for the narrow-band approximation to be valid

$$T_d B \leq \left[\frac{2v}{c}\right]^{-1} \tag{11.5}$$

or for Mach-5 targets $T_d B \leq 90{,}000$ (see also Remley [588]).

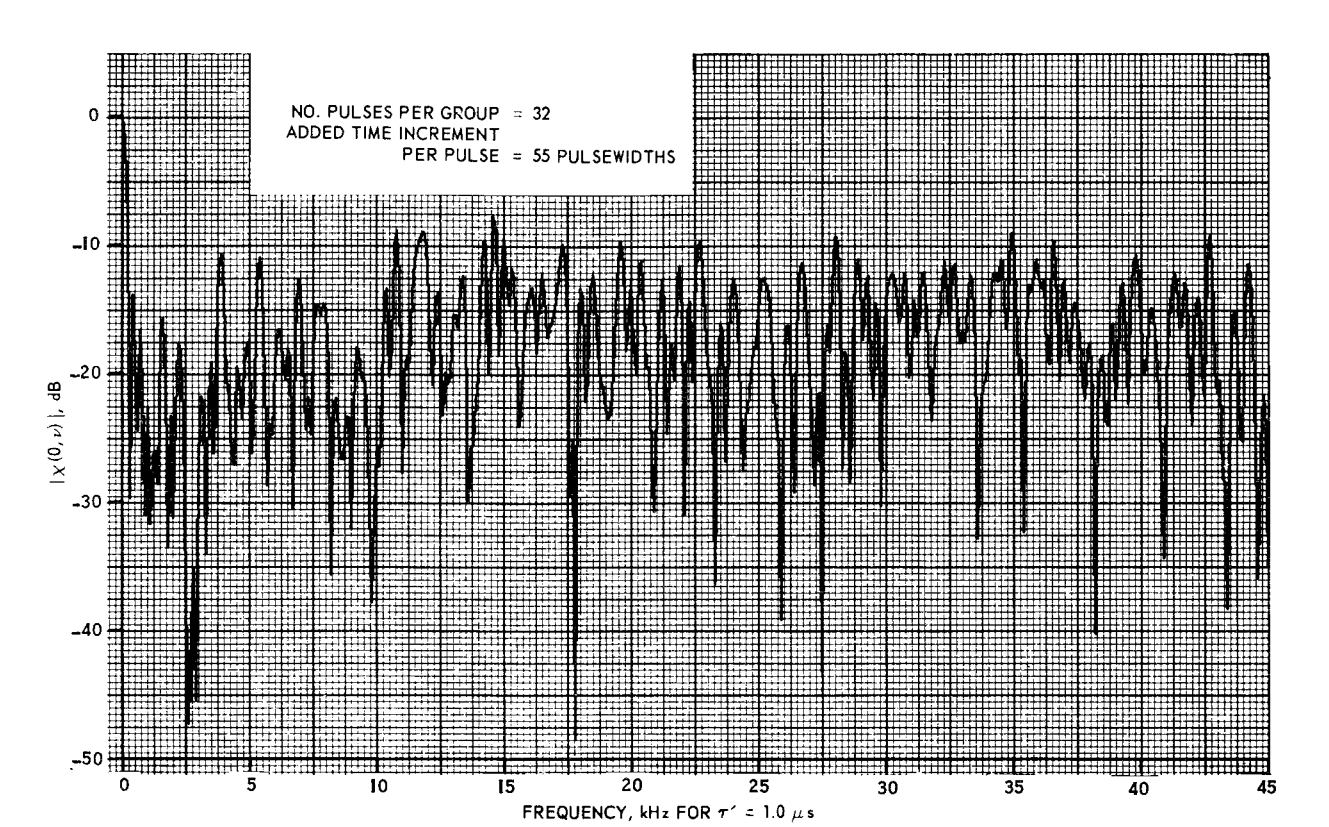

Figure 11.4 Ambiguity function, $20 \log|\chi(0, v)|$ for 32-pulse train. (*Courtesy of M. Davidson*)

TABLE 11.2 Tabulation of T_dB and Sequence of Spacings for Small Values of N

N	T_dB required	Sequence
2‡	1*	1
3‡	3*	1,2
4‡	6*	1,3,2
5	11*	3,1,5,2
6	17*	1,3,6,2,5
7‡	33†	4,7,5,8,6,3
8	35†	7,3,6,2,12,1,4
9	45†	2,8,14,1,4,7,6,3
10	55†	1,5,4,13,3,8,7,12,2
12	85†	2,4,18,5,11,3,12,13,7,1,9
14	127†	5,23,10,3,8,1,18,7,17,15,14,2,4

* Optimum sequence (T_dB minimum possible).

† Extensive but not exhaustive search.

‡ Resnick [589] and E. Paaske and V. G. Hansen, Note on Incoherent Binary Sequences, *IEEE,* vol. AES-4, pp. 128–130, January, 1968.

11.4 Amplitude, Phase, and Pulse-Width Tapering of Finite Pulse Trains

The preceding sections on constant PRF and staggered pulse trains illustrated that the timing of the pulses in the waveform can be chosen to minimize the effects of localized clutter or interference. On the other hand, if there is extended clutter, the average improvement in the signal-to-clutter ratio (S/C) is limited to about the number of pulses in the waveform N. In both cases it was assumed that the transmitted pulses were constant in amplitude and width and the receiver consisted of a matched filter or set of filters.

It was implied (Chap. 8) that there are also *optimum* clutter filters that maximize the output S/C at a small penalty in the output S/N. An analogy to this optimization is the tapering of the transmit and receive apertures of a phased-array antenna wherein the angle sidelobes are reduced at the price of a small reduction in antenna gain and resolution.

One of the limiting factors in achieving clutter reduction by pulse Doppler techniques in narrow-beam rotating or phased-array radar systems is that the limited time allotted per beam position generally restricts the duration of the pulse train and hence the number of pulses. Since it is usually difficult to *transmit* a pulse train with pulses of varying amplitude, it seems best to consider the optimization of the receiver for the constant-amplitude, uniformly spaced pulse train of finite extent. As in all of this section, the effects of target acceleration are neglected, and the targets are assumed to approximate point re-

flectors. The range law of the clutter echoes is not included until Sec. 11.8 and is discussed in Sec 7.9.

Taylor, cosine, Hamming, etc. amplitude weighting of the received pulse train can improve the signal-to-clutter ratio in many situations. It is shown that there are *optimum* complex (both amplitude and phase) weighting techniques that can yield even more improvement if the clutter range and Doppler are known approximately. With all these techniques, there is a slight penalty in signal-to-noise ratio SNR. A figure of merit for these receivers would be the efficiency L_s for a given Doppler sidelobe reduction, defined as

$$L_s = \frac{\text{output signal-to-noise of weighted processor}}{\text{output signal-to-noise of the matched filter}}$$

Both the efficiency and the sidelobe reduction can be made quite high if the unwanted reflectors or targets occupy a small region of the ambiguity plane. If they are less than a pulse length from the target range and are within the first Doppler ambiguity, the reduction in the Doppler sidelobes (compared with the uniform amplitude case of Table 11.1) at the target range can be substantial as shown in Fig. 11.5 for a train of only 21 pulses. The particular taper was based on the Hamming function [699] and the loss in output SNR is only slightly over 1 dB while all Doppler sidelobes are down by 41 dB or more.

The Hamming function is an efficient taper and can be represented in discrete form by its weighting function amplitude [171]

$$W(n) = K - (1 - K)\cos\left[\frac{\pi(2n - N - 1)}{(N - 1)}\right] \tag{11.6}$$

where n = the number of the pulse in the train
K = a constant (equal to 0.54)

There is no phase weighting in this type of taper.

For $K = 0.54$, the theoretical peak sidelobe level is 42.8 dB below the central peak with a 1.3-dB loss in peak signal-to-noise ratio. An approximation for the efficiency with weighting is

$$L_s = \frac{\left[\sum_1^N A_n\right]^2}{N\sum_1^N A_n^2} \tag{11.7}$$

where A_n = the weighted amplitude of the Nth pulse. Other weighting functions are described in Sec. 11.6.

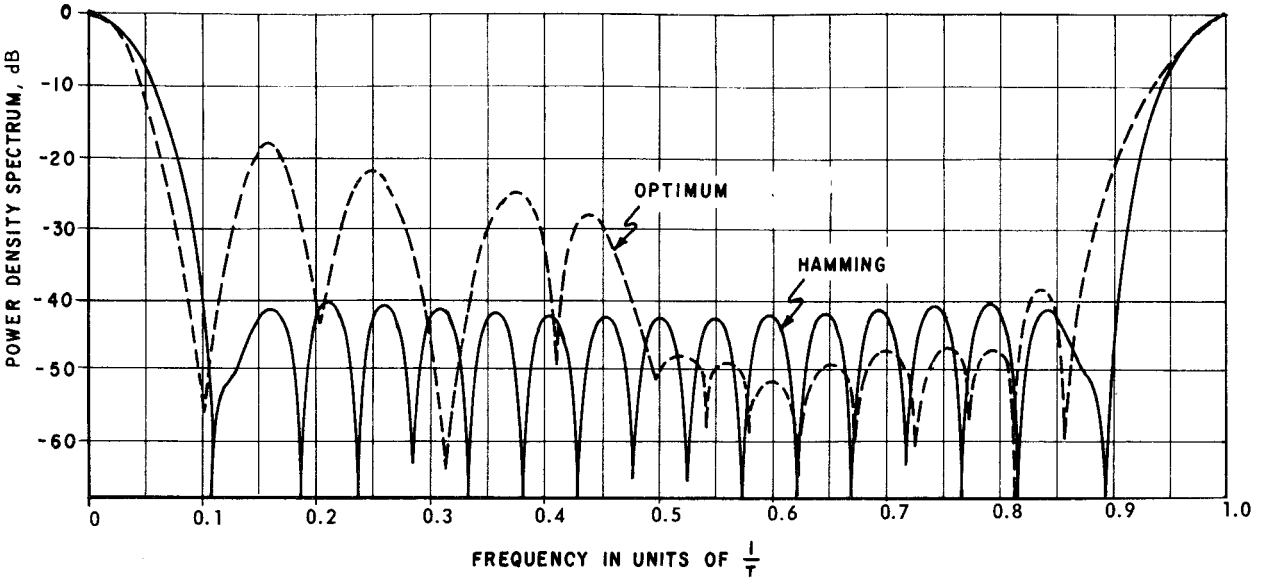

Figure 11.5 Power density spectra for Hamming weighting and for "optimum weighting" in the region of $0.5/T$ to $0.83/T$ for a 21-pulse train. (*Derived by Rummler* [626])

If resolution of targets with nearly the same velocity is desired, there is the additional penalty of the widening of the central Doppler lobe by 40 to 50 percent. Taylor or Dolph-Chebyshev weighting functions [768, 699] can then be used to minimize the degradation in Doppler resolution for a given sidelobe level. One limitation of the *antenna-type* tapers is that they optimize for clutter rejection only at the target range, whereas the clutter often extends into the ambiguous-range intervals. These *antenna* tapers are widely tabulated and usually do not involve phase weighting.

Significantly better efficiency and Doppler sidelobe rejection can be achieved for specific Doppler separations if the interference has a limited range extent. A specific example would be the detection and tracking of a reentry body where the echoes from the wake and tank fragments have comparable ranges and velocities but are not of interest. Descriptions of optimization procedures can be found in Stutt [684, 683], Spafford [678], and Rummler [626, 628].

The value of these optimization techniques can be summarized as follows:

1. If the extent of the *clutter* in range and Doppler is small and its location in the ambiguity plane is approximately known, substantial *S/C* improvements can be achieved over the use of a matched filter. This is achieved with generally less than 1 to 1.5 dB loss in efficiency.
2. As the range extent of the clutter increases to one-half the length of the total waveform and the Doppler extent exceeds one-half the unambiguous velocity, the *optimum* receiver becomes less advantageous. The improvement *I* in *S/C* is limited to 5 to 16 dB over that of matched filters for pulse trains of 20 to 40 pulses.
3. If the range extent of the clutter is comparable to the length of the waveform, the optimization yields only 2.6 to 3.0 dB improvement above the matched filter [626]. An example of this is shown in the section on truncated pulse trains.
4. The penalties of using optimization rather than matched filtering are small if the estimate of the clutter location is poor.
5. Optimization degrades the Doppler resolution. This may or may not be a problem. The efficiency factors that are quoted here are dependent on the width and number of the Doppler filters that are actually implemented.
6. The advantages of optimization are obtained only with tight phase and amplitude tolerances. Rummler [626] stated that the results of the optimization (shown in Figs. 11.5 and 11.6) can be obtained only

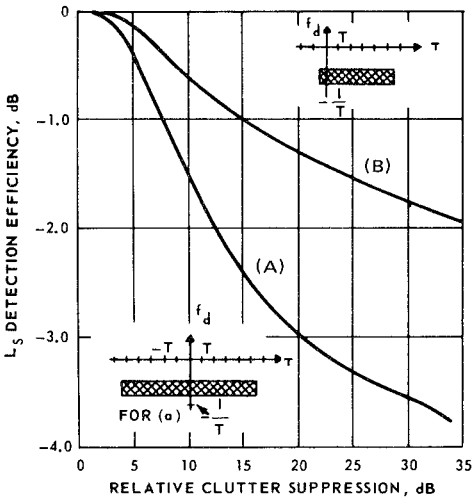

Figure 11.6 Detection efficiency versus relative suppression with a 21-pulse train, clutter cloud distributed in Doppler from $f_d = \frac{5}{6}T$ to $f_d = -\frac{1}{2}T$, in range (A) from $n = -5$ to $n = 5$; (B) from $n = 0$ to $n = 5$. (*After Rummler* [626])

for an rms phase and amplitude uncertainty on each pulse of 1° and 0.2 dB, respectively.

An example that illustrates the loss in detection efficiency for a given clutter reduction as a result of the use of optimum waveforms in moderate clutter extents is contained in Fig. 11.6. Two clutter extents are shown for a clutter velocity spread of from $1/2T$ to $5/6T$ Hz. The ordinate is the efficiency L_s as defined earlier, and the abscissa is the clutter suppression relative to that of a matched filter. For curve *a*, the range extent is 10 interpulse periods (five preceding and five following the target). For curve *b* the extent is five interpulse periods beyond the target ($n = 0$ to 5). It can be seen that even for moderately extensive clutter, significant relative improvement can be obtained with only 1 to 2 dB loss in efficiency. The zero range *cut* of the Doppler response for about a 1.7-dB loss in efficiency (and the clutter extent given for case *a*) is sketched in Fig. 11.6.

A similar optimization is sketched in Fig. 11.7 from Spafford [676]. The clutter is assumed to extend throughout *all* the range ambiguities but was limited to between $0.275/T$ and $0.375/T$ in Doppler. The zero range cut of the ambiguity diagram $\psi(0, \omega)$ is shown for the unweighted and *optimum* pulse trains. The loss in SNR with the optimum weighting is only about 0.1 dB. The zero range error cut is deceptive in that high rejection is shown in the desired Doppler region. However, the Doppler cuts at the distal range ambiguities (where the clutter is also assumed to exist) degrade rapidly, and the overall improvement is only 2.85 dB better than the matched-filter receiver for range-extended clutter.

If the clutter extends throughout the $2N - 1$ range ambiguities, Ares

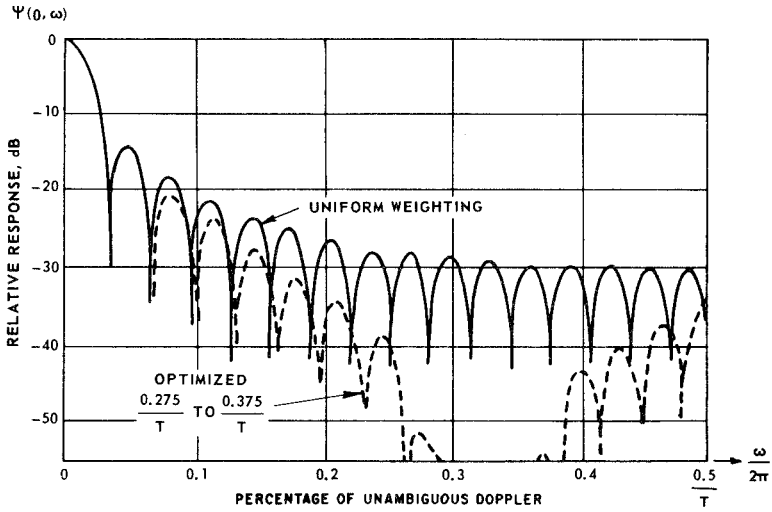

Figure 11.7 Power spectra at target range for 32-pulse transmission. (*After Spafford* [676])

[18] has shown that the use of a constant envelope burst and the optimum mismatched receiver yields a S/C improvement that is within 3 dB of the constant envelope burst and its matched filter.

In some situations, where it is necessary to use a burst of only a few pulses, the signal-to-clutter improvement for constant envelope burst is inadequate for the environment. If the transmitter chain is sufficiently linear, by weighting the amplitude of the pulses in the transmission as a function of time, an additional improvement may be obtained. This is especially useful in range-extended clutter since the clutter echoes from the distal range ambiguities then have relatively lower power at the input to the receiver.

With the aid of a computer and nonlinear optimization routines, Ares [18] computed the improvement in signal-to-clutter ratio over that of a single pulse for bursts of from four to eight pulses. Some typical results are given in Fig. 11.8 for a weighted burst transmission and a matched-filter receiver. The clutter is assumed to be extended in range and have a spectral width of 2 percent of the unambiguous Doppler frequency. The optimization was for the case in which the mean velocity of the clutter is separated from that of the target by one-half the ambiguous velocity. Alternately, the clutter can be assumed to be stationary and the target Doppler located at $1/2T$. With the six-pulse transmission and a clutter spectral width of 10 percent, the improvement factor I is still 26 dB with $1/2T$ Doppler separation, while only 10.8 dB can be obtained with a uniform transmission and receiver-only optimization.

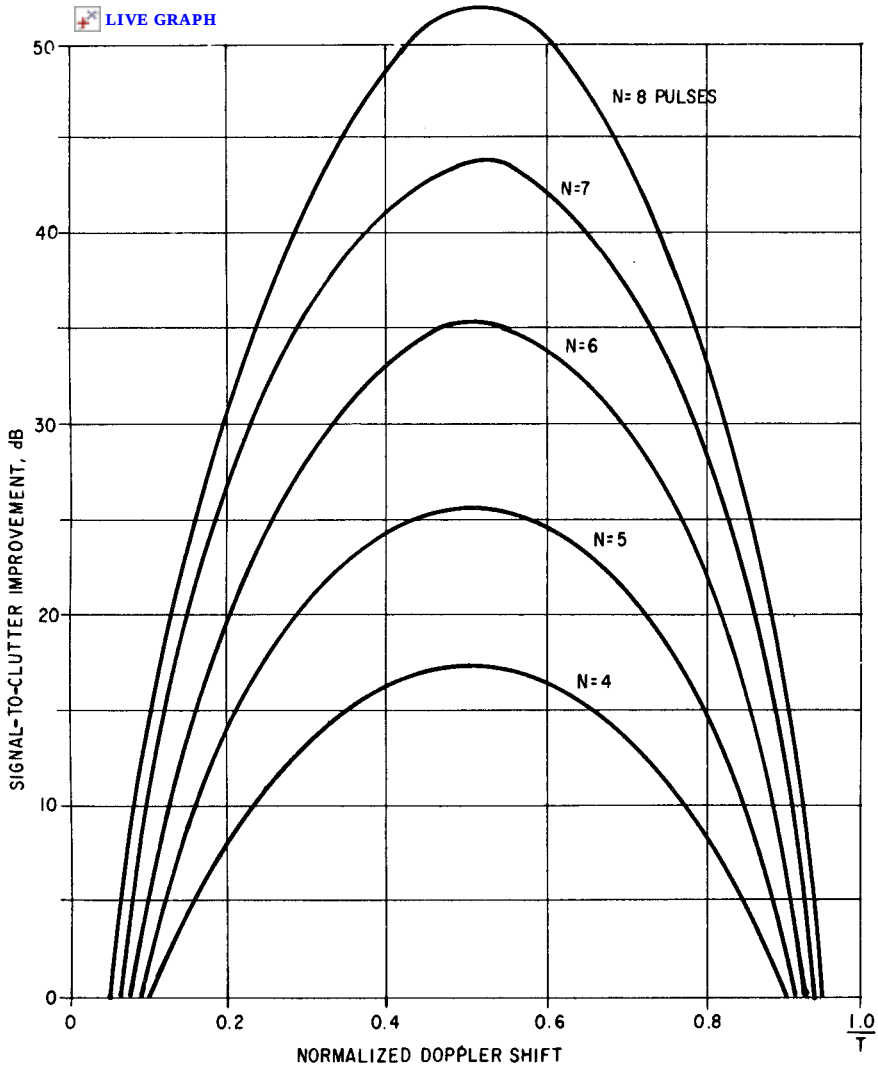

Figure 11.8 Improvement for N-pulse burst with weighted transmission and matched filter (clutter spectral width = $0.02/T$). (*After Ares [18]*)

11.5 Block Diagrams for Pulse Doppler Receivers

There are many pulse Doppler receiver configurations for both search and tracking systems. The choice of configuration is based on the function of the radar. Search radars usually require more sophisticated circuitry than tracking radars since a greater number of range gates

and Doppler filters are needed to *find* the target. Discussions of the choice of carrier frequency are contained in the section on the ambiguity diagram and the section on clutter computations.

The discussion that follows assumes that both coherent range and Doppler processing are needed to reduce clutter as well as integrate the energy from many pulses.

Range gates and Doppler filters at IF

A block diagram of an early pulse Doppler receiver whose Doppler processing was accomplished with narrow-band IF filters is given in Fig. 11.9. Waveform parameters are shown at the top of the figure with the square pulses representing coherent samples of a constant frequency carrier. The received signals are mixed to a convenient first IF, filtered to approximately the inverse of the pulse width, and then mixed again to a second or third IF which is convenient for the final Doppler bandpass filtering, which occurs after range gating. The matched filtering for an individual pulse determines the design of the first bandpass filter and the range gate. In this section a *matched filter* implies optimization with respect to receiver noise unless called a *clutter matched filter*. This is discussed in the section on detection range computations and in Chap. 14.

The reason for using a multiple-conversion receiver is to simplify the filtering processes and remove the Doppler images. The spectrum of a continuous pulse train with interpulse period T and N approaching infinity is shown as the series of impulses centered about the carrier frequency f_0 on Fig. 11.10. The decrease in the height of the spectral lines away from f_0 results from multiplication by the spectrum of a single pulse in the train. If the pulse length is 1 μs and the interpulse period is 200 μs, there are about 400 significant lines in the spectrum.

The dotted lines in the figure represent the echoes from a point-source target approaching the radar at a Doppler frequency of $f_d = 2v/\lambda$. The gaussian-shaped spectra near the transmit spectral lines represent clutter echoes with zero mean velocity but with finite width due to turbulent effects.

If the receiver is to coherently integrate many of the target-echo pulses, the doppler bandpass filter must have a width $b \ll 1/T$. In the example of a 5-kHz PRF, the bandwidth b would be about 100 Hz for 50-pulse coherent integration. If a single-conversion receiver were used at an IF of 500 kHz, the pulse-filter bandwidth ($\approx$ 1 MHz) would become meaningless and the spectral lines and interference near the carrier frequency plus 1 MHz, 1.5 MHz, etc. would *fold* into the desired spectral region. With the double-conversion technique illustrated, the first IF could be about 60 MHz with a pulse-filter bandwidth of 1 MHz.

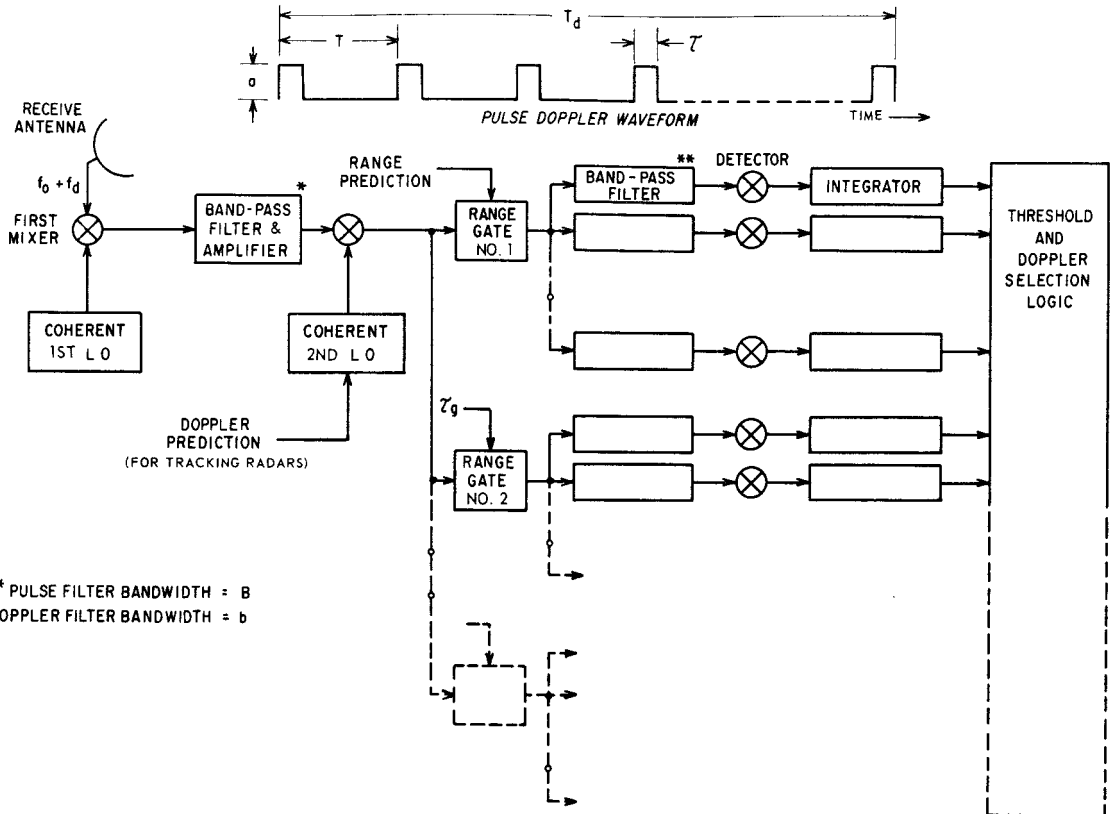

Figure 11.9 Pulse Doppler waveform and basic receiver block diagram.

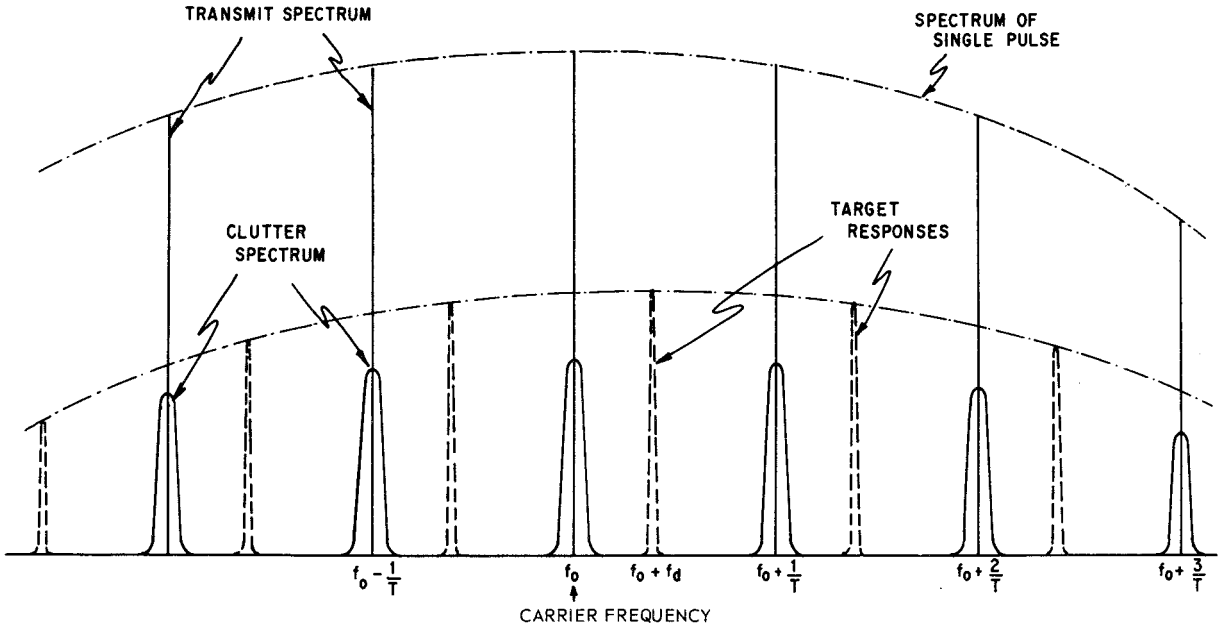

Figure 11.10 Spectrum of returns from a coherent pulse train.

The number of range gates and Doppler filters is dependent on the prior knowledge of target location and radial velocity. In a tracking radar, only two range gates may be needed: an *early* and a *late* gate straddling the predicted range. Each of these gates could be followed by two or three Doppler filters *straddling* the predicted radial velocity. In an acquisition mode or for a search radar the number of range gates and velocity filters may fill the entire unambiguous range including all possible Doppler frequencies up to $1/T$. Since the Doppler response is symmetrical around the PRF lines, the bank of filters may cover either the region between one pair of lines or may straddle a single line.

The minimum number of filters for *all Doppler* coverage is approximately equal to the number of pulses desired for coherent integration N_c with the width of each filter b equal to $1/(N_cT)$ or $1/T_d$. Additional filters tend to reduce the loss when a target echo straddles two Doppler filters but does not give additional unambiguous information. If the filters are not perfectly rectangular, there is a loss of response in the crossover region between the filters. On the other hand, a rectangular bandpass filter is not a matched filter for a uniform pulse train.

After the Doppler filtering, the sinusoidal output of the filters is envelope or square-law detected and is often stored or integrated. The integration at this point is incoherent for all the pulses after the effective time constant of the Doppler filter. The reduction in per-pulse (S/N) below that required for coherent integration of N_c pulses can be approximated by determining N/N_c and entering the appropriate curves of Marcum and Swerling [461] (see Chap. 3). If the signal-to-noise ratio prior to the detector resulting from the coherent integration of N_c pulses is much greater than unity, the loss from incoherent integration is small.

Homodyne or zero-IF processor

Several limitations of the narrow-band IF filter configuration for pulse Doppler receivers have led to the zero-frequency IF (homodyne) configuration described in Sec. 8.8.

A basic block diagram of the homodyne pulse Doppler receiver is shown in Fig. 11.11. The one-step conversion from microwave RF to zero frequency is not necessary but can be accomplished with sufficient preamplification prior to the single sideband mixer. The mixers are of the single sideband type so as to attenuate the Doppler images and to provide the in-phase I and quadrature Q components of the RF pulse signal. Using a signal representation basically that of Rice,

$$f(t) = I \cos(\omega t) + Q \sin(\omega t)$$

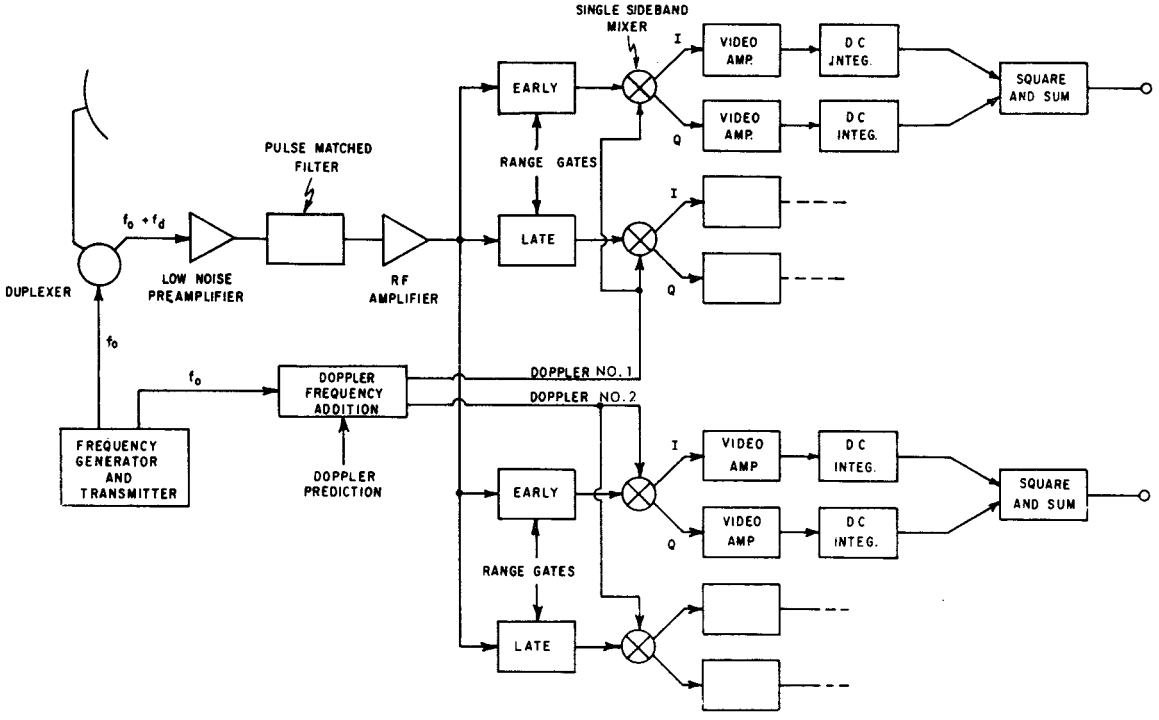

Figure 11.11 Zero IF (homodyne) pulse Doppler receiver.

where ω is the carrier frequency in radians. The mixer outputs are in quadrature (90° phase separation) and the phase and amplitude of each RF pulse are contained in the amplitude of the instantaneous I and Q components. These components are bipolar pulses where $(I^2 + Q^2)^{1/2}$ is the magnitude of the RF pulse. $\text{Tan}^{-1}-(\text{Q/I})$ is the phase angle of the RF pulse. These bipolar pulses then allow reconstruction of the Doppler signal. If the PRF is constant and is greater than the highest target Doppler, the Doppler frequency determination is unique. Otherwise the ambiguities in Doppler must be tolerated or resolved by other measurements such as range rate.

The transmit pulses are usually much shorter than a cycle of the Doppler, therefore the range gating follows a filter that is matched to the transmit pulse width. The determination of which range gate and Doppler filter contain the target signal (or if a signal exists) can be performed by several methods. The dc integration shown in Fig. 11.11 is one of the simplest to consider. If the Doppler prediction is exactly correct in one of the range-gate/Doppler filter channels, all of the outputs from the train of echo pulses in its I channel will have the same polarity, and those in the Q channel will also be unipolar.* The I and Q integrators will simply add the returns from each pulse and after squaring and summing will yield the coherent summation of N_c pulses. If the Doppler prediction in a channel is incorrect by much more than $1/T_d$ Hz, the pulses out of the mixer will vary in both amplitude and polarity during the pulse train. On account of the bipolarity, the output of this integrator will approach an infinitesimal percentage of the amplitude in the *correct* Doppler as N approaches infinity if the integrator time constants also approach infinity. The residues in the incorrect range-Doppler channels are significant only if N_c is small or if the samples are at the ambiguous ranges or Dopplers. Since noise has random phase and amplitude, it will not integrate coherently. Subsequent sections place numerical bounds on the integration of noise and the clutter residues. In current designs this is all performed digitally.

Tapped delay-line and comb-filter processors

If the number of pulses to be coherently integrated is relatively small, a *tapped delay-line implementation* can be used. The portion of this configuration after the mixing processes is shown in Fig. 11.12. The delay lines are matched to the intervals between pulses with T_i cor-

* Both channels are necessary since it is possible for the signal to exist in only one channel.

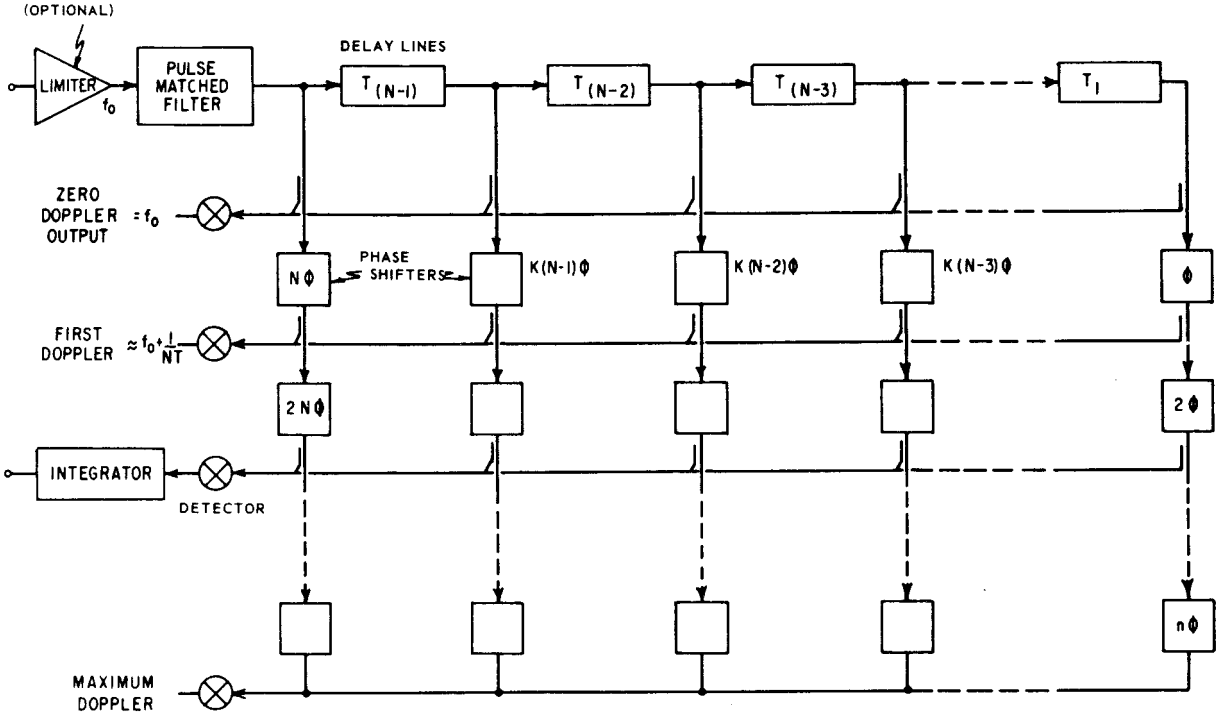

Figure 11.12 Tapped delay line receiver for coherent pulse train.

responding to the time between the transmission of the first and second pulses, etc. The time between the last two transmit pulses to be coherently integrated is then given as $T_{(N-1)}$. This manner of Doppler decoding can be used for a fixed nonuniform pulse train, with the special case of constant PRF resulting in equal lengths for all the delay lines.

The summing bus directly below the delay lines provides the zero-Doppler output if the delay lines are all an integral number of wavelengths at the intermediate frequency. The time delays or phase shifters correspond to the radial distance the target moves between pulses. The arbitrary constant K is shown to indicate that the phase shifts must be adjusted to the individual spacings between pulses if the interpulse period is not constant. The conversion from time delay to phase shift must be made on the basis of target motion in carrier wavelengths. The value of ϕ is often chosen such that $N\phi = 2\pi$ rad, which yields contiguous Doppler coverage with a 4-dB *notch* between Doppler filters for a uniform transmission. Smaller values of ϕ will reduce the depth of the notch but will increase the response of a target in adjacent Doppler filters. The outputs of this processor have the bandwidth of the individual pulses. Coherent integration results from the vector voltage addition of the target echoes in the appropriate channel while noise adds powerwise.

What has been described is often called a *Doppler matrix* or phasing matrix. Its utility is limited by delay-line limitations and the requirement for a large number of components for large number of pulses. One of its advantages is that there is no physical range gating, target range being determined by the time of appearance of echo pulses at Doppler outputs. A *zero range* reference occurs when the first transmit pulse appears at the output of delay line T_1. Quartz delay lines have been used for this technique. A parallel configuration was common for quartz lines rather than the series of lines shown in Fig. 11.12.

If the number of pulses is large enough to achieve CFAR action, a limiter may be placed ahead of the delay lines. Then the normalized maximum output power is obtained from the coherent or voltage sum of N_c pulses (N_c^2 in power). The average noise power level is less than this value by a factor of N_c, the number of pulses coherently integrated.

Since this configuration responds to any set of narrow-band signals associated with all the PRF lines (see Fig. 11.10), it is one of a class of *comb filters*. While it is functionally the same as a range-gated parallel filter bank or a homodyne device it utilizes all the signal's spectral components.

11.6 Fast Fourier Transform Processing

The processing described in the previous sections consisted of various implementations of taking the Fourier transform of the input signals.

Since virtually all processing of pulse-train waveforms is currently performed digitally, and it is necessary to process the echo in each range gate for a number of transmitted pulses, the signal processor is forming the *discrete Fourier transform* (DFT) or something that is equivalent to it. A series of DFTs form the digital filter banks. DFTs can be computed for any number of pulses. The fast Fourier transform (FFT) algorithm is one implementation for rapidly forming near-optimum digital filters for a uniform pulse train-processor. The Cooley-Tukey version illustrated in Fig. 11.13 (often called a bubble chart) is representative of a series of processors now being implemented. A microwave version called the Butler matrix was used for radar beamforming several years before it was suggested for computers. Examining the structure lends insight into the "pipeline" processor, which is one implementation that allows high-speed processing. Other implementations are described in the next section.

For illustration, assume that there is a 16-pulse transmission with uniform time spacing, and that the 16 echoes from a range gate are not weighted and appear on the left as complex video (see Sec. 8.8). The echoes are numbered from 0 to 15 in binary form. Assume also that the processor is set such that the echoes from a stationary point target all have the same phase. The signals flow from left to right with the nodes (circles) representing operations. The number in the circle indicates phase rotation in sixteenths of 2π rad. Signals entering a node on a solid line are phase rotated and passed to the right. A phase rotation means a complex multiplication with a multiplicand of $\exp(j\theta)$. Signals entering on a dashed line are not operated on but also pass to the right.

Observe that all 16 inputs appear at the final node at the upper right corner without any phase shift. This is the zero Doppler channel output. The node at the center of the outputs on the right marked "1" corresponds to the first Doppler channel. The signal from the first pulse has all dashed lines to this output. The signal from the second pulse is phase shifted one-sixteenth of 2π as it enters the first Doppler channel output. Following the third input pulse, it is shifted $2\pi/8$. The last input phase is shifted $^{15}/_{16} \times 2\pi$. Thus, the pulses receive a linear phase shift versus pulse number which corresponds to a linear phase shift versus time, which is a Doppler shift. This is easier to visualize if it is recognized that the number of wavelengths from the radar to an inbound target is decreasing with time.

The pulses arrive at the second Doppler channel with twice the phase shift per input pulse number corresponding to twice the Doppler shift. The inputs to the fifteenth Doppler channel increase by $^{15}/_{16} \times 2\pi$ per pulse, giving a phase slope of 15 times the first Doppler channel. The 16 Doppler outputs respond to 16 different radial velocities. The de-

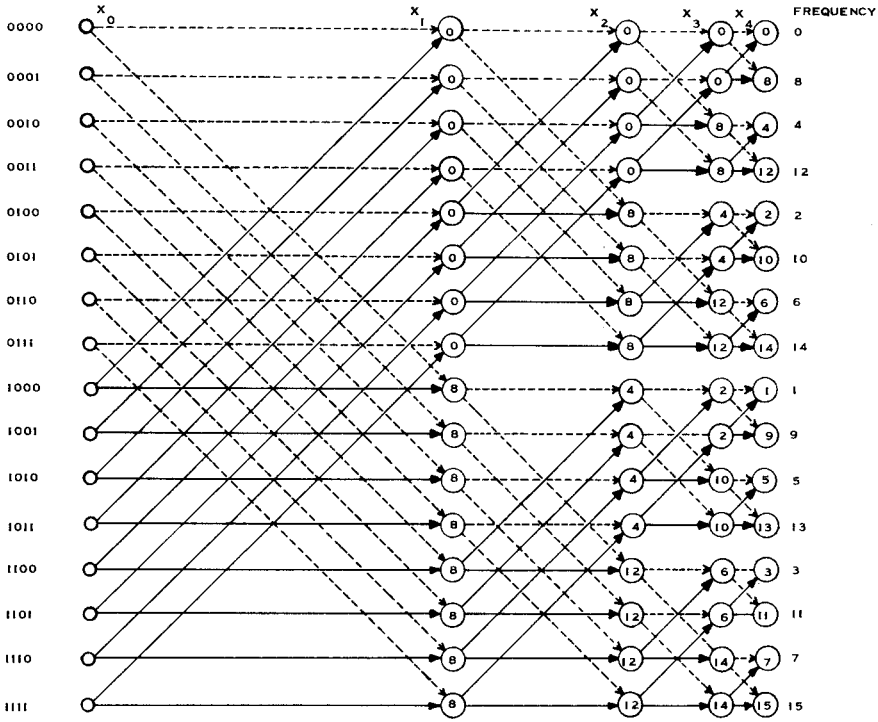

Figure 11.13 Fast Fourier transform (x_n = complex multipliers). Numbers in circles correspond to normalized complex phase rotations; i.e., 13 = ($^{13}/_{16}$) (2π).

termination of which output port is which Doppler channel comes from reading the binary numbers on the left "backwards."

With 16 inputs, there is no reason for any higher Doppler channel. The next output would be phase shifted $^{16}/_{16} \times 2\pi = 0$ degrees per pulse, which is identical to the zero-Doppler channel. This is the Doppler ambiguity at the PRF. Faster targets will "fold over" into the 16 filters as long as the interpulse period is constant. In the FFT algorithm, the number of Doppler channels equals the number of input pulses. The algorithm is designed for binary numbers of pulses (2, 4, 8, 16, etc.). If there is not a binary number of pulses such as 15, "zero-padding" by adding a zero allows use of the FFT algorithms.

The key advantage of the FFT or similar algorithms is the reduction in the number of complex operations (complex multiply and add). For an FFT, it requires only slightly more than $N \log_2 N$ complex operations rather than N^2 operations with a discrete Fourier transform (DFT). In a DFT this means N^2 complex multiplications and $N^2 - N$ complex additions. A complex multiplication requires 4 conventional multiplications and 2 conventional additions. A complex addition requires 2

conventional additions. For 16 pulses this is significant. With numerous pulses, the processing reduction is dramatic. At 64 pulses, $64 \times 64 = 4096$ operations, but 64×6 is only 384.

Figure 11.14 implies withdrawing the inputs from a memory, operating on them, and putting them back into memory as in a general-purpose computer. The faster and more common implementation is the "flowthrough" or "pipeline" processor illustrated in Fig. 11.14. Referring back to Fig. 11.13 it can be seen that the first stage or "pass" involves taking the first half of the inputs and operating on them with the second half of the inputs. Also note that nodes in the first set are either no input or inversion (180° phase shift). This is equivalent to the first stage shown in Fig. 11.14. The second stage in Fig. 11.13 involves operating in quarters of the number of inputs. In Fig. 11.14 another set of gates and adders directly processes the outputs of stage 1. In a similar manner, further processors are added in series. Since these operations are phase rotations of fractions of 2π, complex multipliers and a sine-cosine table are required. There are $\log_2 N$ stages in this configuration.

The power of this pipeline processor is that I-Q samples enter on the left and Doppler filter outputs exit on the right. While there is a latency in the output, the speed of processing is limited only by the speed of complex multiplication. With 25-MHz complex multipliers now available, the available processing speed is quite high and is often limited by the A/D converters that precede the FFT processor. Range gates as short as 0.04 μs can thus be processed. With multiple range gates, there must be more processors or, if the pulses have longer duration, they can be time-multiplexed into a single processor. The Winograd Fourier transform reduces the number of multiplications to the order of N, while only slightly increasing the number of additions. Other algorithms are often used, especially with small numbers of pulses, but this illustration is representative.

The amplitude-versus-frequency response of two of these digital FFT filters is shown in Fig. 11.15. The solid line is the zero Doppler filter response. Since the assumption was that the pulse train was rectangular (unweighted) the Fourier transform has a $\sin x/x$ shape with first sidelobes of 13.3 dB. The dashed curve labeled "uniform illumination filter response" is the shape of the first Doppler filter. With 16 pulses, its peak is at one-sixteenth the PRF. Note that the sidelobes have the opposite polarity of the zero Doppler filter. If the complex signals of the first Doppler filter are added to those of the zero Doppler filter by adding the respective I and Q values a new filter is formed halfway between the zero and first Doppler filters as illustrated. Since the sidelobes are in antiphase, they partially cancel, yielding a first sidelobe of the new filter at -23 dB. All other sidelobes partially cancel. (The

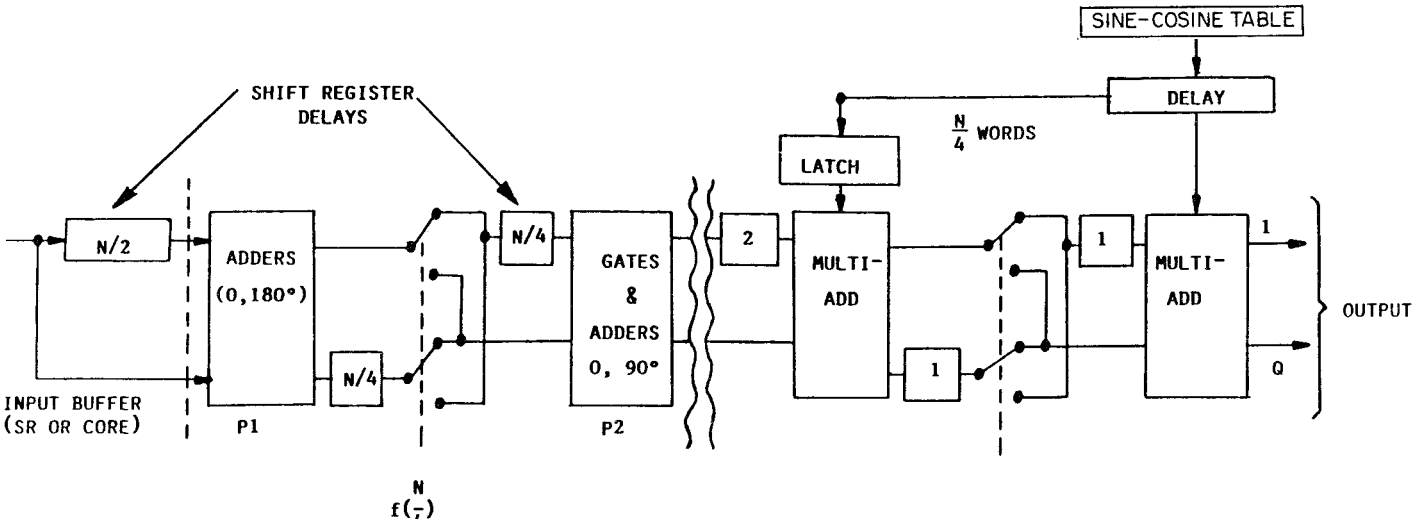

Figure 11.14 Flowthrough FFT (or pipeline) processor (N = number of complex samples = 2^n, n = number of stages).

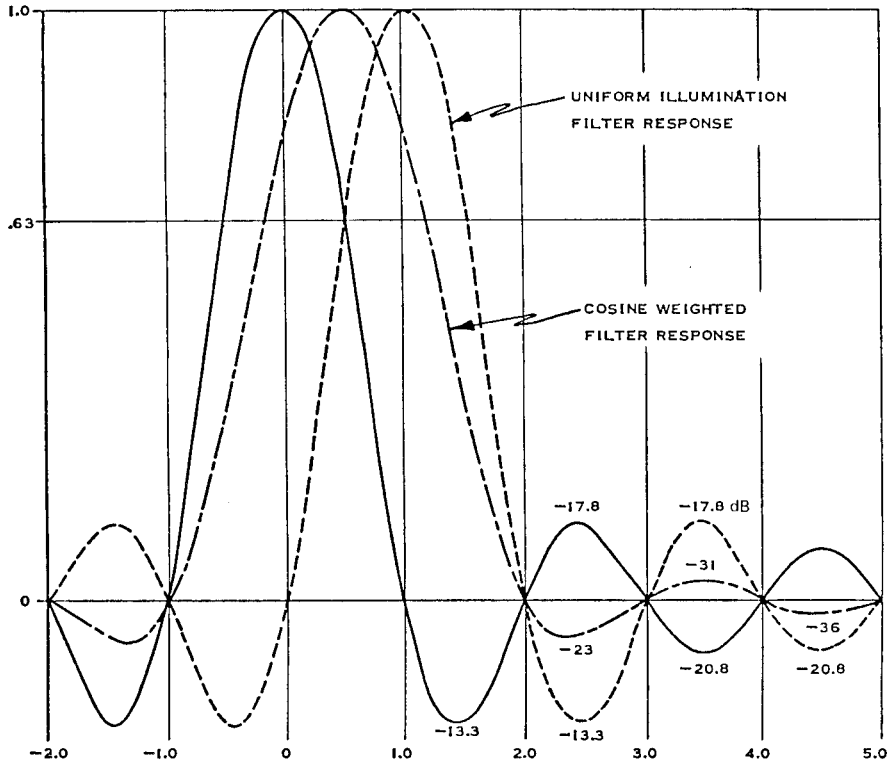

Figure 11.15 Cosine weighting by summation of adjacent filters.

new filter has been normalized in the figure.) This operation can be shown to be equivalent to cosine weighting of the amplitude of the input pulses. This is, in effect, convolving the DFT output with the sequence [1, 1] which is equivalent to multiplying in the signal domain by the inverse DFT of [1, 1], which is the cosine window. There is a 35-percent widening of the filter with the resultant loss in peak signal of about 1.0 dB. The unweighted filters cross at the −4-dB point yielding what is often called a *Doppler cusping* loss, since the target Doppler may be between the peaks of the filters. The cosine-weighted filters cross at the −2.1-dB point. This partially compensates for the loss in peak signal and wider noise bandwidth of the weighted filters. Adding of adjacent filter outputs is often called *windowing* and is mathematically equivalent to amplitude weighting of inputs. The effect of other weighting options is illustrated in Table 11.3 where it is assumed that there are many input pulses. In this table $H(f_k)$ is the complex signal in the kth Doppler filter. For amplitude weighting, $g(t)$ is the time function. For relatively good performance pulse Doppler implementations, the

TABLE 11.3 Weighting or Window Functions

Weighting or window function	Loss in peak, dB	Cross-over point, -dB	Mainlobe broadening ratio	Sidelobe, dB					
				1st	2nd	3rd	4th	5th	Others
1. *Uniform weighting* $g(t) = 1$ $S(w) = 1$	0	4.0	1.0	13.3	17.8	20.8	23	26	$1/f$
2. *Cosine* $S(w) = \frac{1}{2}H(f_k) + \frac{1}{2}H(f_{k+1})$	1.0	2.1	1.35	23.6	30.7	36	39.5	43	$1/f^2$
3. *Hanning or cosine squared** $g(t) = \frac{1}{2}\left(1 + \frac{\cos \pi t}{T}\right) \quad \lvert t \rvert \le T$ $S(w) = \frac{1}{4}H(f_{k-1}) + \frac{1}{2}H(f_k) + \frac{1}{4}H(f_{k+1})$	1.76	1.4	1.59	31.5	41	48	53	59	$1/f^3$
4. *Hamming* $g(t) = 0.54 + 0.46 \cos\left(\frac{\pi t}{T}\right)$ $S(w) = 0.228H(f_{k-1}) + 0.544H(f_k) + 0.228H(f_{k+1})$	1.42	1.7	1.52	44.1	56.1	43.6	42.7	43.2	
5. *Cosine cubed*	2.38	1.1	1.88	39.1	51				$1/f^4$

* $t = 0$ is taken to be the center of the transmission.

TABLE 11.4 Dynamic Range of Digital Fourier Transforms, dB

Number of bits at input	Time samples*				
	32	64	128	256	512
4	38	41	44	47	50
5	44	47	50	53	56
6	50	53	56	59	62
7	56	59	62	65	68
8	62	65	68	71	74
9	68	71	74	77	80
10	74	77	80	83	86
11	80	83	86	89	92
12	86	89	92	95	98

* Assumes that single sine wave fills A/D converter, and that the FFT has an unlimited number of bits. If fluctuating clutter is the input signal, and receiver noise is considered, subtract 6 to 9 dB from the values in the table.

Hamming function is popular (see Sec. 11.4). Other weighting functions such as the Blackman-Harris [120] yield even lower sidelobes when the number of samples is large, but degrade significantly when $N < 32$. Digital filter architecture will be further discussed in Sec. 11.7.

As the signals pass through the various stages of an FFT or DFT, additional dynamic range must be provided to allow for the coherent (voltage) integration of targets while preserving the noise. The increased dynamic range at the output is illustrated in Table 11.4.

With a land-based surveillance radar, where surface clutter is a major problem, the zero Doppler channel can be eliminated, have a separate CFAR channel for large crossing targets, or have its output sent to a *clutter map* (see Sec. 14.1). In this type of radar the Doppler sidelobes should be as low as possible near zero Doppler. Special weighting functions or *finite impulse response* (FIR) filters are often used rather than an FFT implementation, especially if few pulses are transmitted per dwell. Note that in combining adjacent filters in an FFT, all the filters have nulls at zero Doppler. This aids in narrow-band land clutter rejection.

11.7 Architecture for Pulse-Train Processors

Mark A. Richards

As we have seen, signal processing for pulse-train waveforms emphasizes Doppler filtering to separate targets from clutter. Depending on whether a few (perhaps two or three) or many (eight or more) pulses

are to be coherently integrated, a single-channel coherent MTI filter or a multichannel filter bank of bandpass filters might be used. Many systems cascade both. Furthermore, the bandpass filterbank can be implemented either as a collection of individual bandpass filters or indirectly with fast Fourier transform (FFT) processing, as shown in the previous section. While efficient (especially at larger numbers of pulses integrated), the FFT processor places some restrictions on the characteristics of the bandpass filters. Center frequencies must be regularly spaced across the band, i.e., $f_k = kPRF/N$, where N is the number of pulses processed. Also, the shape of each filter's response (passband ripple, sidelobes, transition bandwidth) must be identical.

Once a Doppler filtering approach is chosen, it must be implemented in hardware, usually digital in modern systems. Processor *architecture* is the term used to describe the high-level organization of the implementation. It includes consideration of fundamental algorithm choices, estimation of computational requirements, semiconductor technology, selection between single- and multiple- (e.g., pipeline) processor designs, wordlength requirements, memory sizing, interfaces, and control mechanisms. It does not include detailed logic or circuit designs. Processor architecture is often constrained by external considerations such as the need to interface to certain standard buses, to conform to overall system architectural standards, or to be programmed in particular computer languages.

Processor figures of merit

The most important computational characteristics of a signal processor are its *throughput* and *latency*. Both are measures of speed, which is the major design issue, but they are not the same. Nearly as important are the *dynamic range* and *quantization noise* of a processor, which are determined by its number representation, *e.g.*, whether it uses fixed-point or floating point arithmetic.

Throughput is the rate at which a processor performs a function, such as an FFT, and is most often expressed in units such as MFLOPS (*millions of floating point operations per second*) or MOPS (*millions of operations per second*). Complex arithmetic equivalents such as MCFLOPS are sometimes used. MIPS (*millions of instructions per second*) are frequently used as well. For example, if a processor can complete a 16-point FFT every 100 μs, its throughput is 10,000 16-point FFTs per second. The basic radix-2 implementation of one such FFT requires 128 real multiplies and 192 real additions [98]. If floating-point arithmetic is used, the throughput of this example is then 3.2 MFLOPS.

Unfortunately, these terms are ambiguous and caution must be used

in comparing competing claims. For instance, in the foregoing example, multiplies and additions were assumed to be of equal importance. This is often but not always the case, especially if the arithmetic is implemented in software. Also, in computing real multiplies and adds, it was assumed that a complex multiply requires four real multiplies and two real adds; but a complex multiply can be implemented with only three real multiplies at the cost of five real additions [98].

There are other problems with the use of MIPS, which essentially measure processor clock speed and internal instruction pipelining. MIPS do not account for how many instruction cycles are required to complete an arithmetic operation. For multiplications, this is often more than one. MIPS are more appropriate for sizing control, input/output, and sorting requirements than for arithmetic requirements. Finally, unrealistic peak burst FLOPS and MIPS rates, which ignore pipeline fill times or assume that all data is in a local high-speed cache memory, are often quoted.

Latency is the elapsed time from reading the first (or last) input word in a block of data to be processed into the signal processor until the first (or last) output result is available to be read out of the processor. The concept is illustrated in Fig. 11.16. Short latency times generally require high throughput, but the converse is not true. For example, a multiprocessor architecture with four computational units achieves the same throughput whether the units are arranged as a pipeline or in parallel, but the latency is four times longer for the pipeline. The essential difference is that the pipeline, once filled, processes four FFTs at once with one processor working on each at any given time, while the parallel structure applies all four processors to only one FFT at a time. Latency is frequently critical in certain fast-response jammers and ECM techniques. For filtering and detection processing of radar waveforms, it is generally not as important as throughput.

Processor number representation determines dynamic range and quantization noise. *Processor dynamic range* is the ratio of the largest to smallest nonzero representable numbers, while *quantization noise*

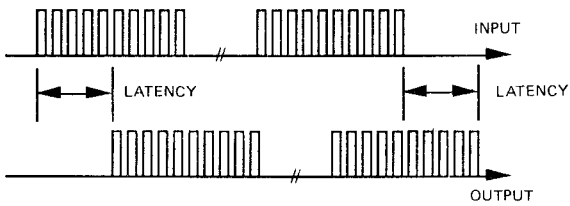

Figure 11.16 Definition of processor latency as the lag time between the input and output data streams.

refers to the noiselike error introduced when real numbers are quantized to one of a finite set of binary numbers. To see why these figures are important, consider a processor with a design goal of a 60-dB improvement factor. If the signal processor's dynamic range is less than 60 dB, then either strong clutter signals must saturate the processor, causing nonlinear effects, or the desired small target signals are too small to be represented by a number other than zero. Alternately, if the signal-to-quantization-noise (SQNR) ratio is less than 60 dB, the target signals are lost in quantization noise.

For B bit fixed-point numbers, processor dynamic range is limited to about $6B - 6$ dB,* while SQNR is about $6B - 1$ dB [525], although both formulas depend on details such as the choice of sign-magnitude or twos complement representation, or the A/D converter gain setting and signal statistics. Thus, an 8-bit processor offers only about 42-dB dynamic range and 47-dB SQNR, while a 16-bit processor can achieve figures in the 90-dB range. While that SQNR is probably adequate, the dynamic range is not. Although the instantaneous dynamic range in a given range cell may be well within 90 dB, when variations due to qualitative clutter differences and R^4 losses over substantial range coverages are considered, the total dynamic range in many systems exceeds 100 dB. The signal dynamic range must then be reduced to match that of the receiver and signal processor with sensitivity time control.

It is also important to realize that signal amplitudes grow in many signal-processing operations. The output of a simple summation can be twice as large as the two signals summed. An N-point FFT can increase signal amplitude by a factor of N, which may be 16 or more, maybe much more. Thus, fixed-point processors require careful attention to signal scaling to avoid overflow and maintain precision.

Many of these limitations are overcome with floating-point processing, which represents each sample by both a fixed point mantissa and an exponent. An increasingly popular floating-point format is the ANSI/IEEE P754 32-bit standard. It uses a 24-bit sign-magnitude mantissa with an 8-bit exponent to achieve 150-dB SQNR with 1600-dB processor dynamic range, clearly more than adequate for virtually all Doppler processors. Floating-point arithmetic requires more complex hardware, and is therefore usually slower. However, as very large scale integration (VLSI) technology advances, floating-point DSP microprocessors are beginning to achieve speeds that make them usable in radar signal processors.

---

* However, it is shown in Chap. 14 that clutter fluctuations limit the actual achievable dynamic range to approximately $6B - 9$ dB.

Architectures for digital filtering

The digital filters used for MTI processing are usually *finite impulse response,* or FIR, filters. FIR filters are aptly named for the fact that the output, when the input is a single nonzero number with all other input samples zero, is nonzero only for a fixed number of samples N equal to one more than the filter *order; N* may be anywhere from two to 10 in MTI processors. Equivalently, FIR filters have no feedback loops. They are useful for Doppler processing because they can be designed to have exactly linear phase response, even when coefficient quantization is taken into account [525]. Consequently, FIR filters need not distort the Doppler-induced phase shifts prior to FFT processing. Furthermore, linear phase FIR filters have symmetric impulse responses, a fact that can be used to approximately halve the number of multiplies required to compute their outputs. While digital filters with feedback (called *infinite impulse response,* or IIR) can achieve greater frequency selectivity with less computation, they strongly distort the phase of the signal near their band edges and are thus unsuitable for coherent Doppler processing.

There are two basic approaches to FIR filter implementation. The first is the straightforward tapped delay line of Fig. 11.17. In this approach, the complex echo amplitude from successive pulses for a given range bin are passed through a delay line whose length equals the number of filter coefficients. Each sample is weighted by multiplication with its corresponding coefficient. For MTI filtering, the coefficients will normally be real-valued. The products are summed to produce one output sample. Each input sample is next fed forward to the next delay stage, and the process repeated.

Tapped delay line filter throughput rates vary widely depending on the implementation technology selected. For example, the Texas Instruments TMS320C25 fixed-point general-purpose digital signal-processing (DSP) microprocessor can implement an N-tap FIR filter at a rate of approximately $11/N$ megasamples per second [700], while the

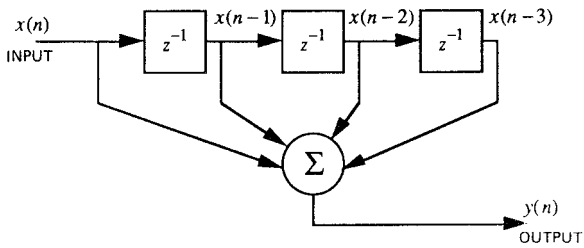

Figure 11.17 Tapped delay line implementation of a 4-tap (third-order) FIR digital filter.

more specialized United Technologies IQMAC IEEE floating-point complex multiplier-accumulator can compute the same filter output at about $15/N$ megasamples per second [726].

The alternative FIR filter implementation approach, known as *fast convolution,* takes advantage of the fact that convolution in the time domain is equivalent to multiplication in the frequency domain. In this approach, illustrated in Fig. 11.18, the input signal is broken into fixed-length blocks, and the FFT of each block computed. The signal spectrum is then multiplied by the filter frequency response, obtained from the FFT of the filter coefficients, to get the output signal spectrum. Normally the filter FFT is computed in advance, rather than in real time. Finally, an inverse FFT returns a block of the output time-domain signal. Because filtering is a linear process, this operation can be repeated block-by-block and the output blocks simply overlapped and added to produce the final output signal [525].

Which procedure is more efficient depends on the filter order K and the number of input signal samples N. The total number of multiplies for a tapped delay-line filter is proportional to NK, while for fast convolution it is proportional to $(N + K)\log_2(N + K)$. While the latter grows more slowly than NK, for the low-order (small K) filters typical of multiple-pulse MTI cancelers, the tapped delay-line implementation is usually fastest. Fast convolution is most efficient for relatively high-order filters.

Figure 11.18 illustrates an additional feature of the fast convolution approach, which is the relative ease with which it can incorporate compensation data. Actual waveforms at the matched-filter input can differ from what was desired for several reasons, such as nonlinearities in the signal generator or amplitude and phase ripple in the transmitter and receiver frequency response. Calibration procedures, whether off-line or real-time, can characterize the deviation of the system response over the operating passband from the constant amplitude, linear phase

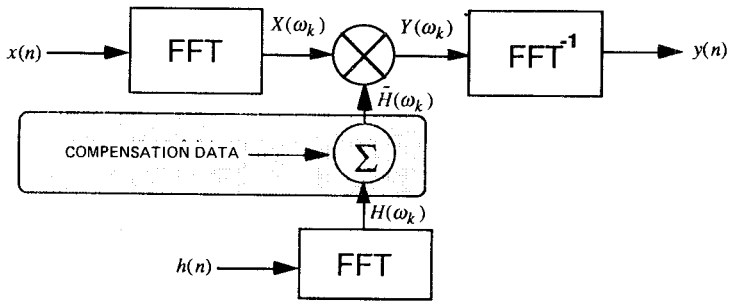

Figure 11.18 Fast convolution frequency domain implementation of an FIR digital filter. Incorporation of frequency domain response compensation data is also shown.

ideal. Since the error characterization is usually in the frequency domain, compensation is most easily done in that domain. The fast convolution structure lends itself readily to frequency domain compensation with minimal extra computation.

Architectures for fast Fourier transforms

The fast Fourier transform is really a growing collection of fast algorithms for computing the discrete Fourier transform (DFT). The best known is the Cooley-Tukey algorithm for signals of length N points, where N is constrained to be of the form R^M for some radix R and integer M. This algorithm breaks the N-point DFT into repeated small elemental R-point DFTs. The example given in the previous section was a radix-2 Cooley-Tukey algorithm; radix 4 is also popular.

There are many other FFT algorithms, most described and compared succinctly by Burruss and Parks [98]. The prime-factor and Winograd algorithms can be applied to signals whose length is a product of relatively prime numbers, $N = N_1N_2 \ldots N_M$. An example would be $N = 2 \times 5 \times 7 = 70$. While these are more efficient than the Cooley-Tukey algorithm in terms of multiplies per output point, they are rarely used in hardware because the structure of these algorithms has other disadvantages [5]. Most important are the lack of an "in-place" signal flow, a requirement for more than one type of elemental DFT block, and computational structures that vary with each stage. The first point has the effect of requiring extra memory in the FFT processor, the second implies multiple basic circuit designs, and the third makes it difficult to pipeline the FFT efficiently and complicates control and addressing circuitry.

Even for the Cooley-Tukey algorithm, there are at least five different high-level hardware architectures: the single processor, pipeline array, parallel array, parallel-pipeline array, and hypercube. We will concentrate on the parallel-pipeline array and the single processor. Figure 11.19 illustrates the high-level architecture of these two implementations. The box marked **R** indicates a processor that performs a single R-point FFT, or "butterfly." If the FFT size $N = R^M$, then there will be M stages in the FFT with N/R butterflies in each stage. This single-butterfly processor might be an entire board of medium- and small-scale integrated circuits, a single custom very large scale integrated (VLSI) circuit, or a microprocessor specialized for digital signal processing.

The important characteristics of an FFT processor are the incremental time between completion of successive FFTs; the throughput in FFTs per second, which is the inverse of the incremental FFT time; the latency; the number of butterfly processors, or *nodes,* required; and

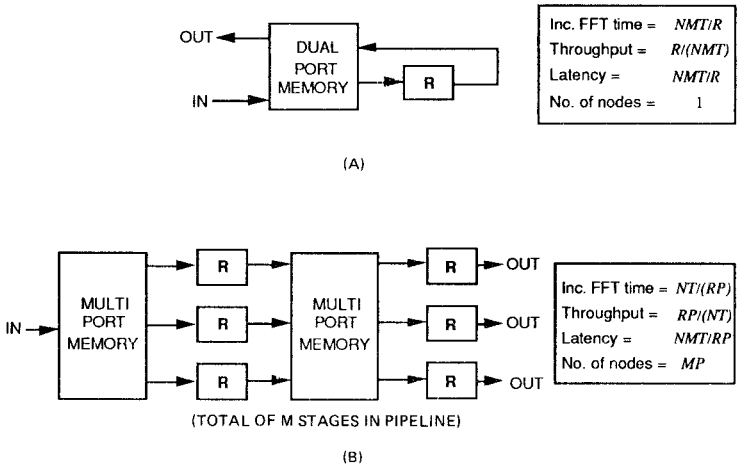

Figure 11.19 Two common FFT architectures and their performance. A box marked **R** denotes a single butterfly computation in radix R. (A) Single processor structure; (B) parallel-pipeline array.

the number of memories required. These characteristics are also shown in Fig. 11.19, with P the number of parallel nodes per pipeline stage and M the number of pipeline stages. T is the time required for a node to compute one butterfly. Generally, pipelining increases throughput but does not affect latency, while using parallel nodes improves both. The conventional pipeline of the previous section corresponds to $P = 1$. In that case, the throughput is increased by a factor M equal to the number of pipeline stages, but the latency is not reduced at all. Increasing the number of nodes per stage, however, both further improves throughput and reduces latency. The disadvantage of multiple nodes per stage is that complex multiport memories are then required to supply all the nodes with inputs and receive their outputs simultaneously.

As with digital filters, FFT times vary widely with the hardware used. The Texas Instruments TMS320C25 can complete a 256-point FFT in 1.408 ms [700], while the United Technologies floating-point IQMAC requires 136.8 μs [726]. A circuit based on an experimental short-block floating-point VLSI radix-4 butterfly circuit was capable of performing the same computation in 81.92 μs [486].

In addition to the nodal computers, all FFT architectures require data memories, coefficient memories, and address generators. The data memories, included in Fig. 11.19, are usually "ping-ponged" and capable of supporting simultaneous read and write operations. If multiple nodes are used per stage, then multiple reads and writes must be accommodated. Coefficient memories are usually read-only memories (ROMs)

which store the $\cos(2\pi nk/N)$ and $\sin(2\pi nk/N)$ values required by the FFT algorithms so that they need not be continuously recomputed. Address generators are special counters that generate the addresses required to access and store both data and coefficients in the special bit-reversed orderings required by the algorithm. These devices offload the simple but high-speed address calculations from the main control processor, and are usually programmable via a few control pins for different DFT sizes. One address generator and coefficient ROM are usually required for each processing node.

An interesting recent development in FFT algorithms is the *split-radix* algorithm, which is an alternative to the Cooley-Tukey method for transform lengths which are powers of 2 [190]. While not as efficient as the Winograd in multiplies per output point, it is more efficient than the Cooley-Tukey algorithm when measured either by multiplies or by total multiplies and additions [596]. This makes it an excellent choice for software or single-node hardware FFT implementations, despite some extra programming complexity. However, it requires more butterflies than the Cooley-Tukey algorithm and its structure does not permit completely efficient pipelining or parallelism. Consequently, it is not well suited to multiple-node parallel or pipeline implementations.

Sizing computational requirements

The first step in developing a processor architecture is to estimate requirements such as throughput, memory size, and latency. This is done by developing a detailed flow graph of the processing and using it along with the radar parameters to "walk through" the processing, estimating the loads at each step. Figure 11.20 gives a simple example of the first level of such an analysis for the Doppler-processor section of a radar comprising a cascade of a three-pulse canceler and a 16-point FFT implemented with the conventional radix-2 algorithm. We assume a *PRF* of 5 kHz with processing of 200 50-m range cells, giving 10 km of total range coverage. Analog pulse compression, perhaps with a *surface acoustic wave* (SAW) device, precedes the analog-to-digital conversion, as does demodulation of the signal to baseband.

The 50-m range resolution implies a 3-MHz signal bandwidth, so the Nyquist sampling rate is also three megasamples per second. Since the receiver is coherent, the samples are complex, *i.e.*, they have I and Q components. The initial PRI buffer holds 1600 8-bit words. This allows for 200 range cells of complex data for each of four pulses. Four pulses of data are stored at a time so that the three-pulse canceler that follows can be working on three rows of data, say numbers 1, 2, and 3, while a new fourth row is collected and stored. When the canceler finishes working through the 200 range bins, it shifts over one row, now op-

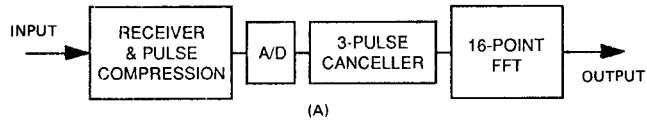

(A)

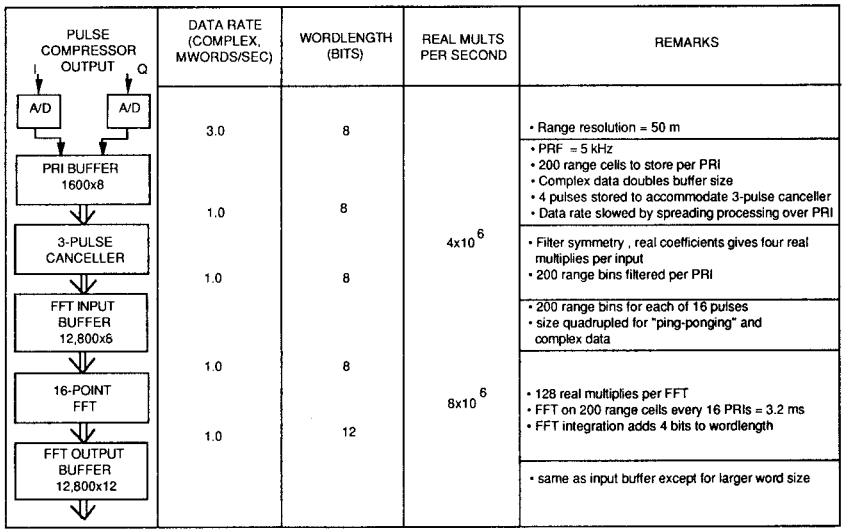

(B)

Figure 11.20 Doppler processor and data rates. (A) Structure of Doppler processor analyzed; (B) rough estimate of Doppler processor data rates, throughput, and word-length requirements.

erating on rows 2, 3, and 4 while row 1 is refilled with new data, and so forth. The data rate is lower coming out of the buffer than going in because the computations can be spread over the entire PRI, even though the data were collected in less than one PRI time.

The three-pulse canceler is a symmetric FIR filter, and therefore needs only two multiplies per output sample. Since the data are complex but the filter coefficients are real, there are only two real multiplies per data-coefficient product. With data arriving at 1.0 megasamples per second, this gives 4 million real multiplies per second. The output goes to an FFT input buffer. Since the FFT size will be 16 points, this buffer must be large enough to accumulate 16 complex samples for each of the 200 range bins, a total of 6400 real words. Furthermore, it must be again doubled in size to 12,800 words so that one-half the memory can be filling with new data while the data in the other half are being processed through the FFT. When all the data in one half have been processed, the roles of the two halves of the buffer are switched: the FFT starts reading the data just placed in the second

half, while the output of the canceler begins refilling the first half. This process, similar to that used in the PRI buffer, is called "ping-ponging." Estimates for the FFT computational rate and the output buffer sizing are outlined in Fig. 11.20 by similar reasoning.

Sizing is an iterative process. The next steps for the MTI section would probably be to expand the FFT structure, perhaps comparing alternatives such as pipelined or single-processor implementations, then to add in missing details such as coefficient memories and control requirements. For a first estimate, however, an analysis like that in Fig. 11.20 is usually reasonably accurate, especially if some design margin is factored in.

Architectural constraints

The designer rarely has full freedom in selecting an architecture. The signal processor is but one part of a larger system, and must conform to overall system constraints. For example, many military signal processors must meet very stringent special requirements for radiation hardness, electromagnetic emissions security, ruggedness, and *built-in-test* (BIT) capability. Radiation hardness requirements, in particular, disqualify certain semiconductor processes from being used, eliminating from consideration some microprocessors that might otherwise be chosen for an application.

Most signal processors are programmable to some degree. The software used to program the device is also frequently constrained. Using military systems as an example again, many require a processor to include a module that implements the military standard (MIL-STD) 1750A low-level computer instruction set. For high-level programming, specific languages such as JOVIAL or Ada are often specified. The lack of a validated Ada compiler can again disqualify some microprocessors from use.

Not all programming of electronic systems is necessarily done in standard assembly or high-level languages, however. So-called *graph* or *block diagram* languages [425] are often used for programming modular signal processors. In these languages, signal-processing algorithms are described by flow graphs in which operations such as summation of two signals or the FFT of a signal are indicated by blocks, and the input signal sources, output signal destinations, and order of operations are indicated by "wiring" the blocks together in the appropriate sequence. Various vendor-specific software tools then "compile" the graph and translate it into real-time commands to route data to specific processor modules and to have those modules execute the appropriate functions.

Graph languages are an attempt to make it easier to implement

signal-processing algorithms efficiently on modular processors. Another approach used in some very highly parallel architectures is to program them in special high-order languages such as OCCAM, which allow explicit specification of processes that can be executed in parallel. Yet another special case arises when the signal processing includes artificial intelligence or expert system concepts. Software for these types of systems is most often written in either LISP or PROLOG.

Military systems are not the only ones that enforce architectural constraints. Many commercial signal processors are modular in construction, using a backplane bus to transfer data and control signals between modules. New modules must therefore conform to the existing bus structure and communication protocols. Examples include the VME and Multibus II standards, which have developed as extensions of buses originally implemented around the popular Motorola 68000 and Intel 80X86 microprocessors, respectively. The others are newer concepts, developed to handle more complex systems and higher data rates.

Signal processors may be subject to other bus constraints as well. Many military processors must provide an interface to the MIL-STD 1553B serial bus. Virtually all processors, military or commercial, require a common RS232 or RS422 serial port as well.

A good example of a more comprehensive set of system constraints is the complete avionics architectural concept known as PAVE PILLAR developed by the U.S. Air Force [527], to which processors designed for the Advanced Tactical Fighter must conform. PAVE PILLAR includes specification of a high-level signal processor architecture like that shown in Fig. 11.21. The key feature of the architecture is the modularity imposed by the requirement that the processor be built up from a small number of relatively generic modules (the "common signal processors" of the figure). Data communication between modules is handled by a high-speed reconfigurable switch, the "data exchange network," which is itself built up from basic modules. Other modules

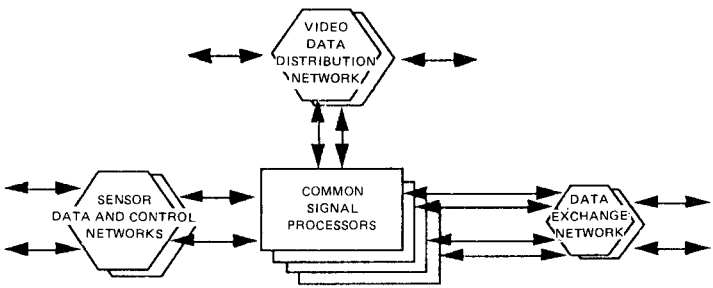

Figure 11.21 The high-level architecture of a PAVE PILLAR signal processor. (*After* [527])

provide the interface to external sensors. The PAVE PILLAR concept specifies a core set of modules including, among others, a 125-MFLOP floating-point processor; a 3 MIPS MIL-STD 1750A CPU used for control and general-purpose computing; a 1-Mword global memory and a 2-Mword nonvolatile memory, both with error detection and correction; interfaces to the MIL-STD 1553B serial bus, a 500-Mbit/s sensor bus; a 24-channel, 25-Mword/s data exchange network; and various utility modules such as timing generators and power supplies. Additional desirable modules for fixed-point arithmetic, sorting, FFTs, and so forth are also identified. The PAVE PILLAR architecture includes a comprehensive treatment of built-in test and diagnosis at the chip, board, and system levels.

11.8 Range Computations for Pulse Doppler Radar

The computation of detection range for a pulse Doppler search radar does not differ substantially from that of the simple pulse radar if the dependence on energy is kept in mind. The pulse radar range equation from Chap. 2 was given as

$$R^4 = \frac{\hat{P}_T G_T L_T A_e L_R L_P L_a L_c L_s \sigma_t}{(4\pi)^2 K T_s B_N (S/N)} \tag{11.8}$$

For a single transmit pulse and approximately a matched filter, the noise bandwidth $B_N \approx 1/\tau'$ where τ' is the pulse width. Since a pulse Doppler system coherently integrates many (N_c) pulses, it is almost sufficient to multiply the numerator of the range equation by N_c if the transfer characteristic of the narrow-band filters following the range gate is such that they optimally integrate N_c pulses, i.e., the narrow-band filter must also be matched to the total transmission time T_d.

The simplest processor to consider is the tapped delay line (Fig. 11.12). In this configuration N_c pulses are added voltagewise (N_c^2 in power), and N_c noise samples are added with random phase (N_c in power). The (S/N) required for a given probability of detection and false alarm probability is thus reduced by N_c after allowance is made for the appropriate number of false alarm opportunities.

In any pulse Doppler system, the false alarm probability must be based on the product of the number of range gates n_g and the number of Doppler filters K per range gate. The number of opportunities for false alarms is not necessarily greater than for a simple pulse radar since the number of independent samples at the output of the filter is proportional to the filter bandwidth b. For a given velocity coverage, the filter bandwidth decreases as the number of Doppler filters in-

creases. Thus, in most cases the number of potential false alarms is independent of the number of Doppler filters.

Another version of the pulse Doppler range equation can be derived from the following relations:

$$d_t = \frac{\bar{P}}{\hat{P}} \tag{11.9}$$

where d_t = transmit duty factor
$\bar{P}$ = average transmit power
$\hat{P}$ = pulse transmit power (average power during pulse)

Also

$$d_t = \frac{\tau' N_c}{T(N_c - 1)} = \frac{N_c}{B_N T(N_c - 1)} \tag{11.10}$$

where T = average interpulse period
N_c = number of coherently integrated pulses

Eliminating the duty factor from Eqs. (11.9) and (11.10),

$$\frac{\hat{P}}{B_N} = \frac{\bar{P}T(N_c - 1)}{N_c} \tag{11.11}$$

A good approximation for the noise bandwidth of the *matched* Doppler filter is

$$b \approx \frac{1}{T_d} = \frac{1}{(N_c - 1)T} \tag{11.12}$$

where T_d = the coherent transmit time of pulse train. Then substituting for $(N_c - 1)T$ in Eq. (11.11) yields

$$\frac{\hat{P}}{B_N} \approx \frac{\bar{P}}{bN_c} \tag{11.13}$$

If Eq. (11.13) is then substituted in the range equation after the numerator has been multiplied by N_c to account for the coherent integration, the alternate pulse Doppler range equation becomes

$$R^4 = \frac{\bar{P}_t G_T L_T A_e L_R L_P L_a L_c L_s \sigma_t}{(4\pi)^2 K T_s b(S/N)} \tag{11.4}$$

It must be emphasized that (S/N) is the per-pulse signal-to-noise ratio in the Doppler filter for the desired probability of detection and false alarm probability.

Deviations from ideal integration

The calculation of the efficiency factor L_s for pulse Doppler must account for some potential added losses:

1. The deviation of the pulse matched filter from the optimum value.
2. The range gate being too narrow, too wide, or not centered on the target return. This loss should not always be directly added to (1) since pulse "stretching" by the pulse matched filter partially compensates for minor errors in the range gating.
3. The Doppler matched-filter shape (or bandwidth) may deviate from the optimum.
4. The target response may straddle more than one Doppler filter or fall in the *notches* between them.
5. There may be a significant Doppler dispersion loss [588] if $2T_d v/\tau' c \geq 1$.
6. Doppler *image noise* may be *folded* onto the desired Doppler spectrum.
7. Phase- and time-delay errors reduce the sensitivity.
8. FM and AM transmitter noise imposed on nearby clutter may exceed receiver noise (see Sec. 14.4).

The characteristics of the individual pulse and the Doppler filters deserve special attention. Analysis of the improvement obtained from coherent integration for various filter shapes has been reported by North [514], George and Zamanakos [263], Galejs [257], and others. For the case of a uniform pulse train of rectangular pulses and a uniform video comb filter with an idealized square passband, it has been shown [263] that

$$\text{Improvement} = (N_c L_s) = 10 \log (0.45\, N_c) \text{ in dB, if } \tau' < \frac{T}{4} \quad (11.15)$$

The assumption here is that the input noise is white, and the rectangular Doppler filters cover the mainlobe of the $(\sin x/x)^2$ energy density spectrum ($\sim$ 90 percent of the energy falls within the filter). The assumed filter bandwidth $b \approx 2/N_c T$ Hz is somewhat wider than the optimum.

By altering the gains of the "teeth" of the comb filter to "match" the amplitudes of the lines of the uniform pulse-train spectrum, an additional improvement of 2.1 dB is obtained. If, in addition, each tooth of the filter is given a $(\sin x/x)^2$ response, the North filter is obtained, the improvement of which is 4.3 dB greater than Eq. (11.15). The improve-

ment in this case $\approx$ 0.8 dB greater than N_c, presumably due to the assumptions of an overly wide bandpass for the single pulse and an idealized integrator.

Galejs [257] has extended this analysis to physically realizable comb filters and to the case in which the pulse-train envelope is in a $|\sin x/x|$ form, which would result from an antenna beam scanning past a target. Using the same general assumptions as George, he obtained the (S/N) power improvements, above $10 \log 0.45 N_c$, for practical filters and rectangular pulse trains. For rectangular pulses the improvement was 3.8, 1.7, and 1.8 dB for the optimum, cascaded delay line, and feedback filters, respectively. The exact values quoted here are for special cases. They should not be used without study of the detailed assumptions in the references, including the discussions on output sampling time.

11.9 Clutter Computations

Perhaps the most difficult part of predicting the performance of a pulse Doppler radar is the calculation of the rejection of extended clutter echoes.* The difficulty arises because the dominant clutter may not be at the target location and may extend over a considerable portion of the ambiguity plane. The differing range dependencies of targets and clutter preclude the use of a single chart of equations. The general pulse Doppler range equation for uniform clutter is derived in this section with some indication of how simplifications can be made. It will be shown that in many cases the right members of the range equation can be factored into the *range in clutter* for a pulse radar and a clutter attenuation CA factor for the pulse Doppler.

The periodic character of the pulse-train spectrum causes Doppler ambiguities at multiples of the repetition frequency. Thus, undesired targets (such as rain, chaff, sea or land clutter) may produce a large response at or near the Doppler frequency of the desired echo, thereby obscuring it. The use of a medium or high pulse repetition frequency to reduce the Doppler ambiguities is common in the design of pulse Doppler radars but aggravates the problem of range ambiguities. With a high PRF, echoes from many different ranges may be received simultaneously so that even though the target might be in a clear region, clutter elsewhere along the antenna beam can cause interference. The peak echo power from clutter at the output of the receiver range gate, neglecting antenna sidelobes, will be

* The majority of this section was prepared by Dr. P. J. Luke, formerly of the Applied Physics Laboratory.

$$\hat{P}_c = \frac{\hat{P} G A_e L}{(4\pi)^2} \Sigma\sigma \int \frac{|f(\theta,\phi)|^4 L_a}{R^4} dV \tag{11.16}$$

where G = antenna gain at beam center
A_e = effective area of the receiving aperture
L = transmitter and receiver loss factors combined
$\Sigma\sigma$ = clutter scattering cross-section density (usually expressed in square meters per cubic meter for volume clutter)
$f(\theta, \phi)$ = antenna amplitude pattern, which is a function of the angular coordinates θ,ϕ measured from the axis of the beam
L_a = attenuation factor due to the transmission medium (a function of range)
R = range to the volume element dV
$dV = R^2\, d\Omega\, dR$
$d\Omega$ = element of solid angle

For volume-extended clutter (e.g., rain, chaff) the integral with respect to the solid angle may be evaluated immediately, giving [563]

$$\int |f(\theta,\phi)|^4\, d\Omega = \frac{\pi\theta_1\phi_1}{8 \ln 2} = 0.57\, \theta_1\phi_1$$

where θ_1 and ϕ_1 are the one-way half-power beamwidths. The echo power from volume-extended clutter is then

$$\hat{P}_c = \frac{\hat{P} G A_e L}{(4\pi)^2} (\Sigma\sigma)\, (0.57\, \theta_1\phi_1) \int \frac{L_a\, dR}{R^2} \tag{11.17}$$

The integral with respect to R is taken over all ranges from which simultaneous or overlapping echoes are received.

Following the range gate, the signal is filtered by the Doppler filter, envelope detected, and compared with a threshold. In order to determine the clutter energy at the detector input, we compute the spectral density of the clutter echo at the input to the filter and from that the clutter energy at the filter output. A similar computation yields the target-echo energy at the detector. The ratio of these two is the signal-to-clutter ratio for the particular range gate and Doppler filter being considered, which are the ones having the most target-echo energy.

Since the clutter return consists of echoes from many small reflectors distributed at random in space and, hence, with random phases, the spectral density for the clutter will be the sum of the spectral densities for the individual returns. The expected value of the resultant spectral density (with respect to both the spatial distribution and the frequency or velocity distribution) integrated over the filter bandwidth yields the mean clutter energy at the detector input.

Constant interpulse period—clutter response

An echo consisting of a uniform train of N pulses with constant amplitude a_i and Doppler shift f_i relative to the filter center frequency has an energy spectral density

$$E_i(f) = \frac{1}{2} a_i^2 \tau_i^2 \left\{ |U_i(f - f_i)|^2 \frac{\sin^2[\pi(f - f_i) NT]}{\sin^2[\pi(f - f_i) T]} + |U_i(f + f_i)|^2 \frac{\sin^2[\pi(f + f_i) NT]}{\sin^2[\pi(f + f_i) T]} \right\} \tag{11.18}$$

where T = the interpulse spacing
τ_i = the pulse width of the echo after range gating (which may truncate the pulse)
$\tau U(f)$ = the single-pulse spectrum (defined in this manner so that $U(f)$ is dimensionless, e.g., for a rectangular pulse $U(f) = \sin \pi f\tau / \pi f\tau$)

After truncation by the range gate the echo from the ith reflector has a single-pulse spectrum $\tau_i U_i(f)$.

The frequencies f_i are distributed over some interval which is usually small relative to the pulse-repetition frequency but may be greater than $1/NT$. Thus, the factor $|U_i(f \pm f_i)|^2/\sin^2 \pi(f \pm f_i)\, T$ does not vary appreciably over this interval and may be given the constant value $U_i(f \pm f_c)^2/\sin^2 \pi(f \pm f_c)\, T$ when averaging $E_i(f)$ with respect to the distribution of f_i. The frequency f_c is an average with respect to the distribution. Noting that the average of the factor $\sin^2 \pi(f \pm f_i)NT$ is $\frac{1}{2}$, the average spectral density is

$$E_{ci}(f) = \frac{1}{2} a_i^2 \tau_i^2 \left\{ \frac{|U_i(f - f_c)|^2}{2 \sin^2 \pi(f - f_c)\, T} + \frac{|U_i(f + f_c)|^2}{2 \sin^2 \pi(f + f_c)\, T} \right.$$

This equation is valid only if $f - f_c > 1/NT$. Since f_i and f_j are independent, this is the spectral density for all the returns.

The total energy in the bandwidth of the filter is

$$E_{ci} = \int_0^{b/2} E_{ci}(f)\, df = \frac{1}{4} a_i^2 \tau_i^2 \int_{f_c - b/2}^{f_c + b/2} \frac{|U_i(f)|^2}{\sin^2 \pi f T}\, df \tag{11.19}$$

where b = the filter bandwidth. Since b is small compared to $1/\tau_i$, $U_i(f)$ is essentially constant throughout the range of integration. Taking $|U_i(f)|^2$ evaluated at f_c outside the integral and evaluating the remaining integral, noting that $a_i^2/2$ is the peak pulse power, and summing over all reflectors, one obtains for the total clutter energy out of the filter

$$E_c = \left[\frac{\hat{P}\,G\,A_e\,L}{(4\pi)^2}\right][(\Sigma\sigma)\,(0.57\,\theta_1\phi_1)]\left[\int\frac{L_a\tau_i^2\,dR}{R^2}\right]\left[\frac{|U(f_c)|^2K}{T}\right] \quad (11.20)$$

where

$$K = \frac{1}{\pi}\left(\frac{\sin\pi bT}{\cos\pi bT - \cos 2\pi f_c\,T}\right)$$

The integral with respect to range is approximately

$$\int\frac{L_a\tau_i^2\,dR}{R^2} \approx \tau^2\frac{c}{2}\left(\tau_g - \frac{\tau}{3}\right)\sum_k\frac{L_a}{R_k^2} = \tau^2\frac{c\tau_e}{2}\sum_k\frac{L_a}{R_k^2}$$

where τ = pulselength, $\tau_e = \tau_g - \tau/3$ if $\tau_g \geq \tau$
τ_g = range-gate length
R_k = range to the kth ambiguous range

If $\tau_g < \tau$, interchange τ_g and τ. Thus, finally one has for the total clutter energy

$$E_c = \frac{\hat{P}\tau\,G\,A_e\,L}{(4\pi)^2}\frac{\tau}{T}(\Sigma\sigma)\left(\frac{c\tau_e}{2}\right)(0.57\,\theta_1\phi_1)\left(\sum_k\frac{L_a}{R_k^2}\right)|U(f_c)^2K \quad (11.21)$$

Target-echo response

The energy spectral density for a target echo consisting of a train of N pulses with amplitude a and Doppler shift f_s relative to the filter center frequency is

$$E_s(f) = \frac{1}{2}a^2\tau^2\left\{|U(f-f_s)|^2\frac{\sin^2\pi\,(f-f_s)\,NT}{\sin^2\pi\,(f-f_s)\,T} + |U(f+f_s)|^2\frac{\sin^2\pi\,(f+f_s)\,NT}{\sin^2\pi\,(f+f_s)\,T}\right\}$$

If the range gate does not match the pulse (so that part of the pulse is eclipsed), τ should be replaced by $\epsilon\tau$ where $0 < \epsilon < 1$. The signal energy out of the Doppler filter is then

$$E_s = \int_0^{b/2} E_s\,(f)\,df = \frac{1}{2}a^2\,\tau^2\,|U(f_s)|^2\int_{f_s-b/2}^{f_s+b/2}\frac{\sin^2\pi fNT}{\sin^2\pi fT}\,df \quad (11.22)$$

The filter bandwidth b is generally much less than the PRF $1/T$, and f_s is less than $b/2$. Otherwise the signal is in another filter, and one

should examine that filter. Therefore, sin (πfT) may be approximated by πfT.

The integral in Eq. (11.22) is then

$$\int_{f_s-b/2}^{f_s+b/2} \frac{\sin^2 \pi fNT}{\sin^2 \pi fT}\, df = \int_{f_s-b/2}^{f_s+b/2} \frac{sin^2\, \pi fNT}{(\pi fT)^2}\, \mathrm{df} = \frac{N}{\pi T} \int_{\pi NT(f_s-b/2)}^{\pi NT(f_s+b/2)} \frac{sin^2 x}{x^2}\, dx = \frac{NY}{T} \tag{11.23}$$

where the function Y represents the fraction of the energy of a single line contained in the filter bandwidth. The signal energy is then

$$E_s = \frac{\hat{P}_\tau\, G\, A_e\, L}{(4\pi)^2} \left(\frac{\tau}{T}\right) \sigma_t\, L_p\, \frac{L_a}{R_t^4} |U(f_s)|^2\, NY$$

where R_t = target range

L_p = pattern loss in case the target is not centered in the beam

With N pulses integrated, the coherent integration on the dwell time is $T_d = NT$.

The ratio of signal energy to clutter energy at the output of the Doppler filter containing the target signal is thus

$$\frac{E_s}{E_c} = \left[\frac{\sigma_t}{(\Sigma\sigma)\,(c\tau_e/2)}\right] \left[\frac{L_p}{0.57\,\theta_1\phi_1}\right] \left[\frac{(L_a/R_t^4)}{\sum_k (L_a'/R_k^2)}\right] \left[\frac{|U(f_s)|^2}{|U(f_c)|^2} \frac{NY}{K}\right] \tag{11.24}$$

or, naming the factors,

$$\frac{E_s}{E_c} = [\text{echo power}][\text{pattern factor}][\text{attenuation}][\text{spectral factor}]$$

For a duty ratio of $\tau/T \leq 0.01$, the single-pulse envelope functions $U(f_s)$ and $U(f_c)$ differ by a small fraction of 1 percent (i.e., both signal and clutter are near the center of the single-pulse spectrum). Hence the ratio $U(f_s)^2$ to $U(f_c)^2$ is essentially unity. The function Y is always < 1 but generally > 0.5.

A number of approximations can be made to make Eq. (11.24) more tractable. A reasonable average value for Y is about two-thirds, the gate length $\tau_g \approx \tau$, the atmospheric attenuation term L_a can be neglected, and $L_p \approx 0.57$. Then Eq. (11.24) simplifies to

$$\frac{E_s}{E_c} = \left[\frac{\sigma_t}{(\Sigma\sigma)\,(c\tau/2)\,\theta_1\phi_1}\right] \left[\frac{1}{R_t^2 \sum_k (R_t/R_k)^2}\right] \left[\frac{N}{K}\right] \tag{11.25}$$

Clutter echoes only at the target

If the clutter is small in extent compared to the interpulse period (less than $cT/2$) and located only at the target, then the energy ratio is

$$\frac{E_s}{E_c} = \left[\frac{\sigma_t}{(\Sigma\sigma)\,(c\tau/2)\,\theta_1\phi_1}\right]\left[\frac{1}{R_t^2}\right]\left[\frac{N}{\frac{1}{\pi}\left(\frac{\sin \pi bT}{\cos \pi bT - \cos 2\pi f_c T}\right)}\right] \tag{11.26}$$

It should be noted that the first two brackets of Eq. (11.26) are the same as the equation for the simple pulse radar in volume clutter. Thus, the terms in the final bracket constitute the clutter attenuation or improvement factor for a train of N pulses using a close approximation to a matched-filter receiver. The detection-range equation for clutter at the target range is then obtained by rewriting Eq. (11.26)

$$R_t^2 = \left[\frac{\sigma_t}{(\Sigma\sigma)\,(c\tau/2)\,\theta_1\phi_1\,(S/C)}\right]\left[\frac{N}{\frac{1}{\pi}\left(\frac{\sin \pi bT}{\cos \pi bT - \cos 2\pi f_c T}\right)}\right] \tag{11.27}$$

Numerical values for the second bracket were given in Table 11.1.

Extended-clutter echoes

For clutter that extends quite close to the radar (uniform rain, etc.), the sum in the denominator of the third bracket of Eq. (11.25) is dominated by the term for the nearest ambiguous range R_1 and the signal-to-clutter ratio is then

$$\frac{E_s}{E_c} = \left[\frac{\sigma_t}{\Sigma\sigma(c\tau/2)\,\theta_1\phi_1}\right]\left[\frac{R_1^2}{R_t^4}\right][L_a(R_t - R_1)]\left[\frac{N}{K}\right] \tag{11.28}$$

where $L_a\,(R_t - R_1)$ = the attenuation between the target and the first clutter region. The significance of this equation is that for volume clutter that is close to the radar at range R_1, the signal-to-clutter ratio varies inversely as R_t^4 rather than as R_t^2 as in unambiguous pulse radars. The first ambiguous clutter range can be approximated by using the largest integer N_1 which satisfies

$$R_1 \approx \left[R_t - N_1\left(\frac{cT}{2}\right)\right] > 0 \qquad \text{if} \qquad \frac{c\tau}{2} \ll \frac{cT}{2} \tag{11.29}$$

The approximation breaks down if R_1 is in the near zone of the antenna or if an STC circuit is used to reduce the near-in clutter.

For the intermediate case in which the clutter extends at least several

interpulse periods but not to the radar (the target may or may not be within the clutter), the sum in Eq. (11.25) may be approximated by

$$\sum_k R_k^{-2} \approx \frac{(N_2 - N_1 + 1)}{[R_t + (2N_1 - 1)\,cT/4]\,[R_t + (2N_2 - 1)\,cT/4]} \tag{11.30}$$

where $R_t + N_1\,cT/2$ = smallest ambiguous clutter range
$R_t + N_2\,cT/2$ = largest ambiguous clutter range
$N_2 - N_1 + 1$ = number of ambiguous ranges from which clutter returns are simultaneously received

Both N_1 and N_2 may be negative as long as $R_t + (2N_1 - 1)\,cT/4$ is positive. If this term is near zero range, the approximation to obtain Eq. (11.30) is poor, and the system is most likely dominated by the first clutter echoes. In this case it will usually suffice to use Eq. (11.29).

Optimum value of filter bandwidth

In order to determine the optimum bandwidth for maximizing S/C, let $b = X/NT = X/T_d$ for large N, where X is a constant factor. The last factor in Eq. (11.24) becomes

$$\frac{NY}{\frac{1}{\pi}\left[\frac{\sin(\pi X/N)}{\cos(\pi X/N) - \cos 2\pi f_c T}\right]} \tag{11.31}$$

Referring to Eq. (11.23), it is easily shown that the function Y is a monotonically increasing function of X which approaches the value 1 for $X = N$. For X decreasing, Y becomes asymptotic to X. Examination of the denominator of the foregoing expression shows it to be also a monotonic increasing function of X which, however, does not approach a constant value for large X but in fact increases indefinitely as X/N approaches $2f_c\,T$. At this point the approximations used to obtain Eq. (11.20) are no longer valid. For small X the denominator is proportional to X/N.

The value of the fraction is thus proportional to N^2 for small X and decreases as X increases. This suggests that the best bandwidth to use is the narrowest obtainable. This is true when clutter is the only interference to consider. In the presence of broadband noise, however, reduction of the bandwidth much below the reciprocal of the signal duration T_d seriously degrades the signal-to-noise ratio. Also, if the target fluctuates rapidly or accelerates, little improvement in signal-to-noise ratio will be obtained by reducing the bandwidth below the spectral width of the fluctuations.

The *best* bandwidth is then obtained by taking X to be of the order of 1, making the signal-to-clutter ratio proportional to N^2. The constant of proportionality depends on f_c. If b is replaced by $1/NT$ in the last bracket of Eqs. (11.27) through (11.31), this term can be written

$$\left[\frac{N}{\frac{1}{\pi}\left(\frac{\sin \pi bT}{\cos \pi bT - \cos 2\pi f_c T}\right)}\right] = \left[\frac{N}{\frac{1}{\pi}\left(\frac{\sin(\pi/N)}{\cos(\pi/N - \cos 2\pi f_c T}\right)}\right] \tag{11.32}$$

If, in addition, N is at least 30, $\sin(\pi/N) \approx \pi/N$, $\cos \pi/N \approx 1$, and the bracketed term becomes

$$N^2[1 - \cos 2\pi f_c T] \approx \text{clutter attenuation} \tag{11.33}$$

As expected, the clutter attenuation term is maximized at $f_c T = \frac{1}{2}$. Then, for $bT = 1/N$ and N large, the maximum clutter attenuation for a Doppler separation of $f_c T \approx \frac{1}{2}$ (averaged over Dopplers in that region) can be approximated by

$$\text{CA}_{\max} \approx 2N^2 \qquad \text{near the optimum Doppler separation} \tag{11.34}$$

Alternately, for an average over all Doppler velocities (except for the ambiguous regions) the improvement factor I is N^2. This analysis does not include effects of weighting described earlier and in Sec. 14.4.

11.10 Truncated Pulse Trains

The previous section on clutter computations emphasized that the *close-in* clutter at range R_0 is often the limiting factor in the performance of pulse Doppler systems in range-extended-clutter environments. For most detection criteria, the overall improvement factor I contains a term of the form R_0^2/R_t^4 for uniform volume clutter extended in range with a high PRF transmission. Thus, the overall improvement may be negligible for targets at a range of many interpulse periods. The type of clutter that is of most concern in this description is assumed to be extended in range and separated from the target velocity but confined in Doppler extent. Rihaczek [601, 603] and others have shown that a uniformly spaced pulse train is desirable since most of the energy under the ambiguity surface is concentrated in finite locations on the axes. The following discussion is based on uniform interpulse spacing of uniform amplitude pulses.

Single-burst pulse train

It can be seen from Eq. (11.30) that the summation of the clutter echoes from many ranges provides a limit to the signal-to-clutter ratio im-

provement in partially extended clutter. Ares [16] has shown that for a given target-to-clutter velocity ratio and interpulse period T there exists for each target range R_t a value of N that maximizes the signal-to-clutter ratio. This *optimization* exists only for clutter that extends for all the $2N - 1$ ridges of the ambiguity diagram. The explanation for this optimization is that for small interpulse periods, the close-in clutter at range R_0 is competing with target signals from distant ranges, and it is the echoes from the later transmitted pulses that constitute the greatest portion of the clutter entering the receiver. The optimum number of pulses found by Ares is

$$N \approx \frac{1}{\sqrt{3}} \left(\frac{R_t}{cT/2} \right) \tag{11.35}$$

and the optimum clutter attenuation is $\mathrm{CA}_{\mathrm{opt}} \approx 2/3N$, the improvement factor then being

$$I_{\mathrm{opt}} \approx \frac{2}{3} N = \frac{2R_t}{3\sqrt{3}(cT/2)} \tag{11.36}$$

It can be seen that the improvement factor increases with target range. The optimum Doppler velocity occurs at approximately $1/2T$, as expected. If the target range and Doppler frequency are approximately known, as in an acquisition or tracking radar, the *optimum* number of pulses and their spacing can be chosen. The target-detection range for uniform range extended clutter can then be written from Eq. (2.30).

$$R_{\mathrm{opt}} = \frac{2L_c L_s' \sigma_t}{3\sqrt{3}(\pi/4)\theta_1 \phi_1 (c\tau'/2)(cT/2)(S/C)\Sigma\sigma} \tag{11.37}$$

It can be noted that the required (S/C) is only first-order dependent on target range and that both short pulse lengths and small interpulse periods are desired. Since a short interpulse period can only result from optimization with respect to a high Doppler frequency, the interpulse period term $cT/2$ in the denominator shows only the desirability of having a large velocity separation between the targets and the clutter.

If the interpulse period is not fixed by other considerations, a double optimization involving the period and the number of pulses can be performed. An example is given in Table 11.5. For a given range R_t (in microseconds) and target Doppler frequency f_d, the optimum number of pulses is shown. Also shown in the table is the length of the burst $T_d \approx 2R_t/3c$ and the Doppler resolution b in kHz.

The improvement factor for these same cases is shown in Table 11.6. The improvement factor is in decibels above the signal-to-clutter ratio

TABLE 11.5 Optimum Number of Uniformly Spaced Pulses for Extended Clutter

Target range R_t, μs	Dwell time T_d, μs	Doppler resolution b, kHz	N_{opt} for Doppler frequency offset, kHz										
			4	5	8	10	12	15	20	25	30	35	40
400	231	4.33	2	2	4	5	6	7	9	12	14	16	18
500	289	3.46	2	3	5	6	7	9	12	14	17	20	23
600	346	2.89	3	4	6	7	8	10	14	17	21	24	28
700	404	2.48	3	4	7	8	10	12	16	20	24	28	32
800	462	2.17	4	5	7	9	11	14	18	23	28	32	37
900	517	1.94	4	5	8	10	12	16	21	26	31	36	42
1000	577	1.73	5	6	9	12	14	17	23	29	35	40	46
1100	635	1.58	5	6	10	13	15	19	25	32	38	44	51
1200	693	1.44	6	7	11	14	17	21	28	35	42	49	55
1300	751	1.33	6	8	12	15	18	23	30	38	45	53	60
1400	808	1.24	6	8	13	16	19	24	32	40	49	57	65
1600	923	1.08	7	9	15	18	22	28	37	46	55	65	74

that would result from a single pulse of the train, and it applies only to an extended-clutter situation. The values shown are slightly better than would be indicated by Eq. (11.36) for certain numbers of pulses (see also [397]).

Ares also considered receiver amplitude weighting of the truncated pulse train and showed that there was little additional improvement. The explanation for this is that the ambiguous clutter returns at other than the target range do not receive the symmetrical weighting that is necessary to reduce the Doppler sidelobes. Fig. 11.22 gives examples

TABLE 11.6 Optimum Improvement Factor, I,dB, for Uniformly Spaced Pulses and Extended Clutter

Target range R_t, μs	Doppler frequency offset, kHz										
	4	5	8	10	12	15	20	25	30	35	40
400	1.3	1.3	4.3	5.2	6.0	6.7	7.8	9.0	9.7	10.3	10.8
500	1.3	3.0	5.2	6.0	6.7	7.8	9.0	9.7	10.5	11.3	11.9
600	3.0	3.0	6.0	6.7	7.3	8.2	9.7	10.5	11.5	12.0	12.7
700	3.0	4.3	6.0	7.3	8.2	9.0	10.3	11.3	12.0	12.7	13.3
800	4.3	5.2	6.7	7.8	8.7	9.7	10.8	11.9	12.7	13.3	13.9
900	4.3	5.2	7.3	8.2	9.0	10.0	11.5	12.4	13.2	13.8	14.4
1000	5.2	6.0	7.8	9.0	9.7	10.5	11.9	12.9	13.7	14.3	14.9
1100	5.2	6.0	8.2	9.4	10.0	11.0	12.2	13.3	14.0	14.7	15.3
1200	6.0	6.7	8.7	9.7	10.5	11.5	12.7	13.7	14.5	15.1	15.6
1300	6.0	7.3	9.0	10.0	10.8	11.9	13.0	14.0	14.8	15.5	16.0
1400	6.0	7.3	9.4	10.3	11.0	12.0	13.3	14.2	15.1	15.8	16.4
1600	6.7	7.8	10.0	10.8	11.7	12.7	13.9	14.9	15.6	16.4	16.9

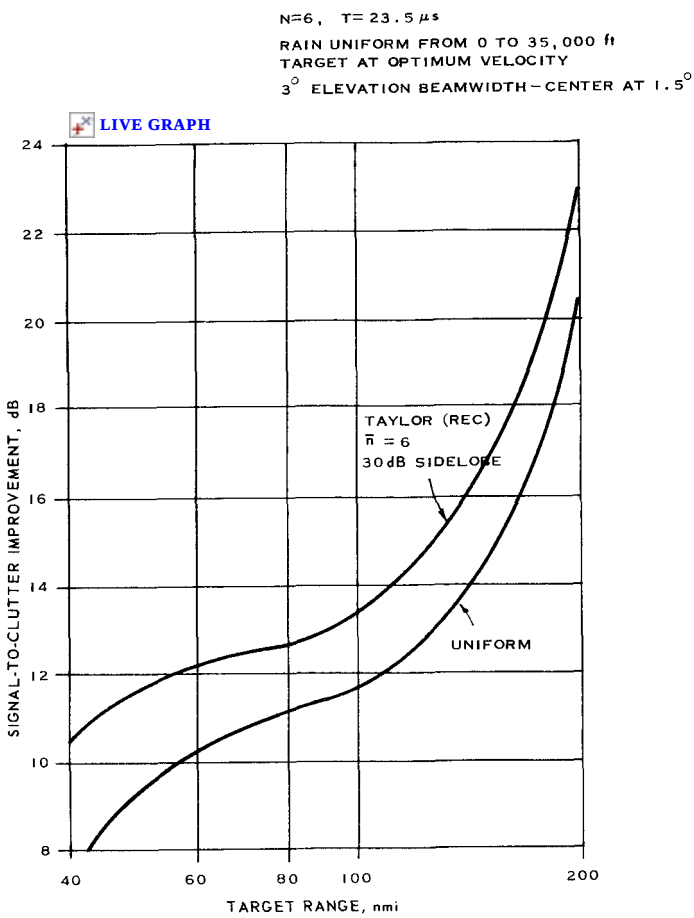

Figure 11.22 Signal-to-clutter improvement versus target range for 16-pulse train and uniform rain. (*From Ares [16]*)

[16] of the improvement obtained with a constant amplitude and a *Taylor*-tapered train of 16 pulses for various target ranges. It is drawn for the case of uniform rain clutter that has a narrow spectrum but is extended in range until the radar antenna beam reaches a 35,000-ft altitude. The improvement increases slowly from 40 to 100 nmi, and then, as the beam extends above the rain, the improvement increases more rapidly. The additional improvement resulting from tapering the received waveform is less than 3 dB at the optimum velocity and almost trivial at other velocities, even with a 40-dB taper. Thus, significant improvement over the uniform case can occur only with complex weighting of the transmitted waveform as well as of the receiver waveform as discussed in Sec. 11.4.

Geometric or burst programming

A pulse Doppler radar operating at high PRF will have blind ranges and close-in clutter problems if the transmit pulse train is not turned off immediately prior to and during the target-echo receive period.* By use of such a turn-off procedure, reduction of close-in clutter echoes can be achieved but at the expense of reducing the total number of pulses on the target during the coherent integration time. A *burst repetition frequency* (BRF) is thus created that is a function of target range and the time allowed for nearby clutter to diminish to a tolerable level. This frequency is nominally equal to $1/(2T_t - T_{cd})$ where T_t is the target echo time and T_{cd} is the *clutter decay time.*

In the case of surface radars, it is often necessary to impose the requirement for a clutter decay time to prevent large clutter returns from regions much closer than the target range from entering the range gate. These returns may be from either the mainlobe or sidelobes of the antenna. For uniform clutter, increasing clutter decay time must be compromised with respect to the number of pulses transmitted. The functional relationship between target range, clutter decay, and the BRF is shown in Fig. 11.23. Here, the maximum percentage of pulses is taken to occur when transmit on and off times are equal; i.e., the clutter decay time is zero.

The adaptive control of the BRF in response to changes in target range and the range extent of the nearby clutter is termed *geometric programming.* Some experimental effects of using geometric programming are shown in the range profiles of Fig. 11.24. The equipment used was a high-PRF (150-kHz) digital implementation of a pulse Doppler radar. In all plots, the zero Doppler channel is displayed (normalized to the largest signal) to illustrate the land-clutter response. In Fig. 11.24A no geometric programming was used. This mode maintains maximum energy on the target (a water tower in this case) but suffers from ambiguous clutter folding onto the target range. Figure 11.24B shows the effect of geometric programming but without any clutter decay time, again allowing nearby clutter to fold onto the target region. In Fig. 11.24C local clutter has been removed by keeping the receiver off for an additional 12.8-μs interval after each burst. Since the system has a constant PRF, range ambiguities still occur beyond the target. In Fig. 11.24D a single-pulse transmission is shown for comparison. With this nonambiguous waveform, the return energy from the target is relatively low (no integration) and cannot yield any Doppler resolution.

The modulation of the transmit waveform with burst timing creates

* Material for this section courtesy of A. Chwastyk.

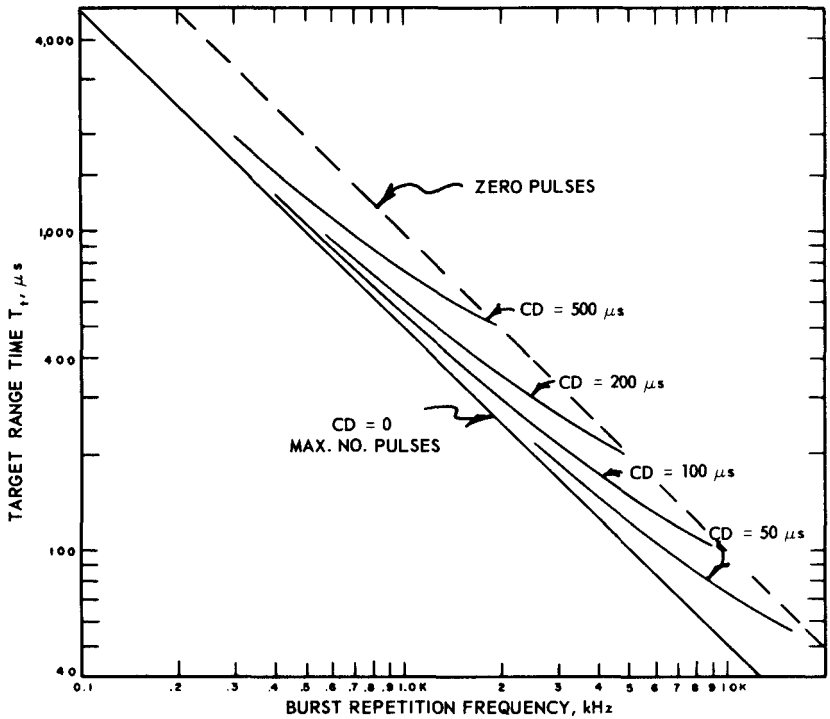

Figure 11.23 Target range delay versus burst repetition frequency for various clutter decay times.

spectral components at the burst repetition frequency and its harmonics. The main Doppler lobe width (the velocity resolution) remains essentially unchanged, but a pair of additional spectral lines due to the burst modulation are less than 4 dB down from the mainlobe. The spectral lines can affect both target parameter estimation and the clutter performance of the system. The worst case for clutter rejection occurs when the clutter Doppler frequency is separated from the target Doppler frequency by the burst repetition frequency. In this case, the clutter residue will often integrate from burst to burst, leaving a substantial residue at the end of the dwell time. Increased coherent integration time will not improve this condition.

11.11 Summary

This chapter showed the evolution of pulse Doppler radar from the original analog to the current digital implementations. There are numerous current variations (the MTD is a widely used variant and is described in Sec. 14.1). Constant PRF bursts generally yield better

Figure 11.24 Effect of geometric programming on land clutter echoes. (A) 3740 pulses, 150 kHz—no programming; (B) 1550 pulses, geometric programming—no clutter decay; (C) 1130 pulses, geometric programming—12.8 μs clutter decay; (D) single 0.15 μs pulse. (*Courtesy of A. Chwastyk*)

clutter rejection, especially in the range-ambiguous regions and are generally preferred to using staggered PRF even though there are blind speeds. Bursts with different PRFs and different carrier frequencies are used to eliminate the blind speeds. With 3 or more PRFs in a beam, m-out-of-n logic is often used for declaring a valid target. Multiple bursts with each on different carriers are also used to reduce losses due to fluctuating targets.

There are various "adaptive" techniques that are used to eliminate clutter in one or more Doppler filters. In some manner the distributed clutter in certain Doppler filters is averaged over range and eliminated. One technique is to perform the Fourier transform on a train of pulses, but store the I-Q inputs in memory. The Doppler filters with high clutter are then determined. The inverse transform (complex) is then deter-

mined on these filters *alone* and the result is subtracted from the stored inputs. The *new* inputs are then reprocessed in the pulse Doppler processor, and the result should have better overall signal-to-clutter ratios.

There can also be a phase code from pulse-to-pulse within a burst. This will allow determining in which range ambiguity the target exists. This is accomplished by parallel processors that decode *assuming* that the target is in the first, second, third ambiguity, etc. Another implementation is applicable where it is known that undesired birds, vehicles, etc. can exist only within the first Doppler ambiguity (their Doppler is less than the PRF), and their range is less than the first ambiguous range. Polarization diversity is also being used for better target discrimination.

There is a steady trend toward using sophisticated software algorithms following pulse Doppler outputs to sort out the uncertainties in range and Doppler, especially in medium-PRF systems. In new systems, especially in airborne multimode radars, the software costs in a total development program exceed the hardware costs.

12

Phase-Coding Techniques

Marvin N. Cohen

Fred E. Nathanson

12.1 Principles of Phase Coding

The next two chapters elaborate on the two primary methods of obtaining range resolution by means of pulse compression. This chapter expands on phase coding of a single-frequency carrier, while Chap. 13 emphasizes pulse coding by shifting the carrier frequency during the waveform. Since the compressed pulse is generally the output of a matched filter, the properties of the output waveforms (in the absence of a Doppler shift) can be discussed in terms of the autocorrelation function of the transmit signal. When there is a Doppler shift, the complete ambiguity function must be discussed. The various forms of phase coding (or phase modulation) provide an excellent basis for general studies of signal processing and can provide for an intuitive grasp of the significance of the ambiguity diagram.

While many of the concepts in this chapter are also applicable to amplitude coding, the emphasis is on the transmission of a constant-amplitude sinusoidal carrier that is divided into N equal segments, each of duration τ. The majority of the material deals with binary phase (biphase) coding, for which the phase of the sine wave in each segment

is set at either 0 or 180° from an arbitrary reference. This is expanded in Sec. 12.5 to include polyphase waveforms, in which each segment can have any one of M possible phases.

Phase coding can be further divided into two general classes depending on the duty cycle of the transmit waveform. The continuous code has wide application in communication systems to convey messages and in continuous wave (CW) radars to provide time (range) resolution. A single pulse whose carrier is phase coded is often used in pulse radar systems to increase range resolution and accuracy when energy requirements dictate a pulse length substantially in excess of the desired resolution. Coded pulses (or coded words) are also used for clutter or interference rejection. Generally, phase coding is utilized as an intrapulse technique, where the coding is overlaid on the carrier during a transmit pulse (or transmit cycle, for CW radars). However, interpulse techniques, such as transmitting code pairs on successive pulses and integrating over several pulses while changing the code on each pulse, are also sometimes utilized.

Consider a carrier divided in time into N segments, each of which is coded either plus or minus as shown in Fig. 12.1. This is called a binary-coded waveform. A plus corresponds to the nominal carrier phase, and a minus corresponds to a 180° phase shift. The amplitude of the kth segment of the waveform is denoted by a_k. Each segment is assumed to have unit amplitude and one of two phases. The effect of the carrier frequency is neglected until the complete ambiguity function is discussed.

In accordance with this notation, the temporal aperiodic autocorrelation function of this waveform can be conveniently written in discrete form

$$\phi(m) = \sum_{k=1}^{N} a_k a_{k+m} \tag{12.1}$$

where the integer index m steps over the domain $-(N-1) \leq m \leq (N-1)$, and we define $a_j = 0$ for all $j < 0$ and for all $j > N+1$. Each

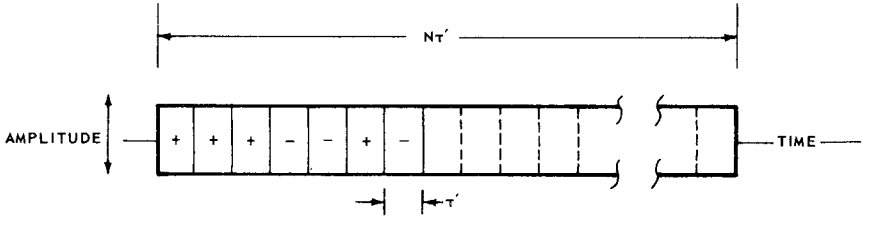

Figure 12.1 Representation of binary phase coding.

step corresponds to a shift in a_{k+m} of one segment duration τ. By describing the autocorrelation function only for discrete steps of τ, the determination of its value for various codes will result in integer values approximating the triangular waveforms that result from an exact autocorrelation. The discrete procedure simplifies the calculation and drawing of the autocorrelation function on the time axis. The loss in accuracy is slight since the response of the system is theoretically linear except for the relatively minor nonlinearities that may be present in the hardware/software implementation of the matched filter.

The autocorrelation function is always a maximum at $t = 0$ and is equal to N. The values of the autocorrelation function away from the origin (that is, the range sidelobes of the waveform, which occur at $\tau \leq t \leq (N-1)\tau$ and $(-N+1)\tau \leq t \leq -\tau$) on the time axis can be computed by numerous techniques, but can easily be visualized by setting up the following tables where, illustratively, the code consists of the first seven segments of Fig. 12.1. For a one-segment offset:

$$
\begin{array}{rl}
 & + \; + \; + \; - \; - \; + \; - \\
 & \quad + \; + \; + \; - \; - \; + \; - \\
\hline
x_1 = & \quad 1 \;\; 1 \;\; -1 \;\; 1 \;\; -1 \;\; -1
\end{array}
= 0, \text{ the first sidelobe}
$$

The logic used in the foregoing example assumes that the occurrence of two pluses or two minuses (a match) gives unity and a plus and a minus equal -1. Thus, in this case, the value of the autocorrelation function at a one-segment offset is zero. Similarly, a two-segment offset would yield

$$
\begin{array}{rl}
 & + \; + \; + \; - \; - \; + \; - \\
 & \quad + \; + \; + \; - \; - \; + \; - \\
\hline
x_2 = & \quad 1 \;\; -1 \;\; -1 \;\; -1 \;\; 1
\end{array}
= -1, \text{ the second sidelobe}
$$

These tables correspond to the computations performed in the tapped delay line given as Fig. 12.2. The incoming signal is clocked through the delay line at a rate of one chip per τ, the multiplication of each chip with its corresponding filter weight is computed, and the sum of these results is computed and output. The entire compression of one occurrence of the code through the filter is given at the bottom of the figure. This corresponds to the compression of a single target through the system. Notice in Fig. 12.2 that the first tap of the filter is the last bit of the code, the second tap is the next-to-last code bit, etc. That is, the process of matched filtering real-valued signals requires that the filter be the time reversal of the signal. For complex signals, the matched filter is the time reversal of the complex conjugate of the signal.

Since such systems are essentially linear, the characteristics of the

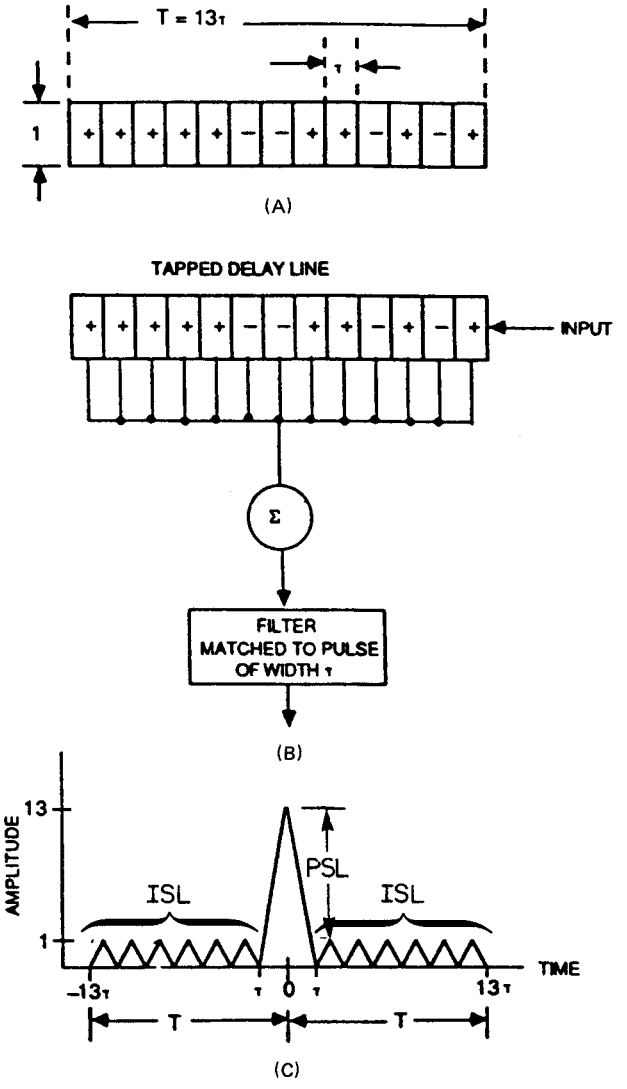

Figure 12.2 Binary phase-coded pulse compression.

compression for a single reflector can be utilized to predict the compression characteristics of the system when many reflectors are present. In particular, when various reflectors are in the scene, the output of the compression system will simply be a superposition of the outputs of the system in response to each of the reflectors.

The characteristics of such systems considered most important for the analysis of performance within the context of a radar system include

the *peak sidelobe level* (PSL), *integrated sidelobe level* (ISL) and *loss in processing gain* (LPG). For an N-bit code

$$\text{PSL} = 10 \log [\text{Max}(x_i^2)/x_0^2]$$

$$\text{ISL} = 10 \log \left[\sum_{i=0} x_1^2/x_0^2 \right]$$

and

$$LPG = 10 \log (x_0^2/N^2)$$

where x_i = all the output-range sidelobes (e.g. all the amplitudes other than that corresponding to $t = 0$ in Fig. 12.2)

x_0 = amplitude of the peak of the compressed pulse (e.g., the response in Fig. 12.2 at $t = 0$)

As suggested in the figure, PSL is a measure of the largest sidelobe as compared with the peak of the compression, ISL is a measure of the total power in the sidelobes as compared with the peak of the compression, and LPG, appropriate when there is an intentional mismatch due to sidelobe suppression weighting (see Sec. 12.3) or due to hardware or Doppler mismatches between the transmitted code and received signal, is a measure of the loss in signal-to-noise ratio in the compression peak as compared with a matched-filter implementation.

12.2 The Barker, MPS, and Other Useful Biphase Codes

In multiple-target environments, it may be significant that the distribution of the time sidelobes of binary phase-coded words is different from that of linear FM pulse compression (Chap. 13). The time sidelobes of linear FM are maximum immediately adjacent to the mainlobe and decrease with distance from the main peak unless some unusual form of tapering is used. This is not generally true for phase codes. Depending on the class of phase code considered, the sidelobes may be fairly uniform, or they may actually exhibit a tendency to be relatively low near the mainlobe. In addition, as seen in Sec. 12.4, mismatched filtering may be applied to sculpt the sidelobes in almost any desired way.

The general assumption to be made in this section, unless otherwise stated, is that the pulse lengths are short enough so that the radial velocity of the target does not cause a significant phase change during the length of the pulse. This limit can be expressed by

$$Tf_d = \frac{2vT}{\lambda} \ll \frac{1}{4} \tag{12.2}$$

or

$$\nu T \ll \frac{\lambda}{8}$$

where λ = transmit wavelength
ν = target radial velocity
$T = N\tau$ = the pulse length

Violation of this inequality necessitates either a bank of Doppler matched filters or causes a loss in (S/N) or (S/C).

It is no coincidence that the example given in Fig. 12.2 exhibited sidelobes of magnitude 1 and 0 only. This was one example of a Barker code [33]. Barker codes are precisely those binary phase codes that have autocorrelation sidelobes only of magnitudes 1 and 0. As such, the Barker codes are the biphase codes with minimum possible peak sidelobe levels. All the known Barker codes, along with their autocorrelation PSL and ISL values, are given in Table 12.1. It has been shown that there are no other such codes of odd length and that there are no other such codes of even length less than 6084 [717, 718]. It is unlikely that any others exist at all, but despite excellent analyses of the problem as in [254], this has not been proven.

These codes are only perfect in the time domain (unknown range, zero Doppler shift). As shown by Key et al. (see [246, p. 108]), the output degrades rapidly in the presence of a Doppler shift. Figure 12.3 provides an ambiguity diagram of a 13-bit Barker code of duration T, where range is given in range bins and Doppler in hertz. Although the code response achieves a Doppler null at $1/T$, significant range sidelobes appear at higher Dopplers, and these can lead to false (ambiguous) returns even if a bank of matched filters is used for all possible Dopplers. That is, interference and clutter return from ranges and velocities other than the target can fold into the target cell and obscure the target return signal. On the other hand, with careful postprocessing, these

TABLE 12.1 The Known Barker Codes

Length of code	Code elements	PSL, db	ISL, dB
1	+		
2	+ −, + +	−6.0	−3.0
3	+ + −	−9.5	−6.5
4	+ + − +, + + + −	−12.0	−6.0
5	+ + + − +	−14.0	−8.0
7	+ + + − − + −	−16.9	−9.1
11	+ + + − − − + − − + −	−20.8	−10.8
13	+ + + + + − − + + − + − +	−22.3	−11.5

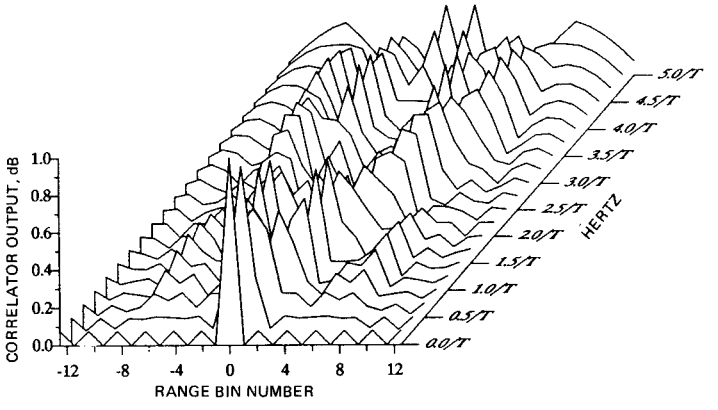

Figure 12.3 13-bit Barker ambiguity surface. (*Courtesy of J. M. Baden*)

false returns can often be sorted out to provide a clear, unambiguous range Doppler map.

The limitation of a maximum length of 13 segments is a serious one, since it does not allow complete decoupling of average power from resolution, a principal aim of pulse compression systems.

The search for longer binary sequences with good sidelobe properties has taken many forms. One useful such effort has been the compilation of the *minimum peak sidelobe* (MPS) codes of lengths 14 through 48 [130]. The MPS codes are those binary sequences that attain the lowest PSL for a given length. The Barker codes are therefore MPS codes. In addition, for example, for length 14, the best peak sidelobe that can be achieved by the autocorrelation of biphase codes is 2, and for length 32, the best peak sidelobe that can be achieved is 3. Table 12.2 [130] summarizes the MPS codes of lengths 14 through 48. The first column of the table is code length and the third gives the minimum autocorrelation peak sidelobe that can be achieved. The second column gives the number of such distinct codes, where code reverses (reversing the order of the bits) and code inverses (inverting each bit) are not counted as distinct. Even though two codes may share the same PSL, they may still exhibit different ISLs. The best ISL among the MPS codes of each length is given in the fourth column, and a single example of such an MPS code is given in notation in the fifth column. Note that this table is not just a compilation of "relatively good" codes for the given lengths, but that these codes are guaranteed to be the best (in terms of PSL) for each given length, since the technique utilized is equivalent to an exhaustive search of all possible sequences of that length.

Other approaches to finding binary sequences with good sidelobes

TABLE 12.2 The Minimum Peak Sidelobe Biphase Codes Through Length 48

Length	Number	PSL	ISL, dB	Sample code (octal)
7	1	1	−9.12	047
8	16	2	−6.02	227
9	20	2	−5.28	327
10	10	2	−5.85	0547
11	1	1	−10.83	1107
12	32	2	−8.57	4657
13	1	1	−11.49	12637
14	18	2	−7.12	12203
15	26	2	−6.89	14053
16	20	2	−6.60	064167
17	8	2	−6.55	073513
18	4	2	−8.12	310365
19	2	2	−6.88	1335617
20	6	2	−7.21	1214033
21	6	2	−8.12	5535603
22	756	3	−7.93	03466537
23	1021	3	−7.50	16176511
24	1716	3	−9.03	31127743
25	2	2	−8.51	111240347
26	484	3	−8.76	216005331
27	774	3	−9.93	226735607
28	4	2	−8.94	1074210455
29	561	3	−8.31	2622500347
30	172	3	−8.82	4305222017
31	502	3	−8.56	05222306017
32	844	3	−8.52	00171325314
33	278	3	−9.30	31452454177
34	102	3	−9.49	146377415125
35	222	3	−8.79	000745525463
36	322	3	−8.38	146122404076
37	110	3	−8.44	0256411667636
38	34	3	−9.19	0007415125146
39	60	3	−8.06	1146502767474
40	114	3	−8.70	02104367035132
41	30	3	−8.75	03435224401544
42	8	3	−9.41	04210756072264
43	24	3	−8.29	000266253147034
44	30	3	−7.98	017731662625327
45	8	3	−8.18	052741461555766
46	2	3	−8.12	0074031736662526
47	2	3	−8.53	0151517641214610
48	8	3	−7.87	0526554171447763

have been undertaken [173, 396, 576]. Delong [173] has discovered a number of these. By means of an extensive computer search, he has found binary codes of length 31, 45, 85, and 99 with peak sidelobe amplitudes of 3, 4, 7, and 7, respectively. More recently, Kerdock [396]

has built a dedicated computer and has successfully applied it to the search for good codes. In neither case ([173] nor [396]) has any attempt been made to ascertain that the discovered codes are MPS, nor to compile a list of all codes of a given length with a given PSL, but long codes with excellent PSL values have been discovered this way. The characteristics of Legendre sequences have been exploited to generate a long list of good codes for prime lengths [576]. Table 12.3 abstracts some of the results of [130], [396], and [576], and it includes some maximal length PN codes for comparisons.

Another, somewhat different approach to achieving longer codes (higher pulse compression ratios) is the process of code *concatenation* (or *combination,* both terms have been used in the literature). In this approach, one utilizes whatever codes are available and codes the transmit pulse at two or more levels so that each segment of a code is again coded with another phase code. This has been called Barker-squared or combined Barker coding, when utilized with Barker codes. The properties of such codes were calculated by Hollis [343]. He combined a Barker code of length 4 with the code of length 13 in two ways. When each bit of the 13-bit word was coded into 4 bits, the zero Doppler autocorrelation function of the waveform yielded four side peaks of amplitude 13 located at range offsets of $\pm$ 1, $\pm$3 segments and 12

TABLE 12.3 Good Binary Phase Codes

Code length	Peak sidelobe value	PSL, dB	Source
13*,†,‡	1	−22.3	[33]
28†,‡	2	−22.9	[130,396]
31**	4	−17.8	[697]
29–48‡	3	−19.7−−24.1	[130]
51†‡	3	−24.6	[130,396]
63**	6	−20.4	[697]
69†	4	−24.7	[396]
88†	5	−24.9	[396]
101†	6	−24.5	[576]
127**	9	−23.0	[697]
127†	7	−25.2	[576]
255**	13	−25.9	[697]
317†	12	−28.4	[576]
511**	19	−28.6	[697]
577†	17	−30.6	[576]
1019†	24	−32.6	[576]
1023**	29	−30.9	[697]

* = Barker
† = Longest known code with given peak sidelobe
‡ = Minimum peak sidelobe code
** = Maximum length PN code

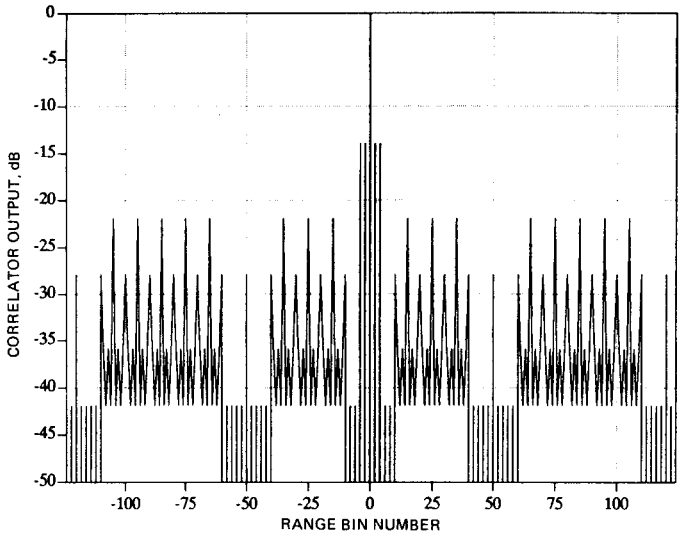

Figure 12.4 25 × 5 concatenated code, matched filter.

peaks of amplitude 4. When each bit of the 4-bit word was coded into 13 bits, the same number of side peaks of amplitude greater than unity appeared, but the location of the side peaks of amplitude 13 occurred at offsets of ±13 and ± 39 segments. The main peak of the autocorrelation function in both cases was 52. The first combination may be useful if the expected interference is considerably separated in range from the target. General properties of concatenated codes have been compiled by Cohen [125].

Figure 12.4 gives the output of a 25 × 5 combined code autocorrelation that provides a 125-to-1 compression ratio. As can be seen from the figure, the structure previously described, where the inner (the 21-bit) code's sidelobes surround the main peak and the outer (the 5-bit) code's sidelobes appear spaced by the length of the inner code, is evident. Such codes up to length 10,985 (a 5 × 13 × 13 × 13 combined Barker code) and mismatch filtering of their range sidelobes was studied in [129]. The sidelobe structures of such codes and special mismatch filtering for reduction of their range sidelobes are discussed further in Sec. 12.4.

When an unwanted target or small regions of clutter are separated by an appreciable portion of the pulse envelope, the linear FM* or chirp waveform is less susceptible to side-peak interference than many phase-

* With a tapered receiver (see Chap. 13).

coded words because of the falloff of the sidelobes as a function of the range from the peak inherent in such waveforms. On the other hand, there are certain binary phase-coded words that are desirable for resolving closely spaced targets or observing missiles in the presence of tank fragments or decoys. There is no apparent method for finding these codes other than observation of a number of autocorrelation functions. For example, the code 453_8 (octal) of length 255 with initial condition 21 has the following time sidelobes adjacent to (and symmetrical about) the main peak:

$$0, -1, 0, -1, 0, 1, 0, 1, 2, 1, 2, -3, -2, -1, 2, 1, 2$$

Thus, within eight segment lengths of the main peak, the ratio of the mainlobe to side-peak amplitude is 255 to 1 or 48 dB. A number of other codes have similar characteristics for six or seven segment offsets. To obtain this degree of discrimination the decoder must be highly linear and have a large dynamic range. As is seen in Sec. 12.4, specific mismatched filtering techniques can also be applied that provide extremely clear (essentially 0), close-in sidelobe regions.

Periodic Barker sequences for $N = 11$ and 13 [186], which are derived from the Barker codes described earlier, also have excellent sidelobes in the absence of Doppler shift. However, they degrade rapidly for targets of moderate velocity. Periodic codes with more than two possibilities of phase per segment have also been reported [323, 250]. A detailed study of ternary codes was made by Tompkins [703] where the coding includes $+$, $-$, and 0. The zero corresponds to the absence of a segment. Properties of ternary codes were tabulated up to $N = 18$ for those cases in which the periodic correlation for $m \neq 0$ or $N = 0$ in the absence of a Doppler shift. In the regions off the range axis, the codes do not seem attractive.

12.3 Random and (Maximal-Length) Pseudorandom Codes

Another class of codes that may be used for generating large pulse compression ratios are those whose sequence of pluses and minuses are chosen in a random or essentially random manner. A random code is obtained when the sequence of pluses and minuses is determined by a random process, where the probability for each occurring is 0.5. A pseudorandom code results when a binary shift register with feedback is utilized for code generation.

For long random codes, the first null in the autocorrelation function tends to occur immediately before and after the compression peak. The power spectrum of such a random sequence, according to the Wiener-

Khintchine theorem, is the Fourier transform of its autocorrelation function. The shape of the power spectrum is thus approximately equal to that of a single rectangular segment τ

$$G(f) = \frac{\sin^2(\pi f\tau)}{(\pi f\tau)^2}$$

This type of power spectrum is shown in Fig. 12.5C for a 255-segment pseudorandom binary code whose starting point was varied from code to code. While not truly a random code, the first nulls appear at a frequency of $1/\tau$ from the carrier, and the first sidelobes are about 13 dB below the peak. The code sequence shown in Fig. 12.5D was used to reverse the phase of the microwave carrier. These photos of the display of a microwave spectrum analyzer have a logarithmic amplitude scale (10 dB per division).

In some implementations of biphase coding, one may restrict the phase change to 90° rather than 180°. This has the effect of reducing the spectral spread of the transmit waveform, which, in turn, can reduce RF interference between radars operating at closely spaced frequencies. Only minor changes are required in the receiver to accommodate such codings.

It has been shown [118] that the amplitude of the autocorrelation function of N bit random sequences for offsets exceeding τ falls between $\pm 0.667\sqrt{N}$ with a 0.5 probability as $N \approx \infty$. The rms sidelobe level is about $0.7\sqrt{N-1}$. It is shown in later sections that by proper choice of code both the PSL and ISL can be held to a lower level and hence yield better clutter rejection. Before describing specific codes and their applications, it is worthwhile to state the properties of a long code in which the choice of the polarity of each segment is made randomly with equal probability [281].

1. The numbers of pluses and minuses are approximately equal.
2. Consecutive segments of the same polarity (or runs) occur frequently. About half of these have a length of one; one-fourth have a length of two; one-eighth have a length of three; etc.
3. The value of the ambiguity function drops rapidly from the origin on both the time and Doppler axes. Thus, random coding constitutes a relatively simple implementation of a thumbtack ambiguity function.

For random and pseudorandom codes, the sidelobes on the time axis are more easily controlled and analyzed than those on the Doppler axis, and thus the bulk of the following discussion emphasizes the properties for zero Doppler shift.

Another class of radar waveforms quite similar to random codes and

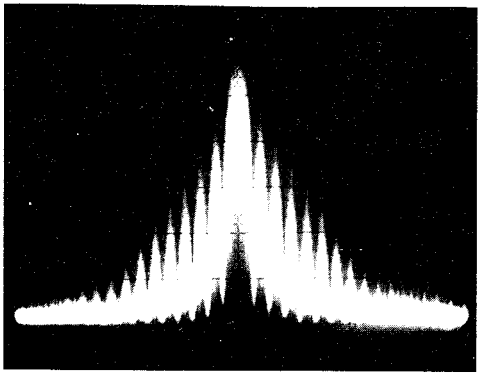

(A)

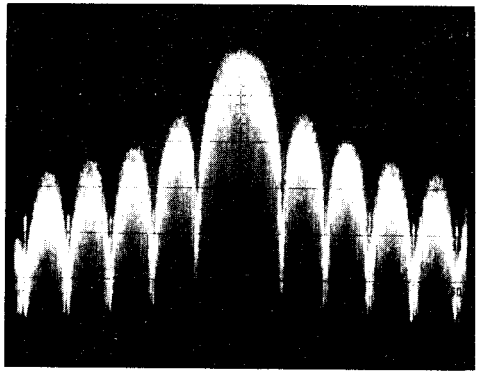

(B)

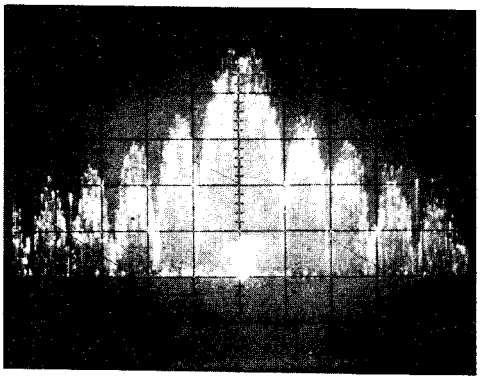

(C)

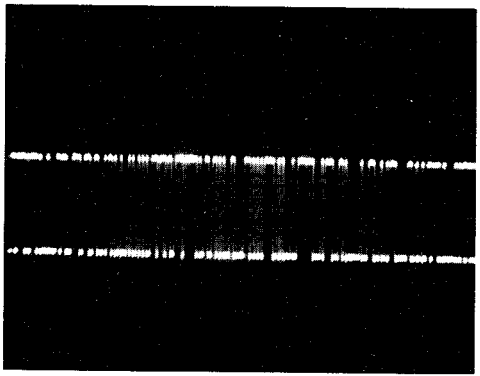

(D)

Figure 12.5 255-to-1 binary phase-coded spectra and waveform 0.1-μs segments. (A) 300-MHz spectrum, cyclic code; (B) 100-MHz spectrum, cyclic code; (C) 100-MHz spectrum, variable starting point; (D) video waveform, 25-μs trace.

having the desired property of high rejection of undesired echoes on the time axis was first reported about 1955 by Elspas [204], Golomb [281], Zierler [784], and several other investigators at M.I.T. There are many names for these maximal-length sequences depending on their application. While there are other sequences of this nature, the terms maximal-length binary shift-register sequences, m-sequences, or maximal-length pseudorandom (PN) sequences/codes are considered synonymous. For random codes, properties (1), (2), and (3) apply only when the codes are relatively long. On the other hand, these properties apply to PN codes of any length. The spectrum of one of these sequences of length 255 was shown in Fig. 12.5). A shift-register encoder is shown as Fig. 12.6.*

A proper discussion of the properties of PN codes requires distinguishing among various utilizations and compressor implementations. The most general radar application entails the use of a pulsed radar for surveillance, and implies all-range compression; that is, the ability to compress the returns from a varied and, theoretically, unlimited number of range bins. Such an application implies compression through some equivalent of the passive, finite impulse response tapped delay line that was shown in Fig. 12.2. This processing represents the linear (aperiodic) correlation of the code with itself (or some mismatched filter). Other applications, such as compression of the return from a CW radar, or implementation of a tracking waveform and filter, can allow circular (periodic) correlation or active demodulation of the re-

* Note that, for radar applications, the zeros in the output sequence are taken as − 1s (phase reversals).

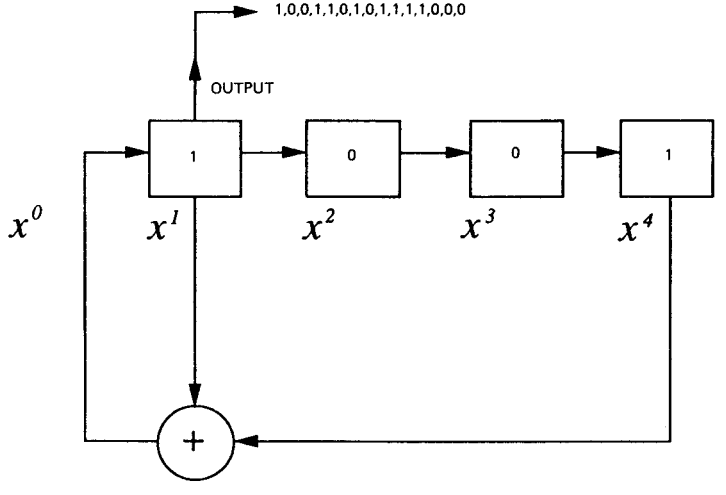

Figure 12.6 Shift register circuit with modulo 2 adder for generating 15-bit PN codes.

ceived waveform. In a CW system, circular correlation occurs naturally even if the compressor is some variant of the tapped delay line shown earlier as Fig. 12.2. In Fig. 12.7, the result of passing a CW waveform through such a tapped delay line is represented. Note that because of the CW nature of the transmission (and hence the reception), the receive registers are always full with repetitions of the received waveform. This, by definition, represents the circular autocorrelation of the transmitted code. *Circular autocorrelation* may be represented mathematically as

$$\phi(m) = \sum_{k=1}^{k=N} a_k \, a_{k+m} \tag{12.3}$$

where N is the (unrepeated) code length, a_k for $k = 1, \ldots, N$ are the code elements, and $a_{k+m} = a_k$ (modulo N). Note that the only difference between this equation and Eq. (12.1) is the definition of $a_k + m$ where $k + m < 1$ and $k + m > N$. In all that follows, we refer to this as circular or periodic correlation. In all other references to correlation, linear (aperiodic) is to be assumed.

While the periodic codes PN have greater application in communications than in radar, they have several properties that make them useful in CW radar [499]. Perhaps the single most important such property is that the periodic autocorrelation function of a PN code has a constant value of minus unity on the time axis for the length of the period except at the origin. The peak amplitude of the autocorrelation function has a height equal to the number of segments in the period. This important property of linear maximal-length sequences means that the rejection of undesired interference is proportional (in amplitude) to the length of one period of the sequence.

The following properties are attributable to pseudorandom sequences [280, 281, 118]. It may be of interest to note the similarities in some of these properties between the PN codes and the random codes, which were discussed earlier.

1. The number of segments of ones (1) in each period of the sequence is within one of the number of segments of zeros (0). This is sometimes called the balance property.
2. In every period, half the runs have length 1, one-fourth have length 2, one-eighth have length 3, etc. (the run property).
3. The PN codes can be generated deterministically through the implementation of shift registers with feedback connections. The initial condition in the shift register determines the starting point of the code. The condition of all pluses is forbidden.
4. The last stage in the shift register must be connected to the feedback circuit and there must be an even number of feedback taps.

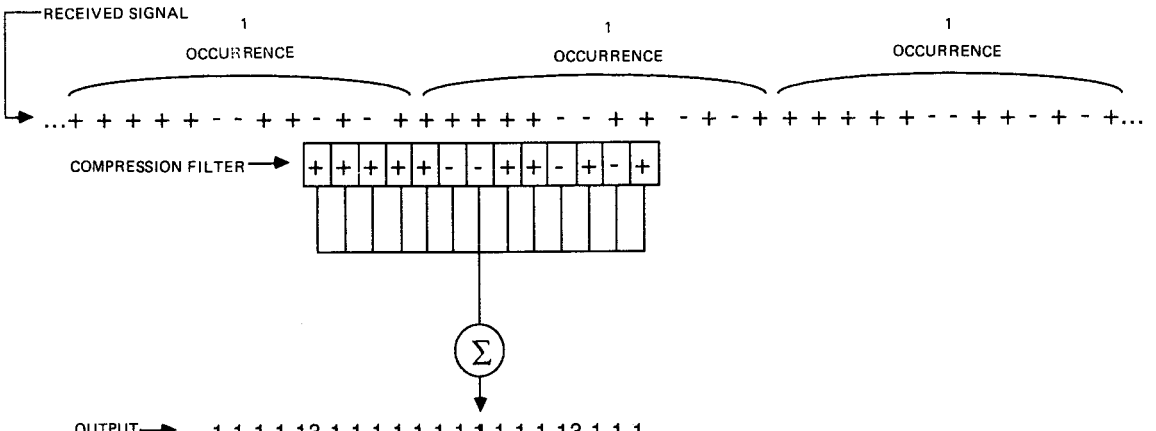

Figure 12.7 A CW signal compressing through a tapped delay line.

5. For maximal-length PN codes, each period has length $2^n - 1$. This is the longest possible period for an n-stage register.
6. In the absence of Doppler shift, the circular autocorrelation function has two levels. Its amplitude at the origin ($t = 0$) is equal to the length of a period N. For all offsets other than multiples of one period the magnitude of the function is unity. This can be written

$$x_m = \sum_{k=1}^{N} a_k a_k + m = \begin{cases} N & \text{if } m = 0, \pm N, \ldots, \pm kN \\ -1 & \text{otherwise} \end{cases} \tag{12.4}$$

7. There are $2N - 1$ side peaks in the autocorrelation function and this function is symmetrical about the origin.
8. There are $2^n - 1$ different maximal-length codes that can be generated from each n-bit shift register, they are simply shifts of each other derived by changing the seed utilized. The number of different n-bit shift registers that yield maximal-length codes (including mirror images) is given by $\phi(2^n - 1)/n$ [45, p. 29; 280, p. 24], where $\phi(m)$ is Euler's phi function. If $2^n - 1$ is a prime number, the number of codes is $(2^n - 2)/n$. If $2^n - 1$ is factorable into prime numbers denoted P_i, then the number of codes is

$$\frac{\phi(2^n - 1)}{n} = \frac{[2^n - 1](P_1 - 1)(P_2 - 1)(P_3 - 1)\ldots}{n(P_1)(P_2)(P_3)\ldots} \tag{12.5}$$

   Each prime P_i is used in the foregoing computation only once even if it appears in the factorization more often.
9. The algebraic sum of all the autocorrelation functions for all the starting points of a given code is $(2^n - 1)^2$ at the origin and $[(N - k)/N](2^n - 1)$ for each segment k away from the origin in either direction [499].
10. The ambiguity function of this waveform is symmetrical about both the time delay and Doppler shift axes.

The notation of 1, 0, 0, 1 in the shift register of Fig. 12.6 represents the initial condition being utilized, and it corresponds to the state of the individual binary elements (flip-flops, etc.) at the start of the code-producing process, where 1 may be interpreted as no phase shift and 0 as requiring a phase shift. The time duration of the segments is determined by the clock generator frequency. The proper choice of the connection of the modulo 2 adder determines whether the sequence will be maximal length. The maximum length of a period will be $2^n - 1$, since if the initial condition of all zeros were to occur in the shift register, the subsequent stages would all remain zero. Adders with

multiple feedback paths are also possible and the various allowable connections* are shown in the literature [204, 280, 63]. Other sequences with similar circular autocorrelation functions have been found, but they cannot be implemented with the convenient shift-and-add property of the binary shift register sequences [118, 279].

To ensure that the output sequence from a shift register with feedback is maximal length, the bits used in the feedback path of Fig. 12.6 must be determined by the 1 coefficients of primitive, irreducible polynominals modulo 2. An example for degree 5, length 31 can be written in binary notation as 100101.† The primitive, irreducible polynominal that this denotes is (see [697, 118])

$$(1)x^4 + (0)x^3 + (0)x^2 + (1)x^1 + (1)x^0$$

The constant (last) 1 term in every such polynominal corresponds to the closing of the loop to the first bit in the register. The shift register corresponding to the preceding polynomials was shown diagrammatically in Fig. 12.6. An excellent compilation of the primitive, irreducible polynomials modulo 2 can be found in the appendix of Peterson's book [542].

A block diagram of a CW radar system with pseudorandom phase coding could look like Fig. 12.8 if the target range is known within a fraction of $\pm \tau$. A CW signal from the RF generator is reversed in phase according to the polarity of the shift register encoder. The 0 to 180° coded CW signal is then amplified and transmitted. Upon reception, the target echoes are mixed to a convenient IF and demodulated. If the time delay of the echo is exactly known, a CW signal appears at the narrow-band filters. Figure 12.8 also represents a top-level example of a limited-range decoder. Such decoder techniques are discussed in more detail in Sec. 12.6, along with range and Doppler tracking circuits. In particular, this is an example of active demodulation (correlation), which is quite similar to stretch processing (described in Section 13.7).

For general surveillance applications, aperiodic (linear) compressions are generally used, and these can be mechanized utilizing the same shift register-type compressor shown in Fig. 12.7 for periodic (circular) correlation of CW signals. PN codes are often chosen over randomly coded words for application because their generation and decoding can be easily mechanized and their sidelobe levels easily predicted. Also, they provide a rich source of good codes for arbitrary length. Due to these properties, they have achieved great popularity for word lengths

* As an example, if the modulo 2 adder were connected to the fourth and fifth stage of the shift register the output would not be maximum length.

† It is often written in octal notation as 45_8. The mirror image is also irreducible and generates the reverse code.

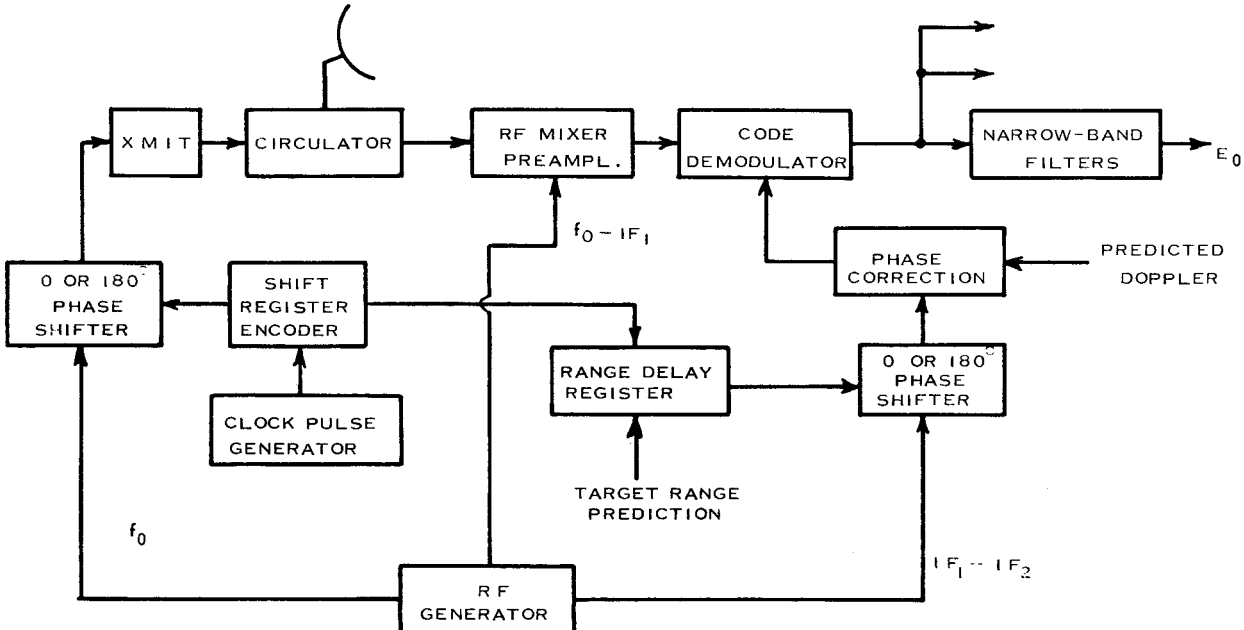

Figure 12.8 Block diagram of phase-coded CW radar with approximate target range and Doppler known.

of $N = 31, 63, 127, 255$. As we have seen, there are several maximal-length binary shift-register codes for each length $2^n - 1$, and there are $2^n - 1$ starting positions for each of these, thus providing a reasonable amount of pulse-to-pulse diversity when this is desirable. Also, within this multiplicity of codes, there are those that have minimum values of either the maximum peak value or rms (equivalently ISL) value of the side peaks. Use of these best maximal-length PN codes can yield desirable performance in both multiple-target and clutter environments. Examples of the performance of such codes were given in Table 12.3.

A summary of maximum-length PN codes and their starting positions is given in Table 12.4 after Taylor [697]. The first column is the degree of the polynomial (number of register stages) and the code length. The second column is the polynomial in octal notation. The feedback conditions can be determined by drawing the shift-register diagram and superimposing the polynomial in binary form on the stages. The polynomial always has an extra one (one bit more than the number of stages), which refers to closing the loop to the first bit of the register. All of the 1 bits in the register are fed to logic circuitry in synchronism with the clock, and the resulting output is entered into the first bit of the shift register. The output for the particular case of Fig. 12.6 is taken from the first stage as shown. The third column lists the lowest peak sidelobe level that can be obtained when a suitable starting position is used. These starting positions are tabulated in the fourth column in the decimal-equivalent form of the required binary state of the register. The fifth column shows the lowest rms sidelobe* amplitude of the codes, and the sixth column shows the decimal equivalent of the initial conditions in the register to achieve this level. In some cases there were too many pertinent starting conditions to list, and only the total number of these is shown.

After degree 8, only a portion of the code properties is available, and only the total number of maximal-length codes and the code with the lowest peak value are shown. None of the mirror images are shown; therefore, the total number of desirable codes is actually twice that contained in the table. Further information on longer codes can be obtained from Roth [622] and Braasch and Erteza [85] or from tables of irreducible polynomials.

Roth's paper also contains an extensive table through degree 9 for determining the minimum number of modulo 2 adders and the cor-

* The mean value of the residues of these codes is 0.5. The values in the table are the rms deviations from this mean except for lengths 3 and 7.

TABLE 12.4 Maximal-Length Binary Code Properties

Degree (number of stages) and length	Polynomial, octal	Lowest peak sidelobe amplitude	Initial† conditions, decimal	Lowest rms sidelobe amplitude	Initial conditions, decimal
1 (1)	003*	0	1	0	1
2 (3)	007*	−1	1,2	0.707	1,2
3 (7)	013*	−1	2	0.707	6
4 (15)	023*	−3	1,2,6	1.39	2,8
5 (31)	045*	−4		1.89	6,25
		−5	(9 conditions)	1.74	31
				1.96	6
6 (63)	103*	−6		2.62	32
		−8			
		−9	(9 conditions)	2.81	35
		−10	(9 conditions)	2.38	7
7 (127)	203*	−9	1,54	4.03	109
	211*	−9	9	3.90	38
	235	−9	49	4.09	12
	247	−9	104	4.23	24,104
	253	−10	54	4.17	36
	277	−10	14,20,73	4.15	50
	313	−9	99	4.04	113
	357	−9	15,50,78,90	4.18	122
8 (255)	435	−13	67	5.97	135
	453	−14	(20 conditions)	5.98	254
	455	−14	124,190,236	6.10	246
	515	−14	54	6.08	218
	537	−13	90	5.91	90
	543	−14	(10 conditions)	6.02	197
	607	−14	(6 conditions)	6.02	15
	717	−14	124,249	5.92	156
9 (511)	(24 codes)	−19 (1743 polynom)		~8.0	
10 (1023)	(30 codes)	−29 (3023 polynom)			
11 (2047)	(88 codes)				
12 (4095)	(72 codes)				
13 (8191)	(315 codes)				

SOURCE: After Taylor and MacArthur [372].
* Only single Mod-two adder required.
† Mirror images not shown.

responding feedback connections for a given polynomial. The number of adders is minimized by using intermediate feedback connections.

It would be desirable if the low value of the circular autocorrelation function for pseudorandom sequences that was obtained on the time axis (except at the origin) was also obtainable throughout the ambiguity plane. This would create a thumbtack ambiguity surface with a height (before normalization) of N^2 at the origin and a plateau of unity height

extending in range for the length of the period and through the Doppler region. Unfortunately, this is not the case, and it has been shown that the squared magnitude of the ambiguity function for these sequences can be written as [204, 118, 246].*

$$
\begin{aligned}
|\chi(t,s)|^2 &= \left| \sum_{\kappa} a_k a_{k+m} \left(exp \frac{2\pi j}{n} \right)^{ks} \right|^2 \\
&= N^2 \quad \text{for } m = 0 \,(\text{mod } N), s = 0 \\
&= 0 \quad \text{for } m = 0 \,(\text{mod } N), s \neq 0 \\
&= 1 \quad \text{for } m \neq (\text{mod } N), s = 0 \bmod \frac{1}{N\tau'} \\
&= N + 1 \text{ elsewhere}
\end{aligned}
\tag{12.6}
$$

Mod N corresponds to the periodicity in time, t is time, and s is the Doppler shift. The region where the value is $N + 1$ is often called the plateau region. Persons [540] has calculated the ambiguity function for a pseudorandom sequence of a length of seven segments. The central peak of height N^2 corresponds to the target response, and all range and Doppler shifts are measured from its location. The Doppler axis is completely free of ambiguities as long as the code contains many periods. The ambiguities along the range axis are unity height except at the code period. The so-called plateau region consists of a series of ridges parallel to the range axis and at multiples of the rate of the periodic repetition.

If the length of the period is sufficient to place the major range ambiguities beyond a range where clutter or undesired targets can occur,† excellent clutter rejection can be obtained for smaller Doppler shifts. If, in addition, the period $N\tau$ is short such that the Doppler difference between desired and undesired targets is less than $1/N\tau$, there will be virtually complete resolution of the desired target. If the radar parameters are such that both of these constraints cannot be met, there is a choice between competing against high-volume, ambiguous-range spikes or the ridge parallel to the range axis at a Doppler shift of $1/N\tau$. In many ways this waveform resembles a pulse Doppler waveform with period $N\tau$.

If the integration time of the narrow-band Doppler filters in Fig. 12.8 is short, the values given for the regions other than the correlation period will fluctuate since the desirable properties of these codes apply only for long sequences. Chandler [118] has placed some limits on this fluctuation.

---

* The segments are all assumed to be contiguous phase modulations of a high carrier frequency.

† Or at any range if the clutter Doppler is sufficiently separated.

12.4 Sidelobe Suppression of Phase-Coded Words

In multiple-target environments where there are large undesired reflectors (point clutter), or in distributed clutter it is often desirable that the time (range) sidelobes of the autocorrelation function of the binary phase-coded pulses be reduced to as low a level as possible. Otherwise the time sidelobes of one large target may appear as a smaller target at another range, or the integrated sidelobes from extended targets or clutter may mask all the interesting structure in a scene. Key, Fowle, and Haggarty [212, 398] seem to have been the first to demonstrate that weighting networks can be designed to reduce these sidelobes to an arbitrarily low level. Their approach consisted of a clever, albeit somewhat heuristic, method for deriving a set of linear equations whose solution provided an effective weighting network.

As an example they used the 13-bit perfect word (Barker code for $N = 13$) whose autocorrelation function has a spectrum

$$\phi(\omega) = (\tau')^2 \left[\frac{\sin(\omega\tau'/2)}{\omega\tau'/2}\right]^2 \left[12 + \frac{\sin(13\,\omega\tau')}{\sin\omega\tau'}\right] \tag{12.7}$$

It was shown that the desired part of the spectrum can be extracted from the signal received from a point target with negligible Doppler shift by a filter whose frequency characteristic is

$$H(\omega) = \frac{13}{12 + [\sin(13\omega\tau')/\sin\omega\tau']} \tag{12.8}$$

For the Barker code they derived two weighting functions to approximate Eq. (12.8), the first of 13th order and the second of 25th order.

The 13th-order weighting network that eliminates the first six sidelobes is shown in Fig. 12.9; and the peak-to-residual sidelobe ratios are given in Table 12.5. Note that the weighting network is placed after the matched filter, necessitating two tapped delay lines in series (one for the matched filter and one for the weighting network). Thus, on the surface, this processing may seem equivalent to utilizing a single filter whose order (length) is 25 (13 + 13 − 1). In fact, since the delays utilized are all 2τ, the 13th-order filter is equivalent to a 26-bit filter in which every other bit is specified as 0. Thus, in terms of total delay through an equivalent single mismatched filter for the suppression of the 13-bit Barker code's range sidelobes, the 13th-order filter shown is equivalent to a 37-bit (13 + (13 × 2 − 1) − 1) tapped delay line, and the 25th-order filter is equivalent to a 61-bit (13 + (25 × 2 − 1) − 1) tapped delay line.

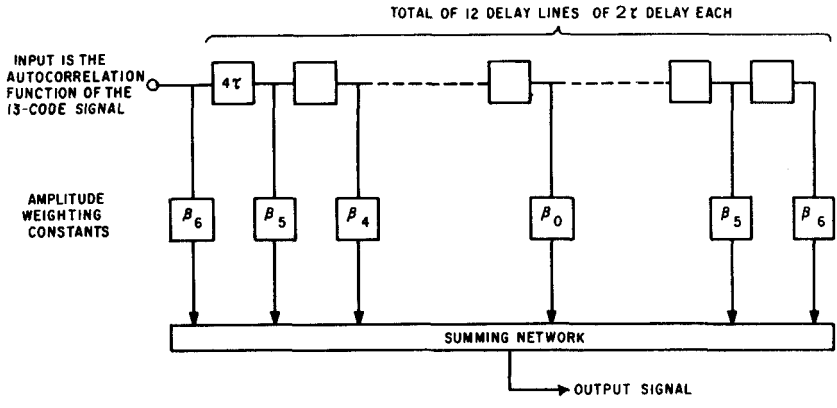

Figure 12.9 Weighting network that controls amplitudes of the close-in sidelobes of the Barker 13 code. (*After Fowle* [246])

The weighting network causes only about a 0.25-dB loss in signal detectability for the higher-order network. The reduction in sidelobes to the −45.6-dB level, while impractical for older systems, may have some real application in current systems that are utilizing 10- and 12-bit A/D converters.

Other, more theoretical, techniques have been applied to this problem as well. Building on work initiated by Ackroyd and Ghani [2], Cohen et al. [127, 126, 128] have continued to apply the theory of Wiener filtering to the problem of range sidelobe suppression for binary phase-coded autocorrelation functions. Implementing an optimal ISL technique, it was shown that the PSL and ISL levels of the 13-bit Barker code can be optimally driven as close to zero as one desires (limited only by A/D quantization levels and other such system considerations) with the application of such mismatched filters. Figure 12.10 shows the performance of these filters as a function of filter length for the 13-bit Barker code. It may be of interest to note that maximum loss (LPG) is in all cases less than 0.21 dB. These filters have also been applied to the other Barker, the MPS, and some maximal-length PN codes with varying results that seem to be a function of code structure. Some codes, such as the Barkers, allow for excellent sidelobe suppression

TABLE 12.5 Sidelobe Reduction of a 13-segment Barker Code

Type of weighting function	Peak signal / Residual peak sidelobes	Peak signal / rms sidelobes
None	13 (22.3 dB)	25.3 dB
13th order	41.9 (32.4 dB)	
25th order	189 (45.6 dB)	

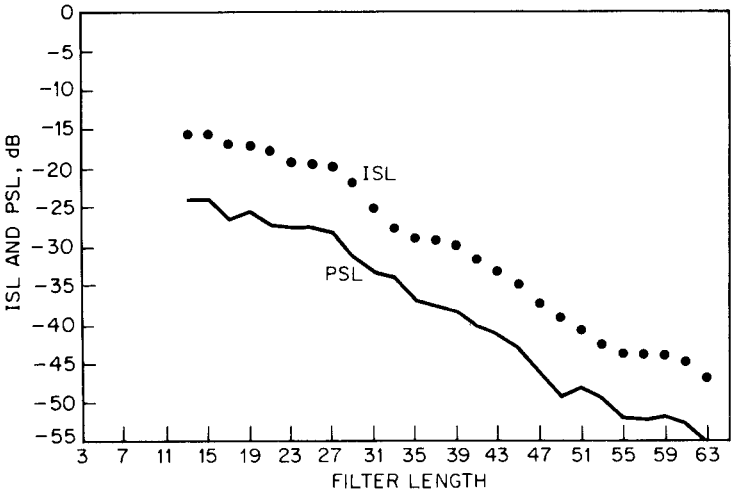

Figure 12.10 Optimal ISL filtering performance as a function of filter length for a 13-bit Barker code. (*From Cohen and Baden [127]*)

with modest filter lengths and losses while others seem to be much less amenable to sidelobe improvement [126, 127]. Most recently, this technique has been generalized via an iterative development approach that allows for minimization of PSL or the establishment of clear regions in the compressed output of arbitrary binary phase codes. Examples of the results of this approach as applied to minimum PSL and clear-region filtering are given in Fig. 12.11A and B [27], respectively. Earlier, Zoraster [785] utilized a minimax optimization technique to derive minimal PSL filters for Barker codes. Comparison of Wiener- and minimax-derived filtering for suppression of sidelobes in Barker code autocorrelations is given in Predrag and Zejak [558].

Optimal ISL filtering has also been applied to combined codes with interesting results. A 125-bit code composed of the concatenation of a 5-bit Barker and a 25-bit MPS code is mismatch filtered to provide a PSL of less than -30 dB and an ISL of less than -25 dB [131] (see Fig. 12.17 in Sec. 12.5 and compare with Fig. 12.4 in Sec. 12.2). Since the technique only requires deriving mismatch filters for the individual codes, that is, the 5- and 25-bit codes separately (and then concatenating the results into an effective filter for the 125-bit code), a great deal of computer time is saved and potential limits to computer memory and accuracy are avoided in the development process. This technique has been applied to significantly reduce the sidelobes of code lengths in excess of 10,000 [129], and there is no practical or theoretical limit to the lengths of the codes that can be so treated.

Another technique to reduce the time sidelobes of a finite-length

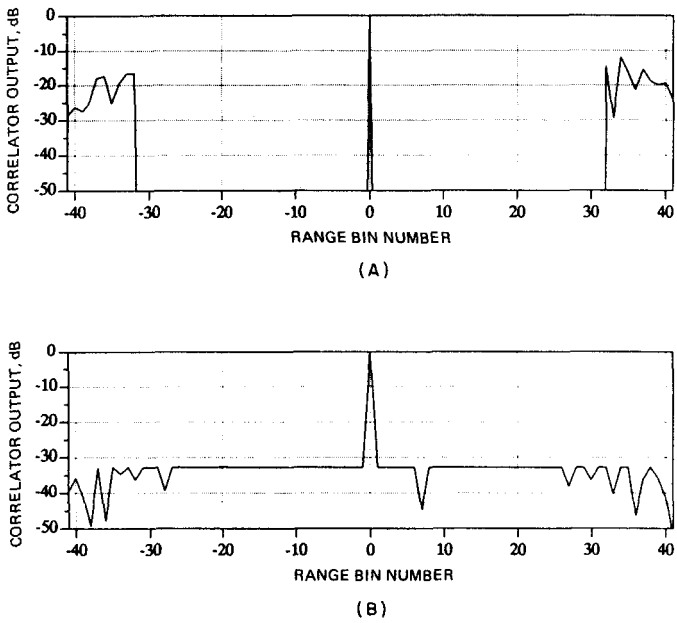

Figure 12.11 (A) 20-bit MPS code; 64-bit tracking filter. (B) 20-bit MPS code; 64-bit optimal PSL filter. (*After Cohen and Baden [128]*)

binary sequence has been reported by Golay [273] and Erickson [208]. They have, it seems independently, found codes of length 2^n that have a complementary code whose autocorrelation function cancels the autocorrelation function of the original code except at the origin. Thus, if the two codes can be transmitted simultaneously and their matched-filter outputs added vectorially,* there will be no residues. A practical problem exists with this approach in a clutter environment. If the two transmitted codes are separated in frequency, there will be decorrelation of the clutter echoes and little cancellation. If the codes are separated in time and the clutter is extensive, the residues may be temporally or spatially decorrelated. Thus the use of this technique is generally restricted to scenarios in which the PRF is sufficiently high to ensure pulse-to-pulse stationarity of the clutter return or to applications in which the principal aim is to prevent the time sidelobes of a large target (or large point clutter) from obscuring a smaller target.

The techniques just described and discussed have dealt primarily with the suppression of sidelobes for linear (aperiodic) correlation. In [617], a technique based on matrix inversion is introduced which pro-

* In the absence of Doppler shift.

vides codes and mismatched filters of arbitrary length that give 0 sidelobes for periodic (circular) correlation. In the paper, actual codes and filters of lengths 3 through 32 are given, and the indication is that codes of all lengths can be found that have this property. Although the inherent loss can be severe for short codes, it approaches zero with increasing code length.

12.5 Polyphase-Coded Words

The Barker codes yield high autocorrelation peak-to-sidelobe ratios of N to 1 in amplitude, but they are known to exist only for lengths up to $N = 13$. Similarly, the MPS codes are known only through length 48. Other good codes are known, but principally for lengths less than 100 or so. The maximal-length PN codes and the technique of combining codes can be used for creating codes of arbitrarily long lengths. While the PN codes are easy to generate and decode, the ratio of amplitude of the central peak to largest side peak remains close to $\sqrt{N}$. The technique of combining codes leads to relatively high peak sidelobes, and even when mismatched filters are used to suppress these sidelobes, a penalty is paid for the code-filter mismatch. In cases in which the word length must be greater than $N \approx 30$ from accuracy, resolution, or automatic detection considerations, there are some additional good codes if the restriction of 0 to 180° phase shifting is removed [173, 250, 249]. Furthermore, and perhaps even more importantly, all the biphase codes share the common quality that they are quite sensitive to Doppler shift in that they exhibit thumbtacklike ambiguity functions, generally showing significant degradation in performance when the shift reaches or exceeds $\pi/2$ rad over the transmit pulse (that is, a Doppler frequency of $1/4T$).

For all these reasons cited, individuals have continued to search for and discover or invent innovative pulse compression codes. In this section three classes of polyphase codes are introduced and discussed: Frank, P4, and Welti codes. By *polyphase coding* we refer to modulation of the carrier with M discrete phases, where M is greater than 2 ($M = 2$ is the biphase case). The *Frank* [249] and Lewis and Kretschmer *P4* [434] codes can be thought of as discrete approximations to linear FM (see Chap. 13). They exhibit better Doppler tolerance for broad range-Doppler coverage than do the biphase codes, and they exhibit relatively good sidelobe characteristics. A Welti code [766] actually consists of a pair of polyphase codes whose autocorrelation sidelobes are equal in magnitude and opposite in sign. Thus, when an N-bit Welti code pair is transmitted, each code is compressed separately through its matched filter, and the compressed outputs are added. The result is an N-to-1 compression, $2N$-to-processing gain, and range sidelobes

that are uniformly zero. The Golay codes, mentioned earlier in Sec. 12.3 are, in fact, those Welti codes that happen to be biphase.

For what follows, let N represent the length of the code and M the number of phases to be utilized. In the case of Frank codes [249] the length of the code is always $N = M^2$. These codes for $M = 3$ through 16 are shown in Table 12.6, in which the numbers correspond to phase shifts of $2\pi/M$ rad from an arbitrary phase reference. The codes for $M = 3$ found by Delong [173] are labeled *b* and *c*. The code length can be the square of any integer, and the properties to be described have been verified up to $M = 13$. The generation of these codes is described in the reference.

The maximum sidelobe level is also shown in the table, and it can be seen that the amplitude ratio of the central peak N to the peak sidelobe is considerably greater than $\sqrt{N}$ and approaches $3\sqrt{N}$ for $M = 3$ to 12. This may be important for surface radars that must cope with land clutter or in multiple-target environments, and it thus may

TABLE 12.6 Frank Codes for $N = 9$ to $N = 256$

M	N	Peak sidelobe amplitude	Code sequence in phase steps of $\frac{2\pi}{M}$
3	9	1.0	(a) 0,0,0;0,1,2;0,2,1 (b) 0,1,1;2,1,2;1,1,0 (c) 0,0,2; 2,0,0;1,0,1
4	16	1.4	(a) 0,0,0,0;0,1,2,3;0,2,0,2;0,3,2,1
5	25	1.6	(a) 0,0,0,0,0;0,1,2,3,4;0,2,4;1,3;0,3,1,4,2;0,4,3,2,1
6	36	2.0	(a) 0,0,0,0,0,0;0,1,2,3,5;0,2,4,0,2,4;0,3,0,3,0,3;0,4,2,0,4,2; 0,5,4,3,2,1
7	49	2.25	(a) 0,0,0,0,0,0,0;0,1,2,3,4,5,6;0,2,4,6,1,3,5;0,3,6,2,5,1,4; 0,4,1,5,2,6,3;0,5,3,1,6,4,2;0,6,5,3,2,1
8	64	2.6	(a) 0,0,0,0,0,0,0,0;0,1,2,3,4,5,6,7;0,2,4,6,2,0,4,6;0,3,6,1,4,7, 2,5;0,4,0,4,0,4,0,4;0,5,2,74,1,6,3;0,6,4,2,0,6,4,2;0,7, 6,5,4,3,2,1
9	814	~2.8	
10	100	~3.1	
12	144	~3.9	
16	256	~4.7	
16*	256	28	
16†	256	13	
16‡	256	26	

* Four-phase approximation to Frank code (rms sidelobes = 5.51).
† Four-phase approximation to good binary codes (rms = 5.99).
‡ Four-phase approximation to linear FM (rms = 6.81).
SOURCE: After Frank [249], Delong [173], and Queen [569].

justify the additional expense of encoding and decoding into many phases. The important properties of Frank polyphase codes can be summarized as follows:

1. The autocorrelation function is symmetrical about $t = 0$. Each set of autocorrelation side peaks for $t > T/N$ or $t < T/N$ (negative offsets) is also symmetrical (for zero Doppler shift).
2. The autocorrelation function equals zero at multiples of M segments.
3. In all cases studied, the amplitude of the largest side peaks is the vector sum of $M/2$ unit vectors (if M is even) or $(M + 1)/2$ unit vectors (if M is odd), where the vectors are separated by angles of $2\pi/M$ rad.
4. Starting points other than the illustrated sequence of all zeros (except for mirror images) seem to result in higher side-peak amplitudes.
5. In the presence of Doppler shift, the autocorrelation function degrades at a much slower rate than for binary codes, but the peak shifts its position rapidly. For $M = 4$, a Doppler shift of M cycles ($4 \times 360°$) per sequence length will shift the main peak by four segment lengths, just as would be the case for a linear FM waveform (see Chaps. 8 and 13).
6. The codes have zero periodic correlation in the absence of Doppler shift [323]. That is,

$$x(m) = 0 \quad \text{for } m \neq 0, N, 2N, \text{ etc.}$$

and

$$x(m) = N - k \quad \text{for } m = kN \text{ and } k < N.$$

Property number (5) implies that the ambiguity function is quite similar to a chirp or linear FM waveform, and in fact it can be seen that the code itself is a discrete approximation to linear FM. In particular, consider the code for $M = 8$ in Table 12.6. After the initial sequence of zeros, the phase versus time is monotonically increasing (mod 2π) for the first eight segments of the code. After that, the phase increases by $4\pi/M$, $6\pi/M$, $8\pi/M$, etc., and the general phase variation approximates

$$d\theta \approx \alpha t^2$$

where t is time in units of the segment length and α is a constant. Since a second-order change of phase versus time is a linear frequency shift, the similarities to linear FM become obvious. This analogy between Frank codes and linear FM is used to introduce Chap. 13.

As with linear FM, property (5) can be advantageous for single-pulse

radars in the presence of Doppler shifts since there is little loss in sensitivity or clutter rejection as compared with biphase codes. On the other hand, a Doppler shift will be interpreted as a range error and the ambiguity diagram will have high diagonal ridges as in linear FM.

An important distinction between Frank codes and linear FM is that Frank codes exhibit distinct signal losses as the compressed peak moves in range as a function of Doppler shift. While linear FM signals exhibit this change smoothly with little or no loss, the discrete nature of the Frank code causes a 3- to 4-dB signal loss at Doppler mismatches of odd-integer multiples of π rad per pulse. In addition, the PSL of the Frank code is degraded with high Doppler mismatches as well [433].

Also included in the table are some four-phase approximations to several pulse-compression waveforms that have desirable properties. Four-phase waveforms are receiving considerable interest since digital decoders are relatively easy to implement. While the four-phase approximations to the Frank $M = 16$ waveforms do not have outstanding range sidelobe properties, Queen [568] has shown that the peak range sidelobe is about 19 dB down from the peak and the rms sidelobes are about 33 dB down. The four-phase approximation to linear FM that was studied yields a peak range sidelobe that is 21 dB down from its peak compression.

Another set of codes that are discrete approximations to linear FM are the P4 codes [434]. The phase of the kth segment of a P4 code is given by

$$\phi_k = (\pi k^2/L) - \pi k$$

where L is the code length and k is an integer, $0 \leq k \leq L$. As L gets large, the maximum subpulse-to-subpulse phase shift, which appears at the beginning and end of the waveform, approaches 2π rad. That is, the transmitted P4 code is a 2-to-1 undersampled discrete approximation to linear FM. By matched filtering on receive, the transmit pulse is compressed, yielding peak sidelobes of -26 dB with respect to the peak. That the PSL is -26 dB rather than the -13 dB of linear FM is not happenstance; the undersampling rate of the P4 codes was chosen precisely to minimize PSL.

Fig. 12.12A, B, and C [128] shows the compressed output of a 169-bit P4 code with no Doppler mismatch and with Doppler mismatches of approximately 95° and 190° per pulse, respectively. As can be seen from the figure, the response to Doppler mismatch is much more like that of linear FM than that of the biphase codes (the structure of which is significantly degraded at such shifts). However, a cusping loss very similar to that of the Frank codes is observed in C. Also, a broadening of the mainlobe is evident in both B and C. This broadening may be

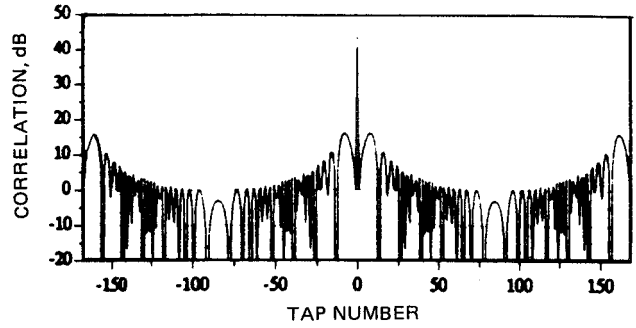

(A)

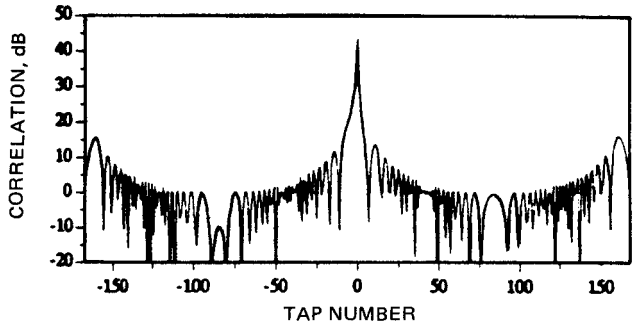

(B)

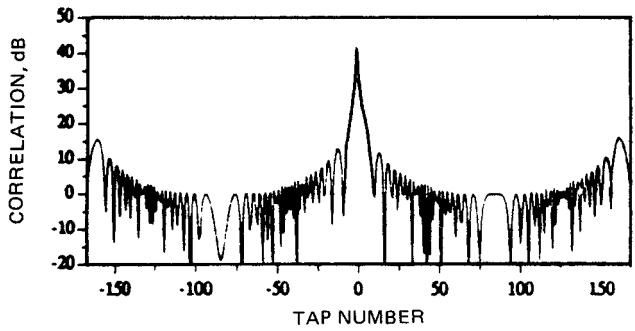

(C)

Figure 12.12 169-bit, P4 code, matched filter; X-band radar, 13-μs pulse. (A) Stationary target; (B) Mach 1 target; (C) Mach 2 target. (*Courtesy of J. M. Baden*)

interpreted either as an increase in the near-in sidelobes or as a coarsening of the range resolution of the waveform.

The final class of codes discussed is the Welti codes [766]. These are four-phase (0, 90, 180, and 270°) code pairs for which the sum of the individual autocorrelations leaves no range sidelobes. Being quaternary, these are polyphase codes; however, unlike the Frank and P4 polyphase codes they are not approximations to linear FM. Rather, they behave much more like biphase codes in that they are extremely sensitive to Doppler mismatch. The Golay codes, discussed in Sec. 12.4, are precisely the subclass of Welti codes that happen to be biphase (no 90 or 270° shifts). Both the Welti and Golay codes are not only sensitive to Doppler shift, but their sidelobe canceling ability is extremely sensitive to any differentials between the two codes of a pair. That is, both a Doppler shift on both codes and minor differences between the Doppler or amplitude content of the two pulses of a pair can result in significant range sidelobes in the sum output.

12.6 Compression Techniques—All-Range Compressors

One of the advantages of the phase-coding technique is that a number of types of simple, efficient, and flexible compressors can be built. This flexibility is an important factor since the particular code can easily be changed from radar to radar or even from pulse to pulse in a single radar, as contrasted to other pulse compression techniques. In general, all the compressors in this section approximate matched-filter or correlation detectors, but they can just as well be implemented with a sidelobe-suppressing mismatched filter.

This discussion is divided into parts, with the functional breakdown indicated below:

Type	General radar function	Typical Doppler coverage
All-range compressors		
Analog	Surveillance—short-coded words	Limited
Digital	Surveillance—long-coded words	Limited
Cross correlators		
	Tracking—words or sequences	Limited

Encoding techniques are not discussed except to state that it is apparent that encoding directly at the microwave carrier frequency is by far the most satisfactory method for binary or four-phase encoding. Multiple, low-power diode crystal switches with good isolation are now available with switching speeds of a few nanoseconds. Microwave "magic tees" provide antiphase outputs, and "hybrids" provide 0 and 90° phase shifts over bandwidths in excess of 20 percent of the carrier

frequency. This type of encoder was used to generate the 0.1-μs-per-segment code of Fig. 12.4D. Digitally controlled phase shifters can also be quite effective.

If little prior information is available about the distance from the radar to the target, the receiver must be implemented to provide a matched filter for a large set of time delays. This is the typical surveillance or search configuration. The class of matched filters for which the filter's output will reach its maximum value for any target range is called the all-range compressors. In the following discussion it is assumed that a phase-coded pulse is transmitted and the Doppler shift imposed on the pulse is negligible or at least known.

Analog compressors

Historically, the processing of phase-coded pulses was accomplished utilizing analog components such as lumped-parameter, glass, or crystal delay lines. More modern analog implementations utilize surface acoustic wave (SAW)–like devices to accomplish the tapped delay-line function at the RF or some intermediate (IF) frequency. While some one-of-a-kind programmable SAW devices—in which the codes and filters can be changed on a pulse-by-pulse basis—have been reported, none, or at least very few, seem available off the shelf. Since one of the powerful features of phase codes is the ability to change the codes and filters rapidly to provide a measure of reduced susceptibility to outside and self-interference as well as intercept, the discussion on SAW devices is deferred to Chap. 13. Of some importance to mention here, however, is that one can, in general, achieve greater bandwidth with SAW devices than with digital compression techniques.* On the other hand, SAW devices are much more susceptible to degradations due to temperature and evidence very high insertion losses.

A different type of analog matched filter for decoding phase-coded words is shown in Fig. 12.13. This is the zero intermediate frequency (dc-IF) or *homodyne configuration* in which bipolar video is fed into each delay line. The local oscillator for the pair of mixers is at the transmitted frequency f_0, and the relative phases of this oscillator at the mixers are in quadrature. The mixer outputs are thus the in-phase I and quadrature Q components of the echoes and contain no carrier frequency as such. In practice both mixers are constructed as a single-sideband mixer whereby the appropriate pair of outputs is obtained with only a single local oscillator input. Minor Doppler shifts (if known) can be added to the LO frequency to prevent degradation of the matched-filter output. Since the total signal may appear in either or

* Unless stepped frequencies are used.

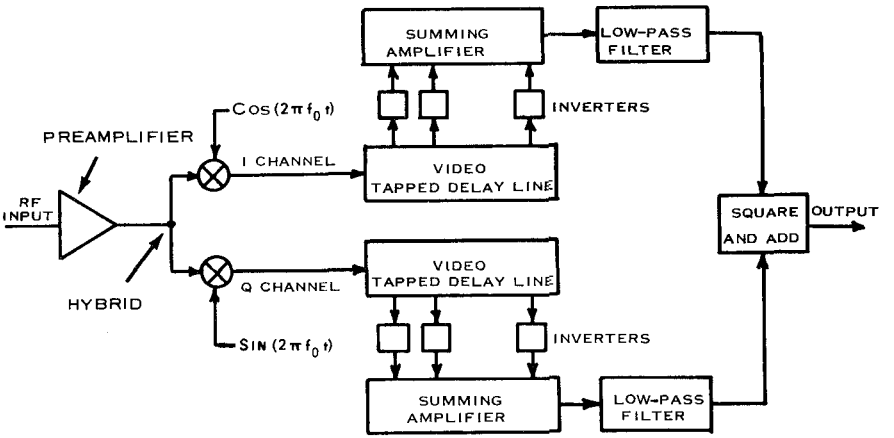

Figure 12.13 Bipolar video matched filter for phase-coded words.

both outputs and the resultant amplitude is $e_0(t) = (I^2 + Q^2)^{1/2}$, both channels are necessary to avoid an average 3-dB loss in signal-to-noise ratio. Another way of stating this is that since the phase of the target is unknown, the received signal may appear in the channel that was not constructed.

While this approach requires twice the number of delay-line elements, it often requires less hardware than the compressors at IF. This results from a combination of two effects. First, the delay-line bandwidth for the video waveform need be only one-half that of the bandpass waveform; second, no IF carrier need be passed through the lines.

The delay tolerances are also less critical for the dc-IF than for the RF or IF implementation. On the other hand, the physical realization of a wideband squaring and summing circuit, which is required for a dc-IF but not for an RF or IF implementation, is not trivial. Effective approximations and the emergence of new components that allow the full computation are described in the next subsection. A final point in favor of the dc-IF is that it lends itself to digital decoding or digital processing of the compressor outputs.

Digital compressors

When binary or quadrature (four-phase) codes are transmitted, a pair of shift registers can be used as a digital tapped delay-line pulse compressor. An all-range implementation of this form of digital pulse compression has been built for maximal length binary codes of up to 255 segments [697] and is illustrated in Fig. 12.14. The shift-register encoder is at the upper left, and the I-Q (homodyne) mixer is at the lower

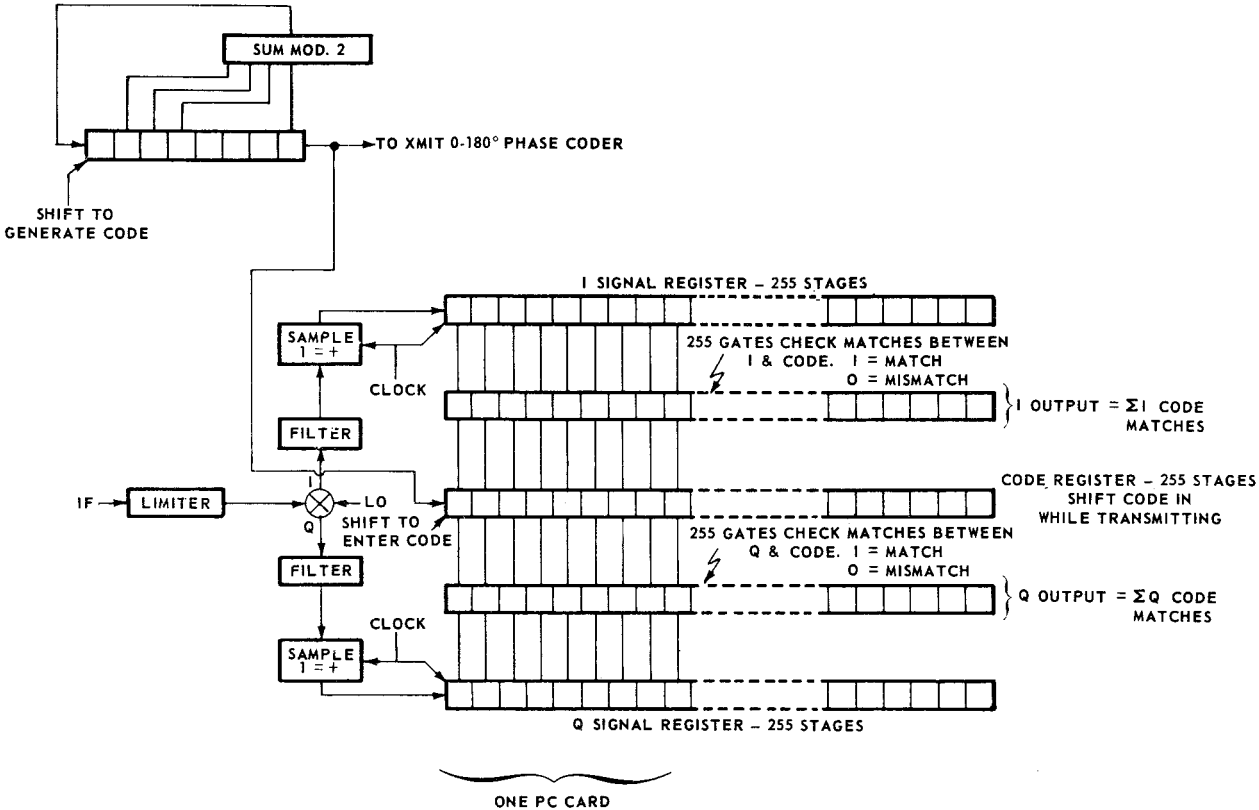

Figure 12.14 Digital pulse compressor using 0–180° binary phase-coded modulation. (*After Taylor and MacArthur* [697])

left of the diagram. The low-pass filters approximate matched filters for the segments of the code. The IF limiter is needed only to ease dynamic range problems and reduce the effect of impulse-type noise. The samplers are normally clocked at the bit rate of the code, and only the polarity of the bits in each channel is shifted down the respective signal registers.

At the time of transmission, the encoded signal is stored in the code register with the polarity of each stage representing the polarity of the corresponding segment of the code. Several unique features of this compressor are worth noting. First, any binary code of length 255 can be transmitted and stored prior to reception of the received echoes. Thus, the code can be changed for each transmitted pulse if desired. In addition, any shorter maximal-length code can be stored if lower-range resolution is desired. Also, if only one code is to be used, the code register can be replaced by fixed wiring.

As the quantized target echoes propagate down the signal registers, their polarity is continuously matched with the stored code in the code register. The number of matches in the 255 gates between the signal and code register is continuously summed. When there is perfect alignment of a target and the stored word, 255 matches should appear in the I or Q summer (or both). The summation of the agreements is combined in a greatest of circuit yielding the larger of $|I|$ or $|Q|$. This summation is fed to a threshold circuit where the threshold level is predetermined by the desired false alarm rate. Since there is broadband limiting prior to the compressor, the false alarm rate should be constant (CFAR) for noise, jamming, or other uncorrelated echoes. Target range is determined by stopping a counter when the threshold is exceeded.

The CFAR effect and an example of clutter reduction are shown in Fig. 12.15.* At the upper left is the uncompressed (all pluses in the code) A-scope output from land-clutter echoes at the beginning of the trace. The backscatter from a localized rainstorm is at the center of the trace. In all of the figures, the transmitted pulse length is the same and is about 3 percent of the illustrated trace length. As the number of bits in the code is increased, the compressor output decreases rapidly for the spatially uncorrelated rain clutter and with moderate rapidity for the partially correlated land-clutter echoes. As the number of bits in the code reaches 255, the clutter is reduced to the noise level, demonstrating the CFAR action. If a point target echo of sufficient energy were present, it would always reach the maximum output (equivalent

* See Chap. 4 for discussion of CFAR. In that chapter it was shown that the desired effect can be achieved only for large time-bandwidth products. With the configuration described here, the number of stages should be ≥ 63 when low false-alarm probabilities are desired.

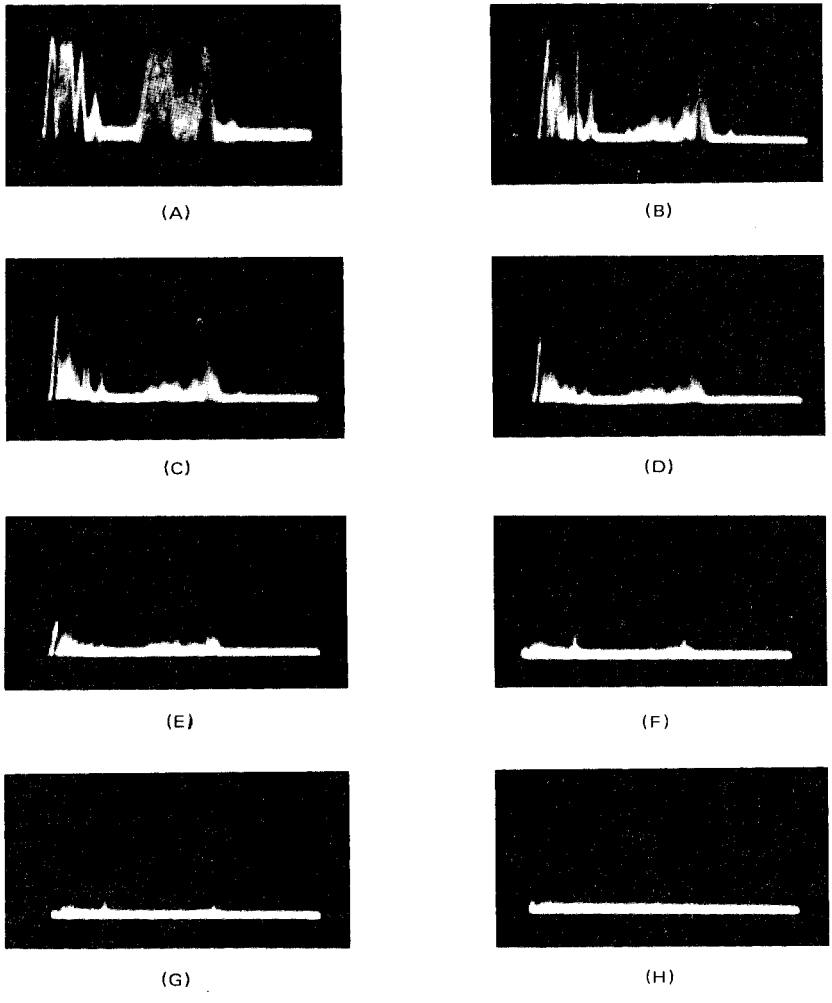

Figure 12.15 Detected video out of digital pulse compressor from rainstorm (100 μs/cm). (A) Long pulse, no ϕ code; (B) pulse compression = 3; (C) pulse compression = 7; (D) pulse compression = 15; (E) pulse compression = 31; (F) pulse compression = 63; (G) pulse compression = 127; (H) pulse compression = 255. (*After Taylor and MacArthur* [*697*])

to voltage addition) while distributed targets would be held to the noise level (equivalent to power addition).

There is some signal-processing loss in the digital processor illustrated in Fig. 12.14. The combination of limiting and quantization causes about a 2-dB loss in efficiency. About 1 dB of this is the loss that is inherent in a CFAR processor. There is an additional fractional decibel loss for using the greatest of circuit. This loss is tabularized in

TABLE 12.7 Signal-to-noise Penalty for Using Single Homodyne Channel or Sum of Magnitudes instead of Square-law Detector

A. Penalty, dB, for Rayleigh fluctuating targets* (case 1 or 2) as compared to $(I^2 + Q^2)^{1/2}$

False alarm probability	$P_D = 0.2$		$P_D = 0.5$		$P_D = 0.9$	
	$\|I\|$	$\|I\| + \|Q\|$	$\|I\|$	$\|I\| + \|Q\|$	$\|I\|$	$\|I\| + \|Q\|$
10^{-1}	1.6	0.2	3.4	0.2	9.1	0.2
10^{-2}	2.2	0.3	3.6	0.3	9.9	0.4
10^{-4}	2.4	0.4	4.0	0.4	10.5	0.5
10^{-6}	2.5	0.5	4.4	0.6	10.7	0.6
10^{-8}	2.5	0.6	4.6	0.7	10.8	0.7

B. Signal-to-Noise penalty for steady target,* dB

False alarm probability, P_N	$P_D = 0.2$		$P_D = 0.5$		$P_D = 0.9$	
	$\|I\|$	$\|I\| + \|Q\|$	$\|I\|$	$\|I\| + \|Q\|$	$\|I\|$	$\|I\| + \|Q\|$
10^{-1}	1.6	0.15	2.4	0.15	10.4	0.25
10^{-2}	1.5	0.30	2.7	0.35	12.0	0.40
10^{-3}	1.5	0.35	2.8	0.40	12.8	0.55
10^{-4}	1.5	0.45	2.8	0.55	13.2	0.70
10^{-6}	1.4	0.50	2.8	0.65	13.7	0.75
10^{-8}	—	0.50	—	0.70	—	0.85

* Averaged over all possible values of target phase. Greatest of $|I|$ or $|Q|$ gives the same loss as $|I|$ or $|Q|$.

Table 12.7. In addition there is about a 2.40-dB average range cusping loss if the full 255 code is used since the target echo may straddle adjacent bits in the registers. This loss is about 1.2 dB if the number of stages in the I and Q registers is twice the number of segments in the code [567]. The range cusping loss is discussed in Chap. 14.

Some advantages of this type of processor that were not mentioned previously include freedom from adjustment and the inherent reliability of microelectronic digital circuitry. Also, the maximal-length code transmitted by one radar does not cause false targets to appear on another radar that uses a different code.

Since two signal registers are effectively four phase quantization levels, a similar configuration can be used to decode four-phase codes.

As in bipolar video processing, one of the principal bottlenecks in digital pulse compression has been the computation of the square root of the sum of the squares of the outputs of the I and Q channels. An excellent approximation to $(I^2 + Q^2)^{1/2}$ is to use the larger of $|I| + 1/2|Q|$ or $|Q| + 1/2|I|$ with a simple logic circuit to decide which is larger.* An even simpler approximation is to use $|I| + |Q|$ or the larger of the

* This will reduce the loss in detectability to about 0.2 dB.

two. With this simplification the loss in detectability is less than 0.65 dB for $P_D = 0.5$ and $P_N = 10^{-6}$ for the steady- or fluctuating-target cases. Table 12.7 shows the losses compared with the sum of squares resulting from the various approximations. The losses are slightly different for steady and fluctuating target models [452, 740].

With the advent of fast, dedicated microprocessor chips such as the Plessey Pythagoras Processor, which is hard-wired to compute $(I^2 + Q^2)^{1/2}$ given I and Q, there should be less need for the approximations already cited.

Modern technology has also made great strides in producing integrated hardware for the computation of the autocorrelation itself. Integrated circuit correlation chips have been introduced that can achieve throughput in the tens of MHz. Figure 12.16 is an example of a compressor configured utilizing Inmos A-100 signal processing chips [131]. A radar system utilizing such a processor could implement a simple pulse, Barker codes, a 5×21 (105-bit) combined Barker and MPS code for operational flexibility. The compressor in the figure can be reconfigured on a pulse-by-pulse basis to accommodate any of these waveforms. The most stringent compression requirements come with utilization of the 105 to 1 pulse compression waveform. The filter implemented for the 105-bit waveform is the concatenation of a 59-bit optimal ISL mismatched filter for the 21-bit MPS component code and a 17-bit optimal ISL filter for the 5-bit component code. The 59-bit filter is implemented by the serial combination of the two processors shown in the upper left of the figure. The outputs from this stage of compression are stored in a 25-MHz random access memory (RAM) in preparation for the second and final stage of compression. The second stage is implemented by the parallel operation of five more A-100 processors, shown on the right-hand side of the figure. Each of these is loaded with the 17 coefficients necessary for compression of the 5-bit outer code. Compression is achieved by routing the outputs of the first stage sequentially, one sample per processor, at a 25-MHz rate, to the bank of five processors. In this way, the input to each processor occurs at a 5-MHz rate, with precisely the spacing between samples that is necessary to accomplish compression of the 5-bit outer code. Thus, one-fifth of the range bins are compressed in each of the five second-stage processors.

What has been described above is the compression of one (either the I or the Q) channel of this fully coherent system. The results of these operations are saved in RAM while the data from the other channel are routed through the same compressor configuration. When the I and the Q channels of all the range bins have been compressed, then the channels are combined as $(I^2 + Q^2)^{1/2}$ in software.

Figure 12.17 gives a simulation of the compression of a point target

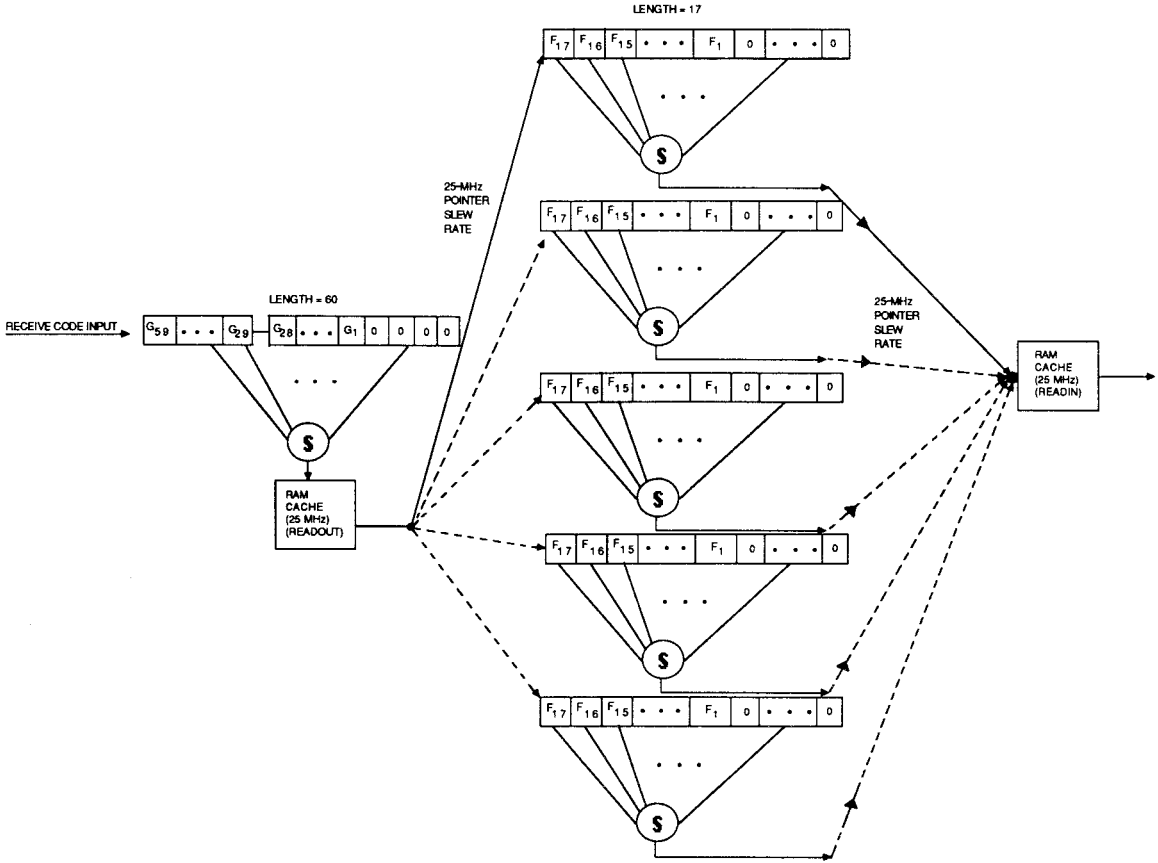

Figure 12.16 Compressor configuration assuming a maximum 5 × 21 transmit code and 17 × 59 mismatch filtering.

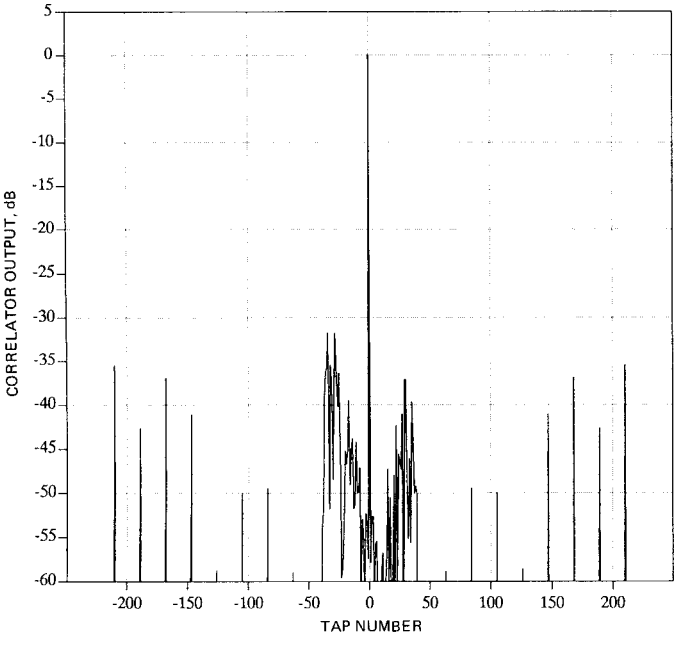

Figure 12.17 Compressed return for 5 × 21 concatenated code through a 17 × 59 mismatched filter.

through the processor. The pulse compression ratio is 105 to 1. The PSL and ISL are less than −30 and −20 dB., respectively. Although it may be difficult to discern in the figure, the structure of the 5-bit Barker code compression (through its 17-bit filter) is present as sidelobes separated by 21 bits, and each of these is surrounded by the structure of the compression of the 21-bit code.

Another implementation for the compression of biphase codes is the utilization of FFT microprocessor chips for the computation of what has come to be called *fast convolution*. Fast convolution consists of computing the Fourier transform of both the code and filter, multiplying the results, and then taking the inverse transform. This technique takes advantage of the fact that convolution in the time domain corresponds to multiplication in the frequency domain, as well as the efficiency of modern FFT computation. Some care must be taken in such an implementation, such as reordering the inputs (to compute correlation instead of convolution) and zero filling one or more of the FFTs to ensure that a linear (aperiodic) correlation rather than a circular (periodic) correlation is computed. Nevertheless, fast convolution is often found to be more efficient than time domain correlations when the codes are, approximately, 64 to 128 bits or longer and the number of range bins to be compressed is not too large.

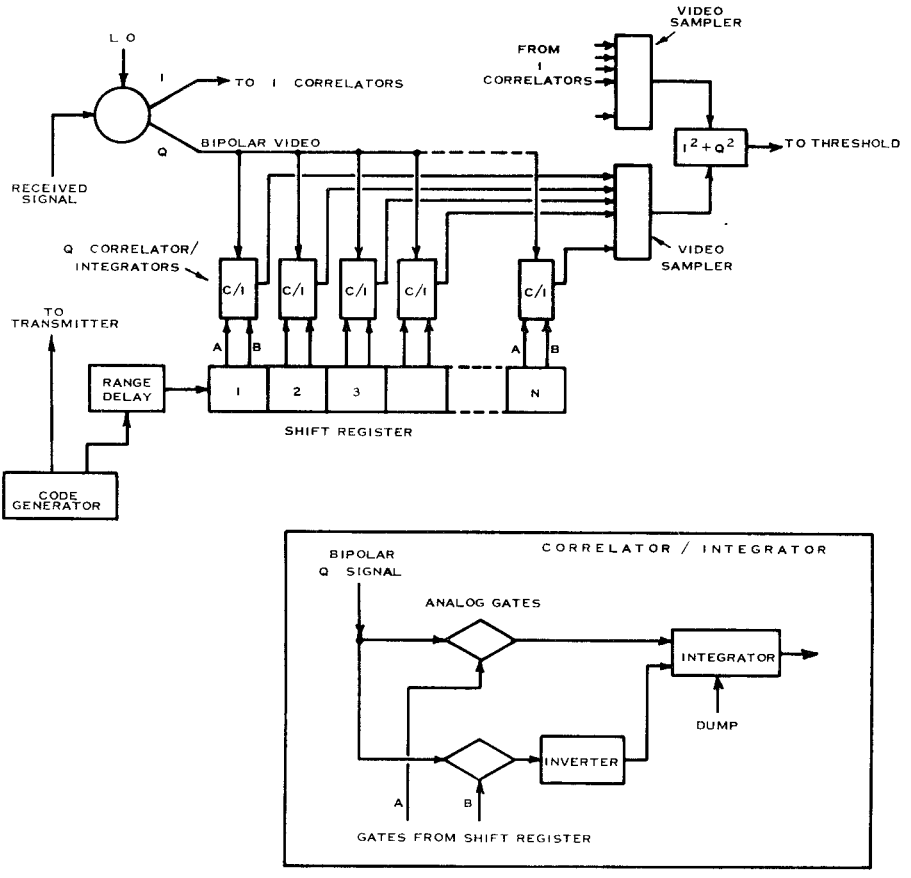

Figure 12.18 Functional block diagram of range-gated correlator. (*Courtesy of M. Davidson*)

12.7 Cross Correlators and Tracking Techniques

If the target range is approximately known, one or more cross correlators can be used to acquire and track the target echoes. The basic block diagram of a multiple correlator that is useful if Doppler shifts can be neglected or compensated for is shown in Fig. 12.18. It is illustrated here in the I-Q configuration. The I and Q components of the signal appear at a succession of correlator-integrators, each of which corresponds to a fixed range delay. To consider the action of a single correlator channel, it is simplest to assume that the code generator* is started at the instant that the bipolar received signal appears at the

* The range delay to the target will be neglected temporarily.

first correlator-integrator. The first stage of the shift register is either in the one or zero state corresponding to the first bit of the code, and energizes either the *a* or *b* line to the correlator-integrator *C/I*. As shown in the insert, this either passes directly or inverts the bipolar video signal while preserving its amplitude. At a subsequent time corresponding to the one-segment duration of the code, the second bit appears at the first stage of the shift register and the first *C/I*. If there was an inversion in the code, the shift register energizes the opposite gate of the *C/I*, and the signal applied to the integrator has the same polarity as the first bit. Thus, if the code is entirely aligned, the received voltage of all N bits is integrated. A similar integration process occurs for signals in the I channel. At the other integrators, cross correlations of the codes appear, and the polarities of the segments are almost random. At the end of the N segments the sidelobes appear on the other integrators. At the termination of the N-segment correlation code the levels in the integrators correspond to the sidelobes of the autocorrelation waveforms as discussed in previous sections. Obviously the integration continues if the code is repeated as a sequence both in the transmission and in the shift register. This circuit then becomes a compressor for a CW code.

When this type of compressor is used for coded words, the range coverage can be increased indefinitely by running the code continuously into the shift register but dumping the integrators at the end of each sequence for each stage. In this case, each *C/I* periodically observes many ranges each separated by $N\tau$. The video sampler must then be sequenced to yield the range-dependent signals (to the $I^2 + Q^2$ circuit) similar to those which would appear on a conventional range display. In any of these alternate configurations the various previously discussed approximations can be made to $I^2 + Q^2$, or the exact output can be obtained with the Plessey Pythagoras Processor or a similar chip [553].

In sum, the basic configuration and its variants represent an excellent example of a discrete matched filter since the integrators perform the filtering on bipolar video signals. Since this is a discrete operation, a loss in sensitivity (range cusping loss) occurs if there is a fractional segment length time mismatch between the shift-register code and the received signal.

The determination of coarse target range is merely the determination of which *C/I* receives a signal that exceeds a preset threshold. If range is known to within approximately plus or minus one code segment, a simple fine-range tracker can be constructed with only two correlator-integrators. The range-delay circuit is set such that the target's expected range straddles the first two *C/I* circuits. If the prediction is good, approximately one-half the voltage will be integrated on each

circuit. For any small errors in estimation the voltage will be split proportionally. Thus, a range error signal can be derived from the ratio of the integrated voltages. This compressor is a version of an early-late gate or split gate range tracker. If short-coded pulses are used, the I and Q signals are gated into their respective integrators only for the predicted duration of the pulse envelope.

An alternate technique of deriving the range error signal is to invert the polarity of the $I^2 + Q^2$ output from the first *C/I* and add it to the $I^2 + Q^2$ output of the second *C/I*. The difference of these signals versus range error has the appearance of a range discriminator characteristic. Such a characteristic is shown in Fig. 12.19, curve *a* (neglecting the self-noise of the range sidelobes of the code). The difference signal can be filtered and used to vary the range-delay circuit with one polarity increasing the range-delay prediction and the other signal decreasing it for subsequent input signals. The amplitude of the difference signal when normalized to the total input signal power determines the amount of correction. The use of a limiting amplifier prior to the final mixer is one such form of normalization.

A somewhat simpler version of the range tracker for phase-coded waveforms is shown in Fig. 12.20. In this form the delayed code is used to switch the phase of the *local oscillator* (LO) signal to decode the received signals. The received signal is amplified (and sometimes limited), divided into the early and late channels, mixed to dc, and integrated. A time delay of the order of the segment length is inserted to form the early channel. In alternate configurations, the delay may be placed in the appropriate LO line or may be obtained from the outputs of successive states of the shift register that forms the delayed-code generator. The shift register outputs are used to switch a pair of phase-inverting switches in two separate LO lines similar to Fig. 12.13. This final variation is sometimes called the delay-lock tracking discriminator [679, 194].

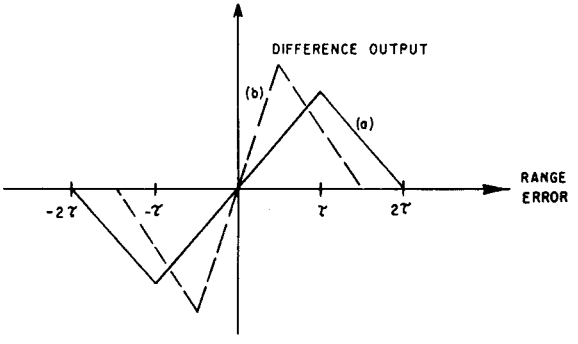

Figure 12.19 Early-late integrator difference output versus range error (unfiltered).

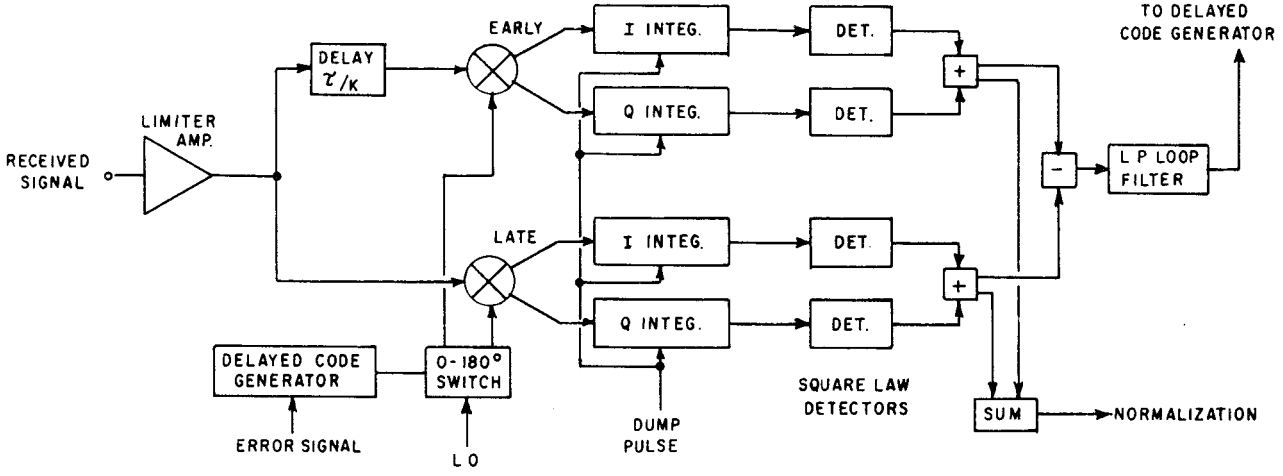

Figure 12.20 Switched LO linear decoder and range tracker, range determined from contents of delayed-code generator.

In all of these compressors, one channel is typically delayed by one-half to two segment lengths from the other, with the variations between them dependent on the nature and location of the delay element. The choice of the delay time* τ/K is a compromise between the error sensitivity of the range circuit, the pull-in range, and the efficiency or threshold level required for small signal-to-noise ratios [478]. If the delay time between early and late channels is less than τ, the discriminator characteristic has a steeper slope as in curve *b* of Fig. 12.19, but a small pull-in range ($\sim \pm 1.5\tau$).† As the delay is increased, the range-error sensitivity decreases, but a greater pull-in range is achieved. Discussions of the optimum choice of parameters for the generalized radar split-gate tracking process are available in texts such as Barton [39] and Mityashev [479, Chap. 2], but descriptions for tracking of phase-coded signals are primarily limited to the communications field.

12.8 Phase-Coded Words—Noise and Clutter Performance

The performance of radar systems using phase-coded waveforms in the presence of noise, clutter, or undesired targets is not difficult to calculate for binary-coded words.

Phase-coded words—noise performance

In computing detection range, either of two methods gives a close approximation to the correct answer for the matched-filter receiver competing with receiver or jamming noise.

1. In the denominator of the range equations, the noise bandwidth term B_N can be made equal to the equivalent matched-filter bandwidth with the uncoded pulse.
2. The noise bandwidth term B_N can be made equal to the matched-filter bandwidth of the segment length, and then the number of segments N must be placed in the numerator of the range equations to account for the coherent integration of the segments.

In both cases the required (S/N) for detection must be determined by using a desired false alarm number n', which is based on the number of segments in the observation range.

---

* K is a constant that is usually between one-half and two.

† In practice, the matched filtering will smooth out these curves and extend them in the range error direction.

The losses due to deviations from a matched-filter L_s are not easy to formulate concisely. Some simple examples include:

Limiting loss: If the signals are limited at RF or IF before decoding, the loss in detectability is approximately 1 dB if N is greater than about 63, for $P_D \cong 50$ percent, $P_N \approx 10^{-6}$ (see Chap. 4).

Quantization loss: If the compressor is all digital (see Sec. 12.5) and only 1 bit deep, as in the polarity-coincidence detector, the quantization loss is approximately 1 dB for large N in addition to the limiting loss (see I. Jacobs [363]). If there are two bits in both the I and Q channels, the total limiting and quantization loss reduces to 0.5 dB [567].

Range cusping loss: If there is a time mismatch between the stored waveform and the target echoes, there is a sampling or range cusping loss. If the time mismatch is one-half a segment length, the target signal in both of the adjacent range outputs is reduced by 6 dB. The average cusping loss is only about 2 to 3 dB and depends on the matched-filter bandwidth and on the type of postdetection filtering or integration. This loss is about 1.2 dB for two samples per τ.

Velocity compensation loss: If the target range changes by an appreciable portion of a carrier wavelength during the time duration of the entire pulse of N segments, the summation of the N segments does not yield N^2 at the matched-filter output. If there are no Doppler filters, the output is proportional to the voltage summation of the N segment vectors, each differing slightly in phase

$$e_o \sim P_o^{1/2} \sim \sum_{n=1}^{N} \cos\left[2\pi f_d \tau n + \Phi\right] \tag{12.9}$$

where p_o = power output
f_d = Doppler frequency
τ = segment duration
ϕ = phase to the target

As an example, for the case of a target with a radial velocity of 1000 ft/s (Mach 1) at a carrier of 3 GHz, the Doppler frequency is about 6 kHz. If the segment length is 3.3 μs, the phase shift per segment is about 0.13 rad. If there are only 10 segments in the code, the loss in signal power is only about 2 dB. If the code length is 50 segments, the signal essentially disappears.

Phase-coded words—clutter performance

The performance of the phase-coded words in a distributed clutter environment can be estimated from the simple pulse radar equations

for clutter (given in Chap. 2) if the segment length is used to determine the resolution cell rather than the envelope of the transmitted pulse. The alternate forms and primary correction factors to these equations are now discussed.

In discrete clutter or in multiple-target environments, the radar cross section of the clutter can be used directly in computation of the signal-to-clutter ratio (S/C). In simplified form, predetection signal-to-clutter ratio is given by

$$\frac{S}{C} = \frac{\sigma_\tau(\text{CA})}{\sigma_c}$$

where σ_c = the radar cross section of the undesired scatterers. The square of the ratio of the number of segments to the time-sidelobe peaks for the rms sidelobe level affects the clutter attenuation factor CA. For the Barker codes, this ratio is simply N^2 for the peaks and $2N^2$ for the rms sidelobe level. The choice of the peak sidelobe level or the rms sidelobe level must correspond to the choice to be used in the denominator of the clutter equations. Figure 12.21 shows that there is a 4- to 5-dB main peak-to-highest sidelobe advantage by using the PN codes with the lowest peaks. Polynomials and starting points corresponding to the better codes were given in Table 12.3.

In a distributed clutter environment where the range extent of the clutter is greater than the transmitted pulse length $N\tau$, the segment length ($c\tau/2$ in distance units) is used to determine the resolution cell. A loss term must be entered to account for the time sidelobe contributions. Since there are $2N - 1$ time sidelobes, the mean-square sidelobe value must be multiplied by $2N - 1$ and compared to N^2 at the peak.* (Note that this measure is very similar to ISL, as defined earlier.) A linear processor is assumed. Table 12.8 has been calculated (see [569]) from Table 12.7 to show this degradation for the maximal-length codes. This table was computed for discrete one-segment length offsets of the autocorrelation functions. A slightly different result would be obtained if correlation between adjacent sidelobes of the autocorrelation functions were included [567]. Several manual calculations have shown that the difference in compuation technique yields a minor error, and the degradation column in the table is slightly pessimistic. It can be seen that, for the better codes, the degradation is only about 1 dB and is almost independent of code length. An entry is shown for

* It is assumed that the transmit pulse length is small enough compared with the target range to neglect the range-dependent terms.

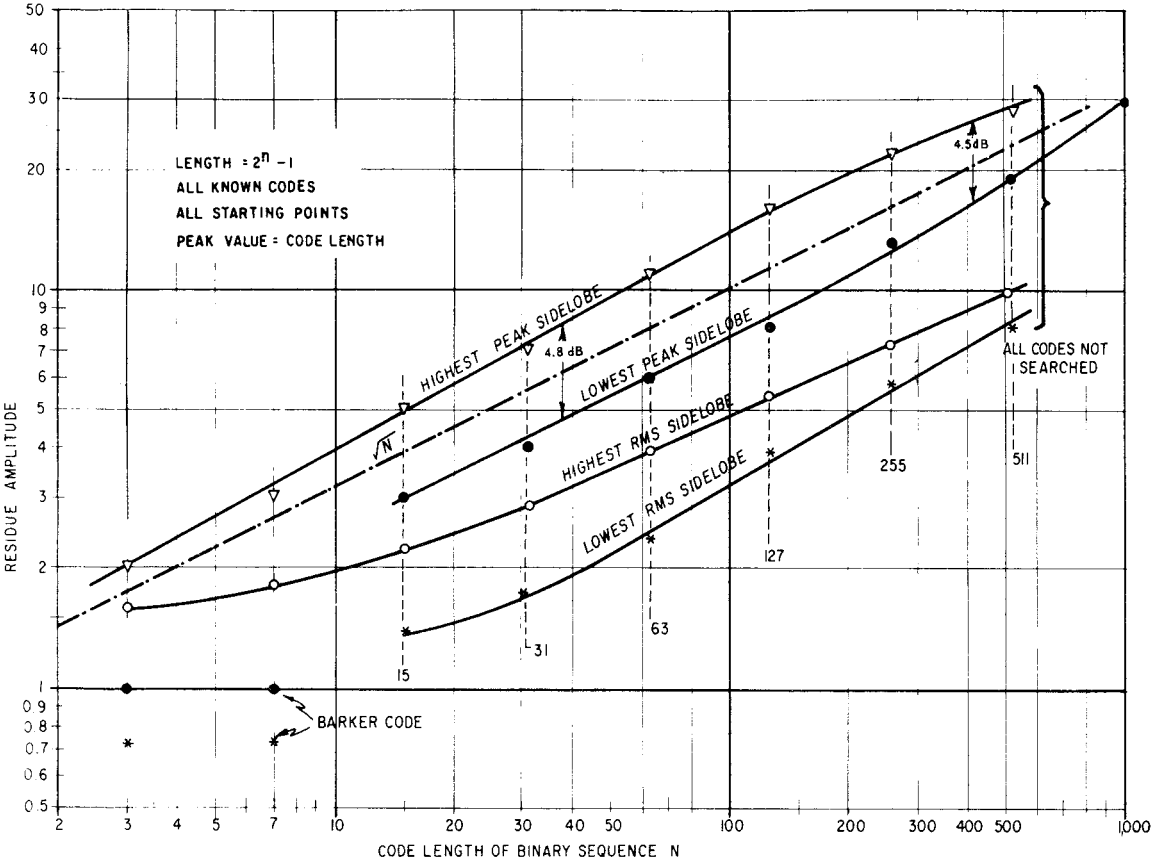

Figure 12.21 Maximum and minimum values of binary PN phase-coded residues.

TABLE 12.8 Range Sidelobe Clutter Contributions for Barker and Maximum-length Binary Phase Codes

Code length, N	Least rms* sidelobes	$1 + \frac{2(N-1)}{N^2}$ (mean-square sidelobes)	Degradation L_S dB
3 (Barker code)	0.707	1.22	0.88
7 (Barker code)	0.707	1.12	0.51
13 (Barker code)	0.707	1.07	0.3
15	1.4	1.24	0.94
31	1.7	1.19	0.75
63	2.4	1.18	0.70
127	3.9	1.24	0.93
169 (Barker squared)§	—	1.15	0.6
255	5.9	1.27	1.05
511†	8.0	1.25	1.0
511 (Noise codes)	~16.0	~2.0	~3.0

* Computed for discrete code shifts of one segment. The mean value is -0.5.

† Not all codes searched.

§ It can be derived from results in [178] that for combinations of Barker codes the rms sidelobe contribution increases the total clutter power by the factor

$$1 + \frac{N-1}{N^2}\left[\frac{L_o^2(L_i-1) + (L_i-1)(L_o-1) + L_i^2 L_o - 1)}{L_o L_i - 1}\right]$$

where L_i = number of segments in the *inner* code
L_o = number of segments in the *outer* code
$N = L_i L_o$

511-segment noise codes, which illustrates that the sidelobe degradation in (S/C) with distributed clutter is about 3 dB for these codes [567]. From Fig. 12.21 it can be seen that the poorest codes give a few decibels of additional degradation for small values of N.

13

Frequency-Modulated Pulse Compression Waveforms

F.E. Nathanson

M.N. Cohen

This chapter includes a discussion of the most widely used forms of pulse compression, those that fall into the general class of frequency modulation. Frequency-modulated (FM) waveforms can entail linear (LFM) or nonlinear (NLFM) modulation of the frequency of the transmit waveform. These modulations can be implemented either within a single coded pulse (intrapulse modulation) or on a pulse-to-pulse basis (interpulse modulation). Also, the frequency modulation may be achieved via either an analog (continuous) or a digital (discrete) process.

Since both frequency and phase modulation are forms of angle modulation, the discussion begins with an example relating FM and phase-coded waveforms. In the rest of the discussion, the formulation, generation, and processing of classical coded pulse LFM as well as more recently developed NLFM and interpulse waveforms are treated.

13.1 Multiplicity of Frequency-Modulation Techniques

It was shown in the chapter on signal processing concepts and waveform design that the basis of improved range resolution is some form of

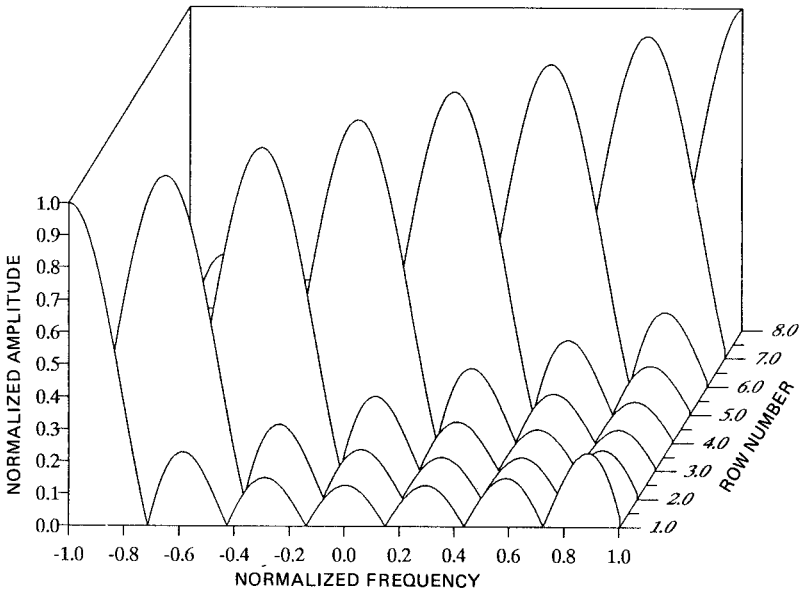

Figure 13.1 Spectra of the rows of a 64-segment Frank code.

modulation or coding within the envelope of the transmit pulse that widens the signal spectrum. While binary or 0-to-180° phase coding accomplishes this same end, it is not categorized as frequency modulation, and was therefore treated separately in Chap. 12.

It is interesting to note that the Frank polyphase codes (Sec. 12.5) are actually a phase approximation to a frequency code. If the Frank code for 64 segments is written as an 8×8 matrix with segments 1 through 8 making up the first row; segments 9 through 16, the second; etc., and the spectrum is calculated for each row, a series of spectra is obtained as shown in Fig. 13.1. Each row approximates a narrow-band carrier, and the movement of the carrier from row to row is linear, as can be seen from the figure. The total spectrum of the 64-segment pulse may be considered as that resulting from the sum of the spectra shown.*

Two conclusions can be drawn from this figure. First, the more or less linear frequency variation versus time makes this waveform somewhat ambiguous in the range Doppler plane of the ambiguity diagram. A single Doppler channel receiver is thus tolerant to greater Doppler shifts with this waveform than with a binary phase-coded waveform, though not as tolerant as FM. Second, the tapering of the spectrum envelope leads to low pulse compression time sidelobes. Typical values

* Details of the overall spectrum can be found in Cook and Bernfeld [71].

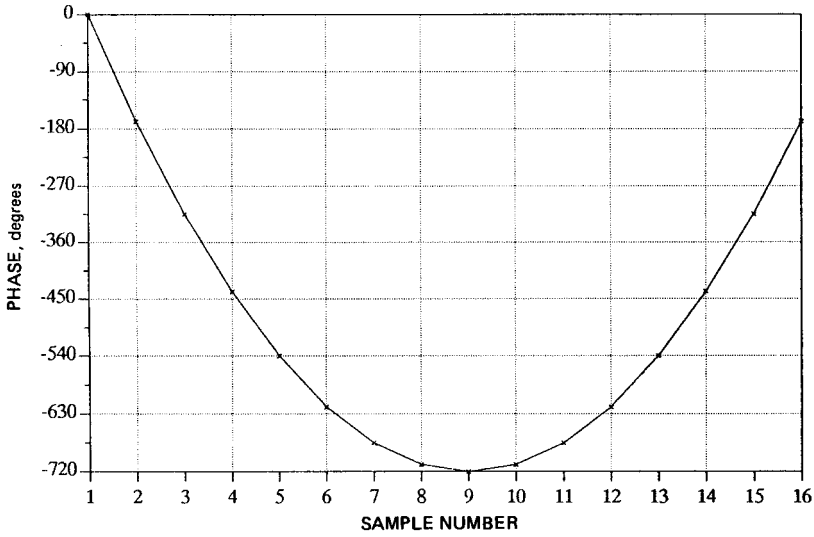

Figure 13.2 The phase function of the P4 code.

for those sidelobes were shown in Chap. 12. The subject of range sidelobe reduction for FM waveforms is explored further in Sec. 13.9. Similarly, the phase function of the P4 codes (Sec. 12.5), as given in Fig. 13.2, can be seen to be a discrete approximation to quadratic phase, and quadratic phase is characteristic of LFM waveforms. Indeed, the P4 codes can be shown to be a 2-to-1 undersampled (both on transmit and receive) discrete representation of an LFM waveform, and so they share many of the properties of such a waveform [128]. Thus, the distinction in terminology between frequency and phase coding is primarily dependent on how the modulation is imposed on the waveform, rather than on the underlying structure of the waveform.

While the generation of linear FM or *chirp** waveforms has in the past been based on the use of passive dispersive delay lines, much of the description in this section is based on active generation of the desired waveform by the use of *voltage-controlled oscillators* (VCOs) and discrete frequency techniques. In the latter implementation of FM waveform generation, the transmit spectrum is formed by the summation of a coherent series of short-duration RF pulse segments, each of which is selected from a comb of coherent frequencies. When passive generation techniques are discussed, *surface acoustic wave* (SAW) devices are emphasized. This departure from the conventional description of chirp systems [403] can be justified in a number of ways:

* A common term for linear FM radar signals coined by B.M. Oliver of the Bell Laboratories in 1951.

1. The description of the properties of chirp techniques is by far the best documented of the radar signal-processing techniques; and rather than repeat earlier analyses, the reader is referred to the excellent articles by the personnel of Bell Laboratories (Klauder and Price [403] and those of the Sperry Rand Corporation [64, 136, 529]. The original FM concepts are contained in patents that date back to 1940 and are described in these references.*
2. Modern technology has allowed the development of VCOs, digital synthesis techniques, and SAWs that permit much tighter control of important transmit waveform parameters, such as linearity with frequency and flat amplitude response, than do the more classical RF and IF dispersive delay techniques that have been employed in older systems.
3. It can be shown that virtually all the desired properties of linear FM are achievable by transmission of discrete frequency segments. These include the reduction of time sidelobes, the ability to improve target resolution and signal-to-clutter ratio, the ability to achieve greater detection range for a given peak transmitter power, and the capability of achieving automatic detection with a hard-limited receiver [664, 521, 767, 260].
4. With discrete transmission of frequencies, it is possible to utilize an approximation to linear FM and accept the range Doppler ambiguity with perhaps slightly more hardware than is needed for analog techniques. However, accepting this penalty yields a more flexible means of waveform generation. For example, it is possible to scramble the ordering of the frequencies to eliminate the FM ambiguity and replace it with a *thumbtacklike* ambiguity function. This would eliminate the major range Doppler uncertainty but yield a general increase in the sidelobe level throughout the ambiguity plane.
5. It is shown that in an interpulse system, extremely high time-bandwidth products can be achieved via discrete frequency stepping, and that this can be accomplished by utilizing receiver components that have instantaneous narrow-band characteristics. Very high bandwidths and time-bandwidth products can also be achieved in systems that utilize phase-locked VCO generation or digital frequency synthesis and upconversion generation techniques in the transmitter and active correlation (stretch) techniques in the receiver.

The summary of general characteristics of chirp-type signals and receivers given in Secs. 13.2 through 13.4 extends the ambiguity dia-

* Darlington's patent (No. 2,678,997) described chirp by means of linearly stepped frequencies as well as dispersive techniques.

gram discussion in the signal-processing section. It was noted there that a rectangular spectrum is generally desirable for maximizing clutter rejection [460]. In addition, a rectangular time function is the simplest to transmit with most types of transmitter power amplifiers. Sec. 13.3 contains a description of how both these goals can be achieved simultaneously.

13.2 Linear FM Pulses (Chirp)

By far the most widely implemented technique for pulse compression is the use of linear frequency modulation during the pulse. Many of the goals of waveform design can be attained with relatively simple dispersive devices. The desired transmission energy can often be obtained by the choice of the requisite pulse length, while the desired resolution can be independently specified by the frequency deviation. Improved performance over uncoded pulses is obtained in distributed clutter environments, and the receiver can be a constant false alarm rate device to cope with broadband noise interference.

Unfortunately, chirp is not a universally desirable waveform; hence the emphasis in previous sections on the multitude of other waveform modulations. The lack of unambiguous range and velocity resolution, discussed in the chapter on signal-processing concepts and waveform design, sometimes results in inadequate performance in sorting out targets, land and sea clutter echoes, decoys, and dense rain and chaff echoes. It would be in sharp contrast to the related field of communications if a single waveform with a single relatively simple matched filter were adequate for all environments.

13.3 Generation and Decoding of FM Waveforms

In the design of a simple chirp system, the first parameter to be chosen is the duration of the pulse envelope, given the peak transmitter power. This determines the pulse energy and allows the prediction of the detectability of a given target model at a given range. Second, the desired resolution determines the bandwidth of the transmission and therefore the performance in a distributed clutter environment.

One class of techniques for generating a long-duration FM signal is the so-called passive one illustrated in Fig. 13.3. An IF pulse of the approximate length of the desired compressed pulse is generated and inserted into a dispersive delay device. Since the compressed pulse for a linear FM waveform has a sin x/x time envelope, it can be shown that the input to a linear dispersive delay should have a time waveform [136]

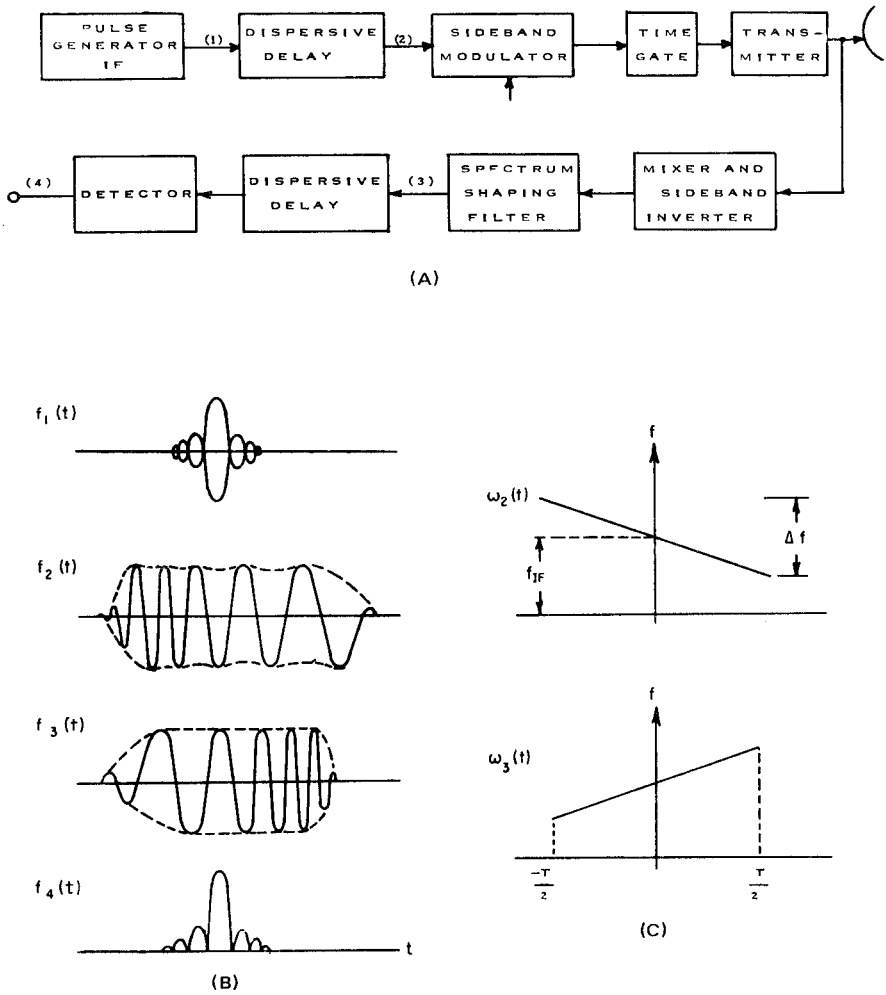

Figure 13.3 Passive system for linear FM pulse compression. (A) Generator and decoder; (B) waveforms (arbitrary time scale); (C) frequency versus time.

$$f_1(t) = \frac{\sin(\mu Tt/2)}{(\mu Tt/2)} \cos(\omega_{IF} t)$$

where $\mu = \Delta\omega/T$, the desired frequency slope at the dispersive delay output (the rate of frequency sweep)

T = the duration of the transmit pulse envelope

$\omega_{IF} = 2\pi f_{IF}$ = the radian center frequency of the dispersive delay line

After traversing the dispersive line the waveform is "up-mixed" (converted) to the desired carrier. Filtering out unwanted sidebands, the transmitted waveform can then be written as [64]

$$f_2(t) = \cos\left[(\omega_0 t) + \frac{\mu T^2}{2}\right] \qquad \text{for } -\frac{T}{2} \le t \le \frac{T}{2}$$

where ω_0 = the transmit carrier frequency. The generating waveform $f_1(t)$ can be obtained by passing a narrow pulse (radian bandwidth $> \Delta\omega$) through a rectangular bandpass filter of width $\Delta\omega/2\pi = \Delta f$. The filter must have a linear phase characteristic.

The dispersive delay devices were historically often composed of cascaded all-pass networks [136, 371]. More modern dispersive implementations include dispersive ultrasonic delay lines [213, 136], waveguide operated near cutoff [183], optical devices, and, most recently, superconductive striplines [455]. For purposes of this discussion assume that the technique utilized has negligible attenuation over the bandwidth Δf and a linear time delay versus frequency. The waveform at its output is shown diagrammatically in Fig. 13.3 as $f_2(t)$, its frequency-versus-time characteristic as $\omega_2(t)$. It should be noted that there is often a certain amount of amplitude ripple versus time at the transmitter input. With the usual saturation in the transmitter, there will consequently be waveform distortion at the receiver output. However, this distortion has a small effect with large compression ratios.

The sideband modulator is used to convert the FM signal to the desired carrier frequency, and a time gate is usually employed to form the rectangular transmit waveform. Upon reception, the echo is mixed with a local oscillator that yields the sideband inverse to that utilized on transmission [575]. By this technique the frequency-versus-time characteristic is inverse with respect to the transmitted signal as illustrated by $f_2(t)$ and $f_3(t)$. This technique permits the use of identical dispersive delays in the transmit and receive lines. In practice, the received signal is often inserted in the same dispersive delay as was used for transmission, thus reducing hardware and tolerance requirements.

The spectral shaping filter is used to reduce the -13-dB time sidelobes to a tolerable level at the cost of a slight reduction in signal-to-noise and signal-to-distributed-clutter ratios and at the further cost of an increase in compressed pulse width. In Sec. 13.9 various shaping filters and their characteristics are discussed. The detected waveform shown has a $|\sin x/x|$ form near its central lobe in the absence of spectral shaping. For a large compression ratio the waveform is similar to that shown in Fig. 13.9. The peak signal amplitude and, more importantly

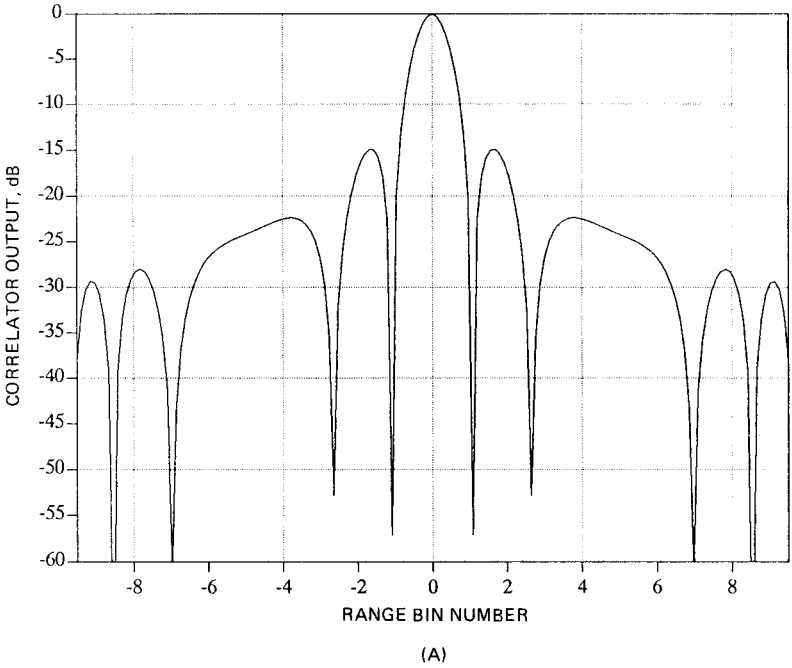

(A)

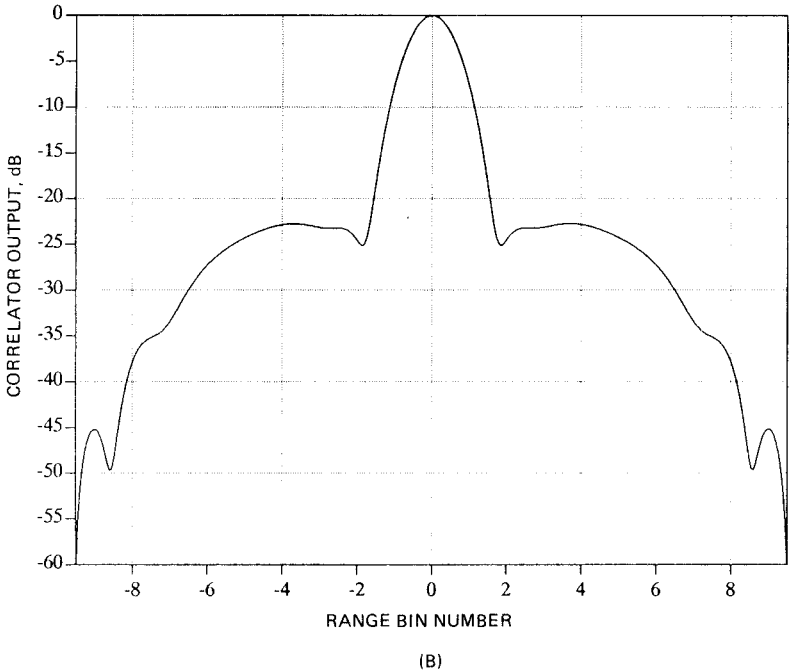

(B)

Figure 13.4 Linear FM code with TB = 10. (A) Matched filter; (B) Hamming weighted filter.

for pulse compression applications, its signal-to-noise ratio is increased by $T\Delta f$, and the pulse width is reduced by approximately the same factor. That is, range resolution is given by $\Delta\tau = c\tau/2 = c/(2\ \Delta f)$. For small time-bandwidth products, say $T\Delta f < 20$, the output waveform deviates from the $(\sin x)/x$ in its sidelobe regions. Figure 13.4A shows the compressed output from such a system whose time-bandwidth product is 10. As can be seen in the figure, the first sidelobes are approximately 15 dB down from the peak. However, whereas a Hamming-weighted, large-time-bandwidth-product LFM waveform exhibits peak sidelobes on the order of -40 dB, the same weighting applied to the waveform of Fig. 13.4A results in peak side-lobes on the order of -24 dB, as exhibited in Fig. 13.4B. The control of range sidelobes in the presence of Doppler mismatch is another potentially troublesome aspect of small-time-bandwidth-product LFM waveforms.

An alternate chirp generation technique that utilizes active generation of the FM waveform is to apply a sawtooth or ramp modulation waveform to a voltage-controlled oscillator or a square-law modulation to a phase-controlled oscillator [136, 64]. Small variations in the modulation function can be injected to compensate for distortions elsewhere in the system.

If target range is not known, a dispersive delay matched filter is usually used in the receiver. Other techniques for generating and compressing a linear FM waveform are discussed in Secs. 13.10 and 13.12, and an excellent summary of more classical dispersive devices is found in Cook and Bernfeld [136, Chaps. 12, 13, and 14]. More recently, the move has been toward utilizing surface acoustic wave (SAW) devices, which typically operate at IF. The theory underlying SAW operation has been known for some time, but it was not until the 1970s that the technology became sufficiently mature for widespread application. Table 13.1 summarizes the operating frequencies, compression ratios, and range side-lobe levels that have been reported in the open literature for various types of surface acoustic wave devices that have been realized for application (that is, that have been built utilizing standard manufacturing procedures). The insertion losses typically associated with such devices range from 25 to 50 dB. Careful custom construction can allow for devices that achieve dispersions to 150 μs, bandwidths in excess of 1 GHz, time-bandwidth products up to 10,000, and sidelobes approaching -40 dB [109]. In most of these cases slight variations in pulse width can be traded for different peak sidelobe levels, but the sidelobe increase due to transmitter distortion (not included in the table) will generally preclude achieving peak sidelobe levels of better than -40 dB anyway. An example of the waveforms of a high-compression-ratio, passive linear FM system with sidelobe suppression is shown in Fig. 13.5. The peak sidelobes are -40 dB for the unit. A

TABLE 13.1 Characteristics of Typical SAW Devices

Center frequency, MHz	Bandwidth, MHz	Dispersion, μs	Compressed-pulse width, μs	TB	Peak sidelobe, dB	Remarks
30	6.3	13	0.22	60	27	Weighted FM*
60	6.5	6.7	0.22	30	33	Weighted FM*
60	10	100	0.175	571	30	Weighted FM†
80	20	20	.05	364	12	LFM†
120	7.5	28.5	0.193	148	30	Weighted FM*
123	54	4	0.02	2700	12	LFM†
240	20	13.4	0.083	161	30	Weighted FM*
266	132	16	0.008	2000	12	LFM†
521	30	15	0.037	405	12	LFM†
1300	500	0.56	.003	187	12	LFM*

* Interdigital transducer device (ITD).
† Reflective array compressor (RAC).

new variation on SAW-like devices is the *acoustic charge transport* (ACT) and *heterojunction acoustic charge transport* (HACT) devices developed in various laboratories around the country [612].

If target range and range rate are approximately known, then pulse compression may be accomplished synchronously via correlation. That is, in a tracking system or in other systems in which the target position is known to within the resolution of the uncompressed pulse, a frequency ramp similar to the transmitter's may be used for decoding in the receiver via active correlation of the received signal with the transmitted modulation. Such a correlation receiver is intrinsically different from the compressive receivers discussed in the foregoing. This technique, sometimes referred to as *stretch,* is discussed in more detail in Secs. 13.7 and 13.13.

13.4 Distortion Effects on Linear FM Signals

The effects of amplitude and phase distortion on pulse compression systems are best described by paired-echo analysis techniques [64, 403, 136] as follows in brief. In the frequency domain the distortion has been related to the transfer admittance of the system [403]

$$Y(\omega) = A(\omega) \exp [jB(\omega)]$$

The terms can be expanded into Fourier series of n terms

$$A(\omega) = a_0 + \sum_n a_n \cos (nc\omega)$$

$$B(\omega) = b_0\omega + \sum_n b_n \sin (nc\omega)$$

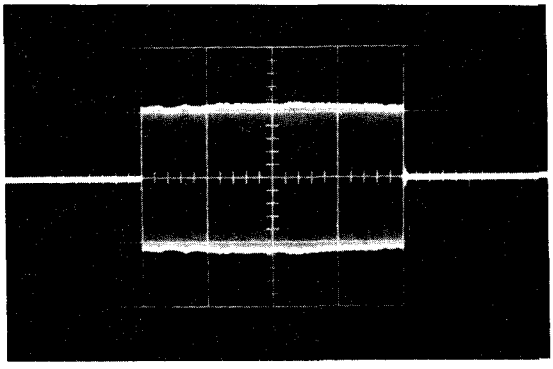

(A)

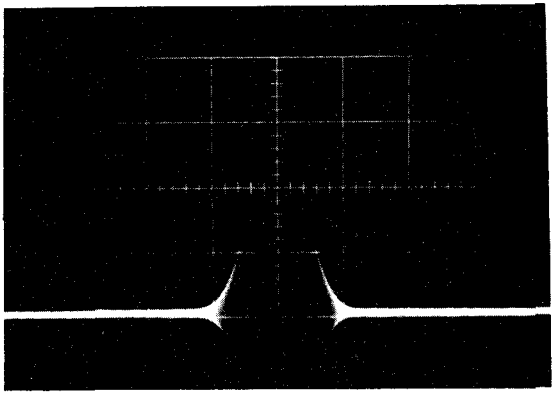

(B)

Figure 13.5 Transmit and receive waveforms of dispersive linear FM pulse-compression system. (A) Expanded pulse, transmit waveform, 30-MHz IF; (B) compressed pulse, 0.58 μs, −40dB sidelobes, horizontal scale 1 μs/cm. (*Permission of Andersen Laboratories*)

where for linear FM signals

$$\begin{aligned} c &= \text{complex constant} \\ a_n \cos(nc\omega) &= \text{amplitude distortion terms} \\ b_n \sin(nc\omega) &= \text{phase distortion terms} \end{aligned}$$

The system is considered ideal when $a_n = b_n = 0$, or the distortion terms are zero.

For small phase deviations ($<25°$), it is sufficient to consider only the $n = 1$ term. A graph of the highest paired-range sidelobes for various peak phase and amplitude errors is shown in Fig. 13.6 [403, 53, 519, 136]. It can be seen that for −40 dB range sidelobes, the amplitude

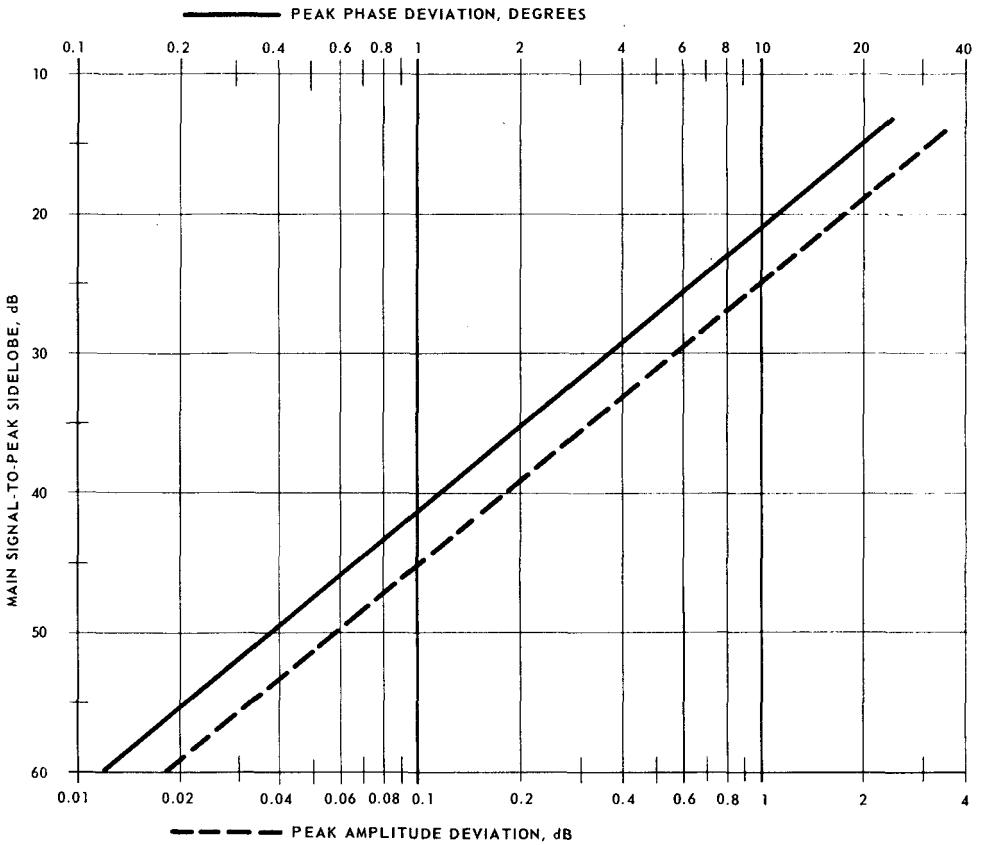

Figure 13.6 Peak sidelobe of linear FM signals with phase and amplitude distortion (paired-echo theory). (*After Klauder et al.* [*403*], *copyright 1960, American Telephone and Telegraph Co. by permission*)

must be held to ± 2 percent and the phase to within $\pm 1.2°$. These results assume a sinusoidal type of error versus time or frequency.

The results for random errors are more difficult to compute. Some limited experimental results involving only phase distortion for $TDf = 50$, uniform amplitude (no weighting); and 10, 20 and 30° of rms phase error are shown in Fig. 13.7. The far-out sidelobes for 20 and 30° error increase to -13.5 and -12.2 dB below the main peak [545]. The corresponding decreases in the mainlobe amplitude were 1 and 2 dB, and the increases in the mainlobe width were 15 and 19 percent. The ordinate is linear in amplitude.

The effect of transmitter-tube phase ripple b_1 on paired-echo sidelobes has been analyzed by Liebman (see Cook [136, p. 395]) and can be given as approximately

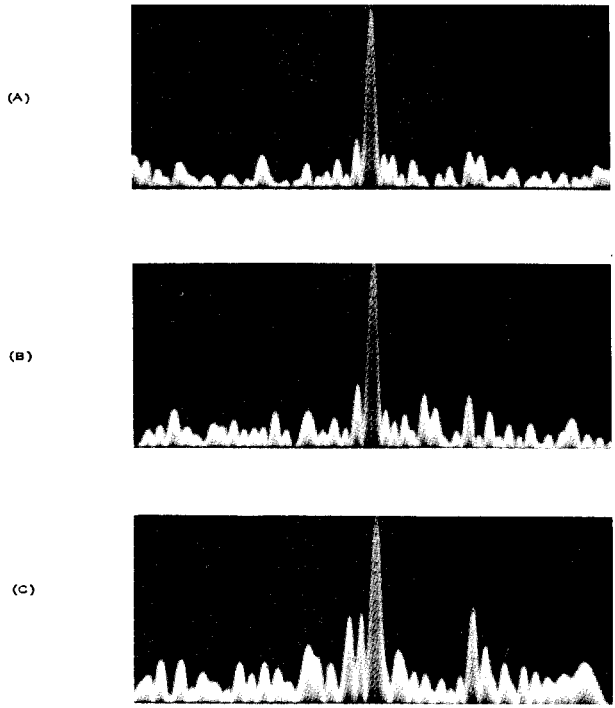

Figure 13.7 Typical compressed-pulse waveform (amplitude) for linear FM signal and random phase errors, $T\Delta F = 50$. (A) 20° phase error (std. dev.); (B) 30° phase error; (C) 40° phase error.

$$b_1 = K\left(\frac{\Delta E}{E}\right)\phi \quad \text{or} \quad b_1 = L\left(\frac{\Delta I}{I}\right) \text{ degrees}$$

that is, b_1 = K (voltage ripple ratio) (electrical length of device in degrees), or
= L (current ripple ratio)

Typical values for modern trasmitter components are given in Chap. 14.

13.5 Spectrum of a Comb of Frequencies

Consider the pulse waveform containing N equal-amplitude rectangular time segments of length t, each on a different frequency f_n. The envelope of this waveform is illustrated in Fig. 13.8A. The time origin will be taken as the midpoint of the first segment but otherwise conforms to an analysis by O'Neill [519]. The waveform of the nth segment or subpulse is given by

$$v_n(t) = A \exp j2\pi(f_n t + \phi_n) \qquad \text{for } \left(n - \frac{3}{2}\right)\tau < t < \left(n - \frac{3}{2}\right)\tau \tag{13.1}$$

where A = segment amplitude
f_n = frequency of the nth segment
ϕ_n = phase of the nth segment
$f_n - f_{n-1} = 1/\tau$ (see Sec. 13.6)

The Fourier transform of the segment can be written

$$V_n(f) = A \int_{(n-3/2)t}^{(n-1/2)t} \exp j2p(f_n t + \phi_n) \exp(-j2pft)dt \tag{13.2}$$

This can be shown to be equal to [519]

$$V_n(f) = A\tau \frac{\sin \pi[(f_0 - f)\tau + n]}{\pi[(f_0 - f)\tau + n]} \exp j[2\pi \left(f_0 - f + \frac{n}{\tau}\right)(n - 1)\tau] \tag{13.3}$$

where f_n is replaced by $f_0 + n\Delta f$ for a frequency spacing of Δf. Now let $\phi_n = n\phi_0 = 0$ (see Sec. 13.6). Then for N subpulses and after removing

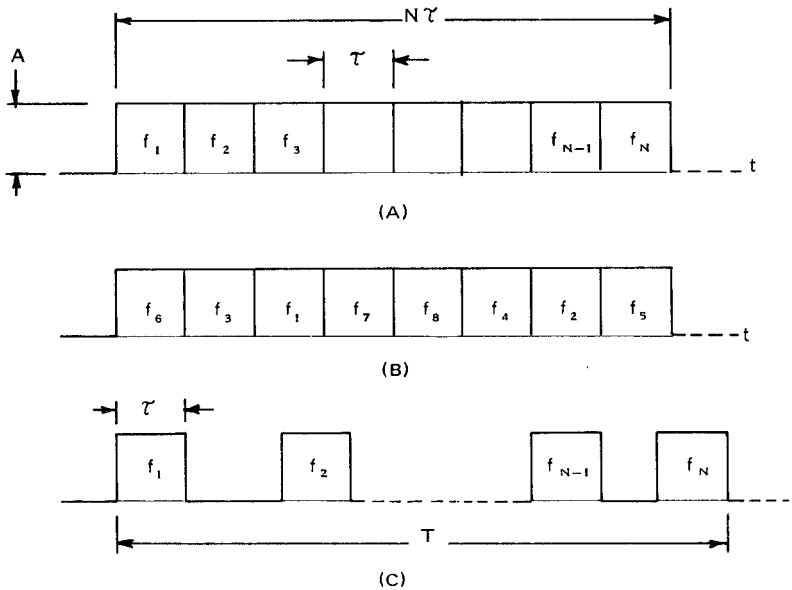

Figure 13.8 Discrete frequency waveforms. (A) Linear stepped-frequency pulse; (B) scrambled frequency-coded pulse; (C) multifrequency pulse train (shown for linear frequency).

the carrier term, the spectrum of the modulation of the entire pulse becomes

$$V(f) = A\tau \sum_{n=1}^{N} \frac{\sin \pi(f\tau - n)}{\pi(f\tau - n)} \exp j[2\pi(f\tau - n)(1 - n)] \qquad (13.4)$$

It is shown in later sections that the envelope of the compressed pulse out of the matched filter for this waveform has a $\sin x/x$ shape in the neighborhood of its mainlobe. The width of the compressed pulse at the 4-dB points is equal to τ/N for uniform weighting of the frequencies. Since the transmit envelope has a duration of $N\tau$, the pulse compression ratio $\approx N^2$. The matched-filter output waveform is illustrated in Fig. 13.9 for $N = 50$. The oscilloscope gain is increased in the lower photograph to show the range-sidelobe details. The response of the scrambled-frequency waveform of Fig. 13.8B yields different outputs depending on the sequencing utilized. In general, random sequencing of the frequencies results in a thumbtacklike ambiguity surface, destroying the range Doppler coupling generally associated with LFM. In Costas [143], ideal patterns for scrambled-frequency waveforms are defined. These patterns are further investigated in [282] and [283] and have since come to be known as Costas Arrays. When they are utilized, not only is the range Doppler coupling destroyed, but the range and Doppler sidelobes vary from $1/N$ far from the peak response to $2/N$ close to it, where N is the number of frequencies utilized.

It should be noted here that coherency is required in such a process to yield a high range resolution profile. That is, as noted earlier, the phases of the individual frequencies must be maintained between transmit and receive and the process must include compression on the IF signal or I and Q sampling of the received waveform. If, instead, one implements such a process by detecting the received signals [that is, by computing $(I^2 + Q^2)^{1/2}$] before compressing, then the result is the autocorelation of the range resolution profile, rather than the range resolution profile itself. While range resolution processing provides an absolute range map of the area of interest, the autocorrelation of the range resolution profile provides only the composite relative ranges between scatterers in the scene [202].

The waveforms depicted in Figs. 13.8A and B represent intrapulse techniques, that is, FM coding techniques that are implemented on a single-pulse basis, much like most of the phase codes from Chap. 12. The waveform depicted in Fig. 13.8C introduces the possibility of implementing frequency modulation of the transmit waveform on an interpulse basis. The preceding analysis, which describes the characteristics of the intrapulse techniques, applies to this waveform as well; however, there are important differences between these classes of tech-

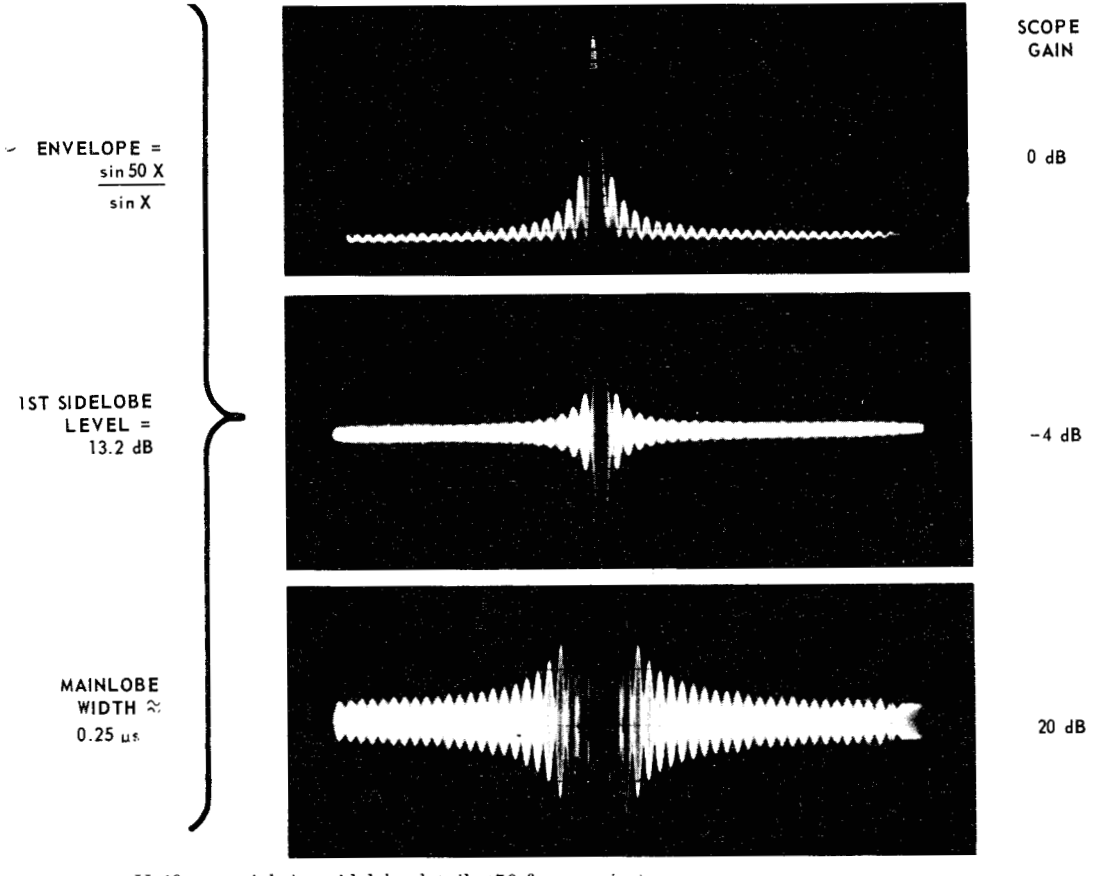

Figure 13.9 Uniform weighting sidelobe details (50 frequencies).

niques in terms of waveform generation, operational applicability, and receiver characteristics. These differences are explored in Secs. 13.6 and 13.7.

13.6 Waveform Analysis for Discrete Frequencies

The rigorous analysis of discrete frequency pulse compression loses touch with physical significance unless some restrictive assumptions are made about the relations among the various parameters, such as the spacing between frequencies Δf, the subpulse or segment length τ, and the phase of each of the subpulses ϕ_n. Figure 13.10 is the time waveform of the envelope of the coherent summation of eight continuous sinusoidal carriers spaced by exactly Δf in frequency. The bandwidth of the RF waveform is $N\Delta f$ and is assumed to be much less than the mean or carrier frequency f_c. The spectrum is periodic in frequency, and, as would be expected, the time waveform is also periodic with a repetition period of $1/\Delta f$. A typical transmit time waveform is shown in Fig. 13.11. With an even number of frequencies, a center carrier frequency does not actually exist as any one of the individual frequencies.*

The necessary condition for compression of the energy is that all the phasors (shown on the figure as small arrows) achieve colinearity at some time during the period. This condition is shown under the first envelope peak at time $t = 2n/\Delta f$. This condition need not be made to occur on transmission as long as there are the appropriate phase adjustments in each channel of a receiver such as shown in Fig. 13.12. As shown, the filters F_n are placed inversely in time to the transmission frequencies f_n. If the filter bandwidths are approximately $1/\tau$, a nearly matched receiver is obtained. Since the bandwidth of each channel is only $1/N$ times the total signal bandwidth, these channels can be seen to be relatively narrow-band as compared with the overall bandwidth achieved. The phase and amplitude response to the received frequency segments is controlled in the individual channels. This eliminates the requirement for components having phase and amplitude linearity across the total transmission bandwidth. In this simplified diagram, the coherent summer is simply a voltage adder, which is then followed by an envelope detector. If the phases are not adjusted for colinear vector addition at some instant of time, the periodic time waveform appears noiselike. However, with the proper adjustment, the phasors can be made to peak up periodically for all time, providing the generated

* From an analytic signal representation point of view involving Hilbert transforms, there would be no need to limit the discussion to a narrow-band comb spectrum or to designate a specific carrier frequency.

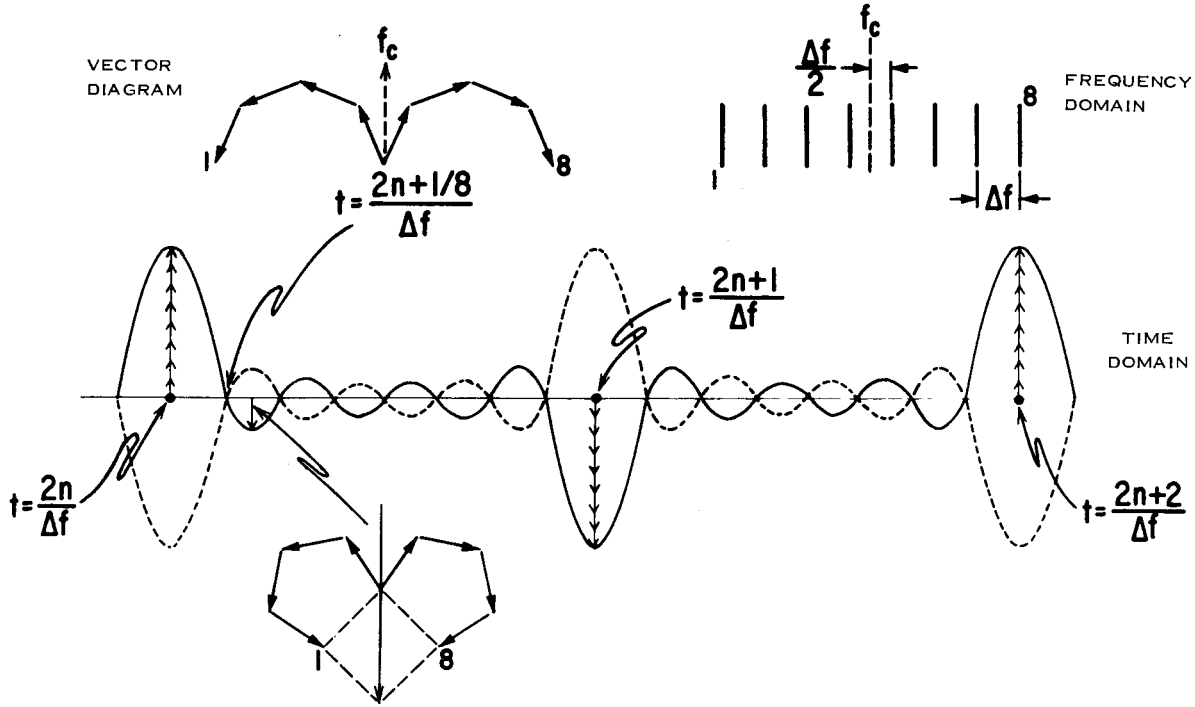

Figure 13.10 Eight-frequency compressed-pulse details.

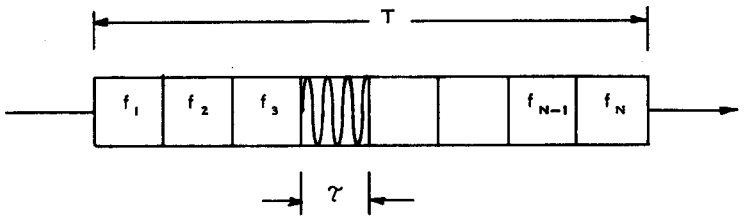

Figure 13.11 Transmit waveform for stepped chirp.

comb frequencies are truly coherent. This is essentially the definition of coherence for multifrequency systems. This condition can be made to occur if all the frequencies are derived from a single stable oscillator, either by mixing or multiplication.

The alternating polarities of the phasors in Fig. 13.10 at the envelope peaks occur with an even number of frequencies. With an odd number of frequencies, the center frequency can be considered the carrier and the phasors at the envelope peak always have the same polarity. In either case, if the mean frequency of the comb is much greater than the total spectral width, there are many RF cycles under the envelope, and the exact time of occurrence or polarity of the mathematical peak is of little importance in the detected output.

A result of these assumptions is that the phase ϕ_n of each of the N transmit frequency segments can be assumed to be zero. While this is a mathematical convenience, the results are valid as long as the phase responses in the individual channels of Fig. 13.12 are equal and opposite in sign to the phases of the corresponding received frequencies.

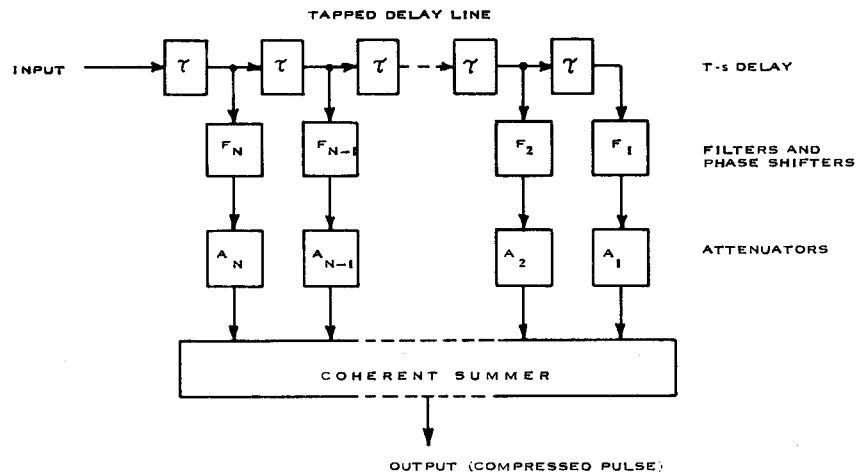

Figure 13.12 Stepped chirp matched filter.

The following discussion is based on the pulse sequential transmission of the frequencies, and the CW-derived periodic time waveform envelope previously discussed is not quite relevant. The envelope of the transmission on each frequency, which is referred to as the subpulse and which has a duration of τ, now determines what portion of that frequency is time selected for coherent summation with the other frequencies of the comb.

Figure 13.12 represents a compressive receiver for the discrete FM waveform and it can be implemented either at IF via analog processing utilizing a tapped delay line; dispersive devices like SAWs; or, at video- via digital processing, by first sampling the received waveforms at rates greater than or equal to $1/\Delta f$ and then implementing the equivalent of digital tapped delay lines for each of the I and Q components of the signal or as a pipelined fast Fourier transform (FFT) processor. As discussed in Sec. 13.13, compressive receivers, in conjunction with any of the discrete intrapulse FM techniques, allow a fairly simple implementation of all-range compression.

Before proceeding further it is desirable to make the assumption that the frequency spacing is equal to the inverse of the pulse length $\Delta f = 1/\tau$, and the subpulse envelopes are rectangular. This has the desirable effect of keeping the mathematics reasonable, but, more importantly, it yields the best waveform properties for most practical situations. The validity of the preceding statement can be illustrated by considering the matched-filter output when $\tau\Delta f \neq 1$.

If $\tau\Delta f > 1$, there are significant range ambiguities at time $t = |1/\Delta f|$ as seen from the autocorrelation function in Fig. 13.13. It can also be seen that when $\tau\Delta f = 1$, the nulls of the autocorrelation function of the subpulse envelope tend to suppress these ambiguous peaks. When $\tau\Delta f < 1$, the subpulse filters F_n shown in Fig. 13.12 overlap, and the contribution of each channel to the coherent summation contains spurious signals. The details of the output waveform for $\tau\Delta f < 1$ depend on the ordering of the frequencies in the pulse envelope.

Another way to motivate the choice $\tau\Delta f = 1$ is to consider the correspondence between processor outputs and range cells. To this end, consider an interpulse stepped frequency waveform whose transmit pulse width is τ, frequency step size is Δf, and total bandwidth is $B = N\Delta f$, where N is the number of pulses utilized. The transmit pulse determines a range gate of extent $c\tau/2$, and one I and Q sample is collected from this range gate for each transmit frequency. These samples are then loaded into an N point complex FFT to provide N complex output values. The total bandwidth utilized in this process is $N\Delta f$. The resulting resolution is therefore $c/2N\Delta f$. It follows that, when $\tau\Delta f = 1$, the range gate is resolved into N range cells, and each FFT output corresponds to precisely one of these cells. If the number of pulses (N) utilized is held constant and Δf is increased so that $\tau\Delta f > 1$, then the

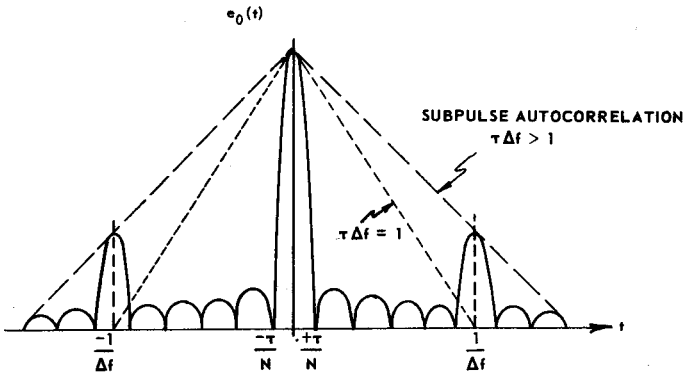

Figure 13.13 Autocorrelation function of frequency-coded pulse.

total bandwidth is increased, and hence resolution cell size is decreased. But N finer resolution cells do not cover the specified range gate. Thus, in this case, only a portion of the range gate is resolved and, in fact, the reflectors in the unresolved portion fold into the resolved portion (hence the "ambiguous peaks" mentioned earlier). In this sense, the cells are not really resolved. Similarly, if the number of pulses utilized is held constant and Δf is decreased so that $\tau\Delta f < 1$ in the example, then the N coarser resolved cells over-cover the specified range gate. That is, certain resolution cells are represented by more than one FFT output, a redundancy that serves no useful purpose.

While in some special cases $\tau\Delta f$ should be made different from unity (such as when the transmit pulse is assumed to have a gaussian rather than rectangular envelope [202]), the remainder of this section is limited to discussions of systems with $\tau\Delta f = 1$.

The transmitted waveform for a linearly stepped-frequency waveform can be written

$$V(t) = \sum_{n=0}^{n-1} [u(t - n\tau) - u(t - [n + 1]\tau)] \cos(\omega_0 + n\Delta\omega)t \quad (13.5)$$

where

$$\begin{aligned} \omega_0 &= 2\pi f_0, \text{ lowest frequency in the transmission comb} \\ \Delta\omega &= \text{frequency spacing} = 2\pi\Delta f \\ u(t) &= \text{unit step function} = \begin{cases} 1, \tau \geq 0 \\ 0, \tau < 0 \end{cases} \\ N &= \text{number of frequencies in transmission} \end{aligned}$$

The phase and time origin is taken to be the leading edge of the first subpulse. It can be shown that the matched filter has an impulse response that can be written [768]

$$\begin{aligned} h(t) &= v(-t) \\ &= \sum_{n=0}^{N-1} [u(-t - n\tau) - u(-t - [n + 1]\tau)] \cos(\omega_o + n\Delta\omega)t \end{aligned} \quad (13.6)$$

If the matched-filter delays and filters are in the inverse order of transmission and the delay to the target is neglected,* the matched-filter output can be written

$$e_o(t) = \sum_{n=0}^{N-1} A_n^2 \exp j(\omega_o + n\Delta\omega)t \tag{13.7}$$

in the region $(N-1)t < t < Nt$. With the assumption that $\Delta f = 1/\tau$, this becomes the only region of interest. Equation (13.7) is the finite sum Fourier series approximation to the matched-filter output, neglecting the detailed shape of the filters in each channel. A_n is the weighting function of the nth frequency segment, and is assumed equal to unity until Sec. 13.9. It follows that:

$$e_o(t) = \exp\left[j\left(\omega_o + \frac{(N-1)\Delta\omega}{2}\right)t\right]\left(\frac{\sin N(\Delta\omega/2)t}{\sin(\Delta\omega/2)t}\right) \tag{13.8}$$

To account for the autocorrelation of the rectangular segment envelope as was illustrated in Fig. 13.8, Equation (13.8) should be multiplied by the triangular function $\tau[1 - (|t|/\tau)]$ for $|t| \leq \tau$, and zero elsewhere.

The term $\omega_o + [(N-1)\Delta\omega/2]$ is the mean frequency of the comb or carrier frequency and can be factored out. Thus, the second term determines the compressed pulse envelope. The nulls in the envelope occur when $\sin[N(\Delta\omega/2)t] = 0$ or when

$$N\frac{\Delta\omega}{2}t = \pm m\pi$$

where m = any integer. The first sidelobe peak is reduced from the mainlobe by 13.46 dB when $N \geq 50$ and is 13.06 dB down for $N = 8$. This envelope has the $\sin(NX)/\sin X$ shape and is similar to that illustrated in Fig. 13.13. At one-half the distance between the nulls, the linear envelope response is down by 4 dB and the width is

$$\text{Compressed pulse}_{(4\text{ dB})} = \frac{1}{N\Delta f} = \frac{\text{transmit envelope}}{N^2} \tag{13.9}$$

The pulse compression ratio is then slightly greater than N^2 with the customary definition of 3-dB pulse widths.

* That is, only differential delays with respect to target location are formulated.

Thus, the compressed-pulse matched-filter output for a stepped linear FM waveform has almost the same shape as that for a continuous linear FM waveform for large compression ratios.

13.7 Capabilities for Extreme Bandwidths and "Stretch" Techniques

In Secs. 13.1, 13.2, and 13.3 it was indicated that among the requirements imposed on very wideband processors, many imply large time-bandwidth products. Phase-coding techniques are generally applicable to systems requiring, at most, 100 to 200 MHz of bandwidth due to limitations in the technological ability to A/D convert at much higher rates. Classical dispersive techniques for LFM waveforms can be utilized to achieve very wide bandwidths, but the devices utilized are often expensive, difficult to mass produce, and prone to performance degradation. However, modern ultrawide-bandwidth and very high time-bandwidth-product systems can generally be configured using one of three available techniques and can be built using reliable, mass-produced devices. Discrete frequency coding on either an intra- or interpulse basis provides two such techniques, and active correlation (*stretch*) processing provides a third. Each of these techniques is treated in the following discussion.

Three major factors favor the use of the discrete frequency techniques. The first is, for certain applications, the ability to eliminate the range Doppler ambiguity of linear FM. It will be seen that the matched-filter response, tapering effects, receiver sensitivities, etc., do not depend on the order in which the frequencies are transmitted. In simple terms, if the price is paid to implement matched filters for all expected target Dopplers, a thumbtack ambiguity function can be obtained (see Sec. 13.12). While there is an increase in the number of low-level residues, there is no range Doppler confusion between targets of comparable size. A related benefit to scrambling the frequencies is that the system does not respond to interfering FM-like signals generated by other radars and will be less susceptible to repeater jammers if the sequencing of frequencies is made to change on a pulse-packet to pulse-packet basis.

The second and perhaps the most significant advantage of multiple-frequency channels is that the components in each channel need only have a bandwidth of $1/N$ times the total processing bandwidth. This is illustrated in the waveform pictorial given in Fig. 13.11 and the receiver block diagram for the stepped–chirp frequency processor shown in Fig. 13.12. It is assumed that all subpulses or segments have the same amplitude upon transmission. The particular waveform shown in Fig. 13.11 is stepped linearly in frequency. After mixing to

the desired RF, the signal is transmitted, received, and mixed down to a convenient intermediate frequency to become the input of the matched filter of Fig. 13.12. In fact, if the stepped-frequency waveform is implemented on an interpulse basis, then the front end of the receiver can be kept instantaneously narrow-band by tuning it to the proper frequency for each transmission.

The third advantage of discrete systems is that channelization allows the capability for selective limiting in automatic detection or CFAR receivers. As was mentioned in Chap. 4, strong CW interference anywhere in the total signal bandwidth can capture a limiting receiver for FM signals. This interference causes suppression of the target-echo signals and prevents the matched-filter output from crossing a preset threshold. In a channelized system, CW interference suppresses the target signal in only one of N channels, and the target signal power output is $(N - 1)^2$ times the output without the interference. If N is greater than about 10, target detection is not prevented with a fixed-threshold system for CW interference which is 20 to 30 dB above the per-channel echo signal power.

In summary, there is virtually no limit to step-frequency-processor time-bandwidth product capability. Many interpulse systems of this nature have been built with over a gigahertz of bandwidth and extremely high time-bandwidth products. Specialized stepped-frequency instrumentation systems have been developed that achieve up to 10 GHz of bandwidth.

Another technique appropriate for achieving extremely high bandwidths is through active generation and active correlational receiver processing, often referred to as *stretch processing* (after Caputi [109]), of intrapulse LFM signals.* Active correlation consists of multiplying returns by a replica of the transmitted waveform, filtering to extract the unmodulated waveform envelope, and then integrating the resulting difference-frequency product across the pulse width to complete the matched-filtering operation. This multiply-and-integrate function must in general be performed for each combination of range gate and Doppler filter instrumented by the radar system.

LFM supports very efficient implementation of active correlation as illustrated in Fig. 13.14. The receiver output is mixed with an LFM signal of the same slope coefficient as the transmitted waveform. Hence, active-correlation multiplication is conducted at RF followed by low-pass filtering to extract the difference-frequency terms. Thereafter, the signal is split into I and Q components and digitized for further processing.

* Much of the following discussion of stretch processing was adapted from material supplied by M. L. Belcher of Georgia Tech.

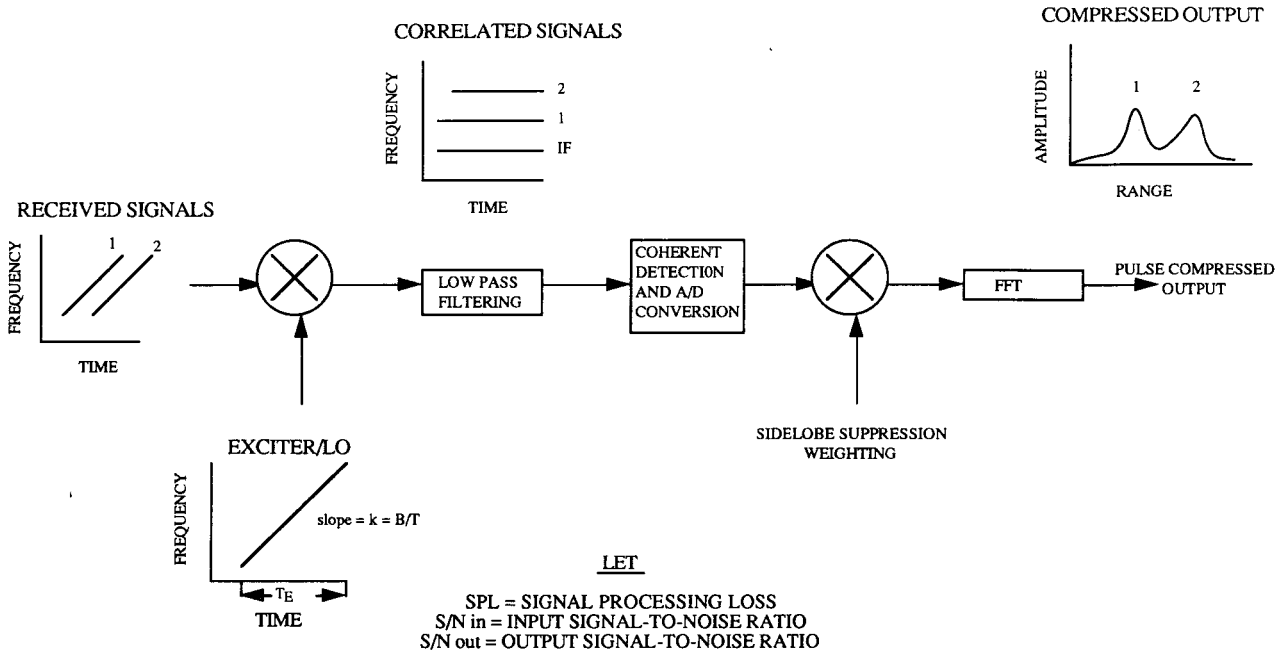

	RF	IF	VIDEO
SNR BANDWIDTH	S/N in B	(S/N in) x BIF IF BANDWIDTH (BIF) = k x T_E	S/N out = FFT + S/N in - SPL BASEBAND = 1/T

Figure 13.14 Active correlation LFM pulse compression. (*Adapted from M. L. Belcher*)

The return from each range bin within the selected range window (gate) thus corresponds to a pulsed tone at the output of the active difference mixer. The frequency of the tone corresponding to the ith range bin from the beginning of the range gate is given by $\tau_i k$, where τ_i is the range delay from the first range bin to the ith range bin, and k is the frequency slope coefficient (that is, $k = B/T$, where B is the bandwidth and T is the transmit pulse duration) of the waveform. Pulse compression is completed by performing a spectral analysis of the difference-frequency output to transform the pulsed tones into corresponding frequency resolution cells. In practice, this spectral analysis is performed by digitizing the difference-frequency output and processing it through an FFT.

Define the *range window* as the range extent over which target returns will be processed. Then, the receive window duration, over which the receiver LFM sweep is implemented, is generally equal to the sum of the transmitted pulse width duration and $2R_e/C$ where R_e is the larger of the range window spatial extent and the uncertainty in range. Let $T_e = 2R_e/C$. As noted earlier for stepped-frequency FM, T_e must be restricted to less than or equal to T, the transmit pulse width.

The Fourier transform relationship implies that LFM sidelobe suppression performance is sensitive to coherent modulation errors. Amplitude or phase ripple across the uncompressed pulse is transformed into corresponding range sidelobes at the FFT output. These sidelobes are not significantly mitigated by the usual sidelobe-suppression weighting techniques.

LFM active correlation reduces computational throughput requirements as compared with other digital compression techniques by performing multiplication within the receiver so that the signal processor must only implement integration (spectral analysis). Active correlation and FFT computation are performed just once for each specified range window, and each FFT output corresponds to the return from a specific range bin within the specified range window.

The required size of the FFT transform is given by

$$N = \{\alpha k\, T_e\, (T + T_e)\}_r \tag{13.10}$$

where $\{\ \}r$ denotes that the number of data points must be rounded to an integer power of r, the FFT radix. The oversampling coefficient is given by α, transmit pulse duration by T, the chirp coefficient by k, and T_e is defined as in the foregoing. Note that if $T_e << T$, for example, $T_e = T/M$ for large M, then $N \approx \{BT/M\}_r$. That is, if the pulse compression ratio is large and only a few range bins need to be compressed and range accuracy is also on the order of a few range bins, then the bandwidth of the receive signal, and thus the size of the required FFT,

is relatively small. On the other hand, if $T_e \approx T$, then $N \approx \{2BT\}_r$. In contrast, two FFTs of approximate length $\alpha\ BW(T + T_e)$ are required to implement matched filtering via fast convolution (i.e., computation of the convolution of two waveforms via an FFT, multiplication, and inverse FFT of the result) if one were to implement an equivalent LFM waveform, digitize, and compress without utilizing an active deramp (stretch) process.

LFM pulse compression gain in decibels is nominally 10log (time-bandwidth product) less the sidelobe-suppression weighting and quantization losses. As indicated in Fig. 13.14, this gain is divided between the front-end mixing processing and the FFT within the signal processor. The number of bits used to represent the signal when converting into the digital domain must be sized to accommodate the signal-to-noise ratio anticipated at the output of the difference mixer and the desired sidelobe suppression.

Active-correlation LFM pulse compression is commonly used for both real-time and postprocessing wideband pulse compression requirements. A number of significant extensions of LFM active-correlation process have been suggested and implemented. For example, specialized techniques have been developed to accommodate the range-walk correlation required in SAR processing.

The stretch technique has been successfully implemented in the satellite altimeters of SEASAT, GEOSAT, and TOPEX, and in the ALCOR long-range instrumentation radar. Implementation of stretch is also planned in several other systems proposed for the 1990s. The intent in the altimeters is precise ranging and wave-height determination over the ocean from an orbiting satellite. If the satellite orbit is known and the vertical distance to the mean sea surface is measured, the shape of the geoid can be accurately determined. The height of the ocean wave distorts the echo from the ocean surface.

The LFM systems implemented in SEASAT [378] and some other similar systems used an LFM waveform with a bandwidth of 300 MHz and a time duration of approximately 3.3 μs. Since the orbit is known, there is relatively little uncertainty in the time delay to the sea surface and thus, stretch processing could effectively be applied. In SEASAT, a modified split-gate tracker was implemented with a 3-ns compressed pulse. The radar altimeter achieved 2 cm (0.14 ns) precision, and the range accuracy from an altitude of 600 km was subsequently measured as 8 cm (0.56 ns) in low to moderate sea states.

As wave height increases, the leading edge of the echo is smeared out in time. By matching the received leading edge to a series of templates representing different wave heights, the wave height is estimated accurately and surface wind speed is derived from the wave height estimate.

In summary, ultrahigh bandwidths and time-bandwidth products can be achieved utilizing discrete as well as active-correlation, FM techniques. Discrete FM techniques can utilize extremely accurate and stable digital synthesizers to generate the required spectrum comb. Intrapulse discrete FM techniques can utilize channelized receivers or a wideband front end with relatively narrow-band IF and digital processing components. Interpulse discrete FM techniques require only a tunable receiver front end to achieve relatively narrow-band instantaneous operation throughout the receiver. Active-correlation techniques can utilize tightly controlled VCOs or digital frequency synthesis techniques for signal generation and a wideband receiver front end. They allow for narrow band signal processing via the conversion of ultrahigh range (time) resolution requirements into ultrahigh frequency (tone) resolution requirements, which is much easier to achieve with modern signal-processing technology. The principal potential difficulties one may encounter with each of these implementations includes: (1) the need for a channelized receiver or finely tuned IF components for the intrapulse discrete FM approach, (2) the required time-on-target and the need for separate signal processors for each desired instrumented range swath for the interpulse FM approach, and (3) the need for a wideband receiver front end and the need for separate signal processors for each desired instrumented range swath with the active-correlation receiver processing approach.

13.8 Resolution Properties of Frequency-Coded Pulses

The virtues of wideband waveforms have been well explored analytically, but it is always useful to show available experimental results. Figures 13.15 and 13.16 are typical outputs from two similar discrete frequency processors each with a coherent bandwidth of ≈80 MHz. These signal processors are described in Secs. 13.11 and 13.12. In one of the systems, the transmission consisted of eight frequency segments of $\tau = 0.13$-μs duration with 10-MHz frequency separation. In the second system, the subpulse length was 0.4 μs, and the frequency Δf was 2.5 MHz. In each system there was also an incoherent output that was simply the summation of the detected envelopes on each frequency. The resolution of the incoherent channel was 0.13 μs in the first processor and 0.4 μs in the second. The compressed-pulse output of each system was $\approx 1/(N\Delta f) \approx 12.5$ ns in duration at the -4 dB points.

The resolution of the echoes from two 6-in metallic spheres is illustrated in Fig. 13.15. They were suspended from a weather balloon 2000 yards from the radar. The A-scope photo was taken when they were 25 ft apart, but they were also resolved with less than 8-ft radial

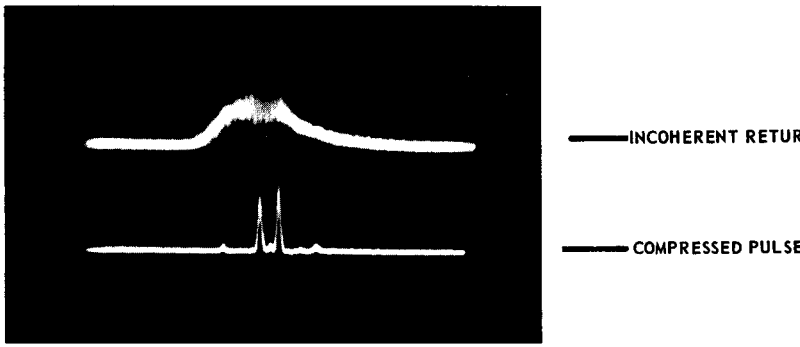

Figure 13.15 Resolution of 6-in spheres (25-ft separation). Trace length = 500 ft, number of frequencies = 8, number of pulses = 32, cross section = 0.2 ft^2, range = 2000 yd, power = 2kW, pulse width = 0.13 μsec, compressed = 0.012 μsec.

separation. The upper trace showing the incoherent output illustrates that resolution was not possible with 0.13-ms (65-ft) resolution. The two small range sidelobes on either side of the echoes from the spheres resulted from having $\tau\Delta f$ slightly greater than unity (see Sec. 13.6).

Figure 13.16 similarly shows the resolution of two men standing in a grassy field. The upper half of each photo is from a TV system boresighted with the antenna. In the left-hand photo, when the men were standing side by side, they could not be resolved; but their reflected echoes did stand out from the local ground clutter. The fluctuation of the incoherent output (center of the photos) was primarily due to the ground-clutter contributions at the left side of the trace. With the two men separated in range by 40 ft, the resolved echoes at the bottom of the right-hand photo are evident. They not only could not be resolved in the incoherent output, but could not be detected in the ground clutter.

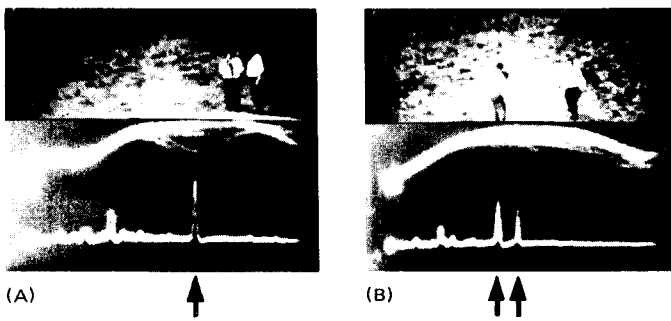

Figure 13.16 Resolution of human targets in ground clutter. Center of each photo shows incoherent echoes; bottom traces show compressed pulses (trace length = 500 ft, range = 300 yd, bandwidth = 80 MHz, beamwidth = 2.0°, antenna elevation = 3°). (A) Two men together; (B) range separation of 40 ft.

While the improvement in target-to-clutter ratio was evident in the grassy areas, the echoes from the men did not stand out very well in a nearby wooded area unless they walked continuously in one direction.

The photos illustrate that high resolution, clutter reduction, and a constant-false-alarm-rate receiver can be achieved in practice as well as in theory. While these results were obtained with discrete frequency coding, they could also have been obtained with phase coding or linear FM.

13.9 Sidelobe Reduction

Just as we saw in Chap. 12 that the range (time) sidelobes of phase-coded waveforms could be improved over the matched-filter case by mismatching the transmit waveform and the receive processor, so can we develop and implement mismatch systems for sidelobe suppression of FM waveforms. Typically, one has a choice to impose an amplitude weighting in either the time or frequency domain in order to achieve sidelobe reduction, and this weighting may be applied to either the transmit or the receive waveform or both. In radar applications it is almost always desirable to operate the transmitter in saturation, so we generally apply the amplitude-weighting mismatches at the receiver. For FM waveforms, the received signals represent the frequency-domain response of the target, and after processing we derive the time- (range-) domain response. Weighting prior to compression requires only a multiplication of the weighting function by the received waveform. Weighting after compression requires convolution of the weighting function by the received waveform. For these reasons, sidelobe reduction for FM signals is usually achieved as an amplitude weighting prior to (or as part of) the compression process. The first sidelobe resulting from a uniformly weighted comb of frequencies was shown to be $\approx$13.5 dB below the mainlobe peak. The remaining sidelobes decay monotonically and symmetrically about the mainlobe. By amplitude weighting the frequencies, the sidelobes, in theory, may be reduced any desired amount.

In addition to the desirable sidelobe reduction, amplitude weighting of the frequencies has undesirable effects on the output waveform, including mainlobe widening and output signal-to-noise ratio degradation. These effects are measured as deviations from the $\sin(nx)/\sin(x)$ envelope waveform, obtained from a uniformly weighted frequency comb. The reason for the mainlobe broadening is deduced intuitively from the Fourier transform reciprocity relationship. When the spectral shape is made narrower, the time-domain waveform becomes broader and vice versa. A bell-shaped or tapered spectrum would then be expected to correspond to a wider time-domain waveform than would

a flat or unweighted spectrum of the same total frequency extent. Therefore, the resultant waveform in the time domain will be broader for an amplitude-weighted comb than for the uniformly weighted comb. Amplitude weighting may be introduced into a pulse compression radar either entirely at the receiver, or at both simultaneously. When the amplitude weighting is imposed equally on both the transmitted waveform and on the corresponding gains of the receiver channels, the system is still considered matched. For a matched system, there will be no decrease in the signal-to-noise ratio due to weighting. However, when the amplitude weighting is introduced either at the transmitter or the receiver alone, the system is mismatched, with a resulting degradation in the signal-to-noise ratio.

Amplitude weighting at the receiver is accomplished in various ways, depending on the type of FM waveform employed. For discrete intrapulse FM, it can be achieved by proper adjustment of the filter gains or by the insertion of the proper value attenuators in each of the parallel channels. It can be conveniently maintained, due to the accessibility of the components and the low power levels involved. For discrete interpulse FM, sidelobe reduction weighting can be simply introduced as a software or hardware multiply in the digital signal processor prior to transformation of the data. For stretch waveforms, the weighting can be applied after digitization of the correlated returns and before (or during) the subsequent FFT computation.

The frequency response of a matched filter is adjusted to maximize the output signal-to-noise ratio and requires that the amplitude response of the matched filter be equal to the amplitude spectrum of the input signal. The amount of mismatch is measured as a degradation from the optimum signal-to-noise ratio normally produced with a matched filter.

The loss in signal-to-noise ratio resulting from the use of weighting at the receiver alone is characterized by the loss factor L_s given by [699]

$$L_s = \frac{(S/N) \text{ weighted}}{(S/N) \text{ matched}} = \frac{\left[\int_T \omega(t)\, dt\right]^2}{T \int_T \omega^2(t)\, dt} \tag{13.11}$$

where $\omega(t)$ = the weighting function
T = the processing time interval or the length of the transmitted waveform

Equation (13.11) states that (S/N) is degraded by a factor L_s times that obtained in the absence of matched weighting. For discrete-frequency amplitude weighting of an N-frequency radar, L_s becomes

$$L_s = \frac{\left[\sum_1^N A_n\right]^2}{N\left[\sum_1^N A_n^2\right]} \tag{13.12}$$

where A_n = the weighted amplitudes for the N. frequencies.

The problem in selecting an appropriate amplitude-weighting function for a pulse compression system is to find what finite spectrum shape can produce a desired time waveform under some condition of optimization. A common criterion for optimization is to find a weighting function that provides a minimum mainlobe widening for a specified peak sidelobe level.

The amplitude-weighting functions that lower the sidelobes in the output time waveform all have a characteristic bell or tapered shape. When this function is applied to, for example, a comb of frequencies, the frequency in the center has the maximum amplitude, and all other frequencies have decreasing amplitudes symmetrically about the center. The output waveform for the more familiar functions, such as cosine and gaussian weighting, can be obtained from the Fourier transform relationship between the input and output of pulse compression systems.

The sidelobe structure for a comb of frequencies, when weighted with a cosine-shaped taper, has been verified experimentally with a multifrequency synthesizer called a DELRA (*delay line range analyzer*) [510, 768]. As used in the following figures, it simulates a 50-channel stepped-frequency generator and receiver. Figure 13.17A shows amplitude versus frequency in 50 discrete steps for cosine weighting. In Fig. 13.17B, the compressed-pulse amplitude is shown with about −22-dB first sidelobes as compared with the theoretical value of −23.6. Figure 13.17C shows the mainlobe region expanded in both dimensions to show the rapid decay of the sidelobes.

Several other amplitude tapers have been used to obtain lower range sidelobes than can be achieved with cosine weighting. As another example, the sidelobe structure for Dolph-Chebyshev [171] tapering for 30-dB sidelobes was obtained on the synthesizer and is shown as Fig. 13.18B and C. DELRA was an analog device with a certain limit of accuracy. Thus, ideally, the sidelobes should be equal in amplitude, but this expected result is only approximated. The sidelobe structure for uniform weighting is illustrated as a reference at the top of the figures. While this taper is not practical for antennas or dispersive lines due to the large values required at the ends of the spectrum, there is no problem in approaching the theoretical limits for discrete frequency systems.

One other class of tapers, the Hamming functions, warrants special

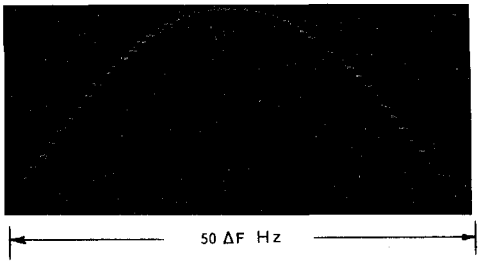

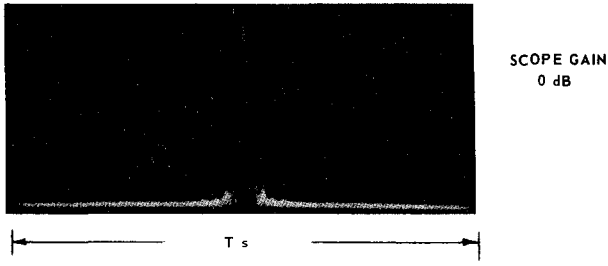

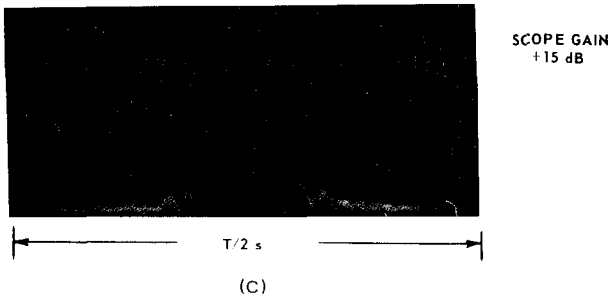

Figure 13.17 Sidelobe reduction with cosine amplitude weighting. (A) Cosine-weighted spectrum; (B) output compressed pulse; (C) expanded output.

consideration for pulse compression systems. The Hamming weighting function in continuous form is described in general terms by [699]

$$G(\omega) = a + (1 - a)\cos\left(\frac{\pi\omega}{W}\right) \qquad \text{for } 0 < a < 1 \qquad (13.13)$$

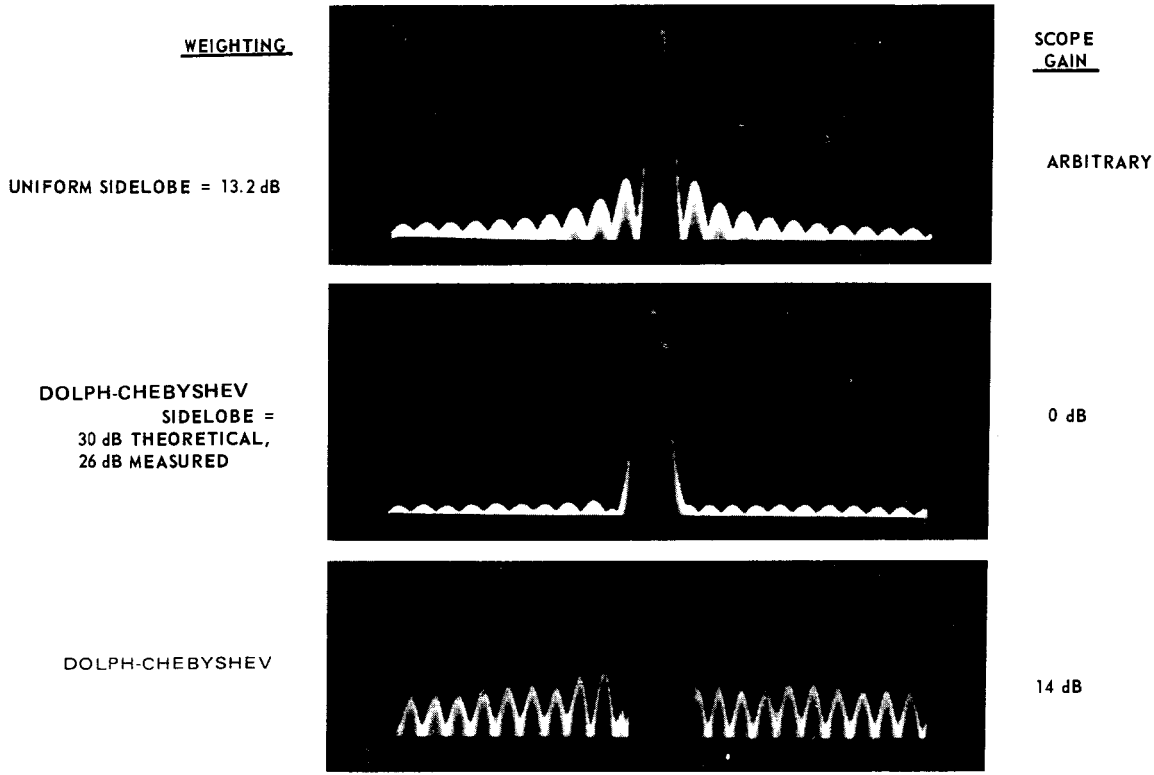

Figure 13.18 Dolph-Chebyshev weighting sidelobe suppression (40 frequencies).

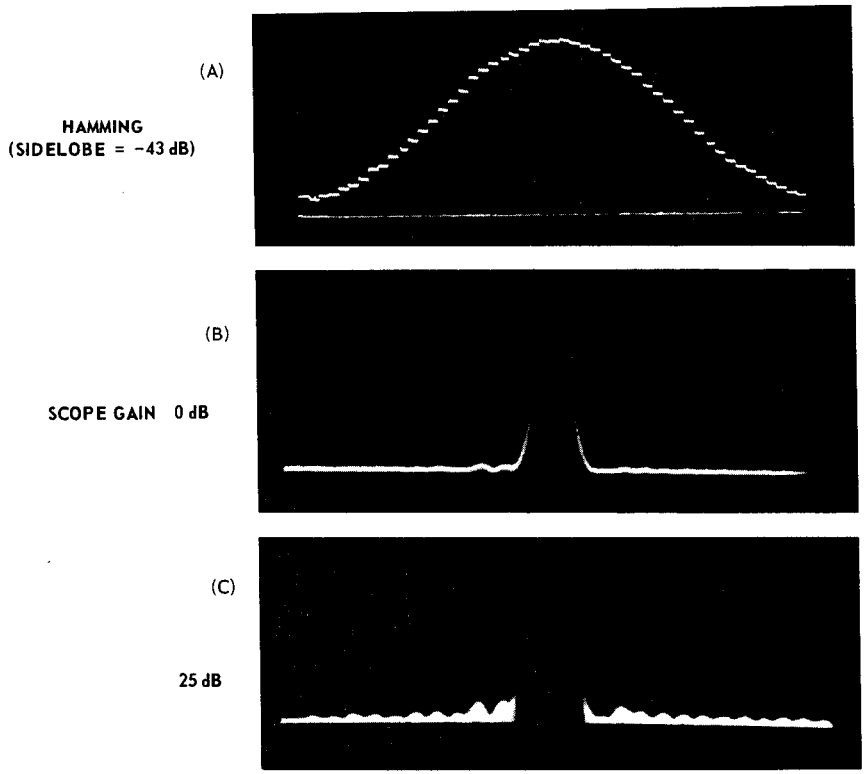

Figure 13.19 Hamming function weighting sidelobe suppression (50 frequencies). (A) Hamming (sidelobe = −43dB); (B) scope gain (0 dB); (C) 25 dB. (*After White and Ruvin* [*769*])

where the center* of the spectrum is assumed to occur at $\omega = 0$. The resultant weighting function for the 50 discrete frequencies and $a = 0.54$ is shown in Fig. 13.19A. The distinguishing feature between this weighting function and the cosine function is that the amplitudes of the frequencies at the edges of the spectrum are not zero. From Eq. (13.13) for $\omega = \pm W$, the amplitude of the frequencies at the edges of the spectrum are equal to 0.08 (compared with a value of 1 at the center of the spectrum).

The output waveform shown in Fig. 13.19 may be described approximately by the Fourier integral used to find the envelope for Hamming weighting. The result for any value of a is

* In some references $\omega = 0$ is taken at the edge of the spectrum. The amplitude at the edge of the spectrum is $a - (1 - a) = 2a - 1$. This is often referred to as the pedestal.

$$e_0(t) = \frac{a}{2}\frac{\sin Wt}{Wt} + \frac{1-a}{2W(1-t^2)}\cos Wt$$

The theoretical maximum sidelobe level for $a = 0.54$ is -42.8 dB, which is beyond the dynamic range of the DELRA. The sidelobes were measured to be ≈ 40 dB below the mainlobe peak. The mainlobe widening over that for uniform weighing is 46 percent. The Hamming weighting function, due to its very low sidelobe level and comparatively low mainlobe widening, serves as a very effective method of amplitude weighting in practical pulse compression receivers.

Some of the properties of various weighting functions are summarized in Table 13.2 [699, 768, 136]. The Hamming class of weighting functions is characterized by the parameter a. The mainlobe broadening and processing loss are referenced to uniform weighting. The lobe decay function describes the rate of decrease of the sidelobes beyond the peak sidelobe. The theoretical and experimental values apply for $N \geq 40$ frequencies, and some additional degradation is to be expected for smaller values of N [305].

The time mismatch column is not directly applicable to short-duration stepped-frequency waveforms, but is pertinent to linear FM when there is a large Doppler shift. It is also significant in clutter computations for pulse Doppler waveforms. The value in the rows for 5- and 10-percent mismatch show the degradation when the weighting function is displaced from the received signal by that amount. The most significant effect is the increase in the range sidelobes. The column on processing loss can also be used for the loss in signal-to-clutter ratio for the case in which clutter has an extent greater than twice the transmit pulse length ([136, pp. 341–343]).

In order to maintain low range sidelobes, careful consideration must be given to the detailed bandpass characteristics of each channel [519]. In practice it has been possible to obtain -40-dB sidelobes by very careful adjustment of receivers employing 35 to 50 frequencies. In a practical operating system, -35 to -40 dB is a limit with most analog configurations. Tolerances are also given in Chap. 14.

13.10 Pulse Compression Decoders and Limiter Effects

In this section a matched-filter processor for a short, random stepped-frequency transmission is described. If the Doppler shift of the target echo is much less than $1/Nt$, a random ordering of frequencies can be used and only a single Doppler channel need be implemented in the receiver. With linear stepping of the frequencies, on the other hand, the tolerance to Doppler shift is much higher (see Fig. 8.8).

TABLE 13-2 Sidelobe Suppression of Frequency-coded Waveforms

Weighting function	a	Time mismatch, %	Main-lobe broadening		Processing loss, dB	Highest sidelobe, −dB	Sidelobe decay function*
			Theor.	Exp.†			
Unweighted		0	1.00	1.00	0	13.2	$1/t$
Cosine		0	1.56		1.0	23.6	$1/t^2$
Hamming	0.54	0	1.47	1.46	1.34	42.8	$1/t$
		5	1.52		1.42	36.6	$1/t$
		10	1.55		1.47	32.2	$1/t$
(Cosine-squared)	0.50	0	1.59	1.70	1.76	31.4	$1/t^3$
Hamming	0.52	0	1.55		1.54	36.1	$1/t$
Hamming	0.56	0	1.45		1.16	37.7	$1/t$
Hamming	0.58	0	1.41		1.01	34.2	$1/t$
Dolph-Chebyshev		0	1.20	1.40	0.80	30.0	1
Dolph-Chebyshev		0	1.35		1.20	40.0	1
Cosine-cubed		0	1.88		2.38	39.1	$1/t^4$
Taylor $\bar{n} = 5$		0	1.34	1.44	1.1	34.0	$1/t$
$\bar{n} = 6$		0	1.41	1.7	1.23	40.0	$1/t$
$\bar{n} = 6$		10	—		—	28.0	$1/t$
$\bar{n} = 8$		0	~1.50		1.46	47.5	$1/t$
$\bar{n} = 8$		10	—		1.66	34.5	$1/t$

* Decay function far from compressed-pulse location.
† Compression ratio = 50:1 (experimental).

The tapped delay-line pulse compression system of Fig. 13.20 is an expansion of Fig. 13.12. The transmit waveform is a contiguous sequence of eight constant-amplitude, 0.1-μs pulses with a frequency spacing Δf of 10 MHz. In a particular system of interest, the comb of frequencies was generated by modulating a carrier at several gigahertz with an impulse-type function. This is represented by the signal generator block. These frequencies are sampled with an eight-pole microwave diode switch, amplified, and then transmitted. The received target echoes are amplified in a low-noise traveling wave tube and then mixed to a convenient intermediate frequency. Since the spectral width is 80 MHz, an intermediate frequency IF centered at 567 MHz was chosen to allow about 14 carrier cycles to occur between the nulls of the compressed-pulse envelope. With a lower IF, detection of the 12.5-ns pulses would become more difficult. With a higher IF, the matched-filter delay-line losses would become excessive.

The signals are then injected into a tapped delay line consisting of eight sections of semirigid coaxial cable. Each section is 67 ft long (1.5 ns/ft delay), is quite stable, has only a 5-dB insertion loss, and coils onto a spool occupying the volume of about a 3-in cube. The delay-line taps are Stripline-type directional couplers with the coupling progressively tapered to account for the delay-line losses. At this point, there is no filtering other than the 100-MHz bandpass of the 567-MHz amplifier. The individual channels are then amplified with either a linear or limiting amplifier whose gain is adjusted for the desired frequency taper. The 10-MHz filters are nominally the matched filters for the 0.1-μs segments. At this point each channel is divided into two outputs. The main output is the coherent summation of the eight segments that have been time aligned. The compressed pulse is then envelope detected and amplified in a wideband video detector. With uniform weighting the measured width of the pulse was close to the theoretical 12.5 ns.

The other eight signals out of the power dividers are detected and then amplified to form the incoherent summation of the eight 0.1-μs segments. This serves both as a reference channel and as a means to compare the detection statistics of complex target returns when simultaneously processed coherently and incoherently. This type of system is easy to adjust and can be quite stable. The loss in peak signal power as a function of a phase error in one of the eight channels or of uncorrelated phase errors in all channels is shown in Fig. 13.21.

It is appropriate at this point to discuss the effects of limiting on the compressed-pulse output. The purpose of using limiting amplifiers prior to the subpulse matched filters is to maintain a constant false alarm rate at the detected matched-filter output and to limit the dynamic range of the output. The statistics of the limiting process were discussed in Chap. 4 on automatic detection by nonlinear, sequential, and adap-

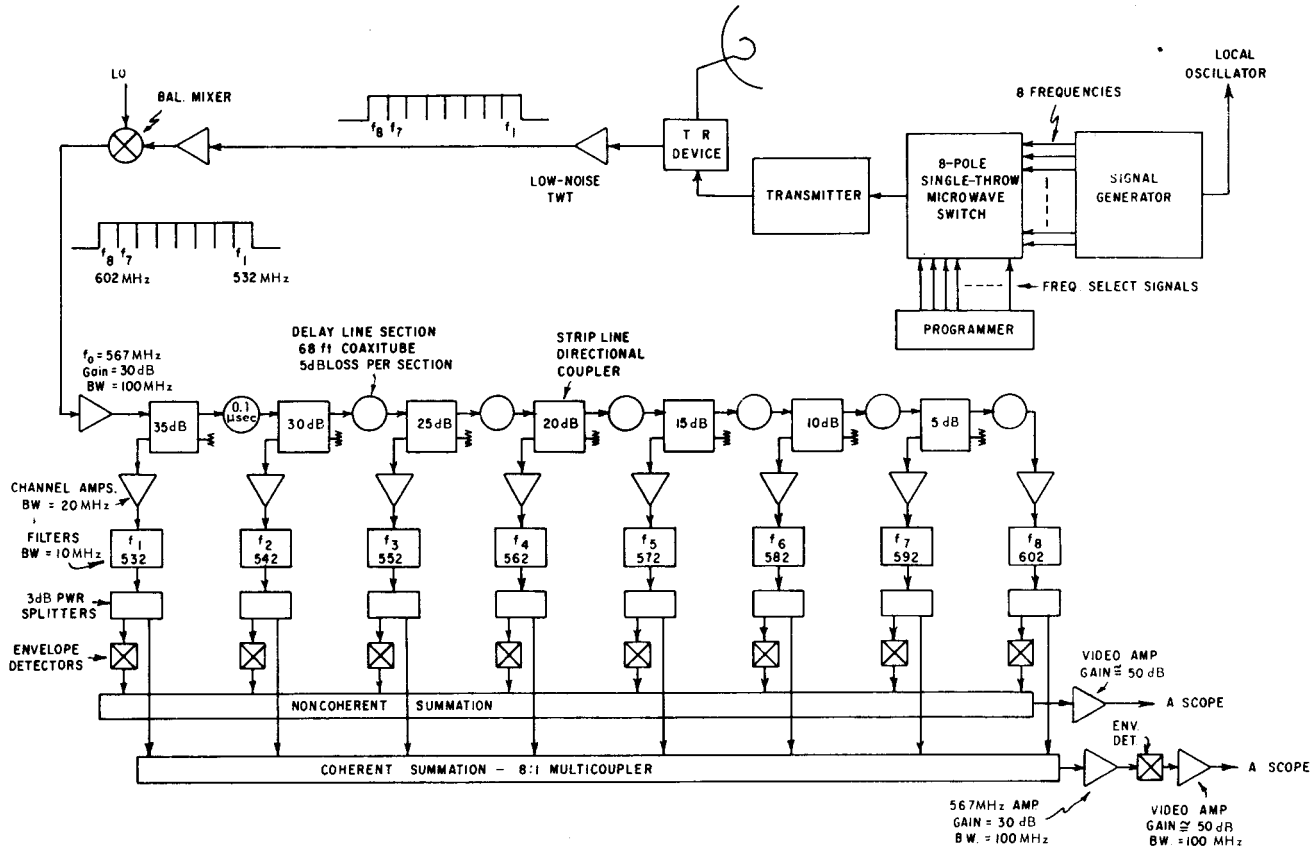

Figure 13.20 Tapped delay-line pulse-compression system.

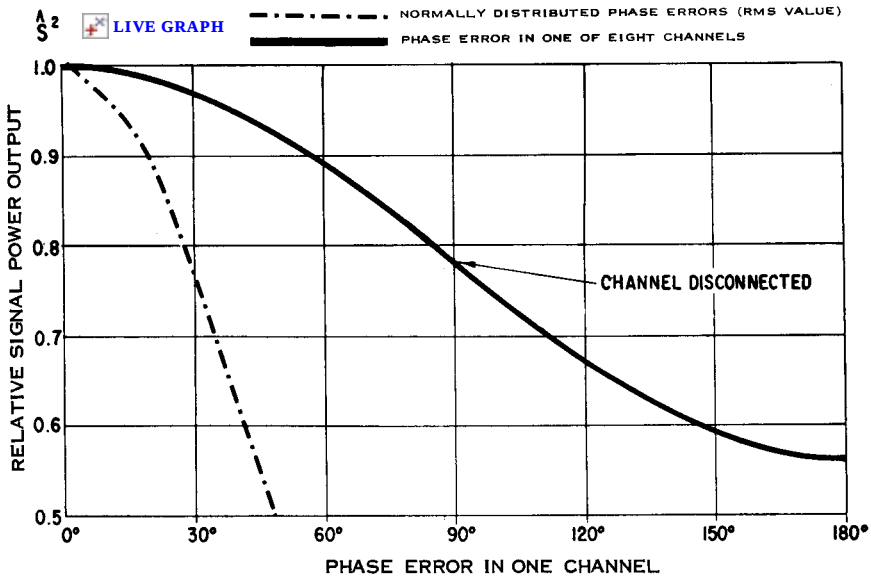

Figure 13.21 Relative signal power loss versus phase errors.

tive processes; however, there are some unique features of a limited receiver for frequency-coded signals which are worth noting here. If N^2 is greater than 64, the channel amplifiers of Fig. 13.20 can each have a hard-limiting characteristic with a bandwidth of slightly over $1/\tau$ (10 MHz); and the coherent summed output signal will still yield desirable CFAR characteristics. Saturated coherent signals of power K out of the limiters will yield KN^2 times this power at the coherent summation output. Random noise, rain, chaff, and most sea clutter echoes appear with random phase and have a relative summation output of KN. Thus S/N′, where N' is the noise power in the absence of signal, has a maximum value of N. While this value may be increased by making the bandwidth of the channel amplifiers wider than $1/t$, as shown by Silber [661], the immunity of the system to strong CW interference then decreases. Strong CW signals capture several of the overlapping channel limiters and suppress significant portions of the target echo.

When the factor of strong CW interference can be ignored, there are advantages in using a prelimiter bandwidth greater than $1/t$, as illustrated in Fig. 13.22. A 30-MHz IF signal out of a channel limiter is shown, along with the eight-frequency pulse-compressed output. The prelimiter bandwidth is 10 MHz for the 0.1-μs subpulse. The upper set of pictures was taken with the signals in each channel just at the limit level. The compressed-pulse output was square-law detected and typ-

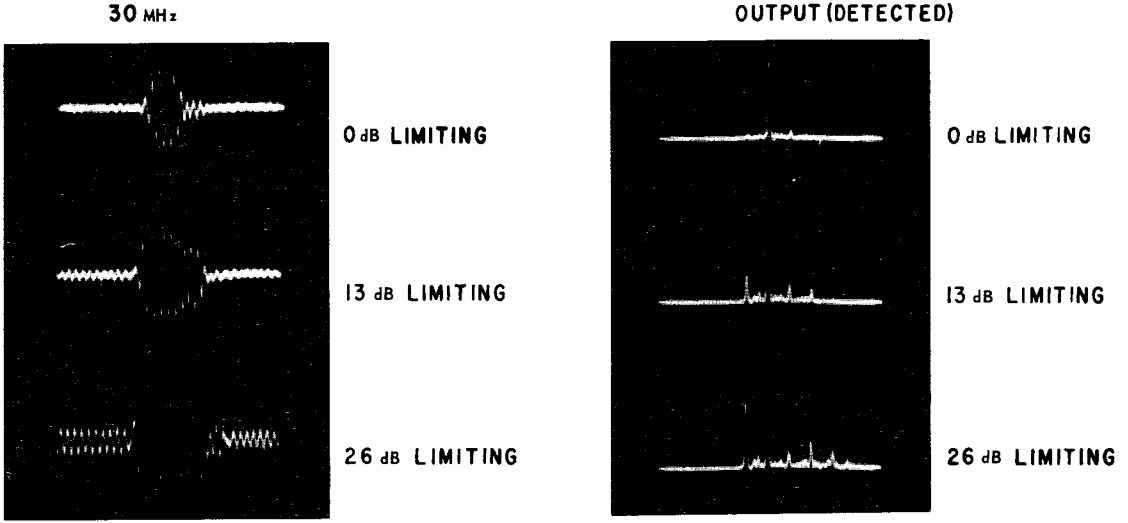

Figure 13.22 Effect of narrow-band limiting on coherent output (transmit pulse = 0.1 μs; limiter bandwidth = filter bandwidth).

ical of the system at that time. In the center photos, the signal level was increased by 13 dB. The output of the limiter has a greater duration ($\tau > 1/\Delta f$) due to the rise and fall portions of the subpulses receiving additional amplification, while the center portion of each subphase is held constant by the limiter. The detected compressed pulse shows that ambiguous outputs at $\pm$ 0.1 μs from the peak are visible and could be confused with other targets.* With 26-dB limiting, the limiter output is doubled in extent and several peaks are apparent at the detector. Tapering to reduce these range sidelobes would be completely ineffective. Some of the extraneous signal was also due to leakage through the transmit switches.

A similar system with $\tau = 0.4$ μs and a limiter bandwidth of 10 MHz does not exhibit this problem. As can be seen in Fig. 13.23, the compressed pulse is not altered and there is negligible increase in the range sidelobes for 55 dB of limiting. Since the prelimiter bandwidth is $4/\tau$, there was a negligible lengthening of the pulses. The dynamic range of this particular system was in excess of 65 dB.

A somewhat surprising result was also obtained in the incoherent summation. With the prelimiter bandwidth of only 4 times the channel filter bandwidth, the dynamic range of the incoherent summation was marginally acceptable for visual target detection with the eight-channel system, and was more than adequate for automatic detection with a 32-channel system.

13.11 Nonlinear FM

To this point in our discussion, we have considered FM waveforms that utilize either linear frequency modulation, discrete approximations to linear frequency modulation, and scrambled stepped-frequency waveforms that, although they are not in themselves linear, are derived from discrete approximations to linear FM waveforms. There is a whole other class of FM waveforms whose frequency functions are decidedly nonlinear with time.

These nonlinear FM (NLFM) waveforms are generally derived so that the spectral amplitude weightings used for sidelobe suppression in the receiver, as described in the foregoing, are instead approximated by a nonlinear time-frequency distribution characteristic that is shared by both the transmitted waveform and the receiver. That is, these waveforms are usually invented by deriving a frequency-time distribution whose square equals the product of a linear FM waveform with a chosen sidelobe-reduction weighting function. Such a frequency-

* It should be recalled that the coherent summation of the ungated comb frequencies has periodic peaks every 0.1 μs.

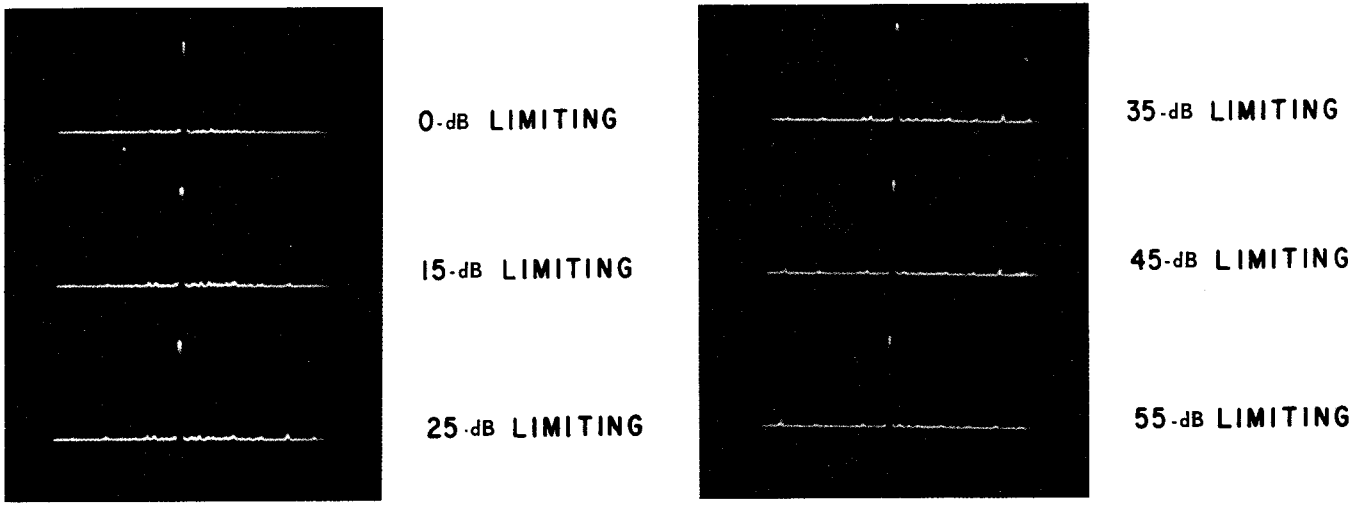

Figure 13.23 Effect of hard limiting on detected coherent output (transmit pulse = 0.4 μs; limiter bandwidth = 4 × postlimiter bandwidth).

modulation function was derived and realized utilizing a cascade of all-pass networks in [473] for cosine-squared-on-a-pedestal weighting. A frequency function whose compression approximates an LFM waveform with Hamming weighting is given here as Fig. 13.24A, and the compression of the waveform through its matched filter is given in Fig. 13.24B. The compressed waveform contains peak sidelobes of approximately −38 dB, with practically no loss in resolution and signal-to-noise ratio, as compared with an LFM matched-filter implementation of the same bandwidth. Similar results, i.e., the ability to derive and implement NLFM waveforms that achieve sidelobe suppression without incurring the SNR and resolution degradations associated with mismatched filtering, have been reported in [376] and [573]. Johnston [376] reported that an NLFM spectrum of truncated gaussian shape was utilized to reduce the peak sidelobe level to −46 dB, with negligible system losses, and showed that the derived NLFM waveform exhibited range Doppler characteristics very similar to those of the LFM waveform. In [573], Taylor weighting of an LFM waveform is emulated via derivation of the appropriate NLFM waveform. The resulting matched system shows peak sidelobes down better than 35 dB, with negligible losses.

As one might expect, these NLFM techniques are also applicable to the other forms of FM- and LFM-derived phase codes. In particular, it is shown in [176] that the equivalent of NLFM waveforms can be derived for a polyphase approximation to LFM, achieving −30 dB sidelobes with essentially no losses due to receiver mismatch.

The Doppler characteristics of these NLFM waveforms are also discussed in the references given in the foregoing. In general, one can expect the NLFM waveforms to exhibit essentially the same range Doppler characteristics that LFM waveforms do for small Doppler shifts (see Fig. 8.8). As the Doppler shift increases, the response drops more rapidly than for linear FM. This can be used to advantage if the targets of interest have a limited range of radial velocities.

13.12 Ambiguity Diagrams for FM Waveforms

Ambiguity diagrams of FM waveforms can take many forms depending on the precise technique utilized. In this section we investigate the range Doppler response of LFM, stepped-frequency, and NLFM waveforms through the study of their ambiguity diagrams. The diagrams for frequency-stepped waveforms are emphasized since they can be quite diverse because their response depends on both the ordering of the frequencies and the time spacing between the segments.

Fig. 13.25 provides the ambiguity diagram of an LFM waveform of

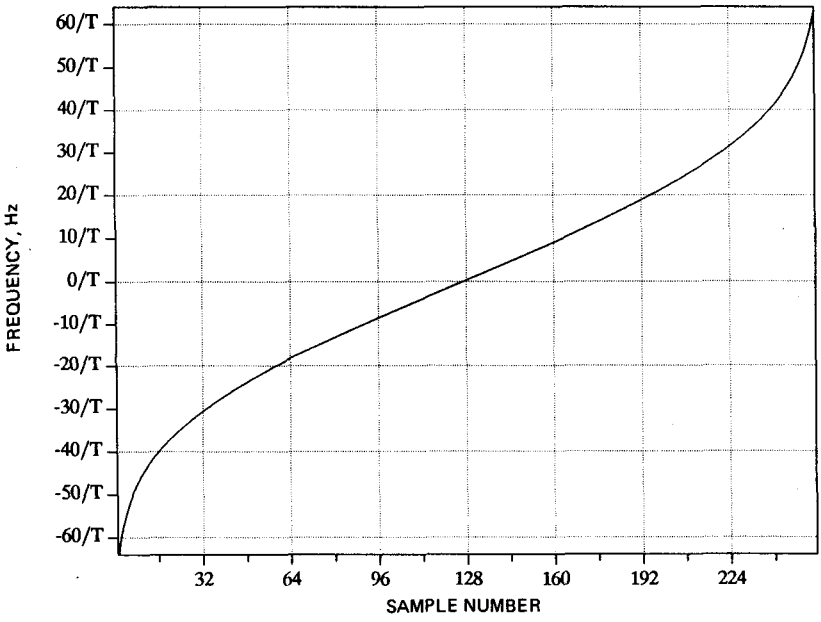

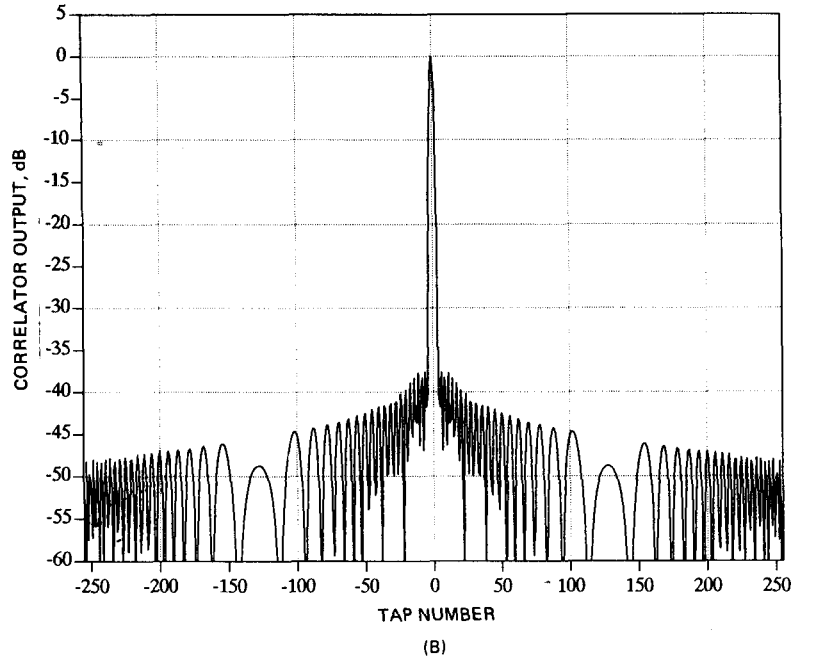

Figure 13.24 (A) Nonlinear FM time-frequency function, TB = 128; (B) nonlinear FM, TB = 128.

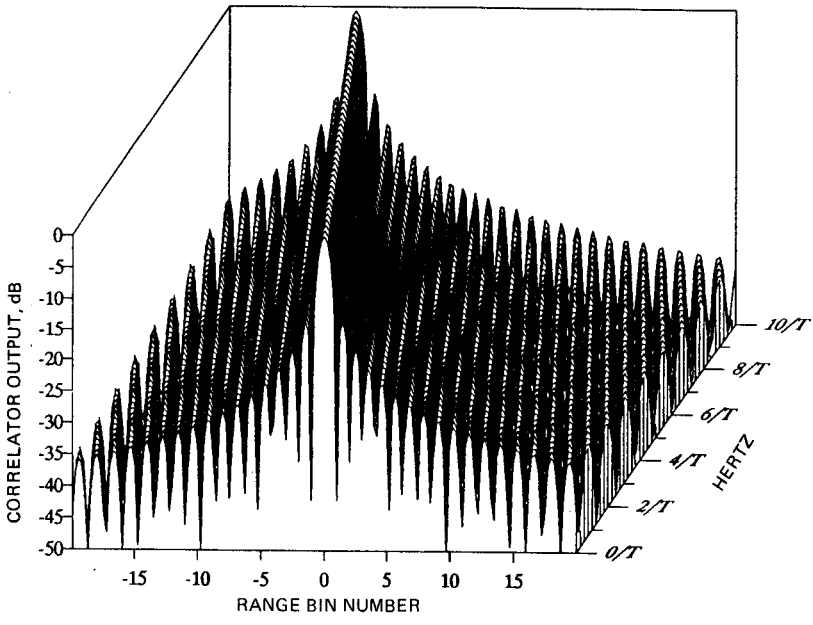

(A)

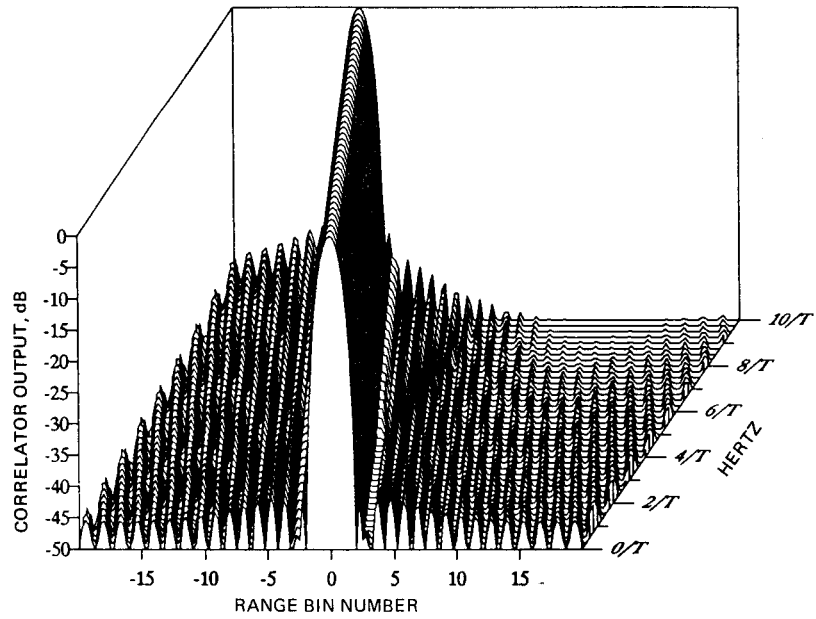

(B)

Figure 13.25 LFM, TB = 128, ambiguity diagram. (A) Matched filtering; (B) Hamming weighting. (*Courtesy J. M. Baden*)

duration T and with a time-bandwidth product of 128. In the figure, range is given in range bins (that is, in multiples of $cT/256$), Doppler in hertz, and power in dB. Figure 13.25A gives the system response assuming matched filtering in the receiver and Fig. 13.25B gives the system response assuming Hamming weighting has been applied to the received signal for range sidelobe suppression. In both cases only the central 40 range bins are shown, for the sidelobes outside this region are quite low and thus of little consequence.

The ambiguity diagram for an NLFM waveform is given in Fig. 13.26A. The waveform utilized for the plot is the same as that utilized for Fig. 13.24; i.e., it represents an NLFM approximation to Hamming-weighted LFM waveform, with time-bandwidth product 128. Most striking, and perhaps most important to notice, is the relative sensitivity of the sidelobe levels of this waveform as a function of Doppler mismatch as compared with Fig. 13.25B. This may be viewed more clearly in Fig. 13.26B, which represents the range response of the waveform when the Doppler mismatch is $5/T$ Hz.

The major contours of the stepped-frequency waveforms given in Fig. 13.8 are shown in Fig. 13.27. The frequency steps in all three cases are separated by $1/\tau$. The diagram at the top is for an intrapulse stepped-frequency approximation to a linear FM pulse. The primary difference between this contour diagram and the chirp diagram of Fig. 13.25 is the result of the poor response of stepped FM to signals with a Doppler shift of $1/2\tau$. At this point the stepped compressed pulse is considerably reduced in amplitude from the value at the origin. This effect is not important for short pulses where $1/N\tau >> f_d$.

The effect of scrambling the order of the frequencies within the pulse envelope is shown in the center diagram. The energy that appeared along the diagonal ridge at $1/\tau$, $2/\tau$, etc. is broken up and forms a pedestal of dimensions $1/\tau$ by τ. There is also a lower spillover pedestal in the range dimension extending from $|\tau|$ to $|N\tau|$. This results from the far-out spectral components of each segment appearing in the wrong frequency channels. The lower-level pedestal is called secondary sidelobes if it occurs mostly along the range axis, or secondary ambiguities if it extends throughout the ambiguity plane [348].

The contour diagram of a constant PRF linear stepped FM pulse train appears in Fig. 13.27C. Both the properties of linear FM and those of a pulse train are combined. As with all constant interpulse-period pulse trains, there are clear regions parallel to the Doppler axis. The major ambiguities appear at multiples of the pulse period T along a diagonal ridge. This is characteristic of linear FM signals as opposed to the nonskewed, rectangular grid appearance of single-frequency pulse trains.

The variations possible with frequency-coded trains are almost in-

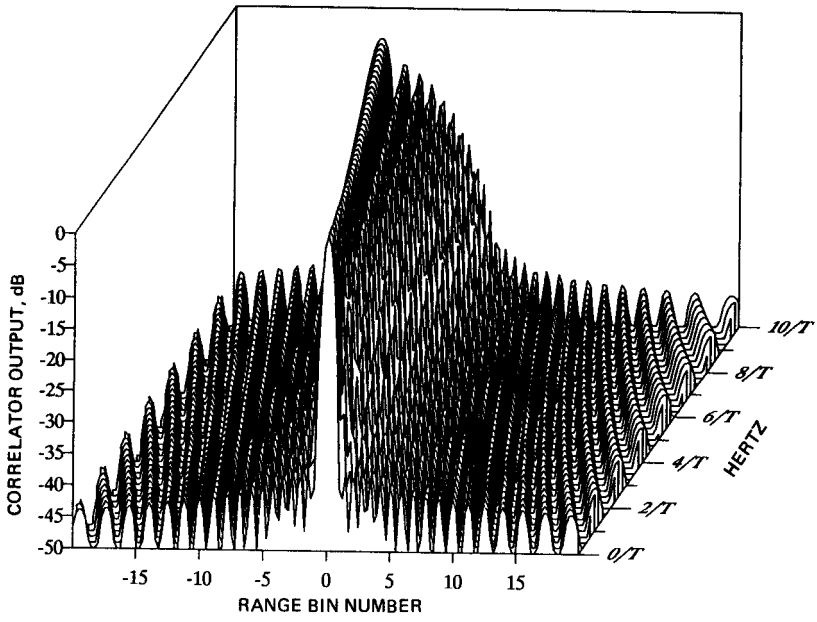

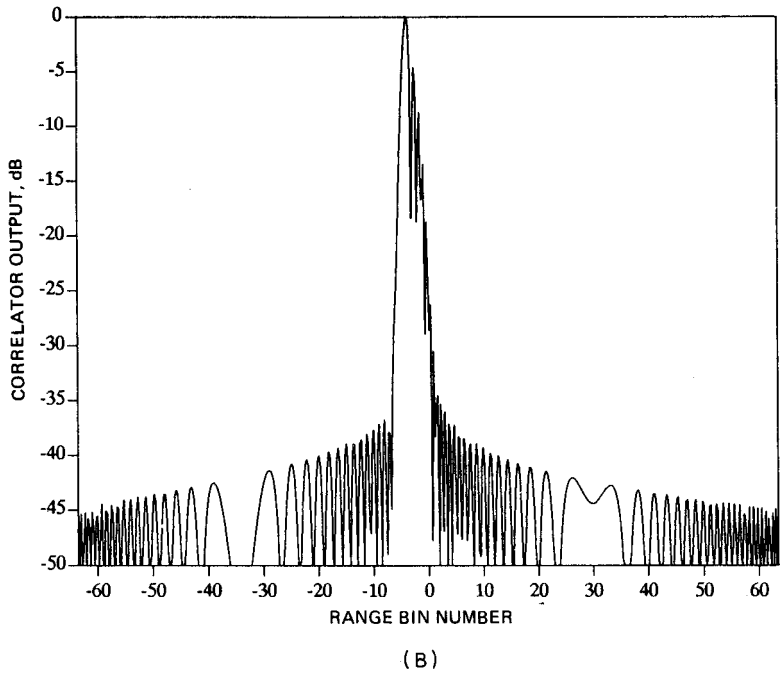

Figure 13.26 (A) Ambiguity diagram of nonlinear FM, TB = 128; (B) range response at 5/T Hz Doppler mismatch. (*Courtesy J. M. Baden*)

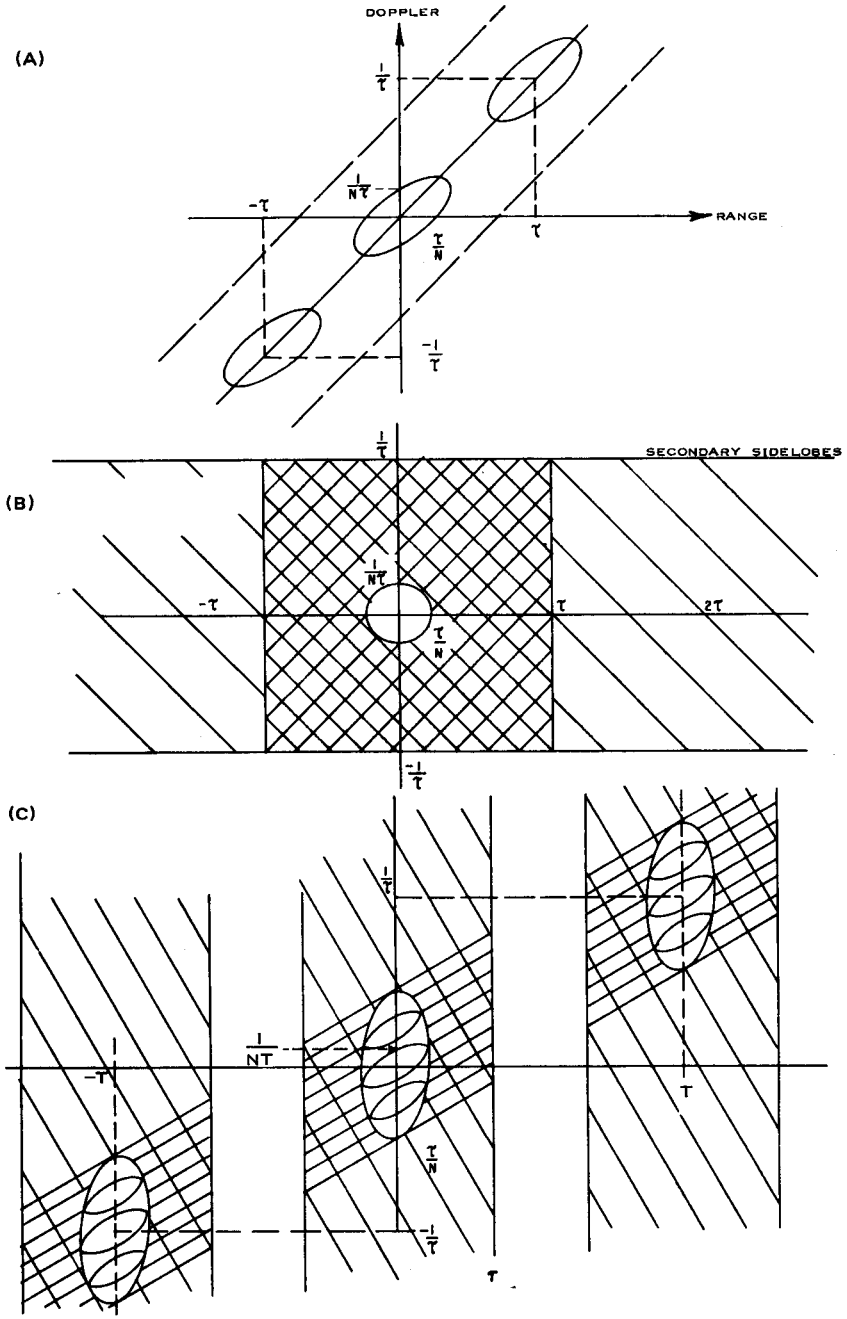

Figure 13.27 Ambiguity contours for discrete frequency waveforms. (A) Linear stepped FM; (B) scrambled pulse; (C) linear stepped FM pulse train.

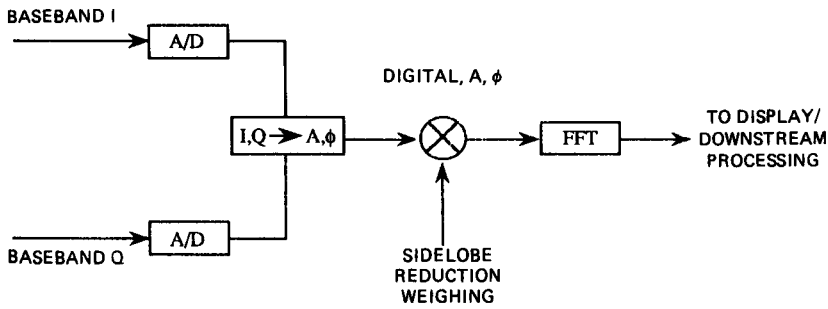

Figure 13.28 Digital processing for a stepped frequency waveform.

finite in that the phase, frequency, and time of transmission of each pulse can be varied. The waveform can be tapered in time and frequency to reduce the sidelobes. Howard [348] has studied the resultant variations in the ambiguity diagram of numerous variations of interpulse timing. Several other specific examples are available in the literature [601, 136].

13.13 Digital Decoders

Interpulse stepped-frequency waveforms are typically processsed as indicated in Fig. 13.28, where we assume N distinct frequencies are transmitted, and it is desired to compress over one transmit pulse footprint. The received RF waveform is downconverted and quadratured to yield I and Q signals at baseband. These values are then digitized, providing one I and one Q digital sample per transmit pulse. The resulting N I and Q samples are then weighted for sidelobe reduction and transformed through an FFT. With some reordering, perhaps, the N FFT outputs then represent the compressed returns from the instrumented range swath. As noted in Sec. 13.7, stretch processors utilize the FFT in a very similar way.

The limiting factor in such decoders is often the time required to process the N-point Fourier transform. Typical performance values for modern processor-on-a-chip FFT devices seem to range between 250 μs and 1 ms per 1024-point complex FFT utilizing single chips, depending on the number of bits required. Many of these chips can be configured to perform in parallel, allowing the computation of 1024-point complex FFTs in as little as 50 μs.

An alternative processing configuration has been implemented for pulse compression in the Southwest Tethered Aerostat System L-88 Radar.* In this implementation, an LFM or NLFM signal is transmitted

* Valuable notes on this system were provided by Dr. Larry Mertens (GE Company).

and digitized on receive. The digitized samples are reordered into an alternating stream of I and Q samples. These samples are Doppler filtered, pulse compressed, demodulated, and azimuth integrated. The pulse compression uses a correlation technique implemented on INMOS A-100 signal-processing chips. The chip is capable of correlating a string of 32 stored, 16-bit real numbers (a stored coefficient set) with an input signal at a throughput rate of 3.3 MHz for 16-bit number representations. The chip is also capable of switching between two such sets of coefficients on a clock-by-clock basis [360].

In the L-88 implementation, the received signal is fed into the A-100 processor as an alternating sequence of 16-bit digitized I and Q samples of the received signal. The filter coefficients are represented to 12 bits of precision. The complex correlation is performed as shown in Fig. 13.29 and is similar to simple real correlation with the exception that the reference waveform coefficients are conjugated prior to the complex multiplication. The desired correlation terms are:

$$I = \Sigma\, I_{sm} \times U_{cm} + Q_{sm} \times Q_{cm}$$

and

$$Q = \Sigma\, Q_{sm} \times I_{cm} - I_{sm} \times Q_{cm}$$

where the subscripts s and c refer to the input signal and reference waveform coefficients, respectively. The subscript m identifies the time sequence.

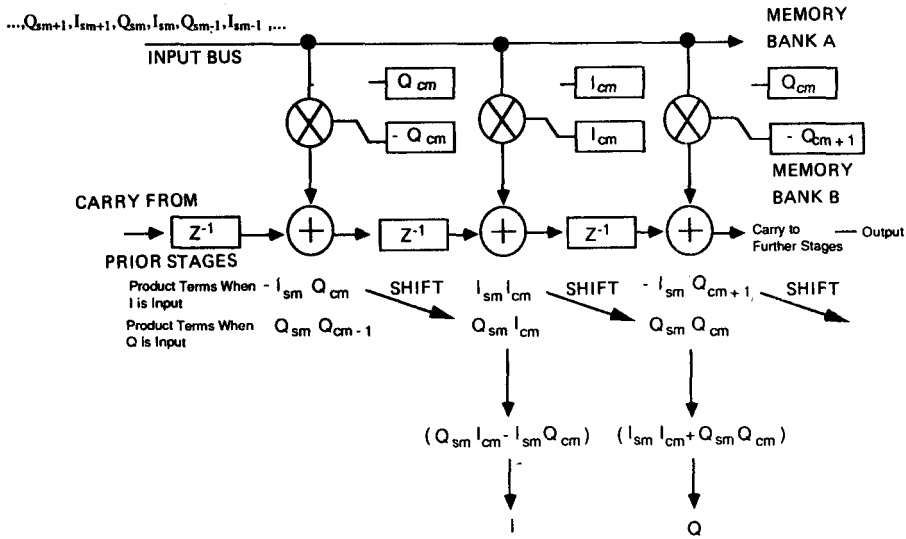

Figure 13.29 L-88 pulse compression processor. (*Courtesy of Dr. Larry Mertens [GE Company]*)

Two correlators are required to produce the in-phase and the quadrature outputs of the complex multiplier. Thus, 16 such processors are required to achieve the system's time-bandwidth product of 250. Each chip time-multiplexes the complex multiplication by storing the complex coefficients in two memory banks and swapping banks every time a new I or Q is input. The correlation sums, computed as indicated in the figure, are accumulated over all the 250 terms as the values propagate down the chain of delays and adders.

Also of interest, perhaps, is the fact that after pulse compression is complete, the L-88 processor utilizes a Plessey PDSP 16330 ("Pythagoras") processing chip to convert the resulting I and Q data to amplitude and phase and to detected video for further processing. Use of this chip eliminates the processing losses associated with the approximations that were discussed earlier (Sec. 12.5).

Chapter

14

Hybrid Processors, Meteorological Radar, and System Performance Analysis

14.1 The Moving Target Detector (MTD)

In the early 1970s the ground-based surveillance radars were bothered by ground clutter, birds, various forms of anomalous propagation, and weather. Air traffic control radars were capable with large commercial aircraft, but marginal in detecting and tracking the increasing general aviation fleet. MTI processors improved and numerous fixes were applied to the radar output. There were still too many false alarms to implement automatic detection and tracking. It was a time of rapid advances in digital processors and memory, but poor communication between the digital community and the radar designers who had a primarily analog background. It was recognized that better clutter rejection could be obtained with a coherent pulse Doppler processor than with an MTI, and that high-clutter locations could be stored in a map with a digital memory.

M.I.T. Lincoln Laboratory brought together several of these concepts into the *moving target detector* (MTD) [493, 385, 284].

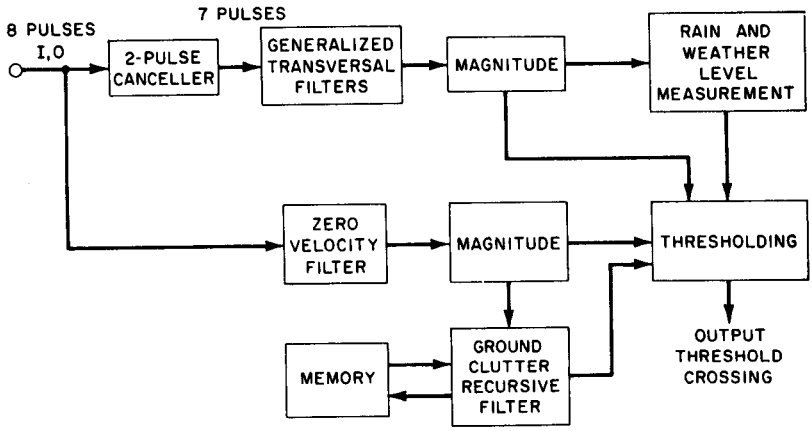

Figure 14.1 Early MTD block diagram.

The first MTD was basically an MTI canceler in cascade with an eight-point FFT or DFT plus some clever digital circuitry called a "clutter map," which collected the output of a zero Doppler filter. An early MTD block diagram is illustrated in Fig. 14.1 (from R. M. O'Donnell). The MTI gave a certain degree of clutter rejection and at the same time reduced the dynamic range of the residual clutter signals into the discrete Fourier transform. This allowed the DFT to be built with fewer bits in the multipliers and accumulators than with a pure pulse Doppler processor.

The clutter map is a recursive digital storage ground map of the residues of the MTI and performs a CFAR-like function (see Sec. 4.9) by taking a time average at each range cell rather than a spatial average over the terrain. This allows better detection of targets near, but not in, high-clutter regions. The clutter map averages the residues at each radar resolution cell over a number of scans to remove the uncertainties due to the fluctuations of the residues.

The MTD is now implemented in numerous air traffic control systems throughout the world. Terminal radars with the nomenclature ASR have a 60-nmi range requirement and are typically at S-band (3 GHz)* where weather clutter is significant. The FAA Enroute radars, denoted ARSR is the United States, have a 160- to 200-nmi range requirement, and due to their higher power levels and larger antennas, they also see precipitation even though their carrier frequency is only 1.3 GHz. In addition, air traffic controllers need estimates of precipitation levels for pilot warnings. Thus, the weather estimation capability is built into the newer MTDs that have only a slightly different block diagram, but

* Current Canadian ones called RAMP are at L-band.

considerably different implementation. This is illustrated in Fig. 14.2 [284]. The block on the left is for a saturation-interference test to eliminate any range cell with strong interference.

The technical data package for the ARSR-4 described the desired capability and a typical configuration. Some of the goals were [224] [663]:

Range	160 nmi
Capacity	550 aircraft
Range accuracy	1/32-nmi bias, 220-ft rms jitter
Angle accuracy	0.16° at $S/N > 30$ dB
Rotation rate	5 to 6 rpm
A/D converter	12 bits I and Q, 1.3-MHz rate
Digital filter	8-point at 0 velocity, 7 at others
Range gates	1280
False-target reports	1 per scan at output
Pulse duration	2 μs
Pulse-pulse phase	0.06° rms
Pulse-pulse jitter	5-ns rms
Instability residue	−60 dB referenced to peak
Stalo noise	(see Fig. 14.3)
Processor dynamic range	66 dB to rms noise
Improvement factor	48 dB for 0.2 to 0.8 PRF
CFAR	13 range cells
Clutter map	seven-eighth feedback factor one-half-mil resolution 1 nmi by 1.4° azimuth

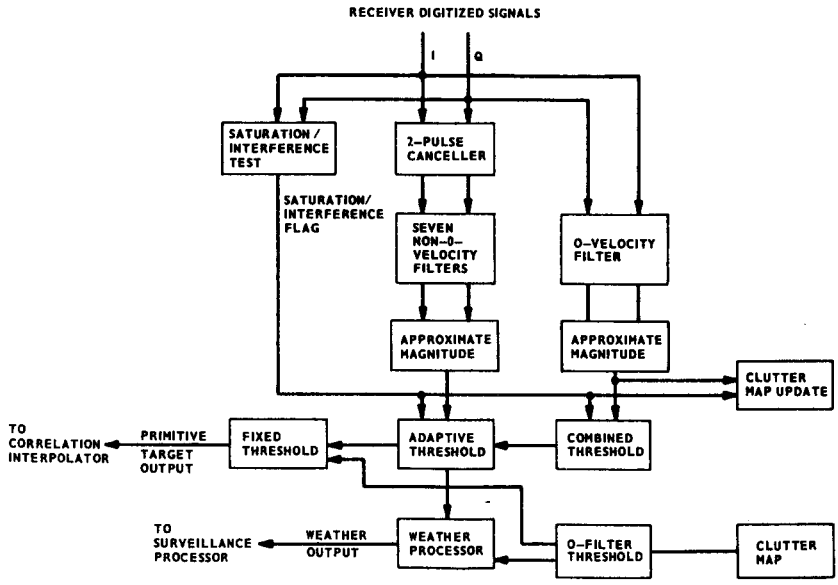

Figure 14.2 MTD II processor block diagram. (*From Goodchild [284]*)

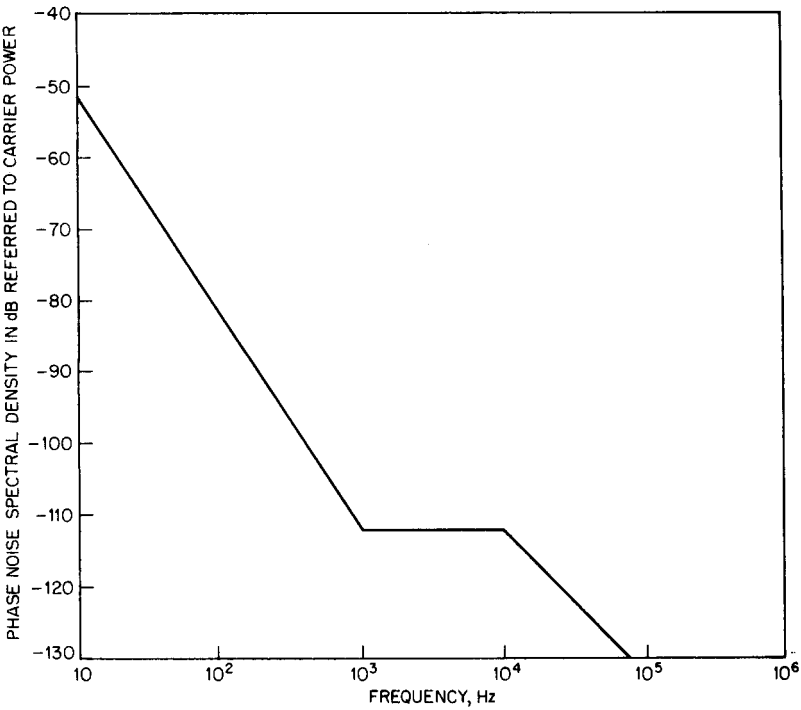

Figure 14.3 Typical permissible phase-noise versus frequency.

Weather data

A typical FIR filter characteristic is shown in Fig. 14.4 with the envelope of several nonzero filters. This response compares favorably with a typical MTI response. A comparison is shown in Fig. 14.5 for an earlier system called MTD II that was implemented on an ASR-7. The ASR-7 MTI improvement factor had a 27-dB maximum. The dramatic improvement is greater than would be expected on a new MTI design. Note that with the fixed PRF of the MTD there are blind speeds that have to be covered. These are due to the fixed PRF. Two PRFs (900 and 1100 Hz) were used in MTD II to achieve full Doppler coverage. In the FAA ASR-9 MTD, there are 10 pulses at a higher PRF and 8 pulses at the low PRF [132]; the bursts are synchronized with the antenna rotation to register the clutter map.

Range cells in the ASR-9 are only $\frac{1}{16}$ nmi, and the predicted range accuracy is $\frac{1}{50}$ nmi. The predicted azimuth accuracy is 0.04 to 0.16 beamwidths, depending on the number of reports (detections) on each PRF.

Processing losses in the target filters of the MTD II included 0.5 dB for azimuth weighting and straddling, 2-dB CFAR loss, 1.3-dB coherent

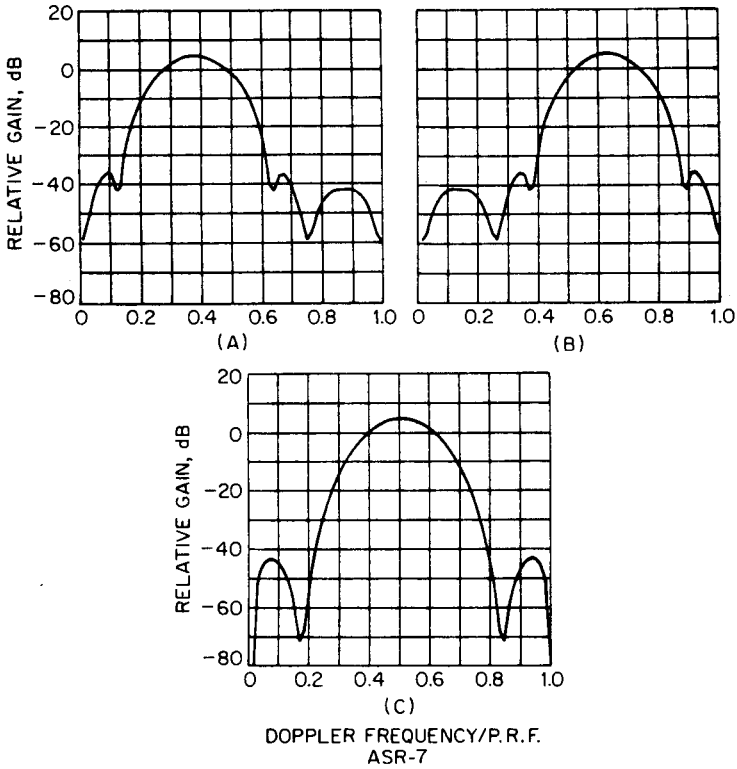

Figure 14.4 Nonzero velocity filter characteristics. (A) Filter 3; (B) filter 5; (C) filter 4. (*From FAA [206]*)

gain loss, 1-dB range-straddling loss, and 0.7-dB Doppler filter straddling loss [284].

Clutter maps

It was shown in Chap. 7 that land clutter is rarely homogeneous, and there is frequently a 30- to 40-dB spread between the reflections from flat rural terrain and either mountains or man-made structures. The clutter-to-noise ratio of these structures may be 60 to 80 dB when observed by long-range surveillance radars. MTI, MTD, or pulse Doppler processors can eliminate most of this clutter, but there will generally be a residue from the largest structures, surface vehicles, ships, rotating or vibrating objects, and flocks of birds. These residues occur at specific locations and may be isolated or clustered. Even though the density may be well less than 1/km, the number in the surveillance area may be large.

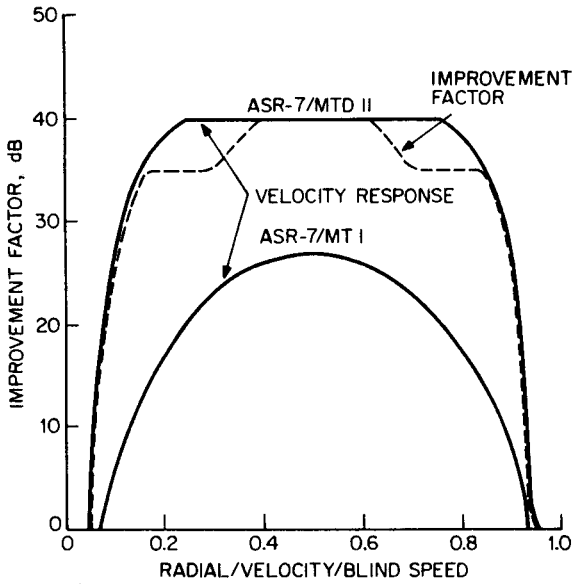

Figure 14.5 Improvement factor and velocity response of ASR-7/MTI and ASR-7/MTD II. (*From Goodchild* [*284*])

Taylor [694] discusses some of the design tradeoffs and how added bits in the weighting coefficients keep the Doppler sidelobes lower.

The spatial statistics of the signal processor residues are not Rayleigh and the CFAR circuits of Chap. 4 are not effective. If the CFAR threshold is set well above the mean to minimize false detections, the overall sensitivity loss is high. If the threshold ratio is reduced, numerous false detections are sent to the data processor, leading to possible saturation.

It is useful to digress briefly to explore the data processor problem. With modern technology, it is not difficult to design a data processor that accepts 500 to 2000 reports per scan if they are distributed more or less randomly around the azimuth scan. The tracking portion of the data processor, often called a *digital target extractor* (DTE), sets up a window about the report with dimensions related to the distance the desired targets can move in the scan period. If the report stays in the window, it is rejected after several scans. However, that report location must be retained, or the same clutter artifact is again reported and the process repeated. The problem comes from the fact that the clutter artifacts (autos, trucks, billboards, towers) fluctuate and are clustered in space. In urban areas, even small ones, the clustering is dramatic and the residues are within the desired windows. The fluctuation of each residue may give a false indication that there is a target moving from one artifact to another or from an artifact to a real target to an

artifact. Thus, a few tens of residue reports in an area can dramatically degrade performance. This is not as large a problem in air traffic control systems, where commercial or general aviation either avoid, or at least stay only briefly in, high-clutter (urban?) areas. It is more of a problem in military or counterinterdiction systems, where a hostile pilot can make a good estimate of where the clutter regions exist. In addition it may be desirable to launch an attack missile along such a path, where radar performance is degraded.

The foregoing problem led to the development and production of clutter maps as another form of CFAR that is based more on spatial nonuniformities than on time fluctuations. It is implemented in a number of systems in which the clutter-to-noise ratio exceeds the improvement factor. Prior to the clutter map era, IF limiters were often placed prior to the signal processors, providing an upper bound to the overall clutter suppression [335].

The clutter map is a radar map, usually in polar coordinates, on which each clutter map cell is a pixel that represents the mean residue power of an area representing one or a few radar resolution cells. The residues are either fixed in space or are slowly moving. Thus ships, which are part of the clutter in an air traffic control system, may be the target in a vessel traffic control system. Obtaining the mean level of the residue is essential because, while the spatial locations may be fixed, there is a temporal fluctuation in the vast majority of the cells. In addition, the desired targets make a contribution to the map on each scan, and the averaging process over many scans minimizes their effect. Aircraft are not likely to stay in a single clutter map cell for many scans.

The most common implementation is to create a simple recursive or single-pole filter at each clutter map cell of the form. [673, Chap. 15; 511, 427].

$$y_i = (1 - w)y_{i-1} + wx_i$$

where y_{i-1} = the old clutter map amplitude
y_i = the updated clutter map value
x_i = the radar output on the current scan
w = the weighting factor, usually $\frac{1}{4}$, $\frac{1}{8}$, or $\frac{1}{16}$

A target is detected when the new value x_i exceeds ky_{i-1} where k is the threshold constant. This is essentially another form of CFAR with some loss based on the number of samples. The effective number of integrations can be expressed as $\eta_e = (2 - w)/w$. For $w = \frac{1}{8}$, $\eta_e = 15$. Shrader and Gregers Hansen developed a clutter map loss (partly

based on the work of Nitzberg) [673]. While not exactly linear, it can be approximated;

$$\text{Clutter map loss (dB)} \approx 5 f_a/\eta_e \tag{14.1}$$

where f_a = the magnitude of the exponent in the false alarm probability, and the loss is from about 0.4 to 2 dB. If the cell maps include several resolution cells η_e is increased. The foregoing calculations are approximate since they assume that the residues are independent. One observation is that current clutter maps at airports vary ± 4 dB over a three-month period. When observing the mountains to the west of a Denver site, the false alarm probability was as high at 0.45 in heavy clutter without the clutter map and dropped to 0.02 with the clutter map.

There is a problem with slowly moving clutter such as ships, bird flocks, vehicles, etc., which move from cell to cell during a scan. Similarly, if the radar is on a ship, all other clutter appears to move. Khoury and Hoyle [399] describe a "spreading" technique. This is accomplished by letting the value in the clutter cells spread into adjacent cells at a selected rate. This requires a desired target to move more rapidly per scan. The result is a velocity response that can be tailored to the desired target's minimum velocity. The clutter map stores echoes from moving targets, including weather, and the velocity discrimination has to be carefully controlled to detect slow-moving aircraft.

The clutter map approach does not work as well for airborne radar. In addition to clutter artifacts moving rapidly from cell to cell, the aspect angle of the artifacts relative to the radar will change, and a face of one building which is quite large at a specific angle to the radar may vanish, and the echo from another building may dramatically appear.

It is not clear whether frequency agility helps or hurts in developing clutter maps. It does increase the number of effective samples, but clutter artifacts appear on some frequencies and not others.

14.2 Meteorological Radar

The backscatter sections in Chap. 6 described the reflections from precipitation as a clutter to a target-detection radar. In meteorological or weather radar this "clutter" is the target and the reflections from land are the clutter. While weather radars have been widely utilized since the 1950s, the signal processing and displays were unsophisticated and indicated only gross precipitation patterns with warning capabilities only when highly skilled operators were watching the displays. In the 1970s, the addition of digital postdetection integrators and digitally

refreshed memories removed much of the "speckled" or "mottled" look on the displays. This was closely followed by color displays that gave a much better indication of the intensity of the precipitation. These were backfitted to the 1950s era WSR-57 National Weather Service radars.

In the 1960s it was shown that Doppler radar could yield added information on the horizontal velocity of the precipitation and, more importantly, indicate the turbulence and/or wind shear in a radar resolution cell (see Nathanson and Reilly [501]). Special-purpose digital circuits were developed to cure certain problems. One of the problems was that land clutter was often misinterpreted as weather echoes, especially when there were ducting conditions. It was called an *anomalous propagation indicator* (API) and was based on measuring the relative fluctuation in a number of pulses [373]. If the relative fluctuation was less than a selected value, those radar cells were inhibited. It is also used in the newest systems.

Experiments in the 1970s related the radar observations to potential hazardous weather [187], and tornado warning time could be increased from about 2 min with a reflectively-only radar to about 20 min with a high-resolution Doppler radar. While experimental Doppler radars were common in the late 1970s and early 1980s, the cost of replacing the National Weather Service radars with new digital Doppler radar delayed the development into the mid 1980s. The system that evolved was called NEXRAD and the radar designated the WSR-88D [324]. About 160 systems are being deployed in the early 1990s for both civil and military uses. The impetus for the development was a combination of the damage and loss of life due to severe storms in the United States plus the growing realization that many aircraft disasters were weather related. About 650 people were killed in numerous U.S. aircraft, weather-related accidents between the mid-1960s and the late 1980s. Most of these are now attributed to microbursts near air terminals. These local phenomena are discussed later.

Several design tradeoffs are necessary to combine the unambiguous, long-range weather-detection goals of a national weather radar network, and the higher PRFs required for Doppler radars to meet sampling requirements for unambiguous Doppler measurements. This is compounded by the requirements for accuracy of measurement of mean radar reflectivity (Z_e), mean radial velocity (V_o), and mean spectral width (σ_v).

To achieve reflectivity accuracies of about 1 dB requires averaging (integrating) numerous (> 30) *independent* measurements, as described in Doviak and Zrnić [187, Chap. 6]. This is compatible with the low PRF required for long-range detection, but not compatible with Doppler measurements. Doppler measurements require samples while

the echoes are still correlated, or, stated in other terms, the sampling rate must be well above the inverse of the spectral width. Thus, while there are ways to do simultaneous reflectivity and Doppler measurements, it is simpler and less prone to range or Doppler foldover problems to sequentially transmit a low-PRF "reflectivity mode" followed by a higher-PRF "Doppler mode." Unfortunately, this takes considerable time for narrow-beam, pencil-beam radars. In NEXRAD the reflectivity mode uses PRFs as low as 318 Hz, while the Doppler mode has PRFs to 1304 Hz. These and other parameters of the WSR-88D are shown in Table 14.1 from Heiss et al. [324]. The time to scan preselected volumes is about 5 to 6 min due to the high resolution goals. This is too long a scan period for timely microburst alerts.

The velocity gradients of interest and the desire for high resolution in severe storm areas led to choice of a 28-ft antenna with a beamwidth of about 1° and range resolution cells of about 0.25 km. A large dish was selected for cost considerations. In early trade studies, the rapid data acquisition properties of phased-array or stacked-beam antennas were considered, but projected costs were excessive. Sidelobes in the elevation plane are specified to be quite low to minimize ground clutter. Echoes from adjacent range cells are often averaged in weather radars to reduce fluctuation and improve accuracy. Thus, the selected radar resolution in the reflectivity mode is often much finer than that required by the user. The slight loss in detectability is more than compensated for by improved accuracy.

The weather radars have MTI circuits to reduce the ground clutter

TABLE 14.1 NEXRAD, WSR-88D Characteristics

Radome diameter	39 ft (12 m) paraboloid
RF loss–two-way	0.3 dB at 2800 MHz
Pedestal	Elevation over azimuth
Steerability	Azimuth: 360° Elevation: −1.0 to 45.0°
Rotational rate—maximum	Azimuth: 36° s^{-1} Elevation: 36° s^{-1}
Antenna polarization	Circular
Reflector diameter	28 ft (8.5 m)
Gain (at 2800 MHz)	45.5 dB
Beamwidth	0.95°
First sidelobe level	29 dB
Transmitter frequency	2700 MHz to 3000 MHz
Peak power	750 kW
Pulse widths (nominal)	1.57 μs and 4.5 μs
rf duty cycle	0.0021 maximum
PRFs	Short pulse: 318 to 1304 HZ Long pulse: 318 to 452 Hz
Receiver dynamic range	95 dB
Noise temperature	450° K
Bandwidth, 3 dB	0.79 MHz

SOURCE: *Microwave Journal* [324]

that would indicate higher rainfall rates if not eliminated. The ground clutter would also bias the velocity measurements. However, the MTI notch does eliminate some weather with low radial velocity.

Ground clutter rejection is achieved by a five-pole, infinite impulse response (IIR) filter and achieves over 50-dB clutter rejection (see Chap. 11). To achieve this, the transmitter and receiver were designed to have a phase noise-to-carrier ratio of -54 dB (integrated over the Nyquist co-interval).

The received echoes are linearly integrated to obtain an accurate measure of radar reflectivity. Specified sensitivity is -8 dB Z_e at 50 km and typical sensitivity is 0.01 mm/h rainfall at this range. Doppler shift is estimated by a pulse pair processor (described later in this section). The standard deviation of the velocity estimate is less than 1 m/s for $S/N > 8$ dB with an input spectral width of 4 m/s. The spectral width is estimated from the autocorrelation function evaluated at a lag equal to the interpulse period (see Chap. 9). The standard deviation of the width estimate is less than 1 m/s at $S/N > 10$ dB for spectral widths of 4 m/s.

In operational tests in August, 1989, severe storms were detected with 91-percent probability relative to a national average of 58 percent for prior systems. The false alarm rate was 21 percent compared with a previous 57 percent. Raw radar outputs are converted to products before dissemination over a national network. Displays are 640 $\times$ 512 pixels, with magnification and storage capabilities.

Long-range (>200 nmi) ground-based weather radars are generally at S-band (3 GHz) to achieve penetration (low attenuation) during heavy rains, even though the reflectivity is about 10 dB higher at C-band (5.5 GHz).

Microburst detection radars

In the early 1980s, microbursts were identified as the cause of most of the aircraft accidents, rather than the gust fronts that had been previously blamed. Microbursts are short-lived phenomena with an average lifetime of 10 min. They are produced by relatively innocuous convective clouds (dry microbursts) as well as by thunderstorms (wet microbursts) [224]. The primary problem is the approach-and-departure corridor to about 3 mi from the ends of the runways. A typical microburst structure is shown in Fig. 14.6. In 1987 tests at Denver, nearly 500 microbursts were recorded. They have also been found to be prevalent near Brisbane in Australia.

The FAA Terminal Doppler Weather Radar (TDWR) Systems Requirement Statement specifies that a wind shear is reportable if it produces a runway-oriented wind speed rate of change of 20 kn per

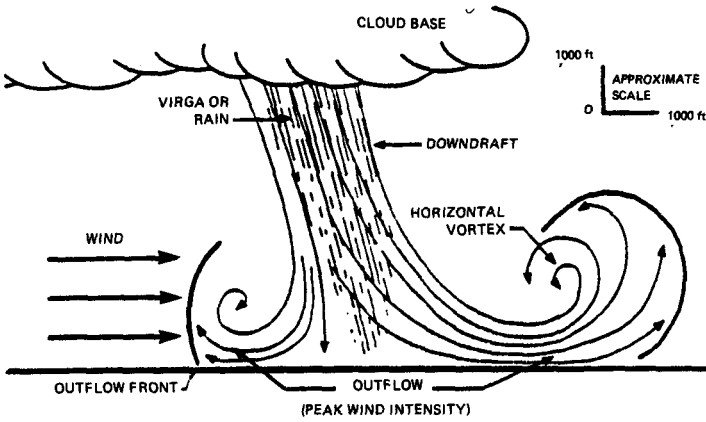

Figure 14.6 Microburst structure. (*From FAA [224]*)

nautical mile over a distance of 0.5 to 4 nmi. The probability of detection must be 90 percent with a false report probability of less than 10 percent.

The electromagnetic spectrum, especially near airports, is overcrowded at S-band with the ASR terminal radar family and NEXRAD both being at that band. Since the TDWR is primarily for shorter ranges, C-band was chosen for the carrier frequency. The transmit power requirements are lower, but there is a problem with Doppler ambiguities. The desired velocity coverage is ± 40 m/s, but the unambiguous Doppler is only ± 22 m/s at the maximum PRF of 1672 Hz. To allow for dealiasing, several PRF from 1066 Hz to the maximum are utilized. A low PRF allows reflectivity data to 460 km. While volume scan is repeated at 5-min intervals, the lowest elevation angles are revisited each minute for microburst detection. About 50 radars are in production at Raytheon [472].

In other respects TDWR is functionally similar to NEXRAD. The major parameters are shown in Table 14.2. Clutter filtering is performed with four-pole equal-ripple elliptic filters with a flat passband. The digital implementation uses 12-bit A/D converters, and has a land clutter suppression goal of 55 dB.

Since microbursts are physically small, point moving targets such as aircraft, automobiles, air terminal vehicles, and birds must be eliminated before detections are declared. Point target algorithms have been tested and are being improved. The key to success is simple timely warnings transmitted to pilots with few false alarms.

Airborne weather radars

Since pilots have to make the final decision as to whether to land or "pull off," it is desirable to have the microburst detection radar capa-

TABLE 14.2 TDWR Performance Parameters

Operating frequency		5.6–5.65 GHz
Instrumented range	Doppler mode	89 km
	Reflectivity	460 km
System clutter suppression		55 dB
Antenna (25 ft)	Gain	50 dB
	Beamwidth	0.55° Pencil beam
	Sidelobes—near-in	−27 dB
	Sidelobes—beyond 5°	−40 dB
	Beam positioning accuracy	0.05°
Transmitter	Peak power	250 kW
	Average power	550 W
	Pulse length	1.1 μs (−6 dB)
	PRF	2000 Hz max
Receiver	Dynamic range	129 dB
	STC	26 dB
	AGC	42 dB
	Linearity	61 dB
	Noise figure	2.3 dB
Signal processor		
	Clutter filters	4-Pole elliptic
Reliability	MTBF	550 hrs
	Inherent availability	0.99967

Clutter canceller	Infinite impulse response design
Notch half-widths	0.5 to 4 m/s (0 to 8 kn)
Reflectivity bias	0 to 1 dB (on 4 m/s width)
Minimum usable velocity	0 to 4 m/s (0 to 8 kn)
Range sampling	0.25 km (0.13 nmi)
Velocity calculation	Pulse pair processing
Estimate accuracy (nominal)	1 m/s (2 kn)
Number of pulses averaged	40 to 200
Range increment	0.25 km (0.13 nmi)
Reflectivity calculation	Linear power average
Estimate accuracy (nominal)	1 dB
Number of pulses averaged	6 to 64
Range increment	1 km (0.54 nmi)

SOURCE: *Microwave Journal* [472]

bility in the aircraft itself. Since there is limited space (about 0.8 m diameter) in the nose of an aircraft, the radar must also have a long-range weather-detection capability. This presents a difficult tradeoff as the beamwidth of NEXRAD is about 1.0° and 0.55° for TDWR. To achieve comparable resolution would require going to 35 GHz, where the attenuation in range is quite high and it would be difficult to avoid both range and Doppler ambiguities.

The starting point is the current airborne weather radars that are either at C- or X-band. The C-band systems have less attenuation in

heavy rain. They are currently being implemented with limited Doppler capability. In level flight, the radar beam can be slightly elevated to minimize ground clutter. In the terminal approach, the glide slope is about 3°, and the radar must look down at the land clutter, automobiles entering and leaving the terminal area, and other vehicles on taxiways, etc. At these angles, the clutter background is considerably higher than for surface radars. In addition, the antenna diameter is limited to about 30 in, precluding beamwidths narrower than 2.5 to 3.0°. Land clutter rejection is made more difficult because of the spectral broadening due to the high aircraft velocities and moderate beamwidths.

The goals for the next generation of airborne weather radars are much broader to justify the added cost and complexity. Studies and experiments are underway at NASA, Langley, VA. and at various contractors [212].

The NASA, Langley program is emphasizing the airborne microburst detection and warning problem. That problem is separated into two subareas: the high reflectivity or "wet" microburst with reflectivity of 20–35 dBZ, and the low reflectivity or "dry" microburst with reflectivity of 0 to 10 dBZ. Obviously both 15- to 20-dB greater sensitivity and clutter rejection are required by the dry microburst. Stable transmitters with 10 to 15 dB more power are being considered. While the ground clutter spectrum is quite narrow, the spectra of the vehicles occupy the same Doppler region as the microbursts. The microbursts have to be selected by algorithms that sort on the basis of spatial Doppler patterns as opposed to the point moving target characteristics of surface vehicles. Microbursts are approximately circular with a diameter of 1 to 4 km at the surface.

Table 14.3 shows an abstract of overall goals for an airborne sensor system that might include optical, as well as radar, sensors. Note that

TABLE 14.3 Goals for Airborne Weather Sensor

	Range/time	Velocities	Angle, etc.
Long-range weather detection	200–300 nmi		± 90° Az 3° Res. clutter suppression
Microburst detection	3–10 km/15–40 s	± 50 m/sec	± 30° Az clutter suppression 100–300 m resolution
Ground mapping			0.5° resolution
Runway imaging	0.5 km		High data rate
Wake vortex detection	10–20 s		± 30° clutter suppression
Clean air turbulence	180 s		

the goals include a mapping capability as a navigation aid, and a high-resolution terminal imaging capability as a landing aid. The detection of wake from other aircraft, especially on parallel runways, and clear air turbulence (CAT) requires a much more sensitive radar or, more likely, a laser radar.

If microburst detection, without the need for long-range weather detection were the only requirement, the improved sensitivity and angular resolution of a 16- or 35-GHz radar would be a possible solution for many of the goals. Meeting most of the goals likely requires either two radar frequencies or an X-band radar and an optical sensor.

The pulse-pair processor

In most target-detection radars that transmit a uniform pulse train, either a matched-filter processor or an MTI filter is used for the signal processor. The matched filter is usually some form of discrete Fourier transform (DFT). The signal level in each discrete filter is tested against a threshold level established by comparing with the signal levels in the adjacent range cells and Doppler filters. If the Doppler of the target is desired, the signal levels in adjacent filters are compared. In weather radar the goals are slightly different. The desired measurements are the power of the echo, the mean radial velocity, and the velocity variance. In weather radars these are computed directly from the autocorrelation function for the 0th, first, and second lag expressed here as R_0, R_1, R_2. If the power spectrum is symmetrical, and a gaussian-shaped spectrum is assumed, one set of algorithms is [418]:

Power or intensity, 0th moment

$$\text{dBZ} = 10 \log (k|R_0|) \tag{14.2}$$

(The noise power should be subtracted from R_0)
Mean radial velocity or first moment

$$V = \lambda/4\pi T \tan^{-1} [I_m(R_1)/R_e(R_1)] \tag{14.3}$$

Velocity variance or second moment

$$\sigma_v^2 = \lambda^2/24\pi^2 T^2 I_m(|R_1|/|R_2|) \tag{14.4}$$

where λ = the radar wavelength
T = the interpulse period
k = a constant from the radar parameters

These turn out to be *maximum entropy* estimators. The estimates are unbiased if the spectrum is symmetrical, but that condition is not

necessary for good estimates. Doviak and Zrnič [187] give slightly different algorithms and an error analysis for various assumptions about the nature of the weather spectrum. The error of these estimates is in some cases less than that obtained from DFT analyses, but degrades when the spectral width becomes an appreciable fraction of the inverse of the interpulse period. The normalized velocity error is shown in Fig. 14.7. The primary virtue is the simplicity of the pulse pair processor (PPP) relative to DFT or FFT implementations. The computation of the autocorrelation function is a simple product of pair of adjacent time samples when the signals are represented in I/Q form. Where detectability is not the main criterion, it is an appropriate choice. It is used in both NEXRAD and TDWR.

Space-based meteorological radar

In the 10 to 15 years after 1992, the ground-based meteorological radar field will be dominated by NEXRAD, TDWR, and their derivatives. They will give good short-term predictions where they are densely deployed. The next advance will be satellite-based radars to extend the capabilities of the passive (optical and microwave) radiometric of the

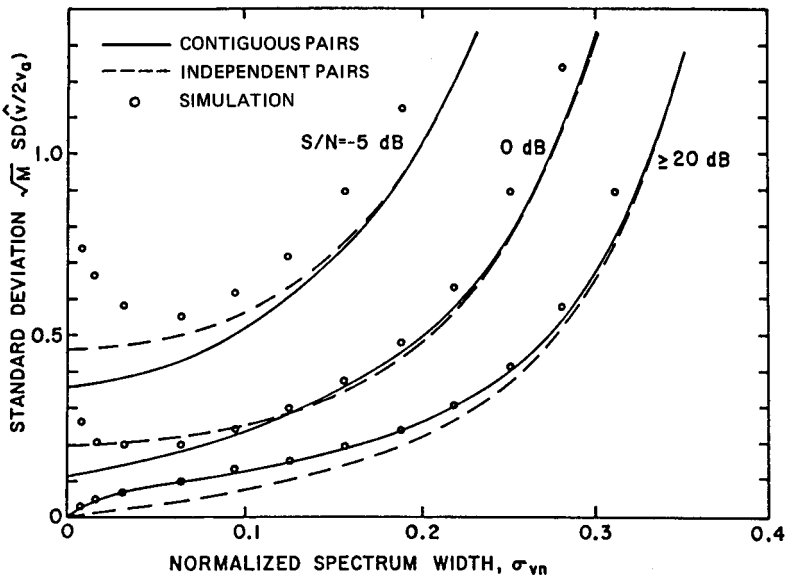

Figure 14.7 Standard deviations of the mean frequency estimate (autocovariance processing). Spectrum width is normalized to the Nyquist interval $2v_a$. Note a gradual increase between 0 and 0.2 and an exponential rise thereafter. (*Courtesy Academic Press* [*187*])

Defense Meteorological Satellite Programs (DMSP) and the NOAA satellites in the United States.

There are several limitations of passive sensors in meeting the primary current goals of determining cloud bottoms, cloud tops, and the altitude of the melting layer. These are required for global weather modeling, longer-term weather prediction, and ground-based military systems that need to estimate visibility for optical instruments. These new requirements are not well served by ground-based radars whose definition is primarily in the horizontal plane.

Space-based meteorological radars (SBMR) have been studied since the early 1970s [673, Chap. 22, 105]. Since the range for low-orbit satellites will be 600 to 1000 km the sensitivity and resolution must be drastically better than for surface systems, which only have 25 to 40 percent of these ranges. In addition, the goal is to see clouds that have 30-dB lower reflectivity than light rains. All this must be accomplished with a total weight and power consumption of a small fraction of ground-based systems.

The studies of the 1970s pointed out that one of the most severe problems is to separate the echoes from clouds and light rain from the dramatically higher echoes from land and oceans. This requires large antennas with narrow beamwidths and low sidelobes. The sidelobe requirement is quite critical, since to obtain the required swath (*coverage area*) means observing low-altitude precipitation at slant angles where these echoes cannot be resolved in time from the ground echoes in the sidelobes just below the precipitation of interest.

The early studies showed that antenna sizes must be 300 to 1000 wavelengths and that carrier frequencies must be 10 GHz or greater. Fortunately, the space-based radar does not have to look through the precipitation for more than a few kilometers, and the millimeter wave radar is practical if the attenuation can be accounted for. In the 1970s the antenna designs were either not practical or too costly.

By the late 1980s, space-band meteorological radar became feasible as a result of relatively large apertures placed into orbit and significantly lower receiver noise temperatures at 10 GHz and higher. Several designs evolved for possible launch in the mid- to late 1990s.

Table 14.4 illustrates the two-way attenuation γ and backscattering coefficient η for hydrometeors from 14 to 140 GHz. Note the dramatic increase in reflectivity and attenuation with increasing carrier frequency. The melting layer has quite high attenuation, but is only about 0.3 km thick. The proposed systems fell into two areas. The first was to monitor tropical rains under the NASA TRMM program. It was originally proposed as a two-carrier frequency system at roughly 13.6 and 35 GHz. The two frequencies were felt to be necessary to calibrate

TABLE 14.4 Attenuation and Scattering Properties

	13.6 GHz		35 GHz		94 GHz		140 GHz	
Frequencies	(dB/km)							
1 mm/h	0.05	−63	0.5	−48	1.9	−43	2.5	−39
Melting	1.8	−47	12.5	−34	22.5	−37	28.5	−39
16 mm/h	1.2	−45	8.7	−32	14.0	−35	17.8	−37
Stratus	0.1	−101	0.9	−85	2.9	−69	4.3	−62
Cirrus	0	−82	0	−65	0	−48	0	−41

the uncertainty in the attenuation. Later designs led to a single-frequency system at 24 GHz due to cost considerations.

Another study for the Air Force [504] evaluated other approaches with the goal of measuring the tops and bottoms of stratus clouds (0.3 gm/m^3 water content). Frequency tradeoffs and system designs were iterated for best overall performance. The bands at 13.6 and 140 GHz were eliminated fairly quickly due to the physically large antennas and large transmitters at the low frequency and excess attenuation encountered at the highest frequency. The appropriate meteorological radar equation can be written in several forms: [105] [673]

$$\bar{P}_r = \frac{K P_t \tau D^2 F M d^3}{\lambda^4 R^2}$$

where attenuation is neglected and

K = constant
P_r = average receive power
P_t = peak transmit power
τ = effective pulse duration (see Chap. 2)
D = antenna diameter
F = beam shape and filling factors
M = liquid water content
d = droplet diameter
λ = carrier wavelength
R = range (related to altitude)

Also in another form

$$\bar{P}_r = \frac{10^{18} P_t G_T G_R C \tau |K|^2 Z}{512 (2 In 2) R^2 \lambda^2} \qquad \text{in MKS units}$$

where G = peak gain (gaussian shape)
c = velocity of light
K^2 = 0.93 for rain, 0.2 for ice
Z = reflectivity in nm^6/m^3 (Chap. 6)

The frequency tradeoff showed that 35 GHz was slightly superior to 94 GHz. This is illustrated in Table 14.5. Note that they would be comparable if only clouds without a melting layer were present. This tradeoff assumed that the state of the art was used for transmitter antenna design. With the large apertures required, tolerances would limit antenna dimensions to 500 to 700 λ.

Another interesting result was that the performance was almost independent of radar configuration. A dish or planar array was compared with a long linear-array system and a synthetic aperture (SAR)

TABLE 14.5 Relative Merits of 35 and 94 GHz

Parameter	35 GHz	94 GHz
Peak transmit power	+6 dB	
Aperture area	+6 dB	
Losses	+1.8 dB	
System noise temperature	+2 dB	
Cloud penetration	+1 dB	
Z_e clouds (light rain)		+16 dB (5–10 dB)
Melting layer penetration	+3 dB	
Total	+19.8 dB	+16 dB

configuration. The SAR was comparable only when a very small swath (< 100 km) was acceptable. Small swaths have little value in global monitoring. The dish was selected as the best option until at least the year 2000. The phased array is heavier, more costly, and probably more "lossy" at millimeter wavelengths.

The parameters of the cloud-sensing radar called ALLRAD are shown in Table 14.6 based on components available in 1990 [504]. It was shown in the study that adding a lower-frequency radar was heavy and only useful for heavier rains. It was also shown that calibration up to about 30-mm/h rainfall rate could be obtained with simple radiometers and by utilizing the reduced backscatter from land or ocean areas to estimate attenuation. A comparison of this cloud radar and the TRMM system which needs only to observe rain is shown in Table 14.7. The difference is the reflectivity of clouds versus light rain.

Other proposed systems were described by Cantafio and Kovalcik [105] including TRAMAR, a dual-frequency system at 9.7 and 24 GHz,

TABLE 14.6 Radar/Radiometer parameters

Frequency—radar	35.6	GHz
Frequency—radiometer	36.6–37.6	GHz
Antenna diameter	4.1	m
Beamwidth (one-way)	0.16	degrees
First sidelobes	31	dB
Gains (40% efficiency)	59.7	dB
Number Transmitters	2	
Peak power/XMIT	6.2	kW
Average power/XMIT	150	W
Pulse repetition frequency	7	kHZ
Pulse duration	3.3	Micro
Losses (approximate)	7	dB
System noise temperature	500	Deg K
Rotation rate	17	rpm
Nadir angles	10–25	degrees
Horizontal resolution (rain)	~2	kM

TABLE 14.7 Rough Comparison of TRMM and ALLRAD

Parameter	TRMM	ALLRAD	*S/N* diff.
Gain (dB)	47.7	59.7	24.4 dB
Peak power (kW)	0.57	6.2	10 dB
Loss diff (dB)	0	−2.5	−2.5 dB
Pulse duration	1.67	3.75	7 dB
Beamwidth (deg)	0.71	0.16	−13 dB
Frequency (GHz)	13.8	35.6	8.2 dB
Noise figure (dB)	2.5	2.5	0 dB
Relative total			~34 dB

PRF and integration area roughly comparable.
TRMM parameters from 1989 Radar Met. Conf.

with a beamwidth as narrow as 0.1° at 24 GHz. They also summarize another concept called LORRA with beamwidths in the azimuth plane of less than 0.05° at 35 GHz. These have advanced antennas with electronic scan in one plane.

Another design problem for SBMR is in the transmitter area. Average power requirements are in excess of 100 W, but resolving low-lying cloud bottoms from the earth's surface limits pulse durations to a few μs. In many systems, this would immediately suggest pulse compression. However, with the typical geometries for weather operation, the ground echo exceeds the cloud echo by 50 to 60 dB, and, thus, the near-in range sidelobes of the pulse compression system must be reduced to a comparable level. It is unlikely that this level has been met in airborne or satellite systems. If the requirement is only to see very light rain, pulse compression may be practical.

Orbiting satellites will have a limited swath, but coverage can exceed 800 km. Multiple satellites are required for global coverage, but nowhere near the number of ground-based systems. In addition, the satellite will provide radar coverage over the oceans that is not currently available.

Eliminating the requirement for multiple satellites in orbit would require the use of a satellite in a geosynchronous orbit. Unfortunately, a monostatic configuration at the 36,000-km range is currently impractical as the relatively large meteorological systems such as NEXRAD have only 1/50 of that range. One possible alternative is a bistatic configuration with the transmitter in geosynchronous orbit and multiple receive-only radar systems on the ground or on aircraft. The direct signal received from the satellite is cross correlated with the bistatic echoes from precipitation (Nathanson in [24 pp. D341–350]).

The signals impinging at a passive receiver, resulting from illumination from a geosynchronous satellite, will yield more or less constant reflective power at reasonable range from a ground station. While the power intensity at a ground receiver falls off inversely as the square

of the range from the receiver, the beam volume increases directly as the square of the range from the receiver. (The angular resolution degrades with increasing range.) There is no need for STC.

The power and aperture sizes are not great due to the volume-search mission of a meteorological radar. Since at any point on the earth's surface it is desired to scan a preselected area (or volume), there is not a significant difference whether that area is scanned with a short, intense beam for a short period of time, or the received power is integrated over a long period of time. Basically, the criterion for an area search is the energy incident on that area in the desired period. It is more efficient to have the satellite illuminate an area of 400 to 700 km in diameter at one time rather than flood the entire country with a lower power density; since this requires only a 1- to 2-m aperture at 12 GHz, there is no severe demand on satellite state of the art. Average levels required to detect light rains near the ground are approximately 200 W radiated from the satellite. This is well within the envelope of what has been accomplished at geosynchronous altitudes. Due to the geometry involved, it is necessary only to scan the satellite beam by $\pm$ 3° in one plane and $\pm$ 1½° in the other plane to cover the United States. This scanning can be accomplished either mechanically, since it is rather slow, or electronically, using multiple feeds or frequency-scanning techniques.

The 12 to 14-GHz carrier frequency was suggested because there are current communication satellite transmitters with scanning arrays operating in that band. The beams from the satellite would periodically scan the surface or concentrate on areas with impending severe weather. The higher carrier frequency is acceptable because although the attenuation coefficient is higher, only one-way horizontal attenuation is involved.

When the technique was proposed (1981), 2- to 4-mm/h rain detection was practical. With new technology, especially low-noise HEMT receivers (see Chap. 2), light-rain detection (< 1 mm/h) is currently practical. Receive antennas of the size of current airborne weather radars (30 in) are adequate.

14.3 Aerostat Surveillance Radars

From the 1970s there have been a few radars attached to aerostats tethered as high as 15,000 ft above sea level. This deployment allows coverage against low-flying aircraft to ranges of 160 to 200 nmi. These surveillance radars are used for military defense and civil purposes such as drug interdiction, and to counter possible smuggling and terrorism.

The United States and other countries are deploying various radars along their borders, coastlines, and islands. These include lightweight

versions of surveillance radars with simplified air traffic control systems, for example, large Customs/Coast Guard aerostat radars by GE which are called L88 (partly based on FPS/117 "SEEK IGLOO" technology), and large Customs/Coast Guard aerostat radars by TCOM/ Westinghouse, which are generally called LASS and are installed as Cariball or Sowrball (these are derivatives of the Marine Corps TPS/ 63). The LASS system is shown in Fig. 14.8. There are also a few older Air Force aerostat radars, and some smaller ones called SASS. The SASS systems are based on Westinghouse X-band airborne Doppler radars.

The aerostat radars are primarily designed to detect and track aircraft; to enable them to have long-range coverage they are deployed at 10,000 to 15,000 ft above sea level. With these geometries they also see numerous vehicles, boats, and ships. The larger systems use L-band, have relatively large lightweight antennas, and transmit several hundred kilowatts of peak power. They can remain at altitude for several days, and all power for the radar is brought up through the tether. A significant advantage is that the motion is quite low, and velocity compensation is not needed as in airborne radars. The smaller aerostats (SASS) are flown at several thousand feet and can be tethered from ships. Typical radar ranges are of the order of 50 nmi.

The large aerostats use fixed- or staggered-pulse, low-PRF MTI and pulse compression. The digital pulse compressor was outlined in Chap. 13. The clutter rejection is high (60 to 65 dB) as they look down at the land at steeper angles than do surface radars.

In some areas they are used for small boat tracking. Maritime channels have been designed to be in parallel with, but not interfering with, the air target channels on the aerostats. These are, in general, designed for radial velocities of about 10 to 70 kn.

The current trackers are basically track-while-scan systems. On each radar scan (about 12 s), the range to the target is measured, as is the centroid of the "run length" or "hits" in azimuth. These are stored for several scans in a *digital target extractor* (DTE), and a velocity vector is derived from the change in target position from scan to scan. Tracking is accomplished in a similar manner to air traffic control systems.

14.4 Performance Estimation for Coherent Pulse Radars*

This section describes the numerous limitations on the actual performance of a coherent pulse radar or a radar mode whose primary purpose is to discriminate a small target in the presence of clutter. The emphasis is on pulse train waveforms that are processed by a moving target

* Portions of this section were developed under an Internal Georgia Tech STGC Program.

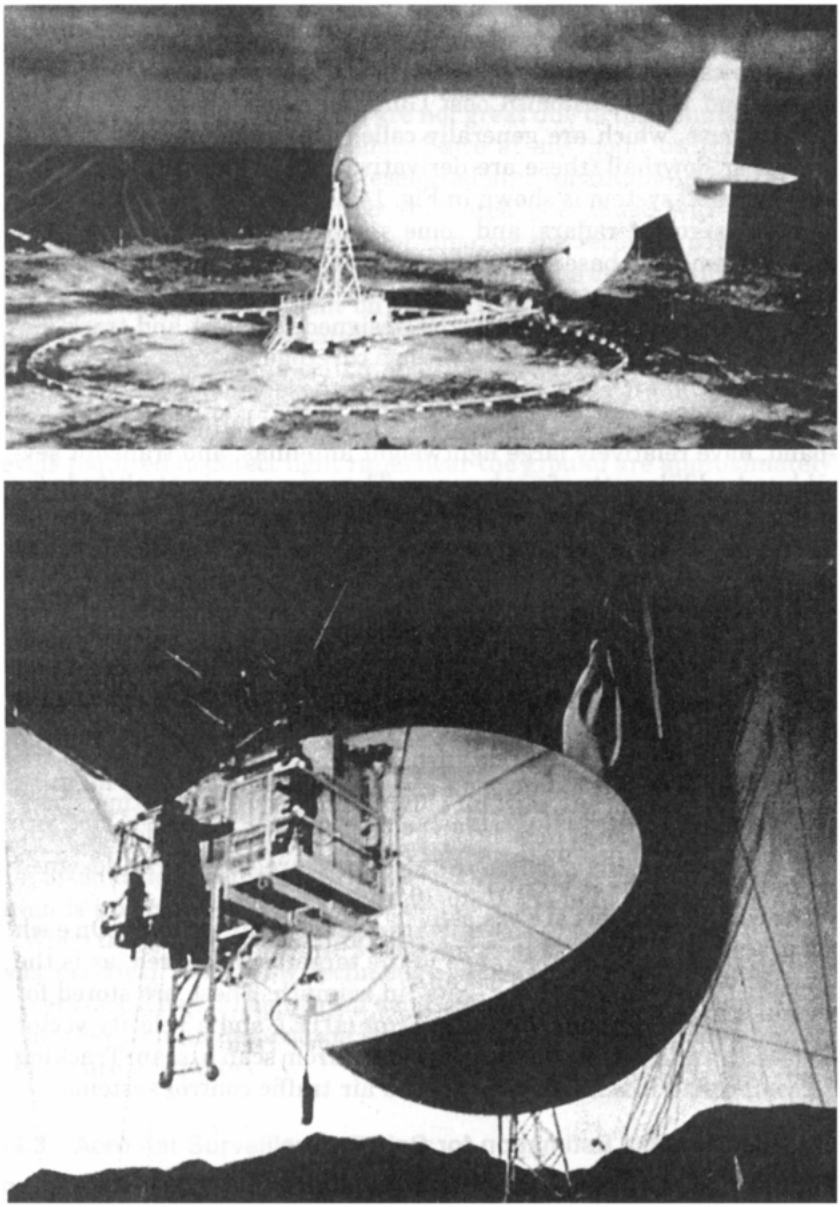

Figure 14.8 Large Aerostat Surveillance System (LASS). (*Courtesy Westinghouse Defense Center*)

indicator (MTI), a pulse Doppler processor (PD), or a moving target detector (MTD), which is roughly a combination of an MTI and a PD. The individual pulses may be coded and introduce other limitations, but that should not alter the following analyses. It is also assumed that the pulse train is coherent, that an attempt has been made to keep the amplitudes of the pulses constant or following some prescribed amplitude taper, and that an attempt has been made to have the relative phases approach what would have been obtained had one sampled a perfectly stable oscillator.

Since the goal is to determine performance, it is necessary to have a reference. The almost universal reference is the performance of the radar if it transmits a single pulse of the pulse train and a matched filter is implemented in the receiver. The equations for performance in receiver noise, jamming, and clutter are widely available. The additional clutter performance obtained by the multiple pulses is expressed by an improvement factor I which combines the benefits from the multiple pulses (and the appropriate processor) with the limitations of nature and the hardware implementation.

There are several terms to describe radar performance in a clutter environment. The oldest term is *subclutter visibility* (SCV), whose definition is given in an IEEE standard as [356]:

> *subclutter visibility* (radar). The ratio by which the target echo power may be weaker than the incident clutter echo power and still be detected with specified detection and false alarm probabilities. Target and clutter powers are measured on a single pulse return and all target velocities are assumed equally likely.

This term combines the performance of the signal processor and the various circuits in the detection process. The numerical value varies with the selected detection and false alarm probabilities. While it may be a useful measure of overall performance of a particular system, it does not lend itself to comparative analysis of radar waveforms and signal processors without a rather complicated detection simulation or analysis. SCV is also dependent on the fluctuation model of the target.

In most stages of radar design or analysis, it seems appropriate to partition the process of waveform and processor evaluation from the detection, CFAR, and thresholding system. In testing, it is also simpler to measure ratios of clutter into and out of the signal processor. The subsequent discussions attempt to discuss processing and detection separately.

The improvement factor is currently formally defined only for MTI processing, but it is often used for pulse Doppler systems. The IEEE Standard definition [356] is:

> *MTI improvement factor* (radar MTI). The signal-to-clutter ratio at the output of the system divided by the signal-to-clutter ratio at the input of the system, averaged uniformly over all target radial velocities of interest. See also: clutter attenuation, moving target indication.

The system is meant to include the clutter filter, but not the post-detection integration process. The input to the radar can be at RF, IF, or even bipolar video as long as these components are all linear. The improvement factor can be expressed as:

$$I = (C_i/C_o)\,(S_o[f]/S_i)$$

where C_i and C_o = the powers of the clutter echoes at the input and output, respectively
S_i and S_o = the powers of the target echoes at the input and output, respectively.

The term $S_o[f]/S_i$ is to normalize I to the average target gain. If one makes the assumption that the potential range of all target Dopplers can be much higher than the PRF, and thus all Dopplers are equally likely, then the bar over the term represents the average over all Dopplers. There is still some ambiguity as to whether to average I over possible Dopplers in absolute units or in decibels. Since noise also has the property that all frequencies are equally likely, the ratio of the signals equals the noise gain of the filter and

$$I = (C_i/C_o)\,(N_o/N_i)$$

This definition has several limitations primarily related to the range of target velocities that is desired or specified. For example, targets up to 50 kn may not be of any interest. More importantly, the velocity response of a bank or Doppler filters might be quite complex with different sensitivities at different velocities. The simple definition also implies linear processing and optimum utilization of the dynamic range. Finally, the use of I does not directly relate to detectability as the amplitude distribution and power spectrum of the residues of an MTI filter are not noiselike.

To make the improvement factor a more general term that is applicable to a number of Doppler processors, we define $I(f)$ as the improvement factor obtained over a range of possible target Dopplers. Its definition is similar to Ward's [747] and Ludloff et al. [451], and is discussed later in this section.

The computation of the performance of a processor for a pulse train waveform is best performed on a computer with some combination of algorithms for computing each limitation, and perhaps a Monte Carlo simulation to evaluate detection and false alarm probabilities. The following outlines the major contributors that limit performance in a clutter environment.

An illustration of the major sources is shown in Fig. 14.9. The signals entering the receiver include the target echo, the clutter echoes, receiver

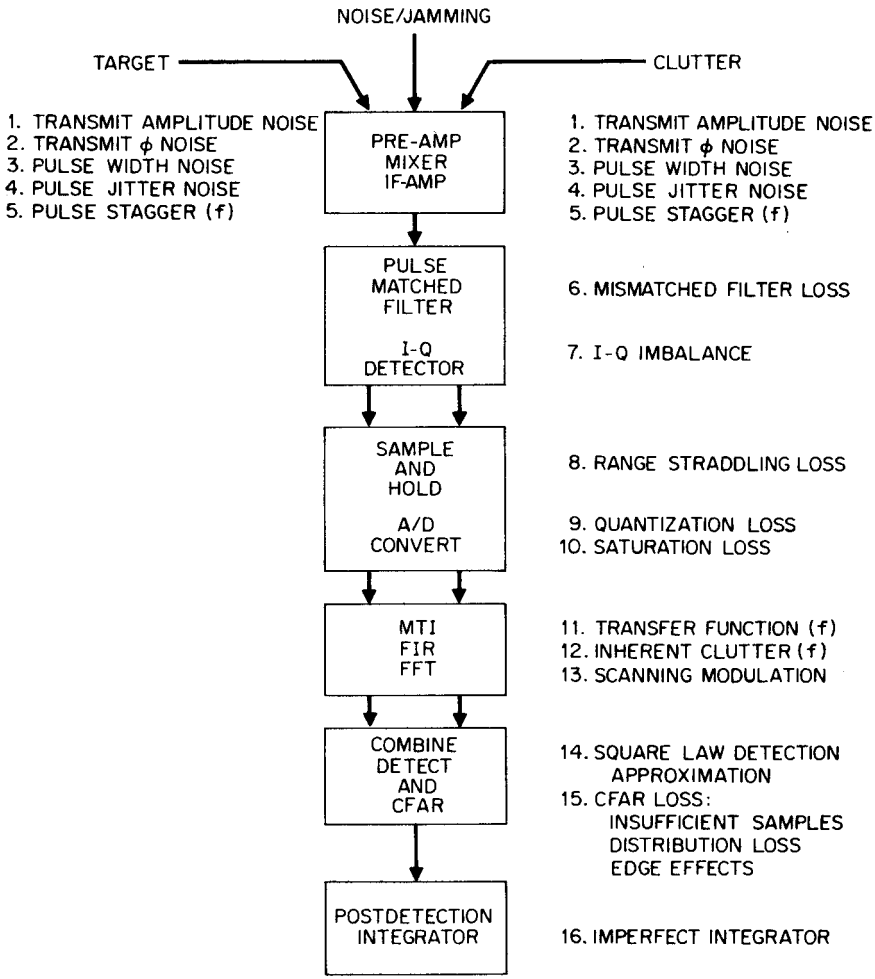

Figure 14.9 Limitations in a pulse train radar processing system.

noise, and jamming. The numbered items represent sources of the limitations on $I(f)$. Note that items one through five are the same for target and clutter, as any modulations or noises in the transmit signal appear on both the target and the clutter. Receiver noise and external jamming do not in general have these modulations, and, if they do, they are generally not important. For example, it is suggested that local oscillator noise be included in the transmitter noise entries, even though they have a minor effect on noise and jamming. In a similar manner, I have not included antenna switching noise or errors that occur with those phased arrays that must be switched between transmit and receive.

Referring again to Fig. 14.9, there is a loss if one does not use a "matched filter" (see Blake's C_b term in [74]) for the individual pulses plus another matched filter for the pulse train. The individual pulses may also be coded and thus there are two losses for not using ideal filters. These are not expanded on here since they have a minor effect on calculating I, and since, at this point, we are assuming that the processor is linear, the errors could just as easily be assigned to the "Combine Detect and CFAR" box.

The "sample and hold" circuits may have instabilities, which are best added elsewhere, but there is a significant loss in that the samples may not occur at the peak of the target echo out of the matched filter. This range-straddling loss cannot be computed independently of the matched-filter loss, as a mismatched filter generally tends to extend the target waveform in time. This tends to counteract the range-straddling loss. Also, the target appears in two range gates and there is a probability of detecting the target in either or both gates. Some designers oversample to reduce the loss, at the price of more hardware.

The *quantization loss* of an A/D converter is a noiselike limitation to the improvement factor. The saturation loss is much more complicated as nonlinear processes are involved. These processes are sensitive to the relation of the dynamic range of the input to the number of bits in the A/D, the ratio of the noise power to the level of the least significant bit, and even the amplitude distribution of the targets and clutter. This is all part of the dynamic range limitation.

Consider a radar with an analog-to-digital converter with a limited number of bits, and the problem of where to set the rms noise and the clutter in the dynamic range.

1. If the noise level is set much below the least significant bit, there is a loss in detectability even in the absence of clutter. This is quantization noise and also affects performance in clutter. Losses decrease as the input is increased to allow accurate quantization of small signals.
2. With noise occupying more of the dynamic range of the A/D, the ratio of clutter to noise that occurs before the clutter saturates is reduced. The clutter cells that saturate create saturation noise that reduces the maximum obtainable improvement factor. Thus, putting the signals higher in the dynamic range increases the saturation loss for a given level of clutter. Saturation noise can often be modeled as white noise, although doing so is not entirely valid.
3. Clutter, like noise, fluctuates and thus its mean level must be well below the maximum so that the peaks do not saturate. This varies for different clutter-fluctuation models.
4. The actual level of the clutter varies from site to site and from one direction to another.

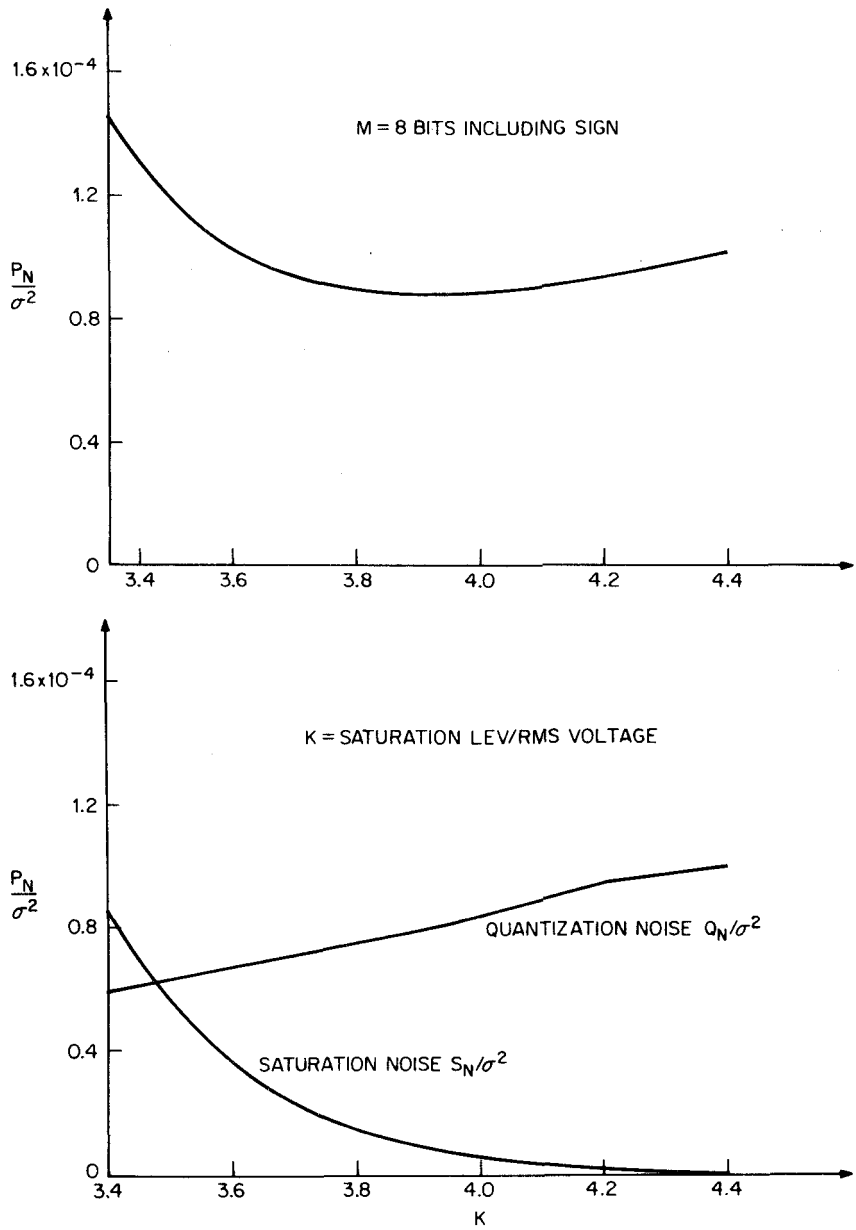

Figure 14.10 Saturation and quantization noise for an 8-bit A/D. (*Adapted from* [292] © *IEEE 1971*)

Figure 14.10, from Gray and Zeoli [292], shows the dynamic range limitations for an 8-bit A/D as a function of K, which is the ratio of the saturation level to the mean signal level. The ordinate is the output noise as a fraction of the input signal. It was assumed that the noise,

or clutter, had a Rayleigh distribution. Note that as the noise level into the A/D is decreased (K increased), quantization noise increases, but saturation noise decreases. The optimum value of K is found on the upper graph. The analysis was repeated for A/D converters of 3 to 10 bits with summary results shown in Fig. 14.11. These results should be interpreted as the noise resulting from large clutter signals at the input to the A/D converter. Note that a 10-bit A/D converter has less than the nominal 60 + dB range when the input is Rayleigh distributed. Taylor (in a TSC short course on MTI) gave a rule of thumb that the dynamic range is $(6N - 9)$ dB where N is the number of bits in the A/D converter. This appears valid for $N = 8 - 10$ but may be pessimistic for $N < 8$. Shrader and Hansen, in the *Radar Handbook* [653], give a different relation:

$$\text{Dynamic range} = 2^{(n-1)}/m\sqrt{2}$$

where n = the number of bits
m = the ratio of the rms value of the noise to the quantization level

The $n - 1$ in this case takes the sign bit into account. The optimum value of m can be found from Gray and Zeoli's work, but a value of 1 will yield better clutter rejection compared with a value of 2, which will give a few tenths of a dB more sensitivity and allow better CFAR performance. Descriptions of this and related limitations are found in Tong [704], Gray and Zeoli [292], Ward [747], and Shrader and Hansen [653].

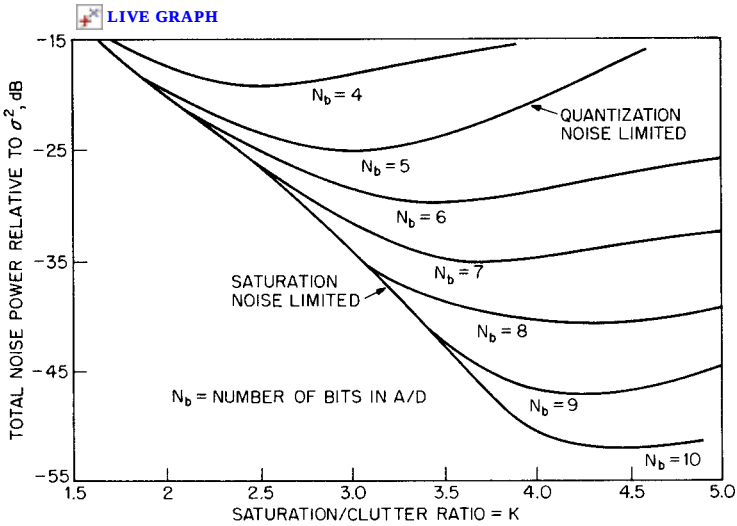

Figure 14.11 Total noise power at A/D output. (*Adapted from Gray and Zeoli [292], © IEEE 1971*)

The box labeled "MIT, FIR, FFT" is to represent the pulse train processor. It is here that the Doppler spectrum of the target and clutter have a major effect, and the ultimate performance of the system is defined. The term MTD (moving target detector) is not included here since it includes clutter maps, etc. that are not directly part of the pulse train processor. Items (11), (12), and (13) are to indicate that the ultimate performance is still limited by the inherent clutter spectrum, which is taken to include wind-blown effects, the variation in clutter Doppler of the scatterers in various parts of the radar beam, plus the uncompensated components due to platform motion and radial motions of the clutter. For MTI, the limitation on improvement factor is described in Chap. 9 and also in Chap. 15 of the second edition of the *Radar Handbook* [673].

There are target velocities, near blind or dim speeds, at which detection is poor or impossible. These are losses if the system is required to detect targets at these velocities. The allocation of these losses is described later.

The scanning modulation of a rotating antenna broadens the inherent clutter spectrum. The transfer function item is to represent the limitations (or benefits) of this block. In a digital processor there are always some additional losses due to quantization and roundoff. There is invariably a Doppler cusping loss due to a target Doppler straddling two adjacent filters in a similar manner to the range-straddling loss. At this point the losses from Doppler cusping are excluded from this box. It may be appropriate to define the term *ultimate performance* to describe the performance of the chosen filter without external hardware limitations.

Following the filter block is the "Combine Detect and CFAR block." At this point there are usually I and Q signals for each pulse from each range gate for an MIT-like processor or from each Doppler filter for each range gate for a batch of pulses for pulse-Doppler-like processors. The I and Q signals are either squared and added to constitute a square-law detector or added by one of several algorithms to approximate a linear detector. There is a small loss in the latter process, but it is usually the preferred approach. These outputs are usually fed to a constant false alarm rate (CFAR) circuit before or after integration, and then to a threshold circuit that establishes the false alarm rate. The CFAR circuit attempts to estimate the mean and some other parameter of the input signals. There are several losses in this process; the first loss results from the CFAR only using a finite number of samples to estimate these parameters. It can be defined as:

CFAR loss. The additional amount that the detection threshold must be raised due to the finite number of samples used to estimate the mean of the distribution plus quantization losses in the estimation. There is an additional loss if the distribution is assumed to be non-Rayleigh, and an attempt is made to estimate

the second parameter as well. This part of the loss can often be neglected if pessimistic estimates are made for the distribution loss, defined later.

The second loss term relates to the uncertainty in knowing which statistical distribution best fits the radar samples. (This is not really a loss in the usual sense of the word.) If the noise or clutter samples are Rayleigh with a constant mean value (in space) and are independent in time, as receiver noise, the distribution is known with only an estimate of the mean value. Otherwise there is a distribution loss. It can be defined as:

Distribution loss. The additional amount that the detection threshold must be raised (or lowered) due to the tails of the clutter distribution exceeding those of the Rayleigh distribution.

CFAR losses were described in Chap. 4. Finally, there is some loss if the postdetection integration is not linear, as is obtained with a recursive integrator. If the inputs are from a rotating antenna, the weighting function and the time constant of the integrator must be matched to the antenna pattern.

Losses attributable to the clutter source

The clutter echo as it enters the radar has first- and second-order statistical properties that limit complete elimination by a filter. The clutter has a mean Doppler component that is related to the winds except in the case of ground clutter. The shift in the clutter spectrum is generally unknown, but can often be estimated by averaging the phase shift from a number of pair of echoes. Similarly, the radar platform may be moving and shift the clutter spectrum. The power spectrum has a width due to environmental considerations, in addition, the finite beamwidth of the radar allows it to simultaneously observe scatterers at different locations with differing velocities (see Chaps. 5, 6, and 7). This inherent clutter spectrum is broadened by the moving platform plus the scanning modulation of a rotating antenna. Additionally, the clutter spectrum may be broadened by staggered pulse transmissions as in a staggered-pulse MTI. It may also be appropriate to include the time jitter of the transmitter at this point, since it has a similar effect to pulse stagger.

Simulation block diagram

It appears appropriate to illustrate and organize the error sources of Fig. 14.9 by the simulation block diagram of Fig. 14.12. The target echo, the receiver noise, clutter, and jamming are assumed to be ad-

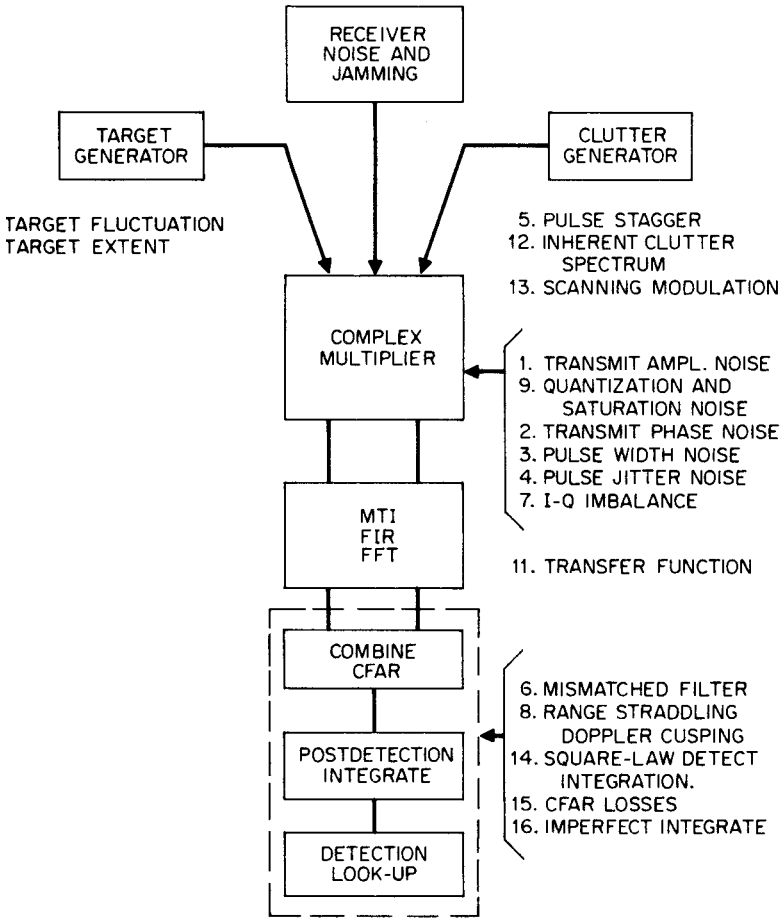

Figure 14.12 Possible simulation block diagram for pulse train radar.

ditive. For convenience, any local oscillator noises are assumed to be included in the transmitter noise components and "sky noise" is included in receiver noise. These are all fed into a "complex multiplier" where most of the signal-processing system noises are introduced. The purpose is to calculate off-line as many of these errors as possible and combine them into a single error modulation function. If the errors can be calculated in this manner, the simulation can be run dramatically faster. This approach appears to be valid if all the errors are small. If one error dominates, there is usually no need for the simulation. Also, since current systems usually achieve $I = 50$ dB or better, and systems in the design phases are striving for 70 to 90 dB, the small error assumption seems valid.

The form of the modulation function is probably $1 + \Sigma e_i$ where the

values of e are obtained by expanding the individual error sources in a Taylor series.

For simulation purposes, the clutter generator might include the velocity offset of the spectrum and a widening due to the other factors. The clutter generator should be derived from the same source as the target generator. The effect of the wider spectrum can be seen at the output of the "MTI, FIR, or FFT" filter in the simulation or the spectral width limitation can be individually calculated for simple MTI systems described in Chap. 9. The intent of this diagram is that the filters are assumed to be perfect. These portions of Fig. 14.12 account for the environmental limitations, those of the transmitter and receiver, and of the signal-processing subsystem. At this point, the signal-to-noise, signal-to-jamming, and signal-to-clutter ratios may be calculated. It is not absolutely necessary to make assumptions about the spatial distribution of the clutter at this time. Spectrum analysis would indicate the nature of the limitations in uniform clutter. However, the detectibility and false alarm probability of the system are not yet available, since the distributions of the target and the sum of noise, jamming, and clutter are unknown as well as their temporal and spatial correlations. The target and clutter distributions have a major effect on the saturation noise component, and should be included in the target and clutter generators. Parameters are suggested in Chaps. 6 and 7.

The I-Q combine, CFAR, integration, and detection block

In the absence of system errors or saturation, the foregoing portions of the simulation are all linear. In this block, the detection process is the first nonlinear operation. A square-law detector is considered optimum, but it is usually approximated by various algorithms, many of which approximate a linear detector. The loss is a few tenths of a decibel. The constant false alarm rate (CFAR) circuit estimates the total interference level in time (range) and often additionally in Doppler in the vicinity of the target echo. The detection curves of Marcum and Swerling and the others *assume* that there is exact estimation of the mean value of the noise background.

As stated previously, there are losses in estimation of the statistics of this interference. The spatial statistics, including temporal correlation of the processors, must be included at the input to have valid results. CFAR circuits can be before or after postdetection integration or both. Postdetection integration can take several forms and be linear or recursive. There is some loss that can be calculated or that show up in the simulation. There is at least one, and often several, thresholds in the detection process. For example, in an m-out-of-n detector, there

is an initial threshold to decide if a single pulse echo is large enough and then a second determination if m of these threshold crossings appeared in the last n transmissions (at a given range). The thresholds are set to establish the false alarm probability (P_{fa}), and the detections are counted. These topics were discussed in Chap. 4, and clutter maps were discussed in Sec. 14.1.

In a simulation, this block can be run separately and operate on stored outputs of the filter block. Thus the diagram of Fig. 14.2 implies that a radar simulation can be split into several subsimulations.

1. A target, noise, jamming, and clutter generator whose outputs are summed into the input of a complex multiplier
2. An error generator, where the individual error sources are approximated and added to form an error modulation
3. A signal-processing filter subsystem simulation
4. A combiner, CFAR, and detection subsystem simulation

There should be several advantages to running the subsimulations sequentially.

1. They can be run on a smaller computer with only the results stored from step to step.
2. The simulations up to the combine/CFAR can be run for a single range gate with and without the target. Other range gates can be subsequently run as along as the distributions are maintained and the spatial and temporal correlations are properly programmed.
3. The subsimulation outputs should be more easily understood.
4. The tasks can be divided among several personnel.
5. Partial results will be available sooner.

Improvement factor as a function of target velocity

As was stated earlier, the improvement factor for an MTI, pulse Doppler, or MTD processor can only be truly evaluated for a target at a specific radial velocity. Each of the processors has velocity regions that are believed to be clutter (the *stopband*) and the corresponding outputs are attenuated. Since realizable filters cannot have a square velocity response for a finite number of pulses transmitted, there is a loss on targets at a slightly higher velocity. There is also a loss on both sides of all the PRF lines for fixed PRF systems, and losses in "batch" transmissions at different PRFs. With most surveillance systems having a limited number of pulses per beam, the losses are significant.

There are several ways of describing the loss. Rivers [611] (private communication) calculates the percentage loss as a fraction of the PRF, and describes this as "wasted" bandwidth. He assumes that in addition to the loss due to the stopband for clutter, the velocity region from the −3-dB point of the adjacent target filter to the velocity at which the filter sidelobes are sufficiently low is wasted. Thus, there is a velocity region that is the sum of the stopband plus the waste bandwidth, at which detection is unlikely. He performed calculations for Dolph-Chebychev filters with varying sidelobe levels.

For design sidelobe levels of 70 dB, the wasted bandwidth was 46, 33, 25, and 13 percent for 8, 12, 16, and 32 pulses. These percentages are in addition to the stopband percentage. Thus, for systems trying to achieve high clutter-rejection levels, using 12 pulses or less per beam is quite inefficient. The alternative of increasing the number of pulses without increasing the total time could be equally damaging if it introduces range-ambiguous clutter. The use of two or more shorter bursts at different PRFs does not present an obvious cure if the total time available is insufficient. Going to higher PRFs to obtain more pulses per burst is highly desirable if it does not introduce or aggravate the range-ambiguous clutter problem. With this approach, a value for detectability versus target radial velocity is determined for the passband, and the waste-plus-stopband percentage is stated separately.

A related approach for MTI processors is described by Kretschmer, 1986 [415]. He shows how the improvement factor increases as the number of pulses is increased, but that the percentage of the Doppler bandwidth at which targets are detected ("visible space") decreases with increasing pulses. An example for clutter centered at zero Doppler and with binomial weights for the MTI is illustrated in Fig. 14.13. If it is required that $I(f)$ is within 3 dB of I, 68 percent of the targets are visible with a two-pulse canceler, but only about 44 percent are visible with a five-pulse canceler. This limitation is alleviated by using staggered-pulse MTI with the appropriate weighting.

These methods are most useful in evaluating initial designs, making tentative choices of the PRF for a single burst, the number of PRFs in a beam, and the value for each PRF; and the system choices of carrier frequency and time per beam position. For evaluating a tentative set of designs, a more analytical evaluation of target detection versus velocity or a simulation is required.

Another approach is probably best described by Ludloff et al. 1981 [451] and expanded on by Taylor [694] [673], who describe a Doppler-dependent signal-to-interference ratio, which is called $I(f_d)$, or simply $I(f)$ when there is no ambiguity. The common expression for the overall improvement factor of a radar system is generally expressed as

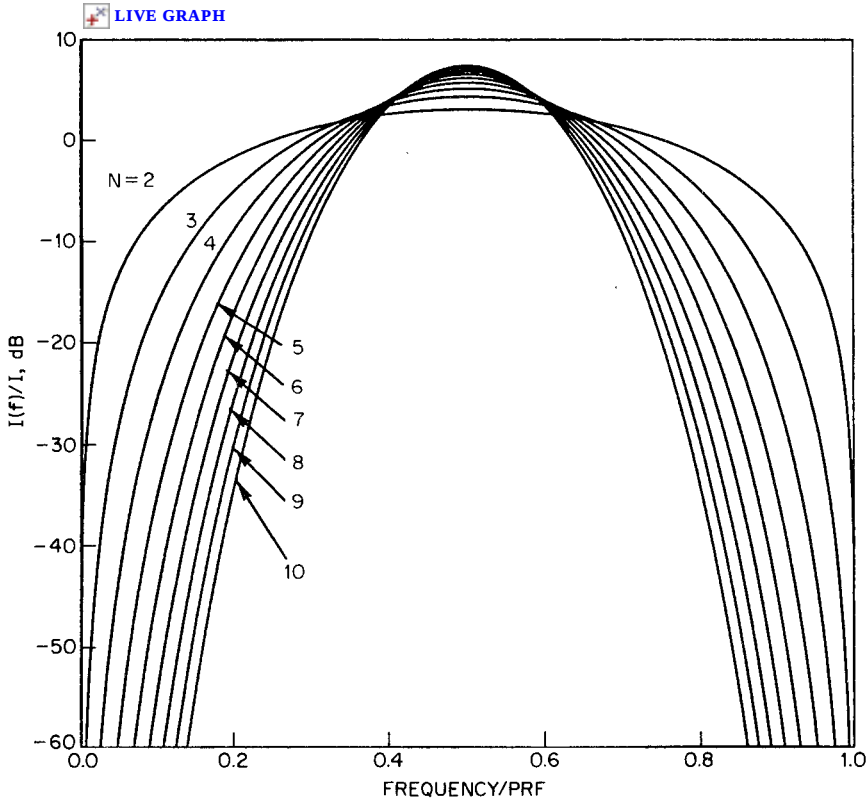

Figure 14.13 Target Doppler visibility space. (*From Kretchmer* [*415*])

$$\frac{1}{I} = \frac{1}{I_1} + \frac{1}{I_2} = \frac{1}{I_3} \cdots$$

where the I_i = the individual limitations, which are usually contained in an improvement factor budget. For this equation to be properly interpreted, either the individual terms must be Doppler independent or they must all be interpreted at each target velocity of interest. The latter approach is quite complicated, and thus most analysts divide the terms into frequency-dependent ones and those that appear as white noise. Unfortunately, some of the ones that are assumed to be white noise, such as A/D limitations (discussed earlier) and transmitter noise, do have a Doppler dependence as described in Echard and Watt [198].

At this point it is useful to point out the major limitation in the use of I *when evaluating a radar system.* The foregoing definition assumes that the clutter-to-noise ratio at an MTI or Doppler filter output is well above unity, and that the dynamic range is adequate to contain the

maximum clutter peaks and have noise alone be adequately described by the least significant bits.

To circumvent this limitation, the term signal-to-interference-ratio improvement, I_{SIR} is defined, but is denoted I_i. It must include the frequency-dependent terms. To try to partition into individual terms that can be calculated, the approach of Ludloff et al. [451] is followed. He defines dynamic range as

$$D = C_{in}, \max/N_{in}$$

where C_{in}, max = the maximum clutter amplitude admissible for clutter processing, divided by 2. Then D is 3 dB less than the processor input dynamic range, usually defined as $(2^n - 1)/2m$, where n is the number of bits including sign, and m is the value of the system noise given in increments of the A/D converter. For $n = 10$ and $m = 1$, D is about 54 dB, which agrees well with Gray and Zeoli's value of 53 dB. Their value assumes that it is possible optimally to set the clutter-saturation ratio at a particular radar site. This is not inconsistent with Taylor, who would reduce the fluctuating clutter-to-A/D-saturation ratio a bit more. His rule of thumb would be $60 - 9 = 51$ dB as a practical value.

With noise alone, there is an improvement in *S/N* due to the *S/N* gain of a multipulse canceler or pulse train processor. This is denoted I_N. Then, in the absence of other limitations, the SIR improvement is DI_N. The more pulses that are transmitted, the greater is the *potential* improvement factor.

To summarize Ludloff's development

$$\frac{1}{I_I} = \frac{1}{DI_N} + \frac{1}{I_C} + \frac{1}{I_{C,E}}$$

where I_C is the frequency-dependent signal-to-clutter improvement, and the last term is the signal-to-equipment-noise ratio at filter output to signal-to-clutter ratio at the filter input. It is the equipment noise limitation.

To illustrate these limitations, Ludloff et al. [451] present a case of an 8-pulse waveform in a ground-clutter environment. A matched filter for each pulse is assumed, along with an optimum maximum likelihood processor that coherently processes the 8 pulses. For each Doppler there is a transversal filter, centered at the target Doppler, whose filter weights are derived from the maximum-likelihood-ratio test of statistics. The sidelobes of the illustrated filter are quite low at the Doppler of the land clutter at the expense of poorer sidelobes in the passband of the filter bank. The envelope of all of the optimum filters, and the filter shape does equal the 59-dB dynamic range maximum that was

assumed. In a real system, with a finite number of filters, there will be other limitations.

Specific limitations on clutter-rejection performance

This section is an expansion of each of the individual limitations on the overall clutter-rejection capability of pulse-train processors. It is assumed that each of the individual limitations does not limit the improvement factor below 30 dB. In many cases the simplified expressions assume a flat spectrum of the error signals. References are given for more exact computations.

Transmitters

The transmitter is becoming the limiting device in systems requiring improvement factors greater than 50 dB, assuming that the A/D converter and number of bits in the processor are adequate. The transmitter is defined here to include the modulator, power supplies, *and the waveform synthesizer,* as well as the master oscillator and the transmit device itself. An essential point to consider is that the transmitter noises are all contained in the reflections from clutter. They are also contained in the target echo, but this is generally not significant unless there is another relatively large target being processed simultaneously with a small one, such as when a radar is looking for a small missile launched from a large ship.

In the frequency domain, the spectrum of the normalized transmitter error sources can be represented by:

$$S_y(f) = k_{-2}f^{-2} + k_{-1}f^{-1} + k_0 + k_1 f$$

where the first term is the so-called flicker noise and the k_0 term is the white noise. These terms usually dominate unless there is a spectral line, usually at a power supply frequency or one or more of its harmonics. It is also possible, but not very likely, to have an f^2 term. Examples of typical devices are shown in Fig. 14.14. These were presumably obtained with stable power supplies.

The effect on radar performance is not a simple calculation as phase, frequency, and amplitude errors must be considered. The limits due to local oscillator shifts are often range dependent. The frequency-dependent terms must be multiplied by the MTI response, and in pulse Doppler systems the components of $S_y(f)$ appear differently in the various Doppler filters. A summary of the effects on MTI is given by Shrader and Hansen [653] in Table 14.8 where they assume that the peak-to-peak values of the instabilities occur on a pulse-to-pulse basis.

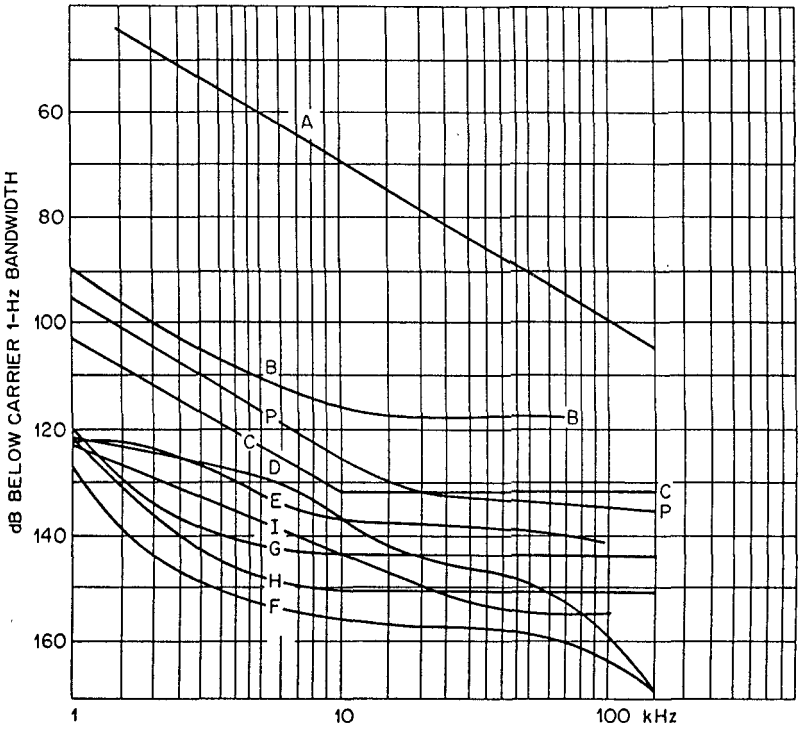

Figure 14.14 FM noise in microwave sources. (A) voltage-controlled *LC* oscillator multiplied to X-band; (B) crystal-controlled oscillator, step recovery multiplier, to X-band; (P) noise floor at X-band of 11729B/8640B combination (*Hewlett-Packard*); (C) crystal oscillator (ST cut) multiplied to X-band (*Westinghouse Corporation*); (D) compact X-band klystron CW amplification (*Hughes*); (E) compact X-band klystron pulsed amplification (*Hughes*); (F) X-band klystron CW amplification (*Varian*); (G) X-band klystron pulsed amplification (*Varian*); (H) S-band electrostatically focused klystron amplifier (*Litton*); (I) stabilized oscillator. Note that curves D and H are additive noise measurements. (*From Saunders in the Radar Handbook* [673]. *Courtesy McGraw-Hill.*)

Note that the local oscillator limitations (STALO and COHO) are range dependent. In pulse Doppler systems, the broadband noise components are divided among the Doppler filters, and there is less susceptibility to random error sources.

Calculating the errors due to transmitter, oscillator, and modulator problems is further complicated in that the phase modulations are often due to current modulations, which are in turn magnifications of power supply voltage modulations. Table 14.9 by Weil [760] illustrates this. The table also includes timing, pulse width, and amplitude jitter relations for MTI systems.

The procedure for determining limitations can proceed from either an estimate of $S_y(f)$ or, preferably, a measured transmitter. These are in turn convolved with the transfer function of the signal processor to

TABLE 14.8 Instability Limitations [673]

Pulse-to-pulse instability	Limit on improvement factor
Transmitter frequency	$I = 20 \log [1/(\pi \Delta f \tau)]$
STALO or COHO frequency	$I = 20 \log [1/(2\pi \Delta f T)]$
Transmitter phase shift	$I = 20 \log (1/\Delta\phi)$
COHO locking	$I = 20 \log (1/(\Delta\phi)$
Pulse timing	$I = 20 \log [\tau/(\sqrt{2}\Delta t \sqrt{B\tau})]$
Pulse width	$I = 20 \log [\tau/(\Delta PW \sqrt{B\tau})]$
Pulse amplitude	$I = 20 \log (A/\Delta A)$
A/D jitter	$I = 20 \log [\tau(J \sqrt{B\tau})]$
A/D jitter with pulse compression following A/D	$I = 20 \log [\tau/(JB\tau)]$

where Δf = interpulse frequency change
τ = transmitted pulse length
T = transmission time to and from target
$\Delta\phi$ = interpulse phase change
Δt = time jitter
J = A/D sampling time jitter
$B\tau$ = time-bandwidth product of pulse compression system ($B\tau$ = unity for uncoded pulses)
ΔPW = pulse-width jitter
A = pulse amplitude, V
ΔA = interpulse amplitude change

obtain the clutter "residue." Alternately, Table 14.9 and other sources can be used as inputs to Table 14.8 for MTI systems, or more elaborate calculations for pulse Doppler systems.

I/Q-channel gain/phase imbalance

The imbalances in gain or phase in the I and Q channels create an image response in addition to the desired signal. A useful approximation for small errors is that the image power is $(\sigma_a/2)^2$, where σ_a is the amplitude imbalance. For 30-dB image power, the gain imbalance must be less than 0.53 dB. The image power from phase imbalance is $(\sigma_\Phi/2)^2$, where σ_Φ is the rms phase imbalance. Phase imbalance must be held to 3.6° to maintain image power below −30 dB. This is illustrated in Fig. 14.15 for a simulated 3-percent gain imbalance with an FFT processor with 128 samples. Figure 14.16 shows a similar image response when there is a 3° nonorthogonality between I and Q. An

TABLE 14.9 Stability Factors

	Frequency- or phase-modulation sensitivity	Impedance: Dynamic, Static	Current or voltage change for 1 percent change in HVPS voltage	
			Line-type modulator	Low-impedance* hard-tube modulator, or dc operation
Magnetron	$\frac{\Delta f}{f} = \begin{pmatrix} 0.001 \\ to \\ 0.003 \end{pmatrix} \frac{\Delta I}{I}$	0.05–0.1	ΔI = 2%	ΔI = 10–20%
Stabilotron or stabilized magnetron	$\frac{\Delta f}{f} = \begin{pmatrix} 0.0002 \\ to \\ 0.0005 \end{pmatrix} \frac{\Delta I}{I}$	0.05–0.1	ΔI = 2%	ΔI = 10–20%
Backward-wave CFA	$\Delta\phi$ = 0.4 to 1° *for* 1% $\Delta I/I$	0.05–0.1	ΔI = 2%	ΔI = 10–20%
Forward-wave CFA	$\Delta\phi$ = 1.0 to 3.0° *for* 1% $\Delta I/I$	0.1–0.2	ΔI = 2%	ΔI = 5–10%
Klystron	$\frac{\Delta\phi}{\phi} = \frac{1}{2}\frac{\Delta E}{E}$ $\phi \approx 5\lambda$	0.67	ΔE = 0.8%	ΔE = 1%
	$\Delta\phi \approx 10°$ *for* 1% $\Delta E/E$			
TWT	$\frac{\Delta\phi}{\phi} = \frac{1}{3}\frac{\Delta E}{E}$ $\phi \approx 15\lambda$	0.67	ΔE = 0.8%	ΔE = 1%
	$\Delta\phi \approx 20°$ *for* 1% $\Delta E/E$			
Triode or tetrode	$\Delta\phi$ = 0 *to* 0.5° *for* 1% $\Delta I/I$	1.0	ΔI = 1%	ΔI = 1%

* A high-impedance modulator is not listed because its output would (ideally) be independent of HVPS voltage.

SOURCE: Weil [760, Chap. 4].

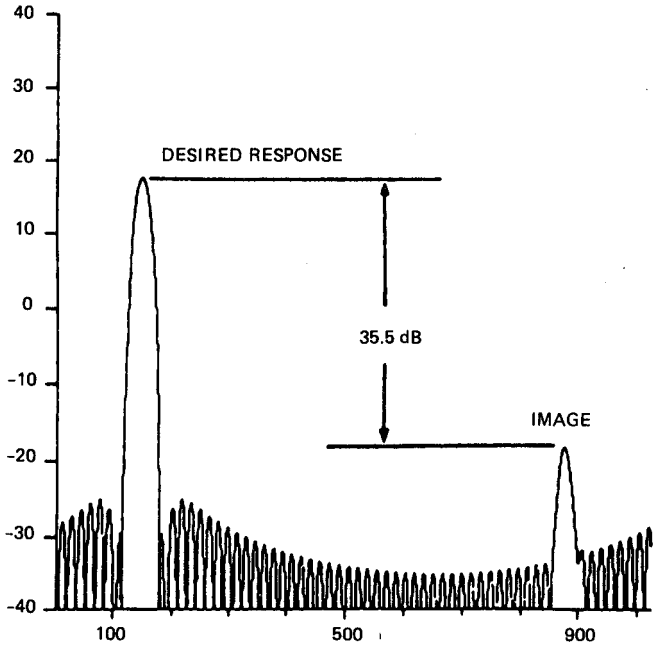

Figure 14.15 FFT response with 3-percent gain imbalance. (*Courtesy of J. Scheer*)

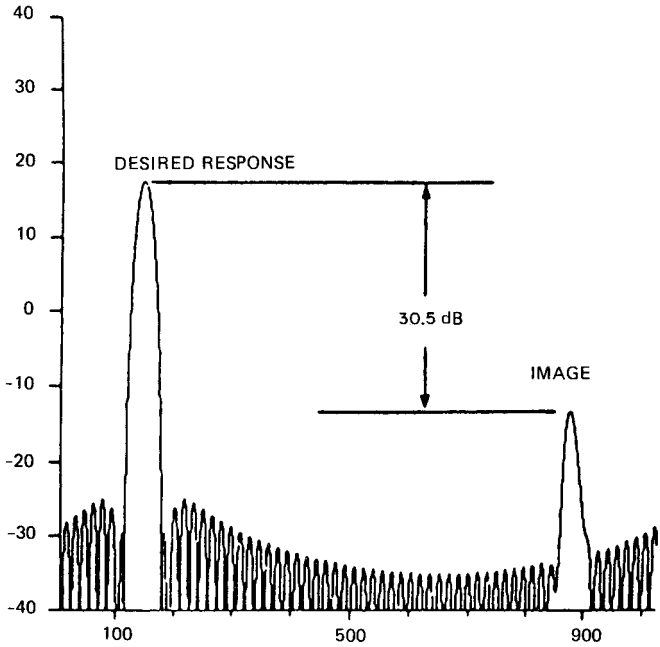

Figure 14.16 FFT response with 3° nonorthogonality. (*Courtesy of J. Scheer*)

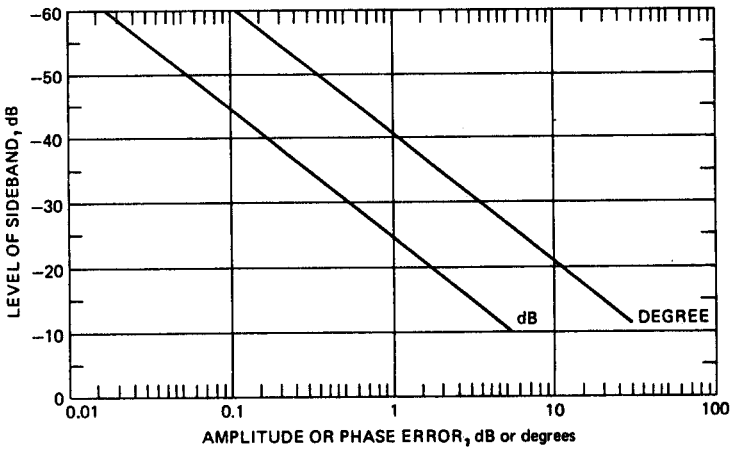

Figure 14.17 Image sideband due to I and Q amplitude and phase errors. (*From* [*653, 673*])

important point to note is that these image responses can appear as a target. The location in Doppler space is dependent on the location of the primary target or clutter. An overall graph of amplitude and phase errors from Taylor in the *Radar Handbook* [653] is shown as Fig. 14.17. To achieve image rejection of 60 dB requires that amplitude errors be held to less than 0.02 dB, and phase errors to about 0.1°.

Internal A/D noise

There are some losses due to imperfections in A/D converters that cause nonlinearities or noise. Suresh Babu and Sorrentino [687] performed a series of simulations of a pulse-train processor that show a loss of about 0.6 dB at $P_{fa} = 10^{-3}$ for an internal noise of 0.4 quantization levels. The receiver noise was set at about 1 quantization level. The increase in the threshold level was almost a linear multiple of the A/D internal noise level. They also simulated nonlinearities, but these had a very small effect.

Summary

This section gave a summary of many of the limitations that are encountered in pulse train processors. Many of these generate partially correlated noise, and the spectrum of this noise is often far from uniform, as in the case of I-Q imbalance. Others, like quantization noise, are not truly uniform, although this assumption is not a bad one. Complete simulations are quite difficult requiring man years of labor, and few have chosen this route. The usual approach is to root-sum-

square the errors and calculate an overall improvement factor. This may yield pessimistic results, as an I-Q imbalance may not be additive with some correlated clutter residue or spurious transmitter signal at some other Doppler frequency. In the absence of a full simulation, it is probably best to identify the three or four major contributors and analyze their effect in the Doppler domain.

Bibliography and References

1. Abramowitz, W., Analytical Signal Processing Techniques in a Reverberation-limited Environment, Grumman Res. Dept. Rept., RE–262, June 1966 (AD485861).*
2. Ackroyd, M., and F. Ghani, "Optimum Mismatched Filters for Sidelobe Suppression," *IEEE Trans. AES,* vol. 9, pp. 214–218, Mar. 1973.
3. Adams, W. B., "Phased Array Radar Performance with Wideband Signals," *EASCON Proc.,* IEEE, Washington, DC, Oct. 1967; *IEEE Trans.,* vol. AES–3, no. 6, pp. 257–271, Nov. 1967.
4. Advanced Radar Systems, AGARD Conference Proceedings No. 66, AGARD–CP–66–70, 1970 (AD715485).
5. AGARD Conference Proceedings No. 197, New Devices, Techniques and Systems in Radar, The Hague, Netherlands, June 14–17, 1976.
6. Airborne Overland Radar Techniques and Testing Study, sec. V., Ground Clutter Model, Illinois Institute of Technology Research Institute, Sept. 1965.
7. Albanese, K., "Pseudorandom Code Waveform Design for CW Radar," *IEEE Trans. AES,* vol. 15, no. 1, pp. 67–75, Jan. 1979.
8. Alekseev, G. V. et al., "Surfaces and Distributions of Reflected Signals in the Meter and Decimeter Wavelength Ranges," *Soviet Radio Physics,* vol. 15, no. 2, pp. 200–210, Feb. 1972.
9. Altshuler, Edward E., "A Simple Expression for Estimating Attenuation by Fog at Millimeter Wavelengths," *IEEE Trans.,* vol. AP–32, no. 7, pp. 757–758, July 1984.
10. Ament, W. S., F. C. MacDonald, H. J. Passerini, and R. O. Shrewbridge, "Quantitative Measurements of Radar Echoes from Aircraft," series of 16 Naval Research Laboratory reports on RCS measurements made between October 1950 and June 1960.
11. Ament, W. S., J. A. Burkett, F. C. MacDonald, and D. L. Ringwalt, Characteristics of Radar Sea Clutter: Observations at 220 Mc, Naval Res. Lab., Rept. 5218, Washington, DC, Nov. 19, 1958.
12. Anderson, John R., and David Karp, "Evaluation of the MTD in a High-Clutter Environment," *IEEE 1980 Inter. Radar Confer.,* pp. 219–224, Washington, DC, April 1980.
13. Andrews, G. A., "Platform Motion Compensation for AMTI Radar," *EASCON '76 Record,* pp. 64A–64H, Washington, DC, Sept. 26–29, 1976.
14. Annett, M. E., Engineering Report on Analysis of ASW Flight Data, Philco Rept. H–1084, July 1952 (AD5707).
15. Ares, M., The Performance of Burst Waveforms in Extended Clutter, Gen. Elec. Heavy Military Electron. Dept., Syracuse, NY, Jan. 12, 1965.

* AD numbers in parentheses refer to NTIC listings.

16. Ares, M., The Performance of Some Uniformly Spaced Burst Waveforms in Extended Clutter, Gen. Elec. Heavy Military Electron. Dept. Rept. R65EMH3, Syracuse, NY, Jan. 12, 1965.
17. Ares, M., Optimum Burst Waveforms for Detection of Targets in Uniform Range-extended Clutter, Gen. Elec. Heavy Military Electron. Dept. Rept. R66EMH16, Syracuse, NY (See also [635] pp. 293–296.), March 1966. Also *IEEE Trans.*, vol. AES–23, no. 1, pp. 138–141, Jan. 1967.
18. Ares, M., Some Anticlutter Waveforms Suitable for Phased Array Radars, Gen. Elec. Heavy Military Electron. Dept. Rept. R66EMH8, Syracuse, NY, Nov. 1965.
19. Ares, M., Postdetection Combining of Multiple Frequency Channel Radar Signals, Gen. Elec. Heavy Military Electron. Dept. Rept. R67EMH20, Syracuse, NY, June 27, 1967.
20. Armendariz, Manuel, and L. J. Rider, Wind Shear for Small Thickness Layers, Atmos. Sci. Lab., ECOM–5040, White Sands Missile Range, NM, Mar. 1966 (AD482329).
21. Aronoff, E., and N. M. Greenblatt, "Medium PRF Radar Design and Performance," *Radars,* vol. 7, pp. 53–67, Artech House, Inc., Dedham, MA, 1978.
22. Ashby, R. M., V. Josephson, and S. Sydoriak, Signal Threshold Studies, Naval Res. Lab. Rept. R–3007, Dec. 1, 1946.
23. Atlas, David, K. R. Hardy, and T. G. Konrad, "Radar Detection of the Tropopause and Clear Air Turbulence," *Proc. 12th Radar Meteorol. Conf.,* Norman, OK, Oct. 19, 1966.
24. Atlas, David, and Otto W. Thiele (ed.), Precipitation Measurements from Space, NASA Workshop Report, NASA, Goddard Space Flight Center, Greenbelt, MD, Oct. 1981.
25. Atlas, David, "Advances in Radar Meteorology," in Landsberg (ed.), *Advances in Geophysics,* vol. 10, Academic Press, Inc., New York, 1964.
26. Baars, Ernst Peter, and Helmut Essen, "Millimeter-Wave Backscatter Measurements on Snow-Covered Terrain," *IEEE Trans. on Geoscience and Remote Sensing,* vol. 26, no. 3, pp. 282–299, May 1988.
27. Baden, J. M., and M. N. Cohen, "Optimal Peak Sidelobe Filters for Biphase Pulse Compression," *Proc. 1990 Inter. Radar Confer.*, Washington, DC, May 1990.
28. Baker, C. J., "Coherent and Polarization Properties of High Resolution Radar Sea Echo," *Proc. of the 1989 Inter. Symposium on Noise and Clutter Rejection in Radars and Imaging Sensors,* pp. 54–59, Tokyo, 1989.
29. Baker, C. H., *Man and Radar Displays,* Pergamon Press, Inc. and The Macmillan Co., New York, 1962.
30. Bakulev, P. A. and Stepin, V. M., "Features of Signal Processing in Modern Surveillance Radars (A Review)," *Izvestiya VUZ. Radioelektronika,* vol. 29, no. 4, 1986 (English translation).
31. Balch, H. T., J. C. Dale, T. W. Eddy, and R. M. Lauver, "Estimation of the Mean of a Stationary Random Process by Periodic Sampling," *Bell Systems Tech. J.,* vol. 45, no. 5, pp. 733–741, May–June 1966.
32. Bardash, M., "Ambiguities in Radar Signal Measurements of Extended Targets," *RCA Damp Tech. Monograph,* DTM–62–18, Moorestown, NJ, Oct. 1962.
33. Barker, R. H., *Group Synchronizing of Binary Digital Systems, Communication Theory,* Academic Press, Inc., New York, 1953. (Papers read at a symposium on Applications of Communication Theory held at the Institution of Electrical Engineers, London, Sept. 22–26, 1952.)
34. Barlow, E. J., "Doppler Radar," *Proc. IRE,* vol. 37, no. 4, pp. 340–355, Apr. 1949.
35. Barrett, C. R., "Adaptive Threshold and Automatic Detection Techniques," in J. L. Eaves and E. K. Reedy (eds.), *Principles of Modern Radar,* Van Nostrand Reinhold Company, New York, 1987.
36. Barrick, D. E., Radar Signal Spectrum Distortions Produced by Volume and Surface Distributed Scatterers, USNC/USRI Spring Meeting, April 9–12, 1968, National Academy of Sciences, Washington, D.C.
37. Barrick, Remote Sensing of the Troposphere, V. E., Derr, NOAA, Aug. 15, 1972.
38. Barry, J. R. et al., Angel Clutter and the ASR Air Traffic Control Radar, vol. 1 Study Results, APL/JHU Technical Report MSO–F–195, AD775 258, Feb. 1973.

39. Barton, David K., *Modern Radar System Analysis,* Artech House, Norwood, MA, 1988.
40. Barton, D. K., "Radar System Performance Charts," *IEEE Trans.,* vol. MIL–9, nos. 3–4, pp. 255–263, July–Oct. 1965.
41. Barton, D. K., and W. M. Hall, "Antenna Pattern Loss Factors for Scanning Radars," *Proc. IEEE (Corr.).* vol. 53, no. 9, pp. 1257, 1258, Sept. 1965.
42. Barton, D. K., "Radar Equations for Jamming and Clutter," *EASCON Proc.,* IEEE Washington, DC, Oct. 1967; *IEEE Trans.,* vol. AES-3, no. 6, pp. 340–355, Nov. 1967.
43. Barton, David K., *Radar Clutter,* Radars Vol. 5, Artech House, Inc., Dedham, MA, 1975.
44. Barton, D. K., Detectability Factor and Integration Loss, Raytheon Co. Intern. Memo. DKB–66, Wayland, MA, Aug. 6, 1965.
45. Barton, D. K., *Radar System Analysis,* Prentice-Hall, Inc., Englewood Cliffs, NJ, 1964.
46. Barton, David K., "Land Clutter Models for Radar Design and Analysis," *Proc. IEEE,* vol. 73, no. 2, pp. 197–204, Feb. 1985.
47. Bath, W. G., and F. R. Castella, "Detection Performance of a Noncoherent MTI," *Proc. IEEE, National Radar Conf.,* pp. 74–78, Mar. 1984.
48. Battan, L. J., *Radar Meteorology,* University of Chicago Press, Chicago, 1959. Also *Radar Observations of the Atmosphere,* University of Chicago Press, 1973.
49. Bean, B. R., "The Radio Refractive Index of Air," *Proc. IRE,* vol. 50, pp. 260–273, Mar. 1962.
50. Beard, C. I., Behavior of Non-Rayleigh Statistics of Microwave Forward Scatter from a Random Water Surface, Boeing Res. Lab. Rept. DI–82–0587, Seattle, WA, Dec. 1966.
51. Beard, C. I., I. Katz, and L. M. Spetner, "Phenomenological Vector Model of Microwave Reflection from the Ocean," *IRE Trans.,* vol. AP–4, no. 2, Apr. 1956.
52. Beard, C. I., and I. Katz, "The Dependence of Microwave Radio Signal Spectra on Ocean Roughness and Wave Spectra," *IRE Trans.,* vol. AP–5, no. 2, pp. 183–191, Apr. 1957.
53. Beard, C. I., "Coherent and Incoherent Scattering of Microwaves from the Ocean," *IRE Trans.,* vol. AP–9, no. 5, pp. 470–483, Sept. 1961.
54. Beasley, E. W., "Effect of Surface Reflections on Rain Cancellation in Radars Using Circular Polarization," *Proc. IEEE* (Letters), vol. 54, no. 12, Dec. 1966.
55. Bechtel, M. E., and H. W. Prensen, "Errors in R-meter Measurements of the Velocity Spread of Meteorological Targets Resulting from Radar Frequency Instabilities," *12th Conf. Radar Meteorol.,* Norman, OK, Oct. 17–20, 1966.
56. Beckmann, P., "Shadowing of Random Rough Surfaces," *IEEE-PGAP,* vol. AP–13, pp. 384–388, May 1965.
57. Beckmann, P., and A. Spizzichino, *The Scattering of Electromagnetic Waves from Rough Surfaces,* The Macmillan Co., New York, 1963.
58. Bell, J., "Propagation Measurements at 3.6 and 11 Gc/s over a Line of Sight Path," *Proc. IEE,* vol. 114, no. 5, pp. 545–549, May 1967.
59. Bello, P., and W. Higgins, "Effect of Hard Limiting on the Probabilities of Incorrect Dismissal and False Alarm at the Output of an Envelope Detector," *IRE Trans. IT,* pp. 60–66, Apr. 1961.
60. Benham, Fredrick C., et al., Pulse Pair Estimation of Doppler Spectrum Parameters, Air Force Cambridge Research Laboratories Final Report, AFCRL–72–0222, Mar. 30, 1972.
61. Bennett, W. R., "Spectra of Quantized Signals," *Bell System Tech. J.,* vol. 27, July 1948.
62. Bennett, John R., Ian G. Cumming, and Robert A. Deane, "The Digital Processing of Seasat Synthetic Aperture Radar Data," *IEEE 1980 Inter. Radar Confer.,* pp. 168–175, Washington, DC, Apr. 1980.
63. Berkowitz, R. S. (ed.), *Modern Radar-Analysis, Evaluation and System Design,* John Wiley & Sons, Inc., New York, 1965.
64. Bernfeld, M., C. E. Cook, J. Paolillo, and C. A. Palmieri, "Matched Filtering Pulse Compresion and Waveform Design" (four parts), *Microwave J.,* pt. 1, pp.

56–64, Oct. 1964; pt. 2, pp. 81–90, Nov. 1964; pt. 3, pp. 70–76, Dec. 1964; pt. 4, pp. 73–81, Jan. 1965.

65. Bickel, H. J., "Spectrum Analysis with Delay-line Filters," *1959 WESCON Conv. Rec.,* pt. 8, pp. 59–67, IRE, 1959.
66. Biernson, G., and I. Jacobs, "Clutter Spectra for an Airborne CW Doppler Radar," *Trans. 1959 Symp. Radar Return,* pp. 377–438, May 11–12, 1959.
67. Birkemeier, W. P., and N. D. Wallace, "Radar Tracking Accuracy Improvement by means of Pulse-to-Pulse Frequency Modulation," *AIEE Trans. Commun. Electron.,* vol. 81, pp. 571–575, Jan. 1963.
68. Bishop, Geffry, Amplitude Distribution Characteristics of X-Band Radar Sea Clutter and Small Surface Targets, Royal Radar Establishment Memo No. 2348, 1970.
69. Bishop, G., "Radar Sea Clutter," in *Determination and Use of Radar Scattering Characteristics,* AGARD Lecture Series No. 59, 1973; also "Amplitude Distribution Characteristics of X-Band Radar Sea Clutter and Small Surface Targets," Royal Signals and Radar Establishment, Malvern, RRE Memorandum No. 2348, 1970.
70. Blackband, W. T., Radar Techniques for Detection, Tracking, and Navigation, 8th Symp. AGARD Avionics Panel, AGARDograph 100, Gordon and Breach, New York, 1966.
71. Blackwell, F., and W. Rogers, Some Measurements of Bistatic Terrain Reflection Coefficient of a Forest Area at X-Band, Royal Radar Establishment, Ministry of Aviation, Malvern Worcs, England, Memo No. 2157, Jan. 1965.
72. Blake, S., "OS-CFAR Theory for Multiple Targets and Nonuniform Clutter," *IEEE Trans. AES,* vol. 24, no. 6, pp. 785–790, Nov. 1988.
73. Blake, L. V., "Recent Advances in Basic Radar Range Calculation Technique," *IRE Trans.,* vol. MIL–5, no. 2, pp. 154–164, Apr. 1961.
74. Blake, L. V., *Radar Range-Performance Analysis,* Lexington Books, 1980 (also Artech House, 1986).
75. Blake, L. V., A Guide to Basic Pulse-radar Maximum-range Calculation Part 1—Equations, Definitions, and Aids to Calculation, Naval Res. Lab. Rept. 5868, Dec. 23, 1969. [Also Radio Ray (Radar) Range-height-angle charts, Naval Res. Lab. Rept. 6650, Jan. 22, 1968.]
76. Blake, L. V., Radar/Radio Tropospheric Absorption and Noise Temperature, Naval Research Laboratory Report 7461, Oct. 30, 1972.
77. Blevis, B. C., R. M. Dohoo, and K. S. McCormick, "Measurements of Rainfall Attenuation at 8 and 15 GHz," *IEEE Trans.,* vol. AP–15, no. 3, pp. 394–403, May 1967.
78. Blood, David W., and Robert K. Crane, "Atmospheric Absorption Loss Algorithm for Radar and Communication Slant Paths," *IGARSS '85, IEEE Geoscience and Remote Sensing Society and USNC/URSI-Commission F,* Oct. 7–9, 1985.
79. Bodnar, Richard A., and Richard M. Smith, "Ambiguity Functions for Quadratic Phase-Coded Pulse Trains," *IEEE Trans. AES,* vol. 20, no. 2, pp. 141–157, Mar. 1984.
80. Bogotch, S. E., and C. E. Cook, "The Effect of Limiting on the Detectability of Partially-time-coincident Pulse Compression Signals," *IEEE Trans.,* vol. MIL–9, no. 1, pp. 17–24, Jan. 1965.
81. Bogush, Alfred, J., Jr., *Radar and the Atmosphere,* Artech House, Norwood, MA, 1989.
82. Bongianni, W. L., and J. B. Harrington, "Ultrawide Bandwidth Pulse Compression in YIG," *Proc. IEEE,* vol. 54, no. 8, pp. 1074–1075, Aug. 1966.
83. Boothe, R. R., The Weibull Distribution Applied to the Ground Clutter Backscatter Coefficient, USAMC Report RE–TR–69–15, June 1969.
84. Boring, J. G., E. R. Flynt, M. W. Long, and V. R. Widerquist, Final Report Project No. 157–96, Sea Return Study, Georgia Inst. Tech. Eng. Exp. Sta. Rept., Aug. 1, 1957 (AD246180).
85. Braasch, R. H., and A. Erteza, "A Recursion for Determining Feedback Formulas for Maximal Length Linear Pseudo-random Sequences," *Proc. IEEE* (Letters), vol. 54, no. 7, pp. 999–1000, July 1966.

86. Bracalante, E. M., C. L. Britt, and W. R. Jones, "Airborne Doppler Radar Detection of Low Altitude Windshear," *AIAA/NASA/AFWAL Sensors and Measurement Technology Conference,* AIAA–88–4657, Atlanta, GA, Sept. 7–9, 1988.
87. Breckhovskikh, L. M., *Waves in Layered Media,* Chap. 5, Academic Press, New York, 1980.
88. Brennan, L. E., and I. S. Reed, "Quantization Noise in Digital Moving Target Indication Systems," *IEEE Trans.,* vol. AES–2, no. 6, pp. 655–658, Nov. 1966.
89. Brennan, L. E., and F. S. Hill, Jr., "A Two-step Sequential Procedure for Improving the Cumulative Probability of Detection in Radars," *IEEE Trans.,* vol. MIL–9, no. 3–4, pp. 278–287, July–Oct. 1965.
90. Britt, C. O. et al., Back Scattering Cross-sections at 4.3 Millimeter Wavelengths of Moderate Sea Surfaces, Univ. Texas Rept. 95 [NONR 375(01)], Nov. 8, 1957.
91. Brookner, E., "Cumulative Probability of Detection," in E. Brookner (ed.), *Radar Technology,* Artech House, Dedham, MA, 1977.
92. Brookner, E., *Radar Technology,* Artech House, Inc., Dedham, MA, 1977 (Chap. 7, Sinsky, A. I., "Waveform Selection and Processing").
93. Brookner, Eli, "Trends in Radar Signal Processing," *Microwave Journal,* pp. 20–39, Oct. 1982.
94. Brookner, Eli (ed.), *Aspects of Modern Radar,* Artech House, Norwood, MA, 1988.
95. Brookner, E., Signal Processing and Synthesis for Optimum Clutter Rejection, Raytheon Space Inform., Syst. Rept. FR–65–343, presented at the *International Conference on Microwave, Circuits, and Information Theory,* Tokyo, Sept. 1964, Oct. 30, 1964; revised May 1, 1965.
96. Buhring, Walter, "Coherent Signal Processing in a Frequency Agile Jittered Pulse Radar," *IEEE 1980 Inter. Radar Confer.,* pp. 17–1–17–6, Washington, DC, Apr. 1980.
97. Burroughs, H. H., Rain Intensity-Time Distributions, Naval Ordnance Lab. Rept. 729, Corona, CA, June 15, 1967 (AD654709).
98. Burruss, C. S., and T. W. Parks, *DFT/FFT and Convolution Algorithms: Theory and Implementation,* John Wiley & Sons, Inc., New York, 1985.
99. Bussgang, J. J., P. Nesbeda, and H. Safran, " A Unified Analysis of Range Performance of CW, Pulse and Pulse Doppler Radar," *Proc. IRE,* vol. 47, no. 10, pp. 1753–1762, Oct. 1959.
100. Bussgang, J. J., and D. Middleton, "Optimum Sequential Detection of Signals in Noise," *IRE Trans. IT–1,* pp. 5–18, Dec. 1955.
101. Cahn, C. R., "A Note on Signal-to-Noise Ratio in Bandpass Limiters," *IRE Trans. IT,* pp. 39–43, Jan. 1961.
102. Camp, W. W., A Short Description of Alcor, Massachusetts Institute of Technology Lincoln Laboratory, Project Rept. RDT-13 (Radar Discrimination Technology), July 20, 1967.
103. Campbell, J. P., "Back-scattering Characteristics of Land and Sea at X-band," *Aeronautical Electron. 1958 Natl. Conf. Proc.,* pp. 12–14, Dayton, Ohio, May 1968.
104. Campbell, C. K., "Applications of Surface Acoustic Wave and Shallow Bulk Acoustic Wave Devices," *Proc. IEEE,* vol. 77, no. 10, pp. 1453–1484, Oct. 10, 1989.
105. Cantafio, Leopold, and Edward Kovalcik, "Space-Based Radar Antennas for Weather Observation Missions," *Microwave Journal,* pp. 131–148, Jan. 1990.
106. Capon, J., "High-speed Fourier Analysis with Recirculating Delay-line Heterodyner Feedback Loops," *IRE Trans. Instr.,* vol. 1–10, no. 1, pp. 32–73, June 1, 1961.
107. Capon, J., "Optimum Weighting Functions for the Detection of Sampled Signals in Noise," *IEEE Trans. Inform. Theory,* Apr. 1964.
108. Capon, J., "On the Properties of an Active Time-variable Network: The Coherent Memory Filter," *Proc. Symp. Active Networks Feedback Systems,* pp. 561–581, Polytechnic Institute of Brooklyn, Apr. 19–20, 1960.
109. Caputi, W. J., "Stretch: A Time Transformation Technique," *IEEE Trans. AES,* vol. 7, no. 2, pp. 269–278, Mar. 1971.
110. Carey, Thomas J., John C. Lovell, and Thomas L. Grisell, "Low-Noise Synthesizer Design," *Hewlett-Packard Journal,* vol. 38, no. 11, pp. 34–38, Dec. 1987.

111. Cartledge, L., and R. M. O'Donnell, Description and Performance Evaluation of the Moving Target Detector, Project Report ATC–69, Lincoln Laboratory, MIT, Mar. 8, 1977.
112. Cassedy, E. S., and J. Fainberg, "Back-scattering Cross Sections of Cylindrical Wires of Finite Conductivity," *IRE Trans. Antennas Propagation,* vol. AP–8, no. 1, pp. 1–7, Jan. 1960.
113. Castella, F. C., "Optimisation of a Generalized Square-law Detector," *IEE Proc.,* vol. 130, pt. F, no. 5, pp. 405–408, 1983.
114. Castella, F. R., and J. P. Reilly, "Radar Detection Statistics for Discrete Scatterer Target Models with Frequency Agile Illumination," *IEE Inter. Radar Conf.,* London, pp. 370–374, Oct. 1987.
115. Celliers, A. F., "Autocorrelation Determines the Coherency of Injection-Locked Pulsed Systems," *Microwave Journal,* pp. 163–165, Jan. 1989.
116. Cha, Chung-Chi, J. Michels, and E. Starczewski, "An RCS Analysis of Generic Airborne Vehicles Dependence on Frequency and Bistatic Angle," *Proc. 1988 IEEE National Radar Confer.,* 88CH2572–6, pp. 214–219.
117. Chadwick, R B., and R. G. Strauch, "Processing of FM-CW Doppler Radar Signals from Distributed Targets," *IEEE Trans. AES,* vol. 15, no. 1, pp. 185–188, Jan. 1979.
118. Chandler, J. P., An Introduction to Pseudo-Noise Modulation, Harry Diamond Lab. Rept. TM-64-4, HDL-16100, Washington, DC, Jan. 30, 1964 (AD479308).
119. Cheston, T. C., and J. Frank, "Antenna Arrays," in M. I. Skolnik (ed.), *Radar Handbook,* Chap. 11, McGraw-Hill Book Co., New York, 1990.
120. Churchill, F. E., "Sidelobe Levels of Weighting Functions with a Platform when the Number of Samples (N) is Small," *Proc. IEEE,* vol. 72, no. 12, Dec. 1984.
121. Clark, N. D., Nielson, G. Hagn, and L. Rorden, An Investigation of the Back-scatter of High Frequency Radio Waves from Land, Sea, Water, and Ice, Stanford Res. Inst. Proj. 2090, May 1960.
122. Clarke, A. S., Target Noise Reduction by Pulse-to-Pulse Frequency Shifting (Non-Coherent Processing), Hughes Aircraft Co. Aerospace Group Rept. TM893, Culver City, Cal., Nov. 1967.
123. Clutter Data Appendixes, vol. II, Evaluation of Airborne Overland Radar Techniques and Testing, Airborne Instrument Laboratories, RTD–TR–65, Sept. 1965 (AD487604).
124. Cochran, W. T. et al., "What is the Fast Fourier Transform?" *Proc. IEEE,* vol. 55, no. 10, pp. 1664–1674, Oct. 1967.
125. Cohen, M., "Pulse Compression in Radar Systems," Chapter 15, in J. L. Eaves and E. K. Reedy (eds.), *Principles of Modern Radar,* Van Nostrand Reinhold, New York, 1987.
126. Cohen, M., and Cohen, P., "Near Perfect Biphase Codes and Optimal Filtering of Their Range Sidelobes," *Proc. 18th European Microwave Confer.,* Stockholm, Sweden, Sept. 1988.
127. Cohen, M., and J. Baden, Pulse Compression Coding Study, Georgia Tech Internal Technical Memo, Project A–3366, Jan. 1983.
128. Cohen, M. N., and J. M. Baden, Unpublished Technical Notes, Dec. 1989.
129. Cohen, M., Binary Phase-Coded Pulse Compression, Internal Report No. 293–R–0021, Norden Systems, Norwalk, CT, 1979.
130. Cohen, M. N., M. R. Fox, and J. M. Baden, "Minimum Peak Sidelobe Pulse Compression Codes," *Proc. 1990 Inter. Radar Confer.,* Washington, DC, May 1990.
131. Cohen, M., Binary Pulse Compression, Standard Elektrik Lorenz, Final Technical Report, Dec. 1988.
132. Cole, E. L., M. J. Hodges, R. G. Oliver, and A. C. Sullivan, "Novel Accuracy and Resolution Algorithms for the Third Generation MTD," *IEEE 1986 National Radar Confer.,* 86CH2270–7, pp. 41–47, 1986.
133. Coleman, S. D., and G. R. Hetrich, "Ground Clutter and Its Calculation for Airborne Pulse Doppler Radar," *Proc. 5th Natl. Conv. Military Electron.,* pp. 409–415, Washington, DC, 1961.
134. Colin, J. M., "Radar Design for Detection in Clutter," *IEEE 1980 Inter. Radar Confer.,* pp. 317–321, Washington, DC, Apr. 1980.

135. Conlon, J. R., High Resolution Radar, Part II-Sea Clutter Measurements, Naval Res. Lab. Rept. NRL-4951, Washington, DC, Aug. 29, 1957.
136. Cook, C. E., and M. Bernfeld, *Radar Signals—An Introduction to Theory and Applications,* Academic Press, Inc., New York, Mar. 1967.
137. Cooley, J. W., and J. W. Tukey, "An Algorithm for the Machine Calculation of Complex Fourier Series," *Mathematics Computation,* vol. 19, pp. 297–301, Apr. 1965.
138. Cope, R., "Tackle Noise Variations at Video," *Electronic Design,* no. 20, pp. 54–56, Sept. 26, 1968.
139. Corriher, H. A., Jr., and B. O. Pyron, Abstracts on Radar Reflectivity of Sea Targets, Georgia Inst. Tech. Eng. Exp. Sta. Proj. A914, vol. 1, Atlanta, GA, Dec. 15, 1966 (AD813955L).
140. Corriher, H. A., Jr. et al., A Bibliography of Radar Reflection Characteristics, vol. 7, ECOM–03759–F, Georgia Institute of Technology, Apr. 14, 1967 (AD820157).
141. Corsini, G. et al., "First Experimental Results Relevant to the Mediterranean Sea-Clutter," *Proc. 1989 Inter. Symposium on Noise and Clutter Rejection in Radars and Imaging Sensors,* pp. 37–41, Tokyo, 1989.
142. Cosgriff, R. L., W. H. Peake, and R. C. Taylor, Terrain Scattering, Properties for Sensor System Design Terrain Handbook II, Ohio State University Antenna Laboratory, May 1960.
143. Costas, J. P., "A Study of a Class of Detection Waveforms Having Nearly Ideal Ambiguity Properties," *Proc. IEEE,* vol. 72, no. 8, pp. 996–1009, Aug. 1984.
144. Cox, Charles, "The Relation of Backscattered Radiation to Wind-Stress at the Sea Surface," *Intern. Symp. Electromagnetic Sensing Earth Satellites,* Miami Beach, FL, Nov. 1965.
145. Crane, R. K., and D. W. Blood, "Handbook for the Estimation of Microwave Propagation Effects—Link Calculations for Earth-Space Paths," ERT Doc. No. P–7376–TRI, prepared under NASA Contract NAS5–25341, 1979.
146. Crane, R. K., and H. K. Burke, The Evaluation of Models for Atmospheric Attenuation and Backscatter Characteristic Estimation at 95 GHZ, Environmental Research and Technology Doc. No. P–3606, Feb. 1978.
147. Crawford, A. B., and D. C. Hogg, "Measurement of Atmospheric Attenuation at Millimeter Wavelengths," *Bell Telephone Monograph* 2646, vol. 35, pp. 907–916, July 1956.
148. Crispin, J. W., Jr., and K. M. Siegel (eds.), *Methods of Radar Cross Section Analysis,* pp. 154–184, Academic Press, New York, 1968.
149. Crispin, J. W., and A. L. Maffett, "Radar Cross Section Estimation for Simple Shapes," *Proc. IEEE,* volo. 53, no. 8, pp. 833–848, Aug. 1965.
150. Crispin, J. W., Jr. et al., A Theoretical Method for the Calculation of Radar Cross Section of Aircraft and Missiles, University of Michigan Radiation Lab. Report 2591-1-H, July 1959.
151. Croney, J., "Improved Radar Visibility of Small Targets in Sea Clutter, *Radio Electron. Engr.,* pp. 135–148, Sept. 1966 (also A.S.W.E. Lab. Note XRA-65-1, Portsmouth, England, June 1, 1965).
152. Currie, Nicholas, C., and Charles E. Brown, *Principles and Applications of Millimeter-Wave Radar,* Artech House, Norwood, MA, 1987.
153. Currie, Nicholas C. (ed.), *Radar Reflectivity Measurement: Techniques & Applications,* Artech House, Norwood, MA, 1989. Also see: Currie, N.C. et al., "Millimeter-Wave Measurements and Analysis of Snow-Covered Ground," *IEEE Trans. on Geoscience and Remote Sensing,* vol. 26, no. 3, May 1988.
154. Curry, G. R., A Study of Radar Clutter in Tradex, M.I.T./Lincoln Lab., Group Rept. 1964-29, May 25, 1964 (also *IRE Trans.,* vol. MIL 9, no. 1, pp. 39–44, Jan. 1965).
155. Daley, J. C., Sea Clutter Measurements at X and C Band, Naval Res. Lab. Letter Rept. 5720–18A:JCD, Aug. 17, 1966.
156. Daley, J. C., Airborne Radar Backscatter Study at Four Frequencies, Naval Res. Lab. Letter Rept. 5270–20A:JCD, Aug. 23, 1966.

157. Daley, J. C., W. T. Davis, and N. R. Mills, Radar Sea Return in High Sea States, NRL Report 7142, Naval Research Laboratory, Washington, DC, Sept. 25, 1970.
158. Daley, J. C. et al., Radar Sea Return-Joss II, NRL Report 7534, Naval Research Laboratory, Washington, DC, Feb. 21, 1973.
159. Daley, J. C. et al., Radar Sea Return-Joss I, NRL Report 7268, Naval Research Laboratory, Washington, DC, May 11, 1971.
160. Dana, Roger A., Dennis Moraitis, and Richard D. Wilmot, "Utilization of Radar Clutter Correlation Characteristics for Automatic MTI Video Selection," *IEEE 1980 Inter. Radar Confer.*, pp. 305–316, Washington, DC, Apr. 1980.
161. Davenport, W. B., Jr., and W. L. Root, *Introduction to the Theory of Random Signals and Noise,* McGraw-Hill Book Co., New York, 1958.
162. Davenport, W. B., Jr., "Signal-to-Noise Ratios in Band-pass Limiters," *J. Appl. Phys.,* vol. 24, no. 6, pp. 720–727, June 1953.
163. Davenport, W. B., Jr., and W. L. Root, *An Introduction to the Theory of Random Signals and Noise,* IEEE Press, New York, 1987.
164. Davidson, M., Dolph-Tschebycheff Amplitude Tapering Factors for Waveforms, Appl. Phys. Lab. Intern. Memo, TWC–3–065, Apr. 1962.
165. Davies, H., "The Reflection of Electromagnetic Waves from a Rough Surface," *Proc. IEE,* pt. 4, vol. 101, pp. 209–214, Jan. 15, 1954 (also Oxford University Inst. Monograph no. 90).
166. Davies, H., and G. G. MacFarlane, "Radar Echoes from the Sea Surface at Centimeter Wave-lengths," *Proc. Phys. Soc.* London, vol. 58, 1946.
167. Davis, D. E. N., and R. A. Bromley, "Measurements on Aircraft Echoes Using Wideband Pulse-Compression Radar," *Proc. IEEE,* vol. 116, no. 8, pp. 1293–1296, Aug. 1969.
168. Dawe, Byron, R., "A Radar Cross Section Model for Icebergs," *IEEE Inter. Radar Confer.,* Arlington, VA, May 6–9, 1985.
169. Delano, R. H., "A Theory of Target Glint or Angular Scintillation in Radar Tracking," *Proc. IRE,* vol. 41, no. 8, pp. 1778–1784, Dec. 1953.
170. Delay Devices for Pulse Compression Radar, *IEE Conf. Publ. 20,* Feb. 21, 1966.
171. Deley, G. W., Width Modulated Pulse-Doppler Waveforms for Clutter Rejection, Def. Res. Corp., Tech. Memo. 364, June 1966 (AD647195).
172. Delisle, G. Y., M. Lecours, G. Gonthier, G. Ratte, and C. Deschenes, "RCS of Projectiles—Analytical and Experimental Results," *Proc. IEEE 1986 National Radar Confer.,* pp. 83–88, 1986.
173. Delong, D. F., Jr., Experimental Autocorrelation of Binary Codes, M.I.T./Lincoln Lab. Rept. 47G–0006, Oct. 24, 1960 (AD245803).
174. Demin, I. D., The Effect of Sea Roughness on Radar Visibility of Small Ships, Leningrad-Central Naval Sci.—Res. Inst. Navigation Commun., no. 20, issue 79 (translation), Air Force Systems Command/Foreign Technology Division, pp. 56–63, Aug. 8, 1966 (AD643974).
175. Di Toro, J. A., Clutter Model for AEW Radar Design, U.S. Naval Air Development Center Rept. NADC–AE–6638, Johnsville, PA, Nov. 29, 1966 (AD644567).
176. Di Vito, A. et al., "Synthesis and Evaluation of Phase Codes for Pulse Compression Radar," *Rivista Technica Selenia,* vol. 9, no. 2, pp. 12–24, 1985.
177. Di Vito, A., G. Galati, and D. Iovino, "A Comparison of Variance Reduction Techniques for Radar Simulation," *Inter. Confer.—Radar 87,* London, UK, 19–21 Oct. 1987.
178. Dickey, F. R., Jr., "Theoretical Performance of Airborne Moving Target Indicators," *IRE Trans.,* vol. ANE–8, pp. 12–23, June 1953.
179. DiFranco, J. V., and W. L. Rubin, *Radar Detection,* Prentice-Hall, Inc., Englewood Cliffs, NJ, 1968.
180. Dike, G., R. Wallenberg, and J. Potenza, "Inverse SAR and its Application to Aircraft Classification," *IEEE 1980 Inter. Radar Confer.,* pp. 161–167, Washington, DC, Apr. 1980.
181. Dillard, George M. and John T. Rickard, "Performance of an MTI Followed by Incoherent Integration for Nonfluctuating Signals," *IEEE 1980 Inter. Radar Confer.,* pp. 194–199, Washington, D.C., Apr. 1980.

182. Dillard, G. A. and R. A. Dillard, "Radar Automatic Detection," *Microwave Journal,* vol. 28, no. 6, pp. 125–130, June 1985.
183. Dockery, G. D., "A Method for Modelling Sea Surface Clutter in Complicated Propagation Environments," *Proc. IEE,* Part F., vol. 137, no. 2, pp. 73–79, 1990.
184. Dockery, G. D., "Modeling Electromagnetic Wave Propagation in the Troposphere Using the Parabolic Equation," *IEEE Trans. Ant. Prop.,* vol. 36, no. 10, pp. 1464–1470, 1988.
185. Domville, A. R., The Bistatic Reflection from Land and Sea of X-band Radio Waves, Part 1 and 2, GEC-AEI (Electronics) Ltd., Stanmore, Middlesex, England, Memos No. SLM. 1802, 2116, July 1967, July 1968, and Supplement July 1969.
186. Douce, J. L., Barker Sequences, Electronics (Letters), p. 159 (British), School of Engineering Science/Univ. of Warwick Coventry, Worcester, Apr. 1966.
187. Doviak, Richard J., and Dusan S. Zrnić, *Doppler Radar and Weather Observations,* Academic Press, Inc., Orlando, FL, 1984.
188. Doviak, Richard J. and Dusan S. Zrnić, "Siting of Doppler Weather Radars to Shield Ground Targets," *IEEE Trans. Weather on Antennas and Propagation,* vol. AP–33, pp. 685–689, July 1985.
189. Drury, W. H., Improved MTI Radar Signal Processor, Project Report ATC–39, Lincoln Laboratory, M.I.T., Apr. 3, 1975.
190. Duhamel, P., and H. Hollmann, "Split-Radix FFT Algorithm," *Electr. Lett.,* vol. 20, no. 1, pp. 14–16, Jan. 5, 1985.
191. Dukeman, Mordechai, and Amnon Hammer, "Weighting Effects on Costas Array Ambiguity Function," *Inter. Radar Confer.,* pp. 168–173, Paris, 1989.
192. Dunn-Rogers, Juliet, "Sea CAS–Sea Clutter Acquisition System," *Proc. 1989 Inter. Symposium on Noise and Clutter Rejection in Radars and Imaging Sensors,* pp. 27, IEICE, 1989.
193. Durlach, N. I., Influence of the Earth's Surface on Radar, M.I.T./Lincoln Lab. Tech. Rept. 373, Jan. 18, 1965 (AD627635).
194. Dye, R. A., "Performance of the Delay-lock Tracking Discriminator with Binary Signals," *1965 IEEE Conf.,* vol. MIL–E–Con 9, pp. 151–158, Sept. 1965.
195. Dyer, F. B., M. J. Gary, and G. W. Ewell, "Some Comments on the Characterization of Radar Sea Return," *Proc. 1974 Inter. IEEE Symp. Ant. and Prop.,* pp. 323–326, Atlanta, 1974.
196. Dyer, F. B., N. C. Currie, and M. S. Applegate, "Radar Backscatter from Land, Sea, Rain, and Snow at Millimeter Wavelengths," *Radar 77,* pp. 559–562, London.
197. Eaves, Jerry L., and Edward K. Reedy (eds.), *Principles of Modern Radar,* Van Nostrand Reinhold Company, New York, 1987.
198. Echard, J. D. and M. L. Watt, The Quantization Noise Spectrum of a Sinusoid in Colored Noise, Submitted for Publication *IEEE Trans.* on Acoustics, Speech, and Signal Processing, Georgia Tech. Research Institute, Atlanta, GA, 1990.
199. Edgar, A. K., E. J. Dodsworth, and M. P. Warden, "The Design of a Modern Surveillance Radar," *Inter. Confer. on Radar–Present and Future,* IEE Conference Publication No. 105, pp. 8–13, Oct. 23–25 1973.
200. Edrington, T. S., Fluctuation of CW Radar Echoes from Aircraft, Def. Res. Lab. Univ. Texas DRL–448, Apr. 1960.
201. Edrington, T. S., "The Amplitude Statistics of Aircraft Radar Echoes," *IEEE Trans.,* vol. MIL–9, no. 1, pp. 10–16, Jan. 1965.
202. Einstein, T. H., Generation of High Resolution Radar Range Profiles and Range Profile Auto-Correlation Functions Using Stepped Frequency Pulse Trains, Project Report TT–54, M.I.T. Lincoln Laboratory, Oct. 1984.
203. Ekstrom, J., "MTI Clutter Locking for Arbitrary Clutter Spectral Shapes," *IEEE Trans.,* vol. AES–10, no. 6, pp. 872–874, Nov. 1974.
204. Elspas, B., A Radar System Based on Statistical Estimation and Resolution Considerations, Appl. Electron. Lab. Stanford Univ. Tech. Rept. 361–1, Aug. 1, 1955 (AD207896).
205. Emerson, R. C., Some Pulsed Doppler MTI and AMTI Techniques, The Rand Corporation, Rept. R–274, March 1954. Reprinted in: D. C. Schleher, *MTI Radar,* Artech House, 1978.

206. En Route Moving Target Detector Technical Data Package, 1980. Federal Aviation Administration, also FAA–E–2763, App. A, Jan. 86, Washington, DC.
207. H. V. Hitney, A. E. Barrios and G. E. Lindem, EREPS, A refractive index prediction software package, available from Code 543 NOSC San Diego, CA 92152, 1988. Rev. 20, Feb. 1990.
208. Erickson, C. W. Clutter Cancelling in Autocorrelation Functions by Binary Sequence Pairing, U.S. Navy Electron. Lab. Rept. 1047, San Diego, Cal., June 13, 1961 (AD01401).
209. Ericson, L. O., "Terrain Return Measurements with an Airborne X-band Radar Station," *Proc. Sixth Conf. Swedish Natl. Comm. Sci. Radio,* March 13, 1963, Research Institute of National Defense, Stockholm, 1963.
210. Estes, Wilmot J., Robert H. Flake, and Claud C. Pinson, "Spectral Characteristics of Radar Echoes From Aircraft Dispensed Chaff," *IEEE Trans. AES,* vol. 21, no. 7, pp. 8–18, Jan. 1985.
211. Evans, G. C., "Influence of Ground Reflections on Radar Tracking Accuracy," *Proc. IEE,* vol. 113, no. 8, pp. 1281–1286, Aug. 1966.
212. Evans, James E., and Daniel Hynek, "Clutter Rejection in Doppler Weather Radars Used for Airport Wind Shear Detection," *Proc. 1989 Inter. Symp. on Noise and Clutter Rejection in Radars and Imaging Sensors,* 1989.
213. Eveleth, J. H., "A Survey of Ultrasonic Delay Lines Operating Below 100 MHz," *Proc. IEEE,* vol. 53, no. 10, pp. 1406–1428, Oct. 1965.
214. Ewell, G. W. and S. P. Zehner "Bistatic Radar Cross Section of Ship Targets," *IEEE Journal of Oceanic Engineering,* vol. OE-5, no. 4, pp. 211–215, Oct. 1980. See also; George W. Ewell and Stephen P. Zehner, "Bistatic Sea Clutter Return Near Grazing Incidence," *IEE Inter. Radar Confer.,* pp. 188–192, London, 1982.
215. Fante, Ronald L., "A Model for Target Detection with Over-The-Horizon Radar," *IEEE Trans. AES,* vol. 26, no. 1, pp. 68–87, Jan. 1990.
216. Farina, A., and F. A. Studer, *Radar Data Processing,* vol. II, Research Studies Press Ltd., 1986.
217. Farina, A., and F. A. Studer, *Radar Data Processing,* vol. I, Research Studies Press Ltd., 1985.
218. Farina, A. and F. A. Studer, "A Review of CFAR Detection Techniques in Radar Systems," *Microwave Journal,* vol. 29, no. 9, pp. 115–128, Sept. 1986.
219. Farina, Alfonso, F. Scannapieco, and F. Vinelli, "Target Detection and Classification with Very High Range Resolution Radar," *International Radar Confer.,* pp. 20–25, Paris, 1989.
220. Farina, A., A. Russo, F. A. Studer, "Coherent Radar Detection in Log-Normal Clutter," *IEE Proc.,* vol. 133, Part F, no. 1, pp. 39–54, Feb. 1986.
221. Farrell, J. L., and R. L. Taylor, "Doppler Radar Clutter," *IRE Trans.,* vol. ANE–11, no. 3, pp. 162–172, Sept. 1964.
222. Farrell, E. B., "Plotting Experimental Data on Normal or Log-normal Probability Paper," *Industrial Quality Control,* vol. 15, no. 1, July 1958.
223. Fay, F. A., J. Clarke and R. S. Peters, "Weibull Distribution Applied to Sea Clutter," *IEE Inter. Radar Confer.,* London, 1977.
224. Federal Aviation Administration Terminal Doppler Weather Radar Operational Demonstration, Fact Sheet, July 1, 1988.
225. Fehlner, L. F., Marcum's and Swerling's Data on Target Detection by a Pulsed Radar, Appl. Phys. Lab./Johns Hopkins Univ. Rept. TG–451, Silver Spring, MD, July 1962 (also supplement TG–451A, Sept. 1964).
226. Fenwick, R. B., and G. H. Barry, "Step-by-Step to a Linear Frequency Sweep," *Electronics,* pp. 66–70, July 16, 1965.
227. Fine, T., "On the Estimation of the Mean of a Random Process," *Proc. IEEE,* vol. 53, no. 2, pp. 187–188, Feb. 1965.
228. Finn, H. M., "A New Approach to Sequential Detection in Phased Array Radar Systems," *Proc. IEEE Natl. Winter Conv. Military Electron.,* vol. 2, pp. 3–4, 1963.
229. Finn, H. M., "Adaptive Detection in Clutter," *Proc. NEC,* vol. 22, p. 562, 1966 (also see RCA APTM–1140–47, Dec. 1, 1966 and "Adaptive Detection with Regulated Error Probabilities," *RCA Rev.,* vol. 28, no. 4, Dec. 1967).
230. Finn, H. M. and R. S. Johnson, "Adaptive Detection Mode with Threshold Control

as a Function of Spatially Sampled Clutter-Level Estimates," *RCA Review,* vol. 29, no. 3, Sept. 1968.
231. Finn, H. M., and R. S. Johnson, "Efficient Sequential Detection in the Presence of Strong Localized Signal Interference," *RCA Rev.,* Sept. 1966.
232. Fiscella, B., and P. P. Lombardini, "Oceanographic Use of a Coastal X Band Incoherent Radar," *IEEE 1980 Inter. Radar Confer.,* pp. 51–55, Washington, DC, Apr. 1980.
233. Fishbein, W., S. W. Graveline, and O. E. Rittenbach, Clutter Attenuation Analysis, USAECOM, Tech. Rept. ECOM–2808, Fort Monmouth, NJ, Mar. 1967. Also [635, pp. 331–354].
234. Fitts, R. E., *The Strategy of Electromagnetic Conflict,* Peninsula Publishing, Los Altos, CA, 1980.
235. Flesher, G. T., and G. I. Cohn, "The General Theory of Comb Filters," *Proc. NEC,* pp. 282–295, Chicago, 1958.
236. Fliss, G. G., and D. L. Mensa, "Instrumentation for RCS Measurements of Modulation Spectra of Aircraft Blades," *IEEE 1986 National Radar Confer.,* IEEE 86CH2270–7, 1986.
237. Fliss, G., and D. Mensa, Spectral Signatures of Rotating Structures (private communication).
238. Flock, Warren L., "Propagation Effects on Satellite Systems at Frequencies Below 10 GHz," NASA Reference Publication 1108, 1983.
239. Flock, Warren L., "Propagation Effects on Satellite Systems at Frequencies Below 10 GHz," 2d ed., NASA Reference Publication 1108(02), Dec. 1987.
240. Floyd, W. L., and T. J. Lund, "Scatterometer Program," *Proc. 1966 Aerospace Electron. Systems Conv. Rec.* (supplement to *IEEE Trans. Aerospace Electron Sys.*), vol. AES–2, no. 6, Nov. 1966.
241. Follin, J. W., Jr., F. C. Paddison, and A. L. Maffett, "Statistics of Radar Cross Section Scintillations," *Electromagnetics,* 4, pp. 139–164, 1984.
242. Fordon, W. A., "Environmental Factors Influencing Radar System Design," *Symposium on Radar Techniques and Systems,* New Delhi, India, May 1970.
243. Fossi, M. et al., "Experimental Results on a Double Polarization Radar," *Inter. Confer. on Radar,* pp. 519–524, Paris, May 21–24, 1984.
244. Fowle, E. N., E. J. Kelly, and J. A. Sheehan, Accuracy and Resolution, Unpublished notes at M.I.T./Lincoln Laboratory, June 1961.
245. Fowle, E. N., E. J. Kelly, and J. A. Sheehan, "Radar System Performance in a Dense-target Environment," *IRE Nat. Conv. Rec.,* pt. 4, pp. 136–145, 1961.
246. Fowle, E. N., The Design of Radar Signals, Mitre Corporation, SR–98, Bedford, MA, Nov. 1, 1963 (AD617711).
247. Fowler, C. A., A. P. Uzzo Jr., and A. E. Ruvin, "Signal Processing Techniques for Surveillance Radar Sets," *IRE Trans.,* vol. MIL–5, no. 2, pp. 103–108, April 1961.
248. Francois, Robert E., Jr., "Geometric Radar Coverage Predictions Using Digital Terrain Elevation Data," *IEEE 1980 Inter. Radar Confer.,* pp. 322–329, Washington, DC, April 1980.
249. Frank, R. L., "Polyphase Codes with Good Nonperiodic Correlation," *IEEE Trans.,* vol. IT–9, pp. 43–45, Jan. 1963.
250. Frank, R. L., and S. A. Zadoff, "Phase Shift Pulse Codes with Good Periodic Correlation Properties," *IRE Trans.,* vol. IT–8, pp. 381–382, Oct. 1962.
251. Freedman, Avraham, and Nadav Levanon, "Staggered Costas Signals," *IEEE Trans. AES,* vol. 22, no. 6, pp. 695–701, Nov. 1986.
252. Freni, A., D. Giuli, M. Gherardelli, S. Minuti, T. A. Seliga, and K. Aydin, "Rainfall-Clutter Discrimination in Dual Linear Polarization Radars," *Radar Meteorology Conference Preprints,* American Meteorological Society, Boston, MA, 1989.
253. G. D. Dockery, and G. C. Konstanzer, "Recent Advances in Prediction of Tropospheric Propagation Using the Parabolic Equation," *Johns Hopkins APL Tech. Digest,* vol. 4, no. 8, pp. 404–412, 1988.
254. Gabbay, S., Properties of Even-Length Barker Codes and Specific Polyphase Codes with Barker Type Autocorrelation Functions," NRL Report 8586, Naval Research Laboratory, Washington, DC, July 1982.

255. Gaheen, A. F., J. McDonough, and D. P. Tice, Frequency Diversity Radar Study, vol. 1, Experimental Verification of Frequency and Polarization Diversity on the Statistics of the Radar Cross Section of Satellite Targets, Westinghouse Electric Corp., Baltimore, MD, Feb. 11, 1966 (AD480358).
256. Galati, G., and M. Orsini, "Doppler-Tolerant Digital Pulse Compression with Minimized Hardware," *Inter. Radar Confer.*, pp. 22–25, Paris, 1989.
257. Galejs, J. "Enhancement of Pulse Train Signals by Comb Filters," *IRE Trans. Inform. Theory,* vol. IT–4, no. 3, pp. 114–125, Sept. 1958.
258. Gallagher, J. M., H. Krason, and W. Todd, Multifrequency Clutter Study, Raytheon Co. Missile Sys. Div. BR–3289, Bedford, MA, March 5, 1965.
259. Gandhi, P. P. and Kassam, S. A., "Analysis of CFAR Processors in Nonhomogeneous Background," *IEEE Trans. AES,* vol. 24, pp. 427–445, July 4, 1988.
260. Garbacz, R. J. and D. L. Moffett, "An Experimental Study of Bistatic Scattering from some Small, Absorber-coated Metal Spheres," *Proc. IRE,* vol. 49, pp. 1184–1192, July 1961.
261. Gardner, R. E., Doppler Spectral Characteristics of Aircraft Radar Targets at S-band, Naval Res. Lab. Rept. 5656, Aug. 3, 1961.
262. Gent, H., I. M. Hunter, and N. P. Robinson, "Polarization of Radar Echoes, Including Aircraft Precipitation and Terrain," *Proc. IEE,* vol. 110, no. 12, pp. 2139–2148, Dec. 1963.
263. George, S. F., and A. S. Zamanakos, "Comb Filters for Pulsed Radar Use," *Proc. IRE,* vol. 42, no. 7, pp. 1159–1165, July 1954.
264. George, T. S., "Fluctuations of Ground Clutter Return in Airborne Radar Equipment," *Proc. IEE (British),* vol. 99, pt. 4, no. 2, pp. 92–98, April 1952.
265. Gill, W. J., "A Comparison of Binary Delay-lock Tracking-loop Implementations," *IEEE Trans.,* vol. AES–2, no. 4, pp. 415–424, July 1966.
266. Giuli, D., "Polarization Diversity in Radars," *Proc. IEEE,* vol. 74, no. 2, pp. 245–269, Feb. 1986.
267. Gjessing, Dag J., and Jens Hjelmstad, "Artificial Perception. Characterization and Recognition of Objects and Scattering Surfaces Based on Electromagnetic Waves. Target Adaptive Matched Illumination Radar (TAMIR)," *International Confer. on Radar,* Paris, May 24–28, 1989.
268. Gjessing, Dag J., "Target Recognition by an Adaptive Radar," *International Confer. on Radar,* Paris, May 21–24, 1984. Also Gjessing, D. T., J. Hjelmstad, and T. Lund, "A Multifrequency Adaptive Radar for Detection and Identification of Objects: Results on Preliminary Experiments on Aircraft Against a Sea-Clutter Background," *IEEE Trans. on Antennas and Propagation,* vol. 30, no. 3, pp. 351–65, May 1982.
269. Glover, K. M., D. R. Hardy, C. R. Landry, and T. Konrad, "Radar Characteristics of Known Insects in Free Flight," *Proc. 12th Radar Meteorol. Conf.,* Norman, OK, Oct. 19, 1966 (also *Science,* vol. 154, no. 967, 1966).
270. Godard, S., Properties of Attenuation of Radiowaves in the 0.86-cm Band by Rain, translated from *J. Rech. Atmos. (J. Atmos. Res.),* vol. 2, no. 4, pp. 121–
271. Goetz, L. P., and J. D. Albright, "Airborne Pulse-Doppler Radar," *IRE Trans.,* vol. MIL–5, no. 2, pp. 116–126, Apr. 1954.
272. Goetz, L. P., and W. A. Skillman, "Master Oscillator Requirements for Coherent Radar Sets," *IEEE-NASA Symp. Short Term Frequency Stability,* NASA SP–80, pp. 19–27, Nov. 23, 1964.
273. Golay, M., *Complementary Series,* vol. 7, no. 2, pp. 82–87, Apr. 1961.
274. Goldhirsh, J., and I. Katz, "Useful Experimental Results for Earth Satellite Rain Attenuation Modeling," *IEEE Trans. Ant. Prop.,* vol. 27, no. 3, pp. 413–415, 1979.
275. Goldhirsh, Julius, "Rain Cell Size Statistics as a Function of Rain Rate for Attenuation Modeling," *IEEE Trans. Ant. Prop.,* vol. 31, no. 5, pp. 799–800, Sept. 1983.
276. Goldman, H., and Bar-David, I., "Analysis and Application of the Excision CFAR Detector," *IEE Proc.,* vol. 135, pt F, no. 6, pp. 563–575, Dec. 1988.
277. Goldstein, G. B., "False-Alarm Regulation in Log-Normal and Weibull Clutter," *IEEE Trans. AES,* vol. 9, no. 1, pp. 84–92, Jan. 1973.

278. Goldstein, H., "Frequency Dependence of the Properties of Sea Echo," *Phys. Rev.*, vol. 70, Dec. 1 and 15, 1956. (See also [211].)
279. Golomb, S. W., and R. A. Scholtz, "Generalized Barker Sequences," *IEEE Trans. Inform. Theory*, vol. IT–11, no. 4, pp. 533–537, Oct. 1965.
280. Golomb, S. W. et al., *Digital Communications*, Prentice-Hall, Inc., Englewood Cliffs, NJ, 1964.
281. Golomb, S. W., Sequences with Randomness Properties, MR–6193–K, Contract Req. no. 639498, Glenn L. Martin Co., June 14, 1955.
282. Golomb, S. W., "Algebraic Constructions for Costas Arrays," *Journal of Combinatorial Theory*, series A 37, 13–21 (1984).
283. Golomb, S. W., and H. Taylor, "Construction and Properties of Costas Arrays," *Proc. IEEE*, vol. 72, pp. 1143–1163, Sept. 1984.
284. Goodchild, W., Moving Target Detector/Airport Surveillance Radar (ASR–7) Field Evaluation, Federal Aviation Administration Technical Center Final Report, Rept. DOT/FAA/RD–81/57, Aug. 1981.
285. Gordon, William B., and Jon D. Wilson, Rain Clutter Statistics, Naval Research Laboratory Report 8639, Washington, DC, Sept. 30, 1982.
286. Gossard, E. E., and R. G. Strauch, *Radar Observation of Clean Air and Clouds* (Development in Atmospheric Science 14–Series), Elsevier Science Publishing Company, Inc., New York, NY, 1983.
287. Gossard, E. E., "The Height Distribution of Refractive Index Structure Parameter in an Atmosphere Being Modified by Spatial Transition at Its Lower Boundary," *Rad. Sci*, vol. 13, no. 3, pp 489–500, 1978.
288. Gossard, Earl E., Richard G. Strauch, Radar Applications in Cloud and Clear-Air Studies, NOAA Technical Memorandum ERL WPL–87, Boulder, CO, Nov. 1981.
289. Grant, C. R., and B. S. Yaplee, "Backscattering from Water and Land at Centimeter and Millimeter Wavelengths," *Proc. IRE*, vol. 45, no. 7, July 1957.
290. Grasso, G., and P. F. Guarguaglini, "Clutter Residues of a Coherent MTI Radar Receiver," *IEEE Trans. Aero. Elect. Sys.*, vol. AES–5, no. 2, pp. 195–204, 1969.
291. Graves, C. D., "Radar Polarization Scattering Matrix," *Proc. IRE*, vol. 44, no. 2, pp. 248–252, Feb. 1956.
292. Gray, G., and G. Zeoli, "Quantization and Saturation Noise Due to A/D Conversion," *IEEE Trans. AES*, pp. 222–223, Jan. 1971.
293. Gray, Glenn A. and Fred E. Nathanson, "Digital Processing of Radar Signals," *IEEE EASCON Proc.*, pp. 208–215, 1971.
294. Green, B. A., Jr., "Radar Detection Probability with Logarithmic Detectors," *IRE Trans.*, vol. IT–4, no. 1, pp. 50–52, Mar. 1958.
295. Grisetti, R. S., M. M. Santa, and G. M. Kirkpatrick, "Effect of Internal Fluctuation and Scanning on Clutter Attenuation in MTI Radar," *IRE Trans.—Aeronautical Navigational Electron.*, pp. 37–41, Mar. 1955.
296. Guinard, N. W., and J. C. Daley, "An Experimental Study of a Sea Clutter Model," *Proc. IEEE*, vol. 58, no. 4, Apr. 1970.
297. Guinard, N. W., J. T. Ransone, Jr., M. B. Laing, and L. E. Hearton, NRL Terrain Clutter Study, Phase I, Naval Res. Lab. Rept. 6487, May 10, 1967 (AD653447).
298. Gunn, K. L. S., and T. W. R. East, "The Microwave Properties of Precipitation Particles," *Quart. J. Roy. Meteorol. Soc.*, vol. 80, pp. 522–545, Oct. 1954.
299. Gustafson, B. G., and B. O. As, "System Properties of Jumping-frequency Radars," *Phillips Telecommun. Rev.*, vol. 25, no. 1, pp. 70–76, July 1964. (See also Lind, G., "Reduction of Radar Tracking Errors with Frequency Agility," *IEEE Trans.*, vol. AES–4, no. 3, pp. 410–416, May 1968.)
300. Hadad, J. D., "Basic Relation Between the Frequency Stability Specification and the Application," *IEE-NASA Symp. Short Term Frequency Stability*, NASA SP–80, Nov. 23, 1964.
301. Hagn, G., Investigation of Direct Backscatter of High Frequency Radio Waves from Land, Sea Water, and Ice, Stanford Res. Final Rept. 2, NONR 2917–(00), Menlo Park, CA, May 1962.
302. Hall, W. M., General Radar Equation, in "Space Aeronautics R&D Handbook, 1962–1963 (also unpublished Appendix A).

303. Hall, W. M., and H. R. Ward, "Signal to Noise Loss in Moving Target Indicators," *Proc. IEEE (Letters)*, vol. 56, no. 2, pp. 233–234, Feb. 1968.
304. Hammond, D. L., and R. E. Morden, "Signal Processing Techniques for a Lunar Radar System," *Suppl. IEEE Trans. Aerospace Electron. Sys.*, vol. AES–2, no. 6, pp. 395–399, Nov. 1966.
305. Hansen, R. C. (ed.), *Microwave Scanning Antennas*, vol. I, Academic Press, Inc., New York, 1964.
306. Hansen, V. Gregers, "Simple Expressions for Determining Radar Detection Thresholds," *IEEE Trans. AES*, vol. 18, no. 4, pp. 510–512, July 1982.
307. Hansen, V. Gregers, Optimum Pulse Doppler Search Radar Processing and Practical Approximations, Raytheon Co. Rept., Wayland, Mass., 1978.
308. Hansen, V. G., "Studies of Logarithmic Radar Receiver Using Pulse-length Discrimination," *IEEE Trans.*, vol. AES–1, no. 3, pp. 246–253, Dec. 1965.
309. Hansen, V. Gregers, and David Michelson, "A Comparison of the Performance Against Clutter of Optimum, Pulsed Doppler and MTI Processors," *IEEE 1980 Inter. Radar Confer.*, pp. 211–218, Washington, DC, Apr. 1980.
310. Hansen, V. G., "Comments on 'Performance Data for a Double-Threshold Detection Radar,' " *IEEE Trans. AES*, vol. 7, no. 3, p. 561, May 1971.
311. Hansen, V. G., and Ward, H. R., "Detection Performance of the Cell Averaging Log/CFAR Receiver," *IEEE Trans. AES*, vol. 8, no. 5, pp. 648–652, Sept. 1972.
312. Hansen, V. G., and J. H. Sawyers, "Detectability Loss Due to 'Greatest of' Selection in a Cell-Averaging CFAR," *IEEE Trans. AES*, vol. 16, no. 1, pp. 115–118, Jan. 1980.
313. Harkness, L. L., Personal Communication, Georgia Tech Research Institute, Atlanta, GA, Feb. 1988.
314. Harmer, J. D., and W. S. O'Hare, "Some Advances in CW Radar Techniques," *IRE Nat. Conv. MIL Electron.*, pp. 311–323, 1961.
315. Harrington, J. V., "An Analysis of the Detection of Repeated Signals in Noise by Binary Integration," *IRE Trans*, vol. IT–1, no. 1, pp. 1–9, Mar. 1955.
316. Harrison, A., "Methods of Distinguishing Sea Targets from Clutter on a Civil Marine Radar," *Radio Electron, Engr.*, vol. 27, pp. 261–275, Apr. 1964.
317. Harrold, T. W., "Attenuation of 8.6-mm Wavelength Radiation in Rain," *Proc. IEE*, vol. 114, no. 2, pp. 201–203, Feb. 1967.
318. Hayes, R. D. et al., "Reflectivity and Emissivity of Snow and Ground at MM Waves," *1980 IEEE International Radar Confer.*, pp. 67–72, Washington, DC.
319. Hayes, R. D., N. C. Currie, and J. A. Scheer, "Reflectivity and Emissivity of Snow and Ground at MM Waves," *IEEE 1980 Inter. Radar Confer.*, pp. 67–72, Washington, DC, Apr. 1980.
320. Hayes, R. D., and F. B. Dyer, Land Clutter Characteristics for Computer Modeling of Fire Control Radar Systems, Technical Report Number 1, EES/GIT Project A–1485 under Contract No. DAAA–25–73–C–0256, May 15, 1973.
321. Heffner, R. W., "A Backscatter-Multipath Model for Ground Wave Pulse Communications Systems," *1964 IEEE Intern. Conv. Rec.*, vol. 6, no. 10, 1964.
322. Heidbreder, G. R., and R. L. Mitchell, "Detection Probabilities for Log-normally Distributed Signals," *IEEE Trans.*, vol. AES–3, no. 1, pp. 5–13, Jan. 1967.
323. Heimiller, R. C., "Phase Shift Pulse Codes with Good Periodic Correlation Properties," *IRE Trans.*, vol. IT–7, pp. 254–257, Oct. 1961.
324. Heiss, William H., Dale Sirmans, and David L. McGrew, "NEXRAD—Next Generation Weather Radar (WSR–88D)," *Microwave Journal*, Jan. 1990.
325. Helgostam, L. F., and B. Ronnerstam, "Ground Clutter Calculation for Airborne Doppler Radars," *IEEE Trans.*, vol. MIL–9, nos. 3 and 4, pp. 294–297, July–Oct. 1965.
326. Helmken, Henry H., and Matthew J. Vanderhill, "Very Low Grazing Angle Radar Backscatter from the Ocean Surface," *IEEE 1990 Inter. Radar Conf.*, Washington, DC, May 1990.
327. Helstrom, C. W., "Performance of Receiver with Linear Detectors," *IEEE Trans.*, vol. AES–26, no. 2, pp. 210–217, Mar. 1990. Analysis of Two-stage Signal Detection System, Westinghouse Res. Lab. Rept. 412 FF 512–R2, Pittsburgh, PA, Apr. 1960.

328. Helstrom, C. W., An Introduction to Sequential Detection in Radar, Westinghouse Res. Lab. Rept. 412 FF 512–R1, R2, Pittsburgh, Penn., March 1960. (Also see "A Range Sampled Sequential Detection System," *IRE PGIT,* vol. IT–8, pp. 43–47, Jan. 1962.
329. Hendry, A. and G. C. McCormick, "Deterioration of Circular-polarization Clutter Cancellation in Anisotropic Precipitation Media," *Electronics Letters,* vol. 10, no. 10, May 16, 1974.
330. Henry, Jean Philippe, "Amplitude and Spectral Characterization of Radar Sea Clutter," *International Radar Confer.,* pp. 126–137, Paris, 1989.
311. *Hewlett-Packard Journal,* Dec. 1987.
332. Hicks, J. J., and J. K. Angell, "Radar Observations of Braided Structures in the Visually Clear Atmosphere," *J. Appl. Meteorol.,* Feb. 1968.
333. Hicks, B. L. et al., Sea Clutter Spectrum Studies Using Airborne Coherent Radar III, Control Sys. Lab./Univ. Illinois Rept. R 105, May 1958.
334. Hicks, J. J., I. Katz, C. R. Landry, and K. R. Hardy, "Clear Air Turbulence: Simultaneous Observations by Radar and Aircraft," *Science,* vol. 157, no. 3790, pp. 808, 809, Aug. 18, 1967.
335. Higgins, William F., and Aditya K. Kamal, "Clutter-Rejection Degradation Due to Limiting," *Proc. 1989 Inter. Symposium on Noise and Clutter Rejection in Radars and Imaging Sensors,* pp. 281–286, IEICE, Tokyo, 1989.
336. Hill, R. T., Performance Characteristics of Radar Phased Arrays, Assoc. Senior Engs.—Bureau Ships 3rd Ann. Tech. Symp., Mar. 25, 1966.
337. Hill, J. E., "Antenna Polarization," Watkins-Johnson Co., *Tech-Notes,* vol. 6, no. 4, pp. 2–15, July–Aug. 1979.
338. Hilst, G. R., Analysis of the Audio-frequency Fluctuations in Radar Storm Echoes: A Key to the Relative Velocities of the Precipitation Particles, M.I.T. Dept. Meteorol. Weather Radar Res. Tech. Rept. 9, pt. A, Nov. 1, 1949 (AD128649).
339. Hitney, H. V., A. E. Barrios, and G. E. Lindem, "Engineer's Refractive Effects Prediction System (EREPS)," *Users Manual,* Naval Ocean Systems Center, Code 543, San Diego, CA, July 1988 (AD 203443).
340. Hoffman, L. A., H. J. Winthroub, and W. A. Garber, "Propagation Observations at 3.2 Millimeters," *Proc. IEEE,* vol. 54, no. 4, pp. 449–454, Apr. 1966.
341. Hoffman, J., Relativistic and Classical Doppler Electronic Tracking Accuracies, AIAA Space Flight Testing Conf., Cocoa Beach, FL, Mar. 18, 1963.
342. Holliday, E. M., W. E. Wood, D. E. Powell, and C. E. Basham, L-band Clutter Measurements, U.S. Army Missile Command Rept. RE–TR–65–1, Redstone Arsenal, AL, Nov. 1964 (AD461590).
343. Hollis, E., "Comparison of Combined Barker Codes for Coded Radar Use," *IEEE Trans. Aerospace Electron. Sys.,* vol. AES–3, no. 1, pp. 141–143, Jan. 1967.
344. Hollis, E. E., "Predicting the Truncated Autocorrelation Functions of Combined Barker Sequences of any Length without Use of a Computer," *IEEE Trans.,* vol. AES–3, no. 2, pp. 368–369, Mar. 1967.
345. Hoover, R. M., and R. J. Urick, "Sea Clutter in Radar and Sonar," *IRE Conv. Rec.,* 1957, pt. 9, p. 17, Nov. 1957.
346. Horst, M. M., F. B. Dyer, and M. T. Tuley, "Radar Sea Clutter Model," *Inter. Confer. on Ant. and Prop.,* IEE Conf. Pub. No. 169, Pts. 1 and 2, London, 1978. (See also R. N. Trebits and B. Perry, Multifrequency Radar Sea Backscatter Data Reduction, Georgia Institute of Technology, Final Technical Report, GIT/EES—A–2717, June 1981–Sept. 1982.)
347. Houghton, E. W., Radar Echoing Areas of Birds, RRE Memorandum No. 2557, Malvern, England, July, 1969.
348. Howard, T. B., "Application of Some Linear FM Results to Frequency-Diversity Waveforms," *RCA Rev.,* vol. 26, no. 1, pp. 75–105.
349. Hsiao, J. K., "On the Optimization of MTI Clutter Rejection," *IEEE Trans. AES,* vol. AES-10, pp. 622–629. Sept. 1974.
350. Hsiao, James K., "Phased Array Sidelobe Level, Gain, Beamwidth, and Error Tolerance," *International Confer. on Radar,* pp. 304–308, Paris, May 21–24, 1984.
351. Hudson, Brian H., and Nicholas C. Currie, "Millimeter Wave Reflectivity of Paved Runway Surfaces," *IEEE Southcon,* 1989.

352. Hughes, P. K. II, "A High-Resolution Radar Detection Strategy," *IEEE Trans. AES,* vol. 19, no. 5, pp. 663–667, Sept. 1983.
353. Hughes, Charles J., "Performance of Digital Signal Processors for MTI and Hard-Limited Radar Detection," *Proc. 1984 International Symposium on Noise and Clutter Rejection, in Radars and Imaging Sensors,* Moorestown, NJ, 1984.
354. Hunter, I. M., and T. B. A. Senior, "Experimental Studies of Sea-surface Effects on Low-angle Radars," *Proc. IEE,* vol. 113, no. 11, pp. 1731–1740, Nov. 1966.
355. Hynes, R., and R. E. Gardner, "Doppler Spectra of S-band and X-band Signals," *IEEE Eastcon Proc.,* Washington, DC, Oct. 16–18, 1967; *IEEE Trans.,* vol. AES–3, no. 6, pp. 356–365, Nov. 1967.
356. IEEE Std 686–1982, IEEE Standard Radar Definitions, New York, NY 10017, USA, Oct. 15, 1982.
357. IEEE Std 521-1984, IEEE Standard Letter Designations for Radar-Frequency Bands, New York, NY 10017, Nov. 30, 1984.
358. IEEE Std. 100–1977, IEEE Standard Dictionary of Electrical and Electronics Terms, 2nd ed., Wiley—Interscience. (See also *IEEE Standard Radar Definitions* 1982.)
359. Ignatova, R. V., V. A. Petrushevskii, and E. Sal'man, "Radar Echo Characteristics of Clouds" (translation), *American Meteorological Society,* 1965.
360. Inmos A–100 Tech. Note, July 1986, and the *Digital Signal Processing Handbook,* Inmos, Colorado Springs, CO, July 1989.
361. Ippolito, Louis, J., "Propagation Effects Handbook for Satellite Systems Design," 4th ed., NASA Reference Publication 1082(04), Feb. 1989.
362. Jacob, J. S., "Graphical Comparison of a Doppler-shift Advantage for Three Pulse-compression Techniques," *1965 IEEE Conf.,* MIL-E-CON 9, pp. 182–187, Sept. 1965.
363. Jacobs, I., "The Effects of Video Clipping on the Performance of an Active Satellite PSK Communication System," *IEEE Trans. Commun. Tech.,* pp. 195–201, June 1965.
364. Jacobus, R. W., A Linear FM 1000:1 Pulse Compression System, Tech. Documentary Rept. ESD–TDR–63–237, Mitre Corp., Bedford, MA, July 1963 (AD411637).
365. Jakeman, E., and P. N. Pusey, "Statistics of Non-Rayleigh Microwave Sea Echo," *IEE Inter. Radar Confer.,* London, 1977.
366. James, W. J., The Effect of the Weather in Eastern England on the Performance of X-band Ground Radars, Royal Radar Establishment Tech. Note, no. 655, July 1961.
367. Janssen, Louis, H., and Gerard A. Van Der Spek, "The Shape of Doppler Spectra from Precipitation," *IEEE Trans. AES,* vol. 21, no. 2, pp. 208–219, Mar. 1985.
368. Janza, F. J., R. K. Moore, B. D. Warner, and A. R. Edison, Radar Cross Sections of Terrain Near-vertical Incidence at 415 Mc, 3800 Mc and Extension of Analysis to X-band, Univ. New Mexico Eng. Expt. Sta. Tech. Rept. EE–21, May 1959.
369. Jeske, H., "Die Ausbreitung elektromagnetischer Wellen im cm- bis m-Band uber dem Meer unter besonderer Berucksichtigung der meteorologicschen Bedingungen in der maritimen Grenzschicht," *Hamberger Geophysikalische Einzelschriften,* De Gruyter, Hamburg, 1965.
370. Jiusto, J. E., and W. J. Eadie, "Terminal Fall Velocity of Radar Chaff," *J. Geophysical Res.,* vol. 68, no. 9, pp. 2858–2861, May 1, 1963.
371. Johnson, C. M., S. P. Schlesinger, J. C. Wiltse, and C. W. Smith, Sea Scattering Measurements in the Region from 9.6 to 38 kMc, Johns Hopkins Univ. Radiation Lab. Tech. Rept. 27, Sept. 1955 (AD605545).
372. Johnson, C. M., S. P. Schlesinger, and J. C. Wiltse, "Backscattering Characteristics of the Sea in the Region from 10 to 50 kMc," Proc. *IRE,* vol. 45, no. 2, pp. 220–228, Feb. 1957.
373. Johnson, C. M., S. P. Schlesinger, and J. C. Wiltse, "Backscattering Characteristics of the Sea in the Region from 10 to 60 kMc," Johns Hopkins Univ. Radiation Lab. Tech. Rept. 35, May 1956.
374. Johnson, G. N. et al., "An Analysis of Techniques for Dealing with Anomalous

Propagation," Preprint volume, *16th Radar Meteorology Conf.*, Houston, Texas, April 22–24, 1975; Amer. Meteor. Soc., pp. 374–377, Boston MA.
375. Johnson, Nicolas, "Cumulative Detection Probability for Swerling III and IV Targets," *Proc. IEEE (Letters)*, vol. 54, no. 11, pp. 1583, 1584, Nov. 1966.
376. Johnston, A., "Improvements to a Pulse Compression Radar Matched Filter," *The Radio and Electronic Engineer*, vol. 53, no. 4, pp. 138–140, Apr. 1983.
377. Jones, J. J., "Hard Limiting of Two Signals in Random Noise," *IEEE Trans.*, vol. IT–9, pp. 34–42, Jan. 1963.
378. Jonsen, G. L., On the Improvement of Detection Range Using Frequency Agile Techniques, Boeing Airplane Co. Transport Div. Doc. D6–6835, Apr. 1964.
379. K_A Radar Weather Performance Data and Analysis, Emerson Elec.-Electron. Space Div. Rept. 1840, St. Louis, Dec. 9, 1964.
380. Kaiteris, C. P., and W. L. Rubin, "Radar Waveform Design for Detecting Targets in Clutter," *Proc. IEE*, vol. 114, no. 6, pp. 696–702, June 1967.
381. Kaiteris, C., and W. L. Rubin, "A Noncoherent Signal Design Technique for Achieving a Low Residue Ambiguity Function," *IEEE Trans. (Corr)*, vol. AES–2, no. 4, pp. 468–471, July 1966.
382. Kalmykov, A. I., and V. V. Pustovoytenko, "On the Polarization Features of Radio Signals Scattered from the Sea Surface at Small Grazing Angles," *Journal of Geophysical Research*, vol. 81, no. 12, pp. 1960–1964, Apr. 20, 1976.
383. Kapitanov, V. A., U. V. Mel'nichuk, and A. A. Chernikov, "Spectra of Radar Signals Reflected from Forests at Centimeter Waves," *Radio Engineering and Electronic Physics*, vol. 18, Scripta Technica, Sept. 1973.
384. Kaplan, E. L., "Signal-Detection Studies with Applications," *Bell Sys. Tech. J.*, vol. 34, Mar. 1955.
385. Karp, D., and J. R. Anderson, Moving Target Detector (Mod II) Summary Report, FAA Project Report FAA–RD–80–77, Lincoln Laboratory, Nov. 3, 1981.
386. Katz, I., "A Polychromatic Radar," 12th Radar Meteorol. Conf., American Meteorological Society, Norman, OK, Oct. 1966.
387. Katz, Isadore, "Wave Length Dependence of the Radar Reflectivity of the Earth and the Moon," *J. Geophysical Res.*, vol. 71, no. 2, pp. 361–366, Jan. 15, 1966.
388. Katz, Isadore, and L. M. Spetner, "Two Statistical Models for Radar Terrain Return," *IRE Trans.*, vol. AP–8, no. 3, pp. 242–246, May 1960.
389. Katz, Isadore, "Radar Reflectivity of the Earth's Surface," *APL Tech. Digest*, vol. 2, no. 3, pp. 10–17, Jan.–Feb. 1963.
390. Katz, Isadore, "Probing the Clear Atmosphere with Radar," *APL Tech. Digest*, vol. 6, no. 1, pp. 2–8, Sept.–Oct. 1966.
391. Katz, Isadore, Radar Backscattering from Terrain at X-band, Appl. Phys. Lab./Johns Hopkins Univ. Rept. CLO–4–002, Silver Spring, MD, June 5, 1963.
392. Katzin, M. "On the Mechanisms of Radar Sea Clutter," *Proc. IRE*, vol. 45, no. 1, pp. 44–54, 1957.
393. Kelly, E. J., and Wishner, "Matched Filter Theory for High Velocity Accelerating Targets," *IEEE Trans.*, vol. MIL 9, pp. 56–59, Jan. 1965.
394. Kennedy, R. W., The Spatial and Spectral Characteristics of the Radar Cross Section of Satellite-type Targets, Air Force Avionics Lab. Tech. Rept. AFAL–TR–66–17, Research and Technology Division, Air Force Systems Command, Wright-Patterson AFB, OH, Mar. 1966.
395. Kennett, Rosemary G., and Fuk K. Li, "Seasat Over-Land Scatterometer Data, Part I: Global Overview of the K_u-Band Backscatter Coefficients," *IEEE Trans. on Geoscience and Remote Sensing*, vol. 27, no. 5, pp. 592–605, Sept. 1989.
396. Kerdock, A. M., R. Mayer, and D. Bass, "Longest Binary Pulse Compression Codes with Given Peak Sidelobe Levels," *Proc. IEEE*, vol. 74, no. 2, Letters, p. 366, Feb. 1986.
397. Kerr, D. E. (ed.), *Propagation of Short Radio Waves*, M.I.T. Radiation Laboratory Series, no. 13, McGraw-Hill Book Co., New York, 1951.
398. Key, E. L., E. N. Fowle, and R. C. Haggarty, A Method of Sidelobe Suppression in Phase-coded Pulse Compression Systems, M.I,T./Lincoln Lab. Tech. Rept. 209, Aug. 28, 1959.

399. Khoury, E. N., and J. S. Hoyle, "Clutter Maps: Design and Performance," Reprinted from *Proc. IEEE Nat. Radar Confer.*, March 13–14, 1984.
400. Kiely, D. G., "Rain Clutter Measurements with CW Radar Systems Operating in the 8mm Wavelength Band," *Proc. IEE (British)*, vol. 101, pt. 3, no. 70, pp. 101–108, March 1954.
401. Kiss, Charles J., Hyperbolic-FM (CHYPE), US Army Missile Command, Redstone Arsenal, Alabama, Tech. Rept. RE–73–32, Oct. 1, 1973.
402. Klauder, J. R., "The Design of Radar Signals Having Both High Range Resolution and High Velocity Resolution," *Bell System Tech. J.*, vol. 39, pp. 808ff, July 1960.
403. Klauder, J. R., A. C. Price, S. Darlington, and W. J. Albersheim, "The Theory and Design of Chirp Radars," *Bell System Tech. J.*, vol. 39, no. 4, pp. 745–808, July 1960.
404. Klein, Albert M., and Masaaki T. Fujita, "Detection Performance of Hard-Limited Phase Coded Signals," *IEEE Trans. AES,* vol. 15, no. 6, pp. 795–802, Nov. 1979.
405. Ko, H. W., J. W. Sari, and J. P. Skura, "Anomalous Microwave Propagation Through Atmospheric Ducts," *The Johns Hopkins APL Tech. Dig.*, vol. 4, no. 2, pp. 12–16, 1983.
406. Kohlenstein, L. C., Effect of Quantization and Limiting on Signal-to-Noise Ratio and System Linearity, Appl. Phys. Lab. Intern. Memo. TWI–3–028, March 1964 (not generally available).
407. Konrad, T. G., J. J. Hicks, and E. B. Dobson, "Radar Characteristics of Known Single Birds in Flight," *Science,* vol. 159, no. 3812, pp. 274–280, Jan. 19, 1968.
408. Konrad, T. G., Statistical Models of Summer Rain Showers Derived from Fine-Scale Radar Observations, The Johns Hopkins University-Applied Physics Laboratory Report, APL/JHU–CP 056, Apr. 1977.
409. Kovaly, J. J. et al., Sea Clutter Studies Using Airborne Coherent Radar, Univ. Illinois Control Sys. Lab. Rept. 37, June 26, 1953.
410. Krason, H., and G. Randig, "Terrain Backscattering Characteristics at Low Grazing Angles for X and S Band," *Proc. IEEE (Letters)* (special issue on computers), vol. 54, no. 12, Dec. 1966.
411. Kraus, J. D., *Antennas,* McGraw-Hill Book Co., New York, 1950.
412. Kretschmer, F. F., "MTI Weightings," *IEEE Trans. Aero. Elect. Sys.*, vol. AES–10, pp. 153–156, Jan. 1974.
413. Kretschmer, Frank F., Jr., and Karl Gerlach, Radar Waveforms Derived from Orthogonal Matrices, Naval Research Laboratory, Rept. 9080, Washington, DC, Feb. 14, 1989.
414. Kretschmer, F. F., C. L. Lin, and B. L. Lewis, "A Comparison of Noncoherent and Coherent MTI Improvement Factors," *IEEE Trans. Aero. Elect. Sys.*, vol. AES–19, no. 3, pp. 398–404, 1983.
415. Kretschmer, Frank F., Jr., "MTI Target Visibility," *IEEE Trans. AES,* vol. 22, no. 2, pp. 216–218, Mar. 1986.
416. Kroszezynski, J., "On the Optimum MTI Reception," *IEEE Trans.*, vol. IT-11, no. 3, pp. 451–452, July 1965.
417. Kunegel, Jacques, "The TVD 900: A Modern Signal Processing Applied to Primary Civilian ATC Radar," *International Radar Confer.*, Paris, pp. 236–240, 1989.
418. Labitt, Melvin, Coordinated Radar and Aircraft Observations of Turbulence, Federal Aviation Administration Project Report, FAA–RD–81–44, May 26, 1981.
419. Lacomme, Philippe, "Ground Clutter Modeling," *Inter. Radar Confer 1989.*, Paris, France, Apr. 24–28, 1989.
420. LaGrone, A., A. Deam, and G. Walker, *Radio Sci., J. Res.* 68D, 895 (1964). (See also: Hajovsky, R. G., A. P. Deam, and A. H. LaGrone, "Radar Reflections from Insects in the Lower Atmosphere," *IEEE Trans. Antennas and Propagation,* vol. 14, pp. 224–227, Mar. 1966.)
421. Lammers, Uve H. W., Dallas T. Hayes, and Richard A. Marr, "Millimeter-Wave Multipath Measurements on Snow Cover," *IEEE Trans. on Geoscience and Remote Sensing,* vol. 26, no. 3, pp. 259–267, May 1988.
422. Lane, P. E., and R. L. Robb, Sea Clutter Measurements at S and X Band, A.S.R.E. Tech. Note NX 55–6, Portsmouth, Hants, England, Aug. 19, 1955 (AD302300).

423. Lane, T. L., C. R. Scheer, and N. C. Currie, "An Overview of MMW Radar Reflectivity," *Proc. of the 1988 IEEE Inter. Radar Confer.*, Ann Arbor, MI, April 20–21, 1988.
424. Lawson, J. L., and G. E. Uhlenbeck, *Threshold Signals,* M.I.T. Radiation Lab. Series, no. 24, McGraw-Hill Book Co., New York, 1950.
425. Lee, E. A. et al., "Gabriel: A Design Environment for DSP," *IEEE Trans. Acoustics, Speech, & Sig. Proc.*, vol. 37, no. 11, pp. 1751–1762, Nov. 1989.
426. Lee, Y. W., *Statistical Theory of Communications,* John Wiley & Sons, Inc., New York, Sept. 1964.
427. Lepere, G., and C. Bruno, "Programmed Processing for Air Traffic Control Radars: Implementation of an MTD Type System," *International Confer. on Radar,* Paris, pp. 479–484, May 21–24, 1984.
428. Lerner, R. M., R. Price, and R. Manasse, "Loss of Detectability in Band-pass Limiters," *IRE Trans.*, vol. IT–4, pp. 34–38, Mar. 1958.
429. Lerner, R. M., "A Matched Filter Detection System for Complicated Doppler Shifted Signals," *IRE Trans. Inform. Theory,* vol. IT–6, pp. 373–385, June 1960.
430. Levanon, N., "Detection Loss Due to Interfering Targets in Ordered Statistics CFAR," *IEEE Trans. AES,* vol. 24, no. 6, pp. 678–681, Nov. 1988.
431. Levine, Daniel, *Radargrammetry,* McGraw-Hill Book Co., New York, 1960.
432. Lewis, E. O., B. W. Currie, and S. Haykin, "Effect of Polarization on the Marine Radar Detection of Icebergs," *IEEE Inter. Radar Confer.*, Arlington, VA, May 6–9, 1985.
433. Lewis, Bernard L., Frank F. Kretchmer, Jr., Wesley W. Shelton, *Aspects of Radar Signal Processing,* Artech House, Norwood, MA, 1986.
434. Lewis, B., and F. Kretchmer, "Linear Frequency Modulation Derived Polyphase Pulse Compression Codes," *Aerospace and Electronic Systems,* vol. 18, no. 5, pp. 637–641, Sept. 1982.
435. Lhermitte, R. M., Motions of Scatterers and the Variance of the Mean Intensity of Weather Radar Signals, Sperry Rand Res. Center Program 38310, SRRC–RR–63–57, Atmospheric Physics Department, Sudbury MA, Nov. 1963.
436. Lhermitte, R. M., "Weather Echoes in Doppler and Conventional Radars," *Proc. 10th Weather Radar Conf.*, Apr. 1965.
437. Lieber, Robert in E. H. Ehling (ed.), *Range Instrumentation,* Chap. 3, Prentice-Hall, Inc., Englewood Cliffs, NJ, 1967.
438. Lind, G., "Measurement of Sea Clutter with Frequency Agility Radar," *Philips Telecommunication Review,* vol. 29, no. 1, Apr. 1970.
439. Linder, R. A., and G. H. Kutz, "Digital Moving Target Indicators," *IEEE Trans. (Suppl.)*, vol. AES–3, no. 6, pp. 374–385, Nov. 1967.
440. Lindgren, B. W., *Statistical Theory,* The Macmillan Co., New York, 1962.
441. Linell, T., "An Experimental Investigation of the Amplitude Distribution of Radar Terrain Return," *6th Conf. Swedish Natl. Comm. Sci. Radio,* Research Institute of National Defense, Stockholm, Mar. 13, 1963.
442. Liu, Bede, "Effect of Timing Jitter on Performance of MTI Filters," *IEEE Trans. AES,* vol. 25, no. 3, pp. 335–342, May 1989.
443. Locke, A. S., *Guidance,* pp. 100–101, D. Van Nostrand Co., Inc., 1955.
444. Long, M. W., *Radar Reflectivity of Land and Sea,* Artech House Inc., 1983.
445. Long, M. W., R. D. Wetherington, J. L. Edwards, and A. B. Abeling, Wavelength Dependence of Sea Echo, Georgia Inst. Tech. Final Rept. Proj. A–840, July 15, 1965 (AD477905).
446. Long, M. W., "A Radar Model for Land and Sea," Prepared for *Proc. of the Open Symposium of URSI,* La Baule, France, 28 April–6 May, 1977.
447. Long, Maurice W., "Polarization and Statistical Properties of Clutter," *Proc. 1984 Inter. Symposium on Noise and Clutter Rejection in Radars and Imaging Sensors,* pp. 25–31, Tokyo, 1984.
448. Long, M. W., "Backscattering for Circular Polarization," *Electron. Letters,* vol. 2, p. 341, Sept. 1966.
449. Long, M. W., "On the Polarization and the Wavelength Dependence of Sea Echo," *IEEE Trans.*, vol. AP–13, pp. 749–754, Sept. 1965. (See also "Polarization and Sea Echo," *Electron. Letters,* Feb. 1967.)

450. Lorti, Daniel C., Bistatic Radar Terrain and Sea Clutter Phenomenology, Xontech, Inc. Report XTI–30518–82, Van Nuys, CA, Sept. 30, 1982.
451. Ludloff, A. et al., "Doppler Processing Waveform Design and Performance Measures for Some Pulsed Doppler and MTD Radars," *Ortung and Navigation,* W. Germany, Mar. 1981 and Jan. 1982.
452. Luke, P. J., Detection of I Channel Only and of I and Q, Appl. Phys. Lab./Johns Hopkins Univ. Intern. Memo MRT–7006, Oct. 5, 1967.
453. Luke, P. J., Rain Clutter for CW Radar, Appl. Phys. Lab./Johns Hopkins Univ. Intern. Memo. MRT–0–0004, Silver Spring, MD, Nov. 5, 1965.
454. Lundy Technical Center, Design of Chaff Units, TM–65RD—38, July 1, 1965.
455. Lynch et al., "Multigigahertz-bandwidth Linear-frequency Modulated Filters Using a Superconductive Stripline," *Applied Physics Letters,* vol. 43, no. 3, pp. 319–321, Aug. 1983.
456. Macdonald, F. C., "Correlation of Radar Sea Clutter on Vertical and Horizontal Polarizations with Wave Height and Slope," *Proc. IRE,* vol. 43, no. 14.2, 1955.
457. Mack, R. B., and B. B. Gorr, Measured Radar Backscatter Cross Sections of the Project Mercury Capsule, Air Force Cambridge Res. Lab. Rept. AFCRL 38, Bedford, Mass., Feb. 1961.
458. Mack, C. L., Jr., and B. Reiffen, "RF Characteristics of Thin Dipoles," *Proc. IEEE,* vol. 52, no. 5, pp. 533–542, May 1964.
459. Mallett, J. D., and L. E. Brennan, "Cumulative Probability for Targets Approaching a Uniformly Scanning Search Radar," *Proc. IEEE,* vol. 51, pp. 596–601, Apr. 1963.
460. Manasse, R., The Use of Pulse Coding to Discriminate against Clutter, M.I.T./Lincoln Lab. Group Rept. 312–12 (rev. 1), June 7, 1961.
461. Marcum, J. I., and P. Swerling, "Studies of Target Detection by Pulsed Radar," *IRE Trans.,* vol. IT–6, no. 2, pp. 59–267, Apr. 1960 (from Rand Corp. Res. Memos RM 753, RM 754, July 1948).
462. Maron, D. A., "Frequency-Jumped Burst Waveforms with Stretch Processing," *Proc. of the 1990 Inter. Radar Conf.,* Washington, DC, May 1990.
463. Marshall, J. S., and Walter Hitschfeld, "Interpretation of the Fluctuating Echo from Randomly Distributed Scatters," *Can. J. Phys.,* vol. 31, pts. 1 and 2, pp. 962–994.
464. Masuko, Harunobu et al., "Measurement of Microwave Backscattering Signatures of the Ocean Surface Using X Band and K_a Band Airborne Scatterometers," *Journal of Geophysical Research,* vol. 91, no. C11, pp. 13,065–13,083, Nov. 15, 1986.
465. Max, J., "Quantizing for Minimum Distortion," *IRE Trans.,* vol. IT–6, no. 1, pp. 962–994.
466. MB Associates (article), *Electronic Warfare,* vol. 4, no. 4, 1972.
467. McEvoy, W. J., Discrete Clutter Measurements Program: Operations in Western Massachusetts, The Mitre Corp., Bedford, Mass. ESD–TR–72–132, MTR–2074, AD 742297, Mar. 1972.
468. McGinn, J. W., and E. W. Pike, "A Study of Sea Clutter Spectra," *Proc. Symp. Statistical Methods Radio Wave Propagation,* UCLA, June 18–20, 1958, Pergamon Press, Inc., New York, 1960.
469. McLane, P. J., L. L. Campbell, and M. F. Meisiya,"Performance of MTI Circuits Due to Amplitude Limiting," *IEEE Trans. Aero. Elect. Sys.,* vol. AES–12, no. 4, pp. 519–522, 1976.
470. Mead, James B., and Robert E. McIntosh, "Observations of Clouds and Fog with a 1.4 mm Wavelength Radar," *PIERS 1989 Proc., Abstracts,* Boston, MA, July 25–26, 1989.
471. Medhurst, R. G., "Rainfall Attenuation of Centimeter Waves: Comparison of Theory and Measurement," *IEEE Trans.,* vol. AP–13, no. 4, pp. 550–564, July, 1965.
472. Menske, R. A., "Detection Probability for a System with Instantaneous Automatic Gain Control," *1965 IEEE Conf. Military Electron,* vol. MIL-E-CON 9, pp. 28–31, Sept. 1965.

473. Michelson, M., W. W. Shrader, and J. G. Wieler, "Terminal Doppler Weather Radar," *Microwave Journal,* vol. 33, no. 2, pp. 139–148, Feb. 1990.
474. Millett, R. E., "A Matched Filter Pulse Compression System Using a Non-Linear FM Waveform," *IEEE Trans. AES,* vol. 6, no. 1, pp. 73–78, Jan. 1970.
475. Milligan, T. A. *Modern Antenna Design,* McGraw-Hill Book Co., New York, 1985.
476. Millman, Jacob, and Herbert Taub, *Pulse and Digital Circuits,* McGraw-Hill Book Co., New York, 1956.
477. Millman, George H., and Gary R. Nelson, "Surface Wave HF Radar for Over-the-Horizon Detection," *IEEE 1980 Inter. Radar Confer.,* Washington, DC, Apr. 1980, pp. 106–112.
478. Mitchell, R. L., "Importance Sampling Applied to Simulation of False Alarm Statistics," *IEEE Trans. AES,* vol. 17, no. 1, pp. 15–24, Jan. 1981.
479. Mityashev, B. N., The Determination of the Time Position of Pulses in the Presence of Noise, translated by Scripta Technica, Inc., D. L. Jones (ed.), MacDonald, London, 1965.
480. Mooney, D., and G. Ralston, "Performance in Clutter of Airborne Pulse, MTI, CW Doppler and Pulse Doppler Radar," *IRE Intern. Conv. Rec.,* 1961.
481. Moore, J. D. and N. B. Lawrence, "Comparison of Two CFAR Methods Used with Square Law Detection of Swerling 1 Targets," *1980 IEEE International Radar Confer.,* pp. 403–409, 1980.
482. Moore, R. K., "Radar Scatterometry–An Active Remote Sensing Tool," *Proc. 4th Symp. Remote Sensing Environment,* Apr. 12, 13, and 14, 1966, University of Michigan 4864–11–x, pp. 339–374, June 1966.
483. Moore, R. K., and W. J. Pierson, Measuring Sea State and Estimating Surface Winds from a Polar Orbiting Satellite, Center for Research in Engineering Science/University of Kansas and the Department of Meteorology and Oceanography/New York University, Nov. 1965.
484. Moore, R. K. et al., "A Radar Clutter Model: Average Scattering Coefficients of Land, Snow, and Ice," *IEEE Trans. AES,* vol. 16, no. 6, pp. 783–799, Nov. 1980.
485. Morchin, William C., *Airborne Early Warning Radar,* Artech House, Norwood, MA, 1990.
486. Morris, C. E. et al., A CMOS/SOS Digital Signal Processing Chip for Front-end Sensor Processing, Digest of Papers, 1987 Government Microcircuit Applications Conference, pp. 305–308, Oct. 1987.
487. Morris, G. V., *Airborne Pulsed Doppler Radar,* Artech House, Norwood, MA, 1988.
488. Moser, R., and J. Stover, "Generation of Pseudo-Random Sequences for Spread Spectrum Systems," *Microwave Journal,* pp. 287–295, May 1985.
489. Muchmore, R. B., "Reply to Comments by Leon Peters and F. C. Weiner," *IRE Trans. Antennas Propagation,* vol. AP–9, pp. 112–113, Jan. 1961.
490. Muchmore, R. B., "Aircraft Scintillation Spectra," *IRE Trans.,* vol. AP–8, pp. 201–212, Mar. 1960.
491. Muehe, C. E., "Moving Target Detector, An Improved Signal Processor," *31st Technical Meeting of the Avionics Panel, AGARD,* pp. 14–18, The Hague, Netherlands, June 1976.
492. Muehe, C. E. et al., "New Techniques Applied to Air Traffic Control Radars," *Proc. IEEE,* vol. 62, no. 6, pp. 716–723, June 1974.
493. Muehe, C. E., "Digital Signal Processor for Air Traffic Control Radars," *NEREM 1974,* Boston MA, Oct. 29–31, 1974.
494. Mueller, E. A., and A. L. Sims, Investigation of the Quantitative Determination Precipitation by Radar Echo Measurements, Illinois State Water Survey, Tech. Rept. ECOM–00032–F, Urbana, IL, Dec. 1966 (AD645218).
495. Myers, G. F., High-resolution Radar, Part 4, Sea Clutter Analysis, Naval Res. Lab. Rept. 5191, Washington, DC, Oct. 21, 1958.
496. Myers, G. F., High-resolution Radar, Part 3, Sea Clutter Analysis, Naval Res. Lab. Rept. 4952, Washington, DC, Oct. 21, 1958.
497. Nathanson, F. E., and J. P. Reilly, "Frequency Agility for Radar Target Detection and Tracking," *APL Technical Digest,* pp. 2–8, July–Aug. 1970.

498. Nathanson, Fred E., *Radar Design Principles,* 1st ed., McGraw-Hill Book Co., New York, 1969.
499. Nathanson, F. E., "Time Sidelobes in a Combined Phase-coded and Pulse-Doppler System," *Proc. IEEE (Corr.),* vol. 53, no. 11, pp. 1775–1776, Nov. 1965.
500. Nathanson, Fred E., and Paul L. Smith Jr., A Modified Coefficient for the Weather Radar Equation, Preprints of the *15th Radar Meteorology Conference,* Champaign-Urbana, Illinois: published by AMS, Boston, MA, pp. 228–230, Oct. 10–12, 1972.
501. Nathanson, F. E., and J. P. Reilly, "Radar Precipitation Echoes," *IEEE Trans.,* vol. AES–4, no. 4, pp. 505–514, July 1968; Also, Radar Precipitation Echoes—Experiments on Temporal, Spatial and Frequency Correlation, Appl. Phys. Lab./ Johns Hopkins Univ. Rept. TG–899, April 1967.
502. Nathanson, Fred E., "Adaptive Circular Polarization," *IEEE Inter. Radar Confer.,* pp. 221–225, 1975.
503. Nathanson, F. E., and J. P. Reilly, "Clutter Statistics that Affect Radar Performance Analysis," *EASCON Proc.* (supplement to *IEEE Trans.*), vol. AES–3, no. 6, pp. 386–398, Nov. 1967.
504. Nathanson, F. E., et al., Radar Sounder, AFGL–TR–88–0300, Air Force Geophysics Lab, Hanscom, AFB, Sept. 1988.
505. Nathanson, F. E., and P. J. Luke, "Loss from Approximations to Square-Law Detectors in Quadrature Systems with Post-Detection Integration," *IEEE Trans. AES,* pp. 75–77, Jan. 1972.
506. Nathanson, F. E., and M. Davidson, "A Coherent Frequency Waveform Synthesizer," *Proc. IEEE (Corr.),* vol. 51, no. 12, pp. 1173–1774, Dec. 1963.
507. Neuf, Don and Steve Spohrer, "Conventional and New Applications for the Quadrature IF Microwave Mixer," *Microwave Journal,* pp. 1–8, Jan. 1983.
508. Nichols, D. E. T., Determination of the Total Refraction of 3.6 cm Wavelength Radiation Passing through the Atmosphere, Royal Aircraft Establishment, RT 66191, June 1966 (AD807747).
509. Nilssen, O. K., "New Methods of Range Measuring Doppler Radar," *IRE Trans.,* vol. ANE–9, no. 4, pp. 255–265, Dec. 1962.
510. Nitzberg, R., "Analysis of the Arithmetic Mean CFAR Normalizer for Fluctuating Targets," *IEEE Trans. AES,* vol. 14, no. 1, pp. 44–47, Jan. 1978.
511. Nitzberg, R., "Clutter Map CFAR Analysis," *IEEE Trans. AES,* vol. 22, no. 4, pp. 419–421, July 1986.
512. Nohara, T. J., S. Haykin, B. W. Currie, and C. Krasnor, "Towards the Improved Detection of Small Ice Targets in *K*-Distributed Sea Clutter," *Proc. 1989 Inter. Symposium on Noise and Clutter Rejection in Radars and Imaging Sensors,* pp. 66–71, IEICE, 1989.
513. Nolen, J. C., J. Schneider, and J. Lacis, Statistics of Radar Detection, Bendix Corporation, Bendix Radio Division, Baltimore, Feb. 1966.
514. North, D. O., "An Analysis of the Factors which Determine Signal Noise Discrimination in Pulsed Carrier Systems," *Proc. IEEE,* vol. 51, no. 7, pp. 1016–1027, July 1963.
515. Novak, L. M., "Radar Target Detection and Map-Matching Algorithm Studies," *IEEE Trans. AES,* vol. 16, no. 5, pp. 620–625, Sept. 1980.
516. O'Clock, George D., Jr., "Improved Matched Filters Sharpen Spread Spectrum," *Microwaves & RF,* pp. 125–129, Sept. 1985.
517. O'Donnell, R. M. et al., Advanced Signal Processing for Airport Surveillance Radars, EASCON 1974, Washington, DC, Oct. 1974.
518. O'Hara, F. J., and G. M. Moore, "A High Performance CW Receiver Using Feedthru Nulling," *Microwave J.,* vol. 6, no. 9, pp. 63–71, Sept. 1963.
519. O'Neill, H. J., A Wideband Stepped Frequency Pulse Compression System," Appl. Electron. Lab. G.E.C. (Electron) LTD Rept. SLR 398, Stanmore, Middlesex, England, Oct. 1966.
520. O'Sullivan, Michael R., Kim M. Harrington, and Robert L. Nevin, "Sidelobe Blanking Systems Performance for Swerling Targets," *International Radar Confer.,* pp. 569–577, Paris, Apr. 1989.

521. Ohman, G. P., "Getting High Range Resolution with Pulse Compression Radar," *Electronics,* vol. 33, no. 41, pp. 53–57, Oct. 7, 1960.
522. Olin, I. D., and F. E., "Queen, Dynamic Measurement of Radar Cross Section," *Proc. IEEE,* vol. 53, no. 8, pp. 954–961, Aug. 1965.
523. Olsen, R. L., D. V. Rogers, and D. B. Hodge, "The aR^b Relation in the Calculation of Rain Attenuation," *IEEE Trans. Ant. Prop.,* vol. 26, pp. 318–329, 1978.
524. Onstott, Robert G., Richard K. Moore, and W. F. Weeks, "Surface-Based Scatterometer Results of Arctic Sea Ice," *IEEE Trans. on Geoscience Electronics,* vol. 17, no. 3, pp. 78–85, July 1979. (See also Robert G. Onstott and Denise J. Gineris, Synthetic Aperture Radar Imagery of Airports and Surrounding Areas, NASA Contractor Report 4275, DOT/FAA/DS–89/14, Contract NAS1–18465, Feb. 1990; Robert G. Onstott and Denise J. Gineris, Synthetic Aperture Radar Imagery of Airports and Surrounding Areas, NASA Contractor Report 4280 DOT/FAA/DS–89/15, Contract NAS1-18465, Mar. 1990.)
525. Oppenheim, A. V., and R. W. Schafer, *Digital Signal Processing,* Prentice-Hall, Englewood Cliffs, NJ, 1975.
526. Optimum Waveform Study for Coherent Pulse Radar, Final Report on Contract NOnr–4649(00)(X), Radio Corporation of America, Moorestown, NJ, Feb. 28, 1965 (AD641391).
527. Ostgaard et al., Architecture Specification for PAVE PILLAR Avionics, US Air Force Wright Aeronautical Laboratories report AFWAL–TR–87–1114, Wright-Patterson Air Force Base, OH, Jan. 1987. DTIC Report no. AD-A188 722.
528. Paddison, F. C. et al. "Large Bistatic Angle Radar Cross Section of a Right Circular Cyclinder," *Electromagnetics,* vol. 5, pp. 63–77, 1985.
529. Palmieri, C. A., Radar Waveform Design, Sperry Eng. Rev. (Radar), pt. 1, Winter, 1962, pp. 32–43.
530. Passarelli, Richard E., Jr., and Dusan S. Zrnic, "An Expression for Phase Noise," *Preprints 24th Radar Meteorology Symposium,* FL, American Meteorological Society, 1989.
531. Peake, W. H., "Theory of Radar Return from Rough Terrain," *1959 IRE Convention Record,* vol. 7, pp. 27–41, 1959.
532. Peake, W. H., The Interaction of Electromagnetic Waves with Some Natural Surfaces, Ohio State Univ. Rept. 898–2, May 30, 1959.
533. Peake, W. H., and S. T. Cost, The Bistatic Echo Area of Terrain at 10 GHz, WESCON 1968, Session 22.
534. Peake, W. H., "Theory of Radar Return from Terrain," *IRE Natl. Conv. Rec.,* pt. 1, pp. 27–41, Antenna Laboratory, Ohio State University, 1959.
535. Pedersen, C., Detectability of Radar Echoes in Noise and Clutter Interference, Columbia Univ. Tech. Rept. T–2/318 CU–28–65–AF–1478–ERL, Sept. 30, 1965.
536. Peebles, P. Z., Jr., and G. H. Stevens, "A Technique for the Generation of Highly Linear FM Pulse Radar Signals," *IEEE Trans.,* vol. MIL.–9, no. 1, pp. 32–38, Jan. 1965.
537. Peebles, Peyton, Z., Jr., "Bistatic Radar Cross Sections of Chaff," *IEEE Trans. AES,* vol. 20, no. 2, Mar. 1984, pp. 133–134.
538. Perlman, S. E., "Staggered Rep Rate Fills Radar Blind Spots," *Electronics,* vol. 31, no. 47, pp. 82–85, Nov. 21, 1958.
539. Perry, James L., "Modern Radar Clutter Suppression Techniques. A Comparison of Theoretical and Measured Results," *International Conf. on Radar Parts,* pp. 485–491, May 21–24, 1984.
540. Persons, C. E., "Ambiguity Function of Pseudo-random Sequences," *Proc. IEEE (Corr.),* vol. 54, no. 12, pp. 1946–1947, Dec. 1966
541. Peters, L., and F. C. Weimer, "Concerning the Assumption of Random Distribution of Scatterers as a Model of an Aircraft for Tracking Radars," *IRE Trans. Antennas Propagation,* vol. AP–9, pp. 110–111, Jan. 1961.
542. Peterson, E., and E. Weldon, *Error Correcting Codes,* Second edition, M.I.T. Press, Cambridge, MA, 1972, Appendix C.
543. Petrushevskii, V. A., R. V. Ignatova, and E. Sal'man, Radar Echo Characteristics of Clouds (translation), American Meteorological Society, 1965 (AD630675).

544. Pham, Kim Khanh, "Improvement of Visibility in Ground Clutter," *Inter. Confer. on Radar 1989,* Paris, April 24–28, 1989.
545. Philippides, C., Degradation of a Pulse Compression System due to Random Phase Errors, Appl. Phys. Lab./Johns Hopkins Univ. Rept. TG–843, Aug. 1966.
546. Pidgeon, V. W., "Time, Frequency, and Spatial Correlation of Radar Sea Return," *Space Sys. Planetary Geol. Geophys.,* American Astronautical Society, May 1967.
547. Pidgeon, V. W., "Bistatic Cross Section of the Sea for a Beaufort 5 Sea," *Space Sys. Planetary Geol. Geophys.,* American Astronautical Society, May 1967.
548. Pidgeon, V. W., "Bistatic Cross Section of the Sea," *IEEE Trans.,* vol. AP–14, no. 3, pp. 405–406, May 1966.
549. Pidgeon, V. W., "Radar Land Clutter for Small Grazing Angles at X and L Band," *Space Sys. Planetary Geol. Geophys.,* American Astronautical Society, May 1967.
550. Pidgeon, V. W., "The Doppler Dependence of Radar Sea Return," *J. Geophys. Res.,* Feb. 15, 1968.
551. Pidgeon, V. W., Private Communication, Applied Physics Laboratory/Johns Hopkins University.
552. Pilié, R. J., J. E. Jiusto, and R. R. Rogers, "Wind Velocity Measurement with Doppler Radar," *Proc. 10th Weather Radar Conf.,* American Meteorological Society, Washington, DC, Apr. 1963.
553. Plessey, "PDSP 16330-Pythagoras Processor," *Plessey Semiconductors,* October 1987.
554. Plessey HP Series of Microwave Absorbing Material—Data Sheet, Plessey Microwave Materials, San Diego, CA, 92138, 1979.
555. Poleman, A. J., "Cross Correlation of Orthogonally Polarized Backscatter," *IEEE AES,* vol. 12, no. 6, pp. 674–682 (also Poleman, A. J., *IEEE Trans. AES,* vol. 11, pp. 660–662, 1975).
556. Potts, B., Memorandum on the Average Radar Echo Area of Orbiting Satellites, Antenna Lab. Ohio State Univ. Rept. 1116–7, Columbus, OH, June 23, 1961 (AD264033).
557. Povejsil, D. J., R. S. Raven, and P. Waterman, *Airborne Radar,* D. Van Nostrand Co., Inc., Princeton, NJ, 1961.
558. Predrag, R., and A. Zejak, "Sidelobe Suppression In Phase-Coded Pulse Compression Radars by LS and MX Filtering," *Proc. 1990 Inter. Radar Confer.,* Washington, DC, May 1990, to appear.
559. Prengaman, R. J., R. E. Thurber, and W. G. Bath, "A Retrospective Detection Algorithm for Extraction of Weak Targets in Clutter and Interference Environments," *IEEE Inter. Radar Confer.,* pp. 341–345, 1985.
560. Presley, J. A., "The Censored Mean-Level Detector for Multiple Target Environments," ORINCON Corporation, Final Report, Contract No. N66001–83–C–0324, Naval Sea Systems Command, 1984.
561. Preston, G. W., "The Search Efficiency of the Probability Ratio Sequential Search Radar," *IRE Intern, Conv. Rec.,* vol. 8, pt. 4, pp. 116–124, 1960.
562. Price, R., and E. M. Hofstetter, "Bounds on the Volume and Height Distributions of the Ambiguity Function," *IEEE Trans. Inform. Theory,* vol. IT–11, no. 2, pp. 207–214, Apr. 1965.
563. Probert-Jones, J. R., "The Radar Equation in Meteorology," *Quart. J. Roy. Meteorol. Soc.,* vol. 88, pp. 485–495, 1962.
564. *Proc. 13th Radar Meteorol. Conf.,* McGill University, Montreal, July 1968.
565. *Proc. IEEE (Radar Reflectivity Issue),* vol. 53, no. 8, Aug. 1965.
566. Prosser, A. G., and W. G. Bath, "Macroscopic Spatial-Temporal Correlation Properties of Radar Clutter," *IEEE 1986 National Radar Confer.,* IEEE 86CH2270–7, 1986.
567. Queen, J. L., Private Communication on detection losses in noise and clutter to Applied Physics Laboratory/Johns Hopkins University.
568. Queen, J. L., 4-Phase Code Correlation Functions, Appl. Phys. Lab. Intern. Memo MRT–00–025, July 18, 1967.
569. Queen, J. L., Effect of Time Sidelobes on Clutter Response of Zero-180° Phase Codes, Appl. Phys. Lab. Intern. Memo. MRT–0–057, May 23, 1967.

570. Radar Cross Section Measurement Systems, System Planning Corporation Brochures, Arlington, VA, Sept. 1988.
571. Radar Workstation. A radar performance calculation software package sold by Technology Service Corporation, Silver Spring, Md. 20910.
572. *RADARCON 90 Proc.,* Adelaide, Australia, Apr. 18, 1990.
573. Radio Corporation of America, Optimum Waveform Study for Coherent Pulse Doppler, Moorestown, NJ, Final Tech Rept. for Office of Naval Research Contract No. NOnr 4649(00) (X), Feb. 1965.
574. Raduziner, D. M., and N. R. Gillespie, "Coherent Radar EM Noise Limitations," *IEEE-NASA Symp. Short-term Frequency Stability,* NASA SP–80, pp. 29–38, Greenbelt, MD, Nov. 23–24, 1964.
575. Ramp, H. O., and E. R. Wingrove, "Principles of Pulse Compression," *IRE Trans.,* vol. MIL–5, pp. 108–116, Apr. 1961.
576. Rao, K. V., and V. U. Reddy, "Biphase Sequence Generation with Low Sidelobe Autocorrelation Function," *IEEE Trans. AES,* vol. 22, no. 2, pp. 128–132, Mar. 1986.
577. Rappaport, S. S., "On Optimum Dynamic Range Centering," *Proc. IEEE (Letters),* vol. 54, no. 8, pp. 1067–1068, Aug. 1966.
578. Ray, Howard, "Improving Radar Range and Angle Detection with Frequency Agility," *Proc. 11th Ann. East Coast Conf. Aerospace Navigational Electron.,* pp. 1.3.6–1 to 1.3.6–7, IEEE, Baltimore, MD, Oct. 21–23, 1964.
579. Rebkopf, H. L., Flight Test Data on Radar Reflection from Terrain, Defense Documentation Center, Defense Supply Agency, Cameron Station, Alexandria, VA, Doc. No. D–16740, Contract No. AF 33(038) 19589, May 18, 1956 (AD93657).
580. Reid, W. S., K. D. Tschetter, and R. M. Johnson, "Analysis of a Rank-Based Radar Detection System Operating on Real Data," *Record of the IEEE 1985 Inter. Radar Confer.,* pp. 435–441, Arlington, VA, May 6–9, 1985.
581. Reilly, J. P., Clutter Reduction by Delay Line Cancellers, masters thesis, George Washington University, Washington, DC, Feb. 1967.
582. Reilly, J. P., "Clutter Rejection Limitations in Ambiguous Range Clutter," *Proc. IEEE Inter. Radar Confer.—1990,* Arlington, VA, May 1990.
583. Reilly, J. P., and G. D. Dockery, "Influence of Evaporation Ducts on Radar Sea Return," *Proc. IEE,* pt F, vol. 137, no. 2, pp. 80–88, 1990.
584. Reilly, J. P., "Short-Range Radar Sea Clutter in Horizon Search Systems: Antenna Pattern Effects," in press.
585. Reilly, J. P., "On the Statistical Representation of Targets for Detection Studies," *IEEE Trans. AES,* vol. 5, no. 3, pp. 560–561, 1969.
586. Reiss, A., W. S. Whitlock, and M. H. A. Smith, Land and Precipitation Clutter Measurements at C Band, A.S.W.E. Laboratory Note–XRE–68–10, Portsdown, June 1968.
587. Reitz, E. A., Radar Terrain Return Study, Final Report, Measurements of Terrain Backscattering Coefficients with an Airborne X-Band Radar, Goodyear Corporation, GERA–463, Sept. 30, 1959.
588. Remley, W. R., "Doppler Dispersion Effects in Matched Filter Detection and Resolution," *Proc. IEEE,* vol. 54, no. 1, pp. 33–39, Jan. 1966.
589. Resnick, J. B., High Resolution Waveforms Suitable for a Multiple Target Environment, masters thesis, Massachusetts Institute of Technology, June 1962.
591. Rice, S. O., in N. Wax (ed.), *Mathematical Analysis of Random Noise* (selected papers on noise and stochastic processes), Dover Publications, Inc., New York, 1954.
592. Rice, S. O., "Statistical Properties of a Sine Wave plus Random Noise," *Bell System Tech. J.,* vol. 27, pp. 109–157, Jan. 1948.
593. Rice, S. O., "Mathematical Analysis of Random Noise," *Bell System Tech. J.,* vols. 23 and 24, pp. 282–332; 45–156, 1945.
590. Rice, P. et al., Transmission Loss Predictions for Tropospheric Communication Circuits, Natl. Bureau Std. Tech. Note 101, vols. 1 and 2, 1965.
594. Richard, Victor W., John E. Kammerer, and Richard G. Reitz, US Army Ballistic

Research Laboratory Memorandum Report, ARBRL–MR–2800, Aberdeen Proving Ground, MD, Dec. 1977.
595. Richard, Victor W., John E. Kammerer, and H. Bruce Wallace, "Rain Backscatter Measurements at Millimeter Wavelengths," *IEEE Trans. on Geoscience and Remote Sensing,* vol. 26, no. 3, pp. 244–252, May 1988.
596. Richards, M. A., "On the Hardware Implementation of the Split-Radix FFT," *IEEE Trans. Acoustics, Speech, & Sig. Proc.,* vol. 36, no. 10, pp. 1575–1581, Oct. 1988.
597. Richman, D., Resolution of Multiple Targets in Clutter, Inst. Defense Analyses Res. Paper P–158 IDA/HQ 66–5086, June 1966, revised Apr., 1967 (AD652578).
598. Rickard, J. T. and Dillard, G. M., "Adaptive Detection Algorithms for Multiple-Target Situations," *IEEE Trans. AES,* vol. 13, no. 4, pp. 338–343, July 1977.
599. Rider, G. C., "A Polarization Approach to the Clutter Problem," *1977 Inter. Radar Confer. Proc.,* pp. 130–134, London, 1977.
600. Riggs, R. F., "The Angular Accuracy of Monopulse Radar in the Presence of Clutter," *Proc. NEC,* vol. 22, 1966.
601. Rihaczek, A. W., "Radar Resolution Properties of Pulse Trains," *Proc. IEEE,* vol. 52, pp. 153–164, Feb. 1964.
602. Rihaczek, A. W., *High Resolution Radar,* McGraw-Hill Book Company, New York, 1969.
603. Rihaczek, A. W., "Radar Signal Design for Target Resolution," *Proc. IEEE,* vol. 53, pp. 116–128, Feb. 1965.
604. Rihaczek, A. W., "Doppler-tolerant Signal Waveforms," *Proc. IEEE,* vol. 54, no. 6, pp. 849–857, June 1966.
605. Rihaczek, A. W., Measurement Properties of the Chirp Signal, Space Sys. Div. Air Force Sys. Command Rept. TDR–469 (5230–43)2, SSD–TR–65–115, Aerospace Corporation, El Segundo, CA, AFO4(695)–469, Aug. 1965.
606. Rihaczek, A. W., "Optimum Filters for Signal Detection in Clutter," *IEEE Trans. AES,* vol. AES–1, no. 3, pp. 297–299, Dec. 1965.
607. Riley, Joseph R., "Radar Cross Section of Insects," *Proc. IEEE,* vol. 73, no. 2, Feb. 1985.
608. Ritcey, J. A., "Performance of Max-Mean Level Detector with and Without Censoring," *IEEE Trans. AES,* vol. 25, no. 2, pp. 213–222, Mar. 1989.
609. Ritcey, J. A., "Performance Analysis of the Censored Mean-Level Detector," *IEEE Trans. AES,* vol. 22, no. 4, pp. 443–454, July 1986.
610. Rivers, Wayne, Low-Angle Radar Sea Return at 3-MM Wavelength, Georgia Institute of Technology, Final Report A-1268, Atlanta, Georgia, Nov. 15, 1970.
611. Rivers, Wayne, Wasted Bandwidth of Doppler Filters, Private Communication, Apr. 18, 1986.
612. Robinson, H. L., "SAW Markets in North America," *Microwave Journal,* vol. 32, no. 12, pp. 26–43, Dec. 1989.
613. Rochefort, J. S., "Matched Filters for Detecting Pulsed Signals in Noise," *IRE Natl. Conv. Rec.,* vol. 2, pp. 30–34, 1954.
614. Rogers, R. R., and B. R. Tripp, "Some Radar Measurements of Turbulence in Snow," *J. Appl. Meteorol.,* pp. 603–610, Oct. 1961.
615. Rogers, R. R., "Radar Measurement of Gustiness," *Proc. 6th Weather Radar Conf.,* pp. 96–106, American Meteorological Society, Boston.
616. Rohling, H., "Radar CFAR Thresholding in Clutter and Multiple Target Situations," *IEEE Trans. AES,* vol. 19, no. 4, pp. 608–621, July 1983.
617. Rohling, H., and Plagge, W., "Mismatched Filter Design for Periodical Binary Phased Signals," *IEEE Trans. AES,* vol. 25, no. 6, pp. 890–897, Nov. 1989.
618. Rohling, H., "New CFAR-Processor Based on an Ordered Statistic," *Record of IEEE 1985 International Radar Confer.,* pp. 271–275, Arlington, VA, May 6–9, 1985.
619. Roll, R. G., Use of the Autocorrelation Function of the Inphase and Quadrature Power from a Turbulent Process . . . ," Appl. Phys. Lab./Johns Hopkins Univ. Rept. BPD 65U–14, Silver Spring, MD, Nov. 10, 1965.
620. Root, W. L., "Remarks, Mostly Historical, on Signal Detection and Signal Parameter Estimation," *Proc. IEEE,* vol. 75, no. 11, pp. 1446–1457, Nov. 1975.

621. Ross, A. W., D. C. Fakley, and L. R. Palmer, Sea-Clutter Investigations, Admiralty Signal and Radar Establishment, England, R4/50/15, Sept. 7, 1950.
622. Roth, H. H., "Linear Binary Shift Register Circuits Utilizing a Minimum Number of MOD-2 Adders," *IEEE Trans. Inform. Theory,* vol. IT–11, no. 2, pp. 215–220, Apr. 1965.
623. Rubin, W. L., and S. K. Kamen, "S/N Ratios in a Two-channel Band-Pass Limiter," *Proc. IEEE,* pp. 389–390, Feb. 1963.
624. Rubin, W. L., and C. P. Kaiteris, "Some Results Concerning Radar Waveform Design for Detecting Targets in Clutter," *Proc. IEEE (Letters),* vol. 54, no. 11, pp. 1609–1610, Dec. 1966.
625. Rummler, W. D., Accuracy of Spectral Width Estimators Using Pulse Pair Waveforms, Tech. Memo MM–68–4121–14, Oct. 29, 1968, Bell Telephone Laboratories, Whipppany, NJ.
626. Rummler, W. D., "Clutter Suppression by Complex Weighting of Coherent Pulse Trains," *IEEE Trans.,* vol. AES–2, no. 6, pp. 689–699, Nov. 1966.
627. Rummler, W. D., Two-Pulse Spectral Measurements, Tech. Memo MM–68–4121–15, Nov. 7, 1968, Bell Telephone Laboratories, Whippany, NJ.
628. Rummler, W. D., "A Technique for Improving the Clutter Performance of Coherent Pulse Train Signals," *IEEE Trans.,* vol. AES–3, no. 6, pp. 898–907, Nov. 1967.
629. Ryan, Joseph, "Sea Clutter Measurements at X-band," *Inter. Conf. on Radar,* pp. 488–493, Paris, Apr. 24–28, 1989.
630. Sakamoto, J. et al., "Coded Pulse Radar System," *J. Faculty Eng. Univ. Tokyo,* vol. 27, no. 1, pp. 119–181, 1964.
631. Sander, J., "Rain Attenuation of Millimeter Waves at Lambda = 5.77, 3.3, and 2mm," *IEEE Trans.,* vol. AP-23, no. 2, Mar. 1975.
632. Sangston, K. J., Coherent Detection of Radar Targets in *K*-Distributed, Correlated Clutter, NRL Report 9130, Naval Research Laboratory, Washington, DC, Aug. 5, 1988.
633. Saxton, J. A., "VHF and UHF Reception, Effects of Trees and Other Obstacles," *Wireless World,* pp. 229–232, May 1955.
634. Schelling, Burrows, and Ferrell, "Ultra-short-wave Propagation," *Proc. IRE,* vol. 21, pp. 440–442, 458–461, March 3, 1933.
635. Schleher, D. Curtis, Ph.D. (ed.), *MTI Radar,* Artech House, Inc., Dedham, MA, 1978.
636. Schleher, D. C., "MTI Detection Performance in Rayleigh and Log-Normal Clutter," *1980 IEEE Inter. Radar Confer.,* pp. 299–304, Washington, DC, 1980.
637. Schlesinger, R. J., *Principles of Electronic Warfare,* Prentice-Hall Space Technology Series, Prentice-Hall, Inc., Englewood Cliffs, NJ, 1961.
638. Scholefield, P. H. R., "Statistical Aspects of Ideal Radar Targets," *Proc. IEEE,* vol. 55, no. 4, pp. 587–590, April 1967.
639. Schwartz, M., "A Coincidence Procedure for Signal Detection," *IRE Trans.,* vol. IT–2, no. 4, pp. 135–139, Dec. 1956.
640. Schwartz, Mischa, *Information Transmission Modulation and Noise,* McGraw-Hill Book Co., New York, 1959.
641. Scoggins, J. R., and M. Susko, FPS–16 Radar/Jimsphere Wind Data Measured at the Eastern Test Range, AGRO-Astrodynamics Laboratory, NASA TM X53290, July 9, 1965.
642. Sekine, M. et al., "Suppression of Weibull-Distributed Weather Clutter," *IEEE 1980 Inter. Radar Confer.,* pp. 294–298, Washington, DC, Apr. 1980.
643. Sekine, M. et al., "On Weibull-Distributed Weather Clutter," *IEEE Trans. AES,* vol. 15, no. 6, pp. 824–828, Nov. 1979.
644. Sekine, Matsuo et al., "MTI Processing and Weibull-Distributed Ground Clutter," *IEEE Trans. AES,* vol. 18, no. 4, pp. 799–830, Nov. 1982.
645. Sekine, M. et al., "Weibull-Distributed Ground Clutter," *IEEE Trans. AES,* vol. 17, no. 4, pp. 596–598, July 1981.
646. Senior, T. B. A., "A Survey of Analytical Techniques for Cross-section Estimation," *Proc. IEEE,* vol. 53, no. 8, pp. 822–833, Aug. 1965.
647. Sevy, J. L., "The Effect of Hard Limiting an Angle-modulated Signal Plus Noise,"

IEEE Trans., vol. AES–4, no. 1, pp. 24–30, Jan. 1968. (See also pp. 125–128.)
648. Shannon, *Electronics*, vol. 35, no. 49, pp. 52–56, Dec. 1962.
649. Sherman, Samuel M., "Comparison of Pure and Doppler-Coupled Range Measurements," *IEEE 1980 Inter. Radar Confer.*, pp. 421–426, Washington, DC, Apr. 1980.
650. Sherwood, E. M., and E. E. Ginston, "Reflection Coefficients of Irregular Terrain at 10 cm," *Proc. IRE (Corr.)*, vol. 43, no. 7, pp. 877–878, July 1955.
651. Short, R. D., "An Adaptive MTI for Weather Clutter Suppression," *IEEE Trans. Aero. Elect. Sys.*, vol. AES–18, no. 5, pp. 552–562, 1982.
652. Shrader, William W., and Thomas A. Weil, "Lens-Effect Loss for Distributed Targets," *IEEE Trans. AES*, vol, 23, no. 4, pp. 594–595, July 1987.
653. Shrader, W., "MTI Radar," in M. I. Skolnik (ed.), *Radar Handbook*, Chap. 17, McGraw-Hill Book Co., New York, 1970.
654. Siebert, W. McC., "A Radar Detection Philosophy," *IRE Trans.*, vol. IT-2, no. 3, pp. 204–221, Sept. 1956.
655. Siegel, K. M. et al., "Radar Calculation of Simple Shapes-Bistatic," *Methods of Radar Cross Section Analysis*, Chap. 5, Academic Press, New York, 1968.
656. Siegel, K. M. "Far Field Scattering from Bodies of Revolution," *Appl. Sci. Res.*, sec. B., vol. 7, pp. 293–328, 1958.
657. Siegel, A. D., and J. J. Wilcox, *Radar Sea Clutter Doppler Characteristics*, System Planning Corp. Report 1327 to USAF RADC, Jan. 22, 1990.
658. Siegel, K. M., "Low Frequency Radar Cross-section," *Proc. IEEE*, vol. 51, pp. 231–233, Jan. 1963.
659. Siegel, K. M. et al., "Bistatic Radar Cross Sections of Surfaces of Revolution," *Journal of Applied Physics*, vol. 26, no. 3, pp. 297–305, Mar. 1955.
660. Siggia, Alan, "Processing Phase-Coded Radar Signals with Adaptive Digital Filters," *21st Radar Meteorology Confer.*, pp. 163–166, Edmonton, Canada, American Meteorological Society, Boston, MA.
661. Silber, D., "Probabilities of Detection and False Alarm for a Coherent Detector with Amplitude Limiting of Arbitrary Hardness," *1966 IEEE Intern. Conv. Rec.*, pt. 7, pp. 107–123, Apr. 1966.
662. Silver, S., *Microwave Antenna Theory and Design*, M.I.T. Radiation Laboratory Series, vol. 12, chap. 6, McGraw-Hill Book Co., New York, 1949.
663. Simkins, William L., Vincent C. Vannicola, and James P. Ryan, Seek Igloo Radar Clutter Study, RADC–TR–77–338, Rome Air Development Center, Griffiss Air Force Base, New York, Oct. 1977 (Also updated in FAA–E–2763 Specification, Appendix A; Jan. 1986.)
664. Simon, L. H., An Analysis of Frequency Step Pulse Compression, RCA-Radar Sys. Memo., Moorestown, N.J., Apr. 12, 1961.
665. Sims, A. L., E. A. Mueller, and G. E. Stout, Investigation of the Quantitative Determination of Point and Areal Precipitation by Radar Echo Measurements, Illinois State Water Survey Interim Rept. 1, Oct. 1, 1964–Mar, 31, 1965 (AD623409).
666. Sinsky, A. I., and Wang, C. P., "Standardization of the Definition of the Radar Ambiguity Functions," *IEEE Trans. AES*, pp. 532–533, July 1974.
667. Sinsky, A. I., Private Communication on Wide Bandwidth Signals in Phase Steered Arrays, 1967.
668. Sittrop, H., X and K_u-Band Radar Backscatter Characteristics of Sea-clutter," Physics Lab TNO, Rept. No. PHL 1975–08, The Netherlands, Apr. 1975.
669. Sittrop, H., "On the Sea-Clutter Dependency on Windspeed," *IEEE Inter. Radar Confer., Radar 77*, pp. 110–114, London, 1977.
670. Sittrop, H., "Characteristics of Clutter and Targets at X- and K_u-Band," *AGARD Confer. Proc.*, No. 197 *Conference on New Devices, Techniques, and Systems in Radar*, The Hague, The Netherlands, pp. 28.1–28.27, June 1977b.
671. Skolnik, Merrill I., *Introduction to Radar Systems*, McGraw-Hill Book Co., New York, 1980.
672. Skolnik, Merrill I., Radar Information from the Partial Derivatives of the Echo Signal Phase from a Point Scatterer, Naval Res. Lab. Rept. 6148, Feb. 17, 1988.
673. Skolnik, Merrill I., *Radar Handbook*, McGraw-Hill, New York, 1990.

674. Skolnik, M. I., *Introduction to Radar Systems,* McGraw-Hill Book Co., New York, 1962 (revised 1980).
675. Smirnova, G. A., Experiments in Radar Measurement of Clear Sky-Turbulence with the Aid of Passive Reflectors, translated from *Tsentr. Aerologicheskaya Observatoriya, Trudy (Central Aerological Observatory Trans.),* no. 57, pp. 72–76, Appl. Phys. Lab/Johns Hopkins Univ. Trans. 1462, Silver Spring, MD, 1965.
676. Spafford, L. J., Optimum Radar Receive Waveforms in the Presence of Clutter, Gen. Elec. Heavy Military Electron. Dept. Rept. R65EMH14, Syracuse, NY, June 3, 1965.
677. Spafford, L. J., Ambiguity Function Catalog of Uniformly Spaced Envelope Recurrent Pulse Trains, Gen. Elec. Heavy Military Electron. Dept. Rept. R66EMH51, Syracuse, NY, Nov. 1966.
678. Spafford, L. J., Optimum Radar Signal Processing in Clutter, Gen. Elec. Heavy Military Electron. Dept. Rept. RG7EMH16, Syracuse, NY, June 1967 (also Ph.D. thesis Polytechnic Institute of Brooklyn, June 1967, and *IEEE Trans.,* vol. IT–14, no. 2, pp. 734–743, Sept. 1968).
679. Spilker, J. J., Jr., "Delay Lock Tracking of Binary Signals," *IEEE Trans,* vol. SET–9, pp. 1–8, Mar. 1963.
680. Steben, J. O., and H. Urkowitz, "An Improved Model for Simulating Radar Sea Return, Including Sea Spikes," *Proc. IRE Radar '87 Conference,* pp. 466–470, London, Oct. 19–21, 1987.
681. Steele, J. G., "Backscatter of 16 Mc/s Radio Waves from Land and Sea," *Austral. J. Phys.,* vol. 18, pp. 317–327, Aug. 1965. (See also *Proc. IEEE,* vol. 55, no. 9, pp. 1583–1590, Sept. 1967.)
682. Stewart, Dorothy A., Wind Shear and Baroclinity in Cross Sections along 80°W, U.S. Army Missile Command Rept. RR–TR–67–4, Redstone Arsenal, AL, Feb. 1967 (AD652256).
683. Stutt, C. A., A Mismatch Filter Approach to Clutter Discrimination, GE Res. Lab Memo., Schenectady, NY, Dec. 1964.
684. Stutt, C. A., Integral Equation for Optimum Mismatched Filter for Suppressing Sidelobes Over a Designated Region of the τ-Δ Plane, GE Res. Lab. Memo., Schenectady, NY, Dec. 1964.
685. Stutt, C. A., and L. J. Spafford, "A 'Best' Mismatched Filter Response for Radar Clutter Discrimination," *IEEE Trans.,* vol. IT–4, no. 2, March 1968.
686. Stutt, C. A., Preliminary Report on Ground-wave-radar Sea Clutter, Lincoln Lab. Tech. Rept. 134, Sept. 21, 1956.
687. Suresh Babu, B. N., and C. M. Sorrentino, "Analog-To-Digital Converter Effects On Airborne Radar Performance," *Proc. 1989 IEEE National Radar Confer.,* pp. 56–61, Dallas, TX, March 29–30, 1989.
688. Swartzlander, Earl E., Jr., "Spectrum Analysis and the Unconventional Butterfly," *Defense Science and Engineering,* pp. 66–75, Oct. 1985.
689. Swerling, P., Probability of Detection for Fluctuating Targets, Rand Corporation, RM–1217, Mar. 17, 1954.
690. Swerling, P., Probability of Detection for Some Additional Fluctuating Target Cases, Aerospace Corp. Rept. TOR–699 (9990)–14, El Segundo, CA, Mar. 1966.
691. Swerling, P., Radar Target Signatures, Intensive Lecture Series, Technology Service Corporation, Santa Monica, CA, Aug. 26–30, 1968.
692. Tamir, T., "On Radio Wave Propagation in Forest Environments," *IEEE Trans.,* vol. AP–15, no. 6, pp. 806–817, Nov. 1967.
693. Taylor, J. W., G. Brunins, "Design of a New Airport Surveillance Radar (ASR–9)," *Proc. IEEE,* vol. 73, no. 2, pp. 284–289, Feb. 1985.
694. Taylor, J. W., Jr., "Sacrifices in Radar Clutter Suppression Due to Compromises in Implementation of Digital Doppler Filters," *IEE International Radar Confer.,* pp. 46–50, London, 1982.
695. Taylor, John W., Jr., and Herman J. Blinchikoff, "Quadriphase Code—A Radar Pulse Compression Signal with Unique Characteristics," *IEEE Trans. AES,* vol. 24, no. 2, pp. 156–170, March 1988.
696. Taylor, R. C., "Terrain Measurements at X-, K_u-Band," *IRE Natl. Conv. Rec.,* on Antennas and Propagation, vol. 7, pt. 1, pp. 27–41, 1959.

697. Taylor, S. A., and J. L. MacArthur, Digital Pulse Compression Radar Receiver, Appl. Phys. Lab. Tech. Digest, vol. 6, no. 4, pp. 2–10, 1967.
698. Taylor, J. W., Jr., and H. J. Blinchikoff, "Quadriphase Code-A Radar Pulse Compression Signal with Unique Characteristics," *IEEE Trans. AES,* vol. 24, no. 2, pp. 156–170, Mar. 1988.
699. Temes, C. L., "Sidelobe Suppression in a Range-channel Pulse Compression Radar," *IRE Trans.,* vol. MIL–6, no. 2, pp. 162–169, Apr. 1962.
700. Texas Instruments Special Report, vol. 5, no. 1, Oct. 1989. Published by Military Products Division, Texas Instruments.
701. Thomas, J. B., "Nonparametric Detection," *Proc. IEEE,* vol. 58, no. 5, pp. 623–631, May 1970.
702. Tolbert, C. W. et al., Back Scattering Cross Sections of Water Droplets, Rain, and Foliage at 4.3 Millimeter Radio Wavelengths, Univ. Texas Elec. Eng. Res. Lab. Rept. 91, Apr. 30, 1957 (AD200368).
703. Tompkins, D. N., Codes with Zero Correlation, Hughes Aircraft Tech. Memo. 651, June 1960.
704. Tong, P. S., "Quantization Requirements in Digital MTI," *IEEE Trans. AES,* vol. 13, no. 5, pp. 512–521, Sept. 1977.
705. Tong, P. S. and P. E. Steichen, "Performance of CFAR Devices in ECM Environments," *DDRE Radar ECCM Symposium* (1976), reprinted in S. L. Johnston (ed.), *Radar ECCM,* Artech House, Dedham, MA, 1979.
706. Totty, R. E. et al., Investigation of Chaff Communications at 4,650 MHz, Tech. Rept. ECOM—0202—3, Radiation Inc., Melbourne, FL, Aug. 1967 (AD664124).
707. Trizna, Dennis B., "Open Ocean Radar Sea Scatter Measurements," *IEEE Inter. Radar Confer.,* Arlington, VA, May 6–9, 1985.
708. Trizna, Dennis B., Measurement and Interpretation of North Atlantic Ocean Marine Radar Sea Scatter, NRL Report 9099, Naval Research Laboratory, Washington, DC, May 31, 1988.
709. Trizna, Dennis B., "Results of a Marine Radar Sea Scatter Experiment for Non-Equilibrium Seas," *Proc. of the 1989 IEEE National Radar Confer.,* Dallas, Texas, Mar. 29–30, 1989.
710. Trunk, G. V., "Range Resolution of Targets Using Automatic Detectors," *IEEE Trans. AES,* vol. 14, no. 5, pp. 750–755, Sept. 1978.
711. Trunk, G. V., "Detection of Targets in Non-Rayleigh Sea Clutter," *Eascon–71,* IEEE, 1971.
712. Trunk, G. V., MTI Integration Loss, Naval Laboratory, Washington DC, Rept. 8132, July 1977.
713. Trunk, G. V., W. B. Gordon, and B. H. Cantrell, "False Alarm Control Using Doppler Estimation," *IEEE Trans, AES,* vol. 26, no. 1, pp. 146–153, Jan. 1990.
714. Turin, G. L., "An Introduction to Matched Filters," *IRE Trans.,* vol. IT–6, pp. 311–329, June 1960.
715. Turin, G. L., A Review of Correlation, Matched-filter and Signal Coding Techniques with Emphasis on Radar Applications, Hughes Aircraft Sys. Devel. Lab. Tech. Memo. 559, vol. 1, Apr. 1957.
716. Turnbull, Donald H., Radar Enhancement of Small Aircraft in the Air Traffic Control System, FAA Report FAA–RD–75–98, Washington, DC, Sept. 1975.
717. Turyn, R., "On Barker Codes of Even Length," *Proc. IEEE (Corr.),* vol. 51, p. 1256, Sept. 1963.
718. Turyn, R., Optimum Codes Study, Contract AF19(604)–5473, Sylvania Electronic Systems Final Report, Jan. 1960.
719. Ulaby, F. T., M. W. Whitt, and M. C. Dobson, Polarimetric Radar Detection of Point Targets in a Forest Environment, Report No. 024825–1–F, Radiation Laboratory, The University of Michigan, Ann Arbor, Apr. 1988.
720. Ulaby, Fawwaz T., Richard K. Moore, and Adrian K. Fung, *Microwave Remote Sensing–Active and Passive,* vol. 1—1981, vol. 2—1982, vol 3—1986, Addison-Wesley, Reading MA.
721. Uliana, E. A. et al., "95 GHz Short Pulse Radar," *IGARSS '89,* Vancouver, Canada, IEEE no. 89 CH2768–0 (Supplement), July 1989.

722. Urkowitz, H., "Filters for Detection of Small Radar Signals in Clutter," *J. Appl. Phys.*, vol. 24, no. 8, pp. 1024–1031, Aug. 1953.
723. Urkowitz, H., "Analysis and Synthesis of Delay Line Periodic Filters," *IRE Trans.*, vol. CT-4, pp. 41–53, June 1957.
724. Urkowitz, H., "Analysis of Periodic Filters with Stationary Random Inputs," *IRE Trans.*, vol. CT–6, no. 4, pp. 330–334, Dec. 1959.
725. Urkowitz, H., Some Properties and Effects of Reverberation in Acoustic Surveillance, Gen. Atronics Corp. Rept. 1594–2041–2, Feb. 1967.
726. UT69532 *IQMAC Applications Handbook,* United Technologies Microelectronics Center, Colorado Springs, CO, Aug. 1989.
727. Valley, S. L., (ed.), *Handbook of Geophysics and Space Environments,* McGraw-Hill Book Co., New York, Apr. 1965.
728. Van Trees, H. L., "Optimum Signal Design and Processing for Reverberation-limited Environments," *IEEE Trans.*, vol. MIL–9, pp. 212–229, July–Oct. 1965.
729. Van Vleck, J. H., and D. Middleton, "The Spectrum of Clipped Noise," *Proc. IEEE,* vol. 54, no. 1, Jan. 1966 (reprint from 1943 report).
730. Vaughn, Charles, R., "Birds and Insects as Radar Targets: A Review," *Proc. IEEE,* vol. 73, no. 2, Feb. 1985.
731. Vinitskiy, A. S., Principles of Continuous Wave Radar, translated from the Russian (Leningrad, 1961), English translation OTS–64–21507, Feb. 6, 1964.
732. Vogel, M., Uber das Statistische Verhalten der Radarechoes von Flugzeugen, Wiss. Ges. Tuftfart E. V. Berlin, Jan. 1962.
733. Voles, R., "Effects of Noise in Clutter-locking MTI Systems," *Proc. IEEE (London),* vol. 122, no. 7, pp. 689–692, 1975.
734. Voles, R., "MTI Clutter Locking When the Spectrum is Asymmetric," *Proc. IEEE (London),* pp. 1169–1172, Nov. 1975.
735. Voles, R., "New Techniques for MTI Clutter Locking," *IEEE International Radar Conference,* London, Oct. 1973.
736. Voles, R., "Frequency Correlation of Clutter," *Proc. IEEE (Letters),* vol. 54, no. 6, pp. 881–882, June 1966.
737. Voles, R., "The Losses Due to the Error in Estimating the Velocity in Clutter-locking MTI Systems," *IEEE Trans. Aero. Elect. Sys.*, pp. 950–951, Nov. 1973.
738. Waddell, M. C., Air Battle Analyzer Handbook, Applied Physics Laboratory/ Johns Hopkins University, TG–421, Silver Spring, MD, Apr. 1963.
739. Wagner, T. C., *Analytical Transients,* John Wiley & Sons, Inc., New York, 1959.
740. Wainstein, L. A., and V. D. Zubakov, *Extraction of Signals from Noise* (translation from Russian edited by R. A. Silverman), Prentice-Hall, Inc., Englewood Cliffs, NJ, 1962.
741. Walcoff, P., Duty Cycle Optimization for a High PRF Radar, Radar Comm., Dev. Engr. Tech. Memo. 39, Westinghouse Air Arm, Baltimore, Feb. 25, 1964.
742. Wald, A., *Sequential Analysis,* John Wiley & Sons, Inc., New York.
743. Walker, J. F., "Performance Data for a Double-Threshold Detection Radar," *IEEE Trans. AES,* vol. 7, no. 1, pp. 142–146, Jan. 1971.
744. Wallace, P. R., "Interpretation of the Fluctuating Echo from Randomly Distributed Scatterers," *Can. J. Phys.*, vol. 31, pt. 2, pp. 995–1009, Sept. 1952.
745. Wallin, Christina, "Experimental Investigation of Correlation Between Fading and Glint for Ship Targets," *International Radar Confer.*, pp. 511–516, Paris, 1989.
746. Wang, H., and L. Cai, "On Adaptive Implementation of Optimum MTI in Severely Nonhomogeneous Environments," *IEEE 1990 Inter. Radar Confer,* Washington, DC, May 1990.
747. Ward, H. R., "Clutter Filter Performance Measures," *IEEE 1980 Inter. Radar Confer.*, pp. 231–239, Washington, DC, May 1980.
748. Ward, H. R., "Dynamic Range Centering for Minimum Probability of Excluding a Rayleigh Distributed Signal," *Proc. IEEE (Letters),* vol. 54, no. 1, pp. 59–60, Jan. 1966.
749. Ward, H. R., and S. S. Rappaport, "Radar Dynamic Range Centering for Log-Normal Target Statistics," *Proc. IEEE,* Dec. 1970.
750. Ward, H. R., and W. W. Shrader, "MTI Performance Degradation Caused by

Limiting," *IEEE EASCON Rec.*, vol. 68–C3 AES, pp. 168–174, Sept. 1968.
751. Ward, Keith D., "Application of the *K* Distribution to Radar Clutter—A Review," *Proc. 1989 Inter. Symposium on Noise and Clutter Rejection in Radars and Imaging Sensors*, pp. 15–21, IEICE, Tokyo, 1989.
752. Ward, R., and W. W. Shrader, "MTI Performance Degradation Caused by Limiting," *Proc. EASCON '68*, pp. 168–171, Washington, DC, Sept. 9–11, 1968.
753. Warden, M. P., An Experimental Study of Some Clutter Characteristics, AGARD Conf. 66, 1970, AD 715485.
754. Waters, P. L., "Frequency Diversity Performance of a Ground Surveillance Radar," *Proc. IEE (Letters)*, vol. 1, no. 10, pp. 282–283, Dec. 1965.
755. Watts, S., and D. C. Wicks, "Empirical Models for Detection Prediction in *K*-Distribution Radar Sea Clutter," *IEEE 1990 Intern. Radar Confer.*, Washington DC, May 1990.
756. Watts, S. and D. C. Wicks, "Empirical Models for Detection Prediction in *K*-Distribution Radar Sea Clutter," *IEEE 1990 Inter. Radar Conf.*, Washington, DC, May 1990.
757. Webb, Richard C., "If Signal Sampling Improves Receiver Detection Accuracy," *Microwave & RF*, pp. 99–103, Mar. 1989.
758. Weber, P. and S. Haykin, "Ordered Statistic CFAR Processing for Two-Parameter Distributions with Variable Skewness," *IEEE Trans. AES*, vol. 21, no. 6, pp. 819–821, Nov. 1985.
759. Weber, P., S. Haykin, and R. Gray, "Airborne Pulse-Doppler Radar: False-Alarm Control," *IEEE Proc.*, vol. 134, pt F, no. 2, pp. 127–134, Apr. 1987.
760. Weil, Thomas A., "Transmitters," in M. I. Skolnik (ed.), *Radar Handbook*, McGraw-Hill Book Co., New York, 1990.
761. Weiner, S. D., A Model of Radar Scattering from the Cone Sphere, M.I.T./Lincoln Lab. Tech. Note 1966–47, Lexington, MA, Oct. 20, 1966 (AD646853).
762. Weinstock, W., Target Cross Section Models for Radar Systems Analysis, doctoral dissertation, University of Pennsylvania, PA, 1964.
763. Weiss, M., "Analysis of Some Modified Cell-Averaging CFAR Processors in Multiple-Target Situations," *IEEE Trans. AES*, vol. 18, no. 1, pp. 102–114, Jan. 1982.
764. Weiss, M. and I. Gertner, "Loss in Single-channel MTI with Post-detection Integration," *IEEE Trans.*, vol. AES–18, no. 2, pp. 205–207, 1982.
765. Weissberger, M., and J. Hauber, Modeling the Increase in Loss Caused by Propagation through a Grove of Trees, *North American Radio Science Meeting*, Quebec, June 1980.
766. Welti, G., "Quaternary Codes for Pulsed Radar," *IRE Trans. on Information Theory*, vol. 7, pp. 82–87, June 1960.
767. Westerfield, E. C., R. H. Prager, and J. L. Stewart, "Processing Gains Against Reverberation (Clutter) Using Matched Filters," *IRE Trans. Inform. Theory*, vol. IT–6, pp. 342–348, June 1960.
768. White, D. M., Synthesis of Pulse Compression Waveforms with Weighted Finite Frequency Combs, Appl. Phys. Lab. Rept., TG–934, Aug. 1967.
769. White, W. O., and A. E. Ruvin, "Recent Advances in the Synthesis of Comb Filters," *IRE Nat. Conv. Rec.*, vol. 5, pt. 2, pp. 186–199, 1957.
770. Whitlock, A., M. Shepherd, and A. L. C. Quigley, Some Measurements of the Effects of Frequency Agility on Aircraft Radar Returns, AGARD Conf. 66, 1970 (AD715485).
771. Wicks, Michael C. et al., "Polarization Radar Processing Technology," *IEEE 1990 Inter. Radar Confer.*, Arlington, VA, May 1990.
772. Widrow, B., "Statistical Analysis of Amplitude Quantized Sampled-data Systems," *AIEE Trans.*, vol. 79, pp. 555–568, Jan. 1961.
773. Wild, T. A., Private Communication on Calculated Return from Total Rainfall in a Collimated Bistatic Radar to Applied Physics Laboratory.
774. Wilkes, M. V., and J. A. Ramsay, "A Theory of the Performance of Radar on Ship Targets," *Proc. Cambridge Phil. Soc.*, vol. 43, pp. 202–231, 1947.
775. Williams, P. D. L., H. D. Crump, and K. Curtis, "Experimental Study of Radar Cross Section of Maritime Targets," *IEEE Journal of Electronic Circuits and Systems*, 1978, vol. 2, no. 4, pp. 121–135, 1978.

776. Williams, P. D. L., M. Phil., "Medium Fading of Radar Targets at Sea with Special Reference to Operation at 3 cm and 10 cm," *IEE Proc.*, vol. 127, pt. F, no. 3., pp. 212–224, June 1980.
777. Williamson, F. R. et al., "Design Criteria for a Microwave Intervisibility Measurement System," *IEEE Inter. Radar Confer.*, Arlington, VA, May 6–9, 1985.
778. Willis, N. J. "Bistatic Radar" Lecture Notes In Technology Service Corp. Intensive Short Course, Dec. 1988. (See also Skolnik, *Radar Handbook,* 1990, Chap. 25, and *Bistatic Radar,* Artech House, 1990.)
779. Woodward, P. M., *Probability and Information Theory, with Applications to Radar,* Pergamon Press, Ltd., London, McGraw-Hill Book Company, New York, 1953.
780. Woodward, P. M., Radar Ambiguity Analysis, RRE Tech. Note 731, Royal Radar Establishment, Malvern Worcs, England, Feb. 1967 (AD653404).
781. Worley, R., "Optimum Thresholds for Binary Integration," *IEEE Trans.*, vol. IT–14, no. 2, pp. 349–352, Mar. 1968.
782. Young, C. A., Signal-to-Noise Ratios, Appl. Phys. Lab./Johns Hopkins Univ. Intern. Memo. MRD–0–013, Silver Spring, MD, Nov. 9, 1965 (not generally available).
783. Zeoli, Gene W., "IF Versis Video Limiting for Two-Channel Coherent Signal Processors," *IEEE Trans. Inform. Theory,* vol. IT–17, no. 5, pp. 579–586, Sept. 1971.
784. Zierler, N., "Linear Recurring Sequences," *J. Soc. Ind. and Appl. Math,* vol. 7, no. 1, pp. 31–48, Mar. 1959.
785. Zoraster, Steven, "Minimum Peak Range Sidelobe Filters for Binary Phase-Coded Waveforms," *IEEE Trans. AES,* vol. 16, Jan. 1980.

INDEX

Index Terms **Links**

S